

NAGW-1001

**LABORATORY INVESTIGATIONS OF STRATOSPHERIC
HALOGEN CHEMISTRY**

FINAL
IN-46-CR
025880

A Final Report for the Period 01/01/87-12/31/96

271360

Submitted to:

National Aeronautics and Space Administration
Upper Atmosphere Research Program
Washington, DC 20654
Attn: Dr. M.J. Kurylo

Submitted by:

Physical and Atmospheric Chemistry Branch (PACB)
Opto-Electronic and Chemical Sciences Division (OECS)
Electro-Optics, Environment, and Materials Laboratory (EOEML)
Georgia Tech Research Institute (GTRI)
Georgia Institute of Technology
Atlanta, GA 30332-0865

Principal Investigator: Dr. Paul H. Wine
Professor, School of Chemistry & Biochemistry
Professor, School of Earth & Atmospheric Sciences
Principal Research Scientist and Head, PACB-OECS-EOEML-
GTRI
(404) 894-3425
paul.wine@chemistry.gatech.edu

Co-Principal Investigator: Dr. J. Michael Nicovich
Dr. Robert E. Stickel
Dr. Anthony J. Hynes

TABLE OF CONTENTS

CHAPTER

	Introduction	1	<i>omit</i>
1.	Progress Report	2	<i>omit</i>
2.	Kinetics and Thermochemistry of the $\text{Cl}(^2\text{P}_1) + \text{C}_2\text{Cl}_4$ Association Reaction.	13	<i>-1</i>
3.	Kinetics of the Reaction of $\text{O}(^3\text{P})$ with CF_3NO	22	<i>-2</i>
4.	Laser Flash Photolysis Studies of Radical-Radical Reaction Kinetics: The $\text{O}(^3\text{P}_1) + \text{BrO}$ Reaction.	31	<i>-3</i>
5.	Quantum Yield for Carbon Monoxide Production in the 248 nm Photodissociation of Carbonyl Sulfide (OCS).	43	<i>-omit P/A</i>
6.	The Fate of Atmospheric Phosgene and the Stratospheric Chlorine Loadings of its Parent Compounds: CCl_4 , C_2Cl_4 , C_2HCl_3 , CH_3CCl_3 , CHCl_3	47	<i>omit P/A</i>
7.	Temperature-Dependent Kinetics Studies of the Reactions $\text{Br}(^2\text{P}_{3/2}) + \text{CH}_3\text{SCH}_2 \leftrightarrow \text{CH}_3\text{SCH}_2 + \text{HBr}$. Heat of Formation of the CH_3SCH_2 Radical.	64	<i>-4</i>
8.	Halogen and Sulfur Reactions Relevant to Polar Chemistry.	72	<i>-5</i>
9.	Kinetics of the $\text{BrO} + \text{NO}_2$ Association Reaction. Temperature and Pressure Dependence in the Falloff Regime.	83	<i>-6</i>
10.	Temperature-Dependent Kinetics Studies of the Reactions $\text{Br}(^2\text{P}_{3/2}) + \text{H}_2\text{S} \leftrightarrow \text{SH} + \text{HBr}$ and $\text{Br}(^2\text{P}_{3/2}) + \text{CH}_3\text{SH} \leftrightarrow \text{CH}_3\text{S} + \text{HBr}$. Heats of Formation of SH and CH_3S Radicals.	100	<i>-7</i>
11.	Laser Flash Photolysis Studies of Atmospheric Free Radical Chemistry Using Optical Diagnostic Techniques.	111	<i>-omit P/A</i>
12.	Deuterium Substitution Used as a Tool for Investigating Mechanisms of Gas Phase Free Radical Reactions.	125	<i>-8</i>
13.	Kinetics of the Reaction of Alkyl Radicals with HBr and Dbr.	143	<i>omit P/A</i>

14.	Kinetics and Thermochemistry of the $\text{Br}(^2\text{P}_{3/2}) + \text{NO}_2$ Association Reaction.	150	9
15.	Thermochemistry and Kinetics of the $\text{Cl} + \text{O}_2$ Association Reaction.	159	-10
16.	Kinetics and Mechanism of the Reaction of Hydroxyl Radicals with Acetonitrile Under Atmospheric Conditions.	166	-11
17.	A Competitive Kinetics Study of the Reaction of Cl with CS_2 in Air at 298 K.	175	-12
18.	Kinetics of the Reactions of IO Radicals with NO and NO_2	181	-13
19.	Kinetics of the Reactions of $\text{Cl}(^2\text{P}_1)$ and $\text{Br}(^2\text{P}_{3/2})$ with O_3	189	-14
20.	Kinetics of the Reactions of $\text{O}(^3\text{P})$ and $\text{Cl}(^2\text{P})$ with HBr and Br_2	205	-15
21.	Kinetics and Thermochemistry of Reversible Adduct Formation in the Reaction of $\text{Cl}(^2\text{P}_1)$ with CS_2	224	-16
22.	Kinetics and Thermochemistry of ClCO Formation from the $\text{Cl} + \text{CO}$ Association Reaction.	232	-17
23.	Kinetics of the $\text{Br}_2\text{-CH}_3\text{CHO}$ Photochemical Chain Reaction.	238	-18
24.	Pulsed Laser Photolysis Kinetics Study of the $\text{O}(^3\text{P}) + \text{ClO}$ reaction.	251	omit p/12
25.	Kinetics of the Reactions of $\text{F}(^2\text{P})$ and $\text{Cl}(^2\text{P})$ with HNO_3	261	19
26.	Temperature-Dependent Absorption Cross Sections for Hydrogen Peroxide Vapor.	267	omit
27.	Temperature Dependence of the $\text{O} + \text{HO}_2$ Rate Coefficient.	272	

Omit to
P. 13

INTRODUCTION

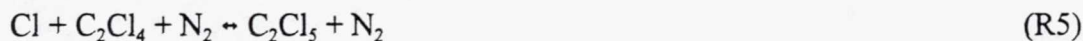
This is the final report for NASA Grant No. NAGW-1001 (Georgia Tech project A-4698) covering the period of 1/1/87 to 12/31/96. A discussion of work which has not yet been published is given in the first section following this introduction. All subsequent chapters contain reprints of published papers that acknowledge support from this grant.

PROGRESS REPORT

In recent years, our NASA-supported efforts have focused on three areas of research: (1) kinetic, mechanistic, and thermochemical studies of reactions which produce weakly bound chemical species of atmospheric interest, (2) development of flash photolysis schemes for studying radical-radical reaction kinetics and implementation of these schemes for studying radical-radical reactions of stratospheric interest, and (3) photochemistry studies of interest for understanding stratospheric chemistry. Progress on the above research tracks is summarized below. Reference numbers in brackets refer to the respective numbers for the subsequent chapters of this report.

Reactions Producing Weakly Bound Species of Atmospheric Interest

We have investigated the formation-dissociation kinetics of a number of weakly bound adducts of halogen atoms with atmospheric trace gases. These studies provide information about the rate coefficient for addition of the halogen atom to the atmospheric trace gas, the lifetime of the adduct toward unimolecular decomposition, and the bond dissociation energy of the adduct. Studies of the following reactions have been completed and written up for publication [21, 22, 15, 14, 2]:



A paper describing our study of R5 appeared in a January 1996 issue of the Journal of Physical Chemistry [2]. Our interest in R5 was stimulated by the use of C_2Cl_4 as a tracer for assessing the importance of chlorine atoms as a tropospheric oxidant [Rudolph et al., 1995; Singh et al., 1996]. While it is known that C_2Cl_4 reacts several hundred times more rapidly with Cl than with OH at $T = 298 \text{ K}$ and $P = 750 \text{ Torr}$ air, the temperature and pressure dependences of the $\text{Cl} + \text{C}_2\text{Cl}_4$ rate coefficient had not been systematically investigated. The results presented in chapter 2 firmly

establish the temperature and pressure dependences of k_5 and the dissociation energy of the $\text{Cl}-\text{CCl}_2\dot{\text{C}}\text{Cl}_2$ bond.

Recently, we have focused attention on formation of weakly bound adducts in reactions of chlorine atoms with haloalkanes. In the atmospheric literature these reactions are assumed to occur via hydrogen atom transfer or, in a few thermochemically favorable cases (such as Cl reactions with CF_3I and CH_2ClI), by halogen atom transfer. At relatively high temperatures, the expected behavior is, indeed, observed. We have characterized the "high-temperature" kinetics of Cl reactions with CH_3F and CH_3Br with sufficient precision and over sufficiently wide temperature ranges to clearly demonstrate non-Arrhenius behavior. Also, we have carried out the first temperature dependent kinetics studies of Cl reactions with CH_3I , CF_3I , CH_2ClI , CH_2ClBr , $\text{C}_2\text{H}_5\text{I}$, and $\text{C}_2\text{D}_5\text{I}$. Our "high temperature" results for the above reactions are summarized in Table I. For Cl reactions with CH_3Br , CF_3I , CH_2ClI , and CH_2ClBr , our results agree well with those reported from other laboratories, although our experiments cover a considerably wider temperature range. The results in Table I represent the first reported kinetic data for Cl reactions with CH_3I , $\text{C}_2\text{H}_5\text{I}$, $\text{C}_2\text{D}_5\text{I}$, and $\text{CF}_3\text{CH}_2\text{I}$.

At sufficiently high pressure and low temperatures (ranging from ≤ 310 K for CH_3I , $\text{C}_2\text{H}_5\text{I}$, and $\text{C}_2\text{D}_5\text{I}$ to ≤ 180 K for CH_3Br) observed kinetic behavior suggests that formation of weakly bound adducts becomes the dominant pathway for Cl reactions with CH_3I , CH_3Br , $\text{C}_2\text{H}_5\text{I}$, $\text{C}_2\text{D}_5\text{I}$, CF_3I , and $\text{CF}_3\text{CH}_2\text{I}$. Through direct observation of association-dissociation kinetics, adduct bond strengths (at 298K) have been evaluated (see Figure 1). Ab-initio calculations employing density functional theory have been carried out by our collaborator, Mike McKee of Auburn University; the calculations reproduce experimental bond strengths reasonably well and predict structures where the C-X-Cl bond angles are close to 90 degrees (X = I or Br). As can be seen by examination of Figure 1, an excellent inverse correlation exists between observed adduct bond strengths and the haloalkane ionization potential. The potential importance of Cl and OH adducts with haloalkanes in atmospheric chemistry cannot be readily assessed without further experimentation. However, it is worth noting that Wallington and co-workers [private communication] have observed complex kinetic behavior and product distributions in the Cl reaction with CH_3I at atmospheric pressure and $T = 298\text{K}$; their observations can only be explained if an adduct is postulated which undergoes chemical transformations other than dissociation back to reactants.

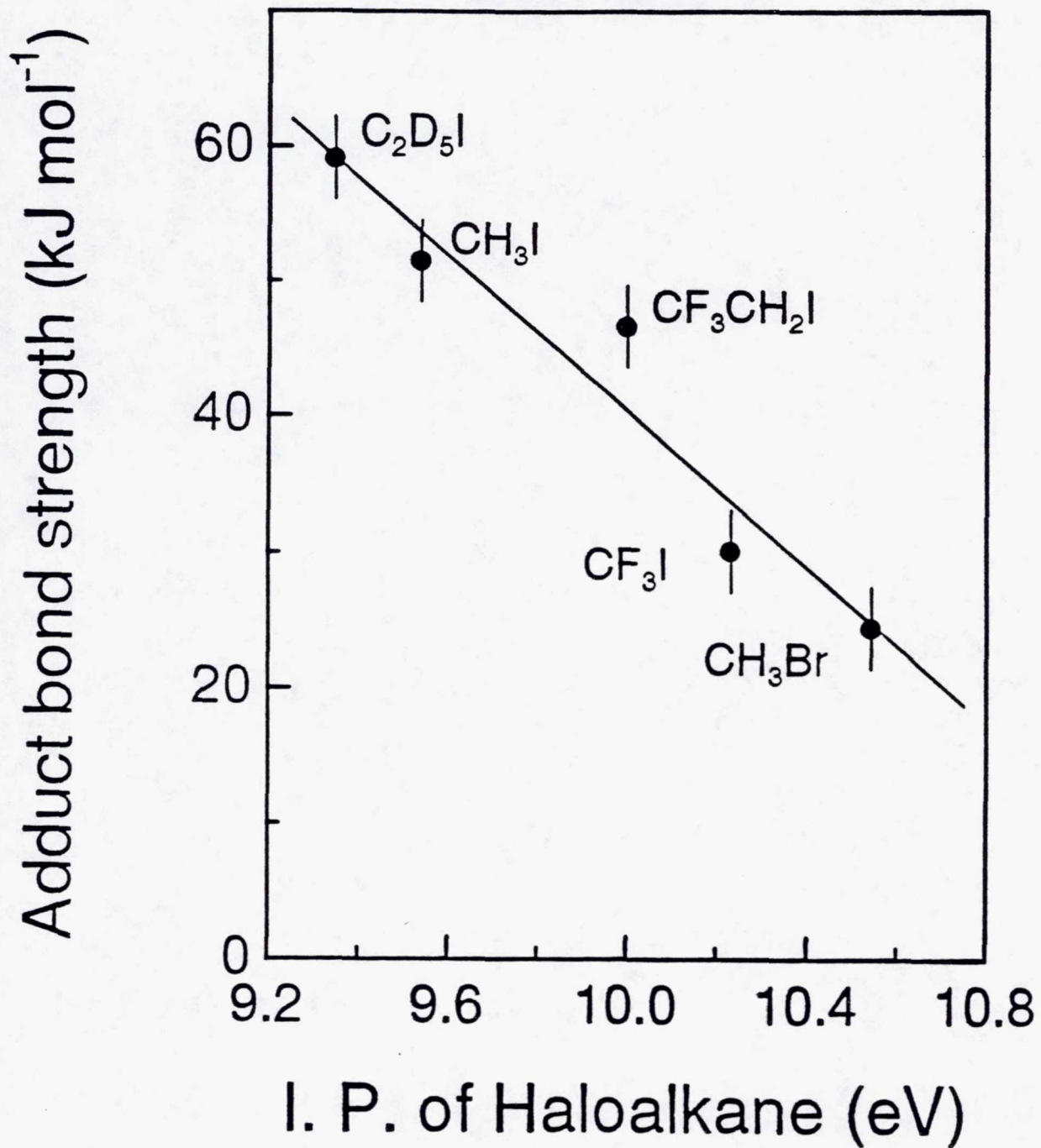
Table I. Rate constants for non-adduct-forming channels in Cl + haloalkane reactions.

haloalkane	Range of T(K)	C ^{a,b}	n ^{ab}	A ^{ab}	D ^{a,b}	E ^{a,b}
CH ₃ F	200-699	3.09 x 10 ⁻¹⁸	2.25	1.08 x 10 ⁻¹¹	2.62	8.20
CH ₃ Br	187-697	3.19 x 10 ⁻¹⁵	1.26	1.47 x 10 ⁻¹¹	5.56	8.55
CH ₃ I	364-694			5.50 x 10 ⁻¹¹		10.48
CF ₃ I	220-418			8.14 x 10 ⁻¹¹		13.05
CH ₂ ClBr	222-400			7.79 x 10 ⁻¹²		7.57
CH ₂ ClI	206-432			4.33 x 10 ⁻¹¹		-1.63
CH ₃ CH ₂ I	350-434			6.34 x 10 ⁻¹¹		3.9
CD ₃ CD ₂ I	350-434			2.67 x 10 ⁻¹¹		3.31
CF ₃ CH ₂ I	274-434			4.50 x 10 ⁻¹²		2.21

a. $k = Ct^n \exp(-D/RT) = A^{-E_a/RT}$, $A = Ct^n e^n$ and $E_a = D + nRT$

b. Units of C and A are cm³ molecule⁻¹s⁻¹; units of D and E_a are kJ mol⁻¹.

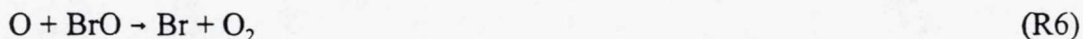
Figure 1.



Dependence of the Cl -- haloalkane bond strength on the ionization potential of the haloalkane.

Radical-Radical Reactions

We invested considerable effort into a detailed study of the reaction



A novel dual laser flash photolysis-long path absorption-resonance fluorescence technique was employed to study the kinetics of R6 as a function of temperature (231-328K) and pressure (25-150 Torr) in N₂ buffer gas. The experimental approach preserves the principal advantages of the flash photolysis method, i.e., complete absence of surface reactions and a wide range of accessible pressures, but also employs techniques which are characteristic of the discharge flow method, i.e., chemical titration as a means for deducing the absolute concentration of a radical reactant and use of multiple detection axes. Our results demonstrate that k_6 is independent of pressure, and that the temperature dependence of k_6 is adequately described by the Arrhenius expression $k(T)_6 = 1.91 \times 10^{-11} \exp(230/T) \text{ cm}^3 \text{ molecule}^{-1} \text{ s}^{-1}$; the absolute accuracy of measured values for k_6 is estimated to vary from $\pm 20\%$ at $T \sim 230 \text{ K}$ (a typical middle stratospheric temperature) to $\pm 30\%$ at $T \sim 330 \text{ K}$. Our results demonstrate that, at mid-stratospheric temperatures, the O + BrO rate coefficient is about a factor of 1.7 faster than previous "guesstimates" suggested. The catalytic cycle with reaction (6) as its rate-limiting step appears to be the dominant BrO_x odd-oxygen destruction cycle at altitudes above 24 km. A paper describing our study of R6 appeared in a March 1995 issue of the Journal of Chemical Physics [4].

Our most recent efforts in the area of radical-radical reaction kinetics have focused on the very important stratospheric reaction



Both $k_7(T)$ and the branching ratio k_{7b}/k_7 must be known quantitatively in order to assess the role of reaction (7) in stratospheric chemistry. While there is a growing consensus based on both laboratory and field observations that k_{7b}/k_7 is very small, some differences have arisen concerning the value of $k_7(298\text{K})$. Two recent studies report $k_7(298\text{K}) > 3 \times 10^{-11} \text{ cm}^3 \text{ molecule}^{-1} \text{ s}^{-1}$ [Bridier et al., 1993;

Larichev et al., 1995] while two other studies report values about a factor of two slower [Elrod et al., 1996; Li, et al., 1995]. There is agreement between Larichev et al., Elrod et al., and Li et al. that R7 has a significant negative activation energy, although one study (Li et al.) reports non-Arrhenius behavior while the other two do not.

Our initial studies of R7 employed 193 nm laser flash photolysis of $\text{H}_2\text{O}_2/\text{O}_3/\text{Br}_2/\text{N}_2$ mixtures, with simultaneous time-resolved detection of BrO (by UV absorption spectroscopy at 338.3 nm) and HO_2 (by infrared diode laser absorption spectroscopy at 1372 cm^{-1}). Typical experimental conditions were $[\text{H}_2\text{O}_2] = (1-2) \times 10^{16}$ per cm^3 , $[\text{O}_3] = (2-5) \times 10^{15}$ per cm^3 , $[\text{Br}_2] = (5-10) \times 10^{13}$ per cm^3 , $P = 10-100$ Torr N_2 , and laser fluence ~ 50 millijoules per cm^2 . In the above scheme, BrO is generated from photolytically produced oxygen atoms via the $\text{O} + \text{Br}_2$ and $\text{Br} + \text{O}_3$ reactions while HO_2 is generated from photolytically produced OH radicals via their reaction with H_2O_2 . Interpretation of observed temporal profiles requires simulations which employ a mechanism consisting of 29 reactions; however, significant time windows exist where BrO removal is dominated by reaction with HO_2 , and where HO_2 removal is dominated by the $\text{HO}_2 + \text{HO}_2$ and $\text{HO}_2 + \text{BrO}$ reactions. The data we have obtained to date support relatively slow values for k_7 , i.e., values in the range $(1-1.5) \times 10^{-11}$ $\text{cm}^3\text{molecule}^{-1}\text{s}^{-1}$. However, the above scheme has two major problems. First, the requirement for high concentrations of H_2O_2 makes the scheme unviable at sub-ambient temperatures. Secondly, we have had problems with reproducibility which we believe result from heterogeneous loss of Br_2 on reactor surfaces; these reactions probably involve H_2O_2 and/or H_2O impurity in the H_2O_2 .

As a solution to the problems mentioned above, we have adopted a new photochemical scheme which involves 351 nm laser flash photolysis of $\text{Cl}_2/\text{CH}_3\text{OH}/\text{O}_2/\text{Br}_2/\text{NO}_2$ mixtures. Studies involving this scheme will carry into the next funding cycle, so details are described in a later section of the proposal.

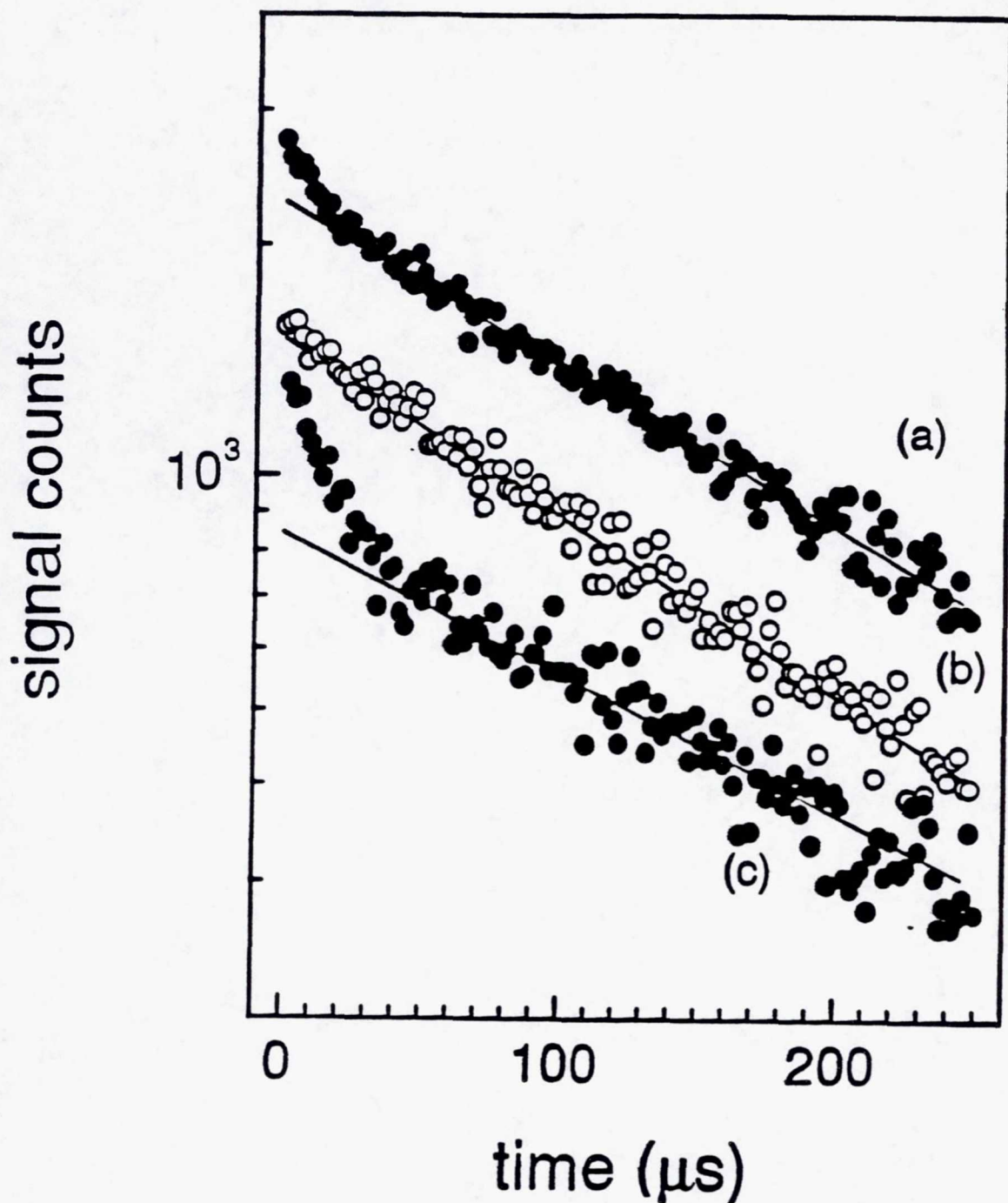
Photochemistry

Carbonyl sulfide (OCS) is thought to be an important photolytic precursor for the background (i.e., non-volcanic in origin) lower stratospheric sulfate aerosol layer [Crutzen, 1976]. We employed time-resolved detection of carbon monoxide (CO) by tunable diode laser absorption spectroscopy to measure the quantum yield for CO production from 248 nm photodissociation of OCS relative to the well-established quantum yield for CO production from 248 nm photolysis of

phosgene (Cl_2CO). The temporal resolution of the experiments was sufficient to distinguish CO formed directly by photodissociation from that formed by subsequent $\text{S}(^3\text{P})$ reaction with OCS. Under the experimental conditions employed, CO formation via the fast $\text{S}(^1\text{D}) + \text{OCS}$ reaction was minimal. Measurements at 297 K and total pressures from 4 to 100 Torr $\text{N}_2 + \text{N}_2\text{O}$ show the CO yield to be greater than 0.95 and most likely unity. This result suggests that the contribution of OCS as a precursor to lower stratospheric sulfate aerosol is somewhat larger than previously thought. A paper describing our study of OCS photochemistry appeared in a March, 1995 issue of Geophysical Research Letters [5].

Recently, we have focused attention on the photochemistry of the halogen nitrates. Recent work at JPL suggests that ClONO_2 photochemistry is much more complicated than previously thought [Nickolaisen et al., 1996]. Both the total photodissociation quantum yield and the fraction of photodissociation events which lead to production of $\text{Cl} + \text{NO}_3$ versus $\text{ClO} + \text{NO}_2$ now appear to depend on wavelength and pressure in a rather complex way. Our initial studies of ClONO_2 photochemistry involved detection of the atomic chlorine photoproduct following photolysis at both 266 nm and 355 nm at pressures in the range 5-200 Torr. Phosgene and molecular chlorine (Cl_2) were used as $\Phi(\text{Cl}) = 2.0$ calibrations at 266 nm and 355 nm, respectively. For reasons which will require further experimentation to sort out, we had considerable difficulty obtaining reproducible Cl atom yields. However, some useful results were obtained from these experiments. First, by monitoring the pseudo-first order chlorine atom decay rate as a function of the ClONO_2 concentration, a value of $1.1 \times 10^{-11} \text{cm}^3 \text{molecule}^{-1} \text{s}^{-1}$ was obtained for the $\text{Cl} + \text{ClONO}_2$ rate coefficient at 298K; this result agrees well with other values reported in the literature [Margitan, 1983; Kurylo, et al., 1983; Yokelson et al., 1995]. Another interesting result is summarized by the data shown in Figure 2, i.e., at very short times after the photolysis flash a fast component in the decay of the resonance fluorescence signal is observed. The fast component is more pronounced in 10 Torr N_2 than in 100 Torr N_2 (compare traces (a) and (c) in Figure 2). Our interpretation of the above observations is that ClONO_2 photolysis produces $\text{Cl}(^2\text{P}_{1/2})$ in considerable excess over the fraction expected to be present in thermal equilibrium with $\text{Cl}(^2\text{P}_{3/2})$. The resonance fluorescence technique simultaneously detects both spin-orbit states, but is more sensitive to the excited state, $\text{Cl}(^2\text{P}_{1/2})$; hence, as the excited state rapidly relaxes, a fast component in the resonance fluorescence temporal profile is observed. When CO_2 , an excellent quencher for $\text{Cl}(^2\text{P}_{1/2})$, is added to the reaction mixture,

Figure 2.



$\text{Cl}(^2\text{P}_{1/2})$ decay profiles in the presence of ClONO_2 , showing the effect of added CO_2 on the Cl signal at short times. Experimental conditions: 298K; N_2 buffer gas - (a) 100 torr, (b) 100 torr, (c) 10 torr; $[\text{ClONO}_2]$ (10^{14} molecules cm^{-3}) - (a) 3.11, (b) 3.11, (c) 2.18; $[\text{CO}_2]$ (10^{16} molecules cm^{-3}) - (a) 0, (b) 2.95, (c) 0.

the fast component in the fluorescence temporal profile disappears (see trace (b) in Figure 2); this confirms the above interpretation. Shortly after carrying out the above experiments, we became aware that the NCAR kinetics group had made similar observations and had, in fact, followed up on their observations to carry out an excellent study of the kinetics of $\text{Cl}(^2\text{P}_{1/2})$ deactivation by a number of collision partners [Tyndall et al., 1995]. Given the excellent work on ClONO_2 photochemistry being done at JPL and NCAR, we decided to shift our attention to the photochemistry of BrONO_2 (see below).

Our initial studies of BrONO_2 photochemistry have involved detection of ground state atomic bromine, $\text{Br}(^2\text{P}_{3/2})$, following laser flash photolysis at 266 nm. CF_2Br_2 has been employed as a $\Phi(\text{Br}) = 1.0$ calibration, and CO_2 has been added to the photolysis mixtures to insure rapid relaxation of any photolytically generated $\text{Br}(^2\text{P}_{1/2})$. Some experiments have been carried out with NO added to the photolysis mixtures in order to rapidly convert photolytically generated BrO to Br ; hence, quantum yield information for both Br and BrO has been obtained. In addition, by measuring the pseudo-first order loss rate of $\text{Br}(^2\text{P}_{3/2})$ as a function of the bromine nitrate concentration, kinetic data for the $\text{Br} + \text{BrONO}_2$ reaction have been obtained. The experimental set-up allows BrONO_2 to be monitored (by UV photometry) in the slow flow system both upstream and downstream from the photolysis/reaction cell. We find that some BrONO_2 is lost upon traversal from the upstream absorption cell to the downstream absorption cell, with the largest differences occurring when the photolysis/reaction cell is cold. Loss of BrONO_2 can be kept very small ($\sim 5\%$) if (a) care is taken to eliminate all leaks from the flow system and (b) the system is treated with N_2O_5 before a set of BrONO_2 photochemistry/kinetics experiments are undertaken; surface reaction of BrONO_2 with H_2O is the probable BrONO_2 loss mechanism. Over the temperature range 228-352 K, our $\text{Br} + \text{BrONO}_2$ kinetic data are well described by the Arrhenius expression (units are $\text{cm}^3 \text{ molecule}^{-1} \text{ s}^{-1}$):

$$k = (2.00 \pm 0.08) \times 10^{-11} \exp [(329 \pm 28)/T]$$

Uncertainties in the above Arrhenius expression are 2σ and represent precision only. The results of quantum yield measurements for Br and BrO are summarized in Table II. We find that the quantum yields for Br and BrO production are similar in magnitude and sum to a value which is unity within experimental uncertainty. Our studies of BrONO_2 photochemistry will extend into the next funding

Table II. Quantum yields (Φ) for Br and BrO from 266 nm photodissociation of BrONO₂.^a

T(K)	P(Torr)	Φ (Br)	Φ (Br)/ Φ (BrO)
245	50	0.52±0.04	1.11 ± 0.10
298	10	0.57±0.010	
	20	0.52±0.06	1.12±0.16
	50	0.51±0.06	1.20±0.20
	200	0.55±0.06	1.24±0.26

a. Uncertainties are 2σ

cycle and will include pressure and temperature dependent studies at two additional photolysis wavelengths (308 nm and 355 nm); in addition, direct observation of two additional possible photoproducts (NO₃ and O) will be carried out.

References

- Bridier, I., B. Veyret, and R. Lesclaux, *Chem. Phys. Lett.* 201, 563 (1993).
- Crutzen, P.J., *Geophys. Res. Lett.* 3, 78 (1976).
- Elrod, M.J., R.F. Meads, J.B. Lipson, J.V. Seeley, and M.J. Molina, *J. Phys. Chem.* 100, 5808 (1996).
- Kurylo, M.J., G.L. Knable, and J.L. Murphy *Chem. Phys. Lett.* 95, 9 (1983).
- Larichev, M., F. Maguin, G. LeBras, and G. Poulet, *J. Phys. Chem* 99, 15911 (1996).
- Li, Z., S.P. Sander, and R.R. Friedl, *Trans. Am. Geophys. Union* 76, F116 (1995).
- Margitan, J.J., *J. Phys. Chem.* 87, 674 (1983).
- Nickolaisen, S.E., S.P. Sander, and R.R. Friedl, *J. Phys. Chem.* 100, 10165 (1996).
- Rudolph, J., R. Koppmann, and Ch. Plass - Dülmer, *Trans. Am. Geophys. Union* 76, F108 (1995).
- Singh. H.B., A.N. Thakur, Y.E. Chen, and M. Kanakidou, *Geophys. Res. Lett.*, submitted, 1996.
- Tyndall, G.S., J.J. Orlando, and C.S. Kegley-Owen, *J. Chem. Soc. Far. Trans.* 91, 3055 (1995).
- Yokelson, R.J., J.B. Burkholder, L. Goldfarb, R.W. Fox, M.K. Gilles, and A.R. Ravishankara, *J. Phys. Chem.* 99, 13976 (1995).

Kinetics and Thermochemistry of the $\text{Cl}(^2\text{P}_j) + \text{C}_2\text{Cl}_4$ Association Reaction

J. M. Nicovich and S. Wang†

Georgia Tech Research Institute, Georgia Institute of Technology, Atlanta, Georgia 30332

M. L. McKee

Department of Chemistry, Auburn University, Auburn, Alabama 36849

P. H. Wine*

School of Chemistry and Biochemistry, School of Earth and Atmospheric Sciences,
and Georgia Tech Research Institute, Georgia Institute of Technology, Atlanta, Georgia 30332Received: August 15, 1995; In Final Form: October 12, 1995[Ⓢ]

A laser flash photolysis-resonance fluorescence technique has been employed to study the kinetics of the $\text{Cl}(^2\text{P}_j) + \text{C}_2\text{Cl}_4$ association reaction as a function of temperature (231–390 K) and pressure (3–700 Torr) in nitrogen buffer gas. The reaction is found to be in the falloff regime between third and second order over the range of conditions investigated, although the second-order limit is approached at the highest pressures and lowest temperatures. At temperatures below 300 K, the association reaction is found to be irreversible on the experimental time scale of ~20 ms. The kinetic data at $T < 300$ K have been employed to obtain falloff parameters in a convenient format for atmospheric modeling. At temperatures above 330 K, reversible addition is observed, thus allowing equilibrium constants for C_2Cl_5 formation and dissociation to be determined. Second- and third-law analyses of the equilibrium data lead to the following thermochemical parameters for the association reaction: $\Delta H^\circ_{298} = -18.1 \pm 1.3$ kcal mol⁻¹, $\Delta H^\circ_0 = -17.6 \pm 1.3$ kcal mol⁻¹, and $\Delta S^\circ_{298} = -27.7 \pm 3.0$ cal mol⁻¹ K⁻¹. In conjunction with the well-known heats of formation of $\text{Cl}(^2\text{P}_j)$ and C_2Cl_4 , the above ΔH values lead to the following heats of formation for C_2Cl_5 at 298 and 0 K: $\Delta H^\circ_{f,298} = 8.0 \pm 1.3$ kcal mol⁻¹ and $\Delta H^\circ_{f,0} = 8.1 \pm 1.5$ kcal mol⁻¹. The kinetic and thermochemical parameters reported above are compared with other reported values, and the significance of reported association rate coefficients for understanding tropospheric chlorine chemistry is discussed.

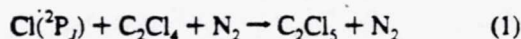
Introduction

Tetrachloroethylene (C_2Cl_4) is used widely for dry cleaning, for metal degreasing, and as an industrial solvent.^{1,2} Global production of C_2Cl_4 over the decade from the early 1980s to the early 1990s averaged around 600 ktons yr⁻¹, and a majority of this production has found its way into the atmosphere.¹ Field observations of the global distribution of atmospheric C_2Cl_4 have been employed in conjunction with spatially resolved emissions data to deduce an average tropospheric lifetime of about 0.4 yr.^{1,3,4} This lifetime is consistent with the notion that C_2Cl_4 removal from the troposphere is dominated by reaction with the OH radical, although uncertainties in the OH + C_2Cl_4 rate coefficient and in tropospheric OH concentrations are such that the lifetime for C_2Cl_4 toward reaction with OH could be anywhere in the range 0.20–0.65 yr.²

Comparison of available kinetic data for the OH + C_2Cl_4 reaction^{5–8} with available data for the $\text{Cl}(^2\text{P}_j) + \text{C}_2\text{Cl}_4$ reaction^{9–16} suggests that the $\text{Cl}(^2\text{P}_j) + \text{C}_2\text{Cl}_4$ rate coefficient is several hundred times faster than the OH + C_2Cl_4 rate coefficient at tropospheric temperatures and pressures. Until recently, it has been thought that chlorine atom levels in the troposphere were so low that $\text{Cl}(^2\text{P}_j)$ could not be an important tropospheric reactant. However, evidence is now mounting which suggests that chlorine atom levels in the marine boundary layer may be as much as one-tenth as high as OH levels,^{17,18} with the chlorine

atom source probably being photochemically labile chlorine species such as Cl_2 and ClNO_2 produced via heterogeneous reactions on the surfaces of moist sea salt particles.¹⁹ Hence, it appears that in certain regions of the troposphere reaction with $\text{Cl}(^2\text{P}_j)$ is an important removal mechanism for C_2Cl_4 .

Reaction 1 must proceed via an addition mechanism, i.e., for N_2 buffer gas,



The current state of knowledge concerning the atmospheric oxidation mechanism for C_2Cl_5 has recently been reviewed by Franklin.² Phosgene (Cl_2CO) is the major end product, but significant yields of carbon tetrachloride, a compound with a large ozone depletion potential, have been reported.²⁰ While CCl_4 can be produced via the gas phase photolysis of the intermediate photooxidation product CCl_3CClO , it is now thought that most CCl_4 observed in laboratory photooxidation studies is formed by heterogeneous photochemical processes.² Hence, yields of CCl_4 observed in laboratory "smog chamber" studies may be larger than those which would actually be produced in the atmosphere.

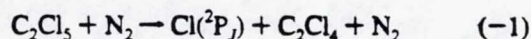
While numerous kinetics studies of reaction 1 have been reported,^{9–16} the temperature and pressure dependences of the rate coefficient have not been systematically investigated. In this paper we report the results of experiments where laser flash photolysis of $\text{Cl}_2/\text{C}_2\text{Cl}_4/\text{N}_2$ mixtures has been coupled with $\text{Cl}(^2\text{P}_j)$ detection by time-resolved atomic resonance fluorescence spectroscopy to investigate the kinetics of reaction 1 over the temperature range 231–298 K and the pressure range 3–700

† Present address: Dalian Institute of Chemical Physics, Chinese Academy of Sciences, P.O. Box 110, Dalian, People's Republic of China.

* To whom correspondence should be addressed.

Ⓢ Abstract published in *Advance ACS Abstracts*, December 15, 1995.

Torr; over this range of experimental conditions the reaction is found to be in the falloff regime between third and second order, although the high-pressure second-order limit is approached at the low-temperature and high-pressure limits of the range of conditions investigated. We also report experiments at higher temperatures (332–390 K) where $\text{Cl}(^2\text{P}_j)$ regeneration is observed on the experimental time scale (10^{-5} – 10^{-2} s), thus indicating the occurrence of the reverse dissociation reaction:



Analysis of equilibration kinetics as a function of temperature provides information about the thermochemistry of reaction 1.

Experimental Technique

The laser flash photolysis–resonance fluorescence apparatus employed in this study was similar to those employed in our laboratory in several previous studies of chlorine atom kinetics.^{21,22} Important features of the apparatus and experimental techniques which are specific to this study are described below.

Chlorine atoms were produced by 355 nm laser flash photolysis of Cl_2 . Third harmonic radiation from a Quanta Ray Model DCR-2 Nd:YAG laser provided the photolytic light source. The photolysis laser could deliver up to 1×10^{17} photons per pulse at a repetition rate of up to 10 Hz; the pulse width was 6 ns. Fluences employed in this study ranged from 5 to 50 $\text{mJ cm}^{-2} \text{ pulse}^{-1}$.

In order to avoid accumulation of photochemically generated reactive species, all experiments were carried out under "slow flow" conditions. The linear flow rate through the reactor was typically 3 cm s^{-1} while the laser repetition rate was varied over the range 2–10 Hz. (It was 2 Hz in most experiments at $T < 300$ K and 10 Hz in most experiments at $T > 330$ K.) Since the direction of flow was perpendicular to the photolysis laser beam, no volume element of the reaction mixture was subjected to more than a few laser shots. Molecular chlorine (Cl_2) and C_2Cl_4 were flowed into the reaction cell from 12 L Pyrex bulbs containing dilute mixtures in nitrogen buffer gas, while N_2 flowed directly from its high-pressure storage tank. The Cl_2/N_2 mixture, $\text{C}_2\text{Cl}_4/\text{N}_2$ mixture, and additional N_2 were premixed before entering the reaction cell. Concentrations of each component in the reaction mixture were determined from measurements of the appropriate mass flow rates and the total pressure. The C_2Cl_4 concentration was also measured *in situ* in the slow flow system by UV photometry at 228.8 nm using a cadmium penray lamp as the light source. The C_2Cl_4 absorption cross section at 228.8 nm was measured during the course of this study and was found to be $8.36 \times 10^{-18} \text{ cm}^2$. Kinetics results were found to be independent of whether the 60.3–201 cm long absorption cell was positioned upstream or downstream from the reaction cell. In the lowest pressure experiments a small correction was required for the pressure differential between the absorption cell and the reaction cell; the pressure differential never exceeded 1%. In all photometric measurements (including the absorption cross section measurements) the absorption cell temperature was 297 ± 2 K.

The gases used in this study had the following stated minimum purities: N_2 , 99.999%; Cl_2 , 99.9%.²³ Nitrogen was used as supplied while Cl_2 was degassed at 77 K before being used to prepare mixtures with N_2 . The liquid C_2Cl_4 sample had a stated purity of 99+%. It was transferred under nitrogen atmosphere into a vial fitted with a high vacuum stopcock and then degassed repeatedly at 77 K before being used to prepare mixtures with N_2 .

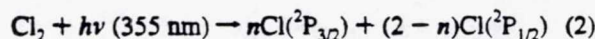
TABLE 1: Summary of Kinetic Data for the Reaction $\text{Cl}(^2\text{P}_j) + \text{C}_2\text{Cl}_4 + \text{N}_2 \rightarrow \text{C}_2\text{Cl}_5 + \text{N}_2$ Obtained under Experimental Conditions ($T < 300$ K) Where the Reaction Was Irreversible on the Time Scale for $\text{Cl}(^2\text{P}_j)$ Decay^a

T	P	$[\text{Cl}_2]$	$[\text{Cl}]_{t=0}$	$[\text{C}_2\text{Cl}_4]_{\text{max}}$	no. of expts ^b	k'_{max}	$k_1 \pm 2\sigma$
231	3.1	77	1.9	6000	6	17500	28.1 ± 0.8
	6.2	69	0.8	2750	5	9300	33.1 ± 1.1
	26	63	0.6	2490	6	10700	43.0 ± 2.5
	101	60	0.6	2320	6	12200	50.3 ± 3.1
	401	61	0.6	1870	6	9770	51.6 ± 0.9
260	702	99	1.4	2500	6	12200	48.0 ± 2.4
	3.1	22–76	1.6	7330	9	11900	15.6 ± 0.3
	6.2	62	0.7	2330	6	5080	20.3 ± 1.8
	26	61	0.6	2130	6	7290	33.6 ± 1.2
	101	54	0.6	2070	5	8630	41.5 ± 3.2
297	402	57	0.7	1630	5	7150	42.8 ± 3.1
	702	85	0.9	2070	5	9740	46.5 ± 2.3
	3.1	70	1.9	6750	10	5700	7.9 ± 0.3
	6.1	27–240	0.2–1.5	2590	20	3020	11.1 ± 0.8
	13	10–56	0.1–0.7	2120	10	3140	14.4 ± 0.9
297	26	10–79	0.1–1.8	3370	21	6490	18.7 ± 0.7
	26	43	0.8	3230	10	6150	18.6 ± 1.1^d
	52	35	0.6	1790	5	4110	22.6 ± 0.8
	101	54	0.9	1620	7	4370	26.9 ± 0.8
	201	32–93	0.3–1.0	2360	12	7830	32.5 ± 2.1
	401	64	1.3	1700	8	6560	37.8 ± 3.2
	701	10	1.3	1760	14	7600	38.7 ± 2.5

^a Units: T (K); P (Torr); concentrations (10^{11} molecules cm^{-3}); k'_{max} (s^{-1}); k_1 (10^{-12} $\text{cm}^3 \text{ molecule}^{-1} \text{ s}^{-1}$). ^b Expt = determination of one pseudo-first-order decay rate. ^c Errors represent precision only. ^d 1.0×10^{15} CF_2Cl_2 per cm^3 added to reaction mixture.

Results and Discussion

In all experiments, chlorine atoms were generated by laser flash photolysis of Cl_2 :



The fraction of chlorine atoms generated in the excited spin-orbit state, $\text{Cl}(^2\text{P}_{1/2})$, is thought to be very small, i.e., less than 0.01.^{24,25} Recently, it has been reported that the rate coefficient for $\text{Cl}(^2\text{P}_{1/2})$ quenching by N_2 is considerably slower than previously thought, i.e., $5.0 \times 10^{-15} \text{ cm}^3 \text{ molecule}^{-1} \text{ s}^{-1}$.²⁶ However, on the basis of reported rate coefficients for $\text{Cl}(^2\text{P}_{1/2})$ deactivation by saturated halocarbons (all gas kinetic except, possibly, CF_4),^{26–29} we expect that the rate coefficient for $\text{Cl}(^2\text{P}_{1/2})$ deactivation by C_2Cl_4 is very fast, i.e., $(2 \pm 1) \times 10^{-10} \text{ cm}^3 \text{ molecule}^{-1} \text{ s}^{-1}$. Hence, it seems safe to assume that all $\text{Cl}(^2\text{P}_j) + \text{C}_2\text{Cl}_4$ kinetic data are representative of an equilibrium mixture of $\text{Cl}(^2\text{P}_{1/2})$ and $\text{Cl}(^2\text{P}_{3/2})$. As a further check on the assumption of spin state equilibration, the rate coefficient at $T = 297$ K and $P = 26$ Torr was measured with and without CF_2Cl_2 , a very efficient $\text{Cl}(^2\text{P}_{1/2})$ quencher,^{26,28,29} added to the reaction mixture; as expected, this variation in experimental conditions had no effect on the observed reaction rate (see Table 1). The equilibrium fraction of chlorine atoms in the $^2\text{P}_{1/2}$ state ranges from 0.0021 at 231 K to 0.019 at 390 K. It is worth noting that, given the small fraction of chlorine atoms in the $^2\text{P}_{1/2}$ state and the fast values for k_1 which are measured (Tables 1 and 2), it must be the case that observed reactivity is dominated by chlorine atoms in the $^2\text{P}_{3/2}$ state.

All experiments were carried out under pseudo-first-order conditions with C_2Cl_4 in large excess over $\text{Cl}(^2\text{P}_j)$. Hence, in the absence of side reactions that remove or produce chlorine atoms, the $\text{Cl}(^2\text{P}_j)$ temporal profile following the laser flash would be described by the relationship

$$\ln\{[\text{Cl}(^2\text{P}_j)]_0/[\text{Cl}(^2\text{P}_j)]_t\} = (k_1[\text{C}_2\text{Cl}_4] + k_3)t = k't \quad (1)$$

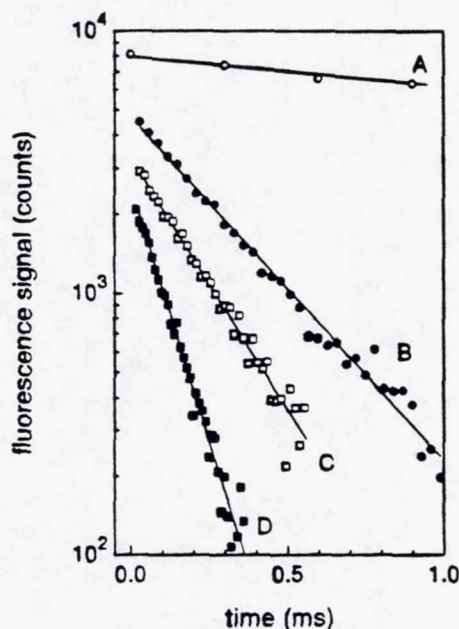


Figure 1. Typical $\text{Cl}(^2P_j)$ temporal profiles observed at $T < 300$ K. Experimental conditions: $T = 259$ K; $P = 100$ Torr; $M = \text{N}_2$; $[\text{Cl}_2] = 5.4 \times 10^{12}$ molecules cm^{-3} ; $[\text{Cl}]_0 = 5.6 \times 10^{10}$ atoms cm^{-3} ; $[\text{C}_2\text{Cl}_4]$ in units of 10^{14} molecules cm^{-3} (A) 0, (B) 0.724, (C) 1.07, and (D) 2.07; number of laser shots averaged (A) 400, (B) 2000, (C) 2000, and (D) 3000. Solid lines are obtained from least-squares analyses and give the following pseudo-first-order decay rates in units of s^{-1} : (A) 245, (B) 3250, (C) 4560, and (D) 8630. For the sake of clarity, traces A and D are scaled by factors of 0.9 and 1.5, respectively.

where k_3 is the rate coefficient for the process

$\text{Cl} \rightarrow$ first-order loss by diffusion from the detector field of view and/or reaction with background impurities (3)

The bimolecular rate coefficients of interest, $k_1([\text{N}_2], T)$, are determined from the slopes of k' versus $[\text{C}_2\text{Cl}_4]$ plots for data obtained at constant $[\text{N}_2]$ and T and under conditions where N_2 is the dominant third body collider with the energized C_2Cl_5 complex. Observation of $\text{Cl}(^2P_j)$ temporal profiles that are exponential, i.e., obey eq 1, a linear dependence of k' on $[\text{C}_2\text{Cl}_4]$, and invariance of k' to variation in laser photon fluence and photolyte concentration strongly suggests that reactions 1 and 3 are, indeed, the only processes that significantly affect the $\text{Cl}(^2P_j)$ time history.

Kinetics at $T < 300$ K. For all experiments carried out at temperatures below 300 K, well-behaved pseudo-first-order kinetics were observed; i.e., $\text{Cl}(^2P_j)$ temporal profiles obeyed eq 1, and k' increased linearly with increasing $[\text{C}_2\text{Cl}_4]$ but was independent of laser photon fluence and photolyte concentration. Typical data are shown in Figures 1–3. Measured bimolecular rate coefficients, $k_1([\text{N}_2], T)$ are summarized in Table 1. As expected for an association reaction in the non-high-pressure-limit regime, $k_1([\text{N}_2], T)$ is found to increase with increasing pressure and with decreasing temperature.

Parametrization of $k_1([\text{N}_2], T)$ for Atmospheric Modeling. For purposes of atmospheric modeling, it is convenient to generate a mathematical expression that can be used to compute $k_1([\text{N}_2], T)$ over the range of relevant temperatures and pressures. (The efficiency of O_2 as a third body collider is generally very similar to that of N_2 .) The expression generally used for this purpose is³⁰

$$k_1([\text{N}_2], T) = \{A/[1 + (A/B)]\} F_c^{1 + [\log(A/B)]^2} \quad (\text{II})$$

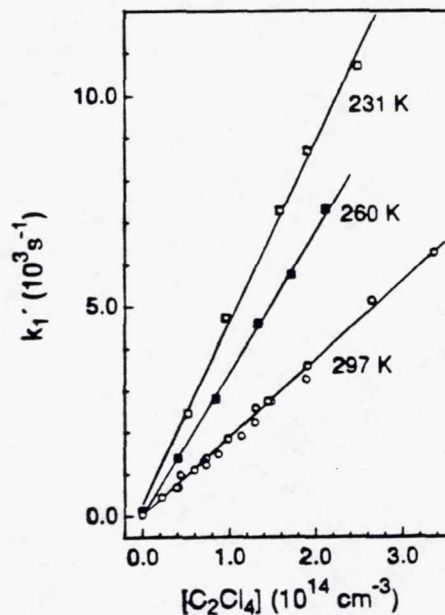


Figure 2. Plots of k' , the $\text{Cl}(^2P_j)$ pseudo-first-order decay rate, versus C_2Cl_4 concentration, as a function of temperature for data obtained at $P = 26$ Torr of N_2 with no added CF_2Cl_2 . The solid lines are obtained from linear least-squares analyses and the resulting rate coefficients, i.e., the slopes of the plots, are listed in Table 1.

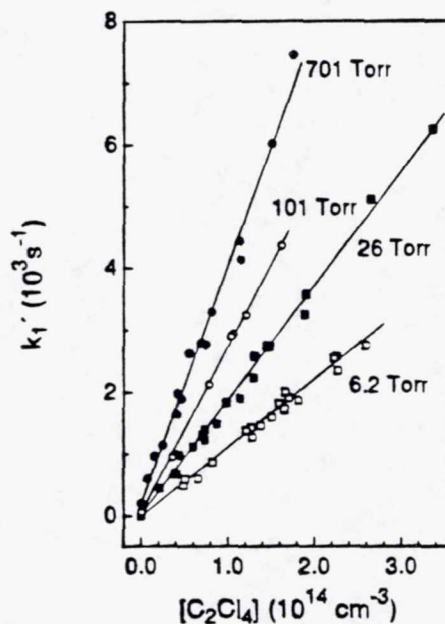


Figure 3. Plots of k' , the $\text{Cl}(^2P_j)$ pseudo-first-order decay rate, versus C_2Cl_4 concentration as a function of pressure for data obtained at $T = 297$ K. The solid lines are obtained from linear least-squares analyses, and the resulting rate coefficients, i.e., the slopes of the plots, are listed in Table 1.

where

$$A = k_{1,0}(T)[\text{N}_2] = k_{1,0}(300 \text{ K})(T/300)^{-n}[\text{N}_2] \quad (\text{III})$$

$$B = k_{1,\infty}(T) = k_{1,\infty}(300 \text{ K})(T/300)^{-m} \quad (\text{IV})$$

$$F_c = 0.6 \quad (\text{V})$$

In the above expression, $k_{1,0}$ and $k_{1,\infty}$ are approximations to the low- and high-pressure limit rate coefficients for reaction 1, and F_c is the "broadening parameter". The value $F_c = 0.6$ is found to fit data for a wide variety of atmospheric reactions reasonably

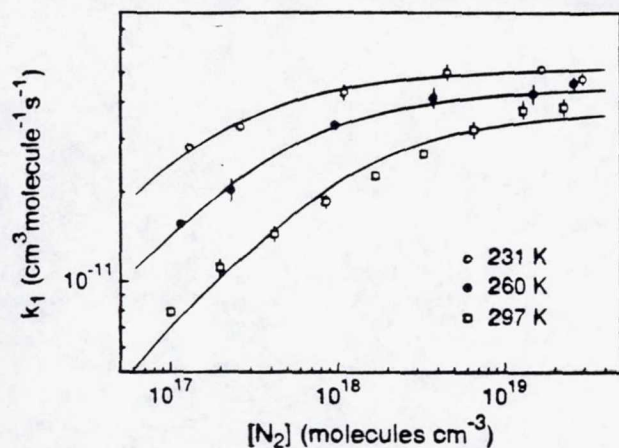


Figure 4. Falloff curves for the reaction $\text{Cl}(^2P_j) + \text{C}_2\text{Cl}_4 + \text{N}_2 \rightarrow \text{C}_2\text{Cl}_5 + \text{N}_2$ at $T = 231, 260,$ and 297 K. Solid lines are best fits of the complete data set to eq II.

well,³⁰ although in principle F_c may vary with temperature and may be different for different reactions.³¹⁻³³ Fitting our measured values for $k_1([N_2], T)$ to eq II gives the following parameters:

$$k_{1,0}(T) = 1.40 \times 10^{-28} (T/300)^{-8.5} \text{ cm}^6 \text{ molecule}^{-2} \text{ s}^{-1}$$

$$k_{1,\infty}(T) = 3.97 \times 10^{-11} (T/300)^{-1.2} \text{ cm}^3 \text{ molecule}^{-1} \text{ s}^{-1}$$

Experimental falloff data are compared with curves calculated using the above parameters in Figure 4. The parametrization represents the experimental data reasonably well. Variation of the parameter F_c does not significantly improve the quality of the fits.

Kinetics at $T > 330$ K. At temperatures above 330 K, chlorine atom regeneration via a secondary reaction became evident. Under these experimental conditions, observed $\text{Cl}(^2P_j)$ temporal profiles were independent of laser fluence and Cl_2 concentration but varied as a function of $[\text{C}_2\text{Cl}_4]$, pressure, and temperature in the manner expected if unimolecular decomposition of C_2Cl_5 was the source of regenerated $\text{Cl}(^2P_j)$. Assuming that C_2Cl_5 decomposition is the source of regenerated $\text{Cl}(^2P_j)$, the relevant kinetic scheme controlling the $\text{Cl}(^2P_j)$ temporal profile includes not only reactions 1 and 3 but also reactions -1 and 4:

C_2Cl_5 — first-order loss by processes

that do not regenerate $\text{Cl}(^2P_j)$ (4)

Assuming that all processes affecting the temporal evolution of $\text{Cl}(^2P_j)$ and C_2Cl_5 are first-order or pseudo-first-order, the rate equations for reactions 1, -1, 3, and 4 can be solved analytically:

$$S_i/S_0 = \{(Q + \lambda_1) \exp(\lambda_1 t) - (Q + \lambda_2) \exp(\lambda_2 t)\} / (\lambda_1 - \lambda_2) \quad (\text{VI})$$

where S_i and S_0 are the resonance fluorescence signal levels at times i and 0, and

$$Q = k_{-1} + k_4 \quad (\text{VII})$$

$$Q + k_3 + k_1[\text{C}_2\text{Cl}_4] = -(\lambda_1 + \lambda_2) \quad (\text{VIII})$$

$$k_3 Q + k_4 k_1[\text{C}_2\text{Cl}_4] = \lambda_1 \lambda_2 \quad (\text{IX})$$

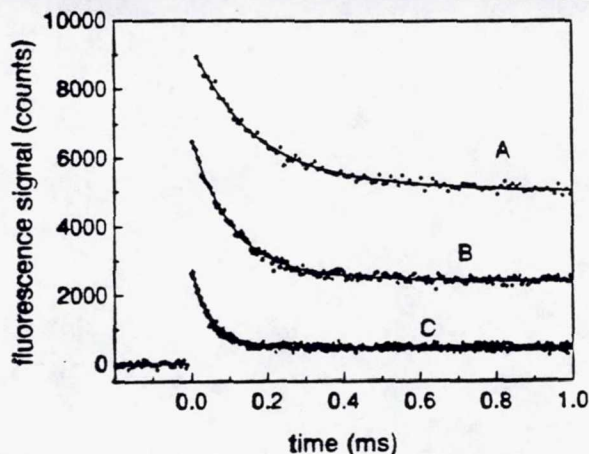


Figure 5. Typical $\text{Cl}(^2P_j)$ temporal profiles observed at $T > 330$ K. Experimental conditions: $T = 360$ K; $P = 100$ Torr; $M = \text{N}_2$; $[\text{Cl}_2] = 7.3 \times 10^{12}$ molecules cm^{-3} ; $[\text{Cl}]_0 = 1.3 \times 10^{11}$ atoms cm^{-3} ; $[\text{C}_2\text{Cl}_4]$ in units of 10^{14} molecules $\text{cm}^{-3} =$ (A) 1.89, (B) 3.90, and (C) 11.2; number of laser shots averaged = (A) 30 000, (B) 30 000, and (C) 40 000. Solid lines are obtained from nonlinear least-squares fits to eq VI. Best fit parameters, i.e., λ_1 , λ_2 , and Q , are summarized in Table 2. For the sake of clarity, traces B and C are scaled by factors of 1.1 and 1.5, respectively.

Observed $\text{Cl}(^2P_j)$ temporal profiles were fit to the double-exponential eq VI using a nonlinear least-squares method to obtain values for λ_1 , λ_2 , Q , and S_0 . The background $\text{Cl}(^2P_j)$ loss rate in the absence of C_2Cl_4 , i.e., k_3 , was directly measured at each temperature and pressure (see Table 2). Rearrangement of the above equations shows that the rate coefficients k_1 , k_{-1} , and k_4 can be obtained from the fit parameters and the measured k_3 using the following equations:

$$k_1 = -(Q + k_3 + \lambda_1 + \lambda_2) / [\text{C}_2\text{Cl}_4] \quad (\text{X})$$

$$k_4 = (\lambda_1 \lambda_2 - k_3 Q) / k_1 [\text{C}_2\text{Cl}_4] \quad (\text{XI})$$

$$k_{-1} = Q - k_4 \quad (\text{XII})$$

Typical $\text{Cl}(^2P_j)$ temporal profiles observed in the high-temperature experiments are shown in Figure 5 along with best fits of each temporal profile to eq VI. The results for all high-temperature experiments are summarized in Table 2. It is worth noting that values for $k_1([N_2], T)$ obtained from analysis of the high-temperature data are consistent with those expected based on extrapolation of the results from $T < 300$ K. We believe that reported values for k_1 , even at high temperature where $\text{Cl}(^2P_j)$ regeneration is fast, are accurate to within $\pm 20\%$. Absolute uncertainties in reported values for k_{-1} are somewhat more difficult to assess. Inspection of Table 2 shows that the precision of multiple determinations of k_{-1} at a particular temperature and pressure (for varying $[\text{C}_2\text{Cl}_4]$) is quite good. An inherent assumption in our analysis is that the only significant C_2Cl_5 loss process that results in chlorine atom production is reaction -1; as long as this assumption is correct (it almost certainly is), we believe the absolute accuracy of our reported k_{-1} values is $\pm 30\%$ over the full range of temperature and pressure investigated.

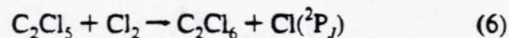
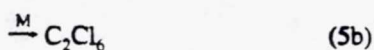
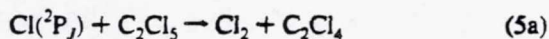
Possible Secondary Chemistry Complications. The photochemical system used to study the kinetics of reactions 1 and -1 appears to be relatively free of complications from unwanted side reactions. The only potential secondary reactions we are aware of which could destroy or regenerate chlorine atoms (other

TABLE 2: Results of the $\text{Cl}(^2P_J) + \text{C}_2\text{Cl}_4 \rightleftharpoons \text{C}_2\text{Cl}_5 + \text{N}_2$ Equilibration Kinetics Experiments^a

<i>T</i>	<i>P</i>	[Cl ₂]	[Cl] _∞	[C ₂ Cl ₄]	<i>Q</i>	-λ ₁	-λ ₂	<i>k</i> ₃	<i>k</i> ₄	<i>k</i> ₁	<i>k</i> ₋₁	<i>K</i> _p
332	25	83	1.6	1390	469	83	2130	187	57	11.2	411	60.3
		83	1.6	2650	484	86	3670	187	73	11.6	411	62.4
		83	1.6	4480	534	127	5670	187	122	11.3	412	60.7
		83	1.6	6950	544	127	8910	187	124	12.0	420	62.9
334	100	87	1.7	1190	864	96	3260	85	100	20.2	764	58.1
		87	1.7	2500	689	44	5370	85	38	18.5	651	62.7
		87	1.7	3920	869	116	8420	85	119	19.3	750	56.7
		87	1.7	6770	1020	217	14100	85	225	19.5	795	53.9
340	6.5	61	0.9	496	327	109	802	319	-63	5.34	390	29.6
		61	0.9	682	424	170	1130	444	10	6.33	414	33.0
		61	0.9	890	506	175	1240	319	93	6.61	414	34.5
		61	0.9	984	420	162	1290	444	37	5.93	383	33.4
		61	0.9	2160	467	185	1960	444	127	5.73	340	36.4
		61	0.9	3080	482	187	2410	444	141	5.42	341	34.3
		61	0.9	3310	592	245	2490	319	230	5.50	362	32.8
340	25	57	0.7	238	536	93	829	188	-188	8.32	655	27.4
		57	0.7	648	628	83	1320	188	-15	9.00	643	30.2
		57	0.7	1550	645	39	2200	188	-25	9.06	669	29.2
		57	0.7	4230	757	103	5180	188	90	10.3	668	33.2
340	100	48	0.7	452	1220	82	2050	88	74	18.2	1150	34.3
		48	0.7	955	1150	71	2860	88	60	17.7	1090	34.8
		74	1.3	1070	1270	83	3210	116	63	17.7	1200	31.7
		48	0.7	1220	1210	64	3470	88	55	17.6	1100	34.6
		48	0.7	1240	1150	66	3350	88	52	18.3	1160	34.0
		48	0.7	1340	1110	61	3440	88	49	17.2	1060	34.9
		48	0.7	1760	1120	62	4340	88	53	18.1	1070	36.7
		48	0.7	2110	1150	72	4940	88	67	17.9	1080	35.7
		74	1.3	3040	1220	73	6720	116	64	17.7	1160	32.9
350	100	57	0.9	529	2150	44	2950	61	1	14.8	2150	14.5
		210	0.7	1630	2130	17	4640	61	-21	15.1	2150	14.7
		210	3.2	1640	2300	66	4790	61	70	15.2	2230	14.3
		57	0.9	1670	2070	19	4750	61	-13	15.8	2080	15.9
		110	0.7	1670	2110	15	4780	61	-21	15.7	2130	15.5
		57	0.9	5190	2550	152	10700	61	178	15.9	2370	14.1
360	25	70	1.0	2120	2040	126	3870	148	103	8.53	1940	8.96
		70	1.0	4920	2020	98	5930	148	73	7.84	1950	8.20
		70	1.0	10700	2070	104	10500	148	94	7.88	1970	8.13
360	100	90	1.7	1110	3780	88	5460	166	-89	14.6	3870	7.71
		73	1.3	1890	3560	53	6200	92	2	13.8	3550	7.92
		73	1.3	3900	3570	43	9280	92	14	14.5	3550	8.34
		90	1.7	6290	4050	67	13200	166	23	14.5	4030	7.31
		73	1.3	11200	4120	233	21500	92	265	15.6	3860	8.25
370	25	68	1.2	4010	3230	129	6080	217	30	6.92	3200	4.29
		68	1.2	8440	3270	111	9350	217	54	7.08	3220	4.37
		68	1.2	11200	3050	50	11000	217	-15	7.01	3070	4.53
370	100	83	1.2	2910	6800	61	11100	87	20	14.7	6780	4.30
		83	1.2	5780	6240	56	13500	87	30	12.5	6210	3.99
		83	1.2	8420	6490	104	18700	87	113	14.6	6380	4.53
		83	1.2	15100	7010	319	30700	87	384	15.9	6630	4.76
380	25	73	1.0	6060	4340	99	7760	199	-28	5.48	4370	2.42
		73	1.0	12700	5110	147	13700	199	117	6.72	4990	2.60
380	100	75	1.2	2200	9820	78	11800	75	90	9.04	9730	1.79
		75	1.2	5060	9690	40	14800	75	-26	10.1	9720	2.01
		75	1.2	6280	11500	124	18700	101	158	11.5	11300	1.96
		75	1.2	9920	10700	78	21300	75	81	10.7	10600	1.95
		210	3.6	10800	9630	54	20300	75	0	9.91	9630	1.99
		210	0.9	10900	10500	117	21700	75	156	10.3	10400	1.91
390	25	89	1.0	6000	7860	174	10700	184	146	4.68	7710	1.14
		89	1.0	21400	8330	203	19000	184	218	4.97	8120	1.15
		89	1.0	24100	8260	128	20000	184	88	4.85	8170	1.12
		89	1.0	27000	8660	242	22600	184	278	5.18	8380	1.16

^a Units: *T* (K); *P* (Torr); concentrations (10¹¹ molecules cm⁻³); *Q*, λ₁, λ₂, *k*₃, *k*₄, *k*₋₁ (s⁻¹); *k*₁ (10⁻¹² cm³ molecule⁻¹ s⁻¹); *K*_p (10⁴ atm⁻¹).

than reaction -1, of course) are the following:



The concentrations of photochemically generated radicals employed in this study, i.e., $\leq 3 \times 10^{11}$ cm⁻³, were sufficiently small that a radical-radical interaction such as reaction 5 could

not be an important Cl(²P_J) removal process even if the rate coefficient were gas kinetic. Experimentally, the fact that observed kinetics were unaffected by significant variations in [Cl]₀ confirms that reaction 5 did not contribute significantly to Cl(²P_J) removal. The only kinetics studies of reaction 6 reported in the literature involved competitive chlorination studies where kinetic information was derived by fitting observed product distributions to a complex chemical mechanism;^{10,34} these studies, while indirect, suggest that *k*₆ is much too slow for reaction 6 to be a significant interference. Experimentally, we found that observed kinetics were unaffected

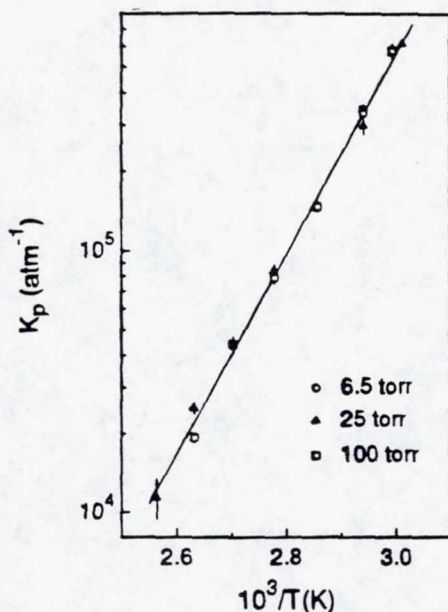


Figure 6. van't Hoff plot for the reaction $\text{Cl} + \text{C}_2\text{Cl}_4 \rightleftharpoons \text{C}_2\text{Cl}_5$. The solid line is obtained from a linear least-squares analysis and gives the second-law thermochemical parameters for the reaction (see Table 4). Different symbols indicate data obtained at different total pressures.

by significant variations in Cl_2 concentration, thus confirming that reaction 6 played no role in controlling observed $\text{Cl}(^2\text{P}_j)$ temporal profiles.

C_2Cl_5 Thermochemistry: Second-Law Analysis. The equilibrium constants, K_p , given in Table 2 are computed from the relationship

$$K_p = k_1/k_{-1}RT = K_c/RT \quad (\text{XIII})$$

Use of eq XIII involves making the *assumption* that reaction -1 is truly the reverse of reaction 1, i.e., that the products of reaction -1 do not contain substantial internal excitation. If, for example, reaction -1 resulted in production of predominantly $\text{Cl}(^2\text{P}_{1/2})$, it would be inappropriate to use the ratio k_1/k_{-1} as a basis for evaluating the thermochemistry of reaction 1. While it seems reasonable to assume that energy is distributed statistically in the translational and internal degrees of freedom of the C_2Cl_4 and $\text{Cl}(^2\text{P}_j)$ products of reaction -1, it should be kept in mind that there presently exists no experimental verification that this assumption is correct.

Assuming that K_p can be computed from the ratio of measured values for k_1 and k_{-1} , a van't Hoff plot, i.e., a plot of $\ln K_p$ versus T^{-1} , can be constructed; such a plot is shown in Figure 6. Since

$$\ln K_p = (\Delta S/R) - (\Delta H/RT) \quad (\text{XIV})$$

the enthalpy change associated with reaction 1 is obtained from the slope of the van't Hoff plot while the entropy change is obtained from the intercept. At 360 K, the midpoint of the experimental T^{-1} range, this "second-law analysis" gives the results $\Delta H = -17.5 \pm 0.6 \text{ kcal mol}^{-1}$ and $\Delta S = -26.1 \pm 1.8 \text{ cal mol}^{-1} \text{ K}^{-1}$, where the errors are 2σ and represent precision only.

C_2Cl_5 Thermochemistry: Third-Law Analysis. In addition to the second-law analysis described above, we have also carried out a third-law analysis, where the experimental value of K_p at 360 K ($79\,800 \pm 8000 \text{ atm}^{-1}$) has been employed in conjunction with a calculated entropy change to determine ΔH .

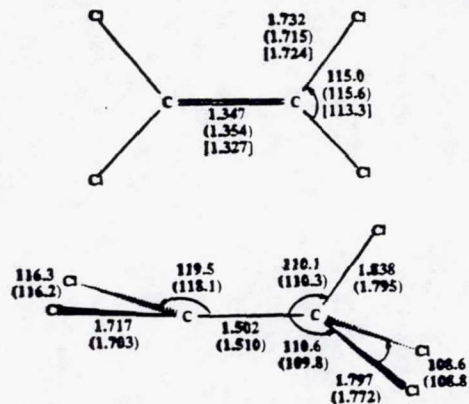


Figure 7. Structure for C_2Cl_4 and C_2Cl_5 derived from *ab initio* calculations at the Becke3LYP/6-31+G(d) level as discussed in the text. Bond lengths and bond angles shown in parentheses are at the MP2/6-31+G(d) level of theory and values for C_2Cl_4 in square brackets are recommendations from the JANAF tables (ref 46).

Since experimental data concerning the structure of C_2Cl_5 are not available, *ab initio* calculations have been carried out for this species. The calculations employed density functional theory³⁵⁻³⁷ as implemented in the GAUSSIAN 92/DFT program system.³⁸ With an appropriate choice of gradient correction and a modest basis set, DFT has been shown to frequently give results of near chemical quality.³⁹⁻⁴⁴ In addition, spin contamination does not seem to be as serious for DFT compared to Hartree-Fock (HF) theory.⁴⁵ Becke3LYP, which seems to be a good choice of exchange and correlational functional, has been used with the 6-31+G(d) basis set to optimize geometries for C_2Cl_5 . Vibrational frequencies have been calculated with the same method. The results for C_2Cl_4 can be compared with experiment to lend credibility to the approach while the results for C_2Cl_5 can be employed to compute its absolute entropy as well as heat capacity corrections. As a check on the DFT results, MP2/6-31+G(d) optimizations were also carried out for C_2Cl_4 and C_2Cl_5 . Only small differences in the geometries were noted. Since the DFT results were closer to experiment for C_2Cl_4 , the DFT geometries and frequencies for C_2Cl_5 were used in the third-law analysis.

Two distinctly different $\text{Cl}(^2\text{P}_j)\text{-C}_2\text{Cl}_4$ adducts are possible. A chlorine atom could add symmetrically to $\text{Cl}_2\text{C=CCl}_2$ to form a π -complex or a three-membered ring with unpaired spin density on chlorine. Alternatively, a chlorine atom could add unsymmetrically to form a σ -complex with unpaired spin density on the β -carbon. Our calculations predict that the most stable form for C_2Cl_5 is the haloalkyl radical CCl_3CCl_2 , i.e., the σ -complex. Calculated structures for C_2Cl_4 and C_2Cl_5 are shown in Figure 7. For comparison, experimental bond lengths and bond angle for C_2Cl_4 ⁴⁶ are also shown in Figure 7; the calculated structure of C_2Cl_4 is in good agreement with experiment.

To carry out the third-law analysis, absolute entropies as a function of temperature were obtained from the JANAF tables⁴⁶ for $\text{Cl}(^2\text{P}_j)$, calculated using vibrational frequencies and moments of inertia taken from the JANAF tables for C_2Cl_4 ,⁴⁷ and calculated using the moments of inertia and vibrational frequencies in Table 3 for C_2Cl_5 . The moments of inertia in Table 3 were computed using the C_2Cl_5 structure shown in Figure 7. The vibrational frequencies in Table 3 were calculated using the approach described above. Because calculated vibrational frequencies for C_2Cl_4 are very close to those given in the JANAF tables,⁴⁶ no scaling of the C_2Cl_5 frequencies is deemed necessary. At 360 K, the third-law analysis gives the results $\Delta H = -18.6 \pm 0.5 \text{ kcal mol}^{-1}$ and $\Delta S = -29.3 \pm 1.0 \text{ cal mol}^{-1} \text{ K}^{-1}$;

Absolute Entropies and Heat Capacity Corrections

species	ν (cm ⁻¹)	σ	I_{ABC} (amu ³ Å ⁶)	g_0	g_1	$\Delta\epsilon$ (cm ⁻¹) ^a
Cl				4	2	882.36
C ₂ Cl ₄	1571	4	7.50 × 10 ⁷	1		
	1000					
	918					
	777					
	512					
	447					
	347					
	324					
	288					
	235					
	176					
	110					
	C ₂ Cl ₅					
942						
782						
721						
624						
447						
406						
342						
327						
264						
233						
231						
173						
129						
39						

^a $\Delta\epsilon \equiv$ assumed energy splitting between lowest two electronic states. C₂Cl₄ has no low-lying excited electronic states, and C₂Cl₅ is assumed to have none.

TABLE 4: Thermochemical Parameters for the Reaction Cl(²P_J) + C₂Cl₄ → C₂Cl₅^a

T	method	-ΔH	-ΔS	ΔH _{f,r} (C ₂ Cl ₅) ^b
360	2nd law	17.5 ± 0.6	26.1 ± 1.8	
	3rd law	18.6 ± 0.5	29.3 ± 1.0	
298	2nd law	17.5 ± 0.7	26.2 ± 1.9	8.5 ± 0.8
	3rd law	18.7 ± 0.6	29.4 ± 1.0	7.4 ± 0.7
0	2nd law	17.1 ± 0.8		8.7 ± 0.9
	3rd law	18.2 ± 0.7		7.5 ± 0.8

^a Units: T (K); ΔH, ΔH_{f,r}(C₂Cl₅) (kcal mol⁻¹); ΔS (cal mol⁻¹ K⁻¹).

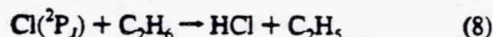
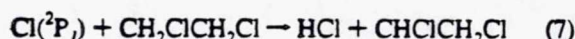
^b Calculated using values for ΔH_{f,r}(Cl) and ΔH_{f,r}(C₂Cl₄) taken from ref 46.

the uncertainties we report reflect an estimate of the uncertainties introduced by our imperfect knowledge of the input data needed to calculate absolute entropies (the low frequency vibrations of C₂Cl₅ are most significant) as well as our estimated uncertainty in the experimental value for K_p(360 K).

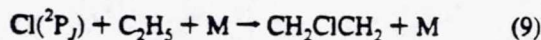
Summary of Thermochemical Results. The thermochemical results of this study are summarized in Table 4. Appropriate heat capacity corrections have been employed to obtain ΔH values at 298 and 0 K. Using literature values⁴⁶ for the heats of formation of Cl(²P_J) and C₂Cl₄ at 298 and 0 K allows the heat of formation of C₂Cl₅ to be evaluated. As can be seen from Table 4, the agreement between the second- and third-law results is not perfect. Since the uncertainties in the ΔH_{f,r}(C₂Cl₅) values obtained by the two methods are about the same, it seems appropriate to report simple averages of the second- and third-law values, while adjusting reported uncertainties to encompass the 2σ error limits of both determinations. Using this approach, we report ΔH_{f,r,298}(C₂Cl₅) = 8.0 ± 1.3 kcal mol⁻¹ and ΔH_{f,r,0}(C₂Cl₅) = 8.1 ± 1.5 kcal mol⁻¹. The Cl-C bond energy can also be directly calculated from theory, where single-point energies are determined with an expanded basis set and zero-point corrections are made with DFT frequencies. The predicted bond energy at 0 K is 14.2 kcal mol⁻¹ at Becke3LYP/

at PMP2/6-311+G(3df) (using the MP2 geometry). While the spin-projected PMP2 value is in reasonable agreement with experiment, the DFT value is several kcal mol⁻¹ too small. It appears that the DFT method calculates the relative strength of the C-C π bond to be too strong relative to the Cl-C σ bond. In a very recent assessment of computational methods for calculating radical addition reactions to alkenes, Wong and Radom found that addition enthalpies may be too positive by DFT by as much as 10 kcal mol⁻¹ when compared to QCISD results.⁴⁸ In light of their work, the underestimation of the Cl-C bond energy by DFT is not unexpected.

Comparison with Previous Research. Although this study represents the first systematic investigation of the temperature and pressure dependence of k₁, there are several published measurements with which our results can be compared. Davis et al.,¹⁴ in one of the pioneering applications of the flash photolysis-resonance fluorescence technique, measured k₁ at 298 K in helium buffer gas; they reported rate coefficients of 4.8 × 10⁻¹² and 6.10 × 10⁻¹² cm³ molecule⁻¹ s⁻¹ at pressures of 15 and 100 Torr, respectively. The magnitude of Davis et al.'s rate coefficients seems a little low compared to values one might expect based on our measurements in N₂ buffer gas, and the ratio k₁(100 Torr of He)/k₁(15 Torr of He) = 1.25 obtained from Davis et al.'s results is smaller than one would predict based on the 297 K falloff curve we have obtained using N₂ as the buffer gas (Figure 4). Breitbarth and Rottmayer have employed a discharge flow system with an EPR detector to study the kinetics of the O(³P_J) + C₂Cl₄ reaction at 298 K and 0.3 Torr total pressure in O₂ buffer gas.¹⁵ They observed that Cl(²P_J) was produced as a reaction product and, by following the temporal evolution of both O(³P_J) and Cl(²P_J), extracted a value of 3 × 10⁻¹³ cm³ molecule⁻¹ s⁻¹ for k₁; this value is slower than one would predict from extrapolation of our 297 K falloff curve down to P = 0.3 Torr under the assumption that N₂ and O₂ are equally efficient as third body colliders. In addition to the two "direct" studies discussed above, there have been a number of competitive kinetics studies of reaction 1,^{9-13,16} two of which^{13,16} report results where meaningful comparisons can be made with our results. Franklin et al. employed CW photolysis of Cl₂ in conjunction with gas chromatographic detection of C₂Cl₄; they employed the reference reactants C₂H₆ and CH₂ClCH₂Cl to measure the ratios k₇/k₁ = 0.0295 at 310 K and k₈/k₁ = 1.66 at 348 K.



Assuming k₇(310 K) = 1.7 × 10⁻¹² cm³ molecule⁻¹ s⁻¹⁴⁹ and k₈(348 K) = 5.9 × 10⁻¹¹ cm³ molecule⁻¹ s⁻¹,³⁰ Franklin et al.'s data give k₁(310 K) = 5.8 × 10⁻¹¹ cm³ molecule⁻¹ s⁻¹ and k₁(348 K) = 3.6 × 10⁻¹¹ cm³ molecule⁻¹ s⁻¹; these rate coefficients are not quantitatively consistent with each other but are in approximate agreement with the values expected based on our data, given the more efficient third-body colliders employed in the Franklin et al. study.³⁰ Atkinson and Aschmann have also employed CW photolysis of Cl₂ in conjunction with gas chromatographic detection of C₂Cl₄ and ethylene to measure k₉/k₁ = 2.56 at 298 K in 735 Torr of air.



Assuming k₉(298 K, 735 Torr of air) = 1.040 × 10⁻¹⁰ cm³ molecule⁻¹ s⁻¹,³⁰ the Atkinson and Aschmann¹⁶ data give k₁(298 K, 735 Torr of air) = 4.1 × 10⁻¹¹ cm³ molecule⁻¹ s⁻¹;

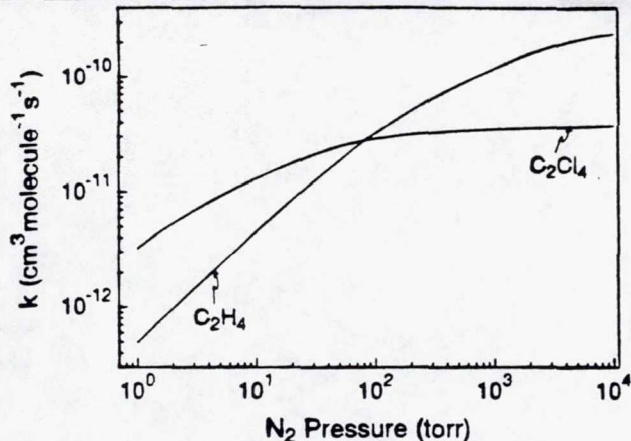


Figure 8. Falloff curves (298 K) for reactions of $\text{Cl}(^2\text{P}_j)$ with C_2Cl_4 and C_2H_4 . The C_2Cl_4 curve is calculated from falloff parameters determined in this study while the C_2H_4 curve is calculated from the falloff parameters recommended in ref 30.

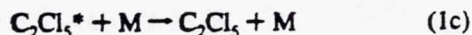
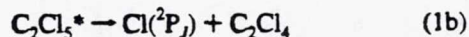
this is slightly faster than the value we report but in agreement within combined experimental uncertainties.

Franklin et al.¹³ in their competitive kinetics studies (described above) derived the following relationship from their data: $\log(k_{-1}/k_6) = 4.90 - 10650/4.576T \text{ mol}^2 \text{ L}^{-2} \text{ s}$. They used their determinations of k_1 in conjunction with the measurements of $k_6(T)$ reported by Dusdeil et al.³⁴ to obtain values for $k_{-1}(T)$. Franklin et al.'s values, when corrected for updated information about $k_7(T)$ and $k_8(T)$, give values for $k_{-1}(T)$ which are somewhat faster than the values we report. A more quantitative comparison does not appear to be worthwhile because (a) the Arrhenius expression for $k_6(T)$ is highly uncertain,^{10,34} (b) Franklin et al. report k_{-1} to be pressure independent while we find k_{-1} to be pressure dependent (Table 2), and (c) as mentioned above, Franklin et al. employed more efficient third-body colliders (C_2Cl_4 , Cl_2 , C_2H_6 , $\text{CH}_2\text{ClCH}_2\text{Cl}$, CO_2 , and SF_6) in their study than we did in ours (N_2). From their evaluations of k_1 and k_{-1} at two temperatures, Franklin et al. derived $\Delta H = -16.9 \pm 1.0 \text{ kcal mol}^{-1}$, i.e., somewhat higher than the value we report but in agreement within combined experimental uncertainties. (We believe the uncertainty in the Franklin et al. determination of ΔH is actually considerably larger than their published estimate¹³ of $\pm 1.0 \text{ kcal mol}^{-1}$.)

The best fit value for the parameter n (describing the temperature dependence of $k_{1,0}$) obtained in this study, i.e., $n = 8.5$, is larger than is typically found for association reactions of atmospheric interest.³⁰ Recommended values of n for 62 atmospheric association reactions range from 0.0 to 6.7, with the largest values found for the $\text{CF}_2\text{ClO}_2 + \text{NO}_2$ and $\text{CCl}_3 + \text{O}_2$ reactions.³⁰ Interestingly, both $\text{CF}_2\text{ClO}_2\text{NO}_2$ and CCl_3O_2 are relatively weakly bound species, with bond strengths only a few kcal mol^{-1} stronger^{51,52} than that of C_2Cl_5 . While the results reported in this paper clearly demonstrate that k_1 increases significantly with decreasing temperature, the value of n is rather uncertain because no data were obtained at pressures anywhere near the low-pressure limit. As a result, extrapolation of our results outside of the experimental temperature regime should be carried out with caution.

The 298 K falloff curves for $\text{Cl}(^2\text{P}_j)$ reactions with C_2H_4 and C_2Cl_4 over the pressure range 1–10 000 Torr of N_2 are compared in Figure 8. The C_2Cl_4 curve is based on the falloff parameters determined in this study while the C_2H_4 curve is calculated from the falloff parameters recommended by the NASA panel for chemical kinetics and photochemical data evaluation,³⁰ which are based on the experimental data of Wallington et al.⁵³ over the pressure range 10–3000 Torr.

Interestingly, $\text{Cl}(^2\text{P}_j)$ reacts much more rapidly with C_2Cl_4 than with C_2H_4 in the low-pressure limit, but much more rapidly with C_2H_4 than with C_2Cl_4 in the high-pressure limit. This interesting reactivity pattern can be rationalized in terms of the simple Lindemann–Hinshelwood mechanism,^{54,55} where reaction 1, for example, proceeds via the following three-step process:



If one makes the steady state approximation for the energized adduct, C_2Cl_5^* , the low- and high-pressure limit rate coefficients are obtained as $k_{1,0} = k_{1a}k_{1c}/k_{1b}$ and $k_{1,\infty} = k_{1a}$. The fact that $k_{9,\infty} > k_{1,\infty}$ implies that $\text{Cl}(^2\text{P}_j)$ adds more rapidly to C_2H_4 than to C_2Cl_4 to form the energized species $\text{C}_2\text{H}_5\text{-}n\text{Cl}_n^*$; this seems reasonable since the four chlorine atoms in C_2Cl_4 would be expected to sterically hinder approach of $\text{Cl}(^2\text{P}_j)$ to a carbon atom. The fact that $k_{9,0} < k_{1,0}$ also seems reasonable since collisional deactivation of $\text{C}_2\text{H}_5\text{-}n\text{Cl}_n^*$ would be expected to be more efficient for C_2Cl_5^* than for $\text{C}_2\text{H}_4\text{Cl}^*$ due to the much higher density of states in C_2Cl_5^* .

Implications for Atmospheric Chemistry. The results reported in this paper confirm that C_2Cl_4 reacts with $\text{Cl}(^2\text{P}_j)$ several hundred times faster than with OH under atmospheric conditions. Hence, in selected atmospheric environments such as the marine boundary layer, where $\text{Cl}(^2\text{P}_j)$ levels appear to be particularly high,^{17–19} reaction with $\text{Cl}(^2\text{P}_j)$ will be the dominant atmospheric removal mechanism for C_2Cl_4 . In addition, C_2Cl_4 is being employed as a "tracer" for analyzing the potential importance of chlorine atoms as an oxidant in the free troposphere;⁵⁶ the temperature- and pressure-dependent values for $k_1(T,P)$ reported in this study are useful for making such an analysis as quantitative as possible.

Acknowledgment. The experimental component of this research was supported by the National Aeronautics and Space Administration, Upper Atmosphere Research Program, through Grant NAGW-1001 to Georgia Institute of Technology. Computer time for this study was made available by the Alabama Supercomputer Network and the NSF-supported Pittsburgh Supercomputer Center. We thank C. A. Piety for helping with some of the experiments.

References and Notes

- (1) Wiedmann, T. O.; Guthner, B.; Class, T. J.; Ballschmiter, K. *Environ. Sci. Technol.* **1994**, *28*, 2321.
- (2) Franklin, J. *Toxicol. Environ. Chem.* **1994**, *46*, 169.
- (3) Wang, C. J.-L.; Blake, D. R.; Rowland, F. S. *Geophys. Res. Lett.* **1995**, *22*, 1097.
- (4) Singh, H. B. In *Composition, Chemistry, and Climate of the Atmosphere*; Singh, H. B., Ed.; Van Nostrand Reinhold: New York, 1995; pp 216–250.
- (5) Winer, A. M.; Lloyd, A. C.; Darnall, K. R.; Pitts, J. N., Jr. *J. Phys. Chem.* **1976**, *80*, 1635.
- (6) Howard, C. J. *J. Chem. Phys.* **1976**, *65*, 4771.
- (7) Chang, J. S.; Kaufman, F. *J. Chem. Phys.* **1977**, *66*, 4989.
- (8) Kirchner, J.; Helf, D.; Ott, P.; Vogt, S. *Ber. Bunsen-Ges. Phys. Chem.* **1990**, *94*, 77.
- (9) Goldfinger, P.; Jeunehomme, M.; Martens, G. *J. Chem. Phys.* **1958**, *28*, 456.
- (10) Ayscough, P. B.; Cocker, A. J.; Dainton, F. S.; Hirst, S.; Weston, M. *Proc. Chem. Soc., London* **1961**, 244.
- (11) Goldfinger, P.; Huybrechts, G.; Martens, G. *Trans. Faraday Soc.* **1961**, *57*, 2210.
- (12) Knox, J.; Waugh, K. C. *Trans. Faraday Soc.* **1969**, *65*, 1585.

- (13) Franklin, J. A.; Huybrechts, G.; Cillien, C. *Trans. Faraday Soc.* **1969**, *65*, 2094.
- (14) Davis, D. D.; Braun, W.; Bass, A. M. *Int. J. Chem. Kinet.* **1970**, *2*, 101.
- (15) Breitbarth, F.-W.; Rottmayer, S. *Plasma Chem. Plasma Proc.* **1986**, *6*, 381.
- (16) Atkinson, R.; Aschmann, S. M. *Int. J. Chem. Kinet.* **1987**, *19*, 1097.
- (17) Jobson, B. T.; Niki, H.; Yokouchi, Y.; Bottenheim, J.; Hopper, F.; Leitch, R. *J. Geophys. Res.* **1994**, *99*, 25355.
- (18) Singh, H. B.; Gregory, G. L.; Anderson, B.; Browell, E.; Sachse, G. W.; Davis, D. D.; Crawford, J.; Bradshaw, J. D.; Talbot, R.; Blake, D. R.; Thornton, D.; Newell, R.; Merrill, J. *J. Geophys. Res.*, in press.
- (19) Finlayson-Pitts, B. J. *Res. Chem. Intermed.* **1993**, *19*, 235.
- (20) Singh, H. B.; Lillian, D.; Appleby, A.; Lobban, L. *Environ. Lett.* **1975**, *10*, 253.
- (21) Stickele, R. E.; Nicovich, J. M.; Wang, S.; Zhao, Z.; Wine, P. H. *J. Phys. Chem.* **1992**, *96*, 9875 and references therein.
- (22) Nicovich, J. M.; Wang, S.; Wine, P. H. *Int. J. Chem. Kinet.* **1995**, *27*, 359.
- (23) Stated minimum purity of liquid phase in high-pressure cylinder.
- (24) Busch, G. E.; Mahoney, R. T.; Morse, R. L.; Wilson, K. R. *J. Chem. Phys.* **1969**, *51*, 449.
- (25) Park, J.; Lee, Y.; Flynn, G. W. *Chem. Phys. Lett.* **1991**, *186*, 441.
- (26) Tyndall, G. S.; Orlando, J. J.; Kegley-Owen, C. S. *J. Chem. Soc., Faraday Trans.* **1995**, *91*, 3055.
- (27) Fletcher, I. S.; Husain, D. *Chem. Phys. Lett.* **1977**, *49*, 516.
- (28) Clark, R. H.; Husain, D. *J. Photochem.* **1983**, *21*, 93.
- (29) Chichinin, A. I.; Krasnoperov, L. N. *Chem. Phys. Lett.* **1989**, *160*, 448.
- (30) DeMore, W. B.; Sander, S. P.; Golden, D. M.; Hampson, R. F.; Kurylo, M. J.; Howard, C. J.; Ravishankara, A. R.; Kolb, C. E.; Molina, M. J. *Chemical Kinetics and Photochemical Data for Use in Stratospheric Modeling*; Evaluation No. 11, Jet Propulsion Laboratory Publication 94-26, 1994.
- (31) Troe, J. *J. Phys. Chem.* **1979**, *83*, 114.
- (32) Luther, K.; Troe, J. *Proc. 17th Int. Symp. Combust.* **1978**, 535.
- (33) Troe, J. *Ber. Bunsen-Ges. Phys. Chem.* **1983**, *87*, 161.
- (34) Dusdeil, S.; Goldfinger, P.; Mahieu-Van Der Auwera, A. M.; Martens, G.; Van Der Auwera, D. *Trans. Faraday Soc.* **1961**, *57*, 2197.
- (35) Parr, R. G.; Yang, W. *Density-Functional Theory of Atoms and Molecules*; Oxford Press: Oxford, United Kingdom, 1989.
- (36) Ziegler, T. *Chem. Rev.* **1991**, *91*, 651.
- (37) *Density Functional Methods in Chemistry*; Labanowski, J., Andzelm, J. W., Eds.; Springer-Verlag: Berlin, 1991.
- (38) Frisch, M. J.; Trucks, G. W.; Schlegel, H. B.; Gill, P. M. W.; Johnson, B. G.; Wong, M. W.; Foresman, J. B.; Robb, M. A.; Head-Gordon, M.; Replogle, E. S.; Gomperts, R.; Andres, J. L.; Raghavachari, K.; Binkley, J. S.; Gonzales, C.; Martin, R. L.; Fox, D. J.; DeFrees, D. J.; Baker, J.; Stewart, J. J. P.; Pople, J. A. *Gaussian 92/DFT (Rev. G. 2)*; Gaussian, Inc.: Pittsburgh, PA, 1993.
- (39) Johnson, B. G.; Gill, P. M. W.; Pople, J. A. *J. Chem. Phys.* **1993**, *98*, 5612.
- (40) Becke, A. D. *J. Chem. Phys.* **1993**, *98*, 5648.
- (41) Gill, P. M. W.; Johnson, B. G.; Pople, J. A.; Frisch, M. J. *Chem. Phys. Lett.* **1992**, *197*, 499.
- (42) Raghavachari, K.; Strout, D. L.; Odom, G. K.; Scuseria, G. E.; Pople, J. A.; Johnson, B. G.; Gill, P. M. W. *Chem. Phys. Lett.* **1993**, *214*, 357.
- (43) Raghavachari, K.; Zhang, B.; Pople, J. A.; Johnson, B. G.; Gonzales, C. A.; Gill, P. M. W.; Pople, J. A. *Chem. Phys. Lett.* **1994**, *220*, 385.
- (44) Johnson, B. G.; Gonzales, C. A.; Gill, P. M. W.; Pople, J. A. *Chem. Phys. Lett.* **1994**, *221*, 100.
- (45) Baker, J.; Scheiner, A.; Andzelm, J. *Chem. Phys. Lett.* **1993**, *216*, 380.
- (46) Chase, M. W., Jr.; Davies, C. A.; Downey, J. R., Jr.; Frurip, D. J.; McDonald, R. A.; Syverud, A. N. *J. Phys. Chem. Ref. Data* **1985**, *14* (Suppl. I).
- (47) We believe that the C₂Cl₄ absolute entropies as a function of temperature tabulated in ref 46 are incorrect.
- (48) (a) Wong, M. W.; Radom, L. *J. Phys. Chem.* **1995**, *99*, 8582. (b) For example, the reaction enthalpy for addition of *tert*-butyl radical to C₂H₄ is too positive by DFT by 9.8 kcal/mol compared to QCISD.
- (49) Wine, P. H.; Semmes, D. H. *J. Phys. Chem.* **1983**, *87*, 3572.
- (50) In their 310 K experiments, Franklin et al. (ref 13) employed gas mixtures containing 80 Torr of Cl₂, 5–20 Torr of C₂Cl₄, 25–100 Torr of CH₂ClCH₂Cl, and 0–500 Torr of CO₂ or SF₆. In their 348 K experiments, the gas mixtures contained 100 Torr of C₂Cl₄, 20 Torr of C₂H₆, and 50–400 Torr of Cl₂. No systematic dependence of *k*₁ on total pressure was reported.
- (51) Xiong, J. Q.; Carr, R. W. *J. Phys. Chem.* **1994**, *98*, 9811.
- (52) Russell, J. J.; Seetula, J. A.; Gutman, D.; Danis, F.; Caralp, F.; Lightfoot, P. D.; Lesclaux, R.; Melius, C. F.; Senkan, S. M. *J. Phys. Chem.* **1990**, *94*, 3277.
- (53) Wallington, T. J.; Andino, J. M.; Lorkovic, I. M.; Kaiser, E. W.; Marston, G. J. *J. Phys. Chem.* **1990**, *94*, 3644.
- (54) Lindemann, F. A. *Trans. Faraday Soc.* **1922**, *17*, 598.
- (55) Hinshelwood, C. N. *The Kinetics of Chemical Change*; Oxford University Press: Oxford, 1940.
- (56) Singh, H. B. Private communication.

JP952396K

Kinetics of the Reaction of O(³P) with CF₃NO

R. P. THORN^{*,**}, J. M. NICOVICH[†], J. M. CRONKHITE[‡], S. WANG^{†,§}, and P. H. WINE^{*,†,§§}
Georgia Institute of Technology, Atlanta, Georgia 30332

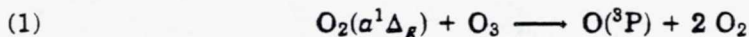
Abstract

A laser flash photolysis-resonance fluorescence technique has been employed to study the kinetics of the reaction of O(³P) with CF₃NO (*k*₂) as a function of temperature. Our results are described by the Arrhenius expression $k_2(T) = (4.54 \pm 0.70) \times 10^{-12} \exp[(-560 \pm 46)/T] \text{ cm}^3 \text{ molecule}^{-1} \text{ s}^{-1}$ (243 K \leq *T* \leq 424 K); errors are 2 σ and represent precision only. The O(³P) + CF₃NO reaction is sufficiently rapid that CF₃NO cannot be employed as a selective quencher for O₂(*a*¹ Δ_g) in laboratory systems where O(³P) and O₂(*a*¹ Δ_g) coexist, and where O(³P) kinetics are being investigated. © 1995 John Wiley & Sons, Inc.

Introduction

The first excited state of molecular oxygen, O₂(*a*¹ Δ_g) ($\epsilon = 0.977$ eV), has a long radiative lifetime of 3900 s and typically is quenched inefficiently by closed-shell molecules [1]. Specifically, the rate coefficient for quenching of O₂(*a*¹ Δ_g) by N₂ is less than 10⁻²⁰ cm³ molecule⁻¹ s⁻¹ [2] which results in a long O₂(*a*¹ Δ_g) lifetime in N₂ even at pressures of hundreds of torr. Although rate coefficients for quenching of O₂(*a*¹ Δ_g) by about 50 small molecules have been reported [1,3,4], only trifluoronitrosomethane, CF₃NO, has been found to have a large quenching rate coefficient at 300 K, i.e., 3.0 \times 10⁻¹² cm³ molecule⁻¹ s⁻¹ [3].

In a recent study of the kinetics of the O(³P) + BrO reaction [5] we employed UV laser flash photolysis of O₃ as a source for generating large concentrations of O(³P). Ozone photolysis at 248 nm (KrF excimer laser) and at 266 nm (fourth harmonic of the Nd:YAG laser) produces primarily electronically excited "singlet" atomic and molecular oxygen, O(¹D) and O₂(*a*¹ Δ_g) [6,7]. O(¹D) is rapidly quenched to the ground state, O(³P), by N₂ on a submicrosecond time scale at pressures greater than 1 torr [8]; hence, further O(¹D) reactions can be neglected in kinetic experiments performed at higher pressures of N₂. However, O₂(*a*¹ Δ_g) is long lived and in O(³P) kinetics experiments with high O₃ concentrations used as the photolyte, the reaction of O₂(*a*¹ Δ_g) with O₃ can generate O(³P):



* School of Earth and Atmospheric Sciences.

** Present Address: Laboratory for Extraterrestrial Physics, N.A.S.A. Goddard Space Flight Center, Code 691, Greenbelt, Maryland 20771.

† Georgia Tech Research Institute.

‡ School of Physics.

§ Present Address: Dalian Institute of Chemical Physics, Chinese Academy of Sciences, P.O. Box 110, Dalian, Peoples Republic of China.

§§ School of Chemistry and Biochemistry.

International Journal of Chemical Kinetics, Vol. 27, 369-377 (1995)

© 1995 John Wiley & Sons, Inc.

CCC 0538-8066/95/040369-09

a MgF₂ lens. Dry N₂ was used as a purge gas in the volume between the lamp window and the cell lens to exclude room air and thus allow transmission of vacuum-UV radiation.

Fluorescence from excited O(³P) atoms within the reaction zone was collected by a MgF₂ lens on an axis orthogonal to both the photolysis laser beam and the resonance lamp beam and imaged onto the photocathode of a solar blind photomultiplier. The region between the reaction cell and the photomultiplier was purged with dry N₂ and contained a CaF₂ window to prevent detection of Lyman- α emission from the resonance lamp. The fluorescence signals were processed using photon counting techniques in conjunction with multichannel scaling. For each O(³P) atom decay rate measured, signals from a large number of laser shots (500 to 15,000) were averaged to obtain a well-defined temporal profile over (typically) three 1/e lifetimes of decay. The multichannel analyzer sweep was triggered approximately 3.2 ms prior to the photolysis laser in order to allow a fluorescence background baseline to be obtained immediately before the laser flash.

All experiments were carried out under "slow flow" conditions so as to avoid accumulation of photolysis or reaction products. The linear flow rate through the reactor was typically around 2 cm s⁻¹ and the laser repetition rate was 10 Hz. Hence, no volume element of the reaction mixture was subjected to more than two or three laser shots. The reactant CF₃NO was flowed from 12 L bulbs containing dilute mixtures in N₂ buffer gas into an absorption cell, which was used for in situ CF₃NO concentration determination as described below. N₂ buffer gas was mixed into the reactant flow before the absorption cell. The flow from a 12 L bulb containing O₃ diluted with N₂ was injected into the reaction cell through a 1/8 inch o.d. Teflon tube positioned such that the O₃ mixed with other components about 1 to 5 cm upstream from the reaction zone.

The concentration of CF₃NO was measured in situ by UV photometry at 202.6 nm using an absorption cell with a 200.3 cm path length and a zinc hollow cathode lamp light source (which emitted the 202.6 nm Zn⁺ line). Because the output of the zinc lamp includes several other strong lines in the same wavelength region, it was necessary to isolate the 202.6 nm line with a 0.25 m monochromator (Jarrell-Ash) positioned at the exit from the absorption cell. A side-on photomultiplier connected directly to the exit aperture of the monochromator provided the signal detection and a 4¹/₂ place digital picoammeter provided the signal readout. A CF₃NO absorption cross section of $(6.08 \pm 0.10) \times 10^{-19}$ cm² at 202.6 nm (error is 2 σ , precision only) was determined with a separate 10.0 cm path length absorption cell and was the value used for all CF₃NO in situ and bulb concentration determinations.

In addition the photometric measurements, the CF₃NO concentration in the reaction mixture was also determined from measurements of the flow rate of the CF₃NO/N₂ mixture, the total flow rate, the cell pressure, and the known CF₃NO/N₂ bulb concentration. There was good agreement between the CF₃NO concentration measured in situ and the values calculated from the flow rate measurements. However, the reported k_2 values are based upon the CF₃NO concentrations determined from the in situ photometry measurements; the flow rate based measurements averaged 7.4% less.

One experiment was performed using in situ visible photometry at 632.8 nm to determine the CF₃NO concentration. The same 200.3 cm length absorption cell was used, but a HeNe laser replaced the zinc hollow cathode lamp as the radiation source. A diffuser was placed in front of the monochromator entrance slit to attenuate the

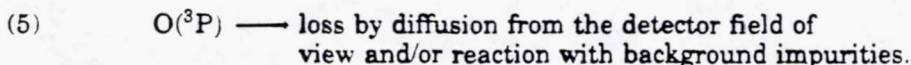
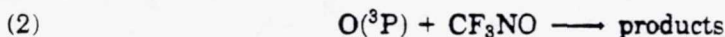
probe beam and prevent saturation of the photomultiplier. A CF_3NO absorption cross section of $(4.26 \pm 0.28) \times 10^{-20} \text{ cm}^2$ was determined with a separate 10.0 cm path length absorption cell and was the value used for all CF_3NO concentration determinations at 632.8 nm. The k_2 value determined with visible photometry was in good agreement with the experiments which used 202.6 nm as the wavelength for CF_3NO monitoring.

The concentration of O_3 in the reaction mixture was determined from measurements of the appropriate mass flow rates, the total pressure, and the known O_3 bulb concentration. The determination of the O_3 concentration in the O_3/N_2 bulb used the in situ UV photometry apparatus described above. At 202.6 nm the O_3 absorption cross section is $3.2 \times 10^{-19} \text{ cm}^2$ [2].

The He and N_2 gases used in this study had stated minimum purities of 99.999% and were used as supplied. Ozone was prepared in a commercial ozonator using UHP oxygen (99.99%). It was collected and stored on silica gel at 195 K, and degassed at 77 K before use. The CF_3NO (95% minimum purity) was obtained from PCR, Inc. and was degassed twice at 77 K before each use. The IR spectrum of the degassed CF_3NO agreed with that reported in the literature [18]. The CF_3NO was also analyzed for the presence of the dimer, $(\text{CF}_3)_2\text{NONO}$, and NO_2 by UV-Visible absorption spectroscopy. $(\text{CF}_3)_2\text{NONO}$ was monitored at 372 nm, where the absorption cross section is $6.38 \times 10^{-20} \text{ cm}^2$ [19]; the CF_3NO absorption cross section at 372 nm is a factor of 640 lower [20]. The upper limit mole fraction of dimer present was determined to be 0.05%. No NO_2 absorption features were observed in the visible region. The CF_3NO gas was used without further purification.

Results and Discussion

All experiments were carried out under pseudo-first-order conditions with CF_3NO in large excess over $\text{O}(^3\text{P})$. Thus, in the absence of secondary reactions which enhance or deplete the $\text{O}(^3\text{P})$ atom concentration, the $\text{O}(^3\text{P})$ atom temporal profile is dominated by the reactions



The background $\text{O}(^3\text{P})$ loss rate, k_5 , was typically $35\text{--}45 \text{ s}^{-1}$ for $P = 100$ torr. The reaction of $\text{O}(^3\text{P})$ with O_3 can be neglected as an $\text{O}(^3\text{P})$ atom loss mechanism since the rate coefficient is small [2] and O_3 concentrations were relatively low (Table I). Similarly, generation of $\text{O}(^3\text{P})$ by reaction (1) can be neglected. Integration of the rate equations for the above scheme yields the following simple relationship:

$$(I) \quad \ln\{S_0/S_t\} = (k_2[\text{CF}_3\text{NO}] + k_5)t = k_2't$$

In eq. (I), S_0 is the $\text{O}(^3\text{P})$ fluorescence signal at a time shortly after the laser fires and S_t is the $\text{O}(^3\text{P})$ fluorescence signal at time t . The bimolecular rate coefficient, k_2 , is determined from the slope of a k_2' vs. $[\text{CF}_3\text{NO}]$ plot.

For the $\text{O}(^3\text{P}) + \text{CF}_3\text{NO}$ reaction, the $\text{O}(^3\text{P})$ temporal profiles were found to be exponential and the $\text{O}(^3\text{P})$ decay rates were found to increase linearly with increasing CF_3NO concentration, i.e., the kinetic observations are consistent with eq. (I). The observed pseudo-first-order decay rates were found to be independent of laser photon fluence and O_3 concentration. This set of observations, coupled with the photometric

TABLE I. Kinetic data for the reaction of O(³P) with CF₃NO.

Temp. (K)	Press. (torr)	Concentrations ^a			Laser Fluence (mJ/cm ²)	Number of Expts. ^c	$k'_{2\max}$ (s ⁻¹)	$10^{13} k_2^d$ (cm ³ molecule ⁻¹ s ⁻¹)
		O ₃	O	CF ₃ NO ^b				
243	100	22.	0.29	523-3150	1.0	5	1550	4.75 ± 0.17
264	100	20.	0.24	376-2700	0.9	5	1540	5.43 ± 0.25
296	25	10.	1.4	195-1130	11.	5	914	7.13 ± 0.10
297	100	7.1	0.27	227-1176	3.0	7	898	7.14 ± 0.054
298	100	56.	0.79	4580-15800 ^e	1.1	5	10570	6.69 ± 0.80 ^e
299	100	56.	0.22	593-2270	0.3	4	1720	7.24 ± 0.44
299	100	4.4	0.25	575-2410	4.4	4	1710	6.93 ± 0.62
301	100	8.0	0.17	332-2180	1.7	5	1560	6.84 ± 0.35
297	400	7.7	0.96	256-759	10.	5	759	6.92 ± 0.44
346	100	7.7	0.14	310-1840	1.4	5	938	8.91 ± 0.27
424	100	11.	0.26	122-1210	1.8	5	1620	12.6 ± 0.93

^aConcentration units are 10¹² molecules cm⁻³.

^bCF₃NO concentration based on in situ UV photometry at 202.6 nm.

^cExperiment = measurement of one O(³P) temporal profile.

^dErrors are 2σ and represent precision only.

^eCF₃NO concentration based on in situ visible photometry at 633 nm.

impurity analyses described above, strongly supports the contention that reactions (2), (4), and (5) are the only processes which affected the post-laser-flash O(³P) time history in these experiments.

Results from our study of reaction (2) are summarized in Table I. Experiments at room temperature (296-301 K) were performed with variations in laser fluence (0.3-11 mJ cm⁻²), O₃ concentration (4.4-56 × 10¹² molecule cm⁻³), initial O(³P) concentration (0.17-1.4 × 10¹² atoms cm⁻³), and N₂ pressure (25, 100, and 400 torr). The rate coefficient, k_2 , is found to be independent of pressure over the range 25-400 torr and at 298 K has the value $k_2(298 \text{ K}) = (6.98 \pm 0.39) \times 10^{-13} \text{ cm}^3 \text{ molecule}^{-1} \text{ s}^{-1}$ (errors are 2σ, precision only). k_2 was found to increase with increasing temperature over the range 243-424 K. Typical O(³P) temporal profiles are shown in Figure 1 while k_2' vs. [CF₃NO] plots for data taken at 264 K, 299 K, and 424 K and $P = 100$ torr are shown in Figure 2.

An Arrhenius plot for reaction (2) is shown in Figure 3. A linear least-squares analysis of the ln k_2 vs. 1/ T data gives the Arrhenius expression

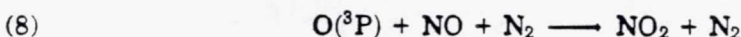
$$(III) \quad k_2(T) = (4.54 \pm 0.70) \times 10^{-12} \exp[(-560 \pm 46)/T] \text{ cm}^3 \text{ molecule}^{-1} \text{ s}^{-1}.$$

Errors in the above expression are 2σ and represent precision only. The estimated absolute uncertainty (2σ) in $k_2(T)$ at any temperature within the range of this study is ±20%. To our knowledge, there have been no previous kinetics studies of the O(³P) + CF₃NO reaction with which to compare our results.

Possible sources of systematic error in this study include secondary reactions arising from the 266 nm photolysis of CF₃NO



Both photolysis products, CF₃ and NO, consume O(³P)



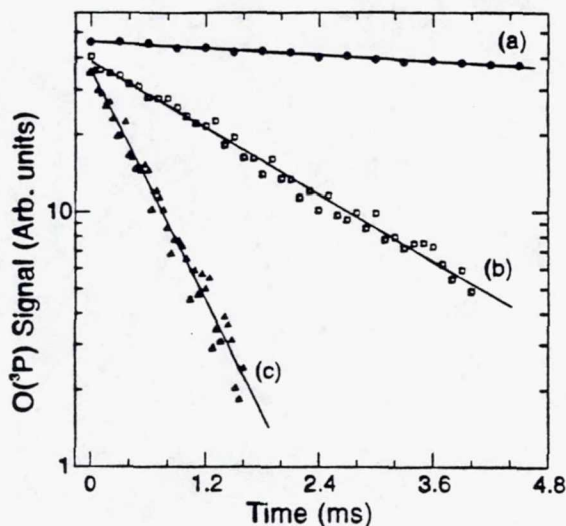


Figure 1. Typical $O(^3P)$ temporal profiles. Experimental conditions: $T = 299$ K; $P = 100$ torr N_2 ; $[O_3] = 5.6 \times 10^{13}$ molecules cm^{-3} ; $[O(^3P)]_0 = 2.2 \times 10^{11}$ atoms cm^{-3} ; $[CF_3NO]$ in units of 10^{14} molecules cm^{-3} = (a) 0.0, (b) 5.93, and (c) 22.7; number of laser shots averaged = (a) 2000, (b) 1500, and (c) 4000. Solid lines are obtained from least-squares analyses and give the following pseudo-first-order decay rates in units of s^{-1} : (a) 44, (b) 489, and (c) 1720.

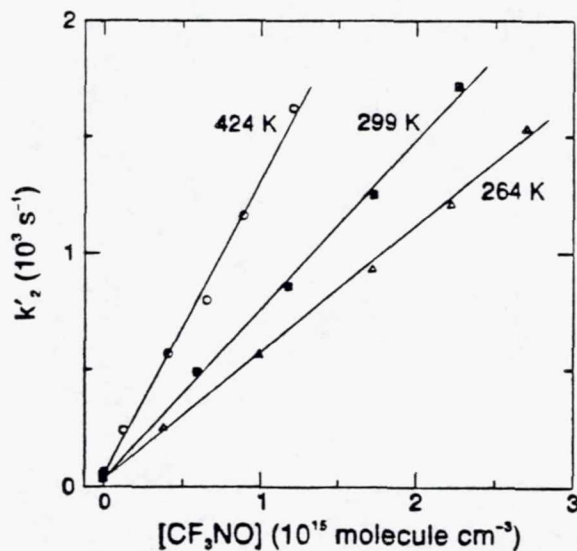


Figure 2. Plots of k_2 vs. $[CF_3NO]$ for data obtained at $T = 424$ K, 299 K, and 264 K and $P = 100$ torr. Solid lines are obtained from linear least-squares analyses and give the following rate coefficients in units of 10^{-13} cm^3 molecule $^{-1}$ s^{-1} : 5.43 ± 0.25 at 264 K, 7.24 ± 0.44 at 299 K, and 12.6 ± 0.93 at 424 K; errors are 2σ , precision only.

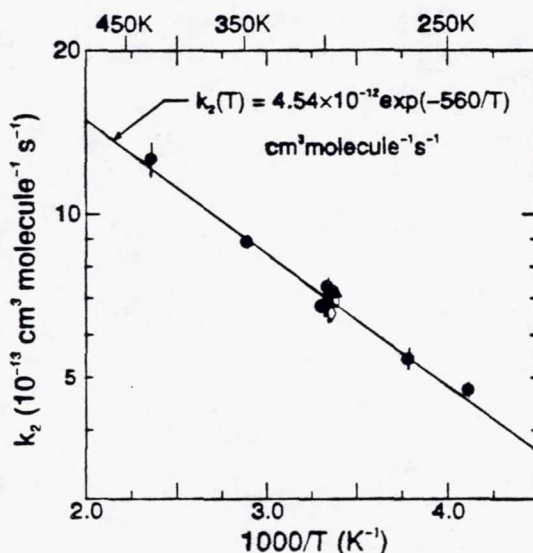
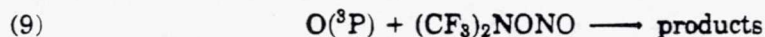


Figure 3. Arrhenius plot for the O(³P) + CF₃NO reaction. Solid line is obtained from a least-squares analysis of all data. Circles are data obtained at $P = 100$ torr. The triangle and square are data obtained at $P = 25$ and 400 torr, respectively. The diamond is data obtained at 100 torr with [CF₃NO] determined in situ by visible photometry at 632.8 nm. Error bars are 2σ and represent precision only.

However, at 298 K and 400 torr total pressure, reaction (7) is approximately 30 times faster than reaction (8) (with $k_7 = 3.1 \times 10^{-11} \text{ cm}^3 \text{ molecule}^{-1} \text{ s}^{-1}$ [20] and $k_8(400 \text{ torr}) = 9.6 \times 10^{-13} \text{ cm}^3 \text{ molecule}^{-1} \text{ s}^{-1}$ [2]). Even at the highest laser fluence and CF₃NO concentrations used (11 mJ/cm^2 and $1.13 \times 10^{15} \text{ molecule cm}^{-3}$), the initial CF₃ concentration is only $1.2 \times 10^{11} \text{ molecule cm}^{-3}$ because of a low CF₃NO absorption cross section at 266 nm ($1.34 \times 10^{-21} \text{ cm}^2$ [21]). Thus, the pseudo-first-order decays do not require correction for reactions (7) and (8).

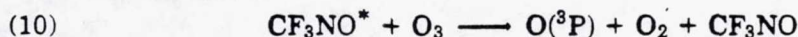
Another possible source of systematic error is O(³P) consumption from impurities present in the CF₃NO sample. In particular, exposure of CF₃NO to light results in production of (CF₃)₂NONO (O-nitrosobis(trifluoromethyl)hydroxylamine). The rate coefficient for reaction (9) is unknown.



To assess the potential role of reaction (9) as a kinetic interference in our study of reaction (2), a crude measurement of k_9 was carried out. A sample of CF₃NO in a 1-liter pyrex bulb was irradiated for 90 h with a tungsten-halogen lamp; a glass cut-off filter prevented radiation at wavelengths shorter than 580 nm from entering the bulb, thus minimizing secondary photolysis of CF₃NO photo-products. UV-visible spectral analysis of the sample after irradiation (and degassing at 77K) showed that (CF₃)₂NONO and NO₂ were present at approximately a 20:1 concentration ratio, and that about 85% of the CF₃NO was converted to (CF₃)₂NONO. Mason [22] has reported observation of CF₃NO₂, CF₃NCF₂, (CF₃)₂NNO₂, NO₂F, NOF, NO, N₂O, CO₂, and SiF₄ as minor products of the photochemical degradation of CF₃NO. When the laser flash photolysis-resonance fluorescence technique was employed to study the kinetics of the reaction of O(³P) with the irradiated mixture, an apparent rate coefficient

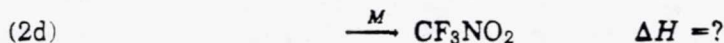
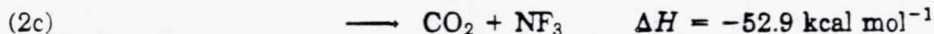
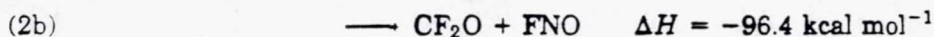
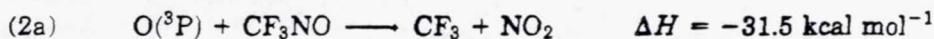
of $2.1 \times 10^{-11} \text{ cm}^3 \text{ molecule}^{-1} \text{ s}^{-1}$ was obtained; this rate coefficient was found to be independent of pressure (25–100 torr) and temperature (298–369 K). Considering that the $\text{O}(^3\text{P}) + \text{NO}_2$ rate coefficient is approximately $1.0 \times 10^{-11} \text{ cm}^3 \text{ molecule}^{-1} \text{ s}^{-1}$ over the temperature range of this study [2], these observations suggest that $k_9 < 3 \times 10^{-11} \text{ cm}^3 \text{ molecule}^{-1} \text{ s}^{-1}$. Therefore, in our studies it was always the case that $k_2/k_9 \geq 0.016$ (see Table I). Since the spectrophotometric analyses discussed above demonstrated that the mole fraction of $(\text{CF}_3)_2\text{NONO}$ in the CF_3NO sample was ≤ 0.0005 , we conclude that reaction (9) could contribute no more than a few percent to observed reactivity in the low temperature studies of reaction (2) and even less at higher temperatures.

Excited state chemistry also represents a potential source of systematic error. The quenching of $\text{O}_2(a^1\Delta_g)$ by CF_3NO is believed to occur via an excitation transfer mechanism which forms a low-energy CF_3NO^* triplet state [3]. Reaction of O_3 with CF_3NO^* could yield $\text{O}(^3\text{P})$



It is, however, very unlikely that reaction (10) occurs. It is not energetically favored; the $\text{O}-\text{O}_2$ bond dissociation energy in O_3 is $25.5 \text{ kcal mol}^{-1}$ which is $3.0 \text{ kcal mol}^{-1}$ higher than the electronic energy possessed by $\text{O}_2(a^1\Delta_g)$. Furthermore, vibrational relaxation of CF_3NO would be expected to compete favorably with the $\text{CF}_3\text{NO}^* + \text{O}_3$ reaction under the conditions of our experiments, i.e., $[\text{N}_2]/[\text{O}_3] > 10^5$.

Using a ΔH_f^0 value for CF_3NO of $-132.2 \text{ kcal mol}^{-1}$ (obtained from a shock tube study of the thermal dissociation of CF_3NO [23]), there appear to be four energetically accessible product channels for reaction (2):



The results reported in this study do not provide information concerning the product branching ratio, although reactions (2a) and/or (2b) would appear to be the most likely reaction channel(s). The observed independence of k_2 to significant variations in pressure argues against the occurrence of reaction (2d) while the large number of (very strong) chemical bonds which must be broken and formed argues against the occurrence of channel (2c). Further studies aimed at quantitative detection of reaction products would be of interest.

Summary

The laser flash photolysis-resonance fluorescence technique has been employed to study the temperature dependence of the thermal rate coefficient for reaction (2); this represents the first kinetics study of the $\text{O}(^3\text{P}) + \text{CF}_3\text{NO}$ reaction. The temperature dependence of k_2 is adequately described by the following Arrhenius expression: $k_2 = (4.54 \pm 0.70) \times 10^{-12} \exp[(-560 \pm 46)/T] \text{ cm}^3 \text{ molecule}^{-1} \text{ s}^{-1}$. The absolute uncertainty in the measured rate coefficient at any temperature within the range studied is estimated to be $\pm 20\%$. Reaction (2) is sufficiently fast to preclude use of CF_3NO as a selective quencher for $\text{O}_2(a^1\Delta_g)$ in laboratory systems where $\text{O}(^3\text{P})$ kinetics are being investigated.

Acknowledgment

This research was supported by the National Aeronautics and Space Administration through grant NAGW-1001. We thank K. A. Walker for assistance with the data analysis and R. E. Stickel for helpful discussions.

Bibliography

- [1] E. A. Ogryzlo, in *Singlet Oxygen Reactions with Organic Compounds and Polymers*; R. Ranby and J. F. Rabek, Eds., Wiley, New York, 1978.
- [2] W. B. DeMore, M. J. Molina, S. P. Sander, D. M. Golden, R. F. Hampson, M. J. Kurylo, C. J. Howard, and A. R. Ravishankara, *Chemical Kinetics and Photochemical Data for Use in Stratospheric Modeling*, Evaluation No. 10, JPL Publication No. 92-20, Jet Propulsion Laboratory, Pasadena, California, 1992.
- [3] J. P. Singh, J. Bachar, D. W. Setser, and S. Rosenwaks, *J. Phys. Chem.*, **89**, 5347 (1985).
- [4] P. Borrell and D. S. Richards, *J. Chem. Soc. Far. Trans. 2*, **85**, 1401 (1989).
- [5] R. P. Thorn, J. M. Cronkhite, J. M. Nicovich, and P. H. Wine, *J. Chem. Phys.*, in press.
- [6] P. H. Wine and A. R. Ravishankara, *Chem. Phys.*, **69**, 365 (1982).
- [7] J. C. Brock and R. T. Watson, *Chem. Phys. Lett.*, **71**, 371 (1980).
- [8] P. H. Wine and A. R. Ravishankara, *Chem. Phys. Lett.*, **77**, 103 (1981).
- [9] G. E. Streit, C. J. Howard, A. L. Schmeltekopf, J. A. Davidson, and H. I. Schiff, *J. Chem. Phys.*, **65**, 4761 (1976).
- [10] S. T. Amimoto, A. P. Force, R. G. Gulotty, Jr., and J. R. Wiesenfeld, *J. Chem. Phys.*, **71**, 3640 (1979).
- [11] P. H. Wine and A. R. Ravishankara, *Chem. Phys. Lett.*, **96**, 129 (1983).
- [12] P. H. Wine, J. M. Nicovich, R. J. Thompson, and A. R. Ravishankara, *J. Phys. Chem.*, **87**, 3948 (1983).
- [13] P. H. Wine, J. M. Nicovich, and A. R. Ravishankara, *J. Phys. Chem.*, **89**, 3914 (1985).
- [14] P. H. Wine, J. R. Wells, and A. R. Ravishankara, *J. Chem. Phys.*, **84**, 1349 (1986).
- [15] A. R. Ravishankara, P. H. Wine, C. A. Smith, P. E. Barbone, and A. Torabi, *J. Geophys. Res.*, **91**, 5355 (1986).
- [16] J. M. Nicovich and P. H. Wine, *Int. J. Chem. Kinet.*, **22**, 379 (1990).
- [17] P. H. Wine, N. M. Kreutter, and A. R. Ravishankara, *J. Phys. Chem.*, **83**, 3191 (1979).
- [18] H. F. Shurvell, S. C. Dass, and R. D. Gordon, *Can. J. Chem.*, **52**, 3149 (1974).
- [19] R. N. Hazeldine and B. J. H. Mattinson, *J. Chem. Soc.*, 1741 (1957).
- [20] C. Tsai, S. M. Belanger, J. T. Kim, J. R. Lord, and D. L. McFadden, *J. Phys. Chem.*, **93**, 1916 (1989).
- [21] T. D. Allston, M. L. Fedyk, and G. A. Takacs, *Chem. Phys. Lett.*, **60**, 97 (1978).
- [22] J. Mason, *J. Chem. Soc.*, 4531 (1963).
- [23] K. Glanzer, M. Maier, and J. Troe, *Chem. Phys. Lett.*, **61**, 175 (1979).

Received July 18, 1994

Accepted August 29, 1994

Laser flash photolysis studies of radical-radical reaction kinetics: The $O(^3P_J)+BrO$ reaction

R. P. Thom^{a)}

School of Earth and Atmospheric Sciences, Georgia Institute of Technology, Atlanta, Georgia 30332

J. M. Cronkhite

School of Physics, Georgia Institute of Technology, Atlanta, Georgia 30332

J. M. Nicovich

Georgia Tech Research Institute, Georgia Institute of Technology, Atlanta, Georgia 30332

P. H. Wine

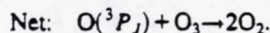
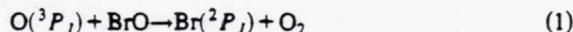
School of Earth and Atmospheric Sciences, Georgia Tech Research Institute,
and School of Chemistry and Biochemistry, Georgia Institute of Technology, Atlanta, Georgia 30332

(Received 18 October 1994; accepted 29 November 1994)

A novel dual laser flash photolysis-long path absorption-resonance fluorescence technique has been employed to study the kinetics of the important stratospheric reaction $O(^3P_J)+BrO \xrightarrow{k_1} Br(^2P_J)+O_2$ as a function of temperature (231–328 K) and pressure (25–150 Torr) in N_2 buffer gas. The experimental approach preserves the principal advantages of the flash photolysis method, i.e., complete absence of surface reactions and a wide range of accessible pressures, but also employs techniques which are characteristic of the discharge flow method, namely chemical titration as a means for deducing the absolute concentration of a radical reactant and use of multiple detection axes. We find that k_1 is independent of pressure, and that the temperature dependence of k_1 is adequately described by the Arrhenius expression $k_1(T)=1.91 \times 10^{-11} \exp(230/T) \text{ cm}^3 \text{ molecule}^{-1} \text{ s}^{-1}$; the absolute accuracy of measured values for k_1 is estimated to vary from $\pm 20\%$ at $T \sim 230$ K to $\pm 30\%$ at $T \sim 330$ K. Our results demonstrate that the $O(^3P_J)+BrO$ rate coefficient is significantly faster than previously "guesstimated," and suggest that the catalytic cycle with the $O(^3P_J)+BrO$ reaction as its rate-limiting step is the dominant stratospheric BrO_x odd-oxygen destruction cycle at altitudes above 24 km. © 1995 American Institute of Physics.

I. INTRODUCTION

The reaction of ground state oxygen atoms, $O(^3P_J)$, with BrO radicals is the rate determining step in a catalytic cycle via which bromine destroys odd oxygen in the middle stratosphere¹⁻³



Reactive BrO_x radicals are produced in the stratosphere primarily by photodissociation of methyl bromide (CH_3Br) and the halons CF_3Br , CF_2ClBr , and CF_2BrCF_2Br .⁴

No direct measurements of k_1 have been reported, although Clyne *et al.* obtained the estimate $k_1(298 \text{ K})=2.5 \times 10^{-11} \text{ cm}^3 \text{ molecule}^{-1} \text{ s}^{-1}$ (factor of 2 reported uncertainty) based on observation of secondary $O(^3P_J)$ consumption and $Br(^2P_J)$ production in a study of $O(^3P_J)+Br_2$ kinetics.⁵ High quality kinetic data for reaction (1) are needed to facilitate quantitative understanding of the role of the above catalytic cycle in stratospheric chemistry. Furthermore, reaction (1) is a likely side reaction in laboratory studies of the Br_2-O_3 photochemical system, so knowledge of

$k_1(T)$ would assist interpretation of experiments designed to study other important BrO_x reactions. Finally, comparison of kinetic data for reaction (1) with available data for other $O(^3P_J)+XO$ reactions ($X=Cl, OH, H, \dots$)⁶ could prove useful for refining theoretical procedures for calculating radical-radical reaction rates.

In this paper we report the results of a direct kinetics study of reaction (1) as a function of temperature (231–328 K) and pressure (25–150 Torr). A dual laser flash photolysis-long path absorption—resonance fluorescence technique (DLFP-LPA-RF) has been employed in our study. This novel experimental approach, which features simultaneous time-resolved detection of BrO (by long path absorption) and $O(^3P_J)$ (by atomic resonance fluorescence) has evolved from our earlier studies of $O(^3P_J)+HO_2$ (Refs. 7 and 8) and $O(^3P_J)+ClO$ (Ref. 9) reaction kinetics. We find that, under midstratospheric conditions, reaction (1) is considerably faster than previously thought; the implications of this result for stratospheric BrO_x chemistry are discussed.

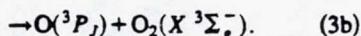
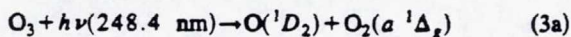
II. EXPERIMENTAL TECHNIQUE AND KINETIC SCHEME

The DLFP-LPA-RF technique preserves the principal advantages of the flash photolysis method, i.e., the complete absence of side reactions catalyzed by wall surfaces and a wide range of accessible pressures, while also incorporating some advantages normally associated with the discharge

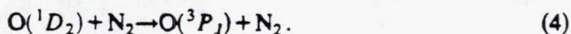
^{a)}Present address: Laboratory for Extraterrestrial Physics, NASA Goddard Space Flight Center, Code 691, Greenbelt, Maryland 20771.

flow method,¹⁰ namely chemical titration as a means for deducing the absolute concentration of a radical reactant and employment of multiple detection axes. Although the two free radical reactants cannot be generated in spatially separated regions (as they can in the discharge flow method), some chemistry complications can be avoided by controlling the time delay between generation of the two reactants. Because the experimental approach is to some extent dictated by the nature of secondary chemistry complications, the experimental technique and the kinetic scheme are best presented in a single section of the paper.

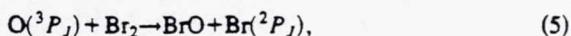
Consider a mixture of N_2 , O_3 , and Br_2 with $[N_2] \gg [O_3] \gg [Br_2]$. When this mixture is subjected to flash photolysis at 248.4 nm (KrF laser), the only species which undergoes significant photodissociation is O_3



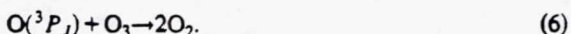
The yields of singlet and triplet photoproducts are 0.91 and 0.09, respectively.¹¹ Since N_2 is present in large excess over O_3 and Br_2 , essentially all $O(^1D_2)$ generated by the photoflash is rapidly quenched by N_2



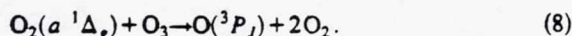
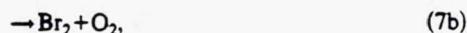
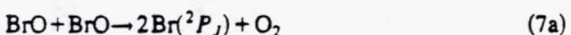
The rate coefficient for the quenching reaction at 298 K is $k_4 = 2.8 \times 10^{-11} \text{ cm}^3 \text{ molecule}^{-1} \text{ s}^{-1}$ with little or no temperature variation.⁶ Suppose that the concentration of oxygen atoms created by the photoflash is greater than the concentration of Br_2 initially present in the reaction mixture; then Br_2 can be titrated to BrO via the following reactions:



Reaction (5) is sufficiently exothermic to generate atomic bromine in the spin-orbit excited electronic state $Br(^2P_{1/2})$. However, if experimental conditions are maintained where $[N_2] \gg [O_3]$, then relaxation of $Br(^2P_{1/2})$ to $Br(^2P_{3/2})$ via collisions with N_2 is rapid compared to the time scale for $Br(^2P_{3/2})$ reaction.¹² Any excess $O(^3P_J)$ remaining after consumption of all Br_2 would be expected to react with O_3 directly via reaction (6) or (primarily) via the catalytic cycle composed of reactions (1) and (2)



If the chemistry in the O_3 - Br_2 - N_2 photolysis system were completely described by reactions (1)–(6), and if experimental conditions could be adjusted such that the rate of $O(^3P_J)$ consumption by the slow⁶ reaction (6) was negligible compared to its rate of consumption by Br_2 and BrO , then k_1 could be evaluated based on measurements of the $O(^3P_J)$ decay rate at long times after the laser flash when Br_2 had been quantitatively converted to BrO ; under such conditions the decay of $O(^3P_J)$ would be essentially pseudo-first-order since BrO lost by reaction with $O(^3P_J)$ would be regenerated via reaction (2). Unfortunately, the following side reactions complicate the measurement of k_1 :

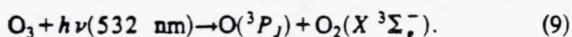


Reaction (7) is moderately fast [$k_7(298 \text{ K}) = 2.7 \times 10^{-12} \text{ cm}^3 \text{ molecule}^{-1} \text{ s}^{-1}$]; both the absolute rate coefficient and the branching ratio for reaction (7) are well established over the range of temperature employed in this study.^{13–16} Fortunately, regeneration of Br_2 via reaction (7) is relatively slow because reaction (7b) is the minor channel.^{13–16}

Although it is quite slow [$k_8(298 \text{ K}) = 3.8 \times 10^{-15} \text{ cm}^3 \text{ molecule}^{-1} \text{ s}^{-1}$; $E_{act} = 5.65 \text{ kcal mol}^{-1}$],⁶ reaction (8) has a profound effect on observed $O(^3P_J)$ temporal profiles. Instead of decaying rapidly to zero concentration via reactions (1) and (5), the $O(^3P_J)$ concentration reaches a near-steady-state level at long times after the laser flash where loss via reactions (1) and (5) is counterbalanced by production via reaction (8). The occurrence of reaction (8) severely complicates the evaluation of k_1 from observations of $O(^3P_J)$ kinetics.

One approach for circumventing the kinetic complications caused by the occurrence of reaction (8) is to identify a quencher which efficiently converts $O_2(a^1\Delta_g)$ to $O_2(X^3\Sigma_g^-)$ but does not otherwise interfere with the chemistry under investigation. Rate coefficients for quenching of $O_2(a^1\Delta_g)$ by small molecules are typically very slow (10^{-16} – $10^{-18} \text{ cm}^3 \text{ molecule}^{-1} \text{ s}^{-1}$) for many quenching reactions which have been studied.¹⁷ One exception is CF_3NO , which quenches $O_2(a^1\Delta_g)$ very efficiently [$k(298 \text{ K}) = 3 \times 10^{-12} \text{ cm}^3 \text{ molecule}^{-1} \text{ s}^{-1}$].¹⁷ We find that CF_3NO also reacts rather rapidly with $O(^3P_J)$ [$k(298 \text{ K}) = 6.9 \times 10^{-13} \text{ cm}^3 \text{ molecule}^{-1} \text{ s}^{-1}$].¹⁸ Hence, a suitable $O_2(a^1\Delta_g)$ quencher for use in our kinetics experiments could not be identified.

A second more successful approach for circumventing the kinetic complications caused by the occurrence of reaction (8) involves the use of a second photolysis laser. Once the concentration of $O(^3P_J)$ has reached its near-steady-state level (typically 10–50 ms after the KrF laser fires) a second pulsed laser operating at 532 nm (second harmonic, Nd:YAG laser) photolyzes a small fraction of the remaining ozone



Computer simulations employing typical experimental conditions strongly suggest that the decay of the additional $O(^3P_J)$ produced by the 532 nm laser back to the near-steady-state level is dominated by reaction (1).

A schematic diagram of the DLFP-LPA-RF apparatus is shown in Fig. 1, and important experimental details are discussed below.

A jacketed borosilicate glass reaction cell was used in all experiments. Thermostated liquids (ethylene glycol–water mixture or methanol) were circulated through the jacket to control the reaction cell temperature (for the sake of clarity, the jacket is not shown in Fig. 1). Measurement of the temperature in the reaction zone under the precise pressure and flow conditions of the experiment was accomplished as described previously.¹⁹ The main body of the reaction cell was a 29.5 cm by 21.5 cm cross which was 4.0 cm in diameter. The longer axis was used for BrO detection while the pho-

absorption measurements was equal within a few percent to the path length estimated by multiplying the measured length of the reaction cell by the number of passes (evaluated by counting the UV spots impinging on a piece of fluorescent paper moved across the White cell mirrors). Typically, the White cell was adjusted for 30 passes. As discussed above, a mask limited the width of the 248.4 nm photolysis beam to 1.0 cm, thus giving an absorption path length for BrO detection of 30 cm. One other modification from our earlier approach²² was the installation of masks with a 1.9 cm height aperture at both reaction cell windows along the BrO detection axis; this ensured complete spatial overlap of the BrO detection volume and the 248.4 nm photolysis region. The slits on the 0.22 m monochromator which isolated 338.3 nm radiation were each set at widths of 100 μm , giving a resolution of 0.36 nm; this monochromator resolution is very close to the 0.4 nm resolution employed to obtain the best available measurements of BrO absorption cross sections.²⁴ Since we find that the observed BrO absorption cross section at 338.3 nm is independent of resolution within the range 0.25–0.50 nm, the BrO absorption cross section values at 338.3 nm of $1.55 \times 10^{-17} \text{ cm}^2$ at 298 K and $1.95 \times 10^{-17} \text{ cm}^2$ at 223 K which were reported by Wahner *et al.*²⁴ can be used to convert the measured BrO absorbance to a concentration (as long as the absorption path length is accurately known). Radiation exiting the monochromator was detected by a photomultiplier, the time-dependent output from which was monitored on channel A of a dual channel signal averager with 1.5 μs time resolution and 10 bit voltage resolution.

Time-resolved detection of $O(^3P_J)$ was accomplished using the resonance fluorescence technique.^{7–9,11,18} An atomic resonance lamp, mounted above the reaction cell and perpendicular to both the photolysis and BrO detection axes, excited resonance fluorescence in photolytically generated $O(^3P_J)$ atoms. The resonance lamp consisted of an electrodeless microwave discharge through about 1 Torr of a flowing mixture containing a trace of O_2 in He. The vacuum-UV resonance radiation (at about 130 nm) was coupled out of the lamp through a magnesium fluoride window and into the reaction cell through a magnesium fluoride lens. The region between the lamp window and the cell lens was purged with dry N_2 . Fluorescence was collected by a magnesium fluoride lens on an axis orthogonal to the resonance lamp beam and imaged onto the photocathode of a solar blind photomultiplier. The region between the reaction cell and the photomultiplier was purged with dry N_2 ; in addition, a calcium fluoride window was inserted into this region to prevent detection of Lyman- α emission from hydrogen impurity in the lamp discharge. Signals were processed using photon counting techniques in conjunction with multichannel scaling. Channel B of the dual channel signal averager could be operated in the multichannel scaling mode [for $O(^3P_J)$ detection] while, simultaneously, channel A was operated in the analog mode (for BrO detection).

Typically, 256–1024 pairs of flashes were averaged to obtain $O(^3P_J)$ and BrO temporal profiles with sufficient signal to noise to allow quantitative kinetic analysis. The shot-to-shot stability of the 248.4 nm laser was about $\pm 10\%$. Because BrO was produced under conditions where

$[O(^3P_J)]_0 > [Br_2]_0$, i.e., under conditions where Br_2 was titrated to BrO, 10% fluctuations in 248.4 nm laser power result in very small shot-to-shot variations in the BrO concentration temporal profile.

In order to avoid accumulation of reaction or photolysis products, all experiments were carried out under "slow flow" conditions. To promote spatial uniformity of concentrations and minimize regions of flow stagnation, each of the four ends of the reaction cell had a port. The gas mixture entered the reaction cell through the two ports on the BrO probe beam axis and exited through the two ports on the laser photolysis axis. This flow pattern exhausted the long-lived BrO radicals from the BrO detection volume more rapidly than if the reaction mixture had exited along the BrO detection axis. The linear flow rate through the reaction cell was (typically) 3.5 cm s^{-1} . The repetition rate of the two laser sequence varied from 1/8 Hz at $P=25$ Torr to 1/5 Hz at $P \geq 100$ Torr. These rates were determined by observing the time required for the BrO signal to return to the pretrigger baseline value under typical experimental conditions.

As shown in Fig. 1, the O_3 , Br_2 , and N_2 gases were premixed before entering the reaction cell. The concentrations of Br_2 and N_2 in the reaction mixture were determined through measurement of the appropriate mass flow rates and the total pressure. The fraction of Br_2 in the Br_2 - N_2 mixture, which was prepared manometrically in a 12 ℓ bulb, was measured by photometry at 404.7 nm as described previously.²² Ozone was flowed from a U-tube containing O_3 adsorbed on silica gel and maintained at dry ice temperature (195 K); nitrogen was passed through the U-tube to obtain a stable O_3 - N_2 flow. The ozone concentration was measured *in situ* in the slow flow system by UV photometry at 253.7 nm using an Hg pen-ray lamp as the light source and a 30.2 cm absorption cell positioned between the mixing cell and the reaction cell; interference from absorption of 253.7 nm radiation by Br_2 was negligible for the reaction mixtures employed ($[O_3] \gg [Br_2]$). Conversion of measured ozone absorbances to concentrations employed an O_3 absorption cross section of $1.145 \times 10^{-17} \text{ cm}^2$ at 253.7 nm.²⁵

The gases used in this study had the following stated minimum purities: N_2 , 99.999% and O_2 , 99.99%; they were used as supplied. Ozone was prepared by passing O_2 through a commercial ozonator. It was collected and stored on refrigeration grade silica gel maintained at a temperature of 195 K. The Br_2 used in this study had a stated minimum purity of 99.94%. It was transferred under nitrogen atmosphere into a glass vial fitted with a high vacuum stopcock, and then was degassed repeatedly at 77 K before being used to prepare Br_2 - N_2 mixtures.

III. RESULTS

Observed $O(^3P_J)$ fluorescence and BrO absorbance temporal profiles for a typical experiment are shown in Fig. 2; in this typical experiment, the time delay between the two lasers was 25 ms. At short times, i.e., $t < 5$ ms for the data shown in Fig. 2, the $O(^3P_J)$ concentration is very high, causing the fluorescence signal to be influenced by radiation trapping effects. Thus, the fluorescence signal is proportional to the $O(^3P_J)$ concentration only after the signal has decayed

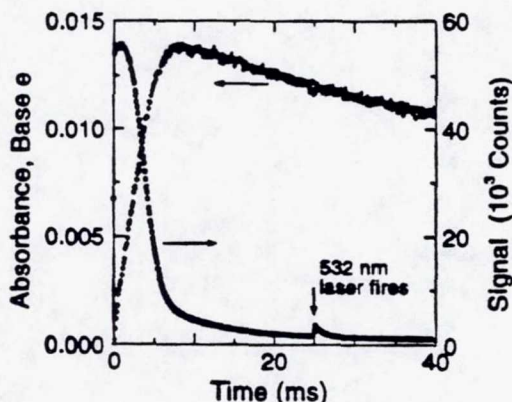


FIG. 2. Typical experimental BrO and $O(^3P_J)$ temporal profiles. Experimental conditions: $T=298$ K; $P=50$ Torr; $[O_3]=7.80 \times 10^{14}$ per cm^3 ; $[Br_2]_0=1.58 \times 10^{13}$ per cm^3 ; $[O]_0=7.4 \times 10^{13}$ per cm^3 ; 512 laser shots averaged; electronic time constant for BrO detection = 50 μs ; $t=0$ is defined to be the time the 248.4 nm laser fires.

significantly from its peak value. The approach to a near-steady-state $O(^3P_J)$ fluorescence level clearly occurs at $t > 10$ ms. Firing of the 532 nm laser at $t=25$ ms results in only a modest increase in the $O(^3P_J)$ fluorescence signal because the ozone absorption cross section at 532 nm is quite low (2.8×10^{-21} cm^2).²⁶ The data in Fig. 2 show that during the first several ms after the 248.4 nm laser fires, BrO appearance "tracks" $O(^3P_J)$ disappearance. Disappearance of BrO at $t > 8$ ms is presumably due to the occurrence of reaction (7b).

The $O(^3P_J)$ fluorescence signal (same data as in Fig. 2) immediately before and after firing of the 532 nm laser is shown in expanded form in Fig. 3. The solid "baseline" in Fig. 3 is obtained by fitting the data in the -10 to -0.1 ms and 7–14 ms time intervals to a double exponential func-

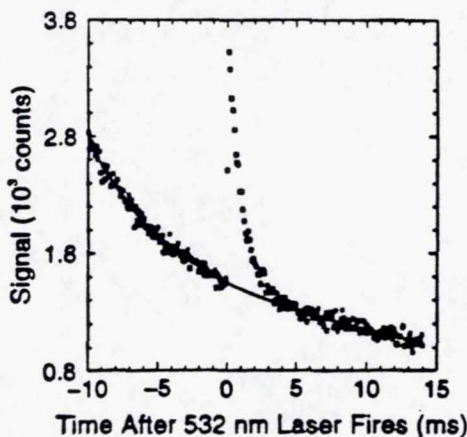


FIG. 3. The same $O(^3P_J)$ temporal profile as shown in Fig. 2 with expanded concentration (i.e., fluorescence signal) scale and expanded time scale around the time the 532 nm laser fired. The solid baseline was obtained from a double exponential fit to the data points in the intervals -10 to -0.1 ms and 7–14 ms where $t=0$ is the time the 532 nm laser fired.

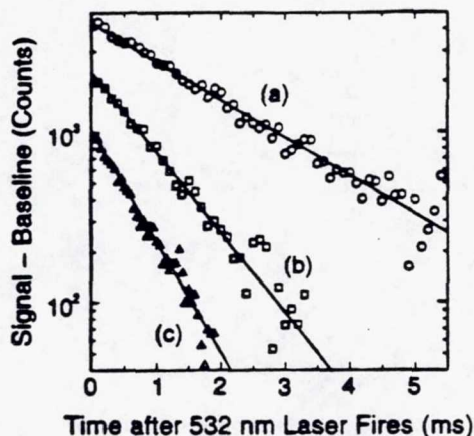


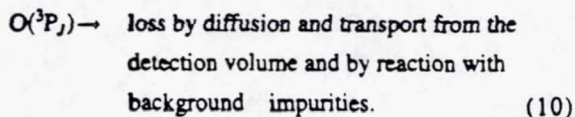
FIG. 4. Typical $[O(^3P_J)]$ relaxation temporal profiles. Trace (b) is the same data as shown in Figs. 2 and 3. $T=298$ K, $P=50$ Torr. Concentrations in units of 10^{13} per cm^3 : $[O_3]_{t=0}=(a) 67.2$, (b) 78.0, (c) 84.4; $[Br_2]_{t=0}=(a) 0.72$, (b) 1.58, (c) 2.25; $[O]_{t=0}=(a) 7.32$, (b) 7.36, (c) 10.0; $[BrO]_{t=0}$ (=average of concentrations deduced by computer simulations and by time-resolved UV absorption measurements)=(a) 1.32, (b) 2.24, (c) 3.16. The 248.4 nm laser fired at $t=0$ and the 532 nm laser fired at $t=t'-\tau$ where τ is the e -folding time for $O(^3P_J)$ relaxation. Number of (pairs of) laser shots averaged=(a) 450, (b) 512, (c) 924. Solid lines are obtained from linear least-squares analyses and give the following pseudo-first-order $O(^3P_J)$ relaxation rates in units of s^{-1} : (a) 515, (b) 1085, (c) 1502. For clarity, traces (a) and (c) are shifted on the vertical axis; the actual signal minus baseline counts for trace (a) are half that shown and for trace (c) are twice that shown.

tional form; the fit is quite good, so the interpolated baseline in the 0–7 ms time interval should be accurate. Subtraction of the interpolated baseline from the total signal yields an $[O(^3P_J)]$ relaxation temporal profile which is exponential, as shown in trace (b) of Fig. 4. Also shown in Fig. 4 are two other $[O(^3P_J)]$ relaxation temporal profiles obtained at the same temperature and pressure as the data shown in Fig. 3; trace (c) was obtained with the highest BrO concentration of the three experiments, while trace (a) was obtained with the lowest BrO concentration. Clearly, the $[O(^3P_J)]$ relaxation rate increases with increasing BrO concentration.

Assuming that all processes contributing to $[O(^3P_J)]$ relaxation are first order or pseudo-first-order, the temporal behavior of the relaxation fluorescence signal should be described by the following relationship:

$$\ln \left(\frac{S_0 - S_{BL,0}}{S_t - S_{BL,t}} \right) = (k_1[BrO] + k_5[Br_2] + k_6[O_3] + k_{10})t = k't, \quad (I)$$

where $t=0$ is defined to be the time at which the 532 nm laser fires, S_0 and S_t are the total signals at times 0 and t , $S_{BL,0}$ and $S_{BL,t}$ are the baseline signals at times 0 and t , and k_{10} is the rate coefficient for the following process:



Equation (I) assumes that the concentrations of BrO, Br_2 , and O_3 are constant over the time interval required for

TABLE I. Assumed mechanism for simulation of $O(^3P_J)$, BrO , $Br(^2P_J)$, Br_2 , and O_3 temporal profiles.

Reaction	Reaction No.	A^{ab}	E/R^{ac}
$O(^3P_J)+BrO \rightarrow Br(^2P_J)+O_2$	(1)	d	d
$Br(^2P_J)+O_3 \rightarrow BrO+O_2$	(2)	17	800
$O(^3P_J)+Br_2 \rightarrow BrO+Br(^2P_J)$	(5)	17.6 ^e	-40 ^f
$O(^3P_J)+O_3 \rightarrow 2O_2$	(6)	8.0	2060
$BrO+BrO \rightarrow 2Br(^2P_J)+O_2$	(7a)	1.4	-150
$BrO+BrO \rightarrow Br_2+O_2$	(7b)	0.060	-600
$O_2(a^1\Delta_g)+O_3 \rightarrow O(^3P_J)+2O_2$	(8)	52.5	2840
$O(^3P_J) \rightarrow \text{bkgrd. loss}$	(10)	10-40 ^f	0

^aArrhenius parameters are taken from Ref. 6 except where otherwise indicated.

^bUnits are 10^{-12} cm³ molecule⁻¹ s⁻¹ except for reaction (10).

^cUnits are degrees kelvin.

^dDetermined from experimental data using an iterative procedure (see the text).

^eFrom Ref. 27.

^fUnits are s⁻¹; rate increases with decreasing pressure; values determined experimentally.

[$O(^3P_J)$] relaxation; this is a good approximation, since the concentrations of all three species change by only a few percent over the time interval of interest. Since [$O(^3P_J)$] relaxation data were typically analyzed over 2-3 e -folding times of decay, we take the (measured or simulated) concentrations of BrO , Br_2 , and O_3 at $t = \tau = 1/k'$ to be the appropriate values for application of Eq. (1). Rate coefficients for reactions (5) and (6) are well established.^{27,28} Values of $k_{10}(P, T)$ were determined experimentally by monitoring the decay of $O(^3P_J)$ following 532 nm laser flash photolysis of O_3/N_2 mixtures; very low O_3 levels were employed in these experiments in order to establish conditions where $k_6[O_3] \ll k_{10}$. Measured values for k_{10} ranged from 10 to 40 s⁻¹; very little temperature dependence was observed, but k_{10} increased with decreasing pressure.

The bimolecular rate coefficients of interest, $k_1(P, T)$, were evaluated from the slopes of k'_{corr} vs [BrO] plots where k'_{corr} is the measured pseudo-first-order decay rate corrected for contributions from Br_2 and O_3

$$k'_{\text{corr}} = k' - k_5[Br_2] - k_6[O_3] = k_1[BrO] + k_{10}. \quad (\text{II})$$

Under the experimental conditions employed in this study, differences between k' and k'_{corr} were dominated by reaction (5), i.e., reaction (6) made a negligible contribution to [$O(^3P_J)$] relaxation. Values for [BrO], [Br_2], and [O_3] as a function of time were determined using the ACUCHEM program²⁹ to numerically integrate the rate equations ([BrO] was, of course, also measured by time-resolved UV absorption). The mechanism assumed for the numerical simulations consisted of reactions (1), (2), (5), (6), (7a), (7b), (8), and (10). Literature values for the temperature-dependent rate coefficients used in the simulations are summarized in Table I. With the exception of k_1 , all other rate coefficients used in the simulations appear to be well established. Because k_1 is highly uncertain, we employed an initial temperature-independent "guesstimate" of 3.0×10^{-11} cm³ molecule⁻¹ s⁻¹ in the simulations.⁶ Concentrations of BrO , Br_2 , and O_3 were then calculated and used to obtain a new value for k_1 ; subsequent iterations had no effect on the

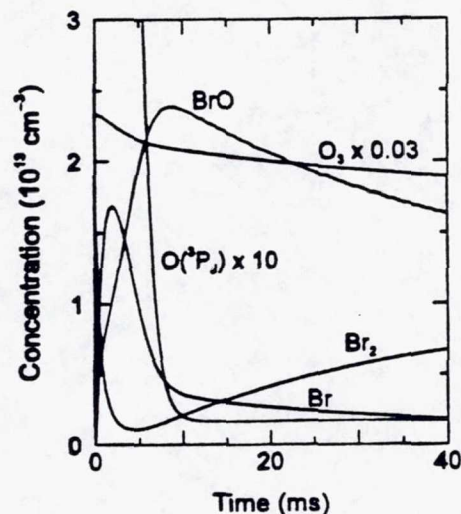


FIG. 5. Simulated temporal profiles for Br_2 , $Br(^2P_J)$, BrO , O_3 , and $O(^3P_J)$ for the conditions employed to obtain the experimental data shown in Figs. 2 and 3. The simulations employ the mechanism and rate coefficients given in Table I, assume $t=0$ is the time that the 248.4 nm laser fires, and ignore concentration changes induced by firing of the 532 nm laser.

derived value for k_1 , i.e., convergence was obtained after a single iteration. Initial concentrations of $O(^3P_J)$ and $Br(^2P_{3/2})$ for use in the simulations were computed from the measured 248.4 nm laser fluence, the measured O_3 and Br_2 concentrations, and well-known O_3 and Br_2 absorption cross sections at 248.4 nm; the O_3 absorption cross section was taken to be 1.05×10^{-17} cm² independent of temperature³⁰ while the Br_2 absorption cross section was taken to be 1.9×10^{-20} cm² (Ref. 31) (assumed to be independent of temperature). Compared to the amount of $Br(^2P_J)$ generated from reactions (1) and (5), the amount generated from Br_2 flash photolysis was very small, ranging from 3×10^9 to 2×10^{10} atoms cm⁻³. Shown in Fig. 5 are simulated temporal profiles for Br_2 , $Br(^2P_J)$, BrO , O_3 , and $O(^3P_J)$ for the conditions employed to obtain the experimental data shown in Figs. 2 and 3.

Typical plots of k' and k'_{corr} vs [BrO] are shown in Fig. 6; for these data ($P=50$ Torr, $T=233$ K), which are typical of all pressures and temperatures investigated, the correction for the $O(^3P_J)+Br_2$ reaction is about 13%. The BrO concentrations plotted in Fig. 6 are averages of the concentrations obtained from the time-resolved absorption measurements and the concentrations obtained from the computer simulations. Typically, BrO concentrations obtained from the absorbance measurements were somewhat higher than those obtained from the simulations. The uncertainty in BrO concentrations is the major source of uncertainty in our reported values for k_1 ; it is discussed in detail below.

The experimental conditions employed in our kinetics experiments are summarized in Table II. Measured bimolecular rate coefficients, $k_1(P, T)$, which are obtained from the slopes of k'_{corr} vs [BrO] plots, are summarized in Table III. It should be noted that values for $k_1(P, T)$ obtained using BrO concentrations evaluated from the UV absorption mea-

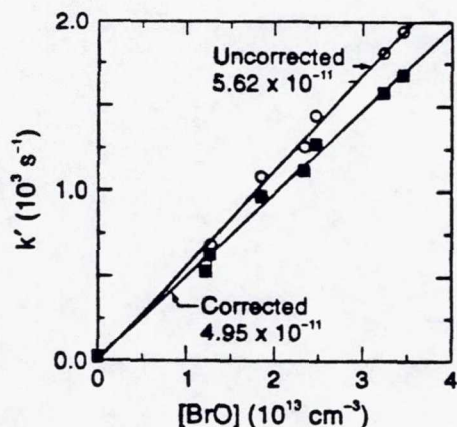


FIG. 6. Typical plots of k' and k'_{corr} vs $[BrO]$, where $t=t'$ is defined as in Fig. 4 and $[BrO]$ is the average of concentrations deduced by computer simulations and by time-resolved UV absorption measurements. $T=233$ K and $P=50$ Torr. Open circles are uncorrected for $O(^3P_J)$ reactions with Br_2 and O_3 while solid squares are corrected for these reactions. Solid lines are obtained from linear least-squares analyses; their slopes give the rate coefficients shown in the figure in units of $\text{cm}^3 \text{molecule}^{-1} \text{s}^{-1}$.

measurements are reported for only six of the twelve P, T combinations for which data are reported. This is because a wavelength calibration error was discovered after some of the experiments were completed; hence, in some of the experiments, BrO was monitored in a wavelength interval which was slightly shifted off the peak of the 7,0 band. Rate coefficients based on UV absorption measurements of $[BrO]$

TABLE III. Rate coefficients for the reaction $O(^3P_J)+BrO \rightarrow Br(^2P_J)+O_2$.

$T(K)$	$P(\text{Torr})$	$k_1(10^{-11} \text{ cm}^3 \text{ molecule}^{-1} \text{ s}^{-1})^{a,b}$	
		A	B
231	25	5.52 ± 0.22	4.68 ± 0.58
233	50	5.30 ± 0.22	4.59 ± 0.38
237	100	5.13 ± 0.20	5.34 ± 0.53
251	50	4.88 ± 0.20	
268	50	5.20 ± 0.48	3.78 ± 0.58
272	50	5.15 ± 0.21	
298	25	4.11 ± 0.37	
298	50	4.94 ± 0.45	3.82 ± 0.52
298	100	4.57 ± 0.18	
298	150	4.52 ± 0.82	
326	50	4.12 ± 0.29	
328	50	4.35 ± 0.14	3.02 ± 0.31

^aErrors are 2σ and represent precision only.

^bA: $[BrO]$ obtained from computer simulations using the mechanism in Table I; B: $[BrO]$ obtained from transient UV absorption measurements.

are reported only for data obtained with BrO monitored at the peak of the 7,0 band.

Examination of Table III shows that, within experimental uncertainty, $k_1(298 \text{ K})$ is independent of pressure over the range 25–150 Torr. Arrhenius plots of the $O(^3P_J)+BrO$ kinetic data are shown in Fig. 7. Separate plots are shown for rate coefficients obtained using (a) BrO concentrations obtained from Acuchem simulations, (b) BrO concentrations obtained from UV absorption measurements, and (c) BrO concentrations obtained from the average of the simulations and the UV absorption measurements. The lines in Fig. 7 are obtained from linear least-squares analyses of the $\ln k_1$ vs

TABLE II. Summary of experimental conditions in the $O(^3P_J)+BrO$ kinetics experiments.

T^a	P^a	Concentrations at $t=0^{a,b}$			$[O]_0/[Br_2]_0$	No. of Expts. ^c	$[BrO]_0^{d,e}$	$k' \text{ }^a$	$k'_{\text{corr}} \text{ }^a$
		O_3	Br_2	O					
231	25	712–1140	3.97–24.0	46.5–70.7	2.9–12	6	6.0–25.0 (9.1–27.2)	372–1580	357–1410
233	50	98–1150	7.56–32.8	55.0–107	3.3–9.5	7	10.0–32.7 (14.4–36.5)	572–1940	529–1680
237	100	944–1160	5.05–21.9	65.7–91.0	4.2–14	4	7.6–25.2 (8.0–23.9)	405–1420	385–300
251	50	852–1070	8.02–25.4	67.8–81.4	2.8–9.4	6	11.7–27.6	650–1580	620–1410
268	50	670–1210	5.94–26.4	61.8–109	3.6–12	6	8.2–28.3 (13.3–37.4)	500–1780	470–1590
272	50	997–1310	6.39–24.8	60.9–82.7	3.3–9.5	5	9.2–26.9	500–1560	466–1370
298	25	664–1250	7.01–25.2	47.1–82.6	3.2–7.3	7	10.0–28.6	556–1480	520–1290
298	50	745–1050	7.60–24.0	62.8–103	4.2–9.9	6	10.5–28.2 (15.8–35.0)	515–1500	483–1380
298	100	818–1030	4.94–18.1	67.6–107	5.1–17	6	7.9–24.5	408–1190	382–1140
298	150	436–1050	6.23–25.5	34.3–106	3.7–14	11	8.7–32.3	350–1650	305–1540
326	50	843–1020	8.40–25.6	64.3–81.6	3.2–7.6	5	11.8–30.3	612–1500	565–1320
328	50	737–967	4.82–19.6	60.4–85.2	4.3–13	4	7.4–23.2 (12.5–34.1)	367–1170	343–1030

^aUnits are $T(K)$; $P(\text{Torr})$; Concentrations ($10^{12} \text{ molecules cm}^{-3}$); k' , $k'_{\text{corr}}(\text{s}^{-1})$.

^b $t=0$ is the time that the 248.4 nm laser fires.

^cExpt. = measurement of one set of $O(^3P_J)$ and BrO temporal profiles.

^dConcentrations in parentheses were obtained from time-resolved UV absorption measurements; other concentrations were obtained from numerical integration of the appropriate rate equations (see the text).

^e t' = one e -folding time for $[O(^3P_J)]$ relaxation after the 532 nm laser fires.

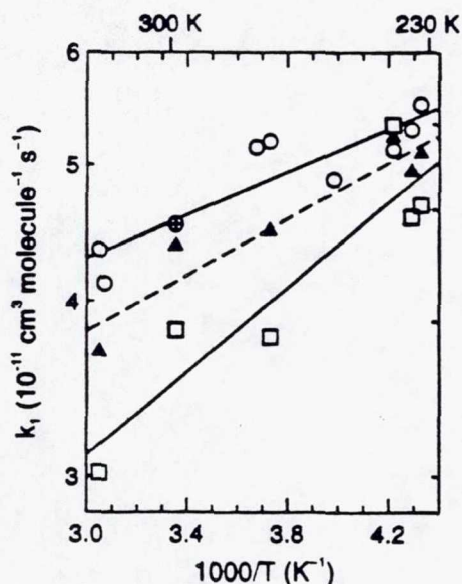


FIG. 7. Arrhenius plots for the $O(^3P_J)+BrO$ reaction. Separate plots are shown for rate coefficients derived from (a) BrO concentrations obtained from computer simulations (open circles, see the text for details), (b) BrO concentrations obtained from time-resolved UV absorption measurements (open squares), and (c) BrO concentrations obtained from the average of the computer simulations and the UV absorption measurements (filled triangles). Solid lines and dashed line are obtained from linear least squares analyses of the $\ln k_1$ vs T^{-1} data and yield the Arrhenius expressions given in the text. The open circle with the "+" inside represents the average of rate coefficients measured at four different pressures (see Table III).

T^{-1} data; these analyses yield the following Arrhenius expressions (units are $10^{-11} \text{ cm}^3 \text{ molecule}^{-1} \text{ s}^{-1}$; uncertainties are 2σ and represent precision only):

[BrO] from simulations:

$$k_1(T) = (2.48 \pm 0.67) \exp[(181 \pm 74)/T],$$

[BrO] from UV absorption:

$$k_1(T) = (1.11 \pm 0.64) \exp[(344 \pm 149)/T],$$

average [BrO]:

$$k_1(T) = (1.91 \pm 0.56) \exp[(230 \pm 76)/T].$$

While the magnitude of the activation energy one would derive from our data depends somewhat on which method for evaluation of the BrO concentration one prefers (see below), our data clearly support a small negative activation energy for reaction (1), i.e., the rate coefficient increases with decreasing temperature.

IV. DISCUSSION

A. Potential systematic errors in $k_1(P, T)$ values

One approach which is commonly employed to validate a kinetics study involves demonstration that the results are independent of wide variations in experimental parameters such as laser fluences and species concentrations. Unfortunately, available laser powers and detection sensitivities as

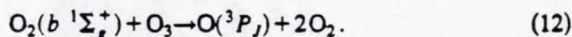
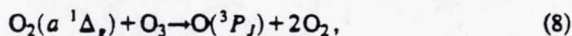
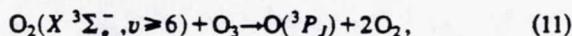
well as constraints dictated by system chemistry limited the range over which important parameters could be varied. Nonetheless a series of experiments were carried out at $P=50$ Torr and $T=269$ K which verified that, for the same initial concentrations of $O(^3P_J)$ and Br_2 , k'_{corr} was independent of a factor of 5 variation in $[O_3]$ ($6-30 \times 10^{14}$ molecules cm^{-3}), a factor of 2 variation in 248.4 nm laser fluence ($5-10 \text{ mJ cm}^{-2}$), and a factor of 1.5 variation in 532 nm laser fluence ($130-195 \text{ mJ cm}^{-2}$). The range of 248.4 nm fluences was limited at the high end by the available laser power and at the low end by the need to generate enough $O(^3P_J)$ to rapidly titrate Br_2 to BrO , thus minimizing interference from the $O(^3P_J)+Br_2$ reaction. The range of 532 nm fluences was also limited at the high end by the available laser power. The lower limit 532 nm fluence was dictated by the requirement that $[O(^3P_J)]$ relaxation temporal profiles be obtained with signal-to-noise ratio suitable for quantitative kinetic analysis, even though the low repetition rate dictated by system chemistry prohibited extensive signal averaging.

Comparison of simulated (Fig. 5) and measured (Fig. 2) $O(^3P_J)$ and BrO temporal profiles shows qualitative but not quantitative agreement. The simulated $O(^3P_J)$ decay to the near-steady-state level is a little faster than observed experimentally while the simulated BrO appearance rate is a little slower than observed experimentally. Also, once near-steady-state conditions are established, the observed $O(^3P_J)$ fluorescence signal continues to decay slowly whereas the simulation predicts that $[O(^3P_J)]$ remains constant or even increases slightly as a function of time; one possible explanation for this difference between observation and simulation would be the existence of a significant (unidentified) $O_2(a^1\Delta_g)$ destruction mechanism other than reaction with O_3 ; an additional first-order $O_2(a^1\Delta_g)$ loss rate of about 90 s^{-1} would yield the best agreement between simulation and experiment. While quantitative differences between simulated and observed $O(^3P_J)$ and BrO temporal profiles do exist, it is important to recognize that (a) the overall agreement is rather good considering the high radical concentrations employed and (b) the accuracy and integrity of this kinetics study is not necessarily dependent upon quantitative agreement between these temporal profiles (although the differences suggest some potential systematic errors which need to be examined). As discussed above, the validity of our determinations of $k_1(P, T)$ is supported by the facts that (a) k'_{corr} values scale linearly as a function of $[BrO]$, (b) k'_{corr} values are independent of the 248.4 and 532 nm laser fluences (at constant $[BrO]$), and (c) $[O(^3P_J)]$ relaxation temporal profiles after the firing of the 532 nm laser are exponential and, according to both observation and simulation, are dominated by reaction (1).

With the exception of the $O(^3P_J)+BrO$ reaction, accurate kinetic data appear to be available for all reactions used in the simulations (Table I). However, additional simulations were carried out where selected rate coefficients were either increased or decreased to see if better agreement between simulation and observation could be obtained. Improved agreement could not be obtained by varying any of the rate coefficients in Table I by factors of 2 or less. Hence, our observations should *not* be considered evidence that one or

more of the Arrhenius parameters in Table I are incorrect.

We have considered in some detail the possibility that the mechanism summarized in Table I is incomplete. This exercise has not led to identification of additional thermal reactions involving species in their ground electronic states which could be important in controlling the temporal behavior of BrO or $O(^3P_J)$. However, reaction (1) is sufficiently exothermic ($62.9 \text{ kcal mol}^{-1}$)⁶ that the O_2 product can be formed with considerable vibrational excitation and/or in any one of three electronic states ($X^3\Sigma_g^-, a^1\Delta_g, b^1\Sigma_g^+$). The production of "hot" O_2 is not only a potential source of the discrepancy between observed and simulated BrO and $O(^3P_J)$ temporal profiles before the firing of the 532 nm laser, it is also a potential kinetic interference in our measurements of k_1 ; this is because $O(^3P_J)$ can be regenerated via the following reactions:



Under the experimental conditions employed to monitor relaxation of $[O(^3P_J)]$ (generated by the 532 nm laser) back to steady state, the rate of production of $O(^3P_J)$ via reaction (8) is several orders of magnitude too slow for this process to represent a significant kinetic interference. Based on time-resolved observation of $O(^3P_J)$ appearance following 300 nm laser flash photolysis of O_3 , Arnold and Comes^{32,33} report the very slow value $k_{11} = 2.8 \times 10^{-15} \text{ cm}^3 \text{ molecule}^{-1} \text{ s}^{-1}$, suggesting that reaction (11) is also too slow to represent a significant kinetic interference. It is, of course, possible that reaction (1) produces $O_2(X^3\Sigma_g^-)$ which is vibrationally hotter than the $O_2(X^3\Sigma_g^-)$ generated by 300 nm photolysis of O_3 and that the rate of reaction (11) increases dramatically with increasing vibrational quantum number. However, Park and Slanger³⁴ have recently shown that the rate of vibrational deactivation of $O_2(X^3\Sigma_g^-, v)$ by N_2 increases with increasing vibrational quantum number up to $v = 19$ (where a two-quantum $v-v$ transfer process is near resonant); hence, any increase in k_{11} as a function of vibrational quantum number would be counterbalanced by a faster competing rate of vibrational relaxation by N_2 buffer gas, so the conclusion that reaction (11) does not contribute significantly to $[O(^3P_J)]$ relaxation should be valid for all energetically accessible vibrational levels of $O_2(X^3\Sigma_g^-)$.

Unlike reactions (8) and (11), reaction (12) is quite fast, i.e., $k_{12}(298 \text{ K}) = 2.2 \times 10^{-11} \text{ cm}^3 \text{ molecule}^{-1} \text{ s}^{-1}$.⁶ Any $O_2(b^1\Sigma_g^+)$ which is generated as a product of reaction (1) would be converted to $O(^3P_J)$ on a time scale which is fast compared to the time scale for $[O(^3P_J)]$ relaxation following the 532 nm laser flash. Hence, our approach for measurement of k_1 is "blind" to a reaction channel which produces $O_2(b^1\Sigma_g^+)$, i.e., we have actually measured $k_{1a} + k_{1b}$, not $k_1 = k_{1a} + k_{1b} + k_{1c}$.

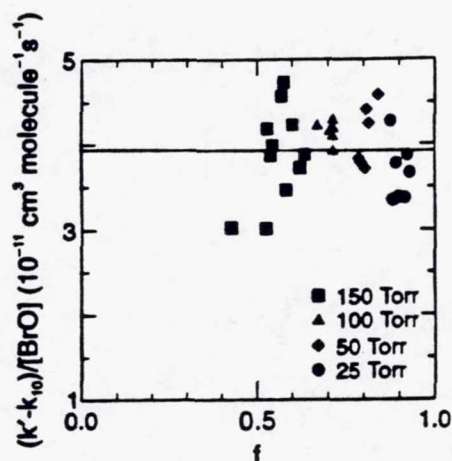
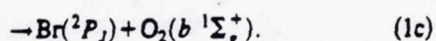
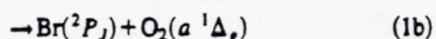
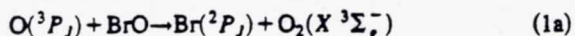
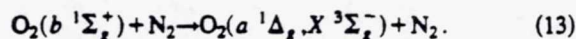


FIG. 8. A plot of bimolecular rate coefficients obtained from individual experiments, i.e., $k_1 = (k'_{\text{corr}} - k_{10})/[BrO]$, vs f , the fraction of $O_2(b^1\Sigma_g^+)$ deactivated by reaction with O_3 . The solid line is obtained from a linear least-squares analysis and gives an $f=0$ intercept of $(3.94 \pm 0.84) \times 10^{-11} \text{ cm}^3 \text{ molecule}^{-1} \text{ s}^{-1}$ and a $f=1$ intercept of $(3.92 \pm 0.32) \times 10^{-11} \text{ cm}^3 \text{ molecule}^{-1} \text{ s}^{-1}$ where the uncertainties are 2σ and represent precision only. These data suggest that the yield of $O_2(b^1\Sigma_g^+)$ from the $O(^3P_J)+BrO$ reaction is very small.

Adiabatic correlation arguments suggest that the branching ratio for channel (1c) should be small, i.e., $BrO(X^2\Pi) + O(^3P_J)$ correlates with $Br(^2P_J) + O_2(X^3\Sigma_g^-, a^1\Delta_g)$ but not with $Br(^2P_J) + O_2(b^1\Sigma_g^+)$. Statistical arguments, which are based on the idea that the most probable products are those with the largest number of energetically accessible quantum states, suggest a negligible branching ratio for channel (1c). Also, Leu and Yung³⁵ have shown that the yield of $O_2(b^1\Sigma_g^+)$ from the analogous $O(^3P_J)+ClO$ reaction is very small, i.e., less than 4.4×10^{-4} . Despite the above rationale for expecting a small $O_2(b^1\Sigma_g^+)$ yield from reaction (1), experimental verification would be reassuring. The rate coefficient for quenching of $O_2(b^1\Sigma_g^+)$ by N_2 is known to be $k_{13} = 2.1 \times 10^{-15} \text{ cm}^3 \text{ molecule}^{-1} \text{ s}^{-1}$ (Ref. 6)



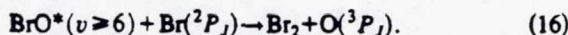
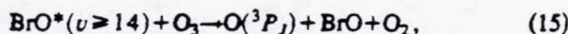
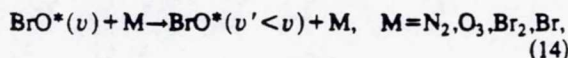
Hence, over the range of N_2 and O_3 partial pressures employed in our study, the fraction of $O_2(b^1\Sigma_g^+)$ which reacts with O_3 , f , spans a considerable range

$$f = k_{12}[O_3]/(k_{12}[O_3] + k_{13}[N_2]). \quad (III)$$

A plot of f vs $(k'_{\text{corr}} - k_{10})/[BrO]$ ($= k_1$) is shown in Fig. 8. Even though reduction in $O(^3P_J)$ detection sensitivity with increasing N_2 pressure prohibited experimentation under conditions where f was very small, the data show no tendency for k_1 to decrease with increasing f [as would be expected if the $O_2(b^1\Sigma_g^+)$ yield from reaction (1) was significant]. We are thus led to conclude that $k_{1a} + k_{1b} \approx k_1$.

Reaction (2) is sufficiently exothermic that BrO can be generated in vibrational levels up to $v = 16$ while reaction (5) can generate BrO in vibrational levels up to $v = 5$. Vibra-

tionally excited BrO (symbolized by BrO^*) could undergo the following transformations upon collision with other species present in the reaction mixture:



There are no kinetic data available in the literature for excited state reactions (14)–(16). Reaction (15) is probably not important in our experimental system because (a) very little BrO is expected to be generated in $v \geq 14$ and (b) vibrational relaxation of $v \geq 14$ by N_2 is almost certainly too fast to allow competition from reaction (15). The chlorine analog of reaction (16) is thought to be responsible for generation of the $O(^3P_J)$ observed when O_3 reacts with an excess of chlorine atoms.⁹ The occurrence of reaction (16) in our experiment could result in increased levels of $O(^3P_J)$ and Br_2 and decreased levels of BrO compared to levels predicted based on the mechanism given in Table I. To examine the potential role of reaction (16) in our study, computer simulations were performed where reactions (14) and (16) were added to the base mechanism (Table I) and values for k_{14} and k_{16} were adjusted over wide ranges. No improvement could be achieved in matching the shapes of the simulated and observed $O(^3P_J)$ temporal profiles. As expected, the inclusion of reaction (16) in the mechanism can depress simulated BrO levels, but only if k_{14} is quite slow. If $k_{14} \sim 10^{-14} \text{ cm}^3 \text{ molecule}^{-1} \text{ s}^{-1}$, i.e., if k_{14} is the same order of magnitude as observed for the analogous $ClO^* + N_2$ relaxation process,⁹ then the dominant fate of BrO^* is deactivation by N_2 . Shown in Fig. 9 is a transient absorption spectrum in the wavelength region of the 7–0 band of the $A^2\Pi-X^2\Pi$ system of BrO; this spectrum, which is discussed in detail below, was obtained using a reaction mixture typical of those employed in the $O(^3P_J)+BrO$ kinetics studies. The spectrum shows no evidence for the presence of BrO^* at “non-thermal-equilibrium” levels; hence, direct experimental evidence supports the idea that vibrational relaxation of BrO^* is rapid in the presence of 25–150 Torr of N_2 .

As discussed briefly above, the most important source of systematic error in this study appears to be evaluation of the absolute concentration of BrO appropriate for use in the kinetic analyses. Two independent methods have been employed to evaluate [BrO]. One method involves numerical integration of a set of rate equations which is based on the mechanism in Table I; experimental photometric, mass flow, and laser fluence measurements allow initial concentrations of O_3 , Br_2 , N_2 , $O(^3P_J)$, and $Br(^2P_J)$ to be evaluated and used as input to the numerical integration routine. The second method involves direct measurement of [BrO] by time-resolved UV absorption at 338.3 nm. Conversion of a measured absorbance at the appropriate time, i.e., one e -folding time for $[O(^3P_J)]$ relaxation after firing the 532 nm laser, employs an experimentally evaluated absorption path length and the best available literature values for the 338.3 nm BrO absorption cross section as a function of temperature,²⁴ since the needed absorption cross sections have been measured at

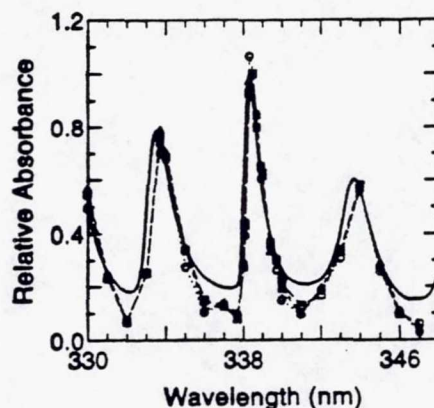


FIG. 9. Transient absorption spectrum over the wavelength range 330–347 nm observed following 248.4 nm laser flash photolysis of an O_3 - Br_2 - N_2 mixture typical of those employed in the $O(^3P_J)+BrO$ kinetics studies. $T=298 \text{ K}$. $P=50 \text{ Torr}$. Concentrations at $t=0$ (= t a time immediately after the 248.4 nm laser fires) in units of 10^{13} per cm^3 are $[O_3]=64.5$, $[Br_2]=2.45$, and $[O]=13.8$. Laser fluence = 13.1 mJ/cm^2 . Absorption path length = 89 cm. Resolution = 0.36 nm. Open squares and long dashed connecting line represent data obtained at the peak of the BrO temporal profile (at $t \sim 7 \text{ ms}$). Open circles and dotted connecting lines represent data obtained at $t=3 \text{ ms}$. Open triangles and short dashed connecting line represent data obtained at $t=20 \text{ ms}$. The solid curve represents the spectrum reported by Wahner *et al.* (Ref. 24) at a resolution of 0.4 nm.

only two temperatures (223 and 298 K),²⁴ the absorption cross section is assumed to depend linearly on temperature over the range of our study, i.e., 231–328 K. Differences between BrO concentrations obtained using the two different methods are largest for experiments with low Br_2 concentrations, and are larger at higher temperatures than at lower temperatures. According to the Arrhenius expressions given above, rate coefficients evaluated based on the two different approaches for determining [BrO] differ by a factor of 1.36 at $T=328 \text{ K}$ and by a factor of 1.10 at $T=231 \text{ K}$ [fortunately, the low temperature regime where agreement is better represents the temperature in the middle stratosphere where reaction (1) is expected to be most important]. In all cases, the slower rate coefficients are obtained using BrO concentrations derived from the time-resolved UV absorption measurements.

A potential systematic error in the UV absorption measurements could arise if BrO were not the only absorbing species at 338.3 nm. To investigate this possibility, experiments were carried out where the time-resolved absorption observed following 248.4 nm laser flash photolysis of Br_2 - O_3 - N_2 mixtures typical of those employed in the $O(^3P_J)+BrO$ kinetics studies was mapped out over a wavelength range (330–347 nm) where the 6–0, 7–0, and 8–0 bands of the BrO $A^2\Pi-X^2\Pi$ system are observed. In particular, we focus on peak-to-valley absorbance ratios to see if there is evidence for continuum absorbance from a species other than BrO. The spectral resolution, 0.36 nm, was the same as employed in the kinetics experiments; it was slightly better than the resolution of 0.4 nm employed by Wahner *et al.*²⁴ to carry out the best available measurements of BrO absorption cross sections as a function of wavelength. To

improve sensitivity in the spectral regions where absorbance was low, the 1 cm mask used in the kinetics studies was removed from the window where the 248.4 nm laser beam entered the reactor; this increased the absorption path length by approximately a factor of 3 at the cost of decreased spatial uniformity in the BrO concentration. Results of a typical experiment are shown in Fig. 9. Experiments employing relatively high and relatively low Br₂ concentrations gave essentially identical results. We find that (1) the observed spectrum is independent of delay time after the 248.4 nm laser fires and (2) peak-to-valley ratios are larger than those reported by Wahner *et al.*²⁴ (the solid line in Fig. 9 represents the spectrum reported by Wahner *et al.*). The low absorbance we observe in the spectral regions between bands could potentially be attributable to changes in the I_0 light level due to depletion of Br₂ and O₃ after the laser flash. However, both Br₂ and O₃ have very low absorption cross sections in the 330–347 nm wavelength region,^{6,30} hence, time-dependent changes in the transmitted light level due to time-dependent changes in the O₃ and Br₂ concentrations are expected to be negligible. The spectroscopy experiments described above lead to two important conclusions. First, it appears that the time-resolved absorption technique employed to monitor BrO in our $O(^3P_J)+BrO$ kinetics experiments is specific to BrO, i.e., there is no evidence for interfering absorptions from other chemical species (such as Br₂O,³⁶ BrOOBr,¹⁵ or O₂^{*}). Also, there are systematic differences in peak-to-valley BrO absorbance ratios obtained in our experiments compared to those reported by Wahner *et al.*;²⁴ these differences, which are potentially important for both laboratory and atmospheric field experiments where [BrO] is deduced from UV absorption measurements, cannot be readily explained at this time.

A number of potential systematic errors in our measurements of $k_1(P,T)$ are discussed above. We believe that errors resulting from excited state reactions or other unidentified side reactions are small. Despite our best efforts, the source of the differences between BrO concentrations evaluated from time-resolved UV absorption measurements and those evaluated from numerical integration of the appropriate rate equations is not clear. At this time, we feel that the best approach is to report $k_1(T)$ values which are based on the average of BrO concentrations obtained by the two methods, and to adjust error bars to span all reasonable possibilities. Based on this strategy, we report the following Arrhenius expression:

$$k_1(T) = 1.91 \times 10^{-11} \exp(230/T) \text{ cm}^3 \text{ molecule}^{-1} \text{ s}^{-1}.$$

The absolute uncertainty in $k_1(T)$ values is estimated to range from $\pm 20\%$ at the low temperature end of the experimental temperature range ($T \sim 230$ K) to $\pm 30\%$ at the high temperature end of the experimental temperature range ($T \sim 330$ K).

B. Comparison with previous research

In the only previous experimental observations relevant to establishing the absolute rate coefficients $k_1(P,T)$, Clyne *et al.*⁵ obtained the estimate $k_1(298 \text{ K}) = 2.5 \times 10^{-11} \text{ cm}^3 \text{ molecule}^{-1} \text{ s}^{-1}$ with an uncertainty range of $(1.0\text{--}5.0) \times 10^{-11} \text{ cm}^3 \text{ molecule}^{-1} \text{ s}^{-1}$; this estimate was ob-

TABLE IV. Arrhenius parameters for $O+XO \rightarrow X+O_2$ radical-radical reactions.

XO	A ^{ab}	E/R ^{bc}	Reference(s)
OH	22	-120	39-41
HO ₂	30	-200	7,8,42-44
NO ₂	6.5	-120	45-49
NO ₃	10	^d	50
ClO	30	-70	9,48,51-55
BrO	19	-230	This work

^aUnits are $10^{-12} \text{ cm}^3 \text{ molecule}^{-1} \text{ s}^{-1}$.

^bValues for XO=OH, HO₂, NO₂, and ClO are recommendations of the NASA panel (Ref. 6), which are based on the references given in the table.

^cUnits are degrees kelvin.

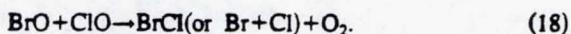
^dThe available temperature dependent data (Ref. 50) suggests that E/R is small, but is insufficient to define the sign of E/R.

tained by observing secondary $O(^3P_J)$ consumption and $Br(^2P_J)$ production in experiments whose primary objective was measurement of rate coefficients for the reactions of $O(^3P_J)$ with Br₂ and BrCl. The experiments of Clyne *et al.* employed a discharge flow-resonance fluorescence technique; total pressures were about 0.5 Torr.⁵ For purposes of stratospheric modeling, the currently recommended Arrhenius expression is $k_1(T) = 3.0 \times 10^{-11} \exp(0/T) \text{ cm}^3 \text{ molecule}^{-1} \text{ s}^{-1}$.⁶ The Arrhenius expression we report in this paper gives $k_1(298 \text{ K}) = 4.13 \times 10^{-11} \text{ cm}^3 \text{ molecule}^{-1} \text{ s}^{-1}$, i.e., 38% faster than the currently recommended value. At 230 K, a temperature characteristic of the stratosphere at altitudes of 30–35 km, our results suggest $k_1(230 \text{ K}) = 5.19 \times 10^{-11} \text{ cm}^3 \text{ molecule}^{-1} \text{ s}^{-1}$, i.e., 73% faster than the currently recommended value. Another discharge-flow study of the $O(^3P_J)+Br_2$ reaction has been reported by Butkovskaya *et al.*³⁷ These authors observed OBrO as a product of secondary chemistry and suggested the wall-catalyzed $O(^3P_J)+BrO$ reaction as a possible OBrO source. This result does not seem relevant for our study where all chemistry occurred in isolation from reactor surfaces.

Arrhenius parameters for $O(^3P_J)+XO \rightarrow X+O_2$ reactions with X=H, OH, NO, NO₂, Cl, and Br are compared in Table IV. All of these reactions are fast with $k(298 \text{ K})$ values ranging from $1.0 \times 10^{-11} \text{ cm}^3 \text{ molecule}^{-1} \text{ s}^{-1}$ for X=NO and NO₂ to $6 \times 10^{-11} \text{ cm}^3 \text{ molecule}^{-1} \text{ s}^{-1}$ for X=OH. Also, with the possible exception of $O(^3P_J)+NO_3$, all reactions are characterized by small negative activation energies, i.e., rate coefficients increase with decreasing temperature. The magnitudes and temperature dependencies observed for $O(^3P_J)+XO$ rate coefficients are characteristic of reactions which occur on potential energy surfaces with a minimum (corresponding to the XO species) along the reaction coordinate. Long range attractive forces result in large cross sections for formation of the energized XO species. Negative activation energies are reasonable because lower energy collisions at lower temperatures result in a longer lifetime for energized XO, thus increasing the probability of passing through the transition state configuration, i.e., reacting, during the energized complex lifetime.

C. Implications for atmospheric chemistry

A one-dimensional photochemical modeling study of stratospheric bromine chemistry has recently been reported by Poulet *et al.*³ This study incorporates up-to-date kinetic information including a much faster rate coefficient for the $BrO+HO_2$ reaction^{3,16} than had been employed in pre-1992 modeling studies. In Fig. 4 of the Poulet *et al.* paper,³ rates of odd oxygen destruction by the most important BrO_x cycles are plotted as a function of altitude and compared with the altitude dependence of the total odd-oxygen destruction rate. Bromine is most significant as a catalyst for odd-oxygen destruction in the lower stratosphere;^{3,38} the key catalytic cycles in this region are those with the following rate-limiting steps:



Poulet *et al.*'s calculations suggest that the catalytic cycle with reaction (1) as the rate limiting step becomes the dominant BrO_x cycle at altitudes above 27 km. Incorporation of our measurements of $k_1(P,T)$ into a model like that employed by Poulet *et al.* will nearly double the rate of odd-oxygen destruction by the $O(^3P_J)+BrO$ cycle in the region around 25 km. As a result the $O(^3P_J)+BrO$ reaction becomes the dominant BrO_x odd-oxygen destruction pathway at all altitudes above 24 km. At 25 km, about 1% of all odd-oxygen destruction occurs via the $O(^3P_J)+BrO$ catalytic cycle.

ACKNOWLEDGMENTS

This research was supported by the National Aeronautics and Space Administration through Grant No. NAGW-1001. We thank T. G. Slanger for making his results on $O_2(X^3\Sigma_g^-)$ vibrational relaxation available to us prior to publication.

- ¹ S. C. Wofsy, M. B. McElroy, and Y. L. Yung, *Geophys. Res. Lett.* **2**, 215 (1975).
- ² Y. L. Yung, J. P. Pinto, R. T. Watson, and S. P. Sander, *J. Atm. Sci.* **37**, 339 (1980).
- ³ G. Poulet, M. Pirre, F. Maguin, R. Ramaroson, and G. Le Bras, *Geophys. Res. Lett.* **19**, 2305 (1992).
- ⁴ P. Fraser, S. Penkett, R. Hariss, Y. Makide, and E. Sanhueza, *Scientific Assessment of Ozone Depletion: 1991*, W. M. O. Global Ozone Research and Monitoring Project, Report No. 25 (unpublished), Chap. 1.
- ⁵ M. A. A. Clyne, P. B. Monkhouse, and L. W. Townsend, *Int. J. Chem. Kinet.* **8**, 425 (1976).
- ⁶ W. B. DeMore, M. J. Molina, S. P. Sander, D. M. Golden, R. F. Hampson, M. J. Kurylo, C. J. Howard, and A. R. Ravishankara, *Chemical Kinetic and Photochemical Data for Use in Stratospheric Modeling*, Evaluation No. 10, JPL Publication No. 92-20, Jet Propulsion Laboratory, Pasadena, CA, 1992.
- ⁷ A. R. Ravishankara, P. H. Wine, and J. M. Nicovich, *J. Chem. Phys.* **78**, 6629 (1983).
- ⁸ J. M. Nicovich and P. H. Wine, *J. Phys. Chem.* **91**, 5118 (1987).
- ⁹ J. M. Nicovich, P. H. Wine, and A. R. Ravishankara, *J. Chem. Phys.* **89**, 5670 (1988).
- ¹⁰ See for example, B. J. Finlayson-Pitts and J. N. Pitts, Jr., *Atmospheric Chemistry: Fundamentals and Experimental Techniques* (Wiley, New York, 1986), Chap. 4-B.

- ¹¹ P. H. Wine and A. R. Ravishankara, *Chem. Phys.* **69**, 365 (1982).
- ¹² R. J. Donovan and D. Husain, *Trans. Faraday Soc.* **62**, 2987 (1966).
- ¹³ S. P. Sander and R. T. Watson, *J. Phys. Chem.* **85**, 4000 (1981).
- ¹⁴ A. A. Turnipseed, J. W. Birks, and J. G. Calvert, *J. Phys. Chem.* **94**, 7477 (1990).
- ¹⁵ R. L. Mauldin III, A. Wahner, and A. R. Ravishankara, *J. Phys. Chem.* **97**, 7585 (1993).
- ¹⁶ I. Bridier, B. Veyret, and R. Lesclaux, *Chem. Phys. Lett.* **201**, 563 (1993).
- ¹⁷ J. P. Singh, J. Bachar, D. W. Setser, and S. Rosenwaks, *J. Phys. Chem.* **89**, 5347 (1985).
- ¹⁸ R. P. Thorn, J. M. Nicovich, J. M. Cronkrite, S. Wang, and P. H. Wine, *Int. J. Chem. Kinet.* (in press).
- ¹⁹ P. H. Wine, J. R. Wells, and J. M. Nicovich, *J. Phys. Chem.* **92**, 2223 (1988).
- ²⁰ A. R. Ravishankara, F. L. Eisele, N. M. Kreutter, and P. H. Wine, *J. Chem. Phys.* **74**, 2267 (1981).
- ²¹ R. P. Thorn, dissertation, Georgia Institute of Technology, 1993.
- ²² R. P. Thorn, E. P. Daykin, and P. H. Wine, *Int. J. Chem. Kinet.* **25**, 521 (1993), and references therein.
- ²³ J. U. White, *J. Opt. Soc. Am.* **32**, 285 (1942).
- ²⁴ A. Wahner, A. R. Ravishankara, S. P. Sander, and R. R. Friedl, *Chem. Phys. Lett.* **152**, 507 (1988).
- ²⁵ K. Yoshino, D. E. Freeman, J. R. Esmond, and W. H. Parkinson, *Planet. Space Sci.* **36**, 395 (1988).
- ²⁶ J. B. Burkholder and R. K. Talukdar, *Geophys. Res. Lett.* **21**, 581 (1994), and references therein.
- ²⁷ J. M. Nicovich and P. H. Wine, *Int. J. Chem. Kinet.* **22**, 379 (1990).
- ²⁸ P. H. Wine, J. M. Nicovich, R. J. Thompson, and A. R. Ravishankara, *J. Phys. Chem.* **87**, 3948 (1983).
- ²⁹ W. Braun, J. T. Herron, and D. K. Kahaner, *Int. J. Chem. Kinet.* **20**, 51 (1988).
- ³⁰ K. Yoshino, J. R. Esmond, D. E. Freeman, and W. H. Parkinson, *J. Geophys. Res.* **98**, 5205 (1993).
- ³¹ J. G. Calvert and J. N. Pitts, Jr., *Photochemistry* (Wiley, New York, 1966).
- ³² I. Arnold and F. J. Comes, *J. Mol. Struct.* **61**, 223 (1980).
- ³³ I. Arnold and F. J. Comes, *Chem. Phys.* **47**, 125 (1980).
- ³⁴ H. Park and T. G. Slanger, *J. Chem. Phys.* **100**, 287 (1994).
- ³⁵ M. T. Leu and Y. L. Yung, *Geophys. Res. Lett.* **14**, 949 (1987).
- ³⁶ J. J. Orlando and J. B. Burkholder, *J. Phys. Chem.* (in press).
- ³⁷ N. I. Butkovskaya, I. I. Morozov, V. L. Tal'rose, and E. S. Vasiliev, *Chem. Phys.* **79**, 21 (1983).
- ³⁸ R. R. Garcia and S. Solomon, *J. Geophys. Res.* **99**, 12937 (1994).
- ³⁹ A. A. Westenbergh, N. deHaas, and J. M. Roscoe, *J. Phys. Chem.* **74**, 3431 (1970).
- ⁴⁰ R. S. Lewis and R. T. Watson, *J. Phys. Chem.* **84**, 3495 (1980).
- ⁴¹ M. J. Howard and I. W. M. Smith, *J. Chem. Soc. Faraday Trans. 2* **77**, 997 (1981).
- ⁴² L. F. Keyser, *J. Phys. Chem.* **86**, 3439 (1982).
- ⁴³ U. C. Sridharan, L. X. Qui, and F. Kaufman, *J. Phys. Chem.* **86**, 4569 (1982).
- ⁴⁴ W. H. Brune, J. J. Schwab, and J. G. Anderson, *J. Phys. Chem.* **87**, 4503 (1983).
- ⁴⁵ D. D. Davis, J. T. Herron, and R. E. Huie, *J. Chem. Phys.* **58**, 530 (1973).
- ⁴⁶ T. G. Slanger, G. J. Wood, and G. Black, *Int. J. Chem. Kinet.* **5**, 615 (1973).
- ⁴⁷ P. P. Bemard, M. A. A. Clyne, and R. T. Watson, *J. Chem. Soc. Faraday Trans. 2* **70**, 564 (1974).
- ⁴⁸ A. P. Ongstad and J. W. Birks, *J. Chem. Phys.* **85**, 3359 (1986).
- ⁴⁹ R. Geers-Muller and F. Stuhl, *Chem. Phys. Lett.* **135**, 263 (1987).
- ⁵⁰ R. A. Graham and H. S. Johnston, *J. Phys. Chem.* **82**, 254 (1978).
- ⁵¹ M. S. Zahniser and F. Kaufman, *J. Chem. Phys.* **66**, 3673 (1977).
- ⁵² A. P. Ongstad and J. W. Birks, *J. Chem. Phys.* **81**, 3922 (1984).
- ⁵³ M. T. Leu, *J. Phys. Chem.* **88**, 1394 (1984).
- ⁵⁴ J. J. Margitan, *J. Phys. Chem.* **88**, 3638 (1984).
- ⁵⁵ J. J. Schwab, D. W. Toobey, W. H. Brune, and J. G. Anderson, *J. Geophys. Res.* **89**, 9581 (1984).

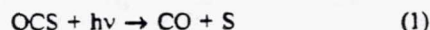
Quantum yield for carbon monoxide production in the 248 nm photodissociation of carbonyl sulfide (OCS)

Z. Zhao, R. E. Stickel, and P. H. Wine
Georgia Institute of Technology, Atlanta

Abstract. Tunable diode laser absorption spectroscopy has been coupled with excimer laser flash photolysis to measure the quantum yield for CO production from 248 nm photodissociation of carbonyl sulfide (OCS) relative to the well-known quantum yield for CO production from 248 nm photolysis of phosgene (Cl_2CO). The temporal resolution of the experiments was sufficient to distinguish CO formed directly by photodissociation from that formed by subsequent $\text{S}(^3\text{P}_1)$ reaction with OCS. Under the experimental conditions employed, CO formation via the fast $\text{S}(^1\text{D}_2) + \text{OCS}$ reaction was minimal. Measurements at 297K and total pressures from 4 to 100 Torr $\text{N}_2 + \text{N}_2\text{O}$ show the CO yield to be greater than 0.95 and most likely unity. This result suggests that the contribution of OCS as a precursor to the lower stratospheric sulfate aerosol layer is somewhat larger than previously thought.

Introduction

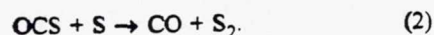
Stratospheric sulfate aerosols, first discovered over three decades ago [Junge and Manson, 1961], have been the subject of numerous investigations motivated by their potential influence on global climate and, more recently, their potential involvement in heterogeneous stratospheric chemistry. Diffusion of carbonyl sulfide (OCS) from the troposphere has been identified as a potentially significant source of stratospheric sulfur [Crutzen, 1976] and at least two studies have suggested that anthropogenic OCS emissions are causing a measurable increase in stratospheric sulfate aerosol levels [Sedlacek et al., 1983; Hofmann, 1990]. In the stratosphere OCS can be photolyzed by solar ultraviolet radiation



or oxidized by reactions with oxygen atoms or OH radicals to produce sulfur species which are readily converted to sulfate aerosol [Berresheim, et al., 1995]. Current estimates of the impact of photolysis reaction (1) are based on consistent measurements of OCS photoabsorption cross sections (discussed below) and two somewhat disparate reports of the photodissociation quantum yield (which equals the quantum yield for CO production) [Sidhu et al., 1966; Rudolph and Inn, 1981]. Both of the quantum yield studies utilized low intensity, continuous light sources which irradiated the OCS sample for periods of several minutes or longer. Under these conditions, the sulfur atom formed in reaction (1) further reacted with OCS to produce a second CO:

Copyright 1995 by the American Geophysical Union.

Paper number 95GL00170
0094-8534/95/95GL-00170\$03.00

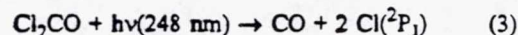


This second step was assumed to be 100% efficient; hence, the primary yield of CO from the photolysis step (Φ) was taken to be one half the measured CO divided by the number of photons absorbed. Sidhu et al. [1966], using the partial pressure of non-condensable (at 77K) gas as their CO measurement technique, reported the values $\Phi = 0.91$ and 0.90 for the photolysis wavelengths 253.7 nm and 228.8 nm, respectively. While they did not quote uncertainty limits, they acknowledged that experimental error may have caused the observed yields to be less than unity. Rudolph and Inn [1981], using resonance fluorescence to detect CO after freezing out unreacted OCS at 77K, made measurements at five photolysis wavelengths from 214.0 to 253.7 nm and reported the value $\Phi = 0.72 \pm 0.08$ essentially independent of wavelength. These authors noted that structured absorption features in the OCS spectrum appear to account for 5–10% of the total oscillator strength while their yield result indicates a 28% bound state contribution. They suggested that perturbations between the $^1\text{A}'$ and $^1\text{A}''$ components of the OCS excited electronic state may obscure some of the structure. However, as noted by Atkinson et al. [1992], there is currently no reported evidence for fluorescence from photoexcited OCS, and this fact, taken together with the observed wavelength independence of the CO quantum yield and the paucity of structure in the photoabsorption spectrum, suggests that dissociation may be the only significant loss channel for electronically excited OCS.

In this letter, we report measurements of the quantum yield for CO production from 248 nm photodissociation of OCS; our results suggest that this quantum yield is unity.

Experimental Technique

In the present work, tunable diode laser absorption was used to follow the concentration of CO after laser flash photolysis of flowing $\text{OCS}/\text{N}_2/\text{N}_2\text{O}$ and $\text{Cl}_2\text{CO}/\text{N}_2/\text{N}_2\text{O}$ gas mixtures. A number of possible systematic errors were avoided by using 248 nm photolysis of phosgene (Cl_2CO) as an *in situ* unit yield calibration standard [Stickel et al., 1993].



The quantum yield for CO production from reaction (1) was determined by performing back-to-back experiments, one with OCS and one with Cl_2CO as the photolyte, and taking the ratio of observed CO absorbances with corrections for small variations in photolysis energy and photolyte concentration. The apparatus is similar to that used for a number of previously published studies [e.g. Stickel et al., 1993]; hence, only a brief description is included here.

The photolytic light source was a KrF excimer laser (Lambda Physik EMG 200) which produced 248 nm pulses of approximately 25 ns duration with an intensity of up to 30

mJ cm⁻² in the sample gas. The infrared probe beam was provided by a lead-salt diode laser (Laser Photonics/Analytics 5622) and detected by HgCdTe detectors cooled to 77K. A portion of the probe beam was diverted to a static CO reference cell. The probe wavelength was modulated (typically at 40 kHz) to give a first derivative reference signal which was used to stabilize the laser output on a CO rotational line near the peak of the P branch of the (1,0) vibrational transition (the P6 line at 2119.68 cm⁻¹ and the P9 line at 2107.42 cm⁻¹ were used). The photolysis and probe beams were merged by a dichroic optic and directed longitudinally through the sample cell, which consisted of a pyrex tube of 25 mm inside diameter and 118 cm length with calcium fluoride windows epoxied to the ends. A second dichroic separated the transmitted IR beam which was then passed through a 0.5 m monochromator for mode selection. The detected signal was digitized, summed over multiple flashes (typically 32) and stored for later second harmonic analysis. The linearity of the second harmonic signal was verified by CO standard addition.

In order to avoid accumulation of photolysis products, all experiments were carried out under "slow flow" conditions such that the contents of the cell were nearly completely replaced between flashes. Photolyte concentrations in the sample cell were determined in two ways: (1) using bulb partial pressures and flow mixing ratios, and (2) using *in situ* photometry at 228.8 nm. For reasons discussed below, the photometric determinations were used exclusively in the quantum yield analysis although the agreement between the photometric and flow measurements was typically 5% or better.

The gases used in this study were supplied with the following stated minimum purities: N₂, 99.999%; N₂O, 99.99%; OCS, 97.5%; Cl₂CO, 99.0%. The N₂ and N₂O were used as supplied. The Cl₂CO was degassed at 77K before use. Three different OCS preparations were used: (1) as supplied, (2) degassed at 77K, and (3) filtered through ascarite and trapped at 77K [Friedl, 1984]. Experimental results were found to be independent of OCS purification technique.

Results and Discussion

Typical data from a single quantum yield measurement are shown in Figure 1. Linear fits to both pre- and post-flash data were extrapolated to the instant of photolysis to give the amount of CO produced by the flash. As explained below, this signal includes CO from both photolysis and fast S(¹D₂) chemistry. The resulting infrared CO absorption signal observed in an OCS experiment (S) can be expressed as

$$S = G * Y * [\text{OCS}] * \sigma(\text{OCS}, 248) * E(\text{OCS}) \quad (\text{I})$$

and the corresponding expression for a Cl₂CO experiment is

$$R = G * [\text{Cl}_2\text{CO}] * \sigma(\text{Cl}_2\text{CO}, 248) * E(\text{Cl}_2\text{CO}) \quad (\text{II})$$

In both cases G is the instrumental response, σ is the appropriate photoabsorption cross section for the excimer laser flash and E is the flash energy. If the concentrations of OCS and Cl₂CO are determined by 228.8 nm photometry in the same absorption cell, the observed CO yield (Y) can be found from

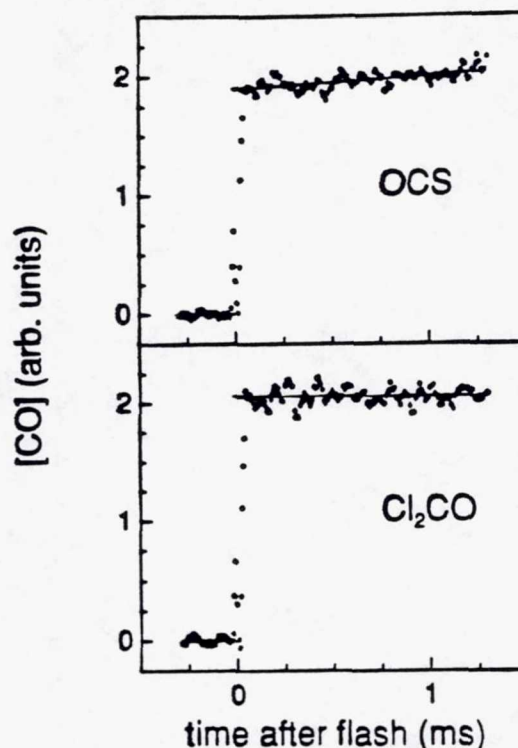


Figure 1. Typical CO temporal profiles observed in back-to-back experiments with first OCS and then Cl₂CO as the photolyte. Experimental conditions: T = 297K; P = 31 Torr. The mean flash intensity was 22.7 mJ cm⁻² for the OCS experiment and 22.4 mJ cm⁻² for the phosgene experiment. Concentrations were, in units of 10¹⁵ molec cm⁻³, [OCS] = 12.6; [Cl₂CO] = 3.25; [N₂O] = 255. The observed yield (Y) is 1.041 which leads to the value $\Phi = 1.035$ when corrected for CO production from the S(¹D₂) + OCS reaction.

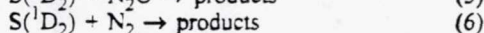
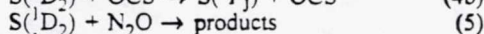
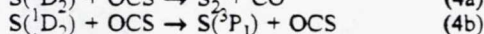
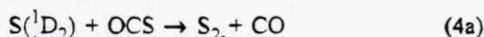
$$Y = \frac{\alpha(\text{OCS}, 229) * \alpha(\text{Cl}_2\text{CO}, 248)}{\alpha(\text{OCS}, 248) * \alpha(\text{Cl}_2\text{CO}, 229)} * \quad (\text{III})$$

$$\frac{S * \ln[I_0(\text{Cl}_2\text{CO})/I(\text{Cl}_2\text{CO})] * E(\text{Cl}_2\text{CO})}{R * \ln[I_0(\text{OCS})/I(\text{OCS})] * E(\text{OCS})}$$

where I₀ and I are the usual photometric intensities. Aside from the experimental results, i.e., S, R, I₀(Cl₂CO), I(Cl₂CO), I₀(OCS), I(OCS), E(Cl₂CO), E(OCS), the observed yield depends on absorption cross section ratios for the two photolytes (i.e., OCS and Cl₂CO) at the photolysis and photometric wavelengths. These ratios depend rather strongly on the exact wavelengths and, for OCS, on the gas temperature. The KrF laser spectrum was measured in the course of this study and found to have a single peak at 248.35 nm with a full width at half maximum of 0.4 nm. The ratio $\sigma(\text{OCS}, 229)/\sigma(\text{OCS}, 248)$ was determined by interpolation from three published tables of absorption cross sections [Molina et al., 1981; Rudolph and Inn, 1981; Locker et al., 1983]. The temperature dependence data of Locker et al. were used to reduce all three results to the center of the experimental temperature range of 296.5 to 298.0 K. The mean and standard deviation of the three OCS absorption cross section ratios are 12.2 ± 0.2. The ratio

$\sigma(\text{Cl}_2\text{CO}, 248)/\sigma(\text{Cl}_2\text{CO}, 229)$ was measured in the course of this study to be 0.657 ± 0.005 . Hence, the factor comprising the four absorption cross sections in equation III is 8.02 ± 0.15 (uncertainty is 1σ).

The only thermodynamically allowed products from 248 nm photolysis of ground state OCS are $\text{CO}(X^1\Sigma^+)$ and a sulfur atom in either the ($^3\text{P}_j$) or ($^1\text{D}_2$) state. Sidhu et al. [1966] observed that at least 74% of the sulfur atoms are formed in the ($^1\text{D}_2$) state, in good agreement with the later work of Breckenridge and Taube [1970]. A more recent study by Sivakumar et al. [1988] has shown that for wavelengths from 222 to 248 nm, $\text{S}(^1\text{D}_2)$ is the only sulfur fragment and that CO is formed only in the lowest vibrational level but with high rotational excitation. In all the OCS experiments, CO formed by the reaction of $\text{S}(^3\text{P}_j)$ with OCS ($k(298\text{K}) = 3.3 \times 10^{-15} \text{ cm}^3 \text{ molecule}^{-1} \text{ s}^{-1}$ [Klemm and Davis, 1974]) was produced slowly enough to be easily distinguished from photolytic CO. However, CO generated via the much faster $\text{S}(^1\text{D}_2) + \text{OCS}$ reaction was essentially indistinguishable from photolytically generated CO. In the Cl_2CO experiments a substantial fraction of the photolytic CO is vibrationally excited and nitrous oxide was added to the sample mixture to relax the excited CO. To minimize differences (such as IR line broadening) between the two sets of experiments, N_2O was also added to the OCS mixtures. Some analysis of the reactions of $\text{S}(^1\text{D}_2)$ with OCS and N_2O is thus required to correct the observed CO yield (Y) to the actual quantum yield (Φ).



The total rate constant for reaction (4), i.e., $k_{4a} + k_{4b}$, in units of $\text{cm}^3 \text{ molecule}^{-1} \text{ s}^{-1}$ has been reported variously as 1.2×10^{-10} [Addison et al., 1979], 3.0×10^{-10} [Addison et al., 1980; van Veen et al., 1983] and 1.5×10^{-10} [Black and Jusinski, 1985]. The branching ratio for reaction (4a), $r_4 \equiv k_{4a}/k_4$, is much less certain; Donovan et al. [1969] suggested $r_4 \geq 0.8$ while Breckenridge and Taube [1970] reported $r_4 \leq 0.8$. More recently Black [1986] observed $r_4 = 0.20 \pm 0.05$.

Table 1. Kinetic data used for correcting observed quantum yields for the occurrence of $\text{S}(^1\text{D}_2) + \text{OCS}$ reaction. The "Best Estimate" values are the result of a critical evaluation of the literature while the "Max. Corr." values were chosen to give the largest correction consistent with literature values for k_4 , r_4 , k_5 , and k_6 . Units of rate constants are $10^{-11} \text{ cm}^3 \text{ molecule}^{-1} \text{ s}^{-1}$.

Parameter	Best Estimate	Max. Corr.
k_4	20	30
r_4	0.25	0.8
k_5	15	5.0
k_6	8.0	6.0

The rate constant for reaction (5) has been reported as $0.6 * k_4$ [Breckenridge and Taube, 1970], $0.4 * k_4$ [Donovan and Breckenridge, 1971] and as $1.6 \times 10^{-10} \text{ cm}^3 \text{ molecule}^{-1} \text{ s}^{-1}$ [Black and Jusinski, 1985]. For reaction (6), Black and Jusinski [1985] measured a rate constant of $8.5 \times 10^{-11} \text{ cm}^3 \text{ molecule}^{-1} \text{ s}^{-1}$ and McBane et al. [1992] reported $(7.1 \pm 1.0) \times 10^{-11} \text{ cm}^3 \text{ molecule}^{-1} \text{ s}^{-1}$. In the present case the observed CO yield (Y) is given by

$$Y = \Phi * \left\{ 1 + \frac{B * r_4 * k_4 * [\text{OCS}]}{k_4 * [\text{OCS}] + k_5 * [\text{N}_2\text{O}] + k_6 * [\text{N}_2]} \right\} \quad (\text{IV})$$

where B is the fraction of sulfur atoms formed in the $^1\text{D}_2$ state (assumed here to be unity). Because the error term depends linearly on the highly uncertain branching ratio r_4 , we have chosen to adopt both "best estimate" and "maximum" corrections for the chemically generated CO signal. The rate constants and branching ratios for both cases are given in Table 1.

Quantum yield results are presented as a function of total gas pressure in Table 2. Averaged over the entire data set, the best estimate correction for secondary CO production reduced the observed yield by 2 percent while the corresponding maximum correction was 10 percent. The apparent pressure dependence of Φ values obtained using the maximum correction (see Table 2) suggests that the maximum

Table 2. Summary of Experimental Results^a

P	Expts.	[OCS]	[Cl ₂ CO]	[N ₂ O]	Laser Fluence	Φ^b		
						A	B	C
3.6	3	9.5 - 9.6	2.1 - 2.2	70 - 72	23.6 - 24.4	1.02	0.99	0.81
7	3	18.8 - 19.9	4.2 - 4.3	137 - 141	23.8 - 24.6	1.07	1.04	0.85
10	36	6.4 - 26.9	1.3 - 6.5	48 - 310	7.6 - 26.3	1.08	1.06	0.94
15	3	12.0 - 12.3	2.7 - 2.8	89 - 90	23.9 - 24.8	1.08	1.07	0.99
20	3	10.6 - 12.4	2.8 - 2.9	90 - 91	23.3 - 24.8	1.05	1.04	0.98
30	7	12.2 - 13.6	2.8 - 4.6	89 - 262	19.1 - 23.3	1.09	1.08	1.03
40	14	10.2 - 44.1	2.4 - 8.5	90 - 203	22.9 - 24.5	1.00	0.99	0.94
50	3	20.5 - 21.5	4.6 - 5.0	151 - 153	23.4 - 23.8	0.96	0.95	0.91
60	3	23.1 - 25.3	5.1 - 5.7	180 - 181	23.6 - 24.0	1.02	1.01	0.97
80	3	30.4 - 32.0	7.2 - 7.7	239 - 240	23.5 - 24.9	1.11	1.10	1.06
100	11	12.2 - 42.4	2.6 - 10.5	302 - 315	23.0 - 24.6	1.06	1.06	1.02
89		6.4 - 44.1	1.3 - 10.5	48 - 315	7.6 - 26.3	1.06 ± 0.04	1.04 ± 0.04	0.96 ± 0.05

(a) Units are P(Torr); Concentrations ($10^{15} \text{ molecules cm}^{-3}$); Fluence (mJ cm^{-2}).

(b) A: uncorrected yield; B: best estimate correction for secondary CO production; C: maximum possible correction for secondary CO production.

corrections are overly severe. The best estimate correction of two percent is smaller than the experimental uncertainty and suggests that reaction (4a) is not a significant source of CO in the present work. The yields and sample standard deviations at each of the pressures shown in Table 2 are all comparable to the overall results. This is a good indication that the measurement errors are uniformly random. The best estimate value for $\Phi \pm 1\sigma$ of 1.04 ± 0.04 represents the weighted mean and standard deviation of the results at each pressure after application of the "best estimate" correction for secondary CO production; the weighting factors are the number of experiments at each pressure. Combining the 4% variability in the measured value for Φ with an estimated 2% standard deviation in the product of absorption cross section ratios appearing in equation (III), leads to an overall 2σ uncertainty of 9%, i.e., $\Phi = 1.04 \pm 0.09$ at the 95% confidence level. Hence, we report $\Phi > 0.95$ with a most probable value of unity. It should be remembered that the value of Φ we report is actually the ratio of the CO yield from OCS photolysis to the CO yield from Cl_2CO photolysis. However, it seems virtually certain that the CO yield from Cl_2CO photolysis is unity.

The role of OCS as a source of stratospheric background (i.e., non-volcanic) sulfur aerosol has recently been analyzed by Chin and Davis [1994]. Using 0.85 as the OCS photodissociation quantum yield, i.e., the average of estimated maximum and minimum values, Chin and Davis conclude that photodissociation is the dominant stratospheric OCS destruction process and calculate a production rate of stratospheric background aerosol from OCS oxidation of $3.2 \times 10^{10} \text{ g S yr}^{-1}$, i.e., only 20–50% of the most recent estimates of the amount needed to maintain the background aerosol level [Servant, 1986; Hofmann, 1990]. Another interesting aspect of the Chin and Davis study is their finding that about 90% of OCS which is transported from the troposphere into the stratosphere is not photochemically destroyed, but instead is transported back to the troposphere where most of it is removed via uptake by vegetation. The OCS photodissociation quantum yield reported in this study will increase the calculated production rate of stratospheric background aerosol from OCS oxidation by about 15%, and will also slightly decrease the percentage of OCS which cycles from the stratosphere back to the troposphere without being photochemically destroyed.

Acknowledgments. This research was supported by the National Science Foundation through grant ATM-9412237 and by the National Aeronautics and Space Administration through grant NAGW-1001. We thank Dr. J. Joens for helpful discussions concerning OCS absorption cross sections.

References

- Addison, M. C., C. D. Byrne, and R. J. Donovan, Direct observation of $\text{S}(3^1\text{D}_2)$ and determination of the absolute rate of reaction with OCS, *Chem. Phys. Lett.*, **64**, 57–59, 1979.
- Addison, M. C., R. J. Donovan, and C. Fotakis, Resonance fluorescence study of electronically excited sulphur atoms: reactions of $\text{S}(3^1\text{D}_2)$, *Chem. Phys. Lett.*, **74**, 58–62, 1980.
- Atkinson, R., D. L. Baulch, R. A. Cox, R. F. Hampson, Jr., J. A. Kerr, and J. Troe, Evaluated kinetic and photochemical data for atmospheric chemistry, supplement IV, *J. Phys. Chem. Ref. Data* **21**, 1125–1568, 1992.
- Berresheim, H., P. H. Wine, and D. D. Davis, Sulfur in the atmosphere, in *Composition, Chemistry, and Climate of the Atmosphere*, edited by H. B. Singh, Van Nostrand Reinhold, 1995, in press.
- Black, G., Branching ratios for quenching and reaction in the interaction of $\text{S}(3^1\text{D}_2)$ with various gases, *J. Chem. Phys.*, **84**, 1345–1348, 1986.
- Black, G., and L. E. Jusinski, Rate coefficients for $\text{S}(3^1\text{D})$ removal at 300K, *J. Chem. Phys.*, **82**, 789–793, 1985.
- Breckenridge, W. H., and H. Taube, Some reactions of ground-state (^3P) and electronically excited (^1D) sulfur atoms, *J. Chem. Phys.*, **53**, 1750–1767, 1970.
- Chin, M., and D. D. Davis, A re-analysis of carbonyl sulfide as a source of stratospheric background sulfur aerosol, *J. Geophys. Res.*, in press, 1995.
- Crutzen, P. J., The possible importance of CSO for the sulfate layer of the stratosphere, *Geophys. Res. Lett.*, **3**, 73–76, 1976.
- Donovan, R. J., L. J. Kirsch, and D. Husain, Rate of the reaction of $\text{S}(3p^4 \ ^1\text{D}_2)$ with OCS, *Nature*, **222**, 1164–1165, 1969.
- Donovan, R. J., and W. H. Breckenridge, Reaction of $\text{S}(3^1\text{D}_2)$ with N_2O , *Chem. Phys. Lett.*, **11**, 520–522, 1971.
- Fiedl, R. R., Spectroscopic and chemical studies of the SH and SD free radicals, *Dissertation, Harvard University*, p. 60, 1984.
- Hofmann, D. J., Increase in the stratospheric background sulfuric acid aerosol mass in the past 10 years, *Science*, **218**, 996–1000, 1990.
- Junge, C. E., and J. E. Manson, Stratospheric aerosol studies, *J. Geophys. Res.*, **66**, 2163–2182, 1961.
- Klemm, R. B., and D. D. Davis, A flash photolysis-resonance fluorescence kinetics study of the reaction $\text{S}(^3\text{P}) + \text{OCS}$, *J. Phys. Chem.*, **78**, 1137–1140, 1974.
- Locker, J. R., J. B. Burkholder, E. J. Bair, and H. A. Webster III, Thermally excited vibrational components of the $\text{A} \leftarrow \text{X}^1\Sigma^+$ system of OCS, *J. Phys. Chem.*, **87**, 1864–1868, 1983.
- McBane, G. C., I. Burak, G. E. Hall, P. L. Houston, The $\text{S}(^1\text{D}) + \text{N}_2$ quenching process: determination of branching ratios to triplet fine structure products, *J. Phys. Chem.*, **96**, 753–755, 1992.
- Molina, L. T., J. J. Lamb, and M. J. Molina, Temperature dependent UV absorption cross sections for carbonyl sulfide, *Geophys. Res. Lett.*, **8**, 1008–1011, 1981.
- Rudolph, R. N., and E. C. Y. Inn, OCS photolysis and absorption in the 200- to 300-nm region, *J. Geophys. Res.*, **86**, 9891–9894, 1981.
- Sedlacek, W. A., E. J. Mroz, A. L. Lazarus, and B. W. Gandrud, A decade of stratospheric sulfate measurements compared with observations of volcanic eruptions, *J. Geophys. Res.*, **88**, 3741–3776, 1983.
- Servant, J., The burden of the sulphate layer of the stratosphere during volcanic "Quiescent" periods, *Tellus*, **38B**, 74–79, 1986.
- Sidhu, K. S., I. G. Csizmadia, O. P. Strausz, and H. E. Gunning, The reactions of sulfur atoms. VII. The ultraviolet spectrum, the photolysis, and the mercury sensitization of carbonyl sulfide, *J. Am. Chem. Soc.*, **88**, 2412–2417, 1966.
- Sivakumar, N., G. E. Hall, P. L. Houston, J. W. Hepburn, and I. Burak, State-resolved photodissociation of OCS monomers and clusters, *J. Chem. Phys.*, **88**, 3692–3708, 1988.
- Stickel, R. E., M. Chin, E. P. Daykin, A. J. Hynes, P. H. Wine, and T. J. Wallington, Mechanistic studies of the OH-initiated oxidation of CS_2 in the presence of O_2 , *J. Phys. Chem.*, **97**, 13653–13661, 1993, and references therein.
- van Veen, N., P. Brewer, P. Das, and R. Bersohn, The adiabatic and diabatic reactions of $\text{S}(^1\text{D})$ atoms with OCS: Internal state distribution of the S_2 products, *J. Chem. Phys.*, **79**, 4295–4301, 1983.

R. E. Stickel, EOEML-GTRI, Georgia Tech, Atlanta, GA 30332-0865
 P. H. Wine, School of Chemistry & Biochemistry, Georgia Tech, Atlanta, GA 30332-0400
 Z. Zhao, School of Earth & Atmospheric Sciences, Georgia Tech, Atlanta, GA 30332-0340

(Received August 10, 1994; revised November 25, 1994; accepted December 27, 1994.)

The fate of atmospheric phosgene and the stratospheric chlorine loadings of its parent compounds: CCl_4 , C_2Cl_4 , C_2HCl_3 , CH_3CCl_3 , and CHCl_3

omit
95A 75017

T. P. Kindler,¹ W. L. Chameides, P. H. Wine,² D. M. Cunnold, and F. N. Alyea

School of Earth and Atmospheric Sciences, Georgia Institute of Technology, Atlanta

J. A. Franklin

Solvay S.A., Central Laboratory, Brussels, Belgium

Abstract. A study of the tropospheric and stratospheric cycles of phosgene is carried out to determine its fate and ultimate role in controlling the ozone depletion potentials of its parent compounds (CCl_4 , C_2Cl_4 , CH_3CCl_3 , CHCl_3 , and C_2HCl_3). Tropospheric phosgene is produced from the OH-initiated oxidation of C_2Cl_4 , CH_3CCl_3 , CHCl_3 , and C_2HCl_3 . Simulations using a two-dimensional model indicate that these processes produce about 90 pptv/yr of tropospheric phosgene with an average concentration of about 18 pptv, in reasonable agreement with observations. We estimate a residence time of about 70 days for tropospheric phosgene, with the vast majority being removed by hydrolysis in cloudwater. Only about 0.4% of the phosgene produced in the troposphere avoids wet removal and is transported to the stratosphere, where its chlorine can be released to participate in the catalytic destruction of ozone. Stratospheric phosgene is produced from the photochemical degradation of CCl_4 , C_2Cl_4 , CHCl_3 , and CH_3CCl_3 and is removed by photolysis and downward transport to the troposphere. Model calculations, in good agreement with observations, indicate that these processes produce a peak stratospheric concentration of about 25-30 pptv at an altitude of about 25 km. In contrast to tropospheric phosgene, stratospheric phosgene is found to have a lifetime against photochemical removal of the order of years. As a result, we find that a significant portion of the phosgene that is produced in the stratosphere is ultimately returned to the troposphere, where it is rapidly removed by clouds. This phenomenon effectively decreases the amount of reactive chlorine injected into the stratosphere and available for ozone depletion from phosgene's parent compounds; we estimate approximate decreases of 14, 3, 15, and 25% for the stratospheric chlorine loadings of CCl_4 , CH_3CCl_3 , C_2Cl_4 , and CHCl_3 , respectively. A similar phenomenon due to the downward transport of stratospheric COFCl produced from CFC-11 is estimated to cause a 7% decrease in the amount of reactive chlorine injected into the stratosphere from this compound. Our results are potentially sensitive to a variety of parameters, most notably the rate of reaction of phosgene with sulfate aerosols. However, on the basis of the observed vertical distribution of COCl_2 , we estimate that the reaction of COCl_2 with sulfate aerosol most likely has a $\gamma < 5 \times 10^{-5}$ and, as a result, has a negligible impact on the stratospheric chlorine loadings of the phosgene parent compounds.

1. Introduction

Phosgene (COCl_2) is produced in the Earth's atmosphere from the degradation of a variety of chlorinated compounds including tetrachloroethylene (C_2Cl_4), trichloroethylene (C_2HCl_3), chloroform (CHCl_3), methylchloroform (CH_3CCl_3), and carbon tetrachloride (CCl_4) [e.g., *Helas and Wilson, 1992*]. These chlorinated compounds fall into two generic reactivity classes:

(1) C_2Cl_4 , C_2HCl_3 , CHCl_3 , and CH_3CCl_3 , the four reactive phosgene parent compounds (referred to here as the RPP compounds) that are destroyed primarily in the troposphere by reaction with OH, and (2) CCl_4 , which is unreactive in the troposphere and is destroyed primarily by photolysis in the stratosphere. Thus the degradation of the RPP compounds leads to the production of tropospheric COCl_2 , while CCl_4 and to some extent also the RPP compounds lead to the production of stratospheric COCl_2 .

Tropospheric COCl_2 is believed to be removed from the atmosphere by rainout and ocean deposition [*Singh, 1976; Singh et al., 1977*] with a residence time of the order of months [*Helas and Wilson, 1992*]. Observations suggest a fairly uniform distribution in the troposphere with an average concentration of about 15-20 pptv and a weak seasonal cycle of about 20% [*Singh, 1976; Singh et al., 1977; Wilson et al., 1988*]. Stratospheric COCl_2 , on the other hand, is believed to be removed by UV-photolysis, and observations indicate a peak concentration of 25-30 pptv at about 25 km [*Crutzen et al., 1978; Wilson et al., 1988*].

¹ Also at Paul Scherrer Institute, Villigen, Switzerland.

² Also at School of Chemistry and Biochemistry, Georgia Institute of Technology, and Georgia Tech Research Institute, Atlanta.

Copyright 1995 by the American Geophysical Union.

Paper number 94JD02518.

0148-0227/95/94JD-02518 \$05.00

While the subcycles of tropospheric and stratospheric COCl_2 have been studied previously [Cruzen *et al.*, 1978; Helas and Wilson, 1992], the interaction between these subcycles has not been studied, and yet, this interaction may potentially affect the ozone depletion potentials (ODPs) of phosgene's parent compounds. For instance, if instead of being removed in the troposphere, a small fraction of the COCl_2 produced in the troposphere from the RPP compounds is transported into the stratosphere and photochemically degraded there, the chlorine released in this degradation could contribute to the destruction of stratospheric ozone and thus cause an increase in the ODPs of the RPP compounds. On the other hand, if a fraction of the COCl_2 produced in the stratosphere were transported to the troposphere before degradation, the ODPs of the compounds producing stratospheric COCl_2 would be decreased.

To address this issue, we have developed a two-dimensional (2-D) model to simulate the tropospheric cycle of COCl_2 and thereby estimate the fraction of COCl_2 produced in the troposphere that is transported to the stratosphere. A one-dimensional (1-D) stratospheric model is then used to estimate the fraction of COCl_2 that is produced in the stratosphere and transported to the troposphere, where it is finally removed. In our discussion it will be convenient to distinguish two types of COCl_2 : (1) "tropospheric phosgene," that is, COCl_2 produced from the OH-initiated oxidation of the RPP compounds in the troposphere, and (2) "stratospheric phosgene," that is, COCl_2 produced from the photolysis of CCl_4 as well as the photolysis and OH-initiated oxidation of the RPP compounds in the stratosphere. By Dalton's law, the total COCl_2 cycle is then represented by the sum of these two independent subcycles. It is important to bear in mind that the terms "tropospheric" and "stratospheric" used in this context refer to the region of the atmosphere where the COCl_2 is produced, not necessarily to where it is found. Thus tropospheric COCl_2 can, in principle, be transported to and reside in the stratosphere, and stratospheric COCl_2 can be transported to and reside in the troposphere.

In the next sections we first describe the sources of atmospheric COCl_2 included in our calculations. We then discuss the basic components of our tropospheric and stratospheric models and the results of our model simulations for COCl_2 as well as phosgene's parent compounds. In the final sections we discuss the implications of our calculations for the ODPs of phosgene's parent compounds.

2. The Production of Phosgene

Atmospheric COCl_2 is produced from the oxidation of chlorinated ethenes and ethanes [Ohta and Mizoguchi, 1980; Nelson *et al.*, 1984; 1990], and a review of the known source strengths of these compounds suggests that the major contributors to this production are C_2Cl_4 , C_2HCl_3 , CHCl_3 , CH_2CCl_3 , and CCl_4 [Singh, 1976; Wilson *et al.*, 1988; Tuazon *et al.*, 1988; Helas and Wilson, 1992]. As was noted earlier, these compounds fall into two generic classes: the RPP compounds, which react with OH and absorb in the UV and thus can produce COCl_2 in both the troposphere and the stratosphere, and CCl_4 , which does not react with OH in the troposphere and thus produces COCl_2 only in the stratosphere.

Because the degradation mechanisms of both the RPP compounds and CCl_4 are not well defined, particularly in the case of the chloroethylenes, the yield of COCl_2 from the oxidation of these compounds is uncertain. Nevertheless, reasonable estimates for these yields can be deduced on the basis of the mo-

lecular structures of the parent compounds along with recent laboratory experiments. In Table 1, we summarize the COCl_2 yields adopted in our calculations from the OH-initiated oxidation and photolysis of each of COCl_2 's parent compounds. Note that as was described earlier, we divide the sources into two components: (1) production of tropospheric phosgene and (2) production of stratospheric phosgene.

3. Model Formulation for Tropospheric Phosgene and Its Parent Compounds

The basic framework for our tropospheric simulation is the 2-D model of Cunnold *et al.* [1983] and Cunnold *et al.* [1986]. The model, which was developed and validated using the Atmospheric Lifetime Experiment and Global Atmospheric Gases Experiment (ALEGAGE) data sets, distributes and transports atmospheric tracers in the vertical and latitudinal directions.

Table 1. COCl_2 Yields Assumed in Model Calculations

Source	Yield	References and Notes
<i>Tropospheric Phosgene Sources</i>		
$\text{C}_2\text{Cl}_4 + \text{OH}$	0.47 COCl_2	Tuazon <i>et al.</i> [1988]
$\text{C}_2\text{HCl}_3 + \text{OH}$	0.4 COCl_2	Tuazon <i>et al.</i> [1988]
$\text{CH}_2\text{CCl}_3 + \text{OH}$	1 COCl_2	upper-limit yield assumed on the basis of molecular structure of parent compound
$\text{CHCl}_3 + \text{OH}$	1 COCl_2	upper-limit yield assumed on the basis of molecular structure of parent compound
<i>Stratospheric Phosgene Sources</i>		
$\text{CCl}_4 + \text{hv}$	1 COCl_2	DeMoore <i>et al.</i> [1992]
$\text{C}_2\text{Cl}_4 + \text{hv}$	1 COCl_2	Berry [1974]
$\text{C}_2\text{Cl}_4 + \text{OH}$	0.47 COCl_2	Tuazon <i>et al.</i> [1988]
$\text{CH}_2\text{CCl}_3 + \text{hv}$	0 COCl_2	Nelson <i>et al.</i> [1984]
$\text{CH}_2\text{CCl}_3 + \text{OH}$	1 COCl_2	upper-limit yield assumed on the basis of molecular structure of parent compound
$\text{C}_2\text{HCl}_3 + \text{hv}$	0 COCl_2	upper-limit yield assumed on the basis of molecular structure of parent compound
$\text{C}_2\text{HCl}_3 + \text{OH}$	0.4 COCl_2	Tuazon <i>et al.</i> [1988]
$\text{CHCl}_3 + \text{hv}$	0 COCl_2	Nelson <i>et al.</i> [1984]
$\text{CHCl}_3 + \text{OH}$	1 COCl_2	upper-limit yield assumed on the basis of molecular structure of parent compound

This is accomplished by apportioning the atmosphere into 12 hydrostatic boxes as illustrated in Figure 1. The concentration, $C^n(J)$, of species J in the n th box is determined in the model by integrating the time-dependent mass continuity equation

$$\frac{\partial C^n(J)}{\partial t} = -\frac{C^n(J)}{\tau^n(J)} + S^n(J) + T^n(J) \quad (1)$$

where $\tau^n(J)$ is the lifetime for species J against photochemical loss and/or wet removal in box n , $S^n(J)$ represents the production of species J from photochemical processes (and emissions for the surface boxes) within box n , and $T^n(J)$ represents the net transport of J into box n .

Transport between boxes in the 2-D model is simulated using zonally averaged meridional and vertical velocities and eddy diffusion coefficients; these parameters were taken from *Newell et al.* [1969] and appropriately modified to optimize the model's ability to reproduce the observed distribution of CFCl_3 as described by *Cunnold et al.* [1986] and *Prinn et al.* [1987]. It should be noted that the model, which includes only transport between neighboring boxes and has transport coefficients inferred from the distribution of long-lived tracers (with lifetimes longer than a few years), is not ideally suited to the simulation of a compound like COCl_2 , whose atmospheric residence time is of the order of a month or two. On the other hand, observations suggest that COCl_2 is relatively well-distributed in the troposphere without major spatial or temporal gradients [*Singh et al.*, 1977; 1978; *Wilson et al.*, 1988]. This is probably due to the fact that COCl_2 's sources and sink are disperse, its sources arising from the photochemical decomposition of its relatively long-lived parent compounds and its sink from slow hydrolysis in cloudwater. (Calculations using the formulation of *Chameides* [1984] indicate that only about 3% of the available COCl_2 within an air mass is removed by hydrolysis over the lifetime of a typical cloud. This estimate is not inconsistent with the observations of *Singh* [1977] who measured COCl_2 concentrations in an air mass before and after a 2 to 3-day storm period and observed a decrease of only about 15-20%.) The absence of significant gradients in the distribution of COCl_2 suggests that the simulations presented here should provide a reasonable estimate of its distribution and atmospheric budget. In fact, as we illustrate in section 9, a sensitivity model calculation in which we alter the transport code to allow for convectivelike transport from the lower troposphere to the stratosphere yields essentially the same results as those from our standard model.

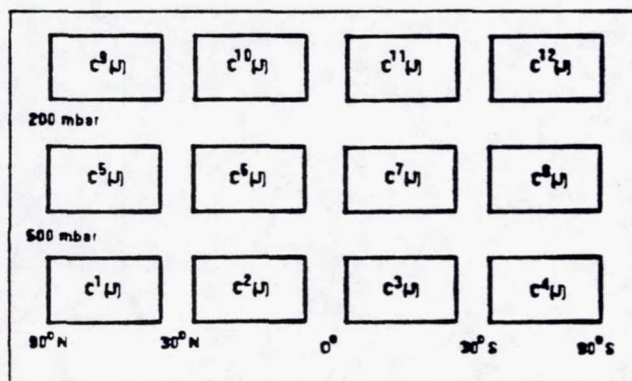


Figure 1. Schematic of the 12-box, two-dimensional model of the atmosphere.

Three loss processes are considered in the determination of $\tau^n(J)$ in our standard model; these are loss via reaction with tropospheric OH, loss in the troposphere by wet removal, and photochemical destruction in the stratosphere, so that

$$\tau^n(J) = \left(\frac{1}{\tau_{\text{OH}}^n(J)} + \frac{1}{\tau_{\text{wet-rem}}^n(J)} \right)^{-1} \quad n = 1 - 8 \quad (2)$$

$$\tau^n(J) = \tau_{\text{strat}}^n(J) \quad n = 9 - 12 \quad (3)$$

The lifetime, $\tau_{\text{OH}}^n(J)$, against loss via reaction with tropospheric OH is calculated using the seasonally varying OH distribution derived to reproduce the CH_3CCl_3 distribution and trend (CH_3CCl_3 atmospheric lifetime = 5.7 years) observed from the ALEGAGE network [*Cunnold et al.*, 1983; *Prinn et al.*, 1992]. Thus

$$\tau_{\text{OH}}^n(J) = \frac{1}{C^n(\text{OH}) k_{\text{OH}}(J)} \quad (4)$$

where $k_{\text{OH}}(J)$ is the rate constant for the reaction of species J with OH. The lifetime, $\tau_{\text{wet-rem}}^n(J)$, against loss due to wet removal is treated in the model using the parameterization described in section 4 and the lifetime, $\tau_{\text{strat}}^n(J)$, against loss in the stratosphere is estimated using a one-dimensional eddy diffusion model, as described in section 5.

It should be noted that the tropospheric lifetimes defined by equation (2) only account for reactions of the RPP compounds with OH. However, it has been proposed that Cl-initiated oxidation in the marine boundary layer could be an important sink for organic compounds such as C_2Cl_4 which react rapidly with Cl [*Singh and Kasting*, 1988; *Keene et al.*, 1990]. On the other hand, the spectroscopic measurements of *Harris et al.* [1992] indicating an upper limit of 0.25 ppbv for HCl (compared to 1 ppbv adopted by *Singh and Kasting*, 1988) in the marine boundary layer suggest that the role of Cl may be more limited. In the calculations presented here Cl-initiated reactions have been neglected. In the case of C_2Cl_4 , however, which has an extremely large rate constant with Cl [*Atkinson and Aschmann*, 1987], a brief discussion of the possible effects of this reaction is presented in section 9.

4. Tropospheric Wet Removal

Kinetic and photochemical data suggest that COCl_2 is essentially unreactive in the troposphere; its reaction with OH is endothermic [*DeMore et al.*, 1992], it is unreactive toward H_2O vapor [*Butler and Snelson*, 1979] and its absorption cross section in the near UV and visible is quite small [*Singh*, 1976; *Heydmann*, 1991]. On the other hand, COCl_2 is known to dissolve in water and hydrolyze [*Manogue and Pigford*, 1960] and as a result is most likely removed from the troposphere by cloudwater and by deposition onto the ocean and other wet surfaces [*Singh*, 1976; *Wine and Chameides*, 1989]. Thus a simulation of the COCl_2 atmospheric cycle requires a quantitative treatment of its wet removal in clouds and to the ocean. (Treatment of deposition to the ocean is also needed in our calculations to accurately simulate the production of COCl_2 from the oxidation of CH_3CCl_3 , since ocean deposition appears to represent a nonnegligible sink for this compound [*Wine and Chameides*, 1989; *Butler et al.*, 1991]). To properly simulate these loss processes, we adopted a wet removal parameterization

based on the formulations of Johnson [1981], Wine and Chameides [1989], and Butler et al. [1991]. This parameterization is described below.

4.1. Wet Removal Parameterization for Phosgene and Other Chlorinated Compounds

A schematic illustration of our wet removal parameterization is presented in Figure 2. We consider two removal pathways: one pathway involving removal by clouds, and the other involving removal by deposition to the ocean. The flux $\Phi_i(J)$ of species J through pathway i is represented by the ratio of the species' atmospheric concentration $C(J)$ and a parameter referred to as the pathway "resistance," R , which has units of second per centimeter [Danckwerts, 1970]. Thus

$$\Phi_i(J) = \frac{C(J)}{R_i} \quad (5)$$

The total flux, $\Phi_{\text{wet-tot}}(J)$, through both pathways is then determined by adding the two resistances as if they formed a parallel circuit, so that

$$\Phi_{\text{wet-tot}}(J) = \frac{C(J)}{R_{\text{tot}}} = C(J) \left(\frac{1}{R_{\text{ocean-tot}}} + \frac{1}{R_{\text{cloud-tot}}} \right) \quad (6)$$

where $R_{\text{ocean-tot}}$ and $R_{\text{cloud-tot}}$ represent the resistances for loss to the ocean and to clouds and rain respectively.

As is illustrated in Figure 2, deposition to the ocean is assumed to be controlled by four processes; these are transport from the free troposphere to the marine boundary layer, transport through a thin "film" or stagnant layer between the atmosphere and the ocean surface, transport through a thin film on the ocean surface, and transport into and loss via hydrolysis in the ocean. In the case of the last process, we consider downward transport and hydrolysis in two ocean layers: the mixed layer and the so-called deep ocean below the thermocline.

Similar to the formulation adopted in equation (5) for the total pathway resistance, the flux or loss due to each of the four processes used to simulate ocean deposition can be represented

in terms of a ratio between a concentration and a resistance specific to that process. Because these process-specific resistances act in series, it can be easily shown that

$$R_{\text{ocean-tot}} = \left(\frac{r_{\text{atm}} + r_{\text{air-film}} + r_{\text{ocean-film}} + r_{\text{ocean}}}{f_{\text{ocean}}} \right) \quad (7)$$

where f_{ocean} is the fraction of the surface covered by ocean and the r are used to represent the resistances for each of the processes listed above. For our simple zeroth order calculations, f_{ocean} is assumed to be 0.7, while for our 2-D model calculations it is allowed to appropriately vary with latitude. The process-specific resistances r , like the total pathway resistance R , have units of seconds per centimeter. In general it can be shown by solving the one-dimensional diffusion equation (or Fick's law), that r is given by the thickness of the layer of transport (often referred to as the film thickness) divided by the appropriate diffusion coefficient [Danckwerts, 1970].

Loss in clouds is assumed to be controlled by three processes: these are transport from the ambient atmosphere to the interstitial air of a cloud, and transport to and accommodation on the droplet surface, and transport into and hydrolysis within the droplet interior. As in the case of ocean deposition, the total resistance due to rainout can be represented as a sum of the regime-specific resistances so that

$$R_{\text{cloud-tot}} = (r_{\text{atm-cloud}} + r_{\text{accommodation}} + r_{\text{cloud}}) \quad (8)$$

where the r are again used to represent the resistances through each of the transport regimes.

The expressions and values adopted here for each of the process-specific resistances are listed in Table 2. While the r values can in general vary considerably depending on the specific species' thermodynamic properties and the assumed state of the atmosphere and ocean, a few generalizations can be made for the range of species considered here and for the conditions assumed for the atmosphere and ocean. We find, for instance, that loss to the ocean in our calculations is always limited by the ocean film resistance ($r_{\text{ocean-film}}$) and/or the ocean resistance (r_{ocean}). The relative contributions of these two resistances largely depends on the species' hydrolysis rate, k_1 . We find that resistance at the thin film generally controls the rate of ocean deposition for species with relatively large rates of hydrolysis (i.e., $k_1 > 3.5 \times 10^{-5} \text{ s}^{-1}$). Ocean deposition for species with relatively small hydrolysis rates, on the other hand, is generally dominated by the ocean resistance. For all cases considered here, the resistances due to transport from the free troposphere to boundary layer (r_{atm}) and to the ocean surface ($r_{\text{air-film}}$) have a negligible impact; these resistances are important only for species with extremely high solubilities and/or hydrolysis rates, and such species are not considered in this work.

For removal by clouds we find that r_{cloud} , the resistance due to transport into and hydrolysis in the droplet, is generally the dominant term, with $r_{\text{atm-cloud}}$, the resistance due to transport from the atmosphere to the interstitial air of the cloud, making a non negligible contribution only in the case of species with relatively large solubilities and/or hydrolysis rates. (In the case of the compounds specifically considered here, including COCl_2 , $r_{\text{atm-cloud}}$ always makes a negligible contribution to the total wet-removal resistance.) Note that for our determination of $r_{\text{accommodation}}$, we have assumed that the accommodation coefficient α is always greater than 10^{-5} ; this assumption seems reasonable in light of several different laboratory experiments

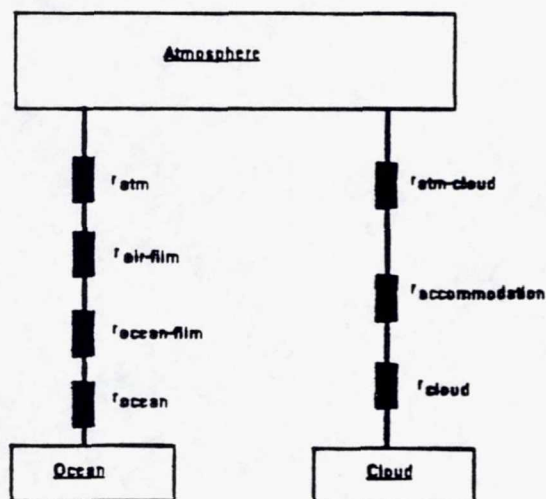


Figure 2. Schematic illustration of the processes included in the wet removal parameterization.

Table 2a. Resistances r Used to Determine Rate of Ocean Deposition for Wet Removal Parameterization

Resistance, r	Value or Expression Used	Comments and References
r_{atm}	3.5 s/cm	Resistance due to transport from the free troposphere to the boundary layer estimated from the inverse of the marine boundary layer entrainment velocity of 2.5 mm/s (Bandy <i>et al.</i> , 1992). Note that this resistance does not have a significant impact on overall ocean deposition rate for the range of species considered here.
$r_{\text{air-film}}$	1.25 s/cm	Resistance due to transport through thin air film between the ocean and atmosphere adopted from Liss [1983]. Note that this resistance does not have a significant impact on overall ocean deposition rate for the range of species considered here.
$r_{\text{ocean-film}}$	$\frac{I_S}{H R T N_A 10^{-3}}$	Resistance due to transport through thin ocean film between the ocean and atmosphere is based on formulation of Liss [1983].
r_{ocean}	$\left(H \sqrt{k_1 D_1} \left(\frac{S-Q}{S+Q} \right) R T N_A 10^{-3} \right)^{-1}$	Resistance due to transport through and hydrolysis in ocean is based on a two-layer ocean transport formulation similar to that of Butler <i>et al.</i> [1991]. Diffusion coefficients D_1 and D_2 were adopted from Johnson [1981]. Latitudinally dependent ocean temperatures for determining hydrolysis rates were taken from Reynolds [1982] for the mixed-layer and were assumed to be one-half of the mixed-layer temperature (in °C) for the thermocline following Butler <i>et al.</i> [1991]. Latitudinally-dependent mixed layer thicknesses were adopted from Li <i>et al.</i> [1984].

Here, $r_f = 170 \text{ s/cm}$. R is gas constant, T is temperature, N_A is Avogadro's number, H is species' solubility constant, $S = (D_1 a_1 + D_2 a_2) / (2 D_1 a_1) e^{-a_1 z_1}$, $Q = (D_1 a_1 - D_2 a_2) / (2 D_1 a_1) e^{-a_1 z_1}$, $a_1 = \sqrt{k_1 / D_1}$, $a_2 = \sqrt{k_2 / D_2}$, k_1 is pseudo first-order hydrolysis rate constant in ocean mixed layer, k_2 = pseudo first order hydrolysis rate constant below ocean thermocline, D_1 is diffusion coefficient in ocean mixed layer ($= 40 \text{ cm}^2/\text{s}$), D_2 is diffusion coefficient below ocean thermocline ($= 1.7 \text{ cm}^2/\text{s}$), and z_1 is thickness of ocean mixed layer

which all yield accommodation coefficients significantly larger than 10^3 for a variety of species of varying solubilities [Mozurkewich *et al.*, 1987; Jayne *et al.*, 1990; Van Doren *et al.*, 1990]. Given this assumption for α , we find that $r_{\text{accommodation}}$ has a negligible impact on the overall rate of rainout for all species considered here. This latter result, which is equivalent to having thermodynamic equilibration of the species between the gas and aqueous phases of the cloud, is consistent with more detailed cloud chemistry calculations which yield gas/aqueous phase equilibration times for soluble species in clouds of only several seconds or less [Chameides, 1984; Schwartz, 1986].

4.2. Zeroth-Order Evaluation of Wet Removal Lifetimes

Before describing the application of the wet removal parameterization to our 2-D model, it is useful to use the parameterization in a zero-dimensional model to roughly estimate the range of wet removal lifetimes that we might expect to find for species as a function of their solubility and hydrolysis rate. To carry out this "zeroth-order evaluation" we first assume, for simplicity, that all species are distributed in the atmosphere with constant mixing ratios; we also neglect longitudinal and latitudinal variations. With these simplifications, the

globally averaged lifetime, $\tau_{\text{wet-tot}}^{\text{ovf}}(J)$, for a species "J" can be estimated by

$$\tau_{\text{wet-tot}}^{\text{ovf}}(J) = \frac{H_A C(J)}{\Phi_{\text{tot}}} = H_A \left(\frac{1}{R_{\text{ocean-tot}}} + \frac{1}{R_{\text{cloud-tot}}} \right)^{-1} \quad (9)$$

where H_A is the atmospheric scale height (taken here to be 8.4 km).

Wet removal lifetimes calculated from equation (9) using ocean and rainout resistances appropriate for globally averaged atmospheric and oceanic conditions (see Table 2) are plotted as a function of the species' solubility and mixed layer hydrolysis rate constants in Figure 3. Not surprisingly, we find that the total wet removal lifetime increases dramatically with decreasing solubility and decreasing hydrolysis rates. Note in Figure 3 that lifetimes of the order of 10 days are obtained for species with solubilities and hydrolysis rates greater than 1 (in units of molar per atmosphere and s^{-1} , respectively). On the other hand, lifetimes of 1000 years or longer are obtained for species with solubilities less than 10^{-4} M/atm and hydrolysis rate constants less than 10^{-2} s^{-1} .

In Figure 4 we plot the ratio of $R_{\text{ocean-tot}}$ to $R_{\text{cloud-tot}}$. When this ratio is greater than one, removal via cloud deposition

Table 2b. Resistances r Used to Determine Rate of Loss in Clouds for Wet Removal Parameterization

Resistance, r	Value or Expression Used	Comments and References
$r_{\text{atm-cloud}}$	1.0 s/cm	Resistance due to transport from the atmosphere to the interstitial air in a cloud assumed to be 1.0 s/cm. This value is adopted to ensure that the minimum lifetime for rainout of an infinitely soluble species is 10 days. Note that this resistance does only have a minor impact on overall rainout rate for the range of species considered here.
$r_{\text{accommodation}}$	$\frac{(1 + (41)/(3r\alpha))r^2}{W_L 1 \sqrt{(8RT)/(m\pi)}}$	Resistance due to transport to and accommodation on the droplet surfaces based on the formulation of Chameides [1984] and Schwartz [1986]. For our zeroth-order calculations, a value of $8.1 \cdot 10^{-6} \text{ L/cm}^2$ was adopted for the cloud liquid water column concentration [Greenwald et al., 1993]. For our two-dimensional model calculations, a latitudinally-dependent cloud liquid water column concentration given by Greenwald et al. interpolated for every month of the year was used. It was further assumed that at each latitude, 75% of the liquid water column resided between 1000 and 500 mbar and the remaining 25% resided between 500 and 200 mbar. Note that as long as $\alpha > 10^{-5}$, this resistance does not have a significant impact on overall wet deposition rate for the range of species considered here.
r_{cloud}	$\frac{1}{Hk W_L R T N_A 10^{-3}}$	Resistance due to transport into the cloud droplet and loss via hydrolysis is based on formulation of Chameides [1984] and Schwartz [1986]. Note that for the range of k adopted here, a dissolved species is always found to be well mixed within the droplet, and thus r_{cloud} is found to be independent of transport parameters such as the molecular diffusion coefficient.

Here, l is mean free path ($= 10^{-5} \text{ cm}$), r is droplet radius ($= 10^{-3} \text{ cm}$), α is accommodation coefficient, m is species' molecular weight, R is gas constant, W_L is total cloud liquid water column concentration in liters per square centimeter, k is first-order hydrolysis rate constant in cloud, N_A is Avogadro's number, H is species' solubility constant, T is droplet temperature for $r_{\text{accommodation}}$, and cloud temperature for r_{cloud} .

dominates, and when the ratio is less than one, removal by ocean dominates. The results indicate two clear regimes, with ocean deposition dominating in one and cloud removal dominating in the other. For the range of H and k considered here, the boundary between these two regimes is found to lie approximately along the $k = 1 \text{ s}^{-1}$ line. When $k < 1 \text{ s}^{-1}$, we find that ocean deposition is the dominant pathway, while when $k > 1 \text{ s}^{-1}$ cloud removal is the dominant pathway. Interestingly, the location of the boundary is largely independent of H . This occurs because for the range of H and k considered here, both $R_{\text{ocean-to-tot}}$ and $R_{\text{cloud-to-tot}}$ vary as $1/H$ and thus their ratio is independent of H .

The general findings presented in Figures 3 and 4 are illustrated in greater detail in Table 3, where we list the relevant input parameters and the resulting lifetimes for three compounds of interest to this work: COCl_2 , the compound with the largest solubility and rate of hydrolysis considered here; CH_3CCl_3 , a compound with a more moderate solubility and hydrolysis rate; and CHCl_3 , a compound with a relatively small solubility and rate of hydrolysis. The wet removal lifetimes are found to vary from less than 0.2 years for COCl_2 , to about 130 years for CH_3CCl_3 , to 50,000 years for CHCl_3 . Consistent with the gen-

eral results illustrated in Figure 4, we find in Table 3 that cloud removal is the dominant wet removal pathway for COCl_2 , while deposition to the ocean dominates for CH_3CCl_3 and CHCl_3 (Note that our CH_3CCl_3 lifetime is essentially consistent with the estimate of Butler et al. [1991] and somewhat longer than that obtained by Wine and Chameides [1989].) As we will see later these lifetimes result in our finding that wet removal is a major sink for tropospheric COCl_2 , a minor sink for CH_3CCl_3 , and a negligibly small sink for CHCl_3 .

4.3. Two-Dimensional Application of Wet Removal Parameterization

In order to apply the wet removal parameterization to the 2-D model, an ocean removal lifetime $\tau_{\text{ocean-1D}}^n$ for the surface boxes (i.e., $n = 1-4$) and a cloud removal lifetime $\tau_{\text{cloud-1D}}^n$ for all the tropospheric boxes (i.e., $n = 1-8$) must be specified. To do this, we assume that within each box, pressure and density are hydrostatically related. We also assume that the deposition flux to the ocean is proportional to C_0^n (J), the concentration of the species

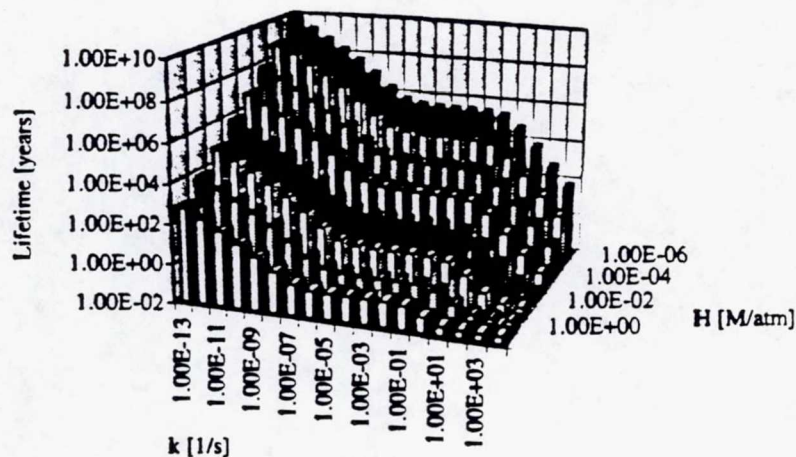


Figure 3. Zeroth-order estimate of species' atmospheric lifetime against wet removal as a function of the species' solubility H and hydrolysis rate constant k. (To produce this figure, we assumed that the mixed-layer hydrolysis rate constant and cloud hydrolysis rate constant were equal and that the deep ocean hydrolysis rate constant was equal to one third of the mixed-layer hydrolysis rate constant. These assumptions made the parameterization a function of only two independent variables and thereby facilitated its illustration. Note that in general our results are insensitive to the exact value of the deep-ocean hydrolysis rate constant.)

at the bottom of the box, while cloud removal is proportional to $C^n(J)$, the average concentration in the box. It then follows that

$$\tau_{\text{ocean-tot}}^n(J) = \frac{C_o^n(J) \int_{1000 \text{ mbar}}^{500 \text{ mbar}} \exp(-z/H_A) dz}{C_o^n(J)/R_{\text{ocean-tot}}^n} =$$

$$0.5 H_A R_{\text{ocean-tot}}^n \quad n = 1 - 4 \quad (10a)$$

$$\tau_{\text{cloud-tot}}^n(J) = \frac{C_o^n(J) \int_{1000 \text{ mbar}}^{500 \text{ mbar}} \exp(-z/H_A) dz}{C^n(J)/R_{\text{cloud-tot}}^n} =$$

$$0.7 H_A R_{\text{cloud-tot}}^n \quad n = 1 - 4 \quad (10b)$$

$$\tau_{\text{cloud-tot}}^n(J) = \frac{C_o^n(J) \int_{500 \text{ mbar}}^{200 \text{ mbar}} \exp(-z/H_A) dz}{C^n(J)/R_{\text{cloud-tot}}^n} =$$

$$0.9 H_A R_{\text{cloud-tot}}^n \quad n = 5 - 8 \quad (10c)$$

5. Stratospheric Model

We determine the stratospheric lifetimes by first estimating the vertical profiles of the species within the stratosphere using a 1-D eddy-diffusion model. These profiles are then used along with their rates of loss in the stratosphere as a function of altitude to calculate the lifetimes in the corresponding boxes of the 2-D model as a function of the solar zenith angle. The 1-D model divides the atmosphere from the tropopause (i.e., $z = 12 \text{ km}$ for global average conditions) to 49 km into 38 layers.

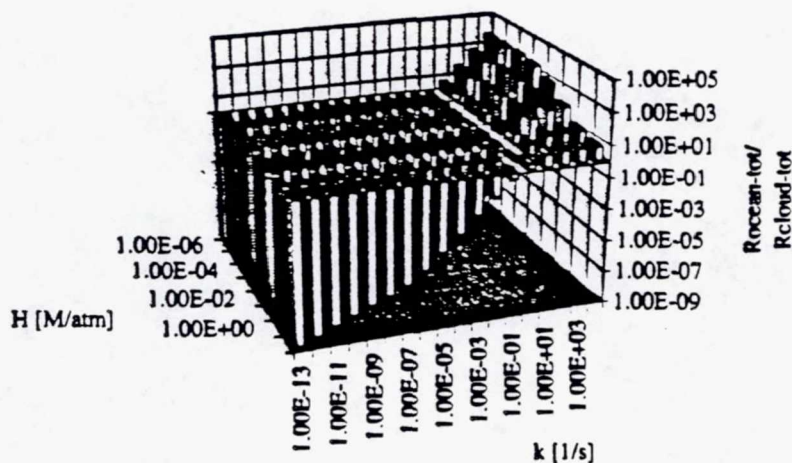


Figure 4. Ratio $R_{\text{ocean-tot}} / R_{\text{cloud-tot}}$ as a function of the hydrolysis rate constant and solubility constant.

Table 3. Zeroth-Order Estimation of $\tau_{\text{wet-ox}}$, the Wet Removal Lifetime of Phosgene (COCl_2), Methylchloroform (CH_2CCl_3), and Chloroform (CHCl_3) Using Equation (5)

	COCl_2	CH_2CCl_3	CHCl_3
<i>Ocean deposition</i>			
H, solubility constant, M/atm	0.2	0.08	0.00554
k_1 , hydrolysis rate constant in mixed layer, s^{-1}	5	1.3^{a}	8.6×10^{-11}
k_2 , hydrolysis rate constant at thermocline, s^{-1}	5	2.3×10^{-9}	1.5×10^{11}
Γ_{atm} , s/cm	3.5	3.5	3.5
$\Gamma_{\text{atm-film}}$, s/cm	1.25	1.25	1.25
$\Gamma_{\text{ocean-film}}$, s/cm	35.37	88.44	1.28×10^3
Γ_{ocean} , s/cm	1.47×10^{-2}	3.37×10^3	1.33×10^6
$R_{\text{ocean-ox}}$, s/cm	40.14	3.47×10^3	1.34×10^6
$\tau_{\text{ocean-ox}}$, years	1.53	131.9	5.08×10^4
<i>Cloud deposition</i>			
H, solubility constant, M/atm	0.2	0.08	0.00554
k, hydrolysis rate constant, s^{-1}	5	7.57×10^{-11}	4.2×10^{-3}
α , accommodation coefficient	$> 10^{-5}$	$> 10^{-5}$	$> 10^{-5}$
$\Gamma_{\text{atm-cloud}}$, s/cm	1.0	1.0	1.0
$\Gamma_{\text{accommodation}}$, s/cm	< 0.69	< 0.80	< 0.76
Γ_{cloud} , s/cm	5.68	9.37×10^{11}	2.46×10^{15}
$R_{\text{cloud-ox}}$, s/cm	6.68	9.37×10^{11}	2.46×10^{15}
$\tau_{\text{cloud-ox}}$, years	0.18	2.5×10^{10}	6.56×10^{13}
<i>Total wet removal</i>			
$\tau_{\text{wet-ox}}$, years	0.16	131.85	5.08×10^4

Calculations carried out assuming a global mean T of 293 K for the mixed layer and 283 K for the thermocline, a mixed layer depth of 75 m [Li *et al.*, 1984], and T for clouds of 265 K. Solubility and hydrolysis rate constants for COCl_2 , CH_2CCl_3 , and CHCl_3 taken from D. Worsnop (private communication, 1993), Gerkens and Franklin [1989], and Jeffers *et al.* [1989], respectively. Note that the data for COCl_2 are uncertain [De Bruyn *et al.*, 1992].

each having a thickness of 1 km. A constant concentration C_0 is specified at the lower boundary (i.e., tropopause), and a flux of zero is assumed at the top boundary. The model then determines the species' concentration C_z as a function of altitude z by integrating the steady state continuity equation

$$0 = S_z(J) + L_z(J) C_z(J) + \frac{d}{dz} \left(K_z n_M \frac{dX_z(J)}{dz} \right) \quad (11)$$

where S_z represents the source of the species (in units of molecules per cubic centimeter per second) as a function of altitude z , L_z the loss of species (in units of reciprocal seconds), K_z the eddy diffusion coefficient (adopted from Luther *et al.*, [1979]), n_M the atmospheric number density, and X_z the species' mixing ratio (v/v).

In our standard model, the rate of stratospheric loss is determined from two photochemical processes: photolysis and reaction with OH. (Calculations indicate that reactions of the compounds considered here with $\text{O}(^1\text{D})$ and with Cl atoms do not play a significant role.) Thus

$$L_z(J) = J_z(J) + k_{\text{OH}}(J) C_z(\text{OH}) \quad (12)$$

where J_z is the photolysis frequency for species J (in units of reciprocal seconds) as a function of altitude z , and the other terms are all defined earlier. Concentrations for OH were adopted from Singh and Kasting [1988] and photolysis frequencies were calculated using the radiative transfer model of Stamnes *et al.* [1988] with cross sections and quantum yields taken from DeMore *et al.* [1992] and Berry [1974] for the RPP compounds and Heydtmann [1991] for COCl_2 .

In addition to the standard model calculations described above, we have carried out three sets of sensitivity model calculations: (1) calculations with K_z increased and decreased by a factor of 2; (2) calculation with $C_z(\text{OH})$ increased and decreased by a factor of 5; and (3) calculations which include an additional sink for stratospheric COCl_2 arising from reaction with sulfate aerosols. The results of these sensitivity calculations are discussed in section 9.

With the exception of the simulation of stratospheric COCl_2 , model calculations are carried out with S_z set equal to zero at all altitudes. As discussed in section 2 and outlined in the bottom section of Table 1, the source term for stratospheric COCl_2 is assumed to be given by

$$\begin{aligned}
 S_2(\text{COCl}_2) = & J_2(\text{CCl}_4) C_2(\text{CCl}_4) + \\
 & k_{\text{OH}}(\text{CH}_3\text{CCl}_3) C_2(\text{CH}_3\text{CCl}_3) + \\
 & J_2(\text{C}_2\text{Cl}_4) C_2(\text{C}_2\text{Cl}_4) + 0.47 k_{\text{OH}}(\text{C}_2\text{HCl}_3) C_2(\text{C}_2\text{HCl}_3) + \\
 & 0.4 k_{\text{OH}}(\text{C}_2\text{HCl}_3) C_2(\text{C}_2\text{HCl}_3) + \\
 & k_{\text{OH}}(\text{CHCl}_3) C_2(\text{CHCl}_3) \quad (13)
 \end{aligned}$$

With the model parameters defined as described above, the stratospheric vertical profiles and loss rates for COCl_2 and its parent compounds are determined by the 1-D model as a function of the solar zenith angle θ , with θ varying from 0° to 80° . An effective lifetime $\tau_{\text{strat}}^q(J)$ as a function of solar zenith angle is then given by

$$\tau_{\text{strat}}^q(J) = \frac{\int_{12\text{ km}}^{50\text{ km}} C_2(J) dz}{\int_{12\text{ km}}^{50\text{ km}} L_2(J) C_2(J) dz} \quad (14)$$

Note that a lower limit of 12 km is chosen for the integrals in equation (14) because this corresponds to the lower boundary of the stratospheric boxes of the 2-D model. Also note that because C_2 appears in both the numerator and denominator of equation (14) and C_2 is linearly dependent on the assumed lower boundary condition C_0 , τ_{strat}^q is independent of this arbitrary model parameter. The seasonally dependent lifetimes for mid-latitudes (i.e., 50°) and tropical latitudes (i.e., 15°) are then used to represent the effective lifetimes for the appropriate stratospheric boxes in the 2-D model as a function of the day of the year.

The stratospheric lifetimes with a solar zenith angle of 60° (assumed to be a global average condition) are listed in Table 4. Note again that in keeping with our earlier discussions, we have calculated two sets of lifetimes for COCl_2 : one for "tropospheric" COCl_2 (i.e., COCl_2 produced in the troposphere and transported into the stratosphere) and one for "stratospheric" COCl_2 (i.e., COCl_2 produced in the stratosphere). Because tropospheric COCl_2 enters the stratosphere at the tropopause and must first be transported to higher altitudes before it can be photolyzed, it has a longer stratospheric lifetime than that of stratospheric COCl_2 , which is produced in the upper and middle stratosphere. In either case, it is also interesting to note that COCl_2 's stratospheric lifetime is of the order of years. This long lifetime is caused by the fact that COCl_2 is a weak absorber in the near and middle ultraviolet and does not react with OH. Because of this long lifetime, a significant fraction of the COCl_2 that is either produced in or transported to the stratosphere will tend to be cycled back to the troposphere before being photochemically destroyed.

6. Source Strengths of Tropospheric Phosgene

As summarized in the top part of Table 1, tropospheric COCl_2 is assumed to be produced from the OH-initiated oxidation of the four RPP compounds. The strength and distribution of each of these sources is determined by first simulating the cycle of each of the four RPP compounds in the 2-D model with the appropriate OH rate constant taken from DeMore et al. [1992] and the appropriate anthropogenic emission rate taken from the literature. With the exception of CHCl_3 , the emission

Table 4. Estimate of Stratospheric Lifetime Calculated With One-Dimensional Model

Species	Stratospheric Lifetimes, years
CH_3CCl_3	7.48
C_2Cl_4	1.79
CHCl_3	3.18
CCl_4	7.14
COCl_2 , troposphere.	8.19
COCl_2 , stratosphere.	1.85
COCl_2 , total.	1.86

A global average solar zenith angle of 60° is assumed for these calculations

rate is assumed to be constant in time and to vary latitudinally in the manner described for CH_3CCl_3 by Midgley [1989]. In the case of CHCl_3 , in addition to the anthropogenic source distribution, an oceanic source has also been considered which varies latitudinally according to Khalil et al. [1983]. In the case of CH_3CCl_3 , we include loss via wet deposition as described in section 4 as well as loss via OH oxidation. The results of these simulations are briefly outlined below and summarized in Table 5.

6.1. Methylchloroform

The annual mean CH_3CCl_3 concentration calculated for the 1987 emission rate of 617 kt/yr [Midgley, 1989] is plotted as a function of latitude and altitude in Figure 5. Also shown in Figure 5 are the average concentrations measured in 1989 from the ALE/GAGE surface network [Prinn et al., 1992]. We find good agreement between the calculated and observed concentrations; however this is not surprising since the model was originally tuned to reproduce the CH_3CCl_3 ALE/GAGE data.

Our calculations yield a globally averaged concentration of 154 pptv and an average atmospheric residence time of 5.6 years. About 83.5% of the CH_3CCl_3 released at the surface is estimated to be destroyed in the troposphere by OH, 4.1% is lost via wet removal, and the remaining 12.4% is lost in the stratosphere. These results are in reasonable agreement with the assessment of Butler et al. [1991]. Assuming that one molecule of COCl_2 is produced for each molecule of CH_3CCl_3 oxidized by OH, we infer an annual tropospheric production rate of COCl_2 of 28 pptv per year (see Table 5).

6.2. Tetrachloroethylene

The annual mean C_2Cl_4 concentrations calculated as a function of altitude and latitude for an emission rate of 580 kt/yr [Class and Ballschmiedt, 1987] are plotted in Figure 6. Our results are compared with the surface C_2Cl_4 concentrations observed by Class and Ballschmiedt [1987] at various sampling sites over the Atlantic and Indian Oceans in the years 1982-1986, and with measurements taken by Koppmann et al. [1993] on a cruise through the Atlantic Ocean made in August-September 1989. As can be seen in Figure 6, our results are in good agreement with the measured concentrations. Our calculations, similar to those of Derwent and Eggleston [1978], yield an average atmospheric residence time of 0.38 years, with about

Table 5. Summary of Simulations of the RPP Compounds and Their COCl₂ Production Rates

RPP Compound	Release Rate, kt/yr	Average Concentration, pptv	Average Residence Time, yr	Phosgene Production Rate, pptv/yr	Percentage of Total Production COCl ₂ , %
CHCl ₃	810	22.8	0.53	47.0	50.8
CH ₂ CCl ₃	614	152.9	5.59	27.7	29.9
C ₂ Cl ₄	580	8.8	0.38	11.4	12.3
C ₂ HCl ₃	300	0.4	0.028	6.4	7.0

98.4% of the annual C₂Cl₄ emissions destroyed by OH in the troposphere and only 1.6% destroyed in the stratosphere. If 0.47 molecules of COCl₂ are produced for each molecule of C₂Cl₄ oxidized by OH, our calculations imply a global COCl₂ source from C₂Cl₄ of about 11 pptv/yr.

6.3. Chloroform

Our model-calculated CHCl₃ concentrations were obtained assuming a total emission rate of 810 kt/yr with 40% distributed as an anthropogenic source and 60% distributed as an oceanic source as discussed above. As is illustrated in Figure 7, an emission rate of this magnitude and distribution yields reasonable agreement with all the measurements, except those of Singh *et al.* [1983]. (We found that model-calculated concentrations fell below observations when the total emission source of 610 kt/yr estimated by Khalil *et al.* [1983] was used.)

We estimate an atmospheric residence time for CHCl₃ of about 0.53 years with approximately 98.3% of the total budget lost in the troposphere and 1.7% in the stratosphere. If one molecule of COCl₂ is produced for each molecule of CHCl₃ oxidized by OH, then our calculations imply a tropospheric source of COCl₂ from CHCl₃ of about 47 pptv/yr.

6.4. Trichloroethylene

In Figure 8, we compare model-calculated concentrations for C₂HCl₃ assuming an emission rate of 300 kt/yr [Gidel *et al.*,

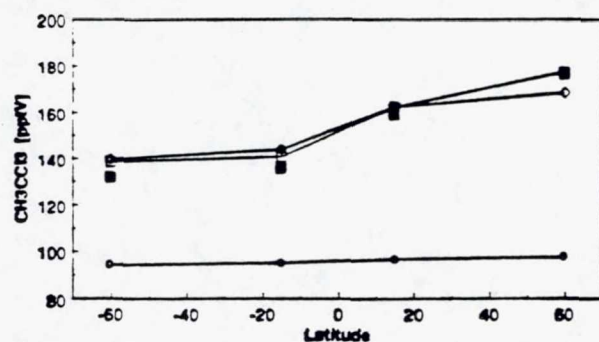


Figure 5. Model-calculated (open symbols) and observed (solid symbols) CH₂CCl₃ concentrations. The open squares represent the lower troposphere, the open diamonds represent the upper troposphere, and the open circles represent the stratosphere. The calculated concentrations were obtained assuming a steady emission rate of 617 kt/yr distributed latitudinally. The solid squares represent annually averaged observations as a function of latitude obtained from the ALE/GAGE remote surface network [Prinn *et al.*, 1992].

1983; A. McCulloch, private communication, 1992] with those measured by Koppmann *et al.* [1993]. Significant discrepancies between the model-calculated and observed concentrations are apparent. Because of C₂HCl₃'s short atmospheric residence time of only 7 days a direct comparison of the model-calculated concentrations with observations is problematic. However, because of its relatively small yield of COCl₂ production, C₂HCl₃ is of only minor importance to the overall COCl₂ cycle, and thus uncertainties in its emissions and distribution have a negligible impact on our conclusions. We infer a tropospheric source of COCl₂ from C₂HCl₃ of about 6.4 pptv/yr. Because of C₂HCl₃'s short lifetime, essentially all of the species is destroyed in the troposphere by OH, and direct injection to the stratosphere is thereby prevented.

6.5. Summary of Tropospheric Sources

Table 5 summarizes the source strengths of COCl₂ to the troposphere from the four RPP compounds. We estimate a total tropospheric rate of COCl₂ production of about 92 pptv/yr, with about half coming from CHCl₃, 30% coming from CH₂CCl₃, 12% from C₂Cl₄, and the remainder from C₂HCl₃. Although not illustrated in a figure, we find that the majority of the COCl₂ is produced in the lower troposphere and in the northern hemisphere; this is to be expected given the distribution of the RPP compounds and their emissions. Comparison of these results with those obtained by Helas and Wilson [1992] using a zero-dimensional box model indicate qualitative agreement with some small discrepancies. Our total COCl₂ source strength is about 10% higher than that of Helas and Wilson [1992], with about 25% and 10% higher source strengths arising from CHCl₃ and CH₂CCl₃, respectively, and 15% and 35% lower source strengths from C₂Cl₄ and C₂HCl₃, respectively. For the most part, these differences can be attributed to the different emission rates assumed for the parent compounds.

7. Fate of Tropospheric Phosgene

Figures 9 and 10 compare model-calculated distributions of tropospheric COCl₂ with measurements made by Wilson *et al.* [1988] and Singh [1976]. The agreement between measurements and simulations is reasonably good, with both the measurements and model calculations indicating an average northern hemispheric mixing ratio of about 15-20 pptv, with at most modest latitudinal and seasonal variations.

Table 6 summarizes the budget of tropospheric COCl₂ inferred by the 2-D model. Of the total 92 pptv of tropospheric COCl₂ produced annually by the oxidation of the RPP compounds, we find that 99.6% is directly removed from the atmos-

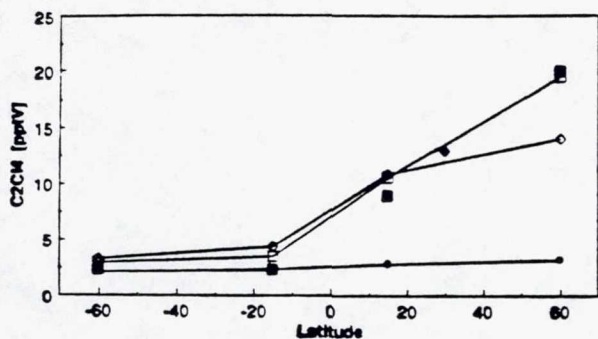


Figure 6. Model-calculated (open symbols) and observed (solid symbols) C_2Cl_4 concentrations. The open squares represent the lower troposphere, the open diamonds represent the upper troposphere, and the open circles represent the stratosphere. The calculated concentrations were obtained assuming a steady emission rate of 580 kt/yr distributed latitudinally. The solid squares represent annually averaged observed surface concentrations as a function of latitude taken by *Class and Ballschmiedt* [1987] and the solid diamond represents averaged surface measurements taken by *Koppmann et al.* [1993].

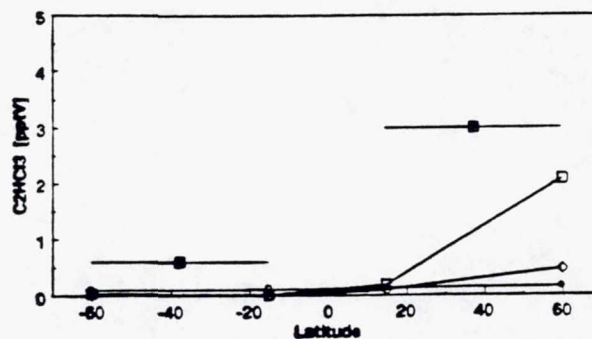


Figure 8. Model-calculated (open symbols) and observed (solid symbols) C_2HCl_3 concentrations. The open squares represent the lower troposphere, the open diamonds represent the upper troposphere, and the open circles represent the stratosphere. The calculated concentrations were obtained assuming a steady emission rate of 300 kt/yr distributed latitudinally. The solid squares represent averaged hemispheric surface observations made by *Koppmann et al.* [1993] on a cruise through the Atlantic Ocean in August-September 1989.

phere via wet deposition and only 0.4% is transported to the stratosphere and photochemically destroyed there. The very small fraction of $COCl_2$ lost to the stratosphere is caused by two effects: (1) the removal of $COCl_2$ by clouds and (2) the slow rate of loss of $COCl_2$ in the stratosphere which allows the vast majority of the $COCl_2$ that is transported into the lower stratosphere to be returned to the troposphere before it is photolyzed. Note that in agreement with our earlier zeroth-order calculations, we find that removal by clouds dominates over that of ocean deposition.

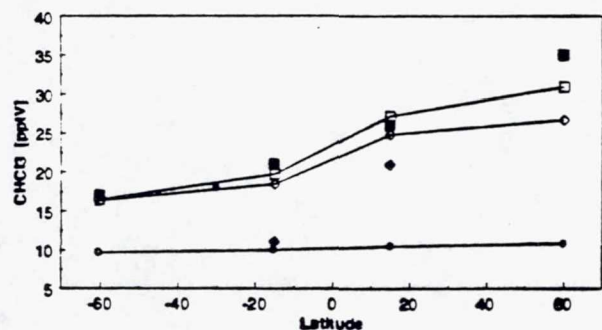


Figure 7. Model-calculated (open symbols) and observed (solid symbols) $CHCl_3$ concentrations. The open squares represent the lower troposphere, the open diamonds represent the upper troposphere and the open circles represent the stratosphere. The calculated concentrations were obtained assuming a steady emission rate of 810 kt/yr distributed latitudinally. The solid squares represent annually averaged surface observations as a function of latitude made by *Khalil et al.* [1983]. The solid diamonds represent averaged surface measurements made by *Singh et al.* [1983] over the Eastern Pacific in December 1981 and the solid circle represents surface measurements made by *Rasmussen et al.* [1982] at $30^\circ S$ in November 1981.

8. Fate of Stratospheric Phosgene

Inspection of Figure 9 reveals that our model simulations of the tropospheric $COCl_2$ cycle predict a stratospheric $COCl_2$ concentration of about 10-15 ppbv. This concentration is considerably smaller than the levels of 20-30 ppbv observed in the lower stratosphere by *Wilson et al.* [1988]. The reason for this discrepancy is the fact that the calculations from the previous section omitted the production of $COCl_2$ in the stratosphere. In this section we address this later aspect of the $COCl_2$ cycle with our 1-D stratospheric model.

As was discussed in section 2 and summarized in the bottom part of Table 1, we consider four sources of stratospheric $COCl_2$. These arise from the photolysis of CCl_4 , the OH oxidation and photolysis of C_2Cl_4 and the oxidation of CH_3CCl_3 and $CHCl_3$. (While OH-initiated oxidation of C_2HCl_3 produces $COCl_2$, its contribution to stratospheric $COCl_2$ is negligible because of the

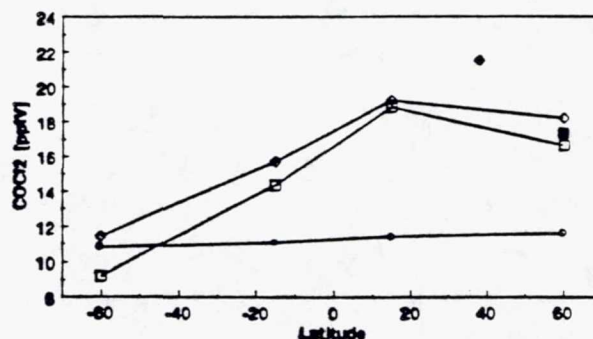


Figure 9. The latitudinal and vertical distribution calculated for tropospheric $COCl_2$ (i.e., $COCl_2$ produced from the tropospheric oxidation of the four RPP compounds). The open squares represent the lower troposphere, the open diamonds represent the upper troposphere, and the open circles represent the stratosphere. The solid square represents annually averaged airborne measurements made by *Wilson et al.* [1988] between Germany and Spitzbergen (50° - $78^\circ N$) at altitudes of 5-12 km. The solid diamond represents surface measurements made by *Singh et al.* [1977] at a remote site in California ($38^\circ N$) in 1976.

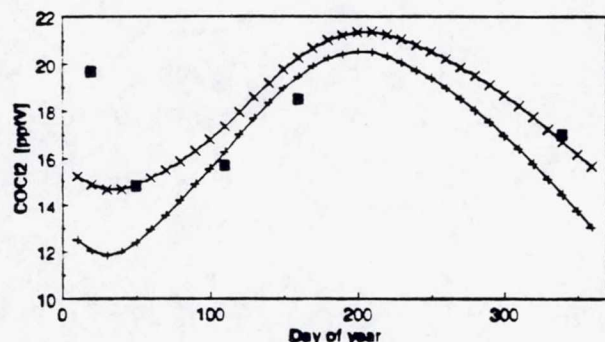


Figure 10. Model-calculated and observed tropospheric COCl_2 concentrations as a function of time of year in the northern hemisphere poleward of 30°N . The model-calculated concentrations are for the lower troposphere (boxes $n = 1$) (represented by pluses) and the upper troposphere (box $n = 5$) (represented by crosses) of the two-dimensional model using the COCl_2 sources from the oxidation of the RPP compounds. The observed concentrations are based on the mid tropospheric airborne measurements of *Wilson et al.* [1988] and are represented by solid squares.

compound's very short tropospheric lifetime). The role of each of the five stratospheric sources relative to that which arises from the upward transport of tropospheric COCl_2 is indicated in Figure 11a, where profiles calculated with the 1-D stratospheric model for equinoctial conditions at midlatitudes are illustrated for each source and all sources together. While the tropospheric COCl_2 profile decreases monotonically from its concentration at the tropopause, the profiles which include stratospheric production increase in concentration in the lower stratosphere and generally reach a maximum at altitudes between 21 and 27 km. The exact altitude of the maximum depends on the species. The COCl_2 produced from C_2Cl_4 , CHCl_3 , and CH_3CCl_3 peak at an altitude of about 22 km because of their reactivity toward OH, while COCl_2 from the unreactive CCl_4 peaks at about 27 km. Interestingly, a comparison of the profile which includes all sources with the profile from the midlatitude measurements of

Table 6. Model-Calculated Budget for Tropospheric COCl_2

Process	Rate, pptv/yr	Percentage of total
Total source (see Table 5)	92.4	100
Loss via cloud removal in lower troposphere	70.9	76.7
Loss via cloud removal in upper troposphere	13.1	14.2
Loss via ocean deposition	8.0	8.7
Total wet deposition	92.0	99.6
Transport to and loss in stratosphere	0.4	0.4
Total loss	92.4	100

Here, tropospheric COCl_2 is produced from the oxidation of the four RPP compounds.

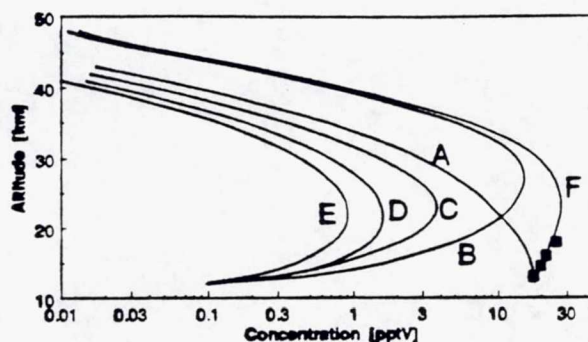


Figure 11a. Calculated profiles for COCl_2 in the stratosphere for a solar zenith angle of 65° . The solid lines are the calculated profiles: A for tropospheric COCl_2 (no stratospheric source), B for stratospheric COCl_2 from CCl_4 , C for stratospheric COCl_2 from C_2Cl_4 , D for stratospheric COCl_2 from CHCl_3 , E for stratospheric COCl_2 from CH_3CCl_3 , and F is total COCl_2 (tropospheric plus stratospheric sources). The squares indicate the measurements of *Wilson et al.* [1988]. The concentration at the lower boundary (i.e., tropopause) for simulations A and F was chosen to be equal to the COCl_2 concentration obtained for the northern, upper tropospheric box in our 2-D model simulation (see Figure 9). Note that the resulting averaged stratospheric concentration obtained from our simulation of tropospheric COCl_2 using this boundary condition (i.e., profile A) is consistent with that obtained for the stratosphere in our 2-D box model simulation.

Wilson et al. [1988] indicates reasonably good agreement in both the concentration magnitude and profile shape in the lower stratosphere (see Figure 11).

The model-calculated budgets of stratospheric COCl_2 produced from CCl_4 , C_2Cl_4 , CHCl_3 and CH_3CCl_3 for global average conditions are presented in Table 7. Because of COCl_2 's relatively long lifetime against destruction in the stratosphere and its rapid removal rate in the troposphere, we find that a significant portion of the COCl_2 that is produced in the stratosphere is

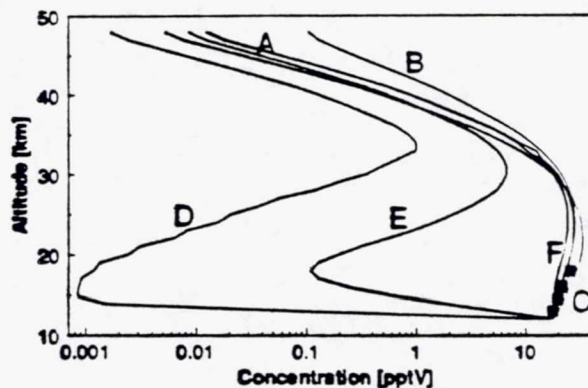


Figure 11b. Calculated profiles for COCl_2 in the stratosphere for a solar zenith angle of 65° . The solid lines are calculated profiles: A is for our standard model, B for K_2 multiplied by a factor of 2, C for $\text{C}_2(\text{OH})$ multiplied by a factor of 5, D for including potential reaction of COCl_2 on sulfate aerosols with $\gamma=1$, E for including potential reaction of COCl_2 on sulfate aerosols with $\gamma = 10^{-2}$, and F for including potential reaction of COCl_2 on sulfate aerosols with $\gamma = 5 \times 10^{-5}$.

Table 7. Model-Calculated Budget for Stratospheric COCl₂

		CCl ₄	CH ₂ CCl ₃	C ₂ Cl ₄	CHCl ₃	Total
P.S.	Rate, (cm ² s) ⁻¹	1.48x10 ⁶	1.25x10 ⁵	3.16x10 ⁵	2.55x10 ⁵	2.18x10 ⁶
	Percent	100.0	100.0	100.0	100.0	100.0
L.S.	Rate, (cm ² s) ⁻¹	1.07x10 ⁶	2.40x10 ⁴	1.01x10 ⁵	4.00x10 ⁴	1.24x10 ⁶
	Percent	72.4	18.9	32.0	15.7	56.9
L.W.	Rate, (cm ² s) ⁻¹	4.09x10 ⁵	1.01x10 ⁵	2.15x10 ⁵	2.15x10 ⁵	9.40x10 ⁵
	Percent	27.6	81.1	68.0	84.3	43.1
T.L.	Rate, (cm ² s) ⁻¹	1.48x10 ⁶	1.25x10 ⁵	3.16x10 ⁵	2.55x10 ⁵	2.65x10 ⁶
	Percent	100.0	100.0	100.0	100.0	100.0

Here, stratospheric COCl₂ is produced from the photolysis of CCl₄, the oxidation of CH₂CCl₃ and CHCl₃, and oxidation and photolysis of C₂Cl₄ calculated with the one-dimensional stratospheric model with a 60° solar zenith angle. Abbreviations are P.S., production in stratosphere; L.S., loss in stratosphere; L.W., loss via transport to troposphere and wet removal; and T.L., total loss. The flux of stratospheric COCl₂ to the troposphere (L.W.) was obtained from the sum of (1) the downward COCl₂ flux at the tropopause calculated for the case when both the stratospheric and tropospheric COCl₂ sources were included, and (2) the upward COCl₂ flux at the tropopause calculated for the case when only the tropospheric COCl₂ flux was included.

transported to the troposphere before it is destroyed. As is indicated in Table 7, the fraction returned to the troposphere is estimated to be roughly one third in the case of CCl₄, two thirds in the case of that produced from C₂Cl₄ and four fifths in the case of stratospheric COCl₂ produced from CH₂CCl₃ and CHCl₃. The larger fractions returned to the troposphere for the COCl₂ produced from CH₂CCl₃, C₂Cl₄, and CHCl₃ are caused by the fact that this COCl₂ is generated at lower stratospheric altitudes, where it encounters less UV radiation and has a shorter distance to travel to reach the tropopause. As we discuss in the next section, the transport of stratospheric COCl₂ into the troposphere can have a significant impact on the stratospheric chlorine loading of these compounds and ultimately therefore on their ozone depletion potentials.

9. Effect of Phosgene Transport on Stratospheric Chlorine Loadings of Phosgene Parent Compounds

An important factor in determining the potential for a compound to deplete stratospheric ozone is its stratospheric chlorine loading, defined here as the percentage of the chlorine contained in the species that is emitted at the surface and ultimately released in the stratosphere as reactive chlorine capable of participating in the catalytic destruction of ozone. Estimates of the stratospheric chlorine loadings of COCl₂'s parent compounds are presented in Table 8 for a variety of model assumptions. (Note that we indicate absolute chlorine loadings in Table 8 rather than the more standard, chlorine loading potentials, which are normalized to the chlorine loading of CFC-11. The reason for this will be discussed in section 10.)

An indication of the effect of tropospheric-stratospheric transport of COCl₂ on the stratospheric chlorine loadings of COCl₂'s parent compounds can be obtained by comparing the results listed in Table 8 for the standard model with those listed for "Model 0," where exchange of COCl₂ across the tropopause was neglected. Because of tropospheric COCl₂'s relative short lifetime and stratospheric COCl₂'s long lifetime, we find that

tropospheric-stratospheric COCl₂ transport tends to lower the stratospheric chlorine loadings of the phosgene parent compounds, and, in some cases the decrease can be significant. Most notable are C₂Cl₄ and CHCl₃; because these species are destroyed efficiently in the lower stratosphere, major fractions (i.e., 70% for C₂Cl₄ and 85% for CHCl₃) of the stratospheric COCl₂ produced from these compound are returned to the troposphere and as a result, consideration of tropospheric-stratospheric transport of COCl₂ produced by C₂Cl₄ and CHCl₃ causes decreases in their stratospheric chlorine loadings of about 15% and 25%, respectively. (However, because the total stratospheric chlorine loadings for these two species are so small, they are not effective agents of stratospheric ozone depletion, and thus the decreased chlorine loadings calculated for these two compounds will not affect overall predictions of ozone depletion from halocarbons.) The impact on the chlorine loading of CCl₄ is somewhat less pronounced (approximately 14%) because the COCl₂ from this compound is produced at higher stratospheric altitudes. A relatively small correction (i.e., 3%) to the chlorine loading of CH₂CCl₃ is predicted because the vast majority of the chlorine atoms from CH₂CCl₃ decomposition in the stratosphere are not converted into COCl₂. Recall that COCl₂ is only produced from CH₂CCl₃ via OH attack (see Table 1), while most of the stratospheric CH₂CCl₃ in our model is destroyed via photolysis.

The sensitivity of our results to variations in model parameters was investigated in a series of additional calculations; in model 1 we varied the stratospheric K₂ by factors of 2, in model 2 we varied C(OH) in the stratosphere by factors of 5, in model 3 we included a reaction between COCl₂ and stratospheric sulfate aerosol; and in model 4 we include convective like transport from the lower troposphere to the stratosphere in the 2-D model. The inclusion of a COCl₂ sink via reaction with sulfate aerosol in model 3 was accomplished by modifying equation (12) for COCl₂ to include an additional loss with an effective first-order rate constant k_{aerosol} given by

$$k_{\text{aerosol}} = v \gamma A/4 \quad (15)$$

Table 8. Stratospheric Chlorine Loadings for Phosgene Parent Compounds and for CFC-11

Species	Model*								
	0	Standard.	1A	1B	2A	2B	3A	3B	4
CCl ₄	100	86.2	87.2	84.4	86.2	86.2	99.5	88.4	86.2
CH ₂ CCl ₃	12.4	12.0	12.3	11.6	10.3	12.5	12.5	12.1	12.0
C ₂ Cl ₄	1.6	1.4	1.3	1.4	1.4	1.4	1.8	1.4	1.4
CHCl ₃	1.7	1.3	1.5	1.2	1.0	1.7	1.8	1.3	1.2
CFC1 ₃	100	93.5	93.2	93.6	93.5	93.5	100	94.9	93.5

The stratospheric chlorine loading of a species is defined here as the percentage of the chlorine atoms released at the surface that are injected into the stratosphere as reactive chlorine capable of participating in the catalytic destruction of ozone. Values are percentages.

*Model 0 assumes no transport of tropospheric COCl₂ to the stratosphere and no transport of stratospheric COCl₂ to the troposphere. Parameters adopted for the standard model are described in the text. Model 1 investigates the effect of varying K₂; in model 1A, K₂ is multiplied by 2, and in model 1B, K₂ is divided by 2. Model 2 investigates the effect of varying stratospheric C(OH); in model 2A C(OH) is multiplied by 5, and in model 2B, C(OH) is divided by 5. Model 3 investigates the effect of including a reaction between stratospheric COCl₂ and sulfate aerosol; in model 3A, $\gamma = 1$, and in model 3B, $\gamma = 5 \times 10^{-5}$. Model 4 investigates the effect of convective like transport from the lower troposphere to the stratosphere.

where v is the COCl₂ thermal velocity, γ is probability of a reaction occurring per collision (and allowed to vary from 5×10^{-5} to 1), and A is the aerosol surface area (taken from World Meteorological Organization, (WMO), [1991], as function of altitude). The inclusion of convective like transport in model 4 was accomplished by altering the transport code in the 2-D model so that 50% of the transport from the troposphere to the stratosphere occurred by direct injection of air from the lower tropospheric boxes, as opposed to the standard model, where all such transport came from the upper tropospheric boxes. The results of our sensitivity calculations are summarized in Table 8 and Figure 11b.

Inspection of Table 8 reveals that the inclusion of a reaction with sulfate aerosol can cause a major shift in our results. For instance, note that when $\gamma = 1$, the stratospheric chlorine loadings for phosgene parent compounds become equal to those obtained for our model 0 calculations. In this case all stratospheric COCl₂ is destroyed in the stratosphere by the aerosol reaction, and there is no transport of stratospheric COCl₂ to the troposphere. Hence our results in this case are identical to those in which we neglected the tropospheric-stratospheric exchange of COCl₂. (Of course, when we let $\gamma < 5 \times 10^{-6}$, the results approach those obtained for our standard model, since the reaction of COCl₂ with the sulfate aerosol becomes too slow to have an impact.) However, it should be noted in this regard that in addition to changing the stratospheric chlorine loadings of the phosgene parent compounds, inclusion of a reaction of COCl₂ with sulfate aerosol can also have a major effect on the distribution of COCl₂ in the lower stratosphere. Note in Figure 11b that when $\gamma > 5 \times 10^{-5}$, the rapid scavenging of COCl₂ by sulfate aerosol causes its concentration to decrease instead of increase as a function of altitude in the lower stratosphere. This result is in direct contradiction with the observed profile of Wilson *et al.* [1988]. It would appear that the reaction of COCl₂ with sulfate aerosol hypothesized in model 3 most likely has a $\gamma < 5 \times 10^{-5}$ and

thus has a negligible impact on the stratospheric chlorine loadings of the phosgene parent compounds (see Table 8).

Inspection of Table 8 reveals that variations in C(OH) cause modest changes in our results; increasing the stratospheric OH concentrations by a factor of 5 leads to a 17 and 40% decrease in the stratospheric chlorine loadings of CH₂CCl₃ and CHCl₃, respectively. This occurs because an increase in stratospheric OH increases the yield of COCl₂ from these two compounds in the stratosphere (see Table 1) and thus effectively increases the percentage of chlorine from these two compounds that can be returned to the troposphere as COCl₂. Finally note that variations in eddy diffusion coefficients by a factor of 2 have a very small impact on our results, and inclusion of convective like transport in the troposphere has essentially no effect on our results. The lack of an impact from convective like transport can be attributed to the absence of strong vertical gradients in the distributions of COCl₂ and its parent compounds (see Figures 5-10).

Another model assumption that bears some discussion is that concerning the role of Cl atoms as oxidizers of the RPP compounds in the troposphere; recall that we assumed that photochemical destruction of these compounds in the troposphere only occurred as a result of reaction with OH and we neglected any contribution that might occur as a result of a reaction with Cl. However, as was noted earlier, C₂Cl₄ reacts extremely rapidly with Cl atoms. Moreover, the Cl-initiated oxidation of C₂Cl₄ has been found to produce trichloroacetyl chloride (TCAC) and COCl₂, in a molar ratio of roughly 3:1 [Sanhueza *et al.*, 1976]. If the Cl-initiated oxidation were a significant sink for C₂Cl₄ and a significant fraction of the chlorine in TCAC produced from this reaction were transported to the stratosphere, the stratospheric chlorine loading for this compound could conceivably be significantly larger than the approximate 1-2% value obtained here in our standard model. It is interesting therefore to briefly consider the fate of tropospheric TCAC. One pathway for TCAC loss is photolysis, a major product being COCl₂ and a

minor product being CCl_4 [Behnke and Zetzsch, 1991]. While the production of CCl_4 from TCAC could potentially increase the stratospheric chlorine loading of C_2Cl_4 , the yield of CCl_4 appears to be quite small (less than 0.3% according to Behnke and Zetzsch) and thus should have a negligible impact. In addition to photolysis, TCAC can be removed from the atmosphere via wet removal. Calculations with the algorithm described in section 4 using $H = 0.3 \text{ M/atm}$ and $k = 2.7 \text{ s}^{-1}$ [D. Worsnop, private communication, 1993] indicate that the lifetime against these removal processes is of order of 20 days and thus that stratospheric chlorine loading from TCAC is insignificant. Thus it appears likely on the basis of present kinetic and thermodynamic data that if a Cl-initiated oxidation pathway represented a major sink for C_2Cl_4 , its stratospheric chlorine loading would be even smaller than the value estimated here.

10. Revised Estimates for ODPs of Phosgene Parent Compounds

The ozone depletion potential, or ODP, of a compound is defined as the steady state ozone reduction calculated for each unit mass of gas emitted per year into the atmosphere relative to that for a unit mass emission of CFCl_3 [MWO, 1989]. Because we find that the inclusion of stratospheric/tropospheric exchange of COCl_2 causes a decrease in the stratospheric chlorine loadings of the phosgene parent compounds, one might assume that it would also cause an approximately equivalent decrease in the ODPs of these compounds, as indicated by the first two columns of Table 9 (calculated according to the semiempirical equation for ODPs given by Solomon *et al.* [1994]).

However, a thorough evaluation of the ODPs of the phosgene parent compounds requires consideration of an additional complication. The ODPs are expressed relative to the ozone depletion of CFCl_3 , and the destruction of CFCl_3 in the stratosphere via photolysis produces COFCl [Jayanty *et al.*, 1975]. COFCl is a compound with properties similar to that of COCl_2 ; it is a weak absorber in the near UV [Noelle *et al.*, 1993] and most likely is hydrolyzed in water at a rate close to that of COCl_2 and thus like COCl_2 is subject to transport to the troposphere and removal by wet deposition. Such an effect would decrease the stratospheric chlorine loading of CFCl_3 and, as a result, would effectively increase the ODP of other compounds, although the actual chlorine loadings of these other compounds would not be changed by the transport of COFCl .

Using the same model approach we used for COCl_2 and its parent compounds, along with spectroscopic data for CFCl_3 and COFCl from DeMore *et al.* [1992] and Noelle *et al.* [1993], we estimate that approximately 21% of all COFCl produced in the stratosphere from the photolysis of CFCl_3 is transported down to the troposphere. Since only one third of the Cl atoms in CFCl_3 are converted to COFCl from photolysis, this implies that roughly 7% of the Cl from CFCl_3 is returned to the troposphere in the form of COFCl and removed in precipitation. Thus we estimate an actual stratospheric chlorine loading for CFCl_3 of 93% instead of 100% (see Table 8). This somewhat smaller chlorine loading for CFCl_3 causes a slight upward revision in the ODPs of the phosgene parent compounds as indicated by the third column of Table 9. Note that in the cases of CCl_4 , CHCl_3 , and C_2Cl_4 , the decreases in their stratospheric chlorine loadings due to the cross-tropopause transport of COCl_2 are estimated to be larger than the decrease in the stratospheric chlorine loading of CFCl_3 due to transport of COFCl , and thus we predict a net

Table 9. Ozone Depletion Potentials for Phosgene Parent Compounds

Compound	Ozone Depletion Potential			
	ODP(0)	ODP(1)	ODP(1)'	Literature Values
COCl_2	0.0030	0.0030	0.0030	n.a.*
CH_3CCl_3	0.086	0.083	0.089	0.11 - 0.13
C_2Cl_4	7.0×10^{-3}	5.7×10^{-3}	6.0×10^{-3}	n.a.
CHCl_3	0.0102	0.0078	0.0083	n.a.
C_2HCl_3	4.9×10^{-4}	7.0×10^{-4}	7.0×10^{-4}	n.a.
CCl_4	1.10	0.95	1.01	1.03 - 1.15

ODP(0) is that obtained using the formulation of Solomon *et al.* [1994] and neglecting the effect of COCl_2 transport (i.e., model 0); ODP(1) obtained by including the effect of COCl_2 tropospheric-stratospheric exchange (i.e., standard model); ODP(1)' is similar to ODP(1) but also includes the effect of the downward transport of stratospheric COFCl to the troposphere. Literature values are taken from WMO [1991]. Note that ODP(0) for CH_3CCl_3 is smaller than the values found in the literature because a shorter lifetime of 5.59 years was adopted here to be consistent with the most recent ALE/GAGE data [Prinn *et al.*, 1992].

* Not available

decrease in the ODPs of these species. The opposite is found for CH_3CCl_3 , and thus in this case we actually predict a slight increase in its ODP.

11. Conclusions

An analysis of the cycle of atmospheric COCl_2 reveals two distinct subcycles. The tropospheric subcycle is driven by production from the OH-initiated oxidation of four reactive halocarbons, namely, CH_3CCl_3 , C_2Cl_4 , CHCl_3 , and C_2HCl_3 . Our calculations indicate that COCl_2 produced from these compounds is removed from the atmosphere by hydrolysis in cloudwater with an average atmospheric lifetime of about 70 days. Simulations of this subcycle with a 2-D model yield reasonably good agreement with observations of tropospheric COCl_2 and its parent compounds. Our calculations suggest that it is unlikely that a significant fraction of the COCl_2 produced in the troposphere is transported and decomposed in the stratosphere and thus that tropospheric COCl_2 has an insignificant role in the depletion of stratospheric ozone.

The stratospheric COCl_2 subcycle is driven by production from the photochemical degradation of CCl_4 , a compound which is essentially inert in the troposphere, as well as of CH_3CCl_3 , CHCl_3 , and C_2Cl_4 . However, because of COCl_2 's weak absorption cross sections in the near and middle ultraviolet, we estimate that a significant fraction of the COCl_2 produced in the stratosphere (perhaps 40%) is probably returned to the troposphere and removed from the atmosphere by clouds. Thus

unless some other sink for stratospheric COCl_2 exists, our calculations suggest the downward transport of stratospheric COCl_2 causes a decrease in the stratospheric chlorine loadings of the phosgene parent compounds. Factoring in a similar effect for COFCl from the photolysis of CFCl_3 , we infer a downward revision in the ODPs of CCl_4 , C_7Cl_4 , and CHCl_3 but a slight increase in the ODP of CH_2Cl_2 .

Finally, our calculations suggest the need for a small correction to the global budget of stratospheric chlorine. For instance, Prather and Watson [1990] estimated that 13% of the total chlorine loading of the stratosphere is caused by CCl_4 , 13% is caused by CH_2Cl_2 , and 22% is caused by CFC-11. However, if about 13.8% of the chlorine atoms from CCl_4 , 3.2% of those from CH_2Cl_2 , and 6.5% of that from CFC-11 are transported back to the troposphere as COCl_2 or COFCl , the global input of chlorine to the stratosphere is about 4% smaller than that originally estimated by Prather and Watson [1990].

There are of course large uncertainties in the results presented here because of the many simplifications inherent in our model's formulation as well as the potential errors in the thermodynamic and kinetic data adopted in the model. However, the results perhaps point to a more fundamental uncertainty in our understanding of halocarbons and their impact on stratospheric ozone. The atmospheric degradation of halocarbons can lead to the production of a wide variety of intermediates. In some cases these intermediates may be long-lived enough to either enhance the amount of chlorine from reactive halocarbons that reaches the stratosphere or decrease the amount of chlorine from unreactive halocarbons that is liberated in the stratosphere. For this reason we believe that priority should continue to be given to research that unravels the detailed degradation pathways of halocarbons and the ultimate fate of the intermediate products of these pathways.

Acknowledgments. The research for this work was supported in part by funds from the European Chlorinated Solvent Association, the Halogenated Solvents Industry Alliance (USA), the Japanese Association for Hygiene of Chlorinated Solvents, and the National Science Foundation under grant ATM-8905901. Participation by P.H.W. was supported by the National Aeronautics and Space Administration under grant NAGW-1001.

References

- Atkinson, R., and S.M. Aschmann, Kinetics of the gas-phase reactions of Cl atoms with chloroethenes at 298 ± 2 K and atmospheric pressure, *Int. J. Chem. Kinet.*, **19**, 1097-1105, 1987.
- Bandy, A.R., D.L. Scott, B.W. Blomquist, S.M. Chen, and D.C. Thornton, Low yields of SO_2 from dimethyl sulfide oxidation in the marine boundary layer, *Geophys. Res. Lett.*, **19**(11), 1125-1127, 1992.
- Behnke, W., and C. Zeitzsch, The yield of carbon tetrachloride from the tropospheric photochemical degradation of perchloroethene, *Fraunhofer-Institut fuer Toxikologie und Aerosolforschung*, Hannover, Germany, 1991.
- Berry, M.J., Chloroethylene photochemical lasers: Vibrational energy content of the HCl molecular elimination products, *J. Chem. Phys.*, **61**, 3114-3143, 1974.
- Butler, R., and A. Snelson, Kinetics of the homogeneous gas phase hydrolysis of CCl_3COCl , CCl_2HCOCl , CH_2ClCOCl and COCl_2 , *J. Air Pollut. Control Assoc.*, **29**(8), 833-837, 1979.
- Butler, J.H., J.W. Elkins, T.M. Thompson, and B.D. Hall, Oceanic consumption of CH_2Cl_2 : Implications for tropospheric OH, *J. Geophys. Res.*, **96**, 22,347-22,355, 1991.
- Chameides, W.L., The photochemistry of a remote marine stratiform cloud, *J. Geophys. Res.*, **89**, 4739-4755, 1984.
- Class, T., and K. Ballschmiter, Atmospheric halocarbons: Global budget estimations for tetrachloroethylene, 1,2-dichloroethane, 1,1,1,2-tetrachloroethane, hexachloroethane and hexachlorobutadiene. Estimation of the hydroxyl radical concentrations in the troposphere of the northern and southern hemisphere, *Fresenius Z. Anal. Chem.*, **327**, 198-204, 1987.
- Crutzen, P.J., I.S. Isaksen, and J.R. McAfee, The impact of the chlorocarbon industry on the ozone layer, *J. Geophys. Res.*, **83**, 345-363, 1978.
- Cunnold, D.M., R.G. Prinn, R.A. Rasmussen, P.G. Simmonds, F.N. Alyea, C.A. Cardelino, A.J. Crawford, P.J. Fraser, and R.D. Rosen, The atmospheric lifetime experiment, 3, Lifetime methodology and application to three years of CFCl_3 data, *J. Geophys. Res.*, **88**, 8379-8400, 1983.
- Cunnold, D.M., R.G. Prinn, R.A. Rasmussen, P.G. Simmonds, F.N. Alyea, C.A. Cardelino, A.J. Crawford, P.J. Fraser, and R.D. Rosen, The atmospheric lifetime and annual release estimates for CFCl_3 and CF_2Cl_2 from 5 years of ALE data, *J. Geophys. Res.*, **91**, 10,797-10,817, 1986.
- Dankwerts, P.V., *Gas-Liquid Reactions*, 276 pp., McGraw-Hill, New York, 1970.
- De Bruyn, W.J., S.X. Duan, X.Q. Shi, P. Davidovits, D.R. Worsnop, M.S. Zahniser, and C.E. Kolb, Tropospheric heterogeneous chemistry of haloacetyl and carbonyl halides, *Geophys. Res. Lett.*, **19**, 1939-1942, 1992.
- DeMore, W.B., S.P. Sander, D.M. Golden, R.F. Hampson, M.J. Kurylo, C.J. Howard, A.R. Ravishankara, C.E. Kolb, and M.J. Molina, Chemical kinetics and photochemical data for use in stratospheric modeling, Evaluation No. 10, NASA Panel for Data Evaluation, *JPL Publ.*, 92-20, 1992.
- Derwent, R.G., and A.E.J. Eggleton, Halocarbon lifetimes and concentration distributions calculated using a two-dimensional tropospheric model, *Atmos. Environ.*, **12**, 1261-1269, 1978.
- Gerken, R.R., and J.A. Franklin, The rate of degradation of 1,1,1-trichloroethane in water by hydrolysis and dehydrochlorination, *Chemosphere*, **19**, 1929-1937, 1989.
- Gidel, L.T., P.J. Crutzen, and J. Fishman, A two-dimensional photochemical model of the atmosphere, 1, Chlorocarbon emissions and their effect on stratospheric ozone, *J. Geophys. Res.*, **88**, 6622-6640, 1983.
- Greenwald, T.J., G.L. Stephens, T.H. Vonder Haar, and D.L. Jackson, A physical retrieval of cloud liquid water over the global oceans using special sensor microwave/imager (SSM/I) observations, *J. Geophys. Res.*, **98**, 18,471-18,488, 1993.
- Harris, G.W., D. Klemp, and T. Zenker, An upper limit on the HCl near-surface mixing ratio over the Atlantic measured using TDLAS, *J. Atmos. Chem.*, **15**, 327-332, 1992.
- Helas, G., and S.R. Wilson, On sources and sinks of phosgene in the troposphere, *Atmos. Environ. Part A*, **26**, (16), 2975-2982, 1992.
- Heydtmann, H., Physics and chemistry of the atmosphere, poster, presented at discussion meeting of the Deutsche Bunsen-Gesellschaft fuer Physikalische Chemie, Schliersee, Germany, 1991.
- Jayanty, P.K.M., R. Simonaitis, and J. Heicklen, The photolysis of chlorofluoromethanes in the presence of O_2 and O_3 at 213.9 nm and their reactions with $\text{O}(^1\text{D})$, *J. Photochem.*, **4**, 381-398, 1975.
- Jayne, J.T., P. Davidovits, D.R. Worsnop, M.S. Zahniser, and C.E. Kolb, Uptake of SO_2 by aqueous surfaces as a function of pH: The effect of chemical reaction at the interface, *J. Phys. Chem.*, **94**, 6041-6048, 1990.
- Jeffers, P.M., L.M. Ward, L.M. Woytowitch, and N.L. Wolfe, Homogeneous hydrolysis rate constants for selected chlorinated methanes, ethanes, ethenes, and propanes, *Environ. Sci. Technol.*, **23**, 965-969, 1989.
- Johnson, J.E., The lifetime of carbonyl sulfide in the troposphere, *Geophys. Res. Lett.*, **8**, 938-940, 1981.
- Keene, W.C., A.A.P. Pszenny, D.J. Jacob, R.A. Duce, J.N. Galloway, J.J. Schultz-Tokos, H. Sievering, and J.F. Boatman, The geochemical cycling of reactive chlorine through the marine troposphere, *Global Biogeochem. Cycles*, **4**, 407-430, 1990.
- Khalil, M.A.K., R.A. Rasmussen, and S.D. Hoyt, Atmospheric chloro-

- form (CHCl₃): ocean-air exchange and global mass balance, *Tellus, Ser. B*, 35, 266-274, 1983.
- Koppmann, R., F.J. Johnen, C. Plass-Duelmer, and J. Rudolph, Distribution of methylchloride, dichloromethane, trichloroethene and tetrachloroethene over the North and South Atlantic, *J. Geophys. Res.*, 98, 20,517-20,526, 1993.
- Li, Y.-H., T. Peng, W. Broecker, and H. Oestlund, The average vertical mixing coefficient for the oceanic thermocline, *Tellus, Ser. B*, 36, 212-217, 1984.
- Liss, P.S., Gas transfer: Experiments and geochemical implications, in *Air-Sea Exchange of Gases and Particles, NATO ASI Series*, vol. 108, pp. 241-298, D. Reidel, Norwell, Mass., 1983.
- Luther, F.M., J.S. Chang, W.H. Duewer, J.E. Penner, R.P. Tarp, and D.J. Wuebbles, Potential environmental effects of aircraft emissions, *UCRL-52861, Lawrence Livermore Natl. Lab.*, Livermore, Calif., 1979.
- Manogue, W.H., and R.L. Pigford, The kinetics of the absorption of phosgene into water and aqueous solutions, *AIChE J.*, 6(3), 494-500, 1960.
- Midgley, P., The production and release to the atmosphere of 1,1,1-trichloroethane (methyl chloroform), *Atmos. Environ.*, 23, 2663-2664, 1989.
- Mozurkewich, M., P.H. McMurry, A. Gupta, and J.G. Calvert, Mass accommodation coefficients for HO₂ radicals on aqueous particles, *J. Geophys. Res.*, 92, 4163-4170, 1987.
- Nelson, L., J.J. Treacy and H.W. Sidebottom, Oxidation of methylchloroform, *3rd European Symposium on Physico-Chemical Behaviour of Atmospheric Pollutants*, pp. 258-263, D. Reidel, Norwell, Mass., 1984.
- Nelson, L., I. Shanahan, H.W. Sidebottom, J. Treacy, and O.J. Nielsen, Kinetics and mechanism for the oxidation of 1,1,1-trichloroethane, *Int. J. Chem. Kin.*, 22, 577-590, 1990.
- Newell, R.E., D.G. Vincent, and J.W. Kidson, Interhemispheric mass exchange from meteorological and trace surface observations, *Tellus*, 21, 641-647, 1969.
- Noelle, A., H. Heydtmann, R. Meller, and G.K. Moortgat, Temperature dependent UV absorption spectra of carbonyl chloro-fluoride, *Geophys. Res. Lett.*, 20, 701-710, 1993.
- Ohta, T., and I. Mizoguchi, Determination of the mechanism of the oxidation of the trichloromethyl radical by photolysis of chloral in the presence of oxygen, *Int. J. Chem. Kin.*, 12, 717-727, 1980.
- Prather, M.J., and R.T. Watson, Stratospheric ozone depletion and future levels of atmospheric chlorine and bromine, *Nature*, 344, 729-734, 1990.
- Prinn, R., D. Cunnold, R. Rasmussen, P. Simmonds, F. Alyea, A. Crawford, P. Fraser, and R. Rosen, Atmospheric trends in methylchloroform and the global average for the hydroxyl radical, *Science*, 238, 945-950, 1987.
- Prinn, R., D. Cunnold, P. Simmonds, F. Alyea, R. Boldi, A. Crawford, P. Fraser, D. Gutzler, D. Hartley, R. Rosen, and R. Rasmussen, Global average concentration and trend for hydroxyl radicals deduced from ALE/GAGE trichloroethane data for 1978-1990, *J. Geophys. Res.*, 97, 2445-2461, 1992.
- Rasmussen, R.A., M.A.K. Khalil, and A.J. Crawford, Natural and anthropogenic trace gases in the southern hemisphere, *Geophys. Res. Lett.*, 9, 704-707, 1982.
- Reynolds, R.W., A monthly averaged climatology of sea surface temperature, *NOAA Tech. Rep. NWS 31*, Natl. Weather Serv., Silver Spring, Md., 1982.
- Sanhueza, E., I.C. Hisatsune, and J. Heicklen, Oxidation of haloethylenes, *Chem. Rev.*, 76, 801-825, 1976.
- Schwartz, S.E., Mass-transport considerations pertinent to aqueous phase reactions of gases in liquid-water clouds, in *Chemistry of Multiphase Atmospheric Systems*, edited by W. Jaeschke, *NATO ASI Ser.*, pp. 415-471, Springer-Verlag, New York, 1986.
- Singh, H.B., Phosgene in the ambient air, *Nature*, 264, 428-429, 1976.
- Singh, H.B., and J.F. Kasting, Chlorine-hydrocarbon photochemistry in the marine troposphere and lower stratosphere, *J. Atmos. Chem.*, 7, 261-285, 1988.
- Singh, H.B., L. Salas, H. Shigeishi and A. Crawford, Urban-nonurban relationships of halocarbons, SF₆, N₂O, and other atmospheric trace constituents, *Atmos. Environ.*, 11, 819-828, 1977.
- Singh, H.B., L.J. Salas, and R.E. Stiles, Selected man-made halogenated chemicals in the air and oceanic environment, *J. Geophys. Res.*, 88, 3675-3683, 1983.
- Solomon, S., J.B. Burkholder, A.R. Ravishankara, and R.R. Garcia, Ozone depletion and global warming potentials of CF₃I, *J. Geophys. Res.*, 99, 20,929-20,935, 1994.
- Stamnes, K., S.-C. Tsay, W. Wiscombe, and K. Jayaweera, Numerically stable algorithm for discrete-ordinate-method radiative transfer in multiple scattering and emitting layered media, *Appl. Opt.*, 27, 2502-2508, 1988.
- Tuazon, E.C., R. Atkinson, S.M. Aschmann, M.A. Goodman, and A.M. Winer, Atmospheric reactions of chloroethenes with the OH radical, *Int. J. Chem. Kinet.*, 20, 241-265, 1988.
- Van Doren, J.M., L.R. Watson, P. Davidovits, D.R. Worsnop, M.S. Zahniser, and C.E. Kolb, Temperature dependence of the uptake coefficients of HNO₃, HCl, and N₂O₅ by water droplets, *J. Phys. Chem.*, 94, 3256-3269, 1990.
- Wilson, S.R., P.J. Crutzen, G. Schuster, D.W.T. Griffith, and G. Helas, Phosgene measurements in the upper troposphere and lower stratosphere, *Nature*, 334, 689-691, 1988.
- Wine, P., and W.L. Chameides, Possible atmospheric lifetimes and chemical reaction mechanisms for selected HCFCs, HFCs, CH₃CCl₃ and their degradation products against dissolution and/or degradation in seawater and cloudwater, in *Scientific Assessment of Stratospheric Ozone*, vol. 2, Appendix: AFEAS Report, *Global Ozone Res. and Mon. Proj.*, Rep. 20, pp. 273-295, World Meteorol. Organ., Geneva, 1989.
- World Meteorological Organization, Scientific Assessment of Stratospheric Ozone, *Global Ozone Res. and Monit. Proj.*, Rep. 20, Geneva, 1989.
- World Meteorological Organization, Scientific Assessment of Stratospheric Ozone, *Global Ozone Res. and Monit. Proj.*, Rep. 25, Geneva, 1991.

F.N. Alyea, W.L. Chameides, D.M. Cunnold, T.P. Kindler, and P.H. Wine, School of Earth and Atmospheric Sciences, Georgia Institute of Technology, Atlanta, GA 30332-0340.

J.A. Franklin, Solvay, S.A., Central Laboratory, B-1120 Brussels, Belgium.

(Received May 21, 1993; revised June 25, 1994; accepted September 22, 1994.)

Temperature-Dependent Kinetics Studies of the Reactions $\text{Br}(^2\text{P}_{3/2}) + \text{CH}_3\text{SCH}_3 \leftrightarrow \text{CH}_3\text{SCH}_2 + \text{HBr}$. Heat of Formation of the CH_3SCH_2 Radical

A. Jefferson,^{†‡} J. M. Nicovich,[†] and P. H. Wine^{*,†,§,||}

Georgia Tech Research Institute, School of Chemistry and Biochemistry, and School of Earth and Atmospheric Sciences, Georgia Institute of Technology, Atlanta, Georgia 30332

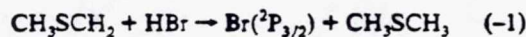
Received: November 2, 1993^o

Time-resolved resonance fluorescence detection of $\text{Br}(^2\text{P}_{3/2})$ atom disappearance or appearance following 266-nm laser flash photolysis of $\text{CF}_2\text{Br}_2/\text{CH}_3\text{SCH}_3/\text{H}_2/\text{N}_2$ and $\text{Cl}_2\text{CO}/\text{CH}_3\text{SCH}_3/\text{HBr}/\text{H}_2/\text{N}_2$ mixtures has been employed to study the kinetics of the reactions $\text{Br}(^2\text{P}_{3/2}) + \text{CH}_3\text{SCH}_3 \leftrightarrow \text{HBr} + \text{CH}_3\text{SCH}_2$ (1, -1) as a function of temperature over the range 386–604 K. Arrhenius expressions in units of $\text{cm}^3 \text{molecule}^{-1} \text{s}^{-1}$ which describe the results are $k_1 = (9.0 \pm 2.9) \times 10^{-11} \{\exp[-(2386 \pm 151)/T]\}$ and $k_{-1} = (8.6 \pm 2.5) \times 10^{-13} \{\exp[(836 \pm 140)/T]\}$; errors are 2σ and represent precision only. To our knowledge, these are the first kinetic data reported for each of the two reactions studied. Second and third law analyses of the equilibrium data for reactions 1 and -1 have been employed to obtain the following enthalpies of reaction in units of kcal mol^{-1} : $\Delta H_{298} = 6.11 \pm 1.37$ and $\Delta H_0 = 5.37 \pm 1.38$. Combining the above enthalpies of reaction with the well-known heats of formation of Br, HBr, and CH_3SCH_3 gives the following heats of formation of the CH_3SCH_2 radical in units of kcal mol^{-1} : $\Delta H_{f,298} = 32.7 \pm 1.4$ and $\Delta H_{f,0} = 35.3 \pm 1.4$; errors are 2σ and represent estimates of absolute accuracy. The C–H bond dissociation energy in CH_3SCH_3 obtained from our data, $93.7 \pm 1.4 \text{ kcal mol}^{-1}$ at 298 K and $92.0 \pm 1.4 \text{ kcal mol}^{-1}$ at 0 K, agrees well with a recent molecular beam photofragmentation study but is 3 kcal mol^{-1} lower than the value obtained from an iodination kinetics study.

Introduction

Accurate thermochemical information for free-radical intermediates is essential to analysis of reaction mechanisms in complex chemical systems. One experimental approach which can be employed to obtain thermochemical parameters for a radical involves measurement of temperature-dependent rate coefficients for the pair of reactions $\text{RH} + \text{R}' \leftrightarrow \text{R}'\text{H} + \text{R}$; the ideal reaction pair for such a study is one where the heats of formation and absolute entropies of R' , $\text{R}'\text{H}$, and R are well-characterized and where kinetic data for the two reactions can be obtained over the same temperature range.

In this paper we report the results of temperature-dependent kinetics studies of the following pair of reactions:



The kinetic results have been employed to derive a value for the heat of formation of the CH_3SCH_2 radical, an intermediate in the oxidation of the important atmospheric reduced sulfur compound dimethyl sulfide (CH_3SCH_3).¹

Experimental Technique

The experimental approach involved coupling reactant radical (i.e., Br or CH_3SCH_2) production by 266-nm laser flash photolysis of suitable precursors with time-resolved detection of ground-state bromine atom disappearance or appearance by atomic resonance fluorescence spectroscopy. A schematic diagram of the apparatus, as configured for bromine atom detection, can be found elsewhere,² as can a detailed description of the experimental

methodology.³ Only those aspects of the experimental approach which are unique to this study are discussed below.

Because the temperature range of this study (386–604 K) was higher than in our previous studies of bromine atom kinetics,^{2–4} a different reaction cell was employed. The cell was constructed of quartz and had an internal volume of about 200 cm^3 . A diagram showing the geometry of the reaction cell as well as a discussion of heating and temperature measurement techniques is published elsewhere.⁵

To avoid accumulation of photolysis or reaction products, all experiments were carried out under "slow flow" conditions. The concentration of each component in the reaction mixtures was determined from measurements of the appropriate mass flow rates and the total pressure. The excess reactant (i.e., CH_3SCH_3 or HBr) concentrations were also determined *in situ* in the slow flow system by UV photometry using a 2-m absorption cell. The monitoring wavelengths employed were 228.8 nm for CH_3SCH_3 (Cd line) and 202.6 nm for HBr (Zn⁺ line); absorption cross sections used to convert measured absorbances to concentrations were $1.16 \times 10^{-18} \text{ cm}^2$ for CH_3SCH_3 ⁶ and $1.02 \times 10^{-18} \text{ cm}^2$ for HBr.⁴ Since it was normally the case that more than one species in the reaction mixture absorbed at the monitoring wavelength, the excess reagent concentration was usually measured upstream from the photolyte addition point; dilution factors required to correct the measured concentration to the actual reactor concentration never exceeded 1.1.

The gases used in this study had the following stated minimum purities: N_2 , 99.999%; H_2 , 99.999%; HBr, 99.997% (liquid phase in cylinder); Cl_2CO , 99.0% (liquid phase in cylinder). Liquid samples were purchased from Aldrich and had the following stated purities: CH_3SCH_3 , 99+%; CF_2Br_2 , 99%. Nitrogen and hydrogen were used as supplied while HBr, Cl_2CO , CH_3SCH_3 , and CF_2Br_2 were degassed at 77 K before being used to prepare gaseous mixtures with N_2 .

Results

In our study of reaction 1, bromine atoms were generated by 266-nm laser flash photolysis of CF_2Br_2 ($[\text{CF}_2\text{Br}_2]$ ranged from

[†] Georgia Tech Research Institute.

[‡] Present address: National Center for Atmospheric Research, Boulder, CO 80307.

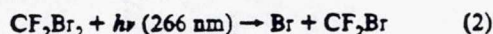
[§] School of Chemistry and Biochemistry.

^{||} School of Earth and Atmospheric Sciences.

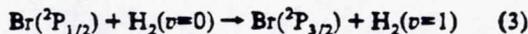
^{*} To whom correspondence should be addressed.

^o Abstract published in *Advance ACS Abstracts*, July 1, 1994.

2.3×10^{13} to 2.7×10^{14} molecules cm⁻³):

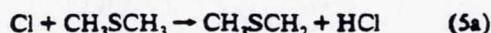
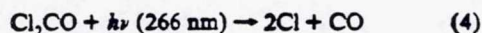


The CF₂Br₂ absorption cross section at 266 nm is approximately 8×10^{-20} cm² molecule⁻¹ while the quantum yield for Br production from CF₂Br₂ photolysis increases from unity at $\lambda = 248$ nm to approximately 2 at $\lambda = 193$ nm.¹⁰ Presumably, at $\lambda \geq 248$ nm, CF₂Br₂ photodissociates as indicated in reaction 2 with unit yield. To ensure rapid relaxation of any photolytically generated Br(²P_{1/2}), about 1 Torr of H₂ was added to the reaction mixture. The reaction

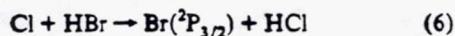


is known to be fast with $k_3 \approx 6 \times 10^{-12}$ cm³ molecule⁻¹ s⁻¹.¹¹

In our study of reaction -1, CH₃SCH₂ radicals were generated as follows:



Reaction 5 is known to occur at a gas kinetic rate,^{12,13} and channel 5a is dominant under the relatively high-temperature, low-pressure conditions employed in this study.¹³ Typical concentrations of Cl₂CO and CH₃SCH₃ were 1×10^{15} and 5×10^{14} molecules cm⁻³, respectively. The concentration of CH₃SCH₃ was kept sufficiently high that >80% of the photolytically generated Cl reacted with CH₃SCH₃ rather than with HBr ($k_6 = 2.25 \times 10^{-11} \exp(-400/T)$ cm³ molecule⁻¹ s⁻¹).¹⁴



On the other hand, the concentration of CH₃SCH₃ was kept sufficiently low that the back-reaction, i.e., reaction 1, had only a minor influence on observed Br(²P_{3/2}) kinetics. The Cl₂CO absorption cross section at 266 nm is approximately 2.3×10^{-20} cm²,^{15,16} while the quantum yield for Cl₂CO photodissociation at 253.7 nm has been shown to be unity.¹⁷ Reaction 4 actually occurs in a two-step process involving a ClCO intermediate. However, even in the unlikely event that ClCO is produced without internal excitation, the ClCO lifetime toward decomposition to Cl + CO is short compared to the experimental time scale of 0.1–1 ms.¹⁸

All experiments were carried out under pseudo-first-order conditions with the stable reactant in large excess (factors of 10³–10⁵) over the free-radical reactant. Concentrations of photolytically generated radicals were typically around 3×10^{11} cm⁻³, although this experimental parameter was varied over a wide range (factor of 30). For both reactions studied, observed kinetics were found to be independent of the photolytic precursor concentration(s) and the concentration of photolytically generated radicals. Observed kinetics were also found to be independent of the linear flow rate of the reaction mixture through the reactor and the photolysis laser repetition rate.

In the absence of side reactions which regenerate or deplete the Br(²P_{3/2}) atom concentration, the observed Br(²P_{3/2}) temporal profile following the laser flash in studies of reaction 1 would be described by the relationship

$$\ln(S_0/S_t) =$$

$$\ln\{[\text{Br}]_0/[\text{Br}]_t\} = (k_1[\text{CH}_3\text{SCH}_3] + k_7)t \equiv k't \quad (1)$$

In the above relationship S₀ and S_t are the signal levels immediately after the laser fires and at some later time t, [Br]₀ and [Br]_t are the bromine atom concentrations corresponding to S₀ and S_t, and

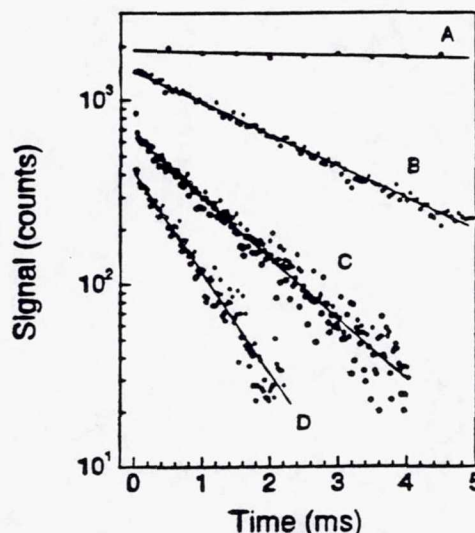


Figure 1. Typical Br(²P_{3/2}) atom temporal profiles observed in the study of reaction 1. Experimental conditions: $P = 50$ Torr, $T = 486$ K, $[\text{H}_2] = 1.3 \times 10^{16}$ molecules cm⁻³, $[\text{CF}_2\text{Br}_2] = 8.0 \times 10^{13}$ molecules cm⁻³, $[\text{Br}(\text{}^2\text{P}_{3/2})]_0 = 1.8 \times 10^{11}$ atoms cm⁻³, $[\text{CH}_3\text{SCH}_3]$ in units of 10^{15} molecules cm⁻³ = (A) 0, (B) 0.577, (C) 1.15, and (D) 1.91. The solid lines represent linear least-squares analyses of the data and give the following pseudo-first-order Br(²P_{3/2}) decay rates in units of s⁻¹: (A) 22, (B) 398, (C) 768, and (D) 1272. For clarity curve C is arbitrarily shifted upward.

k_1 is the first-order rate coefficient for the loss of Br atoms without CH₃SCH₃ present.

Br(²P_{3/2}) → loss by diffusion from the detector field of view and reaction with background impurities (7)

The bimolecular rate coefficients of interest, $k_1(T,P)$, are determined from the slopes of k' versus $[\text{CH}_3\text{SCH}_3]$ plots. Observation of Br(²P_{3/2}) temporal profiles which are exponential (i.e., obey eq 1), linear dependencies of k' on $[\text{CH}_3\text{SCH}_3]$, and invariance of observed kinetics to variations in laser photon fluence and photolytic concentration strongly suggests that reactions 1 and 7 are the only processes which effect the Br(²P_{3/2}) time history, although reactions of Br(²P_{3/2}) with impurities in the CH₃SCH₃ sample are not ruled out by the above set of observations. Typical Br(²P_{3/2}) temporal profiles and a typical k' versus $[\text{CH}_3\text{SCH}_3]$ plot observed in our study of reaction 1 are shown in Figures 1 and 2. Kinetic data for reaction 1 are summarized in Table 1.

In the absence of side reactions that remove or produce Br(²P_{3/2}), the observed Br(²P_{3/2}) temporal profile following the laser flash in our study of reaction -1 can be described by the relationship

$$S(t) = a_1 \exp(-r_1 t) + a_2 \exp(-r_2 t) + a_3 \exp(-r_3 t) \quad (II)$$

where it can be shown that

$$r_1 = 0.5\{J_B + J_R + D\} \quad (III)$$

$$r_2 = 0.5\{J_B + J_R - D\} \quad (IV)$$

$$r_3 = k'_5 + k'_6 + k_9 \quad (V)$$

$$a_1 = -(r_3 - r_2)a_3 + (r_2 - J_B)X + k'_{-1}Y + k'_6/D \quad (VI)$$

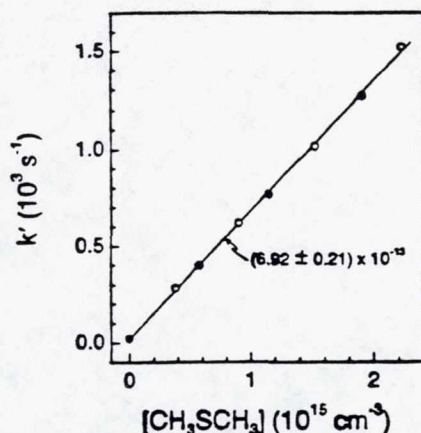


Figure 2. Typical plot of k' versus $[\text{CH}_3\text{SCH}_3]$ observed in the studies of reaction 1. The four closed circles are the data points obtained from the temporal profiles shown in Figure 1. The solid line is obtained from a linear least-squares analysis and gives the bimolecular rate coefficient shown in the figure in units of $\text{cm}^3 \text{ molecule}^{-1} \text{ s}^{-1}$.

TABLE 1: Summary of Kinetic Data for the Reaction $\text{Br}(^2\text{P}_{3/2}) + \text{CH}_3\text{SCH}_3 \rightarrow \text{HBr} + \text{CH}_3\text{SCH}_2^a$

T	P	no. of expts ^b	$[\text{CH}_3\text{SCH}_3]_{\text{max}}$	range of k'	$k_1 \pm 2\sigma^c$
386	50	19	3.70	10–687	1.85 ± 0.05
409	50	11	8.44	37–636	0.716 ± 0.029^d
417	50	5	4.19	13–1339	3.14 ± 0.15
428	50	7	2.82	13–899	3.16 ± 0.07
483	50	6	2.49	18–1556	6.13 ± 0.11
486	50	8	2.22	17–1546	6.92 ± 0.21
487	200	6	2.60	7–1684	6.50 ± 0.30
487	20	5	1.57	21–1177	7.31 ± 0.24
548	50	10	2.40	39–2690	11.0 ± 0.3
604	50	14	1.51	25–2618	17.9 ± 1.1

^a Units are T (K), P (Torr), $[\text{CH}_3\text{SCH}_3]$ ($10^{15} \text{ molecules cm}^{-3}$), k' (s^{-1}), and k_1 ($10^{-13} \text{ cm}^3 \text{ molecule}^{-1} \text{ s}^{-1}$). ^b Expt = measurement of a single pseudo-first-order $\text{Br}(^2\text{P}_{3/2})$ decay rate. ^c Errors represent precision only. ^d Reactant is CD_3SCD_3 .

$$a_2 = \{(r_3 - r_1)a_3 + (r_1 - J_B)X + k'_{-1}Y + k'_6\}/D \quad (\text{VII})$$

$a_3 =$

$$\{k'_6(J_R - r_3) + k'_{-1}k'_3\}/\{(J_B - r_3)(J_R - r_3) - k'_1k'_{-1}\} \quad (\text{VIII})$$

where

$$k'_i = k_i[\text{CH}_3\text{SCH}_3], i = 1, 5 \quad (\text{IX})$$

$$k'_j = k_j[\text{HBr}], j = -1, 6 \quad (\text{X})$$

$$J_B = k'_1 + k_7 \quad (\text{XI})$$

$$J_R = k'_{-1} + k_8 \quad (\text{XII})$$

$$D = \{(J_B - J_R)^2 + 4k'_1k'_{-1}\}^{1/2} = r_1 - r_2 \quad (\text{XIII})$$

$$X = [\text{Br}]_0/[\text{Cl}]_0 \quad (\text{XIV})$$

$$Y = [\text{CH}_3\text{SCH}_2]_0/[\text{Cl}]_0 \quad (\text{XV})$$

and k_3 and k_8 are first-order rate coefficients for the processes

$\text{CH}_3\text{SCH}_2 \rightarrow$ loss by diffusion from the detector field of view and reaction with background impurities (8)

$\text{Cl} \rightarrow$ loss by diffusion from the detector field of view and reaction with background impurities (9)

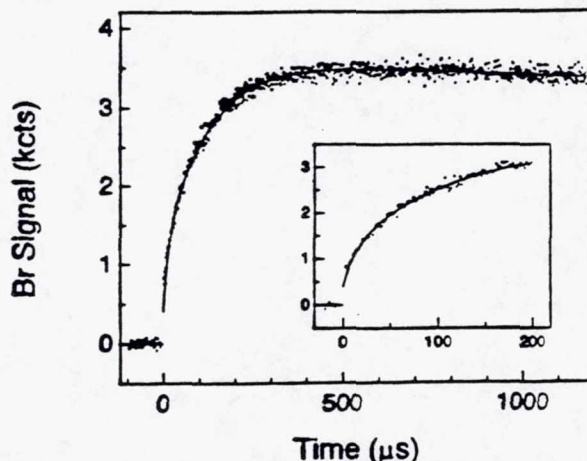


Figure 3. Typical $\text{Br}(^2\text{P}_{3/2})$ atom temporal profile observed in the studies of reaction -1. Experimental conditions: $P = 25$ Torr, $T = 525$ K, $[\text{H}_2] = 5.66 \times 10^{15} \text{ molecules cm}^{-3}$, $[\text{Cl}_2\text{CO}] = 4.24 \times 10^{14} \text{ molecules cm}^{-3}$, $[\text{CH}_3\text{SCH}_3] = 3.53 \times 10^{14} \text{ molecules cm}^{-3}$, $[\text{Cl}]_0 = 5 \times 10^{11} \text{ atoms cm}^{-3}$, and $[\text{HBr}] = 1.83 \times 10^{13} \text{ molecules cm}^{-3}$. The solid curve represents a nonlinear least-squares fit of the data to eq II and gives the following best fit parameters: $a_1 = -2445 \text{ cts}$, $a_2 = 3618 \text{ cts}$, $a_3 = -769 \text{ cts}$, $r_1 = 8167 \text{ s}^{-1}$, and $r_2 = 60 \text{ s}^{-1}$. The parameter r_3 was held fixed at $72\,080 \text{ s}^{-1}$. The time-independent background of 1357 cts (measured immediately prior to the laser flash) has been subtracted from each data point.

It should be noted that

$$r_1 + r_2 = J_B + J_R = k'_1 + k_7 + k_8 + k_{-1}[\text{HBr}] \quad (\text{XVI})$$

Hence, for data obtained with the CH_3SCH_3 concentration held constant, a plot of $r_1 + r_2$ versus $[\text{HBr}]$ should be linear with slope $= k_{-1}$.

In the above equations, it is assumed that $k_5 = k_{5a}$; this assumption is approximately correct in the temperature and pressure regime of our study and is employed only to simplify the mathematics; i.e., the determination of k_{-1} does not critically depend on its validity. A nonlinear least-squares analysis of each experimental temporal profile was employed to determine r_1 , r_2 , a_1 , a_2 , and a_3 . Because k_5 and k_6 are well-known and k_9 is negligible compared to $k'_3 + k'_6$, r_3 was not treated as a variable in the fitting procedure. Under typical experimental conditions, r_3 was considerably larger than $r_1 + r_2$, a requirement for accurate evaluation of $r_1 + r_2$. The bimolecular rate coefficients of interest, $k_{-1}(P, T)$, were determined from the slopes of plots of $r_1 + r_2$ versus $[\text{HBr}]$ for data obtained with $[\text{CH}_3\text{SCH}_3]$ held constant (see eq XVI). It should be noted that accurate determination of k_{-1} in these experiments requires that the concentrations of CH_3SCH_3 and HBr be chosen with care. We require that $k'_{-1} \gg k'_1$ (at least for the larger HBr concentrations employed) so that the dominant contribution to $r_1 + r_2$ is from reaction -1, not from reaction 1.

Similar to the situation discussed above for the study of reaction 1, observation of $\text{Br}(^2\text{P}_{3/2})$ temporal profiles that obey eq II, linear dependencies of $r_1 + r_2$ on $[\text{HBr}]$, and invariance of $r_1 + r_2$ to variation in laser photon fluence and photolyte concentration suggests that reactions 1, -1, and 5-9 are the only processes other than possible impurity reactions which significantly affect the $\text{Br}(^2\text{P}_{3/2})$ time history. A typical $\text{Br}(^2\text{P}_{3/2})$ appearance temporal profile and a typical plot of $r_1 + r_2$ versus $[\text{HBr}]$ observed in our study of reaction -1 are shown in Figures 3 and 4. Kinetic data for reaction -1 are summarized in Table 2, while best-fit values of r_1 , r_2 , a_1 , a_2 , and a_3 for data obtained at four representative temperatures are presented in Table 3.

Listed in Table 2 are values of the intercept of the $r_1 + r_2$ versus $[\text{HBr}]$ plots from each temperature. As can be seen from eq XVI, this intercept is the sum of three terms, i.e., k'_1 , k_7 , and k_8 .

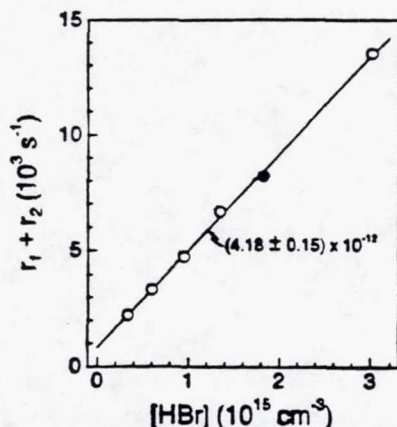
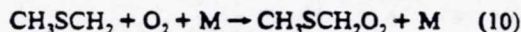


Figure 4. Typical plot of $r_1 + r_2$ versus $[HBr]$ observed in the studies of reaction -1. The closed circle is the data point obtained from the temporal profile shown in Figure 3. The solid line is obtained from a linear least-squares analysis and gives the bimolecular rate coefficient shown in the figure in units of $\text{cm}^3 \text{molecule}^{-1} \text{s}^{-1}$.

Since $[CH_3SCH_3]$ is a known experimental parameter, k'_1 can be subtracted from each intercept, yielding k_4 ($=k_7 + k_8$). In our study of $k_1(T)$ the observed background loss of $Br(^2P_{3/2})$ was always quite small, i.e., $k_7 < 40 \text{ s}^{-1}$; therefore, the values of k_4 listed in Table 2 are dominated by k_8 . It can be seen from Table 2 that k_4 systematically decreases as the temperature increases. A likely explanation for the apparently large background loss of $[CH_3SCH_2]$ is the presence of O_2 impurity possibly due to small leaks or the porosity of the Teflon tubing used in the flow system.



A room temperature value of $5.7 \times 10^{-12} \text{ cm}^3 \text{molecule}^{-1} \text{s}^{-1}$ has been reported for k_{10} in 1 atm of SF_6 .¹⁹ Hence, O_2 levels in the 10 mTorr range could account for our observed values for k_4 (Table 2). In any event the value of the intercept was never more than 25% and typically less than 10% of the maximum value of $r_1 + r_2$ at any temperature. We therefore conclude that the chemistry contributing to the intercept did not significantly impact the accuracy of our measurement of $k_1(T)$.

As indicated in Tables 1 and 2, pressure dependence studies were carried out for reactions 1 and -1; as expected, no evidence for pressure-dependent rate coefficients was observed over the range investigated (20–200 Torr for reaction 1; 10–50 Torr for reaction -1). Arrhenius plots for reactions 1 and -1 are shown in Figure 5. The solid lines in Figure 5 are obtained from linear least-squares analyses of the $\ln k_{\pm 1}$ versus T^{-1} data; these analyses give the following Arrhenius expressions in units of $\text{cm}^3 \text{molecule}^{-1} \text{s}^{-1}$:

$$k_1 = (9.0 \pm 2.9) \times 10^{-11} \exp[(-2386 \pm 151)/T]$$

$$k_{-1} = (8.6 \pm 2.5) \times 10^{-13} \exp[(836 \pm 140)/T]$$

Errors in the above expressions are 2σ and represent precision only. On the basis of observed precision and consideration of possible systematic errors (see below), we estimate the absolute accuracy of each measured bimolecular rate coefficient to be $\pm 15\%$ for $k_1(T)$ values and $\pm 25\%$ for $k_{-1}(T)$ values.

As discussed briefly above, a number of potential systematic errors in our kinetic measurements can be ruled out based on the observed invariance of $Br(^2P_{3/2})$ temporal profiles to variations in laser photon fluence, photolyte concentrations, flow velocity through the reactor, and laser pulse repetition rate; these include contributions to $Br(^2P_{3/2})$ kinetics from radical-radical side reactions, from radical-photolyte side reactions, from reactions involving radicals which are produced by reactant photolysis, or

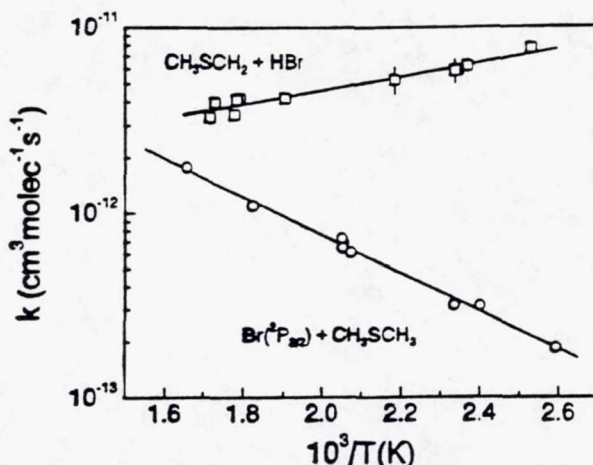
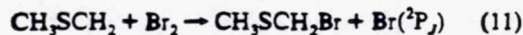


Figure 5. Arrhenius plots for reactions 1 and -1. Solid lines are obtained from linear least-squares analyses which yield the Arrhenius expressions given in the text.

from reactions involving stable products which build up in concentration with successive laser flashes. *In situ* measurements of stable reactant (i.e., CH_3SCH_3 and HBr) concentrations greatly reduce another potential source of systematic error.

One type of kinetic interference which needs to be addressed is the potential contribution to measured rate coefficients from impurity reactions. The relatively unreactive nature of Br atoms makes it unlikely that impurity reactions were a problem in our study of reaction 1. The most likely impurity problem in our study of reaction -1 is from Br_2 . Potential sources of Br_2 are impurity in the HBr sample and residual Br_2 from heterogeneous reactions of HBr (presumably on metal surfaces of valves and fittings). There is no kinetic data in the literature for reaction 11.



However, based on reported rate coefficients for reactions of Br_2 with alkyl radicals²⁰ and thiy radicals,²¹ it seems safe to assume that reaction 11 proceeds at a near gas kinetic rate. Since CH_3SCH_2 probably reacts with Br_2 10–50 times faster than with HBr , the HBr concentration must be several hundred times larger than the Br_2 concentration before Br_2 interferences can be considered unimportant. To investigate the Br_2 interference problem, a 2-m absorption cell was positioned in the slow flow system downstream from the reaction cell and employed to monitor Br_2 photometrically (at 404.7 nm) with typical $Cl_2CO/CH_3SCH_3/HBr/H_2/N_2$ mixtures flowing through the system. No absorption was observed (i.e., $I/I_0 > 0.998$) even at HBr levels as high as $5 \times 10^{16} \text{ molecules cm}^{-3}$. Since the Br_2 absorption cross section at 404.7 nm is about $6 \times 10^{-19} \text{ cm}^2$,²² these experiments suggest that $[Br_2] < 0.0004[HBr]$.

CH_3SCH_3 has a small absorption cross section at 266 nm ($1.2 \times 10^{-21} \text{ cm}^2$).²³ An interference in our measurement of k_{-1} would be present if a significant fraction of the observed Br atom appearance were due to reaction of CH_3SCH_3 photoproducts (rather than CH_3SCH_2) with HBr . As discussed above, the Cl atom photolyte, Cl_2CO , has an absorption cross section at 266 nm of $2.3 \times 10^{-20} \text{ cm}^2$ ^{15,16} with an effective Cl atom yield of 2.17.¹⁸ All experiments to measure k_{-1} were carried out with $[Cl_2CO]$ greater than or equal to $[CH_3SCH_3]$. The concentration of any CH_3SCH_3 photofragments were therefore never more than ~5% of the initial $[Cl]$, and since both CH_3S and CH_3 react more slowly with HBr than does CH_3SCH_3 (see ref 3 and the discussion in the next paragraph), it is concluded that CH_3SCH_3 photolysis did not represent a significant systematic error in our measurements. In our measurements of k_1 , CH_3SCH_3 photo-

TABLE 2: Summary of Kinetic Data for the Reaction $\text{HBr} + \text{CH}_3\text{SCH}_2 \rightarrow \text{Br}({}^2\text{P}_{3/2}) + \text{CH}_3\text{SCH}_3^a$

T	P	no. of expts ^b	range of [HBr]	range of ($r_1 + r_2$) ^c	intercept ^d	k_d ^e	$k_{-1} \pm 2\sigma$ ^f
395	10, 25, 50	8	4.19–36.8	6803–32840	3770	3250	7.67 ± 0.60
422	25	4	6.59–15.1	7132–12810	3300	3130	6.21 ± 0.55
426	25	5	4.13–21.9	5212–15640	2700	2420	5.90 ± 0.12
428	25	5	3.24–20.7	4784–15030	3060	2870	5.85 ± 0.87
458	25	5	1.93–25.0	3211–14750	2350	2150	5.25 ± 0.87
525	25	6	3.32–30.2	2222–13510	820	470	4.18 ± 0.15
558	25	5	3.32–18.6	2738–9142	1350	830	4.17 ± 0.13
561	25	5	5.17–18.1	3681–8943	1450	925	4.09 ± 0.23
563	25	6	3.73–23.4	2798–11180	1500	944	3.43 ± 0.09
578	25	6	2.81–18.3	2526–8690	1310	700	3.96 ± 0.23
583	10, 25, 50	11	1.71–30.7	1997–11450	1570	960	3.33 ± 0.13

^a Units are T (K), P (Torr), [HBr] (10^{14} molecules cm^{-3}), $r_1 + r_2$ (s^{-1}), intercept (s^{-1}), k_d (s^{-1}), and k_{-1} (10^{-12} cm^3 molecule $^{-1}$ s^{-1}). ^b Expt = measurement of a single $\text{Br}({}^2\text{P}_{3/2})$ temporal profile. ^c $r_1 + r_2$ defined in eq XVI. ^d Intercept of ($r_1 + r_2$) versus [HBr] plot. ^e k_d = background radical loss rate (see text). ^f Errors represents precision only.

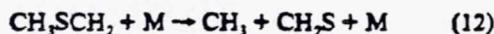
TABLE 3: Experimental Conditions and Best Fit Parameters at Four Representative Temperatures Obtained from Observation and Analysis of $\text{Br}({}^2\text{P}_{3/2})$ Temporal Profiles Observed following 266-nm Laser Flash Photolysis of $\text{Cl}_2\text{CO}/\text{H}_2/\text{CH}_3\text{SCH}_3/\text{HBr}/\text{N}_2$ Mixtures

temp, K	total press.	[H ₂]	[Cl ₂ CO]	[CH ₃ SCH ₃]	[HBr]	a_1	r_1	a_2	r_2	a_3	r_3^b	
395	10.0	237	15.5	11.2	4.19	-637	8023	822	221	258	208 400	
	47.3	89	5.90	4.12	5.56	-1693	6810	1927	-7.2	-44	80 200	
	24.2	124	8.17	5.88	5.64	-1613	8045	1830	56	-131	112 600	
	25.0	125	8.36	5.77	10.9	-1669	11880	1878	24	186	114 900	
	24.6	120	7.40	5.59	15.8	-1329	16060	1618	-0.5	-119	115 600	
	24.7	80	7.38	5.31	23.6	-1845	22530	2104	-23	167	116 800	
	10.3	135	8.65	6.42	32.7	-1256	27430	1540	48	-26	114 500	
	25.6	107	6.83	5.13	36.8	-1555	32870	1892	-29	-164	124 100	
	458	23.0	699	4.36	4.39	1.93	-872	3108	1034	68	92	73 880
		23.6	691	4.31	4.26	6.91	-1489	5725	1660	56	134	76 410
23.5		662	4.13	4.08	11.7	-1459	8353	1636	49	91	77 950	
24.1		647	4.04	3.92	17.9	-983	12840	1187	34	11	81 080	
25.0		636	3.97	3.85	25.0	-1361	14730	1739	23	-61	86 710	
24.5		630	4.73	3.89	3.32	-3483	2156	4049	66	-195	61 730	
525	24.4	614	4.54	3.79	5.98	-3282	3268	3994	71	-465	62 980	
	25.1	607	4.54	3.78	9.52	-3017	4668	3819	67	-537	66 680	
	25.1	586	4.38	3.72	13.5	-2758	6612	3725	61	-694	69 850	
	25.3	566	4.24	3.53	18.3	-2445	8167	3618	60	-769	72 080	
	26.1	525	3.93	3.33	30.1	-1979	13460	3445	46	-1051	81 600	
	24.9	113	9.42	4.39	2.81	-1875	2429	2303	97	-188	65 350	
	25.0	111	9.17	4.41	4.60	-1695	3025	2139	102	-272	67 560	
578	25.1	105	8.78	4.24	7.67	-1465	4123	2004	91	-470	68 640	
	25.2	107	8.93	4.17	9.66	-1873	5126	2536	97	-490	69 840	
	24.9	105	8.48	3.96	13.4	-1804	6336	2605	95	-618	71 060	
	25.1	96	8.08	3.86	18.3	-1666	8606	2541	84	-565	75 180	

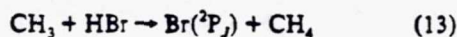
^a Units are pressure (Torr), concentrations (10^{14} molecules cm^{-3}), a_i (signal counts), and r_i (s^{-1}). ^b This parameter was fixed during the regression analysis (see text).

products could only interfere via radical-radical reactions that would affect the atomic bromine concentration. Under the conditions of our experiments the amount of CH_3SCH_3 photolyzed (a maximum of 3×10^{10} molecules cm^{-3}) was small enough that radical-radical reactions would not occur on the time scale for $\text{Br}({}^2\text{P}_{3/2})$ loss via reaction with CH_3SCH_3 .

Another potential systematic error in our study of reaction -1 centers around the possible occurrence of the reaction



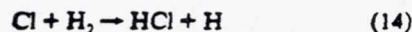
Using the CH_3SCH_2 heat of formation determined in this study (see below) in conjunction with the best available heats of formation for CH_3 ²⁴ and CH_2S ²⁵⁻²⁷ leads to the conclusion that the $\text{H}_3\text{C}-\text{SCH}_2$ bond strength is 30 ± 3 kcal mol^{-1} . Hence, it is conceivable that, near the high-temperature end of our range of experimental conditions (i.e., $T \sim 600$ K), reaction 12 could occur rapidly enough that the rate-limiting step in production of bromine atoms was not reaction -1, but rather reaction 13.



To examine this possibility, we have directly measured k_{13} at 573 K by monitoring $\text{Br}({}^2\text{P}_{3/2})$ appearance following 266-nm laser

flash photolysis of $\text{Cl}_2\text{CO}/\text{CH}_4/\text{HBr}/\text{H}_2/\text{N}_2$ mixtures, i.e., using the $\text{Cl} + \text{CH}_4$ reaction as a source of methyl radicals. A plot of $r_1 + r_2$ versus [HBr] for this experiment is shown in Figure 6; the slope, $(2.09 \pm 0.13) \times 10^{-12}$ cm^3 molecule $^{-1}$ s^{-1} , is k_{13} (573 K). This value agrees well with the value 2.04×10^{-12} cm^3 molecule $^{-1}$ s^{-1} obtained via extrapolation of the Arrhenius expression we report elsewhere,⁴ which is based on kinetics studies carried out over the temperature range 257–422 K ($k_{13} = 1.3 \times 10^{-12} \exp(-233/T)$ cm^3 molecule $^{-1}$ s^{-1}). When CH_3SCH_3 was employed in the reaction mixtures instead of CH_4 , a significantly faster value, $k(573 \text{ K}) \sim 3.7 \times 10^{-12}$ cm^3 molecule $^{-1}$ s^{-1} , was obtained for the "apparent" rate coefficient (see Figure 5). This observation, coupled with the fact that the "apparent" activation energy (i.e., the slope of the $\ln k$ versus T^{-1} plot) did not change as a function of temperature, leads to the conclusion that reactions 12 and 13 were not a significant interference in our study of reaction -1.

Another possible interference in our measurement of $k_{-1}(T)$ results from the presence of H_2 which was added to ensure that any atomic bromine formed in the ${}^2\text{P}_{1/2}$ state was rapidly quenched to the ${}^2\text{P}_{3/2}$ ground state. At the higher end of our temperature range the reaction



becomes rapid enough to be significant.²⁸ The hydrogen atom

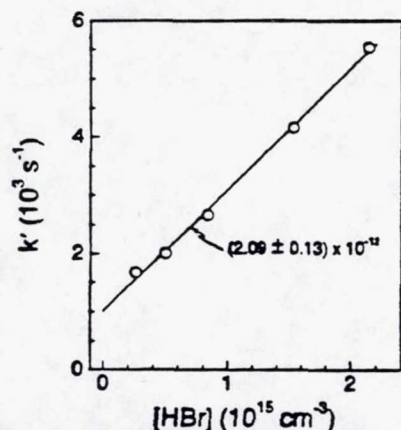
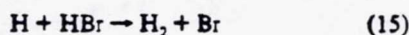


Figure 6. Plot of k' versus $[\text{HBr}]$ observed in the study of reaction 13. Experimental conditions: $T = 573 \text{ K}$, $P = 25 \text{ Torr}$, $[\text{H}_2] = 1.0 \times 10^{16} \text{ molecules cm}^{-3}$, $[\text{Cl}_2\text{CO}] = 9.1 \times 10^{14} \text{ molecules cm}^{-3}$. The solid line represents a linear least-squares analysis of the data which gives the bimolecular rate coefficient shown in the figure in units of $\text{cm}^3 \text{ molecule}^{-1} \text{ s}^{-1}$.

will then quickly react with HBr^{29}



In order to access the contribution of this additional Br production process, we simulated the chemistry under typical experimental conditions at 583 K using a numerical integration routine. The reaction mechanism included reactions ± 1 , 5–9, and 14–16.

H → loss by diffusion from the detector field of view and reaction of background impurities (16)

Simulated Br time dependencies were generated at several typical levels of $[\text{HBr}]$ and at constant $[\text{CH}_3\text{SCH}_3]$. Each simulated Br temporal profile was then subjected to the same nonlinear least-squares fitting routine as was used in analyses of the experimental data. The slope of the resulting $r_1 + r_2$ versus $[\text{HBr}]$ plot was $\approx 3\%$ lower when $[\text{H}_2] = 0$ than when $[\text{H}_2]$ was set to the experimental value of $6 \times 10^{15} \text{ molecules cm}^{-3}$. Since this simulation was carried out under conditions where the contribution of reactions 14 and 15 would be greatest, no corrective action was deemed necessary to account for this minor interference.

Discussion

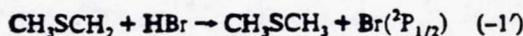
Reaction Mechanisms. Since we wish to employ our kinetic data to evaluate thermochemistry, the identity of the reaction products is a crucial issue. Can we be sure that $\text{Br}({}^2\text{P}_{3/2}) + \text{CH}_3\text{SCH}_3$ produces $\text{CH}_3\text{SCH}_2 + \text{HBr}$ with unit yield, and can we be sure that $\text{CH}_3\text{SCH}_2 + \text{HBr}$ produces $\text{Br}({}^2\text{P}_{3/2}) + \text{CH}_3\text{SCH}_3$ with unit yield? In the case of the $\text{Br}({}^2\text{P}_{3/2}) + \text{CH}_3\text{SCH}_3$ reaction, we have found that addition to the sulfur atom is the dominant reaction pathway at $T \leq 300 \text{ K}$.³⁰ However, at the temperatures employed in this study, $T \geq 386 \text{ K}$, the adduct lifetime toward unimolecular decomposition back to reactants is so short that its existence is kinetically inconsequential. At temperatures around 400 K, we have obtained strong evidence that the dominant pathway for the $\text{Br}({}^2\text{P}_{3/2}) + \text{CH}_3\text{SCH}_3$ reaction is hydrogen transfer. First, we find that at $T = 409 \text{ K}$ $\text{Br}({}^2\text{P}_{3/2})$ reacts with CD_3SCD_3 a factor of 3.7 more slowly than with CH_3SCH_3 (Table 1); this result strongly suggests that the reaction mechanism involves breaking a carbon–hydrogen bond. Second, in experiments which will be published elsewhere, we have employed time-resolved tunable diode laser absorption spectroscopy to directly monitor HBr production from the $\text{Br}({}^2\text{P}_{3/2}) + \text{CH}_3\text{SCH}_3$ reaction;³¹ using the $\text{Br}({}^2\text{P}_{3/2}) + (\text{CH}_3)_3\text{CH}$ reaction

TABLE 4: Thermochemical Parameters for the Reaction $\text{Br}({}^2\text{P}_{3/2}) + \text{CH}_3\text{SCH}_3 \rightarrow \text{CH}_3\text{SCH}_2 + \text{HBr}$

T, K	$\Delta H_i^\circ \text{ kcal mol}^{-1}$		$\Delta S_i^\circ \text{ cal mol}^{-1} \text{ deg}^{-1}$	
	2nd law	3rd law	2nd law	3rd law
470	6.40 ± 0.58	6.67 ± 1.37	9.25 ± 0.40	9.82 ± 1.30
298	5.98 ± 0.58	6.24 ± 1.37	7.83 ± 1.96	8.72 ± 1.30
0	5.24 ± 0.59	5.50 ± 1.38		

^a Errors are 2σ and represent best estimate of absolute accuracy.

as a "unit yield calibration", we find that the HBr yield from $\text{Br}({}^2\text{P}_{3/2}) + \text{CH}_3\text{SCH}_3$ is near unity. For the $\text{CH}_3\text{SCH}_2 + \text{HBr}$ reaction, qualitative thermochemical considerations suggest that production of $\text{CH}_3\text{SCH}_3 + \text{Br}$ should be the dominant reaction pathway. Observed resonance fluorescence signal levels confirm that atomic bromine is produced with high yield. However, production of electronically excited bromine atoms, $\text{Br}({}^2\text{P}_{1/2})$, is a possibility which warrants consideration.



If the $\text{CH}_3\text{SCH}_2 + \text{HBr}$ reaction proceeded exclusively or a significant fraction of the time via channel $-1'$, then we would be overestimating the rate of the true reverse of reaction 1 and our reported enthalpy change for reaction 1 (see below) would be in error. A simple thermochemical argument based on the measured activation energy for reaction 1 can be used to place a reasonable upper limit on k_{-1}' . It is reasonable to assume that the activation energy for reaction $-1'$ is greater than $-2.0 \text{ kcal mol}^{-1}$. Since the bromine atom spin–orbit splitting is $10.5 \text{ kcal mol}^{-1}$, reaction $-1'$ must be endothermic by at least $3.7 \text{ kcal mol}^{-1}$, i.e., $10.5 - 2.0 - 4.8 \text{ kcal mol}^{-1}$ where $4.8 \text{ kcal mol}^{-1}$ is the measured activation energy for reaction 1. Taking $1 \times 10^{-11} \text{ cm}^3 \text{ molecule}^{-1} \text{ s}^{-1}$ as an upper limit A factor for reaction $-1'$ (a polyatomic + diatomic reaction) and $3.7 \text{ kcal mol}^{-1}$ as a lower limit activation energy for reaction $-1'$ leads to the result $k_{-1}' \leq 9.0 \times 10^{-14} \text{ cm}^3 \text{ molecule}^{-1} \text{ s}^{-1}$ at 395 K and $k_{-1}' \leq 4.1 \times 10^{-13} \text{ cm}^3 \text{ molecule}^{-1} \text{ s}^{-1}$ at 583 K; comparison of these limits with the rate coefficients reported in Table 2 shows that upper limit branching ratios for formation of $\text{Br}({}^2\text{P}_{1/2})$ are 0.013 at 395 K and 0.11 at 583 K. We conclude that it is safe to ignore the possible occurrence of reaction $-1'$ in our thermochemical analysis.

Thermochemistry. From the Arrhenius parameters determined in this study, we can obtain the enthalpy change and entropy change associated with reaction 1. One approach, the "second law method", employs the following relationships to obtain thermochemical parameters:

$$\Delta H_i = E_i - E_{-i} \quad (\text{XVII})$$

$$\Delta S_i = R \ln(A_i/A_{-i}) \quad (\text{XVIII})$$

where ΔH_i , ΔS_i , E_i , and A_i are the enthalpy change, entropy change, activation energy, and A factor for reaction i . Thermochemical parameters for reaction 1 obtained from the second law analysis are tabulated in Table 4. The temperature 470 K is the arithmetic mean of the T -ranges employed in the determinations of $k_1(T)$ and $k_{-1}(T)$. Values of ΔH at 298 and 0 K were computed using heat capacity corrections obtained from the JANAF tables²⁴ for Br and HBr and calculated using the structural information in Table 5 for CH_3SCH_3 and CH_3SCH_2 . Second law values for ΔS at 298 K were computed from the relationship

$$\begin{aligned} \Delta G_{298} &= \Delta H_{298} - T\Delta S_{298} = -RT \ln K_{eq}(298 \text{ K}) \\ &= RT \ln[k_{-1}(298 \text{ K})/k_1(298 \text{ K})] \end{aligned} \quad (\text{XIX})$$

Values for $k_1(298 \text{ K})$ and $k_{-1}(298 \text{ K})$ were computed from the Arrhenius expressions reported above.

TABLE 5: Structural Parameters Used in the Evaluation of Absolute Entropies and Heat Capacities for CH₃SCH₃ and CH₃SCH₂^a

	CH ₃ SCH ₃ ^b	CH ₃ SCH ₂	symmetry	
vibrational frequencies, cm ⁻¹	2998, 2998, 2990, 2970, 2930, 2930, 1444, 1444, 1439, 1430, 1331, 1315, 1030, 973, 940, 903, 743, 695, 282	3157, 3025, 3006, 2997, 2897, 1419, 1407, 1358, 1294, 991, 929, 866, 811, 689, 282, 281 3139, 3010, 3005, 2996, 2896, 1418, 1407, 1357, 1294, 993, 930, 872, 807, 689, 398, 282		C ₁ C ₁
barriers to internal rotation, kcal mol ⁻¹	V ₀ (CH ₃) = 1.89 ^c (doubly degenerate)	V ₀ (CH ₃) = 1.68 V ₀ (CH ₂) = 1.40–6.15 ^d		
moments of inertia ABC, amu ³ Å ⁶	173180	129724 (C ₁) 129976 (C ₁)		
I _r (CH ₃), amu Å ²	3.24	3.01		
I _r (CH ₂), amu Å ²		1.77		

^a Except where noted otherwise all parameters are from *ab initio* calculations at the UMP2/g-31+G(2d) level³² (see text for further discussion).

^b Experimentally observed values from ref 33. ^c From ref 34. ^d Extremes of suggested barrier heights, the lower from ref 35 and the higher from ref 32; thermochemical parameters calculated at extremes and averaged.

TABLE 6: Comparison of CH₃SCH₂ Thermochemical Results from This Study with Literature Values^a

T, K	ΔH _{L,T}	C–H bond strength in CH ₃ SCH ₂	ref
298	32.7 ± 1.4	93.7 ± 1.4	this work
	35.6 ± 1.0 ^b	96.6 ± 1.0 ^b	35
0	35.3 ± 1.4	92.0 ± 1.4	this work
	34.8 ± 2.5	91 ± 2.5	38
	37.3		39

^a Units are kcal mol⁻¹ for the thermochemical parameters. ^b These values were arrived at using an assumed activation energy for the CH₃SCH₂ + HI reaction of 1.0 ± 0.5 kcal mol⁻¹.

An alternate approach for obtaining thermochemical parameters is the "third law method" where the entropy change is calculated using standard statistical mechanical methods³⁶ and employed in conjunction with an experimental value for $K_{eq}(T)$ to obtain ΔH_T (from eq XIX). Absolute entropies as a function of temperature were obtained from the JANAF tables²⁴ for Br and HBr, and calculated using the structural information in Table 5 for CH₃SCH₃ and CH₃SCH₂. The uncertainty in the third law ΔS value is based on estimated uncertainties in key structural parameters, most notably the low-frequency vibrational modes and internal rotation barriers in CH₃SCH₂. The structural parameters for CH₃SCH₂ listed in Table 5 are based on *ab initio* quantum chemical calculations carried out by McKee.³² His calculated bond angles and bond lengths (for the structure with C₁ symmetry) agree well with those reported in a recent *ab initio* theoretical study by Baker and Dyke.³⁷ McKee finds that two structures with C₁ and C_s symmetry, respectively, are very close in energy. The calculated frequency of the CH₂ wag changes considerably between the two structures; its values (scaled downward by 5% from those actually calculated) are 281 cm⁻¹ (C₁) and 398 cm⁻¹ (C_s). Another major source of uncertainty is the barrier for internal rotation of the CH₂ group. McKee's calculations suggest that this barrier could be very large (6.15 kcal mol⁻¹) while Shum and Benson³⁵ estimate a barrier of 1.40 kcal mol⁻¹. We have carried out four separate calculations of the absolute entropy of CH₃SCH₂ (S⁰) using different pairs of the above values for the CH₂ wag frequency and the barrier to CH₂ internal rotation. Reported heat capacity corrections and third law ΔS values employ the average result with uncertainties adjusted to span the range of reasonable possibilities. The four calculations give S⁰ values which range from 70.84 to 73.09 cal mol⁻¹ K⁻¹; the average value is 71.89 cal mol⁻¹ K⁻¹.

Values for ΔH_{L,0} and ΔH_{L,298} for CH₃SCH₂, which are given in Table 6, were calculated from our ΔH_{rxn,T} determinations using literature values for the heats of formation of Br,²⁴ HBr,²⁴ and CH₃SCH₃.⁴⁰ Simple averages of the second and third law enthalpies of reaction have been employed to obtain our reported heat of formation; this approach seems reasonable since (a) estimated uncertainties in the second and third law determinations

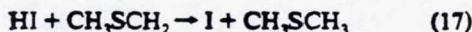
do not differ greatly and (b) the second and third law values for ΔH_{L,T} agree to within a few tenths of a kcal mol⁻¹. The reported uncertainties in ΔH_{L,T} represent 2σ estimates of absolute accuracy; since the 2σ error estimates for the individual second and third law determinations are significantly larger than the deviations of the two determinations from their mean, we take the larger of the (second and third law) error estimates to be the error for the mean. The possible small contribution from reaction -1', i.e., a channel forming Br(²P_{1/2}) (see above), represents an insignificant source of systematic error.

Comparison with Previous Research. To our knowledge there have been no previous kinetics studies of either reaction 1 or -1. The preexponential factor that we observe for reaction 1 is similar to those observed for other atom plus polyatomic hydrogen abstraction reactions. In the case of the reverse process, reaction -1, a significant negative activation energy is observed. It is interesting to note that in recent studies negative activation energies have been observed for reactions of carbon-centered radicals with HBr^{4,41} and HI,⁴² while positive activation energies have been measured for reactions of sulfur-centered radicals with HBr.³ In fact, the Arrhenius parameters reported here for reaction -1 are similar to the Arrhenius parameters for the C₂H₅ + HBr and *t*-C₄H₉ + HBr reactions.^{4,41}

While the experimental evidence for negative activation energies in reactions of carbon-centered radicals with HBr and HI is very strong, the theoretical interpretation of this counterintuitive phenomenon is less clear. Apparently, reaction proceeds via formation of a weakly bound complex. As shown by Mozurkewich and Benson,⁴³ if the transition state leading from reactants to complex (TS1) is loose and the transition state leading from complex to products is both tighter and lower in energy compared to TS1, then a negative activation energy should be observed. McEwen and Golden⁴⁴ have reported a two-channel RRKM calculation that models the *t*-C₄H₉ + HI (DI) reactions as proceeding via formation of a weakly bound (CH₃)₂C–I–H (D) complex. They were able to reproduce the kinetic results of Seetula et al.⁴² for *t*-C₄H₉ + HI with complex binding energies as low as 3 kcal mol⁻¹. Interestingly, their models which are capable of reproducing experimental $k(T)$ values for *t*-C₄H₉ + HI also predict an inverse kinetic isotope effect (KIE), i.e., $k_{\text{HI}} < k_{\text{DI}}$; this prediction results from the fact that the transition state leading from complex to products becomes looser with the lower vibrational frequencies associated with deuterium substitution. No experimental determination of the KIE for *t*-C₄H₉ + HI, DI has been reported. However, "normal" kinetic isotope effects are observed for CH₃, C₂H₅, and *t*-C₄H₉ reactions with HBr, i.e., $k_{\text{HBr}} > k_{\text{DBr}}$.⁴ A detailed theoretical study of the CH₃ + HBr reaction, which has an activation energy of about -0.4 kcal mol⁻¹,^{44,45} has been reported by Chen et al.^{46,47} They calculated a potential energy surface at the G1 level of theory and deduced

the existence of a hydrogen-bridged complex with C_{2v} symmetry which is bound by 0.28 kcal mol⁻¹ and is formed without activation energy. Chen et al. calculated rate constants for CH₃ + HBr, CH₃ + DBr, and CD₃ + HBr from RRKM theory with corrections for tunneling. By adjusting the height of the barrier toward dissociation to products, they were able to obtain values for $k(T)$ which agreed fairly well with experiment,^{4,45} furthermore, their calculated isotope effects agreed quantitatively with experiment.⁴

Table 6 contains a comparison of our thermochemical results with previously reported values. Shum and Benson³⁵ reported a value of ΔH_{L0}° for CH₃SCH₂ that is approximately 3.0 kcal mol⁻¹ larger than the result reported in this study; these investigators studied the iodination of CH₃SCH₃ at elevated temperatures (630–650 K). Kinetic information was arrived at indirectly by monitoring the rate of change of [I₂] and total pressure. In order to obtain their reported thermochemical results, Shum and Benson assumed a value of 1.0 ± 0.5 kcal mol⁻¹ for the activation energy for the reaction



If the activation energy for reaction 17 is actually negative (as we report for the analogous CH₃SCH₃ + HBr reaction), then the difference between Shum and Benson's value for $\Delta H_f^\circ(\text{CH}_3\text{SCH}_2)$ and the value reported in this study would be even larger. The only other experimental thermochemical information available in the literature is from a recent molecular beam photofragmentation study of CH₃SCH₃ by Ng and co-workers,³⁸ in which they report a value of 91 ± 2.5 kcal mol⁻¹ for the C–H bond strength in CH₃SCH₃; their result is in good agreement with our reported value of 92.0 ± 1.4 kcal mol⁻¹ although our error limits are nearly a factor of 2 smaller. A recent *ab initio* calculation by Ma et al.³⁹ obtains $\Delta H_{L0}^{\circ} = 37.3$ kcal mol⁻¹, somewhat higher than our value of 35.3 ± 1.4 kcal mol⁻¹ but in agreement within estimated combined uncertainties.

Acknowledgment. We thank S. Wang for assisting with some of the preliminary experiments, M. L. McKee for providing theoretical calculations of structural parameters for CH₃SCH₂, and R. E. Stickel for several helpful discussions. This research was supported by Grant ATM-9104807 from the National Science Foundation and Grant NAGW-1001 from the National Aeronautics and Space Administration.

References and Notes

- Stickel, R. E.; Zhao, Z.; Wine, P. H. *Chem. Phys. Lett.* **1993**, *212*, 312.
- Nicovich, J. M.; Shackelford, C. J.; Wine, P. H. *J. Photochem. Photobiol., A: Chem.* **1990**, *51*, 141.
- Nicovich, J. M.; Kreutter, K. D.; van Dijk, C. A.; Wine, P. H. *J. Phys. Chem.* **1992**, *96*, 2518.
- Nicovich, J. M.; van Dijk, C. A.; Kreutter, K. D.; Wine, P. H. *J. Phys. Chem.* **1991**, *95*, 9890.
- Nicovich, J. M.; Gump, C. A.; Ravishankara, A. R. *J. Phys. Chem.* **1982**, *86*, 1684.
- Wine, P. H.; Kreutter, N. M.; Gump, C. A.; Ravishankara, A. R. *J. Phys. Chem.* **1981**, *85*, 2660.
- Molina, L. T.; Molina, M. J.; Rowland, F. S. *J. Phys. Chem.* **1982**, *86*, 2672.
- Gillotay, D.; Simon, P. C. *J. Atmos. Chem.* **1989**, *8*, 41.
- Burkholder, J. B.; Wilson, R. R.; Gierczak, T.; Talukdar, R.; McKeen, S. A.; Orlando, J. J.; Vaghjiani, G. L.; Ravishankara, A. R. *J. Geophys. Res.* **1991**, *96*, 5025.
- Talukdar, R. K.; Vaghjiani, G. L.; Ravishankara, A. R. *J. Chem. Phys.* **1992**, *96*, 8194.
- Nesbitt, D. J.; Leone, S. R. *J. Chem. Phys.* **1988**, *73*, 6182.
- Nielsen, O. J.; Sidebottom, H. W.; Nelson, L.; Rattigan, O.; Treacy, J. J.; O'Farrell, D. *Int. J. Chem. Kinet.* **1990**, *22*, 603.
- Stickel, R. E.; Nicovich, J. M.; Wang, S.; Zhao, Z.; Wine, P. H. *J. Phys. Chem.* **1992**, *96*, 9875.
- Nicovich, J. M.; Wine, P. H. *Int. J. Chem. Kinet.* **1990**, *22*, 379.
- Heicklen, J. *J. Am. Chem. Soc.* **1965**, *87*, 445.
- Moule, D. C.; Foo, P. D. *J. Chem. Phys.* **1971**, *55*, 1262.
- Okabe, H. *J. Chem. Phys.* **1977**, *66*, 2058.
- Nicovich, J. M.; Kreutter, K. D.; Wine, P. H. *J. Chem. Phys.* **1990**, *92*, 3539.
- Wallington, T. J.; Ellermann, T.; Nielsen, O. J. *J. Phys. Chem.* **1993**, *97*, 8442.
- Timonen, R. S.; Seetala, J. A.; Gutman, D. *J. Phys. Chem.* **1990**, *94*, 3005.
- Fenter, F. F.; Anderson, J. G. *J. Phys. Chem.* **1991**, *95*, 3172.
- Calvert, J. G.; Pitts, J. N., Jr. *Photochemistry*; Wiley: New York, **1966**.
- Hearn, C. H.; Turcu, E.; Joens, J. A. *Atmos. Environ.* **1990**, *24A*, 1939.
- Chase, M. W., Jr.; Davies, C. A.; Downey, J. R., Jr.; Frurip, D. J.; McDonald, R. A.; Syverud, A. N. *J. Phys. Chem. Ref. Data* **1985**, *14* (Suppl. I).
- Nobes, R. H.; Radom, L. *Chem. Phys. Lett.* **1992**, *189*, 554.
- Curtiss, L. A.; Nobes, R. H.; Pople, J. A.; Radom, L. *J. Chem. Phys.* **1992**, *97*, 6766.
- Ruscic, B.; Berkowitz, J. *J. Chem. Phys.* **1993**, *98*, 2568.
- DeMore, W. B.; Sander, S. P.; Golden, D. M.; Hampson, R. F.; Kurylo, M. J.; Howard, C. J.; Ravishankara, A. R.; Kolb, C. E.; Molina, M. J. *Chemical Kinetics and Photochemical Data for Use in Stratospheric Modeling*; JPL Publication 92-20; Jet Propulsion Laboratory: Pasadena, CA, **1992**.
- Seakins, P. W.; Filling, M. J. *J. Phys. Chem.* **1991**, *95*, 9878.
- Wine, P. H.; Nicovich, J. M.; Stickel, R. E.; Zhao, Z.; Shackelford, C. J.; Kreutter, K. D.; Daykin, E. P.; Wang, S. In *The Tropospheric Chemistry of Ozone in the Polar Regions*; NATO ASI Series, Vol. 17; Niki, H., Becker, K. H., Eds.; Springer-Verlag: Berlin, **1993**; pp 385–395.
- Stickel, R. E.; Zhao, Z.; Wine, P. H. To be published.
- McKee, M. L. Private communication.
- Sverdlov, L. M.; Kovner, M. A.; Krainov, E. P. *Vibrational Spectra of Polyatomic Molecules*; Wiley: New York, **1974**.
- Durig, J. R.; Griffin, M. G. *J. Chem. Phys.* **1977**, *67*, 2220.
- Shum, L. G. S.; Benson, S. W. *Int. J. Chem. Kinet.* **1985**, *95*, 27.
- See, for example: Knox, J. H. *Molecular Thermodynamics*; Wiley-Interscience: London, **1971**.
- Baker, J.; Dyke, J. M. *Chem. Phys. Lett.* **1993**, *213*, 257.
- Nourbakhsh, S.; Norwood, K.; Yin, H.-M.; Liao, C.-L.; Ng, C. Y. *J. Chem. Phys.* **1991**, *95*, 5014.
- Ma, Z.-X.; Liao, C.-L.; Yin, H.-M.; Ng, C. Y.; Chiu, S.-W.; Ma, N. L.; Li, W.-K. *Chem. Phys. Lett.* **1993**, *213*, 250.
- McCullough, J. P.; Hubbard, W. N.; Frow, F. R.; Hosenlopp, L. A.; Waddington, G. *J. Am. Chem. Soc.* **1957**, *79*, 561.
- Seakins, P. W.; Filling, M. J.; Niiranen, J. T.; Gutman, D.; Krastopirov, L. N. *J. Phys. Chem.* **1992**, *96*, 9847.
- Seetala, J. A.; Russell, J. J.; Gutman, D. *J. Am. Chem. Soc.* **1990**, *112*, 1347.
- Mozurkewich, M.; Benson, S. W. *J. Phys. Chem.* **1984**, *88*, 6429.
- McEwen, A. B.; Golden, D. M. *J. Mol. Struct.* **1990**, *224*, 357.
- Russell, J. J.; Seetala, J. A.; Gutman, D. *J. Am. Chem. Soc.* **1988**, *110*, 3092.
- Chen, Y.; Tschuikow-Roux, E.; Rank, A. *J. Phys. Chem.* **1991**, *95*, 9832.
- Chen, Y.; Rank, A.; Tschuikow-Roux, E. *J. Phys. Chem.* **1991**, *95*, 9900.

NDB

55-25

S 9.30 026123

HALOGEN AND SULFUR REACTIONS RELEVANT TO POLAR CHEMISTRY

273539

P. H. Wine,^{1,2,3} J. M. Nicovich,³ R. E. Stickel,³ Z. Zhao,²
C. J. Shackelford,⁴ K. D. Kreutter,^{1,3,5} E. P. Daykin,^{3,6} and S. Wang^{3,7}
Georgia Institute of Technology
Atlanta, GA 30332, U.S.A.

11P.

INTRODUCTION

It is widely hypothesized that catalytic cycles involving BrO_x species play an important role in the episodic destruction of ground-level ozone which is observed in the springtime Arctic boundary layer, although the exact mechanism for production of BrO_x radicals remains an open question [Barrie et al., 1988; Bottenheim et al., 1990; Finlayson-Pitts et al., 1990; McConnell et al., 1992]. The critical evidence linking ozone depletion with BrO_x chemistry is an observed negative correlation between ozone and filterable bromine [Bottenheim et al., 1990; Kieser et al., 1992]. In a recent field study of springtime Arctic boundary layer chemistry [Kieser et al., 1992], ozone concentrations and ethane concentrations were found to be correlated; this observation suggests that chlorine atoms (which react rapidly with ethane) may also be an important catalyst for ozone destruction under springtime Arctic conditions.

The possibility that reactions occurring on surfaces of sea-salt aerosol particles can lead to significant production of halogen atoms in the marine boundary layer has received considerable attention in recent years. Production of photochemically labile $\text{X}_2(\text{g})$ ($\text{X} = \text{Cl}, \text{Br}$) via heterogeneous degradation of ozone (possibly involving free radical intermediates) is one suggested pathway for generation of gas phase bromine atoms [McConnell et al., 1992] and chlorine atoms [Zetzsch et al., 1988; Behnke and Zetzsch, 1989; Keene et al., 1990]; however, recent laboratory and modeling studies [Behnke and Zetzsch, 1990; Chameides and Stelson, 1992a, 1992b] suggest that, at least in the case of chlorine, this pathway is not important in the atmosphere. On the other hand, it appears that ClNO_2 , generated via heterogeneous reaction of N_2O_5 vapor with moist $\text{NaCl}(\text{s})$, may represent a

¹ School of Chemistry and Biochemistry
² School of Earth and Atmospheric Sciences
³ Electro-optics and Physical Sciences Laboratory, GTRI
⁴ School of Physics
⁵ Now at Dept. of Biochemistry, Brandeis Univ., Waltham, MA 02254
⁶ Now at EG&G, P. O. Box 1912, MS A1-24, Las Vegas, NV 89125
⁷ Now at Dalian Institute of Chemical Physics, Chinese Academy of Sciences, P.O. Box 110, Dalian, Peoples Republic of China

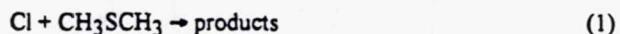
photolytic precursor for atmospherically significant levels of atomic chlorine, even in the remote marine boundary layer where NO_x levels are typically quite low [Behnke and Zetzsch, 1990; Zetzsch and Behnke, 1992; Ganske et al., 1992]. The analogous reaction of $\text{N}_2\text{O}_5(\text{g})$ with $\text{NaBr}(\text{s})$ is one proposed source of springtime Arctic BrO_x radicals [Finlayson-Pitts et al., 1990], although it has been pointed out that generation of sufficient levels of the photolytic precursor BrNO_2 would require a longer residence time for Arctic air than is actually observed [McConnell et al., 1992; Patterson and Husar, 1981]. The frequency of ice fogs in the springtime Arctic boundary layer suggests that heterogeneous chemistry similar to that which occurs in polar stratospheric clouds [Poole et al., 1992] may result in partitioning of XO_x ($\text{X} = \text{Cl}, \text{Br}$) species largely into the reactive forms X and XO .

Dimethylsulfide (CH_3SCH_3 , DMS) is a key atmospheric sulfur species. Roughly half the global flux of sulfur into the atmosphere is thought to be natural in origin [Cullis and Hirschler, 1980; Schwartz, 1988] and a significant fraction of all natural sulfur enters the atmosphere as DMS volatilized from the oceans [Andreae, 1986; Bates et al., 1987]. Levels of DMS in polar regions typically peak during springtime when microorganisms which produce DMS are exposed to light after a long dark period [H. Berresheim, private communication]. Hence, under conditions which exist in the springtime Arctic marine boundary layer, reactions of chlorine and bromine atoms with DMS may play an important role in coupling the halogen and sulfur cycles.

Discussed below are the results of recent laboratory studies we have carried out to investigate the kinetics and mechanisms of the $\text{X} + \text{DMS}$ reactions ($\text{X} = \text{Cl}, \text{Br}$) [Stickel et al., 1992; Nicovich et al., 1992a]. We also present estimates of sea level (i.e., 760 torr) unimolecular decomposition rates for BrNO_2 which are based on kinetic and thermochemical information obtained in our recent study of the $\text{Br} + \text{NO}_2$ association reaction [Kreutter et al., 1990].

THE CL + DMS REACTION

Time-resolved resonance fluorescence detection of chlorine atoms following 266 nm laser flash photolysis of $\text{Cl}_2\text{CO}/\text{DMS}/\text{N}_2$ mixtures has been employed to study the kinetics of R1 over the temperature and pressure ranges 240–421K and 3–700 torr.



A complete description of the experimental approach can be found in a recent publication describing our study of the $\text{Cl} + \text{CS}_2$ reaction [Nicovich et al., 1990]. In agreement with a recent competitive kinetics study [Nielsen et al., 1990], we find that R1 is very fast, i.e., reaction occurs on essentially every $\text{Cl} + \text{DMS}$ encounter. Measured rate coefficients at

240K, 297K, and 421K are plotted as a function of pressure in Figure 1. The reaction rate is found to increase with decreasing temperature as would be expected for a very fast reaction whose rate is determined by the magnitude of long range attractive forces between the reactants. The somewhat surprising aspect of the data in Figure 1 is our observation of a clear pressure dependence for k_1 . It appears that reaction 1 occurs via both pressure-independent and pressure-dependent pathways; the pressure-dependent pathway must involve collisional stabilization of a $(\text{CH}_3)_2\text{S}-\text{Cl}$ adduct.

To gain further insight into the mechanism for reaction 1, we carried out a separate set of experiments where laser flash photolytic (LFP) production of Cl (via 248 nm photolysis of phosgene) was coupled with tunable diode laser absorption spectroscopy (TDLAS) to

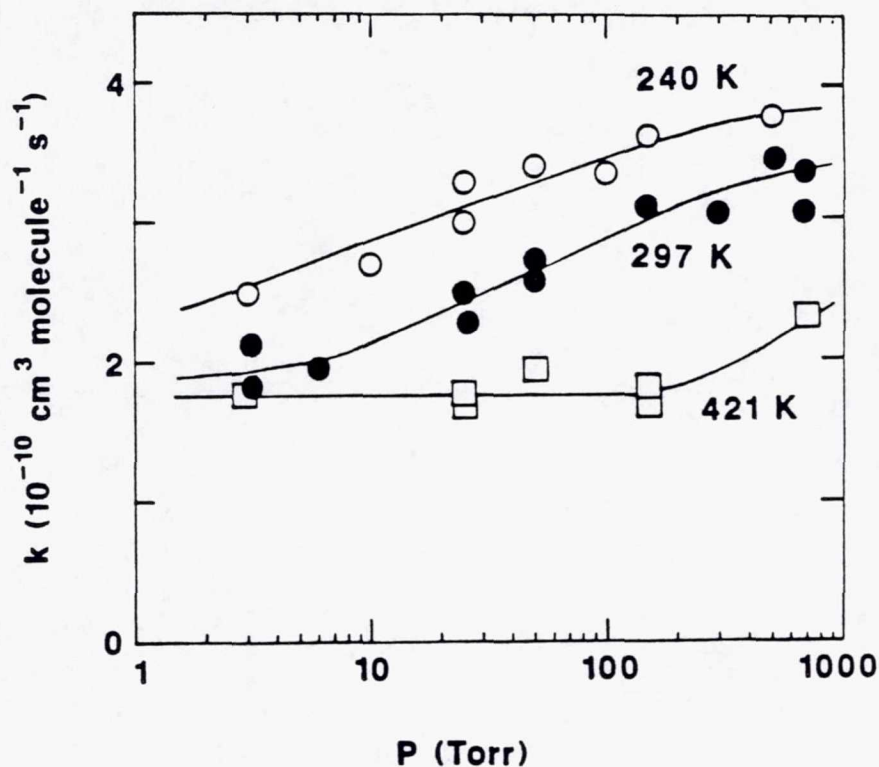


Fig. 1. Rate constants for the $\text{Cl} + (\text{CH}_3)_2\text{S}$ reaction at three temperatures plotted as a function of pressure. The solid lines are "eyeball" fits to the data; their significance is simply as an aid in visualizing the observed pressure dependencies.

Table 1. Yield of HCl from the Cl + DMS reaction as a function of pressure at T = 297 K

Buffer Gas	P(torr)	N ^(a)	HCl Yield
CO ₂	0.6	2	0.98
	2.0	19	0.89
	5.0	4	0.79
	10.1	4	0.74
	26	2	0.62
N ₂ ^(b)	5.0	2	0.85
	10.0	2	0.80
	25	2	0.68
	50	2	0.59
	100	2	0.54
	203	2	0.51

(a) N = number of experiments.

(b) includes one torr of CO₂

measure the HCl product yield at 297K as a function of pressure. A detailed description of the LFP-TDLAS apparatus is given elsewhere [Stickel et al., 1992]. To obtain the HCl yield we carried out back-to-back experiments where the photolytically produced Cl reacted with DMS, then with ethane (C₂H₆); the yield of HCl from the Cl + C₂H₆ reaction is known to be unity. In all experiments, at least 0.6 torr CO₂ was present in the reaction mixture to (a) facilitate rapid equilibration of the atomic chlorine spin-orbit states and (b) facilitate rapid relaxation of any HCl formed in the $v = 1$ level. Typical experimental HCl appearance temporal profiles are presented elsewhere [Stickel et al., 1992]. The results of the yield experiments are summarized in Table 1.

The HCl yield approaches unity as $P \rightarrow 0$ but decreases with increasing pressure. Although extrapolation of kinetic and yield data to zero pressure is non-trivial, examination of the results in Figure 1 and Table 1 strongly suggests that the following relationship is obeyed:

$$\Phi(P) = k_1(P \rightarrow 0) / k_1 P = 1$$

where $\Phi(P)$ is the HCl yield at pressure P.

The experiments described above demonstrate that hydrogen abstraction is the dominant pathway for reaction 1 in the low pressure limit. With increasing pressure, stabilization of a (CH₃)₂SCI adduct apparently becomes competitive with the hydrogen

abstraction pathway. Under the pressure and temperature conditions of the springtime Arctic boundary layer, it appears that $k_1 \sim 4 \times 10^{-10} \text{ cm}^3 \text{ molecule}^{-1} \text{ s}^{-1}$ and that 60-80% of the overall reaction proceeds via the adduct-forming pathway. The fate of the stabilized adduct remains uncertain, although it clearly does not dissociate to Cl or HCl on the time scale of our experiments (several milliseconds). One interesting possibility is reaction with O_2 to form $(\text{CH}_3)_2\text{SO} + \text{ClO}$; this reaction could represent an unrecognized source of atmospheric $(\text{CH}_3)_2\text{SO}$. Another energetically feasible pathway for degradation of $(\text{CH}_3)_2\text{SBr}$ is unimolecular decomposition to $\text{CH}_3\text{S} + \text{CH}_3\text{Cl}$, a process which could possibly represent an important source of atmospheric methyl chloride. Clearly, the atmospheric fate of $(\text{CH}_3)_2\text{SBr}$ warrants further investigation.

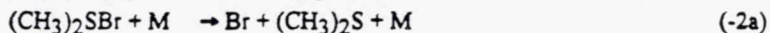
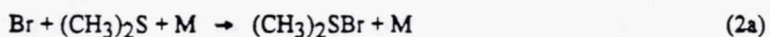
THE BR + DMS REACTION

Time-resolved resonance fluorescence detection of bromine atoms following 266 nm laser flash photolysis of $\text{CF}_2\text{Br}_2/\text{DMS}/\text{H}_2/\text{N}_2$ mixtures has been employed to study the kinetics of reaction 2 as a function of temperature and pressure.



A complete description of the experimental approach can be found in a recent publication describing our studies of the reactions $\text{Br} + \text{H}_2\text{S} \rightleftharpoons \text{SH} + \text{HBr}$ and $\text{Br} + \text{CH}_3\text{SH} \rightleftharpoons \text{CH}_3\text{S} + \text{HBr}$ [Nicovich et al., 1992b]. Distinctly different kinetic behavior is observed in the two temperature regimes 260-310K and 375-425K.

In the low temperature regime, i.e., 260-310K, the dominant reaction pathway is found to be reversible adduct formation:



Observation of the kinetics of the approach to equilibrium allows evaluation of $k_{2a}(P,T)$, $k_{-2a}(P,T)$ and, therefore, $K_{eq}(T)$ ($K_{eq} = k_{2a}/k_{-2a}$). Measured rate coefficients are summarized in Table 2. A van't Hoff plot of $\ln K_p$ versus T^{-1} is shown in Figure 2. From the slope of the van't Hoff plot (and a small heat capacity correction) we obtain a value for the enthalpy change associated with reaction 2a, i.e., the $(\text{CH}_3)_2\text{S-Br}$ bond strength; the result is $\Delta H_{298} = -14.5 \pm 1.2 \text{ kcal mole}^{-1}$. We have recently carried out similar measurements of the $(\text{CH}_3)_2\text{S-OH}$ bond strength [Hynes et al., 1992] and find it to be approximately equal to the

Table 2. Rate constants for the reactions $\text{Br} + (\text{CH}_3)_2\text{S} + \text{M} \rightleftharpoons (\text{CH}_3)_2\text{SBr} + \text{M}$ as a function of temperature and pressure^(a)

T	P	k_{2a}	k_{-2a}	notes
263	50	4.49	410	
265	50	3.90	380	
267	200	8.25	1,350	
268	50	6.07	730	(b)
269	200	10.1	2,050	(b)
272	25	2.63	500	
274	50	4.16	920	
274	100	5.70	1,380	
274	200	7.49	2,400	
274	400	10.2	3,150	
274	600	11.9	3,600	
285	50	3.18	2,360	
285	200	6.70	5,900	
291	50	2.96	3,210	
291	200	6.69	7,730	
298	50	2.74	5,150	(c)
299	50	3.44	7,430	(b)
300	25	1.77	3,750	
300	50	2.62	5,920	
310	25	1.43	6,810	
310	50	2.11	10,500	

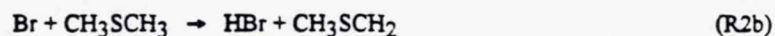
(a) Units are T(K), P(torr), $k_{2a}(10^{-11} \text{ cm}^3 \text{ molecule}^{-1}\text{s}^{-1})$, $k_{-2a}(\text{s}^{-1})$.

(b) Reactant was DMS- d_6 .

(c) Photolyte was Br_2 (it was CF_2Br_2 in all other experiments); Br_2 was photolyzed at 355 nm.

$(\text{CH}_3)_2\text{S}$ -Br bond strength. Hence, a reasonable "guesstimate" for the $(\text{CH}_3)_2\text{S}$ -Cl bond strength is 14-15 kcal mole⁻¹.

At temperatures above 375K, $(\text{CH}_3)_2\text{SBr}$ decomposition is so rapid that the addition reaction effectively does not occur. In this temperature regime sulfide reactivity toward atomic bromine follows the trend $(\text{C}_2\text{H}_5)_2\text{S} > (\text{CH}_3)_2\text{S} > (\text{CD}_3)_2\text{S}$, strongly suggesting that the dominant reaction pathway is hydrogen abstraction:



Interestingly, we measure an activation energy for reaction 2b of 5.0 kcal mole⁻¹, while the literature value for CH_3SCH_2 heat of formation [Shum and Benson, 1985] suggests that

reaction 2b is endothermic by $9.0 \text{ kcal mole}^{-1}$; hence, our kinetic results strongly suggest that the C-H bond strength in DMS is $2\text{--}4 \text{ kcal mole}^{-1}$ weaker than currently thought.

Extrapolation of our kinetic data to conditions typical of the springtime Arctic boundary layer (760 torr, 230-270K) suggests that under the conditions of interest (a) addition of Br to DMS is four to five orders of magnitude faster than hydrogen abstraction; (b) the rate coefficient for the addition reaction is $(1.3 \pm 0.2) \times 10^{-10} \text{ cm}^3 \text{ molecule}^{-1} \text{ s}^{-1}$;

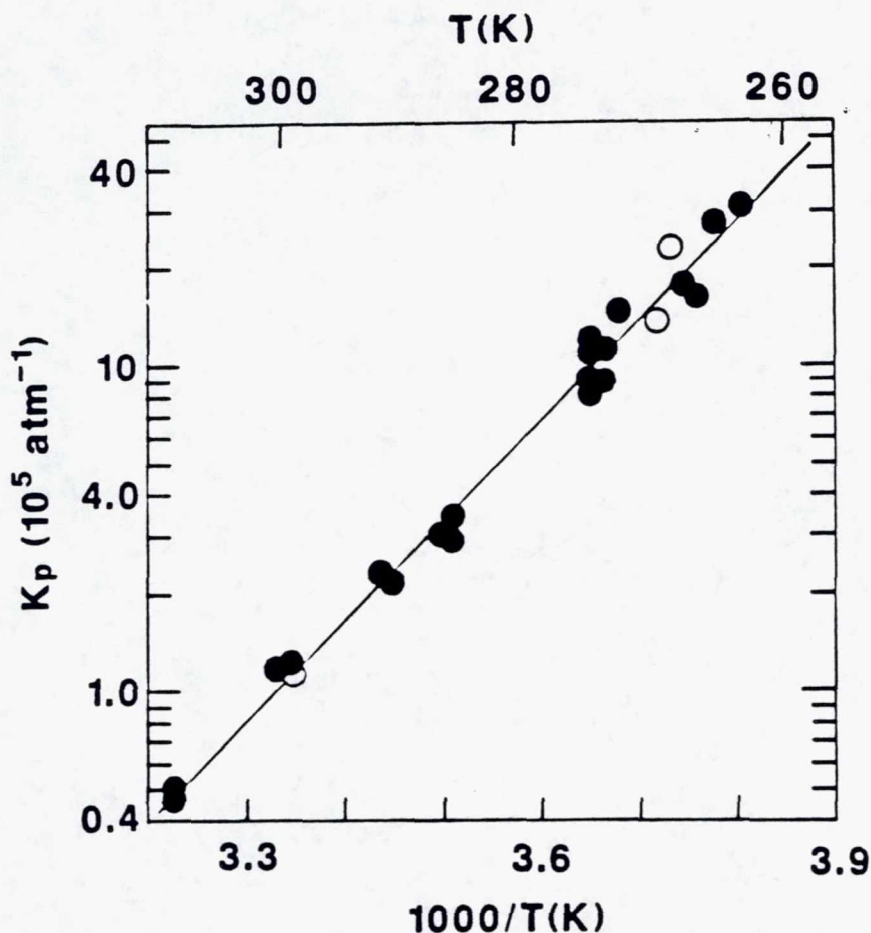
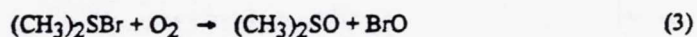


Fig. 2. van't Hoff plot for the equilibrium $\text{Br} + (\text{CH}_3)_2\text{S} \rightleftharpoons (\text{CH}_3)_2\text{SBr}$. Open circles are data obtained using $(\text{CD}_3)_2\text{S}$ as the sulfide reactant. Solid line is obtained from a least squares analysis; the slope gives $\Delta H(334\text{K}) = -14.6 \pm 1.1 \text{ kcal mole}^{-1}$ while the intercept gives $\Delta S(334\text{K}) = -22.9 \pm 3.9 \text{ cal mole}^{-1} \text{ deg}^{-1}$ (errors are 2σ and represent precision only).

and (c) the lifetime of the $(\text{CH}_3)_2\text{SBr}$ adduct toward unimolecular decomposition is 0.01-0.0001 seconds. The short lifetime of $(\text{CH}_3)_2\text{SBr}$ toward unimolecular decomposition suggests that the only atmospheric species capable of scavenging $(\text{CH}_3)_2\text{SBr}$ is O_2 .

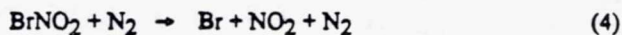


To search for BrO production from reaction 3, a separate set of experiments was carried out (at 297K) where time-resolved longpath absorption detection in the near ultraviolet was coupled with 248 nm laser flash photolysis of $\text{CF}_3\text{Br}/\text{DMS}/\text{H}_2/\text{N}_2/\text{O}_2$ mixtures; a description of the apparatus is given elsewhere [Daykin and Wine, 1990]. Production of BrO was not observed, but a strong, broad, unstructured absorption feature with $\lambda_{\text{max}} \sim 370$ nm was observed. Studies of the appearance kinetics of the absorption feature demonstrate rather conclusively that it is due to $(\text{CH}_3)_2\text{SBr}$, i.e., a plot of pseudo-first order appearance rate versus [DMS] is linear with slope equal to the (previously measured) k_2 and intercept equal to the (previously measured) k_{-2a} . At 50 torr total pressure the strength and temporal behavior of the transient absorption signal was independent of whether N_2 or O_2 was employed as the buffer gas; this observation suggests that $k_3 < 3 \times 10^{-16} \text{ cm}^3 \text{ molecule}^{-1} \text{ s}^{-1}$. For assessing the potential role of reaction 3 in atmospheric chemistry under springtime Arctic boundary layer conditions, it will be necessary to extend the time-resolved absorption studies to higher O_2 partial pressures and lower temperatures.

UNIMOLECULAR DECOMPOSITION OF BrNO_2

As mentioned in the introduction, Finlayson-Pitts et al. [1990] have proposed that BrNO_2 (nitryl bromide), formed via the heterogeneous reaction of N_2O_5 with NaBr on the surface of sea salt aerosol particles, may be an important photolytic precursor to BrO_x radicals in the springtime Arctic boundary layer. However, McConnell et al. [1992] have pointed out a potential problem with the Finlayson-Pitts et al. proposal – the residence time for an air mass in the Arctic may not be long enough for sufficient buildup of BrNO_2 to occur prior to polar sunrise.

Recently, we reported a detailed study of the kinetics and thermochemistry of $\text{Br} + \text{NO}_2$ association reaction [Kreutter et al., 1990]. Given in Table 3 are upper and lower limit lifetimes toward BrNO_2 unimolecular decomposition (i.e., k_4^{-1}) under springtime Arctic boundary layer conditions; the lifetimes are obtained by extrapolation of our data [Kreutter et al., 1990] to 760 torr and low temperature.



The range of values for k_4^{-1} which are consistent with our data is rather large because the possible roles of the (short lived) isomer BrONO and/or excited electronic state potential energy surfaces could not be quantified due to lack of information. Nonetheless, the data in Table 3 lead to an important conclusion. At temperatures typical of the wintertime and springtime Arctic, i.e., 220 - 260 K, the lifetime of BrNO₂ toward unimolecular decomposition is rather short, i.e., usually less than one day. Hence, bromine atoms would be released from the BrNO₂ reservoir not only when the sun comes up, but continuously during the dark BrNO₂ production period.

Table 3. Lifetime of BrNO₂ toward unimolecular decomposition at atmospheric pressure

T(K)	k_4^{-1} (days)	
	lower limit	upper limit
200	2.1	840
220	0.054	5.8
240	0.0021	0.14
260	0.00013	0.0057
280	0.000014	0.00029
300	0.0000024	0.000027

Acknowledgments: The research described in this paper was supported by the NSF Atmospheric Chemistry Program (grant ATM-9104807), the NASA Upper Atmosphere Research Program (grant NAGW-1001), and the Georgia Tech Research Institute (internal grant E-8904-038).

REFERENCES

- Andreae, M. O., The ocean as a source of atmospheric sulfur compounds, in *The Role of Air-Sea Exchange in Geochemical Cycling*, edited by P. Buat-Menard, pp. 331-362, D. Reidel, Hingham, MA, 1986.
- Barrie, L. A., J. W. Bottenheim, R. C. Schnell, P. J. Crutzen, and R. A. Rasmussen, Ozone destruction and photochemical reactions at polar sunrise in the lower Arctic atmosphere, *Nature*, **334**, 138-141, 1988.
- Bates, T. S., J. D. Cline, R. H. Gammon, and S. R. Kelly-Hansen, Regional and seasonal variations in the flux of oceanic dimethylsulfide to the atmosphere, *J. Geophys. Res.*, **92**, 2930-2938, 1987.

- Behnke, W. and C. Zetzsch, Heterogeneous formation of chlorine atoms from various aerosol in the presence of O₃ and HCl, *J. Aerosol Sci.*, 20, 1167-1170, 1989.
- Behnke, W. and C. Zetzsch, Heterogeneous photochemical formation of Cl atoms from NaCl aerosol, NO_x, and ozone, *J. Aerosol Sci.*, 21, Suppl. 1, s229-s232, 1990.
- Bottenheim, J. W., L. A. Barrie, E. Atlas, L. E. Heidt, H. Niki, R. A. Rasmussen, and P. B. Shepson, Depletion of lower tropospheric ozone during Arctic spring: The polar sunrise experiment 1988, *J. Geophys. Res.*, 95, 18,555-18,568, 1990.
- Chameides, W. L. and A. W. Stelson, Aqueous-phase chemical processes in deliquescent seasalt aerosols, *Ber. Bunsenges. Phys. Chem.*, 96, 461-470, 1992a.
- Chameides, W. L. and A. W. Stelson, Aqueous-phase chemical processes in deliquescent seasalt aerosols: A mechanism that couples the atmospheric cycles of S and seasalt alkalinity, *J. Geophys. Res.*, in press, 1992b.
- Cullis, C. F., and M. M. Hirschler, Atmospheric sulfur: Natural and man-made sources, *Atmos. Environ.*, 14, 1263-1278, 1980.
- Daykin, E. P., and P. H. Wine, Kinetics of the reactions of IO radicals with NO and NO₂, *J. Phys. Chem.*, 94, 4528-4535, 1990.
- Finlayson-Pitts, B. J., F. E. Livingston, and H. N. Berko, Ozone destruction and bromine photochemistry at ground level in the Arctic spring, *Nature*, 343, 622-625, 1990.
- Ganske, J. A., H. N. Berko, and B. J. Finlayson-Pitts, Absorption cross sections for gaseous ClNO₂ and Cl₂ at 298K: Potential organic oxidant source in the marine troposphere, *J. Geophys. Res.*, 97, 7651-7656, 1992.
- Hynes, A. J., A. J. Pounds, T. McKay, J. D. Bradshaw, and P. H. Wine, Detailed mechanistic studies of the OH initiated oxidation of biogenic sulfur compounds under atmospheric conditions, *Twelfth International Symposium on Gas Kinetics*, paper no. G6, Reading, United Kingdom, 1992.
- Keene, W. C., A. A. P. Pszenny, D. J. Jacob, R. A. Duce, J. N. Galloway, J. J. Schultz-Tokos, H. Sievering, and J. F. Boatman, The geochemical cycling of reactive chlorine through the marine troposphere, *Global Biogeochem. Cycles*, 4, 407-430, 1990.
- Kieser, B. N., T. Sideris, H. Niki, J. W. Bottenheim, and W. R. Leitch, Spring 1989 observations of tropospheric chemistry in the Canadian high Arctic, *Atmos. Environ.*, in press, 1992.
- Kreutter, K. D., J. M. Nicovich, and P. H. Wine, Kinetics and thermochemistry of the Br(²P_{3/2}) + NO₂ association reaction, *J. Phys. Chem.*, 95, 4020-4028, 1991. Correction, *J. Phys. Chem.*, 96, 7146, 1992.
- McConnell, J. C., G. S. Henderson, L. Barrie, J. Bottenheim, H. Niki, C. H. Langford, and E. M. J. Templeton, Photochemical bromine production implicated in Arctic boundary-layer ozone depletion, *Nature*, 355, 150-152, 1992.
- Nicovich, J. M., C. J. Shackelford, and P. H. Wine, Kinetics and thermochemistry of reversible adduct formation in the reaction of Cl(²P_{1/2}) with CS₂, *J. Phys. Chem.*, 94, 2896-2903, 1990.
- Nicovich, J. M., C. J. Shackelford, K. D. Kreutter, E. P. Daykin, S. Wang, A. Jefferson, and P. H. Wine, Kinetic and mechanistic studies of the reactions of atomic bromine with dimethylsulfide, to be published, 1992a.
- Nicovich, J. M., K. D. Kreutter, C. A. van Dijk, and P. H. Wine, Temperature-dependent kinetics studies of the reactions $\text{Br}({}^2\text{P}_{3/2}) + \text{H}_2\text{S} \rightleftharpoons \text{SH} + \text{HBr}$ and $\text{Br}({}^2\text{P}_{3/2}) +$

- $\text{CH}_3\text{SH} \rightleftharpoons \text{CH}_3\text{S} + \text{HBr}$. Heats of formation of SH and CH_3S radicals, *J. Phys. Chem.*, **96**, 2518-2528, 1992b.
- Nielsen, O. J., H. W. Sidebottom, L. Nelson, O. Rattigan, J. J. Treacy, and D. J. O'Farrell, Rate constants for the reactions of OH radicals and Cl atoms with diethyl sulfide, di-n-propyl sulfide, and di-n-butyl sulfide, *Int. J. Chem. Kinet.*, **22**, 603-612, 1990.
- Patterson, D. E. and R. B. Husar, A direct simulation of hemispherical transport of pollutants, *Atmos. Environ.*, **15**, 1479-1482, 1981.
- Poole, L. R., R. L. Jones, M. J. Kurylo, and A. Wahner, Heterogeneous processes: Laboratory, field, and modeling studies, in *Scientific Assessment of Ozone Depletion: 1991*, edited by D. L. Albritton, R. T. Watson, S. Solomon, R. F. Hampson, and F. Ormond, chapter 3, World Meteorological Organization, Global Ozone Research and Monitoring Project - Report No. 25, 1992.
- Schwartz, S. E., Are global cloud albedo and climate controlled by marine phytoplankton?, *Nature*, **336**, 441-445, 1988.
- Shum, L. G. S., and S. W. Benson, Iodine catalyzed pyrolysis of dimethyl sulfide. Heats of formation of $\text{CH}_3\text{SCH}_2\text{I}$, the CH_3SCH_2 radical, and the pi bond energy in CH_3S , *Int. J. Chem. Kinet.*, **17**, 277-292, 1985.
- Stickel, R. E., J. M. Nicovich, S. Wang, Z. Zhao, and P. H. Wine, Kinetic and mechanistic study of the reaction of atomic chlorine with dimethyl sulfide, *J. Phys. Chem.*, in press, 1992.
- Zetzsch, C., G. Pfahler, and W. Behnke, Heterogeneous formation of chlorine atoms from NaCl in a photosmog system, *J. Aerosol. Sci.*, **19**, 1203-1206, 1988.
- Zetzsch, C. and W. Behnke, Heterogeneous photochemical sources of atomic Cl in the troposphere, *Ber. Bunsenges. Phys. Chem.*, **96**, 488-493, 1992.

5-9-30
NDB
56-25
026124
17P
273540

Kinetics of the BrO + NO₂ Association Reaction. Temperature and Pressure Dependence in the Falloff Regime

R. P. THORN, E. P. DAYKIN,* and P. H. WINE†

School of Earth & Atmospheric Sciences, School of Chemistry & Biochemistry, and Georgia Tech Research Institute, Georgia Institute of Technology, Atlanta, Georgia 30332

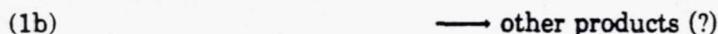
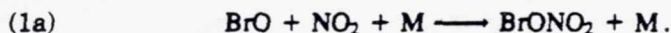
Abstract

A laser flash photolysis-long path absorption technique has been employed to study the kinetics of the reaction BrO + NO₂ + M[‡] products as a function of temperature (248–346 K), pressure (16–800 torr), and buffer gas identity (N₂, CF₄). The reaction is found to be in the falloff regime between third and second-order over the entire range of conditions investigated. This is the first study where temperature-dependent measurements of $k_1(P, T)$ have been reported at pressures greater than 12 torr; hence, our results help constrain choices of $k_1(P, T)$ for use in models of lower stratospheric BrO_x chemistry. Approximate falloff parameters in a convenient form for atmospheric modeling are derived. © 1993 John Wiley & Sons, Inc.

Introduction

Despite its relatively low concentration (about 25 pptv) in the stratosphere, bromine plays an important role in stratospheric odd oxygen chemistry. Due to differences in the rates of formation and destruction of the HX reservoir species, under “normal” stratospheric conditions (i.e., unperturbed by heterogeneous chemistry) a much larger fraction of bromine is partitioned into the “active” form (Br + BrO) compared to chlorine. Hence, on a per molecule basis, bromine is thought to be 30–120 times more effective than chlorine as a catalyst for odd oxygen destruction [1]. The chlorine-to-bromine concentration ratio in the stratosphere is currently about 160 [1]; this ratio is expected to drop to about 100 over the next century as anthropogenic sources of both halogen species are greatly reduced [1].

The most important BrO_x reservoir species in the lower stratosphere is bromine nitrate, which is formed via the BrO + NO₂ association reaction



*Present address: EG&G Energy Measurements Division, P.O. Box 1912, MS A1-24, Las Vegas, Nevada 89125.

†To whom correspondence should be addressed.

In fact, recent model calculations suggest that BrONO_2 is the dominant BrO_x species at altitudes below 35 km [2,3]. The calculated partitioning between BrONO_2 and BrO , the two most concentrated species, is critically dependent on the assumed values for $k_1(P, T)$.

Two studies of the kinetics of reaction (1) are reported in the literature. Sander et al. [4] employed both discharge flow and flash photolysis techniques to obtain values for $k_1(P, 298\text{ K})$ over the pressure range 1–700 torr N_2 , while Danis et al. [5] employed a laser flash photolysis-time resolved mass spectrometry technique to study the temperature dependence of k_1 (over the range 263–343 K) at low total pressures (4–12 torr O_2). Where the two studies overlapped, i.e., $T = 298\text{ K}$ and $P = 4\text{--}12$ torr, the rate coefficients reported by Sander et al. [4] are about 25% faster than those reported by Danis et al. [5].

In this article we present the results of a study where 351 nm laser flash photolysis of $\text{Br}_2/\text{NO}_2/\text{N}_2$ (or CF_4) mixtures has been coupled with detection of BrO by time-resolved long path ultraviolet spectroscopy to study the kinetics of reaction (1) over the temperature and pressure ranges 248–346 K and 16–800 torr. The motivation for this study is primarily to improve the accuracy with which $k_1(P, T)$ values can be estimated under atmospheric conditions, particularly under the low temperature, high pressure conditions of the lower stratosphere. In addition, this study improves somewhat the accuracy with which $k_{1,\infty}(T)$, the rate coefficient in the high pressure limit, can be estimated.

Experimental

The kinetics of reaction (1) were investigated by monitoring the temporal behavior of BrO absorbance following 351 nm laser flash photolysis of $\text{Br}_2/\text{NO}_2/\text{N}_2$ (or CF_4) mixtures. The laser flash photolysis-long path absorption apparatus was similar to the one we employed recently to investigate the reactions of F and Cl atoms with HNO_3 [6] and the reactions of IO radicals with NO and NO_2 [7]. A schematic diagram of the apparatus and descriptions of the reaction cell and temperature measurement techniques can be found elsewhere [6]. As in the IO kinetics study [7], a 150 watt xenon arc lamp was employed as the probe light source.

The XeF laser photolysis beam was expanded by means of cylindrical lenses to be 11–12 cm wide and 2 cm high as it traversed the reactor. The xenon arc lamp beam was multipassed through the reactor at right angles to the photolysis beam using modified White cell optics [8]; 42 or 46 passes were employed, giving absorption path lengths through the photolyzed volume of 462 or 552 cm. Output radiation from the multipass cell was focused onto the entrance slit of a 0.22-m monochromator adjusted to transmit radiation at 338.3 nm, the peak of the strong 7–0 band of the $\text{BrO } A^2\pi \leftarrow X^2\pi$ transition [9].

Reflective losses in the multipass system were minimized by using White cell mirrors coated for high reflectivity around 338 nm and reaction cell windows coated for maximum transmission around 338 nm. As a tradeoff between light throughput and resolution, the monochromator slit widths

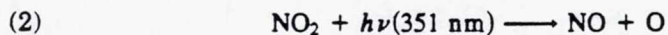
were set at 200 μm (resolution 0.72 nm FWHM). Radiation exiting the monochromator was detected by a photomultiplier (Hamamatsu R928), the time-dependent output from which was monitored by a signal averager with 1.5 μs time resolution and 10 bit voltage resolution. The results of 32–512 laser shots were averaged to obtain data with suitable signal-to-noise ratio for quantitative kinetic analysis. Digitized voltage vs. time data were transferred to a small computer for storage and analysis.

In order to avoid accumulation of reaction or photolysis products, all experiments were carried out under "slow flow" conditions. The linear flow rate through the reaction cell was typically 2 cm s^{-1} , and the excimer laser repetition rate was 0.2 Hz. Hence, the gas mixture in the photolysis zone was replenished between laser shots. Br₂ and NO₂ were flowed into the reaction cell from 12-L bulbs containing dilute mixtures in nitrogen (Br₂) or zero grade air (NO₂). Preparation of the NO₂ bulb with air as the diluent gas prevented conversion of NO₂ to NO during storage. To prevent reaction of Br₂ with the antireflection coated reaction cell windows, a four-port gas input/output system was employed [6,7]. The NO₂/Br₂ mixture and 85–90% of the N₂ buffer gas entered the reactor through an inner port while the remaining 10–15% of the N₂ buffer gas entered the reactor through both outer ports. The gas mixture was exhausted through an inner port. The concentration of Br₂ was determined from the known bulb concentration, measurement of the appropriate mass flow rate, and the total pressure. The NO₂ concentration was measured in situ in the slow flow system by UV photometry using a 216.2 cm long absorption cell plumbed in series with the reaction cell. Radiation at 326.1 nm emitted by a cadmium penray lamp was employed as the light source for NO₂ detection. With the combination of the Cd lamp light source and the band-pass filter employed to isolate the 326.1 nm line, we determined the effective NO₂ absorption cross section to be $(2.89 \pm 0.04) \times 10^{-19} \text{ cm}^2$. This value is in reasonable agreement with the recent measurements of Schneider et al. [10], who report $\sigma = 2.815 \times 10^{-19} \text{ cm}^2$ at $326.0 \pm 0.5 \text{ nm}$. The absorption cross section for Br₂ at 326.1 nm is about $4.0 \times 10^{-20} \text{ cm}^2$ [11], which is too low to interfere with the photometric determination of the NO₂ concentration. UV photometry at 404.7 nm was used to determine the Br₂ concentration in each 12-L Br₂/N₂ bulb used. With the combination of an Hg pen-ray lamp light source and a band-pass filter employed to isolate the 404.7 nm line, we measured the effective Br₂ absorption cross section to be $5.95 \times 10^{-19} \text{ cm}^2$.

The gases used in this study were obtained from Matheson and had the following stated minimum purities: N₂, 99.999%; NO, 99.0%; O₂, 99.99%; and CF₄, 99.99%. Air was ultra zero grade with total hydrocarbons less than 0.1 ppm. The procedures employed to synthesize pure NO₂ from the NO + O₂ reaction are described elsewhere [7]. The Br₂ used in this study had a stated minimum purity of 99.94% (liquid phase). The Br₂ was transferred under nitrogen into a vial fitted with a high-vacuum stopcock and then degassed repeatedly at 77 K before being used to prepare Br₂/N₂ gas mixtures.

Results and Discussion

The following scheme was employed to generate BrO radicals:



Based on literature values for k_3 and k_4 [12,13] and the concentrations of Br_2 and NO_2 employed to measure values for $k_1(P, T)$ (Table I), it was always the case that BrO production was at least 15 times faster than BrO removal, and that at least 70% of the photolytically generated oxygen atoms reacted with Br_2 to produce BrO.

For the optical path lengths traversed by the probe beam through the reactor (around 13 meters in most experiments) and the NO_2 concentrations employed (up to 6.31×10^{15} molecules per cm^3), a large fraction of the probe radiation was absorbed by NO_2 . Hence, destruction of NO_2 by reactions (2) and (4) led to a noticeable difference between the (baseline) signal levels before and after the laser fired in experiments where NO_2 was photolyzed in the absence of Br_2 . In the presence of Br_2 , the magnitude of the rapid baseline shift upon firing the laser was reduced due to the occurrence of reaction (3) in competition with reaction (4). A majority of the BrO generated via reaction (3) decayed by reacting with NO_2 to form BrONO_2 while, as will be discussed in more detail below, a small fraction decayed by reaction (5), a process which regenerates NO_2 .



Based on reported 338.3 nm absorption cross sections for BrO [9], NO_2 [10], and BrONO_2 [14], it appears that absorption of analytical light by BrONO_2 was negligible, i.e., the BrONO_2 absorption cross section is a factor of 4 smaller than the NO_2 absorption cross section and more than a factor of 100 smaller than the BrO absorption cross section. Furthermore, Sander and Watson [15] have shown that if an elementary reaction results in an absorbance change due to removal of an absorbing excess reagent and/or formation of an absorbing product, the correct decay rate is obtained from the first-order decay of the overall absorbance by using the signal level at $t \rightarrow \infty$ as the baseline. All of our kinetic data were analyzed in this manner. As typified by the data in Figure 1, the observed transmission after BrO had decayed away was found to be slightly lower than the transmission before the laser fired; this implies either that the BrONO_2 absorption cross section at 338.3 nm is larger than reported in the literature, or that another species is formed whose absorbance more than offsets the increased transmission due to NO_2 removal. A likely explanation for the lower than expected postdecay transmission is production of BrNO_2 via the reaction of atomic bromine with NO_2 .

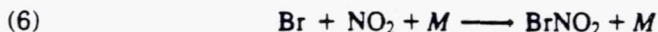


TABLE I. Summary of kinetic data for the reaction BrO + NO₂ + N₂ products.

T ^a	Concentrations ^a			[NO ₂]/[O] ₀	no. of expts ^b	Range of k'	k ₁ ^{a,c}	
	N ₂	Br ₂	NO ₂				Uncorrected	Corrected ^d
248	622	4.5	0.86 - 4.20	700-800	6	503-2230	5.32 ± .16	4.88 ± .18
248	1560	5.5	0.93 - 4.07	730-980	7	999-4160	9.88 ± .71	9.54 ± .69
249	3880	7.5	1.66 - 4.52	740-950	9	3000-8500	19.7 ± 1.4	19.3 ± 1.4
253	11400	12.	0.59 - 3.47	350-410	5	1920-11800	33.9 ± 1.2	33.2 ± 1.1
256	24100	7.8	0.55 - 2.90	420-540	7	2520-12400	42.1 ± 4.1	41.5 ± 4.1
267	579	7.2	0.94 - 5.48	810-900	6	373-2130	3.88 ± .21	3.54 ± .22
268	1440	5.4	0.88 - 3.62	920-1100	5	353-2630	7.44 ± .53	7.17 ± .51
268	3610	5.6	0.84 - 3.73	370-1200	7	1220-5870	14.7 ± 1.7	14.2 ± 1.5
268	10800	6.2	0.74 - 3.84	520-720	5	1810-10850	28.2 ± 1.1	27.7 ± 1.0
268	23100	5.2	0.49 - 2.12	390-580	6	1680-8600	40.8 ± 2.6	40.1 ± 2.6
298	518	8.1	0.42 - 2.73	650-1200	8	137-754	2.66 ± .26	2.40 ± .22
298	1300	7.9	0.62 - 5.22	560-1240	11	306-2840	5.39 ± .29	5.13 ± .23
298	3240	9.6	1.84 - 4.41	230-1120	11	1850-4340	9.75 ± .78	9.16 ± .58
298	9720	6.0	0.23 - 3.30	260-860	8	559-6460	19.6 ± .66	18.8 ± .79
298	20700	5.0	0.31 - 1.90	280-1230	10	808-5940	30.0 ± 3.0	29.3 ± 2.8
345	448	8.1	1.92 - 4.40	1040-1200	5	350-761	1.65 ± .16	1.48 ± .14
347	1110	8.9	0.93 - 5.45	240-1380	14	353-2020	3.17 ± .41	2.72 ± .26
345	2800	9.0	0.73 - 6.31	570-660	6	375-3410	5.50 ± .28	5.12 ± .26
345	8400	6.0	1.04 - 4.44	510-580	5	1040-5150	11.4 ± .85	11.0 ± .83
346	17900	5.9	0.78 - 3.39	370-400	5	1370-5630	16.9 ± 1.3	16.2 ± 1.4
346	22300	5.2	0.70 - 3.41	350-460	5	1350-6760	20.6 ± 1.8	20.1 ± 1.7

^a Units are: T, K; concentration, 10¹⁵ molecules per cm³; k', s⁻¹; k₁, 10⁻¹³ cm³ molecule⁻¹ s⁻¹.

^b Experiment = measurement of one BrO temporal profile.

^c Errors are 2σ and represent precision only.

^d Corrected for contributions from the BrO + NO reaction.

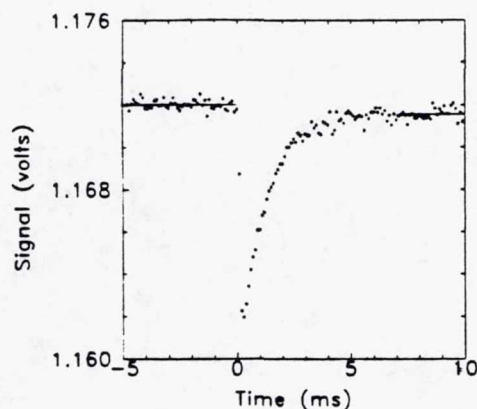


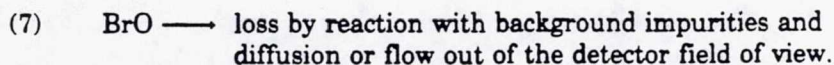
Figure 1. Typical absorbance temporal profile. Experimental conditions: $T = 298\text{ K}$; $P = 40\text{ torr N}_2$; $1.59 \times 10^{15}\text{ NO}_2\text{ per cm}^3$; $8.73 \times 10^{15}\text{ Br}_2\text{ per cm}^3$; electronic time constant = $16\ \mu\text{s}$; and 225 laser shots averaged. Note that the transmitted light level after absorbance has decayed away is lower than the pretrigger transmitted light level by 0.00048 volts , the equivalent of 0.041% absorption.

In our experiments, bromine atoms were generated via reactions (3) and (5), and also via 351 nm photolysis of Br_2 . In fact, under typical experimental conditions, bromine atoms were in about three-fold excess over BrO . Values for $k_6(P, T)$ over the pressure and temperature range of this study are reported in the literature [16], but the BrNO_2 absorption spectrum is unknown. The possible systematic error resulting from BrNO_2 absorption will be discussed below after the kinetic data are presented. It is worth pointing out that the Br -to- BrO concentration ratio could have been reduced somewhat by employing 308 nm as the photolysis wavelength, i.e., XeCl laser rather than XeF laser. However, the excimer laser available for this study had been used for many years exclusively at fluoride wavelengths and, as a result, could not be passivated for operation with chloride gas mixtures.

To ensure that we were detecting the BrO radical, the spectrum of the absorbing species was mapped out over the wavelength range $333\text{--}339\text{ nm}$. As expected [9], the $8\text{--}0$ and $7\text{--}0$ bands of BrO were clearly observed. The apparent BrO absorption cross section at the peak of the $7\text{--}0$ band was estimated based on the measured laser fluence, the measured NO_2 and Br_2 concentrations, and the known rate coefficients for reactions (3) and (4) [12,13]. An absorption cross section of $(1.4 \pm 0.4) \times 10^{-17}\text{ cm}^2$ was obtained (at 0.72 nm resolution). This agrees very well with the literature value of $(1.55 \pm 0.15) \times 10^{-17}\text{ cm}^2$ at 0.4 nm resolution [9].

Reaction mixtures employed to study reaction (1) contained $0.007\text{--}0.226\text{ torr NO}_2$, $0.116\text{--}0.322\text{ torr Br}_2$, and $16\text{--}800\text{ torr N}_2$ or CF_4 buffer gas. As mentioned above, a small amount of O_2 was also present in the reaction mixture because the NO_2 storage bulb contained air rather than N_2 as the diluent gas, typically, $[\text{O}_2]\text{ ca. } 10\text{ [NO}_2]$. Concentrations of BrO radicals generated via reactions (2) and (3) were in the range $(0.4\text{--}8.5) \times 10^{12}\text{ molecules per cm}^3$; these concentrations were sufficiently low that contributions from the BrO self reaction were negligible. In all experiments, BrO removal was

dominated by reaction (1), but also had small contributions from reactions (5) and (7).



Under the assumption that all processes contributing to BrO removal are first order or pseudo-first-order, the data can be analyzed using the following relationship:

$$(I) \quad \ln\{[\text{BrO}]_{t'}/[\text{BrO}]_t\} = \ln[\ln(S_{t'}/S_{t''})/\ln(S_t/S_{t''})] \\ = (k_1[\text{NO}_2] + k_5[\text{NO}] + k_7)t = k't$$

In eq. (I), t' represents a time shortly after the laser fires when BrO production is complete but little or no BrO decay has occurred, t'' represents a time after BrO removal has gone to completion but before NO₂, BrONO₂, and BrNO₂ diffuse or flow into or out of the detection volume, and S_t represents the signal level at time t . The bimolecular rate coefficients of interest, $k_1([M], T)$, are determined from the slopes of k'_{corr} vs. [NO₂] plots where k'_{corr} is the measured pseudo-first-order decay rate, k' , corrected for the contribution from flash-generated NO:

$$(II) \quad k'_{\text{corr}} = k' - k_5[\text{NO}]_f$$

In eq. (II), [NO]_f is the concentration of flash-generated NO; the method used to determine [NO]_f is described below. Observation of BrO temporal profiles that are exponential (i.e., obey eq. (I)) and a linear dependence of k' on [NO₂] strongly suggests that reactions (1), (5), and (7) are, indeed, the only processes significantly contributing to BrO removal.

As mentioned above, all measured BrO pseudo-first-order decay rates were corrected for contribution from reaction of BrO with flash-generated NO using eq. (II). Values for [NO]_f were determined from the peak BrO absorption signals using the following relationships:

$$(III) \quad [\text{BrO}]_{t'} = \ln(S_{t'}/S_{t''})/\sigma(\lambda, T)l$$

$$(IV) \quad [\text{O}]_0 = [\text{BrO}]_{t'}/f$$

$$(V) \quad f = k_3[\text{Br}_2]/(k_3[\text{Br}_2] + k_4[\text{NO}_2])$$

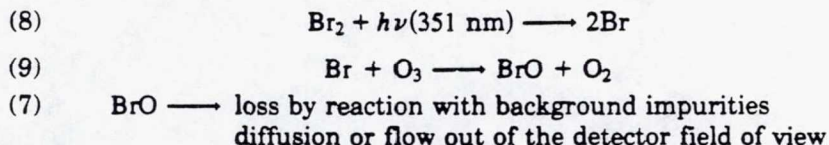
$$(VI) \quad [\text{NO}]_f = (2 - f)[\text{O}]_0$$

In the above equations $\sigma(\lambda, T)$ is the BrO absorption cross section (estimated at each temperature based on the results presented in ref. [9]), l is the absorption pathlength through the region photolyzed by the laser beam, and [O]₀ is the oxygen atom concentration immediately after the laser fired. At 298 K, the ratio $k_5[\text{NO}]_f/k'$ decreased from about 0.12 at $P = 16$ torr to about 0.02 at $P = 640$ torr.

In making the correction for the reaction of BrO with flash-generated NO, it was assumed that the NO concentration was time-independent over the course of the BrO decay. Computer simulations of representative experiments indicated that the ratio [NO]_f/[NO]_{t''} never exceeded 1.1 in any experiment. Hence, errors in evaluation of corrected pseudo-first-order BrO decay rates resulting from the approximation that [NO] was time-

independent never exceed 1%, and errors in evaluation of bimolecular rate coefficients, i.e., $k_1([M], T)$, resulting from this approximation never exceeded a few tenths of a percent.

In order to evaluate the magnitude of k_7 , experiments were conducted where BrO removal was monitored following 351 nm laser flash photolysis of $\text{Br}_2/\text{O}_3/\text{N}_2$ mixtures.



Experiments were carried out using the lowest detectable BrO concentrations to minimize contributions to BrO removal from the self reaction. At all pressures and temperatures relevant to this study, we found that $k_7 < 3 \text{ s}^{-1}$. Observed intercepts of k'_{corr} vs. $[\text{NO}_2]$ plots also suggest a very small value for k_7 ; averaging the intercepts observed from experiments at all temperatures and pressures gives $k_7 = 9 \pm 140 \text{ s}^{-1}$, where the uncertainty represents two standard deviations of the average.

As typified by the data in Figures 2-4, well-behaved pseudo-first-order kinetics were observed in all experiments, i.e., BrO decays were exponential and decay rates increased linearly as a function of $[\text{NO}_2]$. The data in Figure 4 demonstrate, as expected, that the bimolecular rate coefficient, $k_1([M], T)$, increases with increasing pressure. Measured bimolecular rate coefficients are summarized along with other pertinent information in Tables I and II. Uncertainties in $k_1([M], T)$ given in the tables are 2σ and represent precision only. Small systematic errors are possible in the

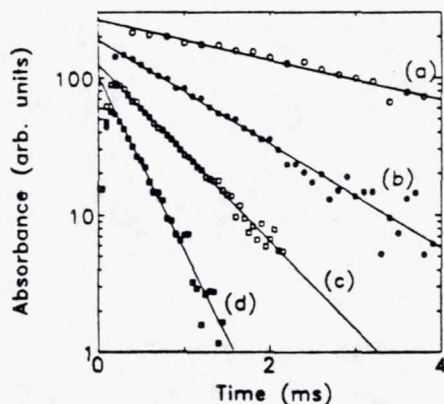


Figure 2. Typical plots of log (absorbance) vs. time obtained assuming that the post-decay transmitted light level is the correct baseline. Experimental conditions: $T = 298 \text{ K}$; $P = 40 \text{ torr N}_2$; $[\text{Br}_2]$ in units of $10^{15} \text{ molecules cm}^{-3}$ (a) 6.7, (b) 8.7, (c) 6.8, and (d) 8.4; $[\text{NO}_2]$ in units of $10^{15} \text{ molecules cm}^{-3}$ = (a) 0.62, (b) 1.59, (c) 2.70, and (d) 5.22; and number of laser shots averaged = (a) 128, (b) 225, (c) 128, and (d) 200. Solid lines are obtained from least-squares analyses and give the following pseudo-first-order decay rates in units of s^{-1} : (a) 306, (b) 878, (c) 1520, and (d) 2840. For the sake of clarity, temporal profiles are shifted on the absorbance scale; peak base e absorbances are (a) 0.0060, (b) 0.0082, (c) 0.020, and (d) 0.010. Note that trace (b) is obtained from the data shown in Figure 1.

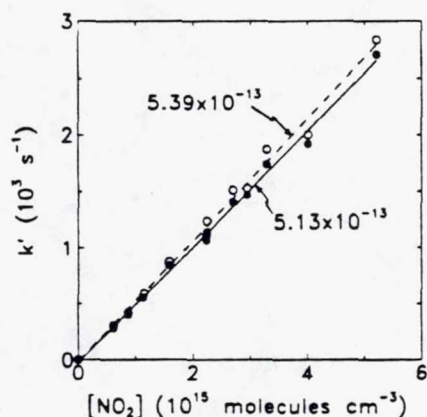


Figure 3. Typical plots of k' and k'_{corr} vs. $[\text{NO}_2]$. Experimental conditions: $T = 298 \text{ K}$, $P = 40 \text{ torr N}_2$. Open circles are uncorrected for BrO reaction with flash generated NO, while filled circles are corrected for this reaction. Lines are obtained from linear least-squares analyses. Their slopes give the uncorrected (dashed line) and corrected (solid line) rate coefficients shown in the figure (units are $\text{cm}^3 \text{ molecule}^{-1} \text{ s}^{-1}$).

NO₂ concentration determination, in the correction for reaction with flash-generated NO, and because of contributions to the absorbance signal from species other than BrO, NO₂, and BrONO₂ (the potential magnitude of errors resulting from BrNO₂ absorption is considered below). We estimate the accuracy of any measured rate coefficient, $k_1([M], T)$, to be $\pm 20\%$ (2σ).

Our kinetics studies of reaction (1) were restricted to $T \geq 248 \text{ K}$ because, for the range of NO₂ concentrations employed, dimerization becomes a significant problem at lower temperatures [17]. At the low temperature extreme of our study, a small fraction of NO₂ existed as the dimer ($[\text{NO}_2] \geq 6.7 [\text{N}_2\text{O}_4]$ in all experiments). Under experimental conditions where N₂O₄ levels were significant, i.e., low temperature (where the NO₂ \leftrightarrow N₂O₄ equilibrium is

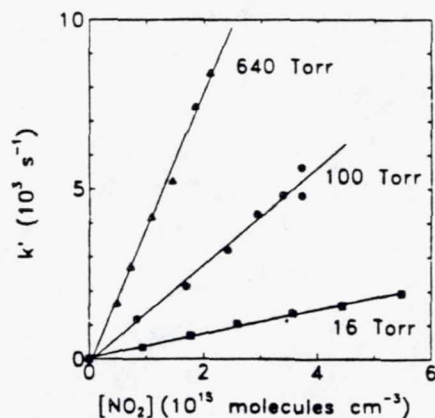


Figure 4. Plots of k'_{corr} vs. $[\text{NO}_2]$ for data obtained at $T = 267\text{--}268 \text{ K}$ in N_2 buffer gas. Solid lines are obtained from linear least-squares analyses and give the following bimolecular rate coefficients in units of $10^{-13} \text{ cm}^3 \text{ molecule}^{-1} \text{ s}^{-1}$: 3.54 ± 0.22 at 16 torr; 14.2 ± 1.5 at 100 torr; and 40.1 ± 2.6 at 640 torr (errors are 2σ , precision only).

TABLE II. Summary of kinetic data for the reaction $\text{BrO} + \text{NO}_2 + \text{CF}_4 \rightarrow \text{products}$ at $T = 298 \text{ K}$.

Concentrations ^a				no. of expts ^b	Range of k' ^a	k_1 ^{a,c}	
CF_4	Br_2	NO_2	$[\text{NO}_2]/[\text{O}]_0$			Uncorrected	Corrected ^d
518	4.5	1.10-3.35	630-910	6	419-1200	3.52 ± 0.44	3.24 ± 0.38
1300	4.9	1.01-4.97	880-1000	6	634-3590	6.91 ± 0.70	6.64 ± 0.69
3240	8.8	1.30-5.48	330-880	6	1580-6890	12.2 ± 0.78	11.9 ± 0.67
9720	3.1	1.03-3.23	590-600	5	2560-7840	24.6 ± 1.6	24.1 ± 1.6
20700	3.8	1.00-4.02	440-460	5	3660-15,900	40.1 ± 2.6	39.4 ± 2.5

^a Units are: concentration, 10^{15} molecules per cm^3 ; k' , s^{-1} ; k_1 , 10^{-13} cm^3 molecule $^{-1}$ s^{-1}

^b Experiment = measurement of one BrO temporal profile.

^c Errors are 2σ and represent precision only.

^d Corrected for contributions from the BrO + NO reaction.

shifted toward N₂O₄) and low pressure (where higher concentrations of NO₂ are employed due to the slower BrO + NO₂ rate coefficient), a potential interference could result from the reaction



A plot of k' vs. [NO₂] for our data at $T = 248 \text{ K}$, $P = 16 \text{ torr}$ is shown in Figure 5. A linear dependence of k' on [NO₂] is observed; the slope gives an apparent BrO + NO₂ rate coefficient of $4.83 \times 10^{-13} \text{ cm}^3 \text{ molecule}^{-1} \text{ s}^{-1}$ and a reasonable intercept of $34 \pm 36 \text{ s}^{-1}$ (uncertainty is 2σ , precision only). If we assume that $k_{10} = 1.0 \times 10^{-12} \text{ cm}^3 \text{ molecule}^{-1} \text{ s}^{-1}$, then a simulated k' vs. [NO₂] plot with a slope of $4.83 \times 10^{-13} \text{ cm}^3 \text{ molecule}^{-1} \text{ s}^{-1}$ can be obtained by assuming a value of $3.01 \times 10^{-13} \text{ cm}^3 \text{ molecule}^{-1} \text{ s}^{-1}$ for k_1 (248 K, 16 torr N₂). However, the simulated k' vs. [NO₂] plot differs from the experimental plot in two important ways (see Fig. 5). First, the simulated plot is not as linear as the experimental plot, i.e., it displays a small but distinct upward curvature. Secondly, the intercept of the simulated plot is distinctly negative, i.e., $-184 \pm 96 \text{ s}^{-1}$ (uncertainty is 2σ , precision only). The observed positive intercept of the k' vs. [NO₂] plot for data obtained at the lowest temperature and pressure of our study strongly suggests that reaction (10) did not contribute significantly to BrO removal over the range of experimental conditions employed. Therefore, analysis of all low temperature data employed the good approximation that $k_{10}[\text{N}_2\text{O}_4] \ll k_1[\text{NO}_2]$.

As mentioned above, one potential source of systematic error in our data analysis procedure results from the fact that a species other than BrO, NO₂, and BrONO₂ appears to absorb probe radiation at 338.3 nm. The probable absorbing species is BrNO₂, produced via reaction (6). The kinetics of reaction (6) as a function of temperature and pressure are well characterized [16]. The bimolecular rate coefficients k_1 and k_6 are similar in magnitude but

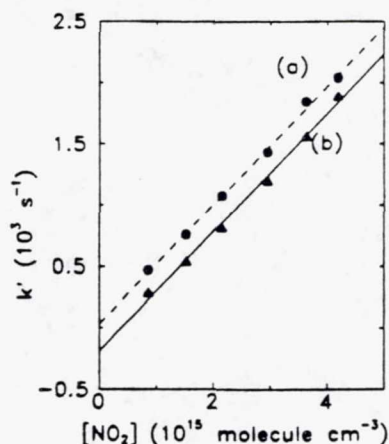
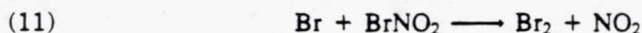


Figure 5. Plots of k' vs. [NO₂] for (a) experimental data at $T = 248 \text{ K}$, $P = 16 \text{ torr}$ and (b) a simulation with k_1 assumed equal to $3.01 \times 10^{-13} \text{ cm}^3 \text{ molecule}^{-1} \text{ s}^{-1}$ and k_{10} assumed equal to $1.0 \times 10^{-12} \text{ cm}^3 \text{ molecule}^{-1} \text{ s}^{-1}$. Note the significant nonlinearity in the simulated k' vs. [NO₂] data. Lines are obtained from linear least-squares analyses and give equal slopes ($4.83 \times 10^{-13} \text{ cm}^3 \text{ molecule}^{-1} \text{ s}^{-1}$) but significantly different intercepts.

have somewhat different temperature and pressure dependences. Over the range of temperatures and pressures employed in this study, the ratio k_1/k_6 varies from 1.4 in the low P , low T extreme (16 torr, 248 K) to 0.4 in the high P , high T extreme (800 torr, 346 K). As discussed above, the kinetic data reported in Tables I and II were obtained based on an analysis which assumed a time-independent baseline equal to S_{∞} , the postdecay signal level. The assumption that all absorbance not due to BrO, NO₂, or BrONO₂ is attributable to BrNO₂ leads to a time-dependent baseline which, since the time constant for baseline change is different from the time constant for BrO attenuation, should be accounted for in the data analysis [15]. To address this problem, we have reanalyzed the 346 K, 640 torr, and 248 K, 16 torr data sets using a time-dependent baseline calculated from our kinetic data for reaction (6) [16] under the assumptions that (a) all absorbance at $t = t''$ not attributable to BrO, NO₂, or BrONO₂, is due to BrNO₂, and (b) removal of BrNO₂ via reaction (11) is negligible on the time scale of interest.



The results of a typical reanalysis are summarized in Figures 6 and 7. Individual pseudo-first-order decay rates computed using the time-dependent baseline differ from those computed using the time-independent baseline by 2–6% with the largest differences coming at the lowest NO₂ concentrations. Bimolecular rate coefficients obtained using the two methods of analysis differ by less than 2% in the high pressure, high temperature case (the more exact analysis gives a slightly higher rate coefficient), and by less than 5% in the low pressure, low temperature case (the more exact analysis gives a slightly lower rate coefficient). Because the errors associated with neglecting the time-dependent baseline are small and identification of the fourth absorbing species as BrNO₂ is somewhat tenuous, we have chosen to report rate coefficients obtained using the less exact time-independent baseline analysis. The above-mentioned accuracy estimate of $\pm 20\%$ for individual values of $k_1([M], T)$ includes possible systematic errors due to the time-independent baseline assumption. It is worth noting that a small systematic error in the shape of reported fall off curves probably results from the time-independent baseline assumption, because high pressure rate coefficients are expected to be slightly underestimated while low pressure rate coefficients are expected to be slightly overestimated.

Our results demonstrate that reaction (1) is in the "falloff" regime between third- and second-order kinetics over the temperature and pressure ranges investigated. Troe and co-workers [18–21] have shown that bimolecular rate coefficient vs. pressure curves (i.e., falloff curves) for association reactions can be approximated by the three-parameter equation

$$(VII) \quad k_i([M], T) = k_{i,\infty}(T) F_{LH} F([M], T)$$

where F_{LH} is the Lindemann-Hinshelwood factor.

$$(VIII) \quad F_{LH} = X/(1 + X)$$

$$(IX) \quad X = k_{i,0}([M], T)[M]/k_{i,\infty}(T)$$

In the above equations, $k_{i,0}([M], T)$ is the rate coefficient for reaction (i) in the low-pressure-third-order limit, $k_{i,\infty}(T)$ is the rate coefficient for reaction

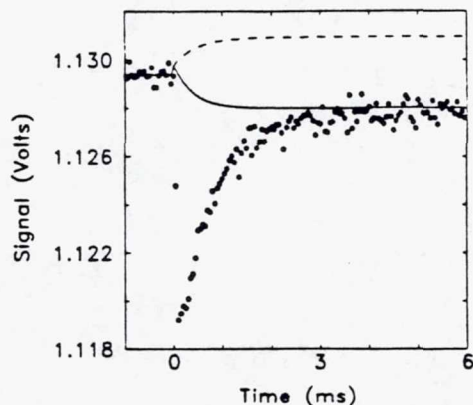


Figure 6. Solid circles are experimental transmitted 338.3 nm probe intensity vs. time data for an experiment at $T = 346$ K, $P = 640$ torr N₂ with $[\text{NO}_2] = 7.75 \times 10^{14}$ molecules cm^{-3} , and $[\text{Br}_2] = 6.7 \times 10^{15}$ molecules cm^{-3} . The dashed line is the expected "baseline" transmitted probe intensity assuming that BrNO₂ is transparent at 338.3 nm. The solid line is calculated assuming that the difference between the postdecay experimental signal level and the postdecay dashed line level can be attributed to absorption by BrNO₂; the BrNO₂ absorption cross section required to account for the difference is 1.14×10^{-18} cm^2 .

(i) in the high-pressure-second-order limit, and $F([M], T)$ is the parameter which characterizes the broadening of the falloff curve due to the energy dependence of the rate coefficient for decomposition of the energized adduct. $F([M], T)$ can be calculated from the spectroscopic and thermodynamic properties of the adduct.

For parameterization of the temperature and pressure dependences of atmospheric association reactions, the following approximate form for $F([M], T)$

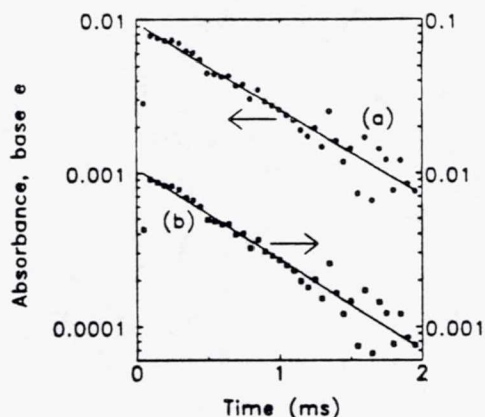


Figure 7. Plots of $\log(\text{absorbance})$ vs. time for the data shown in Figure 6. In trace (a), the baseline is assumed to be time-independent and equal to the postdecay value of the solid line in Figure 6. In trace (b) the baseline (B) is assumed to be time-dependent with $B(t)$ given by the solid line in Figure 6. Solid lines are obtained from least-squares analyses and give the following pseudo-first-order decay rates in units of s^{-1} : (a) 1290 and (b) 1360.

is typically employed [13,22]:

$$(X) \quad F([M], T) = F_c(M, T) [1 + (\log_{10} X)^2]^{-1}$$

In eq. (X), $F_c(M, T)$ is the broadening parameter at the center of the falloff curve, i.e., when $k_{i,0}[M] = k_{i,\infty}$. The NASA panel for data evaluation assumes $F_c(N_2, T) = 0.6$ for all reactions at all temperatures [13]. On the other hand, the IUPAC subcommittee on gas kinetic data evaluation for atmospheric chemistry employs F_c values which are both reaction and temperature dependent. For reaction (1) the IUPAC panel recommends $F_c(N_2, T) = \exp(-T/327)$ [22]; the recommended value at 298 K, $F_c = 0.402$, is based on the detailed analysis of Sander et al [4]. We have fit our data to eqs. (VII) and (X) using both $F_c(N_2, T) = 0.6$ and $F_c(N_2, T) = \exp(-T/327)$. Corresponding values for $F_c(CF_4, T)$ were computed from the relationship [18]

$$(XI) \quad \frac{F_c(CF_4, 298 K)}{F_c(N_2, 298 K)} = \left[\frac{k_{i,0}(CF_4, 298 K) Z_{LJ}(N_2, 298 K)}{k_{i,0}(N_2, 298 K) Z_{LJ}(CF_4, 298 K)} \right]^{0.14}$$

In eq. (XI), $Z_{LJ}(M, 298 K)$ is the Lennard-Jones collision frequency for $BrONO_2 - M$ encounters; it is calculated using a relationship and Lennard-Jones parameters given elsewhere [23].

Experimental data along with best fit (to our data only) falloff curves for $M = N_2$ at 298 K are shown in Figure 8 while experimental data along with best fit (to our data only) falloff curves for $M = N_2$ at 268 K and 346 K are shown in Figure 9. Rate coefficients reported in the two previous studies of $BrO + NO_2$ kinetics [4,5] are also plotted in Figures 8 and 9. The fits for the two different choices of F_c are virtually indistinguishable over the range of pressures where our data were obtained although, as expected, values for $k_{1,\infty}(T)$ obtained using the two different F_c parameterizations differ considerably; the $k_{1,\infty}(T)$ values obtained using $F_c = \exp(-T/327)$ are

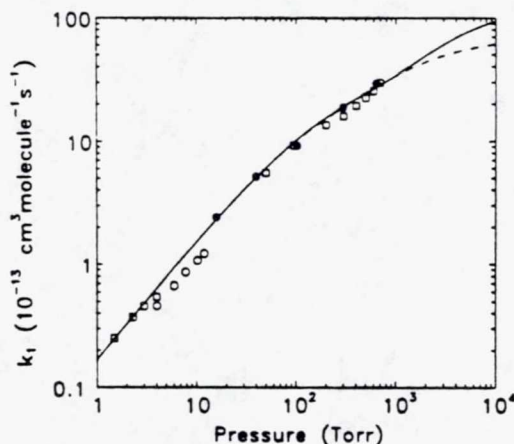


Figure 8. Falloff curve for the reaction $BrO + NO_2 + N_2 \rightarrow$ products at 298 K. Closed circles are rate coefficients reported in this article; open squares are rate coefficients reported by Sander et al. [4]; open circles are rate coefficients reported by Danis et al. [5]. Solid line is the best fit of our data only to eqs. VII and X with $F_c = \exp(-T/327) = 0.402$. Dashed line is the best fit of our data only to eqs. VII and X with $F_c = 0.6$. Best fit values for $k_{1,0}$ and $k_{1,\infty}$ are given in Table III.

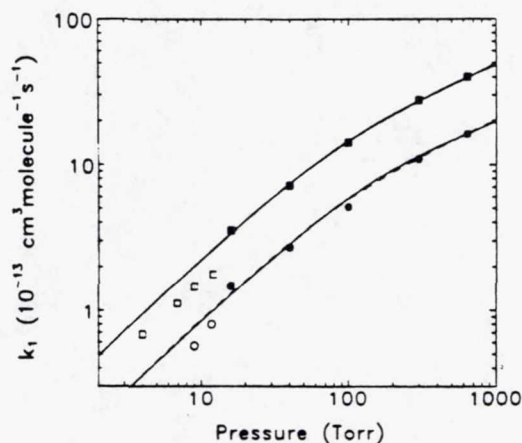


Figure 9. Falloff curves for the reaction $\text{BrO} + \text{NO}_2 + \text{N}_2 \rightarrow \text{products}$ at 268 K and 346 K. Closed squares and circles are rate coefficients reported in this article at 268 K and 346 K, respectively; open squares and circles are rate coefficients reported by Danis et al. [5] at 263 K and 343 K, respectively. Solid lines are the best fits of our data only to eqs. VII and X with $F_c = \exp(-T/327)$. Dashed lines are the best fits of our data only to eqs. VII and X with $F_c = 0.6$. Best fit values for $k_{1,0}$ and $k_{1,\infty}$ are given in Table III.

undoubtedly closer to the real high pressure limit rate coefficients because (a) F_c is expected to be temperature dependent [18–21] and (b) the 298 K value $\exp(-298/327) = 0.402$ is supported by the experimental and theoretical results of Sander et al. [4]. Best fit falloff parameters are summarized in Table III.

Examination of Figure 8 shows that our 298 K results agree very well with the extensive 298 K study of Sander et al. [4], who used two different experimental techniques (one of which was very similar to ours) to measure $k_1([\text{N}_2], 298 \text{ K})$ over the pressure range 1–700 torr. On the other hand, as shown in Figures 7 and 8, the low pressure rate coefficients reported by Danis et al. [5] in O_2 buffer gas are lower than our (extrapolated) low pressure rate coefficients by about 25%. It has now been established that the lower rate coefficients reported by Danis et al. can be attributed to heterogeneous loss of NO_2 in their slow flow system [24]. Hence, it appears that values of $k_1(P, T)$ for use in stratospheric models should be based on our results and the 298 K results of Sander et al. [4]. This approach leads

TABLE III. Summary of "best fit" falloff parameters for reaction (1).^a

T	M	$F_c = 0.6^b$		$F_c = \exp(-T/327)^b$	
		$k_{1,0}$	$k_{1,\infty}$	$k_{1,0}$	$k_{1,\infty}$
252 ± 4	N ₂	9.9	10.9	10.1	17.4
268	N ₂	7.3	10.5	7.6	18.5
298	N ₂	5.5	7.6	5.7	15.6
	CF ₄ ^b	7.2	9.0	7.6	18.2
346 ± 1	N ₂	3.6	4.7	3.7	12.7

^a Units are: T, K; $k_{1,0}$, $10^{-31} \text{ cm}^6 \text{ molecule}^{-2} \text{ s}^{-1}$; $k_{1,\infty}$, $10^{-12} \text{ cm}^3 \text{ molecule}^{-1} \text{ s}^{-1}$.

^b These F_c values are for N₂; $F_c(\text{CF}_4) = 1.056 F_c(\text{N}_2)$.

to the following two sets of recommended falloff parameters ($k_{1,0}$ values are for N_2 buffer gas):

I. $F_c = 0.6$

$$k_{1,0} = 5.2 \times 10^{-31}(T/300)^{-3.2} \text{ cm}^6 \text{ molecule}^{-2} \text{ s}^{-1}$$

$$k_{1,\infty} = 6.9 \times 10^{-12}(T/300)^{-2.9} \text{ cm}^3 \text{ molecule}^{-1} \text{ s}^{-1}$$

II. $F_c = \exp(-T/327)$

$$k_{1,0} = 5.4 \times 10^{-31}(T/300)^{-3.2} \text{ cm}^6 \text{ molecule}^{-2} \text{ s}^{-1}$$

$$k_{1,\infty} = 1.4 \times 10^{-11}(T/300)^{-1.2} \text{ cm}^3 \text{ molecule}^{-1} \text{ s}^{-1}$$

Either of the above sets of falloff parameters can be employed to accurately compute $k_1(P, T)$ over the range of temperatures and pressures relevant to the atmosphere. However, it should be kept in mind that the values for $k_{1,0}$ and $k_{1,\infty}$ given above are parameters which only approximate the actual low- and high-pressure-limit rate coefficients. Because data are available near the low pressure limit, and because derived values for $k_{1,0}$ are only weakly dependent on the choice of F_c , we expect that the reported $k_{1,0}$ values are within $\pm 20\%$ of the actual low pressure limit rate coefficient. On the other hand, because data are not available near the high pressure limit, and because derived values for $k_{1,\infty}$ are strongly dependent on the choice of F_c , the uncertainty in the actual high pressure limit rate coefficient is rather high, i.e., at least a factor of two. If accurate values for $F([M], T)$ could be calculated from available spectroscopic and thermodynamic information about $BrONO_2$, then a reasonably accurate value for $k_{1,\infty}$ could be obtained by extrapolation of available kinetic data. However, for reasons discussed below, available structural and thermodynamic information for $XONO_2$ species must be viewed with skepticism. Measurements of $k_1(P, T)$ up to very high pressures, i.e., tens of atmospheres, would provide the data needed for accurate evaluation of $k_{1,\infty}$ (and F_c).

One interesting aspect of reaction (1) is the magnitude of the low-pressure-limit termolecular rate coefficient. Theoretical values of $k_{1,0}$ have been calculated using RRKM theory [5] and the factorized expression of Troe [5,23]; theoretical values for $k_{1,0}$ are slightly lower than experimental low pressure rate coefficients; for typical N_2 collisional efficiency factors of 0.1 to 0.3, this means that theoretical $k_{1,0}$ values are about a factor of five too low to be consistent with experiment. As pointed out by DeMore, et al. [25], "Even though isomer formation seems to have been ruled out for the $ClO + NO_2$ reaction (i.e., the isomer stability is too low to make a significant contribution to the measured rate constant), this does not eliminate the possibility that $BrO + NO_2$ leads to more than one stable compound. In fact, if the measured low pressure limit rate constant for $BrO + NO_2$ is accepted, it can only be theoretically reconciled with a single isomer, $BrONO_2$, which would have a 6-7 kcal mol⁻¹ stronger bond than $ClONO_2$! This would fix the heat of formation of $BrONO_2$ to be the same as $ClONO_2$, an unlikely possibility." Interestingly, a similar situation exists when comparing the measured low-pressure-limit rate coefficient for the $IO + NO_2$ reaction [7], with those for $ClO + NO_2$ and $BrO + NO_2$. Clearly, the thermochemistry of $XONO_2$ ($X = Br, I$) requires further investigation, as does the possible formation of isomers such as $OXNO_2$, $XOONO$, or $OXONO$. Regarding $XONO_2$ thermochemistry, we have recently become aware of a theoretical study which suggests a higher than expected value for the

BrONO₂ bond dissociation energy [24]; the higher bond dissociation energy, if correct, would lead to good consistency between calculated $k_{1,0}(T)$ values and experimental low pressure rate coefficients [24].

Acknowledgment

This research was supported through grant NAGW-1001 from the National Aeronautics and Space Administration. We thank Dr. R. Lesclaux for helpful discussions.

Bibliography

- [1] M. J. Prather, T. Sasaki, A. M. Ibrahim, F. Stordal, and G. Visconti, in *Scientific Assessment of Ozone Depletion: 1991*, D. L. Albritton, R. T. Watson, S. Solomon, R. F. Hampson, and F. Ormond, Eds., WMO Global Research and Monitoring Project-Report No. 25, 1992, Chap. 8.
- [2] G. Poulet, M. Pirre, F. Maguin, R. Ramoroson, and G. LeBras, *Geophys. Res. Lett.*, **19**, 2305 (1992).
- [3] M. Pirre, M. J. Marceau, G. LeBras, F. Maguin, G. Poulet, and R. Ramoroson, *Proc. Quadrennial Ozone Symp.*, Charlottesville, Virginia, 1992, in press.
- [4] S. P. Sander, G. W. Ray, and R. T. Watson, *J. Phys. Chem.*, **85**, 199 (1981).
- [5] F. Danis, F. Caralp, J. Masanet, and R. Lesclaux, *Chem. Phys. Lett.*, **167**, 450 (1990).
- [6] P. H. Wine, J. R. Wells, and J. M. Nicovich, *J. Phys. Chem.*, **92**, 2223 (1988).
- [7] E. P. Daykin and P. H. Wine, *J. Phys. Chem.*, **94**, 4528 (1990).
- [8] J. U. White, *J. Opt. Soc. Am.*, **32**, 285 (1942).
- [9] See for example, A. Wahner, A. R. Ravishankara, S. P. Sander, and R. R. Friedl, *Chem. Phys. Lett.*, **152**, 507 (1988).
- [10] W. Schneider, G. K. Moortgat, G. S. Tyndall, and J. P. Burrows, *J. Photochem. Photobiol. A:Chem.*, **40**, 1985 (1987).
- [11] J. G. Calvert and J. N. Pitts, Jr., *Photochemistry*, Wiley, New York, 1967.
- [12] J. M. Nicovich and P. H. Wine, *Int. J. Chem. Kinet.*, **22**, 379 (1990).
- [13] W. B. DeMore, M. J. Molina, S. P. Sander, D. M. Golden, R. F. Hampson, M. J. Kurylo, C. J. Howard, and A. R. Ravishankara, *Chemical Kinetics and Photochemical Data for Use in Stratospheric Modeling*, Evaluation No. 10, JPL Publication No. 92-20, 1992.
- [14] J. E. Spencer and F. S. Rowland, *J. Phys. Chem.*, **82**, 7 (1978).
- [15] S. P. Sander and R. T. Watson, *J. Phys. Chem.*, **84**, 1664 (1980).
- [16] K. D. Kreutter, J. M. Nicovich, and P. H. Wine, *J. Phys. Chem.*, **95**, 4020 (1991).
- [17] H. Blend, *J. Chem. Phys.*, **53**, 4497 (1970).
- [18] K. Luther and J. Troe, *Proc. Symp. (Int.) Combust.*, **17**, 535 (1978).
- [19] J. Troe, *J. Phys. Chem.*, **83**, 114 (1979).
- [20] J. Troe, *Ber. Bunsenges. Phys. Chem.*, **87**, 161 (1983).
- [21] R. G. Gilbert, K. Luther, and J. Troe, *Ber. Bunsenges. Phys. Chem.*, **87**, 169 (1983).
- [22] R. Atkinson, D. L. Baulch, R. A. Cox, R. F. Hampson, Jr., J. A. Kerr, and J. Troe, *Atmos. Environ.*, **26A**, 1187 (1992).
- [23] R. Patrick and D. M. Golden, *Int. J. Chem. Kinet.*, **15**, 1189 (1983).
- [24] R. Lesclaux, private communication.
- [25] W. B. DeMore, M. J. Molina, S. P. Sander, D. M. Golden, R. F. Hampson, M. J. Kurylo, C. J. Howard, and A. R. Ravishankara, *Chemical Kinetics and Photochemical Data for Use in Stratospheric Modeling*, Evaluation No. 8, JPL Publication 87-41, 1987.

Received December 2, 1992

Accepted February 1, 1993

NDB
 5-9 36
 57-25
 026125
 11P.
 073542
 5-10.1

Temperature-Dependent Kinetics Studies of the Reactions $\text{Br}(^2\text{P}_{3/2}) + \text{H}_2\text{S} \leftrightarrow \text{SH} + \text{HBr}$ and $\text{Br}(^2\text{P}_{3/2}) + \text{CH}_3\text{SH} \leftrightarrow \text{CH}_3\text{S} + \text{HBr}$. Heats of Formation of SH and CH_3S Radicals

J. M. Nicovich, K. D. Kreutter, C. A. van Dijk, and P. H. Wine*

Physical Sciences Laboratory, Georgia Tech Research Institute, Georgia Institute of Technology, Atlanta, Georgia 30332 (Received: August 5, 1991)

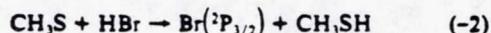
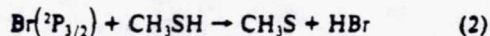
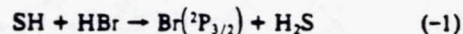
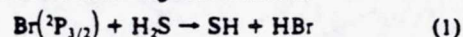
Time-resolved resonance fluorescence detection of $\text{Br}(^2\text{P}_{3/2})$ atom disappearance or appearance following 266-nm laser flash photolysis of $\text{CF}_3\text{Br}_2/\text{H}_2\text{S}/\text{H}_2/\text{N}_2$, $\text{CF}_3\text{Br}_2/\text{CH}_3\text{SH}/\text{H}_2/\text{N}_2$, $\text{Cl}_2\text{CO}/\text{H}_2\text{S}/\text{HBr}/\text{N}_2$, and $\text{CH}_3\text{SSCH}_3/\text{HBr}/\text{H}_2/\text{N}_2$ mixtures has been employed to study the kinetics of the reactions $\text{Br}(^2\text{P}_{3/2}) + \text{H}_2\text{S} \rightleftharpoons \text{SH} + \text{HBr}$ (1, -1) and $\text{Br}(^2\text{P}_{3/2}) + \text{CH}_3\text{SH} \rightleftharpoons \text{CH}_3\text{S} + \text{HBr}$ (2, -2) as a function of temperature over the range 273–431 K. Arrhenius expressions in units of $10^{-12} \text{ cm}^3 \text{ molecule}^{-1} \text{ s}^{-1}$ which describe the results are $k_1 = (14.2 \pm 3.4) \exp[(-2752 \pm 90)/T]$, $k_{-1} = (4.40 \pm 0.92) \exp[(-971 \pm 73)/T]$, $k_2 = (9.24 \pm 1.15) \exp[(-386 \pm 41)/T]$, and $k_{-2} = (1.46 \pm 0.21) \exp[(-399 \pm 41)/T]$; errors are 2σ and represent precision only. By examining $\text{Br}(^2\text{P}_{3/2})$ equilibration kinetics following 355-nm laser flash photolysis of $\text{Br}_2/\text{CH}_3\text{SH}/\text{H}_2/\text{N}_2$ mixtures, a 298 K rate coefficient of $(1.7 \pm 0.5) \times 10^{-10} \text{ cm}^3 \text{ molecule}^{-1} \text{ s}^{-1}$ has been obtained for the reaction $\text{CH}_3\text{S} + \text{Br}_2 \rightarrow \text{CH}_3\text{SBr} + \text{Br}$. To our knowledge, these are the first kinetic data reported for each of the reactions studied. Measured rate coefficients, along with known rate coefficients for similar radical + H_2S , CH_3SH , HBr , Br_2 reactions are considered in terms of possible correlations of reactivity with reaction thermochemistry and with IP - EA, the difference between the ionization potential of the electron donor and the electron affinity of the electron acceptor. Both thermochemical and charge-transfer effects appear to be important in controlling observed reactivities. Second and third law analyses of the equilibrium data for reactions 1 and 2 have been employed to obtain the following enthalpies of reaction in units of kcal mol^{-1} : for reaction 1, $\Delta H_{298} = 3.64 \pm 0.43$ and $\Delta H_0 = 3.26 \pm 0.45$; for reaction 2, $\Delta H_{298} = -0.14 \pm 0.28$ and $\Delta H_0 = -0.65 \pm 0.36$. Combining the above enthalpies of reaction with the well-known heats of formation of Br , HBr , H_2S , and CH_3SH gives the following heats of formation for the RS radicals in units of kcal mol^{-1} : $\Delta H_f^\circ(\text{SH}) = 34.07 \pm 0.72$, $\Delta H_f^\circ(\text{CH}_3\text{S}) = 34.18 \pm 0.68$, $\Delta H_f^\circ(\text{CH}_3\text{S}) = 31.44 \pm 0.54$, $\Delta H_f^\circ(\text{CH}_3\text{S}) = 29.78 \pm 0.44$; errors are 2σ and represent estimates of absolute accuracy. The SH heat of formation determined from our data agrees well with literature values but has reduced error limits compared to other available values. The CH_3S heat of formation determined from our data is near the low end of the range of previous estimates and is 3–4 kcal mol^{-1} lower than values derived from recent molecular beam photofragmentation studies.

Introduction

Accurate thermochemical information for free-radical intermediates is essential to analysis of reaction mechanisms in complex chemical systems. One experimental approach which can be employed to obtain thermochemical parameters for a radical R involves measurement of temperature-dependent rate coefficients for the pair of reactions $\text{RH} + \text{R}' \rightleftharpoons \text{R}'\text{H} + \text{R}$; the ideal reaction pair for such a study is one where the heats of formation and absolute entropies of R' , $\text{R}'\text{H}$, and RH are well characterized and

where kinetic data for the two reactions can be obtained over the same temperature range.

In this paper we report the results of temperature-dependent kinetics studies of the following four reactions:



* Author to whom correspondence should be addressed.

The kinetic results have been employed to derive the most precise (and hopefully the most accurate) values currently available for the heats of formation of SH and CH₃S, two radicals which are important intermediates in the oxidation of a number of atmospheric reduced sulfur compounds including H₂S, CH₃SH, CH₃SCH₃, and CH₃SSCH₃.^{1,2} To our knowledge there are no kinetics studies of any of the reactions 1, -1, 2, and -2 reported in the literature.

Experimental Technique

The experimental approach involved coupling reactant radical (i.e., Br, SH, CH₃S) production by laser flash photolysis of suitable precursors with time-resolved detection of ground state bromine atom disappearance or appearance by resonance fluorescence spectroscopy. A schematic diagram of the apparatus, as configured for bromine atom detection, can be found elsewhere.³ A description of the experimental methodology is given below.

A Pyrex-jacketed reaction cell with an internal volume of 150 cm³ was used in all experiments; a diagram showing the geometry of the reaction cell is published elsewhere.⁴ The cell was maintained at a constant temperature by circulating ethylene glycol ($T > 298$ K) or methanol ($T < 298$ K) from a thermostatically controlled bath through the outer jacket. A copper-constantan thermocouple with a stainless steel jacket was inserted into the reaction zone through a vacuum seal, thus allowing measurement of the gas temperature under the precise pressure and flow rate conditions of the experiment.

The reactant radicals Br, SH, and CH₃S were generated by 266-nm laser flash photolysis of CF₂Br₂, Cl₂CO/H₂S, and CH₃SSCH₃, respectively. In a few experiments Br atoms were generated by 355-nm laser flash photolysis of Br₂. Third (355 nm) or fourth (266 nm) harmonic radiation from a Quanta Ray Model DCR-2 Nd:YAG laser provided the photolytic radiation. The laser could deliver up to 3×10^{16} photons per pulse at 266 nm and up to 1×10^{17} photons per pulse at 355 nm; the maximum repetition rate was 10 Hz and the pulse width was approximately 6 ns.

A bromine resonance lamp, situated perpendicular to the photolysis laser, excited resonance fluorescence in the bromine atoms produced photolytically or as a reaction product. The resonance lamp consisted of an electrodeless microwave discharge through about 1 Torr of a flowing mixture containing a trace of Br₂ in helium. The flows of a 0.2% Br₂ in helium mixture and pure helium into the lamp were controlled by separate needle valves, thus allowing the total pressure and Br₂ concentration to be adjusted for optimum signal-to-noise ratio. Radiation was coupled out of the lamp through a magnesium fluoride window and into the reaction cell through a magnesium fluoride lens. Before entering the reaction cell, the lamp output passed through a flowing gas filter containing 50 Torr-cm of methane in nitrogen. The methane filter prevented radiation at wavelengths shorter than 140 nm (including impurity emissions from excited oxygen, hydrogen, nitrogen, and chlorine atoms) from entering the reaction cell, but transmitted the strong bromine lines in the 140–160-nm region.

Fluorescence was collected by a magnesium fluoride lens on an axis orthogonal to both the photolysis laser beam and resonance lamp beam and was imaged onto the photocathode of a solar blind photomultiplier with a CsI photocathode. The region between the reaction cell and the photomultiplier was purged with N₂ to prevent absorption of fluorescence photons by O₂, H₂O, and other trace gases in the laboratory air. Signals were processed using photon counting techniques in conjunction with multichannel scaling. A large number of laser shots were typically averaged to obtain a bromine atom temporal profile with signal-to-noise sufficient for quantitative kinetic analysis. It is worth noting that

TABLE I: Parameters Relevant to In Situ Monitoring of H₂S, CH₃SH, and HBr

species	λ , nm	light source ^a	λ isolation ^b	$10^{19} \sigma$, cm ²
H ₂ S	202.6	A	M	57.5 ^c
	228.8	B	BPF	4.58 ^c
CH ₃ SH	202.6	A	M	87.1 (ref 67)
	213.9	A	M	14.8 ^c
HBr	202.6	A	M	10.2 (ref 24)

^aA, zinc hollow cathode lamp; B, cadmium penray lamp. ^bM, 1/4-m monochromator; BPF, band-pass filter. ^cMeasured during the course of this investigation.

the resonance fluorescence detection scheme is sensitive to both ground-state (²P_{3/2}) and spin-orbit excited-state (²P_{1/2}) bromine atoms.

Tests were carried out to evaluate the sensitivity of the detection system toward O, H, Cl, CO, and Br using 266-nm laser flash photolysis of O₃/N₂, CH₃SH/N₂, Cl₂CO/N₂, and CF₂Br₂/H₂/N₂ mixtures as the respective sources for O, H, Cl + CO, and Br (the reason for adding H₂ to the CF₂Br₂/N₂ mixture is discussed below). Production of $\sim 1 \times 10^{12}$ O or H cm⁻³ resulted in no observable signal. Similarly, production of 1×10^{12} Cl cm⁻³ + 5×10^{11} CO cm⁻³ resulted in no observable signal. The detection sensitivity for Br atoms was sufficient to allow temporal profiles to be followed down to [Br] < 1×10^9 atoms cm⁻³ with a reasonable level of signal averaging.

The emission spectrum of the bromine lamp (transmitted through the methane filter) was measured using a scanning vacuum UV monochromator (resolution ~ 0.05 nm) and the same solar blind photomultiplier as was employed in the kinetics experiments. In addition to the ⁴P → ²P and ²P → ²P bromine transitions, major impurity emissions were the ²P → ²P, ²P → ²D, and ²D → ²P transitions of atomic nitrogen at 174 nm (strong), 149 nm (strong), and 141 nm (weak), respectively, and the ³P → ³P transitions of atomic carbon at 166 nm (weak). The above-mentioned sensitivity tests confirmed that N(²P), N(²D), and/or C(³P) were not produced in sufficient quantity in the reaction cell (by multiphoton photodissociation of N₂ or Cl₂CO) to be detected via fluorescence excited by impurity lamp emissions; if this were not the case, then fluorescence signal would have been observed following 266-nm laser flash photolysis of O₃/N₂, CH₃SH/N₂, and/or Cl₂CO/N₂ mixtures. The tests described above demonstrate quite conclusively that the detection system was specific to bromine atoms.

To avoid accumulation of photolysis or reaction products, all experiments were carried out under "slow flow" conditions. The linear flow rate through the reactor was in the range 1.5–4.5 cm s⁻¹ and the laser repetition rate was varied over the range 1–10 Hz (5 Hz typical). Hence, no volume element of the reaction mixture was subjected to more than a few laser shots. Reactants and radical photolytic precursors were flowed into the reaction cell from bulbs (12 L volume) containing dilute mixtures in nitrogen while hydrogen and additional nitrogen were flowed directly from their storage cylinders. Except where specified in later discussions, all gases were premixed before entering the reactor. The concentrations of each component in the reaction mixtures were determined from measurements of the appropriate mass flow rates and the total pressure. The excess reactant (i.e., H₂S, CH₃SH, or HBr) concentration was also determined in situ in the slow flow system by UV photometry. Monitoring wavelengths, light sources, and absorption cross sections relevant to the photometric measurements are summarized in Table I. Since it was normally the case that more than one species in the reaction mixtures absorbed at the monitoring wavelength, the excess reactant concentration was usually measured upstream from the photolyte addition point; dilution factors required to correct the measured concentration to the actual reactor concentration never exceeded 1.1. Some experiments were carried out with the absorption cell positioned downstream from the reactor. Although the determinations of the excess reactant concentration were less precise in this experimental configuration (due to the presence in the absorption cell of more than one absorbing species), ex-

- (1) Tyndall, G. S.; Ravishankara, A. R. *In: J. Chem. Kinet.* 1991, 23, 483.
- (2) Yin, F.; Grosjean, D.; Seinfeld, H. *J. Atmos. Chem.* 1990, 11, 309.
- (3) Nicovich, J. M.; Shackelford, C. J.; Wine, P. H. *J. Photochem. Photobiol., A: Chem.* 1990, 51, 141.
- (4) Wine, P. H.; Kreutter, N. M.; Ravishankara, A. R. *J. Phys. Chem.* 1979, 83, 3191.

perimental results were found to be independent of whether the absorption cell was positioned upstream or downstream relative to the reactor.

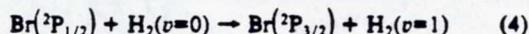
The gases used in this study had the following stated minimum purities: N₂, 99.999%; H₂, 99.999%; Cl₂, 99.99%;⁵ HBr, 99.8%;⁵ H₂S, 99.5%;⁵ CH₃SH, 99.5%.⁵ Nitrogen and hydrogen were used as supplied while Cl₂, HBr, H₂S, and CH₃SH were degassed repeatedly at 77 K before being used to prepare mixtures with N₂. It is worth noting that HBr gas samples taken directly from the storage cylinder contained significant (25–50%) levels of a noncondensable (at 77 K) impurity which was determined by weighing to be H₂. The stated minimum purity of the CF₂Br₂ liquid sample was 99%. It was transferred under nitrogen into a vial fitted with a high vacuum stopcock and subjected to repeated freeze (77 K)–pump–thaw cycles before being used to prepare gaseous mixtures with N₂.

Results and Discussion

In studies of reactions 1 and 2 bromine atoms were generated by 266-nm laser flash photolysis of CF₂Br₂ ([CF₂Br₂] ranged from 0.2 × 10¹⁴ to 11 × 10¹⁴ molecules cm⁻³):

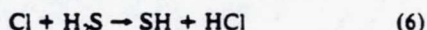


The CF₂Br₂ absorption cross section at 266 nm is approximately 8 × 10⁻²⁰ cm² molecule⁻¹ while the quantum yield for Br production from CF₂Br₂ photolysis increases from unity at λ ≥ 248 nm to around 2 at λ = 193 nm.⁹ Presumably, at λ ≥ 248 nm CF₂Br₂ photodissociates as indicated in reaction 3 with unit yield. To ensure rapid relaxation of any photolytically generated Br(²P_{1/2}), about 1 Torr of H₂ was added to the reaction mixture. The reaction



is known to be fast with $k_4 = 6 \times 10^{-12} \text{ cm}^3 \text{ molecule}^{-1} \text{ s}^{-1}$.¹⁰

In studies of reaction -1, SH radicals were generated as follows:



The Cl₂CO concentration was typically 1 × 10¹⁵ molecules cm⁻³ while the H₂S concentration was typically 1 × 10¹⁶ molecules cm⁻³. We have recently shown that $k_6 = 3.6 \times 10^{-11} \exp(210/T) \text{ cm}^3 \text{ molecule}^{-1} \text{ s}^{-1}$ ¹¹ and $k_7 = 2.25 \times 10^{-11} \exp(-400/T) \text{ cm}^3 \text{ molecule}^{-1} \text{ s}^{-1}$.¹²



Based on the above rate coefficients, experimental conditions were maintained where >90% of the photolytically generated Cl reacted with H₂S and <10% reacted with HBr. The Cl₂CO absorption cross section at 266 nm is approximately 1 × 10⁻¹⁹ cm²,^{13,14} while the quantum yield for Cl₂CO photodissociation at 253.7 nm has been shown to be unity.¹⁵ Reaction 5 actually occurs in a two-step process involving a ClCO intermediate. However, even in the unlikely event that ClCO is produced without internal excitation, the ClCO lifetime toward decomposition to Cl + CO is short compared to the experimental time scale (hundreds of microseconds) for SH removal.¹⁶ Reaction -1 was studied employing reaction mixtures containing no H₂ in order to avoid potential complications from the reaction Cl + H₂ → HCl + H.

(5) Stated purity of liquid phase in cylinder.

(6) Molina, L. T.; Molina, M. J.; Rowland, F. S. *J. Phys. Chem.* 1982, 86, 2672.

(7) Gillotay, D.; Simon, P. C. *J. Atmos. Chem.* 1989, 8, 41.

(8) Burkholder, J. B.; Wilson, R. R.; Gierczak, T.; Talukdar, R.; McKeen, S. A.; Orlando, J. J.; Vaghjiani, G. L.; Ravishankara, A. R. *J. Geophys. Res.* 1991, 96, 5025.

(9) Talukdar, R.; Vaghjiani, G. L.; Ravishankara, A. R., to be published.

(10) Nesbitt, D. J.; Leone, S. R. *J. Chem. Phys.* 1980, 73, 6182.

(11) Nicovich, J. M.; van Dijk, C. A.; Kreutter, K. D.; Wine, P. H., to be published.

(12) Nicovich, J. M.; Wine, P. H. *Int. J. Chem. Kinet.* 1990, 22, 379.

(13) Heicklen, J. *J. Am. Chem. Soc.* 1965, 87, 445.

(14) Moule, D. C.; Foo, P. D. *J. Chem. Phys.* 1971, 55, 1262.

(15) Okabe, H. *J. Chem. Phys.* 1977, 66, 2058.

(16) Nicovich, J. M.; Kreutter, K. D.; Wine, P. H. *J. Chem. Phys.* 1990, 92, 3539.

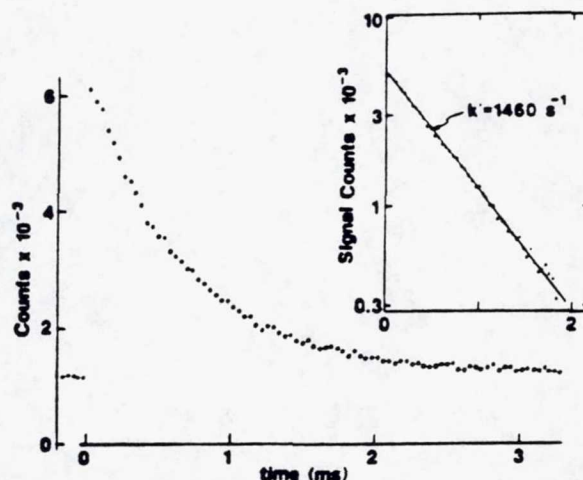
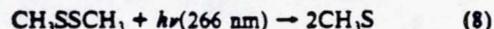


Figure 1. Typical Br(²P_{3/2}) atom temporal profile observed in the studies of the Br(²P_{3/2}) + RSH reactions (R = H, CH₃). Reaction: Br(²P_{3/2}) + CH₃SH. Experimental conditions: T = 332 K, P = 50 Torr, [CF₂Br₂] = 8.1 × 10¹⁴ molecules cm⁻³, [CH₃SH] = 5.04 × 10¹⁴ molecules cm⁻³, [Br(²P_{3/2})]₀ ~ 8 × 10¹⁰ atoms cm⁻³, number of laser shots averaged = 2000. The inset shows the same data plotted as ln S, versus time. The solid line in the inset is obtained from a least-squares analysis and gives the pseudo-first-order Br(²P_{3/2}) decay rate shown in the figure.

In studies of reaction -2, CH₃S radicals were generated by 266-nm laser flash photolysis of dimethyl disulfide:



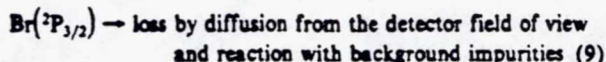
Concentrations of CH₃SSCH₃ ranged from 2 × 10¹³ to 32 × 10¹³ molecules cm⁻³. The CH₃SSCH₃ absorption cross section at 266 nm is approximately 1 × 10⁻¹⁸ cm²,¹⁷ and the quantum yield for producing CH₃S is thought to be 2.¹⁸ Reaction mixtures employed to study reaction -2 did contain 1 Torr of added H₂.

All experiments were carried out under pseudo-first-order conditions with the stable reactant in large excess (factors of 10²–10⁵) over the free-radical reactant. Concentrations of photolytically generated radicals were typically in the range (5–15) × 10¹⁰ cm⁻³, although this experimental parameter was varied over a wide range (factor of 50). For all four reactions studied, observed kinetics were found to be independent of the photolytic precursor concentration(s) and the concentration of photolytically generated radicals. Observed kinetics were also found to be independent of the linear flow rate of the reaction mixture through the reactor and the photolysis laser repetition rate.

In the absence of side reactions which regenerate or deplete the Br(²P_{3/2}) atom concentration, the observed Br(²P_{3/2}) temporal profile following the laser flash in studies of reactions 1 and 2 would be described by the relationship

$$\ln(S_0/S_t) = \ln\left\{\frac{[\text{Br}(\text{}^2\text{P}_{3/2})]_0}{[\text{Br}(\text{}^2\text{P}_{3/2})]_t}\right\} = (k_i[\text{R,SH}] + k_9)t = k't \quad (i = 1 \text{ or } 2, \text{R}_1 = \text{H}, \text{R}_2 = \text{CH}_3) \quad (I)$$

In the above relationship, S₀ and S_t are the signal levels immediately after the laser fires and at some later time t, [Br(²P_{3/2})]₀ and [Br(²P_{3/2})]_t are the bromine atom concentrations corresponding to S₀ and S_t, and k₉ is the first-order rate coefficient for the process



The bimolecular rate coefficients of interest, k_i(P,T), are determined from the slopes of k' versus [R,SH] plots. Observation of Br(²P_{3/2}) temporal profiles which are exponential (i.e., obey eq I), linear dependencies of k' on [R,SH], and invariance of observed

(17) Calvert, J. G.; Pitts, J. N., Jr. *Photochemistry*; Wiley: New York, 1966.

(18) Balla, R. J.; Heicklen, J. *Can. J. Chem.* 1984, 62, 162.

TABLE II: Summary of Kinetic Data for the Reaction Br(²P_{3/2}) + H₂S → SH + HBr^a

T	P	no. of expts ^b	[H ₂ S] _{max}	range of k'	k ₁ ± 2σ
319	100	6	456	10-138	2.65 ± 0.10
334	50	7	198	22-99	3.77 ± 0.29
341	100	6	550	12-229	4.44 ± 0.15
348	250	5	199	15-120	5.33 ± 0.42
351	50	7	197	23-135	5.23 ± 0.62
361	100	7	511	13-378	7.09 ± 0.18
362	50	10	137	28-121	6.95 ± 0.73
376	50	7	152	28-168	9.08 ± 0.48
388	50	11	149	30-212	12.0 ± 0.7
403	50	5	142	31-263	16.0 ± 1.0
417	50	5	157	34-333	19.0 ± 0.9
420	250	7	151	19-297	18.7 ± 0.8
423	100	8	492	13-1065	22.3 ± 0.7
431	50	5	122	40-350	25.1 ± 0.8

^aUnits are T (K); P (Torr); [H₂S] (10¹⁴ molecules cm⁻³); k' (s⁻¹); k₁ (10⁻¹⁵ cm³ molecule⁻¹ s⁻¹). ^bExpt = measurement of a single pseudo-first order Br(²P_{3/2}) decay rate. ^cErrors represent precision only.

TABLE III: Summary of Kinetic Data for the Reaction Br(²P_{3/2}) + CH₃SH → CH₂S + HBr^a

T	P	no. of expts ^b	[CH ₃ SH] _{max}	range of k'	k ₂ ± 2σ
273	50	10	23.8	31-5310	2230 ± 50
297	200	5	14.9	42-4000	2640 ± 70
298	50	10	21.8	27-5390	2480 ± 90
332	50	7	9.78	27-2810	2830 ± 90
383	50	6	12.0	34-4120	3350 ± 80
409	50	10	9.86	40-3570	3590 ± 60
431	50	6	12.8	37-5060	3820 ± 50

^aUnits are T (K); P (Torr); [CH₃SH] (10¹⁴ molecules cm⁻³); k' (s⁻¹); k₂ (10⁻¹⁵ cm³ molecule⁻¹ s⁻¹). ^bExpt = measurement of a single pseudo-first order Br(²P_{3/2}) decay rate. ^cErrors represent precision only.

kinetics to variations in laser photon fluence and photolyte concentration strongly suggest that reactions 1 and 9 are the only processes which affect the Br(²P_{3/2}) time history, although reactions of Br(²P_{3/2}) with impurities in the R,SH samples are not ruled out by the above set of observations. A typical Br(²P_{3/2}) temporal profile and a typical k' versus [R,SH] plot observed in our studies of reactions 1 and 2 are shown in Figures 1 and 2. Kinetic data for reactions 1 and 2 are summarized in Tables II and III.

In the absence of side reactions that remove or produce Br(²P_{3/2}), the observed Br(²P_{3/2}) temporal profile following the laser flash in studies of reactions -1 and -2 would be described by the relationship

$$S_i = k_2 C_1 (k_9 - k_2)^{-1} [\exp(-k_2 t) - \exp(-k_9 t)] + C_2 \exp(-k_9 t) \quad (\text{II})$$

In eq II, S_i and k₉ are as defined above, k₂ is the pseudo-first order rate coefficient for Br(²P_{3/2}) appearance, and the parameters C₁ and C₂ are defined as follows:

$$C_1 = \alpha [R,S]_0 \quad (\text{III})$$

$$C_2 = \alpha [\text{Br}(\text{}^2\text{P}_{3/2})]_0 \quad (\text{IV})$$

In the above equations [R,S]₀ and [Br(²P_{3/2})]₀ are the radical concentrations after photolysis and (in the case of the SH + HBr study) reaction 6 have gone to completion, but before significant removal of R,S radical has occurred, f is the fraction of R,S radicals which are removed via a reaction which produces Br, and α is the proportionality constant which relates S_i to [Br(²P_{3/2})]_i. For the reaction systems of interest, we expect that

$$k_2 = k_{-i}[\text{HBr}] + k_{10} \quad (\text{V})$$

$$f = k_{-i}[\text{HBr}] / k_2 \quad (\text{VI})$$

where i = 1 or 2, R = H for i = 1 and CH₃ for i = 2, and k₁₀ is the rate coefficient for the following reaction(s)

R,S → first-order loss by processes which do not produce Br (10)

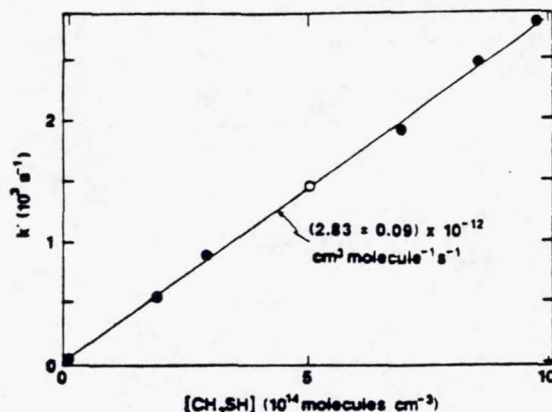


Figure 2. Typical plot of k' versus [RSH] observed in the studies of the Br(²P_{3/2}) + RSH reactions (R = H, CH₃). Reaction: Br(²P_{3/2}) + CH₃SH. T = 332 K, P = 50 Torr. The solid line is obtained from a linear least-squares analysis and gives the bimolecular rate coefficient shown in the figure. The open circle is the data point obtained from the temporal profile shown in Figure 1.

A nonlinear least-squares analysis of each experimental temporal profile was employed to determine k₂, k₉, C₁, and C₂. The bimolecular rate coefficients of interest, k_i(P,T) (i = 1, 2), were determined from the slopes of k₂ versus [HBr] plots. It is worth pointing out that the accuracy with which k₂ could be determined via the nonlinear least-squares fitting technique was quite good because it was always the case that k₂ ≫ k₉ and C₁ ≫ C₂. It was also always the case that the intercepts of the k₂ versus [HBr] plots were small compared to the k₂ values measured; i.e., k₁₀ was always slow enough to exert little or no influence on the precision of the measured bimolecular rate coefficients. Application of eq II for analysis of SH + HBr kinetic data requires that Cl conversion to SH and Br via reactions 6 and 7 is instantaneous on the time scale for SH removal; under our experimental conditions, reactions 6 and 7 were complete within a few microseconds while reaction -1 occurred on a time scale of several hundred microseconds.

Similar to the situation discussed above for the studies of reactions 1 and 2, observation of Br(²P_{3/2}) temporal profiles that obey eq II, linear dependencies of k₂ on [HBr], and invariance of k₂ to variation in laser photon fluence and photolyte concentration suggests that the R,S + HBr reaction and reaction 9 are the only processes other than possible impurity reactions which significantly affect the Br(²P_{3/2}) time history (once photolysis and Cl reaction with H₂S and HBr are complete). A typical Br(²P_{3/2}) temporal profile and typical k₂ versus [HBr] plot observed in our studies of reactions -1 and -2 are shown in Figures 3 and 4. Kinetic data for reactions -1 and -2 are summarized in Tables IV and V.

As indicated in Tables II-V, pressure dependence studies were carried out for reactions 1, 2, and -2; as expected, no evidence for pressure-dependent rate coefficients was observed over the range investigated (30-300 Torr). Arrhenius plots for reactions 1, 2, -1, and -2 are shown in Figure 5. The solid lines in Figure 5 are obtained from linear least-squares analyses of the ln k_i(T) versus T⁻¹ data; these analyses give the following Arrhenius expression in units of cm³ molecule⁻¹ s⁻¹:

$$k_1 = (1.42 \pm 0.34) \times 10^{-11} \exp[(-2752 \pm 90)/T], \quad 319-431 \text{ K}$$

$$k_{-1} = (4.40 \pm 0.92) \times 10^{-12} \exp[(-971 \pm 73)/T], \quad 299-423 \text{ K}$$

$$k_2 = (9.24 \pm 1.15) \times 10^{-12} \exp[(-386 \pm 41)/T], \quad 273-431 \text{ K}$$

$$k_{-2} = (1.46 \pm 0.21) \times 10^{-12} \exp[(-399 \pm 41)/T], \quad 273-426 \text{ K}$$

Errors in the above expressions are 2σ and represent precision only. On the basis of observed precision and consideration of possible

TABLE IV: Summary of Kinetic Data for the Reaction $\text{SH} + \text{HBr} \rightarrow \text{Br}(^2\text{P}_{3/2}) + \text{H}_2\text{S}^a$

T	P	no. of expts ^b	$[\text{HBr}]_{\text{max}}$	range of k_a	range of k_b	$k_{10} \pm 2\sigma$	$k_{-1} \pm 2\sigma$
299	100	7	161	590-2910	29-45	49 ± 106	176 ± 10
321	100	6	125	411-2980	24-35	64 ± 76	209 ± 8
341	100	5	153	626-4050	28-39	92 ± 140	253 ± 14
402	100	7	117	1100-4740	31-37	302 ± 286	385 ± 34
423	100	12	91.2	622-4330	23-43	112 ± 143	457 ± 22

^aUnits are T (K); P (Torr); $[\text{HBr}]$ (10^{14} molecules cm^{-3}); k_a , k_b , k_{10} (s^{-1}); k_{-1} (10^{-15} cm^3 molecule $^{-1}$ s^{-1}). ^bExpt = measurement of a single $\text{Br}(^2\text{P}_{3/2})$ temporal profile. ^cErrors represent precision only.

TABLE V: Summary of Kinetic Data for the Reaction $\text{CH}_3\text{S} + \text{HBr} \rightarrow \text{Br}(^2\text{P}_{3/2}) + \text{CH}_3\text{SH}^a$

T	P	no. of expts ^b	$[\text{HBr}]_{\text{max}}$	range of k_a	range of k_b	$k_{10} \pm 2\sigma$	$k_{-2} \pm 2\sigma$
273	100	10	77.9	261-2870	11-29	99 ± 114	347 ± 29
295	200	10	82.1	419-3360	17-61	247 ± 116	383 ± 25
297	30	11	72.4	334-2700	20-32	81 ± 50	363 ± 12
297	100	14	66.2	439-2570	10-19	56 ± 82	382 ± 20
297	300	10	69.4	436-2770	9-23	-18 ± 130	385 ± 28
330	100	6	65.9	473-2970	14-20	49 ± 82	438 ± 21
366	100	7	56.4	252-2690	25-48	65 ± 26	468 ± 8
403	100	8	56.0	294-3120	30-37	55 ± 42	546 ± 12
426	100	12	54.7	287-3341	24-44	22 ± 77	592 ± 25

^aUnits are T (K); P (Torr); $[\text{HBr}]$ (10^{14} molecules cm^{-3}); k_a , k_b , k_{10} (s^{-1}); k_{-2} (10^{-15} cm^3 molecule $^{-1}$ s^{-1}). ^bExpt = measurement of a single $\text{Br}(^2\text{P}_{3/2})$ temporal profile. ^cErrors represent precision only.

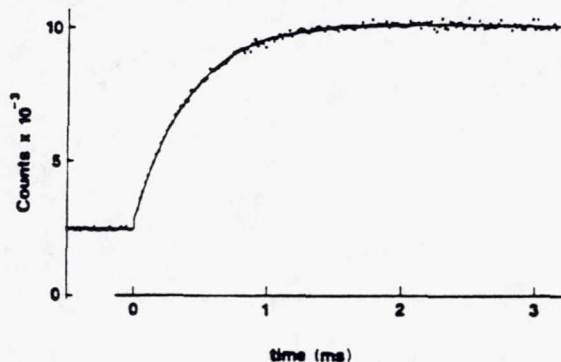


Figure 3. Typical $\text{Br}(^2\text{P}_{3/2})$ atom temporal profile observed in the studies of $\text{RS} + \text{HBr}$ reactions ($\text{R} = \text{H}, \text{CH}_3$). Reaction: $\text{CH}_3\text{S} + \text{HBr}$. Experimental conditions: $T = 330$ K, $P = 100$ Torr, $[\text{CH}_3\text{SSCH}_3] = 3.29 \times 10^{13}$ molecules cm^{-3} , $[\text{HBr}] = 5.12 \times 10^{13}$ molecules cm^{-3} , $[\text{CH}_3\text{S}]_0 \sim 1.2 \times 10^{11}$ molecules cm^{-3} , number of laser shots averaged = 5000. The solid line is obtained from a nonlinear least-squares analysis and gives the following best fit parameters: $k_a = 2270$ s^{-1} , $k_b = 15$ s^{-1} , $C_1 = 7470$, $C_2 = 396$.

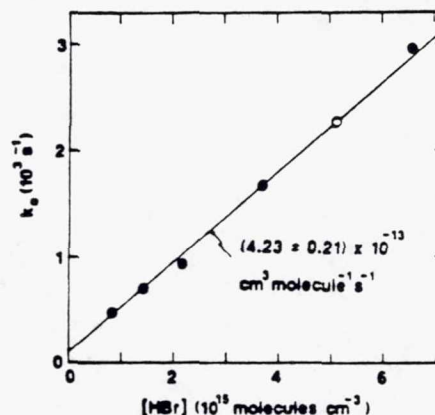


Figure 4. Typical plot of k_a versus $[\text{HBr}]$ observed in the studies of the $\text{RS} + \text{HBr}$ reactions ($\text{R} = \text{H}, \text{CH}_3$). Reaction: $\text{CH}_3\text{S} + \text{HBr}$. $T = 330$ K, $P = 100$ Torr. The solid line is obtained from a linear least-squares analysis and gives the bimolecular rate coefficient shown in the figure. The open circle is the data point obtained from the temporal profile shown in Figure 3.

systematic errors (see below), we estimate the absolute accuracy of each measured bimolecular rate coefficient to be $\pm 15\%$ for the $\text{Br}(^2\text{P}_{3/2}) + \text{R}_2\text{SH}$ reactions and $\pm 20\%$ for the $\text{R}_2\text{S} + \text{HBr}$ reactions.

Reaction Mechanisms. One important question one can ask about reactions 1, -1, 2, and -2 concerns the identity of the reaction products. Can we be sure that $\text{Br}(^2\text{P}_{3/2}) + \text{R}_2\text{SH}$ produces $\text{R}_2\text{S} + \text{HBr}$ with unit yield and that $\text{R}_2\text{S} + \text{HBr}$ produces $\text{Br} + \text{R}_2\text{SH}$ with unit yield? The answer to this question appears to be yes for reactions -1 and -2. We have investigated the possibility of adduct formation in the $\text{Br}(^2\text{P}_{3/2}) + \text{H}_2\text{S}$ reaction and find no evidence for the occurrence of an addition reaction, even at temperatures as low as 190 K. Hence, it appears that reaction 1 must produce $\text{SH} + \text{HBr}$ with unit yield. However, there are a number of possible channels via which reaction 2 could proceed:

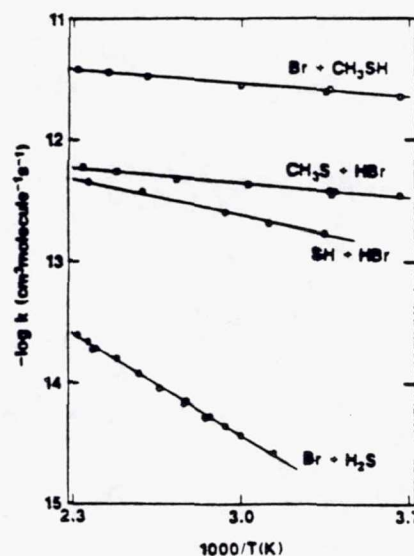
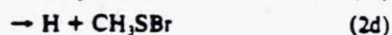
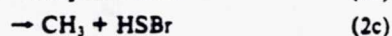
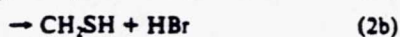
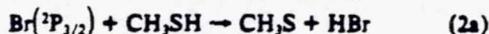
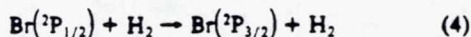
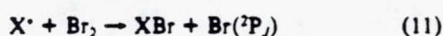
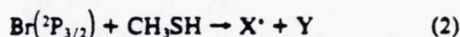


Figure 5. Arrhenius plots. Solid lines are obtained from least-squares analyses which yield the Arrhenius expressions given in the text.

The occurrence of reaction 2b seems unlikely since the C-H bond in CH₃SH is thought to be about 6 kcal mol⁻¹ stronger than the S-H bond.^{19,20} For the similar though considerably more exothermic reactions of Cl and OH radicals with CH₃SH, abstraction of a methyl hydrogen is known to be a very minor reaction channel,^{21,22} since channel 2b is probably significantly endothermic, the yield of CH₃SH from reaction 2 is probably smaller than the (very small) yields of CH₃SH from the reactions of Cl and OH with CH₃SH. Assuming the RS-Br bond strength to be 57 kcal mol⁻¹, i.e., intermediate between published estimates of the RS-Cl²³ and RS-I²⁰ bond strengths, reactions 2c and 2d are highly endothermic. Using the CH₃S and SH heats of formation derived from our data (see below) to calculate the enthalpy change for reaction 2c leads to the conclusion that this reaction is endothermic by 4.6 kcal mol⁻¹; assuming an *A* factor of 1 × 10⁻¹¹ cm³ molecule⁻¹ s⁻¹ for *k*_{2c} and an activation energy equal to the endothermicity suggests that reaction 2c could contribute no more than 1% to the measured *k*₂ at 431 K and much less at lower temperatures. Recent unpublished experiments in our laboratory have obtained kinetic evidence for reversible adduct formation in the Br + CH₃SH reaction at temperatures below 235 K. At *T* ≥ 273 K, the temperature range of interest for this study, our results suggest that the adduct lifetime is too short for its existence to be kinetically important.

As an experimental check on the above conclusions, experiments were carried out where Br(²P_{3/2}) kinetics were observed following 355-nm laser flash photolysis of Br₂/CH₃SH/HBr/H₂/N₂ mixtures. To avoid complications from a heterogeneous dark reaction between Br₂ and CH₃SH, it was necessary to inject Br₂ into the gas flow just upstream from the reaction zone. Long-wavelength photolysis was necessary in order to completely avoid production of CH₃S and H via photodissociation of CH₃SH. Following Br(²P_{3/2}) production by the laser flash, the following reactions occur:



Br(²P_{3/2}) → loss by diffusion from the detector field of view and reaction with background impurities (9)

X* → first-order loss by processes which do not produce Br (13)

Assuming that all reactions are first order or pseudo first order and that Br(²P_{1/2}) deactivation to Br(²P_{3/2}) is instantaneous on the time scale for the occurrence of reactions 2, 11, and 12, the rate equations for the above reaction scheme can be solved analytically:

$$\frac{[\text{Br}(\text{}^2\text{P}_{3/2})]_t}{[\text{Br}(\text{}^2\text{P}_{3/2})]_0} = \frac{(Q + \lambda_1) \exp(\lambda_1 t) - (Q + \lambda_2) \exp(\lambda_2 t)}{(\lambda_1 - \lambda_2)} \quad (\text{VII})$$

where

$$\lambda_1 = 0.5[(a^2 - 4b)^{1/2} - a] \quad (\text{VIII})$$

$$\lambda_2 = -0.5[(a^2 - 4b)^{1/2} + a] \quad (\text{IX})$$

$$Q = k_{11}[\text{Br}_2] + k_{12}[\text{HBr}] + k_{13} \quad (\text{X})$$

$$a = Q + k_2[\text{CH}_3\text{SH}] + k_9 = -(\lambda_1 + \lambda_2) \quad (\text{XI})$$

$$b = k_9 Q + k_{13} k_2[\text{CH}_3\text{SH}] = \lambda_1 \lambda_2 \quad (\text{XII})$$

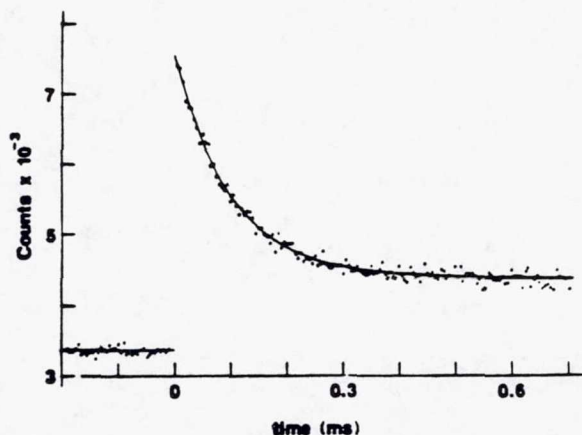


Figure 6. Typical Br(²P_{3/2}) temporal profile observed following 355-nm laser flash photolysis of Br₂/CH₃SH/HBr/H₂/N₂ mixtures. Experimental conditions: *T* = 298 K, *P* = 30 Torr, [Br₂] = 5.3 × 10¹² molecules cm⁻³, [CH₃SH] = 3.50 × 10¹⁵ molecules cm⁻³, [HBr] = 2.99 × 10¹⁵ molecules cm⁻³, [Br(²P_{3/2})]₀ = 4 × 10¹⁰ atoms cm⁻³, number of laser shots averaged = 10000. The solid line is obtained from a nonlinear least-squares analysis and gives the best fit parameters *Q* = 2540 s⁻¹, -λ₁ = 67.1 s⁻¹, and -λ₂ = 10250 s⁻¹.

Observed Br(²P_{3/2}) temporal profiles were fitted to the predicted double-exponential functional form (eq VII) using a nonlinear least-squares procedure to obtain values for λ₁, λ₂, and *Q*. The rate coefficient *k*₉ was directly measured and was always small (10–40 s⁻¹). Hence, the elementary rate coefficients *k*₂ and *k*₁₃ could be obtained from the relationships

$$k_2 = -(Q + k_9 + \lambda_1 + \lambda_2)/[\text{CH}_3\text{SH}] \quad (\text{XIII})$$

$$k_{13} = (k_9 Q - \lambda_1 \lambda_2)/(Q + k_9 + \lambda_1 + \lambda_2) \quad (\text{XIV})$$

Values for *k*₁₃ were always found to be relatively small, ranging from 14 to 127 s⁻¹ for the 45 double-exponential decays which were analyzed. For a set of experiments where [HBr] is varied at constant (low) [Br₂], a plot of (*Q* - *k*₁₃) versus [HBr] should, according to eq X, be linear with slope = *k*₁₂ and intercept = *k*₁₁[Br₂]. With the exception of CH₃SH, 298 K rate coefficients for reactions of all possible radicals X* with HBr are known and are significantly different from each other, in units of 10⁻¹³ cm³ molecule⁻¹ s⁻¹ the rate coefficients of interest are 1.7 for X* = SH (this work), 3.9 for X* = CH₃S (this work), 30 for X* = CH₃,²⁴ and 65 for X* = H.²⁵ Hence, determination of *k*₁₂ as described above should provide strong evidence concerning the identity of X*.

A typical Br(²P_{3/2}) temporal profile observed following 355-nm laser flash photolysis of Br₂/CH₃SH/HBr/H₂/N₂ mixtures is shown in Figure 6, while typical plots of (*Q* - *k*₁₃) versus [HBr] are shown in Figure 7. The data in Figure 7 suggest that *k*₁₂(298 K) = 4.6 × 10⁻¹³ cm³ molecule⁻¹ s⁻¹; considering the nature of the fitting procedure, we estimate the uncertainty in *k*₁₂(298 K) to be ±30%. This determination of *k*₁₂(298 K) strongly supports the contention that the dominant reaction channel for the Br(²P_{3/2}) + CH₃SH reaction is production of CH₃S + HBr. The intercepts of the plots in Figure 7 indicate that the CH₃S + Br₂ reaction is very fast, i.e., *k*₁₄ = (1.7 ± 0.5) × 10⁻¹⁰ cm³ molecule⁻¹ s⁻¹. To our knowledge there are no measurements of *k*₁₄ reported in the literature.



However, very fast rate coefficients have recently been reported for the reactions of alkyl radicals²⁶ and SD radicals²⁷ with Br₂.

(19) Dill, B.; Heydtmann, H. *Chem. Phys.* 1978, 35, 161.

(20) Shum, L. G. S.; Benson, S. W. *Int. J. Chem. Kinet.* 1983, 15, 433.

(21) Nesbitt, D. J.; Leone, S. R. *J. Chem. Phys.* 1981, 75, 4949.

(22) Tyndall, G. S.; Ravishankara, A. R. *J. Phys. Chem.* 1989, 93, 4707.

(23) Benson, S. W. *Chem. Rev.* 1978, 78, 23.

(24) Nicovich, J. M.; van Dijk, C. A.; Kreutter, K. D.; Wine, P. H. *J. Phys. Chem.* 1991, 95, 9890.

(25) Umemoto, H.; Wada, Y.; Tsunashima, S.; Takayanagi, T.; Sato, S. *Chem. Phys.* 1990, 143, 333.

(26) Timonen, R. S.; Seetula, J. A.; Gutman, D. *J. Phys. Chem.* 1990, 94, 3005.

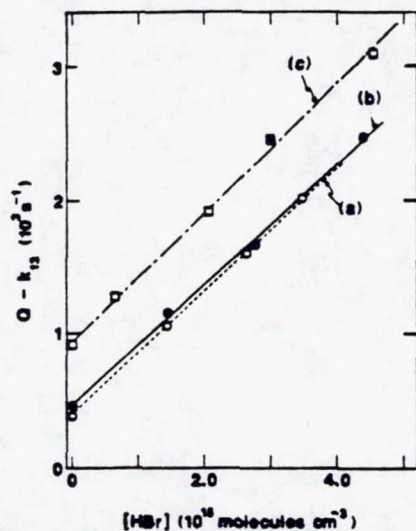


Figure 7. Plots of $(Q - k_{13})$ versus $[HBr]$. Experimental conditions: $T = 298$ K; P (Torr) = (a) 100, (b) 30, (c) 30; $[Br_2]$ (10^{12} molecules cm^{-3}) = (a) 2.15, (b) 3.25, (c) 5.3; $[CH_3SH]$ (10^{15} molecules cm^{-3}) = (a) 1.24, (b) 1.33, (c) 3.61. The lines are obtained from linear least-squares analyses; the slopes give the following values for $k_{13} \pm 2\sigma$ in units of 10^{13} cm^3 molecule $^{-1}$ s $^{-1}$: (a) 4.60 ± 0.19 , (b) 4.51 ± 0.26 , (c) 4.81 ± 0.28 ; the intercepts suggest a gas kinetic value for k_{14} . The filled square is the data point obtained from the temporal profile shown in Figure 6.

Reactivity in these systems seems to correlate with properties that reflect the strength of long-range attractive forces, particularly those associated with stabilization of transition states via charge separation. The highly polarizable nature of both CH_3S and Br_2 , the low ionization potential of CH_3S (8.06 eV 28), and the large electron affinity of Br_2 (~ 2.55 eV 28) are electronic properties which contribute to the very fast rate of reaction 14.

Potential Systematic Errors. As discussed briefly above, a number of potential systematic errors in our kinetic measurements can be ruled out based on the observed invariance of $Br(^2P_{3/2})$ temporal profiles to variations in laser photon fluence, photolyte concentrations, flow velocity through the reactor, and laser pulse repetition rate; these include contributions to $Br(^2P_{3/2})$ kinetics from radical-radical side reactions, from radical-photolyte side reactions, from reactions involving radicals which are produced by reactant photolysis (H and CH_3S from CH_3SH photolysis, for example) or from reactions involving stable products which build up in concentration with successive laser flashes. In situ measurements of stable reactant (i.e., H_2S , CH_3SH , HBr) concentrations greatly reduce another potential source of systematic error.

One type of kinetic interference which needs to be addressed is the potential contribution to measured rate coefficients from impurity reactions. The relatively unreactive nature of Br atoms makes it unlikely that impurity reactions were a problem in our studies of reactions 1 and 2. Gas chromatographic analyses of the H_2S and CH_3SH samples were carried out using a flame photometric detector to search for sulfur-containing impurities; none were observed, lending further confidence that impurity reactions were not a problem. The most likely impurity problem in our studies of reactions -1 and -2 is from Br_2 . Potential sources of Br_2 are impurity in the HBr sample, residual Br_2 (from Br recombination) not swept out of the reaction zone between laser flashes, and catalytic formation of Br_2 from heterogeneous reactions of HBr (presumably on the metal surfaces of valves and fittings). As discussed above, reactions 14 and 15 are very fast (the 298 K rate coefficient for the $SD + Br_2$ reaction has recently been reported to be 9.8×10^{-11} cm^3 molecule $^{-1}$ s $^{-1}$ 27).



Since SH and CH_3S react with Br_2 several hundred times faster than with HBr , the HBr concentration must be several thousand times larger than the Br_2 concentration before Br_2 interference can be considered to be unimportant. To investigate the Br_2 interference problem, a 2-m absorption cell was positioned in the slow flow system downstream from the reaction cell and employed to monitor Br_2 photometrically (at 404.7 nm) with typical $Cl_2CO/H_2S/HBr/N_2$ or $CH_3SSCH_3/HBr/H_2/N_2$ mixtures flowing through the system. No absorption was observed (i.e., $I/I_0 > 0.998$) even at HBr levels as high as 1×10^{17} molecules cm^{-3} . Since the Br_2 absorption cross section at 404.7 nm is about 6×10^{-19} cm^2 , 17 these experiments suggest that $[Br_2] < 0.0002[HBr]$.

Another potential systematic error in our studies of reactions -1 and -2 concerns the possibility that SH and CH_3S are produced in vibrationally or electronically excited states and do not relax much more rapidly than they react. The spin-orbit splittings in SH and CH_3S are 377 cm^{-1} 29 and 257 cm^{-1} , 30,31 respectively, i.e., only slightly larger than the average collision energy at 298 K ($kT = 207$ cm^{-1} at 298 K). Hence, extremely rapid equilibration of the SH and CH_3S spin orbit states via collisions with the nitrogen buffer gas can be safely assumed. It is known from infrared chemiluminescence experiments that much of the available exothermicity of the $Cl + H_2S$ reaction appears as vibrational excitation in the HCl product, but that the SH product is formed with little or no internal excitation. 19 Furthermore, vibrational relaxation of SH by H_2S is expected to be a very efficient process due to the near resonance ($\Delta\bar{\nu} \sim 40$ cm^{-1}) between the SH vibrational frequency 29 and the $S-H$ stretch frequencies in H_2S . 32 Hence, it seems safe to conclude that SH was thermalized in our study of reaction -1. Black and Jusinski have studied the time dependence for populating the ground vibrational level of CH_3S following 248-nm pulsed laser photolysis of CH_3SSCH_3 in the presence of a number of inert collision partners. 33 They find that nearly all CH_3S is produced in excited vibrational levels, but that relaxation is very efficient. A phenomenological rate coefficient of 5.1×10^{-12} cm^3 molecule $^{-1}$ s $^{-1}$ was measured for populating the ground vibrational level (from the unknown initial vibrational state distribution) via collisions with N_2 . Hence, under our experimental conditions (Table V), CH_3S relaxation times ranged from 0.02 to 0.2 μs while CH_3S reaction times ranged from 300 to 4000 μs .

As mentioned above, the $SH + HBr$ experiments were carried out with no H_2 added to the reaction mixtures in order to avoid potential complications from the $Cl + H_2$ reaction. This variation in experimental conditions does, however, introduce a different possible complication. As mentioned in the Experimental Section, the resonance fluorescence detection technique is sensitive to both bromine atom spin-orbit states, and the relative sensitivities for detecting the two states are different and difficult to quantify. If $Br(^2P_{1/2})$ was generated in significant quantity, and if its relaxation to $Br(^2P_{3/2})$ occurred on the same time scale as the $SH + HBr$ reaction, then temporal profiles for appearance of the fluorescence signal would deviate systematically from the quantity we actually want to measure—the temporal profile for appearance of bromine atoms. Rate coefficients for deactivation of $Br(^2P_{1/2})$ by N_2 and HBr are, in units of cm^3 molecule $^{-1}$ s $^{-1}$, 2.5×10^{-15} 34 and $\sim 1 \times 10^{-12}$, 34,35 respectively. Hence for the N_2 and HBr levels employed (Table IV), any $Br(^2P_{1/2})$ generated via HBr photolysis, via reaction 7, or via reaction -1, was deactivated to $Br(^2P_{3/2})$ on a time scale which was faster by factors of 3–20 than the time scales for the occurrence of reaction -1. Although the rate coefficient for $Br(^2P_{1/2})$ deactivation by H_2S does not appear to

(29) Ramsay, D. A. *J. Chem. Phys.* 1952, 20, 1920.

(30) Hsu, Y.-C.; Liu, X.; Miller, T. A. *J. Chem. Phys.* 1989, 90, 6852.

(31) Lee, Y. P.; Chiang, S.-Y. *J. Chem. Phys.* 1991, 95, 66.

(32) Sverdlov, L. M.; Kovner, M. A.; Krainov, E. P. *Vibrational Spectra of Polyatomic Molecules*; Wiley: New York, 1974.

(33) Black, G.; Jusinski, L. E. *J. Chem. Soc., Faraday Trans. 2* 1986, 82, 2143.

(34) Donovan, R. J.; Husain, D. *Trans. Faraday Soc.* 1966, 62, 2987.

(35) Leone, S. R.; Wodarczyk, F. J. *J. Chem. Phys.* 1974, 60, 314.

(27) Fenter, F. F.; Anderson, J. G. *J. Phys. Chem.* 1991, 95, 3172.

(28) Lias, S. G.; Bartmess, J. E.; Liebman, J. F.; Holmes, J. L.; Levin, R. D.; Mallard, W. G. *J. Phys. Chem. Ref. Data* 1988, 17, Suppl. 1.

TABLE VI: Kinetic Parameters, Enthalpy Changes, and IP - EA Values for a Series of Hydrogen Transfer Reactions R + XH → RH + X

R	X	kinetic parameters ^a			ref	-ΔH ₂₉₈ ^b	electronic properties ^c		
		A	E _{act}	k(298 K)			IP(R) - EA(XH)	IP(XH) - EA(R)	IP(R)
Br	HS	140	5.5	0.013	TW ^d	-3.6	10.70	7.08	
Cl	HS	360	-0.4	710	11	11.9	11.86	6.83	
OH	HS	60	0.15	47	68	28.0	12.57	8.62	
Br	CH ₃ S	92	0.8	24	TW ^d	0.1	11.6 ^e	6.08	
Cl	CH ₃ S	120	-0.3	2000	11	15.7	12.8 ^e	5.82	
OH	CH ₃ S	99	-0.7	320	68	31.8	13.5 ^e	7.61	
Cl	Br	230	0.8	60	12	15.6	12.8 ^e	8.04	
OH	Br	110	0	110	68	31.7	13.5 ^e	9.83	
SH	Br	44	1.9	1.8	TW ^d	3.6	10.2 ^e	9.36	
CH ₃ S	Br	15	0.8	3.9	TW ^d	-0.1	7.9 ^e	9.78	
CH ₃	Br	14	-0.5	32	24	17.8	9.6 ^e	10.5	
C ₂ H ₅	Br	13	-1.1	83	24	13.7	7.9 ^e	10.7	
t-C ₄ H ₉	Br	11	-1.9	270	24	8.9	6.5 ^e	11.0	

^aUnits for A and k(298 K) are 10⁻¹³ cm³ molecule⁻¹ s⁻¹ and units for E_{act} are kcal mol⁻¹. ^bUnits are kcal mol⁻¹; values are computed using heats of formation from this work (SH and CH₃S), ref 24 (CH₃, C₂H₅, t-C₄H₉), ref 28 (t-C₄H₁₀), and ref 68 (all others). ^cUnits are electronvolts; ionization potentials and electron affinities taken from ref 28. ^dTW = this work. ^eThe unknown (but presumably very small) EA(XH) is assumed to be 0.2 eV.

be known, it appears likely (based for example on analogy with the known fast rate for Br(²P_{1/2}) deactivation by H₂O³⁶) that H₂S levels of 1 × 10¹⁶ molecules cm⁻³ were sufficient to contribute significantly to the overall rate of Br(²P_{1/2}) deactivation.

Comparison of Reaction Rates for a Series of Radical + H₂S, CH₃SH, HBr Reactions. To our knowledge, there are no previous kinetics studies of reactions 1, -1, 2, or -2 with which to compare our results. However, kinetic data are available for many "similar" reactions. Kinetic parameters, reaction enthalpies, and relevant electronic properties for a series of hydrogen-transfer reactions involving free-radical attack on H₂S, CH₃SH, and HBr are summarized in Table VI.

When one considers series of similar reactions such as those in Table VI, a correlation between the activation energy (in the exothermic direction) and the reaction exothermicity is often observed. Such correlations were clearly established by Evans and Polanyi in the 1930s³⁷ and are heavily documented in the literature.³⁸ Examination of Table VI, however, shows the correlation between activation energy and reaction exothermicity to be rather poor. Only the small subset of reactions Cl, OH, SH + HBr appear to follow such a trend.

As mentioned above when considering the very fast rate observed for the CH₃S + Br₂ reaction, it is often possible to correlate reactivity with properties that reflect the strength of long-range attractive forces, particularly those associated with stabilization of transition states via charge separation. For some classes of reactions, reactivity is found to be strongly correlated with the parameter IP - EA, the difference between the ionization potential of one reactant and the electron affinity of the other reactant. Bayes and co-workers have observed that low values of IP - EA correlate with enhanced reactivity in the alkyl + O₂, O₃ reactions.^{39,40} Gutman and co-workers have observed a similar reactivity trend for the reactions of alkyl radicals with Cl₂,⁴¹ Br₂,²⁶ HI,⁴² and HBr;⁴³⁻⁴⁵ recent work in our laboratory has confirmed the reactivity trend in the alkyl + HBr series²⁴ (Table VI). Anderson and co-workers have observed correlations between IP - EA and reactivity in reactions of OH and SD radicals with

halogen molecules^{27,46} and in the reactions of Br, Cl, F, O, N, and OH radicals with ClNO⁴⁷ and with O₃.⁴⁸ The property IP - EA has been found to correlate with both activation energies^{24,26,42-48} and A factors.³⁹⁻⁴¹ As discussed by Abbatt et al.,⁴⁷ the barrier (i.e., activation energy) to reaction can be lowered through an interaction with low-lying ionic states. Presumably, the ionic character of the reaction potential energy surface in the region of the transition state is enhanced when IP - EA is relatively small; this ionic character presumably lowers the barrier by increasing the stability of charge separation at the transition state. The long-range electronic interaction which can occur when IP - EA is relatively low can result in formation of highly polar, loose transition states, an effect which leads to abnormally large A factors.

Examination of the kinetic parameters and IP - EA values in Table VI leaves little doubt that ionic interactions exert an important influence on reactivity in the reactions considered. The low ionization potential of CH₃SH and high electron affinity of Cl allow these reactants to interact via a charge-transfer mechanism at large separation, thus leading to a very large A factor and very fast reaction rate. Differences in reactivity of H₂S and CH₃SH toward Cl and OH correlate very well with the value of IP(RSH) - EA(X), X = Cl, OH. For Br(²P_{3/2}) reactions with H₂S and CH₃SH, however, the above correlation would predict faster rate coefficients than are actually observed as a result of the high electron affinity of Br. The reactions of Cl and OH with H₂S and CH₃SH, all of which are significantly exothermic, are barrierless processes. However, the thermoneutral Br(²P_{3/2}) + CH₃SH reaction has an activation energy of 0.8 kcal mol⁻¹ and the endothermic Br(²P_{3/2}) + H₂S reaction has an activation energy 1.9 kcal mol⁻¹ larger than the endothermicity. It seems clear that Br(²P_{3/2}) can form (very weakly bound) long-range polar complexes with H₂S and CH₃SH. However, the unfavorable thermochemistry of the Br + RSH reactions apparently leads to significant barriers for H atom transfer within the complexes, such that complex dissociation back to reactants can compete effectively with the H-transfer reaction.

Observed A factors for the radical + HBr reactions in Table VI follow the well-established trend of decreasing with increasing complexity of the reactant radical (i.e., atomic > diatomic > polyatomic).⁴⁹ As mentioned above, alkyl + HBr reactivity correlates well with the alkyl radical ionization potential, i.e., the lower the radical ionization potential, the faster the reaction; alkyl + HBr reactivity does not correlate with reaction exothermicity.

(36) Taatjes, C. A.; Lovejoy, C. M.; Opansky, B. J.; Leones, S. R. *Chem. Phys. Lett.* 1991, 182, 39.

(37) Evans, M. G.; Polanyi, M. *Trans. Faraday Soc.* 1938, 34, 11.

(38) see for example, Semenov, W. N. *Some Problems in Chemical Kinetics and Reactivity*, Princeton University Press: Princeton, NJ, 1958.

(39) Ruiz, R. P.; Bayes, K. D. *J. Phys. Chem.* 1984, 88, 2592.

(40) Pallenghi, R.; Ogryzlo, E. A.; Bayes, K. D. *J. Phys. Chem.* 1984, 88, 2595.

(41) Timonen, R. S.; Gutman, D. *J. Phys. Chem.* 1986, 90, 2987.

(42) Seetula, J. A.; Russell, J. J.; Gutman, D. *J. Am. Chem. Soc.* 1990, 112, 1347.

(43) Russell, J. J.; Seetula, J. A.; Timonen, R. S.; Gutman, D.; Nava, D. *J. Am. Chem. Soc.* 1988, 110, 3084.

(44) Russell, J. J.; Seetula, J. A.; Gutman, D. *J. Am. Chem. Soc.* 1988, 110, 3092.

(45) Seetula, J. A.; Gutman, D. *J. Phys. Chem.* 1990, 94, 7529.

(46) Loewenstein, L. M.; Anderson, J. G. *J. Phys. Chem.* 1985, 89, 5371.

(47) Abbatt, J. P. D.; Toohey, D. W.; Fenter, F. F.; Stevens, P. S.; Brune, W. H.; Anderson, J. G. *J. Phys. Chem.* 1989, 93, 1022.

(48) Toohey, D. W.; Brune, W. H.; Anderson, J. G. *Int. J. Chem. Kinet.* 1988, 20, 131.

(49) see for example, Johnston, H. S. *Gas Phase Reaction Rate Theory*; Ronald Press Co.: New York, 1966; Chapter 12.

TABLE VII: Thermochemical Parameters for the Reactions $\text{Br}(^2P_{3/2}) + \text{H}_2\text{S} \rightarrow \text{SH} + \text{HBr}$ (1) and $\text{Br}(^2P_{3/2}) + \text{CH}_3\text{SH} \rightarrow \text{CH}_3\text{S} + \text{HBr}$ (2)

reaction	T, K	ΔH_i° , kcal mol ⁻¹		ΔS_i° , cal mol ⁻¹ deg ⁻¹	
		2nd law	3rd law	2nd law	3rd law
1	360	3.54 ± 0.32	3.96 ± 0.21	2.33 ± 0.60	3.50 ± 0.15
	298	3.46 ± 0.33	3.82 ± 0.17	2.04 ± 1.56	3.24 ± 0.12
	0	3.08 ± 0.35	3.44 ± 0.19		
2	333	-0.03 ± 0.17	-0.17 ± 0.32	3.67 ± 0.44	3.23 ± 0.53
	298	-0.08 ± 0.19	-0.20 ± 0.28	3.48 ± 1.09	3.07 ± 0.51
	0	-0.59 ± 0.27	-0.71 ± 0.36		

* Errors are 2σ and represent best estimates of absolute accuracy.

On the other hand, for the Cl, OH, and SH reactions with HBr, a reasonable correlation of activation energy with reaction exothermicity is observed. These reactions apparently proceed through transition states which are not strongly influenced by ionic interactions. The thermoneutral $\text{CH}_3\text{S} + \text{HBr}$ reaction appears to be an intermediate case. Unlike the alkyl + HBr reactions, the $\text{CH}_3\text{S} + \text{HBr}$ reaction does have a positive activation energy. However, the barrier is much smaller than one would predict based on the ΔH versus E_{act} trend observed for the Cl, OH, SH + HBr reactions. Apparently, the low ionization potential of CH_3S facilitates ionic interactions which reduce but do not eliminate the barrier.

SH and CH_3S Thermochemistry. From the Arrhenius parameters determined in this study we can obtain the enthalpy changes and entropy changes associated with reactions 1 and 2. One approach, the "second law method", employs the following relationships to obtain thermochemical parameters for reaction *i*:

$$\Delta H_i = E_i - E_{-i} \quad (\text{XV})$$

$$\Delta S_i = R \ln (A_i/A_{-i}) \quad (\text{XVI})$$

where A_i and E_i are the A factor and activation energy for reaction *i*. Thermochemical parameters for reactions 1 and 2 obtained from the second law analyses are tabulated in Table VII. The temperature, 360 K for reaction 1 and 333 K for reaction 2, is defined as the arithmetic mean of the T^{-1} ranges employed in the determinations of k_i and k_{-i} . Values for ΔH at 298 and 0 K were computed using heat capacity corrections obtained from the JANAF tables⁵⁰ for Br, HBr, SH, and H_2S , and calculated from available spectroscopic data for CH_3S ^{30,31} and CH_3SH .^{32,51,52} Second law values for ΔS at 298 K were computed from the relationship

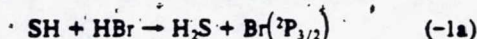
$$\Delta G_{298} = \Delta H_{298} - T\Delta S_{298} = RT \ln K_{\text{eq}}(298 \text{ K}) = RT \ln [k_{-i}(298 \text{ K})/k_i(298 \text{ K})] \quad (\text{XVII})$$

Values for $k_i(298 \text{ K})$ and $k_{-i}(298 \text{ K})$ were computed from the Arrhenius expressions reported above.

An alternate procedure for obtaining thermochemical parameters is the "third law method" where the entropy change is calculated using standard statistical mechanical methods⁵³ and employed in conjunction with experimental values for $K_{\text{eq}}(T)$ to obtain ΔH_T° (from eq XVII). Absolute entropies as a function of temperature were obtained from the JANAF tables⁵⁰ for Br, HBr, SH, and H_2S , and calculated from available spectroscopic data for CH_3S ^{30,31} and CH_3SH .^{32,51,52} Uncertainties in the third law ΔS values are estimated based on uncertainties in key structural parameters. For reaction 1, the calculated ΔS appears to be quite accurate. For reaction 2, a significant uncertainty in the calculated ΔS arises from uncertainty in the frequency of the doubly degenerate ν_6 mode of CH_3S , which was recently assigned a value of 586 cm^{-1} by Lee and Chiang;³¹ we "guesstimate" the error in this assignment to be $\pm 100 \text{ cm}^{-1}$. In units of cal mol^{-1}

deg⁻¹, the 298 K entropies of SH and CH_3S used in our third law determinations are 46.77 and 58.32, respectively. Results of the third law determinations are summarized in Table VII.

The analysis presented above is based on the idea that reactions -1 and -2 are the reverse of reactions 1 and 2. In the case of reactions 1 and 2 we know that the reacting bromine atom was in the $^2P_{3/2}$ ground state because sufficient H_2 was present in the reaction mixtures to instantaneously (on the time scale for Br reaction) deactivate any photolytically generated $\text{Br}(^2P_{1/2})$. Hence, the reverse reactions we wish to determine the rates of are



Our method, however, actually measures $k_{-1} = k_{-1a} + k_{-1b}$ and $k_{-2} = k_{-2a} + k_{-2b}$ where reactions -1b and -2b are the channels producing $\text{Br}(^2P_{1/2})$:



Clearly, if reactions -1 and/or -2 proceed exclusively or a significant fraction of the time via channels -1b and/or -2b, then we would be overestimating the rate of the true reverse reaction(s) and our reported enthalpy changes would be in error. Simple thermochemical arguments based on the measured activation energies for reactions 1 and 2 can be used to place reasonable upper limits on k_{-1b} and k_{-2b} . Our measured activation energy for reaction 1 is 5.5 kcal mol⁻¹. It is reasonable to assume that the activation energy for reaction -1a is greater than -1.0 kcal mol⁻¹. Since the bromine atom spin-orbit splitting is 10.5 kcal mol⁻¹, reaction -1b must be endothermic by at least 4.0 kcal mol⁻¹. Taking $1 \times 10^{-11} \text{ cm}^3 \text{ molecule}^{-1} \text{ s}^{-1}$ as an upper limit A factor for reaction -1b and 4.0 kcal mol⁻¹ as a lower limit activation energy for reaction -1b leads to the result $k_{-1b}(299 \text{ K}) \leq 1.2 \times 10^{-14} \text{ cm}^3 \text{ molecule}^{-1} \text{ s}^{-1}$ and $k_{-1b}(423 \text{ K}) \leq 8.6 \times 10^{-14} \text{ cm}^3 \text{ molecule}^{-1} \text{ s}^{-1}$, i.e., $k_{-1b}/k_{-1} \leq 0.068$ at 299 K and $k_{-1b}/k_{-1} \leq 0.19$ at 423 K. We have repeated the second and third law analyses of the reaction 1 data assuming that the above upper limits were the correct values for k_{-1b} . Under this scenario, the second law ΔH values for reaction 1 which are given in Table VII would be increased by 0.29 kcal mol⁻¹ while the third law ΔH values for reaction 1 would be decreased by 0.09 kcal mol⁻¹. Our measured activation energy for reaction 2 is 0.8 kcal mol⁻¹. If we assume as above that the activation energy for reaction -2a is greater than -1.0 kcal mol⁻¹, then we are led to the conclusion that reaction -2b must be endothermic by at least 8.7 kcal mol⁻¹. Taking $1 \times 10^{-11} \text{ cm}^3 \text{ molecule}^{-1} \text{ s}^{-1}$ as an upper limit A factor for reaction -2b and 8.7 kcal mol⁻¹ as a lower limit activation energy for reaction -2b leads to the result $k_{-2b}(273 \text{ K}) \leq 1.1 \times 10^{-16} \text{ cm}^3 \text{ molecule}^{-1} \text{ s}^{-1}$ and $k_{-2b}(426 \text{ K}) \leq 3.4 \times 10^{-16} \text{ cm}^3 \text{ molecule}^{-1} \text{ s}^{-1}$, i.e., $k_{-2b}/k_{-2} \leq 3.1 \times 10^{-6}$ at 273 K and $k_{-2b}/k_{-2} \leq 5.7 \times 10^{-6}$ at 426 K. Clearly, the contribution of channel -2b to our measured values for k_{-2} must be negligible over the entire temperature range investigated.

The enthalpy changes for reactions 1 and 2 determined in this study can be combined with the accurately known heats of formation of Br, HBr, H_2S , and CH_3SH ^{28,50} (Table VIII) to obtain SH and CH_3S heats of formation. Values for $\Delta H_f^\circ(\text{R,S})$ and

(50) Chase, M. W., Jr.; Davies, C. A.; Downey, J. R., Jr.; Frurip, D. J.; McDonald, R. A.; Syverud, A. N. *J. Phys. Chem. Ref. Data* 1985, 14, Suppl. 1.

(51) Kojima, T.; Nishikawa, T. *J. Phys. Soc. Jpn.* 1957, 12, 680.

(52) Kojima, T. *J. Phys. Soc. Jpn.* 1960, 15, 1284.

(53) See, for example: Knox, J. H. *Molecular Thermodynamics*; Wiley-Interscience: London, 1971.

TABLE VIII: Gas-Phase Heats of Formation

species	ΔH_f°	ΔH_f° ₂₉₈	ref
H	51.634 ± 0.001	52.103 ± 0.001	50
S	65.662 ± 0.060	66.200 ± 0.060	50
Br	28.184 ± 0.014	26.735 ± 0.014	50
HBr	-6.836 ± 0.060	-8.710 ± 0.040	50
H ₂ S	-4.203 ± 0.191	-4.900 ± 0.191	50
CH ₃	35.62 ± 0.19	34.82 ± 0.19	50
CH ₃ SH	-2.89 ± 0.14	-5.47 ± 0.14	28
CH ₃ SCH ₃	-5.09 ± 0.12	-8.96 ± 0.12	28
CH ₃ SSCH ₃	-1.63 ± 0.24	-5.78 ± 0.24	28
SH	34.07 ± 0.72	34.18 ± 0.68	this work
		33.3 ± 1.2	50
		33.6 ± 1.1	57
	33.9 ± 1.5		58
CH ₃ S	31.44 ± 0.54	29.78 ± 0.44	this work
		29.4 ± 2.1 ^{bc}	28
		34.2 ± 2.0 ^a	59
		31.4 ± 2.0 ^a	60
		33.2 ± 1.5 ^{bc}	61
		30.5 ± 2.0	63
		≥29.5 ± 2.0	20
	35.4 ± 1.5		65
	35.5 ± 2		58
	34.2 ± 1.5		66

^aUnits are kcal mol⁻¹. ^bThese values are obtained by coupling the kinetic data of Colussi and Benson (ref 59) with different values (ranging from 44 to 49 kcal mol⁻¹) for the benzyl radical heat of formation. ^cCritical review.

TABLE IX: Bond Strengths Derived Using the SH and CH₃S Heats of Formation Determined in This Study in Conjunction with Other Heats of Formation Given in Table VIII^a

bond	D ^o	D ^o ₂₉₈
S-H	83.23 ± 0.78	84.12 ± 0.74
HS-H	89.91 ± 0.91	91.18 ± 0.87
H ₃ C-SH	72.58 ± 1.05	74.47 ± 1.01
		(75.0 ± 1.3) ^b
H ₃ C-S	69.84 ± 0.79	71.24 ± 0.69
		(71.7 ± 1.0) ^b
H ₃ CS-H	85.96 ± 0.68	87.35 ± 0.58
H ₃ CS-CH ₃	72.15 ± 0.85	73.56 ± 0.75
		(74.0 ± 1.1) ^b
H ₃ CS-SCH ₃	64.51 ± 1.32	65.34 ± 1.00

^aUnits are kcal mol⁻¹. ^bComputed using $\Delta H_{f,298}(\text{CH}_3) = 35.3 \pm 0.5$ kcal mol⁻¹ as reported in ref 24.

$\Delta H_{f,298}^\circ(\text{R,S})$ are given in Table VIII. Simple averages of the second and third law enthalpies of reaction have been employed to obtain our reported R,S heats of formation; this approach seems reasonable since (a) estimated uncertainties in the second and third law determinations do not differ greatly and (b) the second and third law values for $\Delta H_{f,298}^\circ(\text{R,S})$ agree to within a few tenths of a kcal mol⁻¹ for both SH and CH₃S. The reported uncertainties in $\Delta H_{f,298}^\circ(\text{R,S})$ represent 2 σ estimates of absolute accuracy; since the 2 σ error estimates for the individual second and third law determinations are significantly larger than the deviation of the two determinations from their mean, we take the larger of the (second and third law) error estimates to be the error estimate for the mean. In the case of SH, we increase the uncertainty by an additional 0.1 kcal mol⁻¹ to account for the fact that reaction -1 could have a small but not negligible channel forming Br(²P_{1/2}) (see above). Our estimated uncertainties in $\Delta H_{f,298}^\circ(\text{R,S})$ of 0.44-0.72 kcal mol⁻¹ are substantially smaller than those reported previously (Table VIII). The SH or CH₃S heat of formation represents the least well-known parameter required for evaluation of a number of bond dissociation energies (BDEs); in Table IX we give values for these BDEs derived using our reported values for $\Delta H_{f,298}^\circ(\text{R,S})$ in conjunction with the other heats of formation given in Table VIII. For consistency, we employ the JANAF⁵⁰ value of 34.82 ± 0.19 kcal mol⁻¹ for $\Delta H_{f,298}^\circ(\text{CH}_3)$ to derive H₃C-SH, H₃C-S, and H₃C-SCH₃ bond strengths. It should be pointed out, however, that combining our recent measurement of the CH₃ + HBr rate coefficient with the literature value for the

Br + CH₃ rate coefficient leads to a value of 35.3 ± 0.5 kcal mol⁻¹ for $\Delta H_{f,298}^\circ(\text{CH}_3)$;²⁴ bond strengths derived using this value for the methyl heat of formation are given in parentheses in Table IX.

Values for $\Delta H_{f,298}^\circ(\text{SH})$ reported in this study are compared with literature values in Table VIII. The current JANAF recommendations⁵⁰ are based on measurements of the SH ionization potential^{54,55} and the appearance potential of SH⁺ from photoionization of H₂S.⁵⁶ Hwang and Benson have obtained a value for $\Delta H_{f,298}^\circ(\text{SH})$ based on a study of the I₂ + H₂S reaction at 555-595 K;⁵⁷ derivation of $\Delta H_{f,298}^\circ(\text{SH})$ from their kinetic data required the assumption that the activation energy for the SH + HI reaction is 1 ± 1 kcal mol⁻¹. A value for $\Delta H_{f,0}^\circ(\text{SH})$ has recently been obtained by Nourbakhsh et al. based on time-of-flight measurements of CH₃ and SH photofragments from 193-nm photodissociation of CH₃SH in a supersonic molecular beam.⁵⁸ Within combined uncertainties, the results reported in this study agree with all three literature values mentioned above. However, the error limits in the present study are somewhat smaller than those reported previously.

Values for $\Delta H_{f,298}^\circ(\text{CH}_3\text{S})$ reported in this study are compared with literature values in Table VIII. An early determination of $\Delta H_{f,298}^\circ(\text{CH}_3\text{S})$, reported by Colussi and Benson,⁵⁹ involved studying the kinetics of benzylmethyl sulfide pyrolysis; their data analysis required knowledge of the benzyl radical heat of formation. A number of subsequent evaluations of $\Delta H_{f,298}^\circ(\text{CH}_3\text{S})$ have appeared in the literature^{28,60,61} which involve reevaluation of Colussi and Benson's results based on different assumed values for $\Delta H_{f,298}^\circ(\text{benzyl})$; the recommendation of Lias et al.,²⁸ which shows the best agreement with our results, is based on an assumed benzyl heat of formation of 49 kcal mol⁻¹, as recommended by Tsang.⁶² Janousek et al.⁶³ have measured the electron affinity of CH₃S and combined their result with gas-phase acidity data for CH₃SH⁶⁴ to derive a value for $\Delta H_{f,298}^\circ(\text{CH}_3\text{S})$ which agrees quite well with our findings. Shum and Benson²⁰ have studied the kinetics of the I₂ + CH₃SH reaction over the temperature range 476-604 K and obtain a lower limit value for $\Delta H_{f,298}^\circ(\text{CH}_3\text{S})$ which is consistent with our findings. Hence, the value for $\Delta H_{f,298}^\circ(\text{CH}_3\text{S})$ which we obtain from kinetics studies of reactions 2 and -2 seems to be consistent with (but more precise than) most earlier work, although uncertainties in the heat of formation of benzyl radical^{61,62} somewhat hinders the comparison. However, an interesting discrepancy exists between our results and the recent molecular beam photofragmentation studies of Nourbakhsh et al.^{58,65,66} These authors have obtained three independent measurements of $\Delta H_{f,0}^\circ(\text{CH}_3\text{S})$ based on time-of-flight measurements of photofragments from 193-nm photodissociation of CH₃SH,⁵⁸ CH₃SSCH₃,⁶⁵ and CH₃SCH₃,⁶⁶ they report values for $\Delta H_{f,0}^\circ(\text{CH}_3\text{S})$ (with uncertainties of 1.5-2 kcal mol⁻¹) which are all 3-4

- (54) Morrow, B. A. *Can. J. Phys.* 1966, 44, 2447.
 (55) Palmer, T. F.; Lossing, F. P. *J. Am. Chem. Soc.* 1962, 84, 4661.
 (56) Dibeler, V. H.; Liston, S. K. *J. Chem. Phys.* 1968, 49, 482.
 (57) Hwang, R. J.; Benson, S. W. *Int. J. Chem. Kinet.* 1979, 11, 579.
 (58) Nourbakhsh, S.; Norwood, K.; Yin, H.-M.; Liao, C.-L.; Ng, C. Y. *J. Chem. Phys.* 1991, 95, 946.
 (59) Colussi, A. J.; Benson, S. W. *Int. J. Chem. Kinet.* 1977, 9, 295.
 (60) Rossi, M.; Golden, D. M. *J. Am. Chem. Soc.* 1979, 101, 1230.
 (61) McMillen, D. F.; Golden, D. M. *Annu. Rev. Phys. Chem.* 1982, 33, 493.
 (62) Tsang, W. In *Shock Tubes in Chemistry*; Lifshitz, A., Ed.; Dekker: New York, 1981.
 (63) Janousek, B. K.; Reed, K. J.; Brauman, J. I. *J. Am. Chem. Soc.* 1980, 102, 3125.
 (64) Bartmess, J. E.; McIver, R. T., Jr. In *Gas Phase Ion Chemistry*; Bowers, M. T., Ed.; Academic Press: New York, 1979; Vol. 2.
 (65) Nourbakhsh, S.; Liao, C.-L.; Ng, C. Y. *J. Chem. Phys.* 1990, 92, 6587.
 (66) Nourbakhsh, S.; Norwood, K.; Yin, H.-M.; Liao, C.-L.; Ng, C. Y. *J. Chem. Phys.* 1991, 95, 5014.
 (67) Wine, P. H.; Thompson, R. J.; Semmes, D. H. *Int. J. Chem. Kinet.* 1984, 16, 1623.
 (68) DeMore, W. B.; Sander, S. P.; Golden, D. M.; Molina, M. J.; Hampson, R. F.; Kurylo, M. J.; Howard, C. J.; Ravishankara, A. R. *Chemical Kinetics and Photochemical Data for Use in Stratospheric Modeling*; JPL Publication 90-1; Jet Propulsion Laboratory, Pasadena, CA, 1990.

kcal mol⁻¹ higher than the value of 31.44 ± 0.54 kcal mol⁻¹ obtained in this study. The error in our determination of k_2/k_{-2} needed to rationalize a 3–4 kcal mol⁻¹ increase in $\Delta H_{f,0}(\text{CH}_3\text{S})$ is a factor of several hundred in the direction where k_2 would have to be slower or k_{-2} would have to be faster; errors of this magnitude seem unlikely.

Summary

Time-resolved resonance fluorescence detection of $\text{Br}(^2\text{P}_{3/2})$ disappearance following 266-nm laser flash photolysis of $\text{CF}_2\text{Br}_2/\text{H}_2\text{S}/\text{H}_2/\text{N}_2$, $\text{CF}_2\text{Br}_2/\text{CH}_3\text{SH}/\text{H}_2/\text{N}_2$, $\text{Cl}_2\text{CO}/\text{H}_2\text{S}/\text{HBr}/\text{N}_2$, and $\text{CH}_3\text{SSCH}_3/\text{HBr}/\text{H}_2/\text{N}_2$ mixtures has been employed to study the kinetics of reactions 1, 2, -1, and -2 as a function of temperature. In units of 10^{-12} cm³ molecule⁻¹ s⁻¹, Arrhenius expressions which describe our results are $k_1 = (14.2 \pm 3.4) \exp[(-2752 \pm 90)/T]$, $k_{-1} = (4.40 \pm 0.92) \exp[(-971 \pm 73)/T]$, $k_2 = (9.24 \pm 1.15) \exp[(-386 \pm 41)/T]$, and $k_{-2} = (1.46 \pm 0.21) \exp[(-399 \pm 41)/T]$. By examining $\text{Br}(^2\text{P}_{3/2})$ equilibrium kinetics following 355-nm laser flash photolysis of $\text{Br}_2/\text{CH}_3\text{SH}/\text{H}_2/\text{N}_2$ mixtures, a 298 K rate coefficient of $(1.7 \pm 0.5) \times 10^{-10}$ cm³ molecule⁻¹ s⁻¹ has been obtained for the $\text{CH}_3\text{S} + \text{Br}_2$ reaction. To our knowledge, these are the first kinetic data reported for each of the reactions studied. Comparison of A factors and activation energies for reactions 1, -1, 2, and -2 with known kinetic parameters for other radical + H_2S , CH_3SH , HBr hydrogen-transfer reactions suggests that both thermochemistry and electronic properties (i.e., $\text{IP} - \text{EA}$) exert important influences on observed reaction rates.

Second and third law analyses of the equilibrium data, i.e., k_1/k_{-1} and k_2/k_{-2} , have been employed to obtain the enthalpy changes associated with reactions 1 and 2. At 298 K, reaction 1 is endothermic by 3.64 kcal mol⁻¹ while reaction 2 is exothermic by 0.14 kcal mol⁻¹. Combining the experimentally determined enthalpies of reaction with the well-known heats of formation of Br , HBr , H_2S , and CH_3SH gives the following heats of formation for RS radicals in units of kcal mol⁻¹: $\Delta H_{f,0}^\circ(\text{SH}) = 34.07 \pm 0.72$, $\Delta H_{f,298}^\circ(\text{SH}) = 34.18 \pm 0.68$, $\Delta H_{f,0}^\circ(\text{CH}_3\text{S}) = 31.44 \pm 0.54$; $\Delta H_{f,298}^\circ(\text{CH}_3\text{S}) = 29.78 \pm 0.44$; errors are 2σ and represent estimates of absolute accuracy. The SH heat of formation determined from our data agrees well with literature values but has reduced error limits compared to other available values. The CH_3S heat of formation determined from our data is near the low end of the range of previous estimates and is 3–4 kcal mol⁻¹ lower than values derived from recent molecular beam photofragmentation studies.^{28,64,65}

Acknowledgment. We thank Professor C. Y. Ng and Dr. A. R. Ravishankara for communicating their results to us prior to publication, Drs. D. M. Golden and S. A. Safron for helpful discussions, Dr. H. Berresheim for carrying out the GC analyses, and J. M. Cronkhite for assistance with some of the experiments. We also thank the two anonymous reviewers for a number of helpful comments. This work was supported by grants ATM-8802386 and ATM-9104807 from the National Science Foundation and grant NAGW-1001 from the National Aeronautics and Space Administration.

PROCEEDINGS REPRINT

EUROPTO*
SERIES

Reprinted from

***Optical Methods in
Atmospheric Chemistry***

22-24 June 1992
Berlin, FRG



Volume 1715

©1993 by the Society of Photo-Optical Instrumentation Engineers
Box 10, Bellingham, Washington 98227 USA. Telephone 206/676-3290.

omit
93A 51502

Laser flash photolysis studies of atmospheric free radical chemistry using optical diagnostic techniques

Paul H. Wine, J. Michael Nicovich, Anthony J. Hynes, Robert E. Stickel,
R. Peyton Thorn, Mian Chin, Jeffrey A. Cronkhite,
Christie J. Shackelford, Zhizhong Zhao, Edward P. Daykin,
Cornelius A. van Dijk, Shouzhi Wang, and Jill V. Steidl

Physical Sciences Laboratory, Georgia Tech Research Institute,
Georgia Institute of Technology, Atlanta, Georgia 30332

ABSTRACT

Some recent studies carried out in our laboratory are described where laser flash photolytic production of reactant free radicals has been combined with reactant and/or product detection using time-resolved optical techniques to investigate the kinetics and mechanisms of important atmospheric chemical reactions. Discussed are (1) a study of the radical-radical reaction $O + BrO \rightarrow Br + O_2$ where two photolysis lasers are employed to prepare the reaction mixture and where the reactants O and BrO are monitored simultaneously using atomic resonance fluorescence to detect O and multipass UV absorption to detect BrO; (2) a study of the reaction of atomic chlorine with dimethylsulfide (CH_3SCH_3) where atomic resonance fluorescence detection of Cl is employed to elucidate the kinetics and tunable diode laser absorption spectroscopy is employed to investigate the HCl product yield; and (3) a study of the aqueous phase chemistry of Cl_2^- radicals where longpath UV absorption spectroscopy is employed to investigate the kinetics of the $Cl_2^- + H_2O$ reaction.

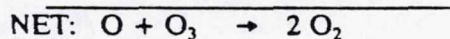
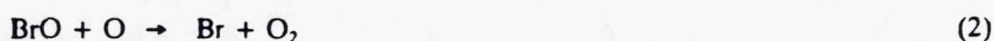
1. INTRODUCTION

The combination of reactant radical production by laser flash photolysis (LFP) with reactant and product detection by time-resolved optical techniques (TROT) has proven to be a powerful method for investigating the kinetics and mechanisms of important atmospheric chemical reactions. While not without limitations, this approach offers several advantages over other commonly used techniques. First, studies can be carried out which employ both short reaction times and low radical concentrations, thus minimizing interferences from secondary reactions. Secondly, in gas phase studies a wide range of pressure, covering more than five orders of magnitude for some detection techniques (0.001 - 200 atmospheres), is experimentally accessible. Finally, and probably most importantly, the chemistry of interest occurs in complete isolation from reactor surfaces, so interferences from heterogeneous reactions can be completely avoided.

In this paper some recent LFP-TROT studies conducted in our laboratory are described. These include a study of the kinetics of the radical-radical reaction $O + BrO \rightarrow Br + O_2$, a kinetic and mechanistic study of the $Cl + CH_3SCH_3$ reaction, and a study of the potentially important cloudwater reaction of Cl_2^- radicals with H_2O where very sensitive detection of $Cl_2^-(aq)$ by multipass UV absorption spectroscopy provides information not attainable using less sensitive detection techniques.

2. THE O + BrO REACTION

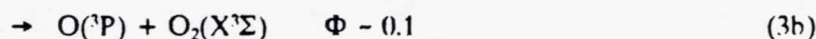
The radical-radical reaction of ground state atomic oxygen ($O \equiv O(^3P)$) with bromine monoxide is the rate-determining step in a potentially important mid-stratospheric ozone destruction cycle:



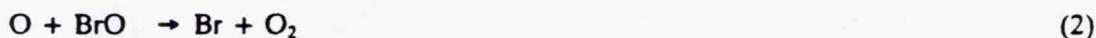
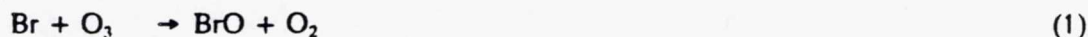
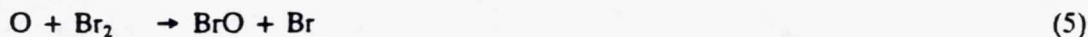
The only value for the BrO + O rate coefficient reported in the literature, $k_2(298 \text{ K}) = (2.5^{+2.5}_{-1.5}) \times 10^{-11} \text{ cm}^3 \text{ molecule}^{-1} \text{ s}^{-1}$, is based on measurements of O atom consumption rates and Br atom production rates observed in a study which was actually designed to measure the O + Br₂ rate coefficient.¹

Traditionally, most studies of radical-radical reaction kinetics have employed flow tube techniques.² Advantages of the flow tube method which make it well-suited for studying radical-radical reactions include the following: (1) absolute concentrations of unstable chemical species can be readily determined via chemical titration; (2) unstable reactants can be generated in spatially separated regions, thus allowing improved control over potential chemical interferences; and (3) multiple detection axes can be readily employed. Our study of O + BrO kinetics attempts to preserve the advantages of the flash photolysis method (discussed in the introduction), while also incorporating some of the advantages of the flow tube method. The experimental approach is an improved version of one we have employed previously to study the kinetics of the O + HO₂^{3,4} and O + ClO⁵ reactions. Despite improvements in experimental sophistication, however, the O + BrO study has proven quite challenging due to difficulties in controlling interferences from unwanted side reactions.

To study O + BrO kinetics, a reaction mixture containing O₃, Br₂, and N₂ is subjected to 248 nm laser flash photolysis using a KrF excimer laser. Concentrations are (5-30) × 10¹⁴ O₃ per cm³, (3-20) × 10¹² Br₂ per cm³, and 25-150 Torr N₂. The laser fluence is sufficient to produce O atoms in 5-10 fold excess over Br₂:



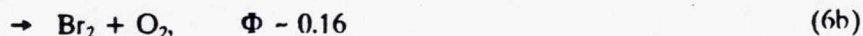
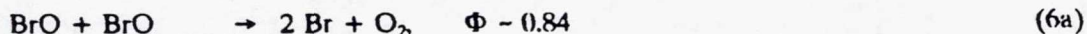
Ozone photolysis at 248 nm produces primarily electronically excited singlet products.⁶ However, at the N₂ levels employed in the experiment, relaxation of O(¹D) to ground state O(³P)(≡O) atoms occurs on a sub-microsecond time scale.⁷ Subsequent to O(¹D) relaxation, O atoms titrate Br₂ to BrO and the catalytic cycle defined by reactions (1) and (2) converts all remaining O atoms to O₂:



The O + BrO reaction is sufficiently exothermic to generate atomic bromine in the excited spin-orbit electronic state Br(²P_{1/2}). However, relaxation to the ground electronic state, Br(²P_{3/2}), via collisions with N₂ is rapid compared to the time scale for bromine atom reaction.⁸ The kinetics of reactions (1) and (5) are well established, having been investigated recently in our laboratory^{9,10} as well as elsewhere.¹¹

If the chemistry in the O₃/Br₂/N₂ photolysis system were completely described by reactions (1) - (5), then we could evaluate the O + BrO rate coefficient based on measurements of the O atom decay rate at long

times after the laser flash, i.e., when $[\text{Br}_2] \rightarrow 0$. However, there are complicating side reactions which must be considered:



The kinetics of reactions (6a), (6b), and (7) are reasonably well-established.¹¹ Reaction (6b) results in regeneration of some Br_2 on the time scale for O decay. The relatively slow reaction (7) prevents complete decay of O atoms. Instead, a near-steady-state situation is established at long time after the excimer laser flash where O production via reaction (7) and O loss via reactions (2) and (5) occur at similar rates; as a result, quantitative information about the O + BrO rate coefficient is not easily obtained from the oxygen atom temporal profile. To circumvent the above complications, we employ a second photolysis laser. After the near-steady state oxygen atom concentration is established, 532 nm radiation (Nd:Yag laser, 2nd harmonic, 7 ns pulsewidth) is employed to photolyze a small fraction of the remaining O_3 , thus perturbing the steady state O atom concentration. Computer simulations show that relaxation of the O atom concentration back to steady state is dominated by the O + BrO reaction.

A schematic diagram of the apparatus for the O + BrO kinetics study is shown in Figure 1. A "slow flow" configuration is employed such that the reaction mixture is essentially static on the time scale of the experiment (10-50 milliseconds) but is completely replaced during the 5-10 seconds between excimer laser flashes. The reaction cell is jacketed to allow control of temperature by flowing a cooled or heated fluid through the outer jacket (which is not shown in Figure 1). Ground state oxygen atoms are monitored by time-resolved atomic resonance fluorescence spectroscopy¹⁰ while BrO radicals are monitored by time-resolved UV absorption spectroscopy at 338.3 nm, the peak of the strongest band in the BrO A-X spectrum;¹² details of our application of the long path absorption technique are given elsewhere.^{13,14} A dual channel signal averager simultaneously accumulates the O atom fluorescence signal in the multichannel scaling mode (i.e., photon counting techniques are employed to process the fluorescence signal) and the BrO absorption signal in the peak height analysis mode. A segmented aperture optical integrator is employed to make the excimer laser photolysis beam spatially uniform. Hence, the excimer laser photolysis flash produces a spatially uniform concentration of oxygen atoms. Several hundred flashes are typically averaged to obtain the desired O and BrO temporal profiles. The shot-to-shot stability of the excimer laser is about $\pm 10\%$. Because experimental conditions are such that $[\text{O}]_0 > [\text{Br}_2]_0$, ten percent fluctuations in excimer laser fluence result in very small shot-to-shot variations in $[\text{BrO}]_0$.

Results from a typical experiment are summarized in Figures 2-4; the experimental conditions employed to obtain the results in Figures 2-4 are as follows: $T = 298\text{K}$; $P = 50 \text{ Torr}$; $[\text{O}_3]_0 = 7.68 \times 10^{14} \text{ per cm}^3$; $[\text{Br}_2]_0 = 1.56 \times 10^{13} \text{ per cm}^3$; $[\text{O}]_0 = 8.6 \times 10^{13} \text{ per cm}^3$; time delay between the excimer and Nd:Yag laser pulses = 0.025 seconds. Observed O and BrO temporal profiles are shown in Figure 2. At short times when [O] is very high, the fluorescence signal is reduced due to radiation trapping effects; hence, the fluorescence signal is proportional to the O atom concentration only after the signal has decayed significantly from its peak value. Computer simulations of the O, BrO, and Br_2 temporal profiles are shown in Figure 3. The simulations were obtained by numerical integration of the rate equations assuming that the chemistry governing the desired temporal profiles is described completely by reactions (1), (2), (5), (6), and (7), and using the best available kinetic data from the literature;⁹⁻¹¹ since $[\text{BrO}]$ values are based (at least in part) on the simulations, an iterative procedure was required in order to allow the value of k_5 , determined from our data to be used in the simulations. Comparison of simulated O and BrO temporal profiles with experiment shows qualitative but not quantitative agreement. The simulated O decay to

steady state is somewhat faster than that observed experimentally, the simulated BrO appearance rate is a little slower than that observed experimentally, and the simulated BrO decay is a little faster than that observed experimentally. Typically, we find that the simulated BrO concentration at the time the Nd:Yag laser fires is about 10% lower than the concentration derived from the measured BrO absorbance using the best available literature value for the BrO absorption cross section at 338.3 nm^2 to convert absorbance to concentration. The difference between observed and simulated O and BrO temporal profiles could indicate that the chemistry in the model is incomplete or that one or more rate coefficients for reactions (1), (2), (6), and/or (7) are inaccurate. Another possibility which may account for all observations is the production of electronically excited oxygen, $\text{O}_2(^1\Delta)$, as a product of the O + BrO reaction. The oxygen atom fluorescence data around the time that the 532 nm laser fires is shown in Figure 4. The solid "base line" is obtained from fitting the data in the -10 to -0.1 ms and 7 to 14 ms time intervals to a double exponential decay function. The relaxation of the O atom population generated by the 532 nm laser is found to be exponential; for the data shown in Figure 4, the relaxation time (τ) is 950 microseconds. A plot of k' ($\equiv \tau^{-1}$), the pseudo-first order rate of O atom relaxation back to steady state following the 532 nm laser pulse, versus [BrO] is shown in Figure 5; the BrO concentrations are those obtained from the computer simulations of system chemistry. Also shown in Figure 5 is the k' versus [BrO] data corrected for the contribution to the O decay from the O + Br₂ reaction; in this case (which is typical of all pressures and temperatures examined) about 10% of the oxygen atom decay is attributable to the O + Br₂ reaction. The slope of the corrected k' versus [BrO] plot gives a rate coefficient of $4.8 \times 10^{11} \text{ cm}^3 \text{ molecule}^{-1} \text{ s}^{-1}$ for the O + BrO reaction at 298 K in 50 Torr N₂.

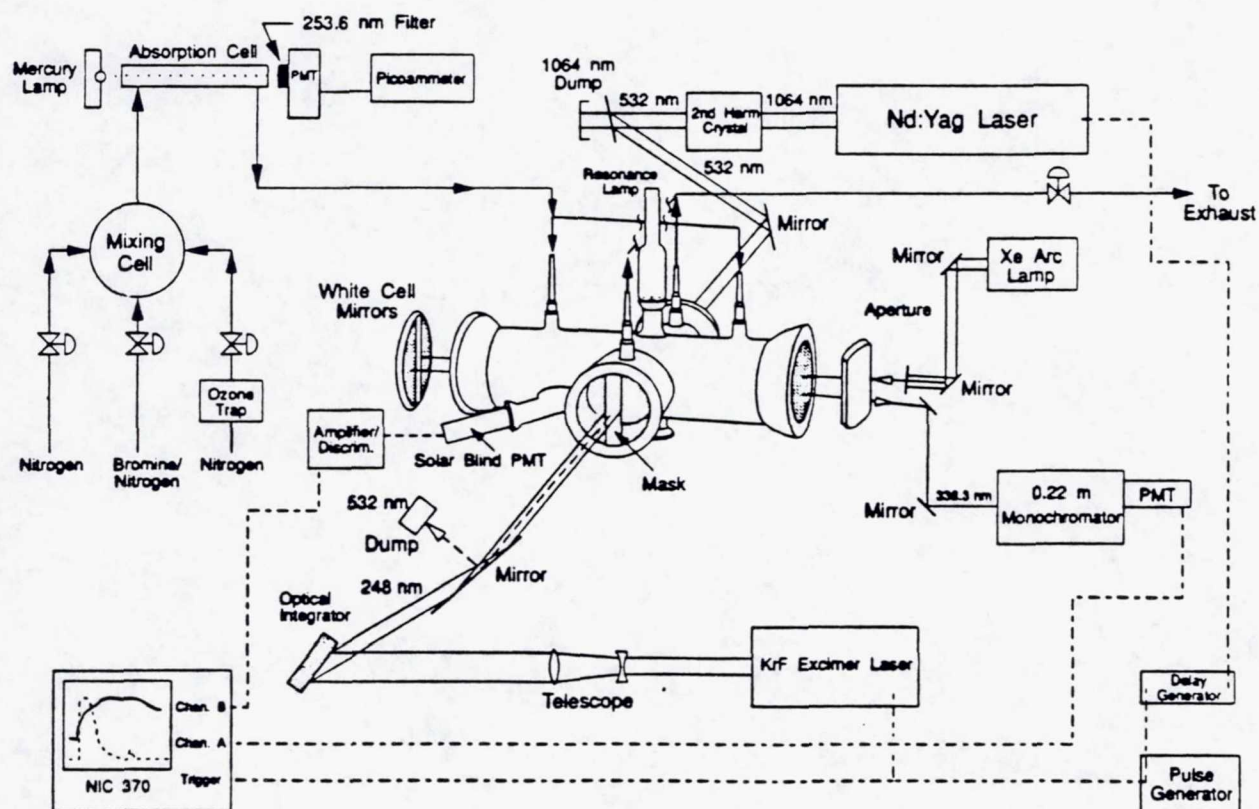


Fig. 1. Apparatus for the O + BrO kinetics study.

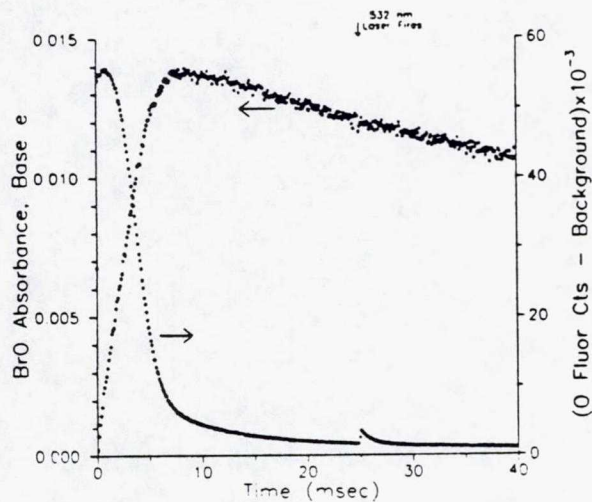


Fig. 2. Typical O and BrO temporal profiles. $T = 298 \text{ K}$, $P = 50 \text{ Torr}$. $[\text{O}_3]_0$, $[\text{O}]_0$, and $[\text{Br}_2]_0$ in units of $10^{13} \text{ cm}^{-3} = 76.8, 8.6,$ and 1.56 , respectively.

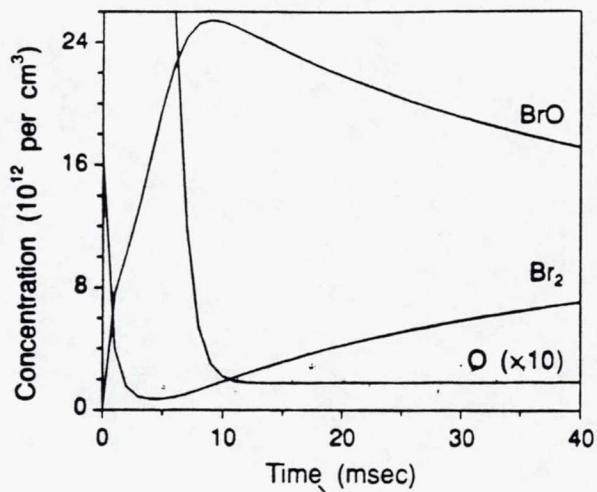


Fig. 3. Computer simulation of temporal profiles. Experimental conditions same as Fig. 2, but no 532 nm laser pulse.

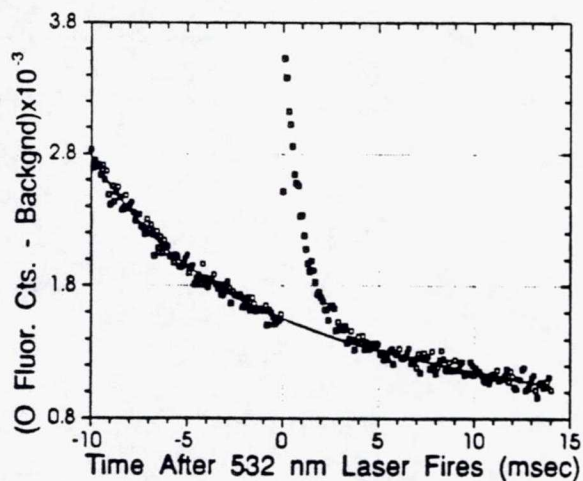


Fig. 4. O atom temporal profile around the time that the 532 nm laser fires; same data as in Fig. 2 but with scales expanded.

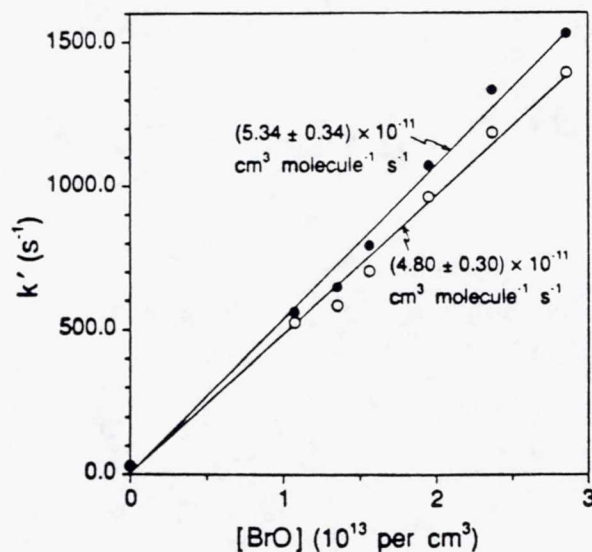
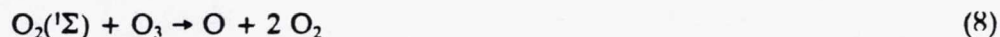


Fig. 5. Plots of k' versus $[\text{BrO}]$. $T = 298 \text{ K}$, $P = 50 \text{ Torr}$. Open circles are corrected for the $\text{O} + \text{Br}_2$ contribution.

We have investigated the kinetics of the O + BrO reaction at 298 K over the pressure range 25 - 150 Torr and at 50 Torr pressure over the temperature range 233 - 328 K. We find that $k_5(298 \text{ K}) = (4.4 \pm 0.6) \times 10^{-11} \text{ cm}^3 \text{ molecule}^{-1} \text{ s}^{-1}$ and that $k_5(T) = (2.4 \pm 0.4) \times 10^{-11} \exp [(190 \pm 100)/T] \text{ cm}^3 \text{ molecule}^{-1} \text{ s}^{-1}$, i.e., k_5 increases slightly with decreasing temperature; "negative activation energies" are often observed for radical-radical reactions because the potential energy surface typically contains a minimum corresponding to a bound intermediate complex (BrOO in the case of reaction (5)).

At this time the O + BrO kinetic results reported above must be considered preliminary. In particular, the potential importance of $\text{O}_2(^1\Delta)$ or $\text{O}_2(^1\Sigma)$ production from reaction (5) needs to be addressed. As mentioned above, a high yield of $\text{O}_2(^1\Delta)$ from reaction (5) could account for important differences between observed and simulated O and BrO temporal profiles; however, $\text{O}_2(^1\Delta)$ production could have only a small effect on the simulated BrO concentration at the time the 532 nm laser fires and, therefore, would not significantly alter reported values for k_5 . Production of $\text{O}_2(^1\Sigma)$ as a product of the O + BrO reaction is potentially a more serious problem because the $\text{O}_2(^1\Sigma) + \text{O}_3$ reaction is several orders of magnitude faster than the $\text{O}_2(^1\Delta) + \text{O}_3$ reaction.¹⁵



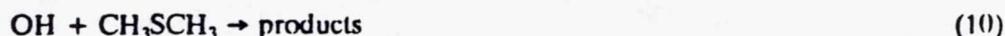
Hence, any O atoms which reacted with BrO to form $\text{O}_2(^1\Sigma)$ would immediately be regenerated via reaction (8). Since efficient $\text{O}_2(^1\Sigma)$ quenchers which are also chemically inert in the $\text{O}_3/\text{Br}_2/\text{N}_2$ photolysis system do not seem to be available, direct evidence for $\text{O}_2(^1\Sigma)$ production will require observation of its infrared emission in an experimental system where O_3 is not present. Adiabatic correlation arguments¹⁶ as well as statistical arguments (i.e., arguments based on the assumption that all sets of energetically accessible product quantum states are equally probable) suggest that the $\text{O}_2(^1\Sigma)$ yield from reaction (5) should be very small; however, experimental confirmation that this is the case would be highly desirable. Our results indicate that the O + BrO reaction is considerably faster than previously thought, even though we are observing only those reaction channels which produce O_2 in the $\text{X}^3\Sigma$ or $^1\Delta$ states.

3. KINETIC AND MECHANISTIC STUDY OF THE Cl + CH₃SCH₃ REACTION

It has recently been suggested that significant chlorine concentrations may be present in the marine boundary layer, possibly as a result of ClNO₂ or Cl₂ generation via reactions on surfaces of marine aerosol particles.¹⁶ A recent competitive kinetics study of reaction (9) at 298 K in one atmosphere of air¹⁷ suggests that this reaction is extraordinarily fast, i.e., $k_9(298 \text{ K}) = 3.2 \times 10^{10} \text{ cm}^3 \text{ molecule}^{-1} \text{ s}^{-1}$.



Combining the above result with the findings of our study of the kinetics and mechanism of the OH + CH₃SCH₃ (DMS, dimethylsulfide) reaction¹⁸ suggests that $k_9/k_{10} \approx 50$ at 298 K and one atmosphere of air.



DMS is the dominant reduced sulfur species in the marine boundary layer and its primary removal mechanism from the atmosphere is thought to be reaction with OH. Hence, if Cl concentrations in the marine boundary layer are as large as 10⁴ atoms per cm³, and if reaction (9) is as fast as the available kinetic data¹⁷ suggest, then the Cl + DMS reaction could be very important in marine atmospheric chemistry.

The above considerations have led us to carry out a detailed study of the kinetics and mechanism of the Cl + DMS reaction. Laser flash photolysis of Cl₂CO (phosgene) at 266 nm was combined with time-

resolved atomic resonance fluorescence detection of chlorine atoms to measure values for k , as a function of temperature and pressure. A complete description of the experimental approach can be found in a recent publication describing our study of the complex $\text{Cl} + \text{CS}_2$ reaction.¹⁹ All experiments were carried out under pseudo-first order conditions with DMS in large excess over chlorine atoms. Observed chlorine atom decays were exponential and increased linearly as a function of $[\text{DMS}]$, as would be expected if chlorine atom removal is dominated by reaction with DMS. The bimolecular rate coefficients of interest, $k_0(P,T)$, are obtained from the slopes of plots of k' , the pseudo-first order decay rate, versus DMS concentration; measured rate coefficients at 239 K, 297 K, and 421 K are plotted as a function of pressure in Figure 6. Our results confirm that reaction (9) occurs on virtually every Cl-DMS encounter. The reaction rate is found to increase with decreasing temperature as would be expected for a very fast reaction whose rate is determined by the magnitude of long range attractive forces between the reactants. The surprising aspect of the data in Figure 6 is our observation of a clear pressure dependence for k_0 , at least at temperatures of 297 K and below. Reaction (9) appears to occur via both pressure-independent and pressure-dependent pathways; the pressure-dependent pathway must involve collisional stabilization of a $(\text{CH}_3)_2\text{S}\text{-Cl}$ adduct.

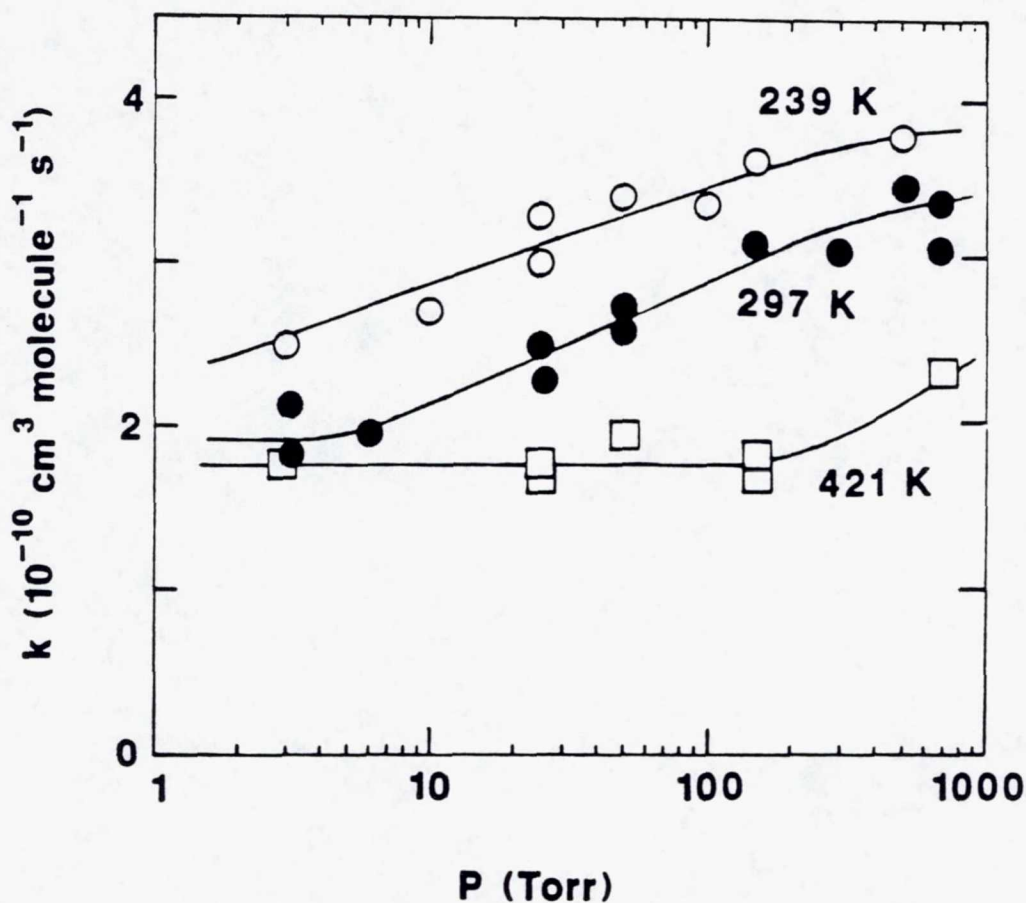


Fig. 6. Rate constants for the $\text{Cl} + \text{DMS}$ reaction as a function of temperature and pressure.

To gain further insight into the mechanism for reaction (9), we have carried out additional experiments where laser flash photolytic production of Cl (via 248 nm photolysis of phosgene) has been coupled with tunable diode laser absorption spectroscopy (TDLAS) to measure the HCl product yield at 297 K as a function of pressure. A schematic of the LFP-TDLAS apparatus is shown in Figure 7. The excimer laser photolysis beam and the diode laser probe beam traverse the one-meter-long reaction cell coaxially; the beams are combined and separated using dichroic optics. The experiments are carried out under slow flow conditions as described above for the O + BrO study. An absorption cell is positioned in the flow system upstream from the reaction cell to allow UV photometric monitoring of the Cl₂CO concentration. Other important components of the apparatus are a He/Ne alignment laser, a liquid helium closed cycle refrigerator which cools the diode laser housing, electronics for controlling the diode laser frequency via temperature or current tuning, an infrared monochromator for diode laser mode isolation, and infrared detectors with associated electronics for monitoring the transmitted intensities of the probe and reference beams. To obtain the HCl yield we carry out back-to-back experiments where the photolytically produced Cl reacts with DMS, then with ethane (C₂H₆); the yield of HCl from the Cl + C₂H₆ reaction is known to be unity. About 1 Torr of CO₂ is added to the reaction mixture to facilitate rapid relaxation of any HCl which is formed in the v = 1 level. Typical data, obtained in 10 Torr N₂ buffer gas, are shown in Figure 8. It is clear from the data in Figure 8 that HCl is a major product of reaction (9). However, it is also clear that the HCl yield is less than unity. A plot of the HCl yield as a function of pressure is shown in Figure 9. The HCl yield approaches unity as P → 0, but decreases with increasing pressure.

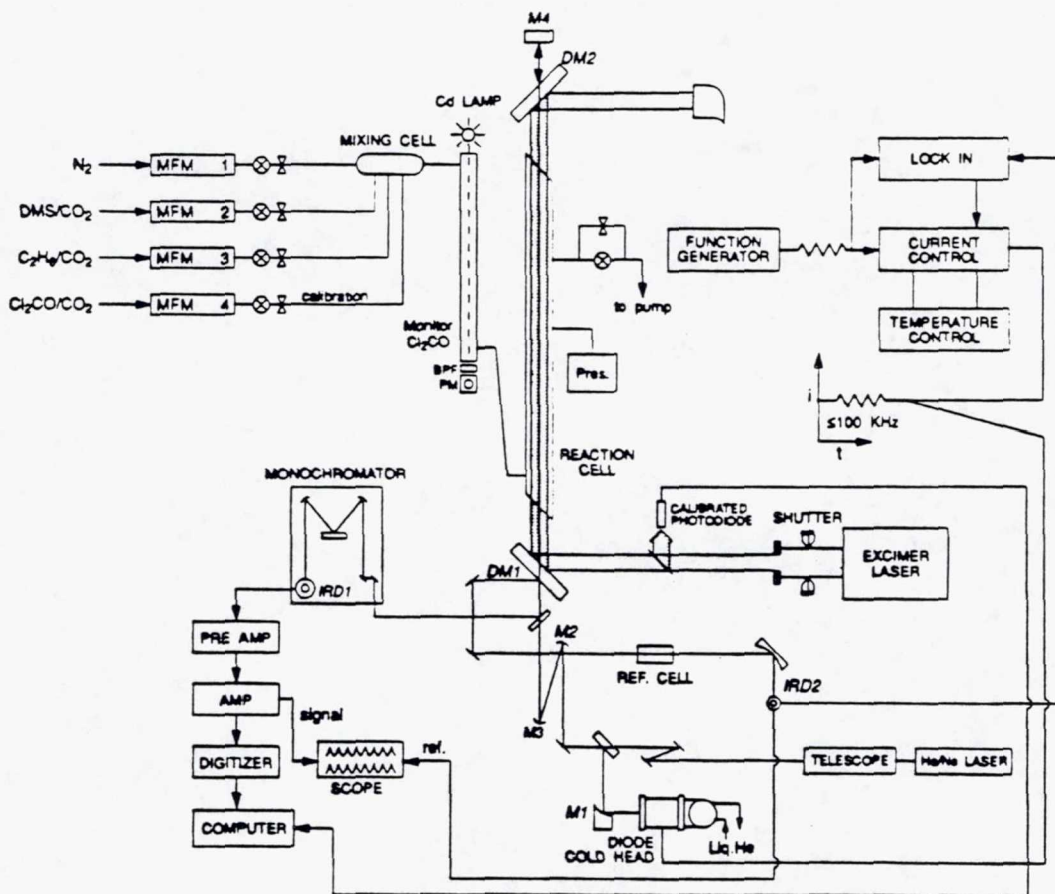


Fig. 7. Apparatus for LFP-TDLAS measurements of the HCl yield from the Cl + DMS reaction.

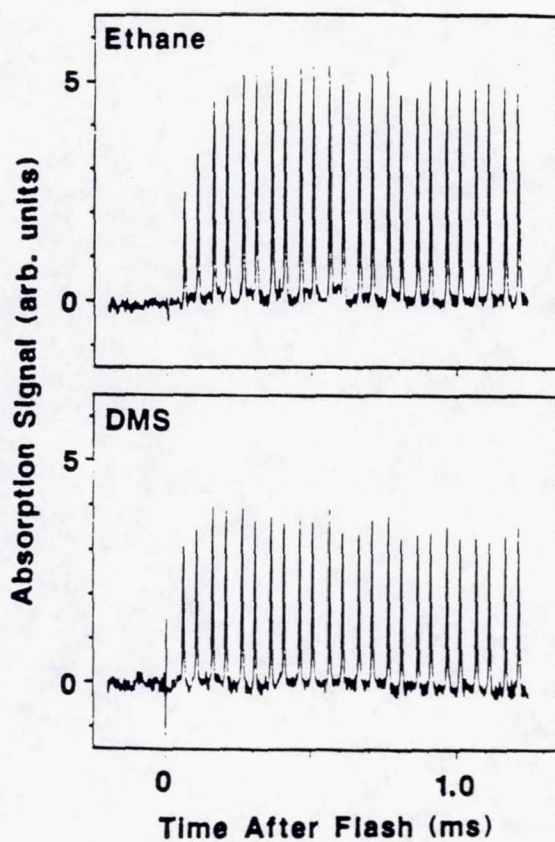


Fig. 8. Typical HCl yield data. $P = 10$ Torr, $T = 298$ K. Ethane and DMS concentrations in units of 10^{14} cm^{-3} are 1.5 and 1.1, respectively. The diode laser is swept back and forth through an HCl absorption feature, thus obtaining a concentration measurement every $50 \mu\text{s}$.

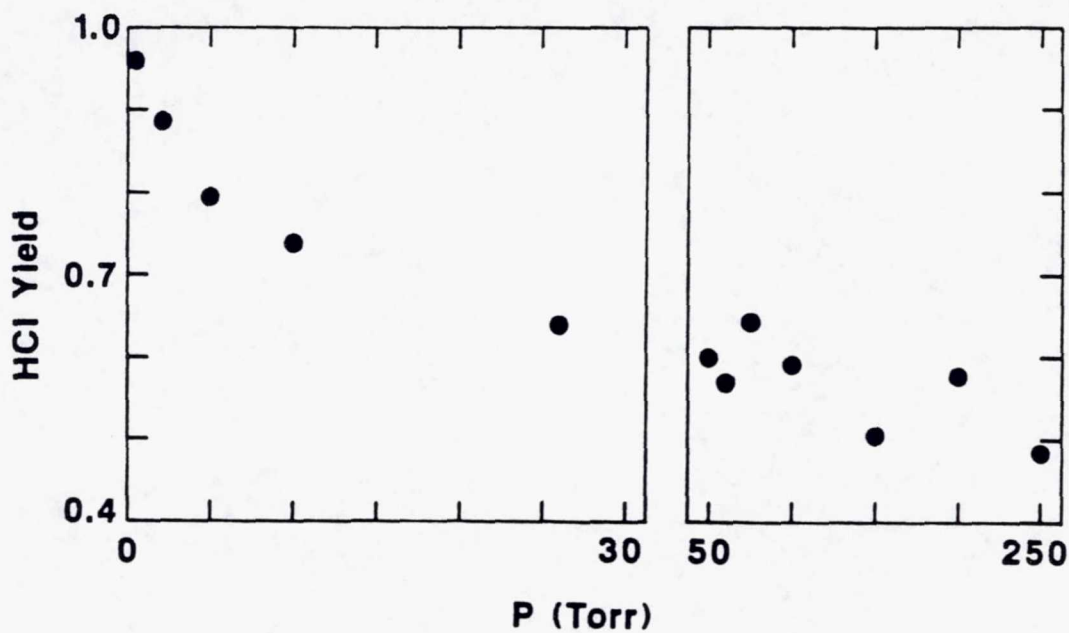
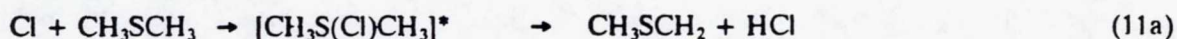


Fig. 9. Pressure dependence of the HCl yield from the $\text{Cl} + \text{DMS}$ reaction.

Possible reaction channels for the Cl + DMS reaction include the following:



Comparison of the kinetic data and the HCl yield data strongly suggests that reaction (11a) is the dominant channel in the low pressure limit, but that reaction (11d) becomes competitive at higher pressures. Whether the adduct formed via reaction (11d) is stable on the time scale of our experiment, or decomposes to products other than HCl or Cl, remains to be determined.

4. LABORATORY STUDIES OF FREE RADICAL CHEMISTRY IN CLOUD WATER

Free radical reactions occurring in cloud water play a role in the generation of acid precipitation²⁰ and may affect gas phase concentrations of key species such as O₃, HO_x, and NO_x in the remote troposphere.²¹ In recent years we have developed a laser flash photolysis - long path absorption (LFP-LPA) technique for studying the kinetics of aqueous phase free radical reactions, and applied the technique to studies of potential importance in cloud chemistry.²²⁻²⁵ The improved sensitivity afforded by the LPA detection technique has allowed us to carry out kinetics studies employing much lower radical concentrations than have typically been employed in pulse radiolysis and/or flash photolysis studies; examples of results which could only be obtained because of this improved detection sensitivity include (1) our measurement of the rate coefficient for the slow SO₄⁻ + H₂O reaction²³ and (2) our demonstration that previous measurements of the SO₄⁻ + HSO₃⁻ rate coefficient had not (as had been suggested in the literature) been affected by secondary reactions which regenerate SO₄⁻.²⁴

In order to further improve the ultimate detection limit of our LFP-LPA apparatus, we have recently constructed a new reactor which is considerably longer than the reactor we employed in earlier studies.²²⁻²⁴ A cylindrical lens is employed to expand the excimer laser photolysis beam in the horizontal direction, thus allowing a 10 cm wide region of the reaction cell to be photolyzed. We typically employ 34 passes of the probe light through the reactor, giving an absorption pathlength of ~340 cm.

Chlorine radical chemistry initiated by, for example, pulse radiolysis of N₂O-saturated chloride solutions, is quite complex; the following three rapid equilibria are thought to be involved:²⁶



At relatively high [Cl⁻] and [H⁺], the radical pool in the above equilibria exist almost entirely as Cl₂⁻, a species which absorbs strongly in the near UV (ε_{max} = 8800 M⁻¹cm⁻¹, λ_{max} = 340 nm);²⁶ both HOCl⁻ and Cl also absorb in the near UV, but not as strongly as Cl₂⁻.^{26,27} A convenient method for generating chlorine radicals by flash photolysis is as follows:



$\text{S}_2\text{O}_8^{2-}$ can be photolyzed efficiently at the excimer laser wavelength 248 nm, and does not react at an appreciable rate with $\text{SO}_4^{\cdot -}$, OH, Cl, $\text{Cl}_2^{\cdot -}$, or $\text{HOCl}^{\cdot -}$. Reaction (16), which happens to be the dominant sink for chloride in cloud water,²⁴ is reasonably fast with $k_{16}(298 \text{ K}) = 2.6 \times 10^8 \text{ M}^{-1}\text{s}^{-1}$ in the limit of zero ionic strength.^{24,28}

In a recent study of chlorine radical chemistry initiated by reaction (16) McElroy²⁸ concludes that the $\text{Cl}_2^{\cdot -} + \text{H}_2\text{O}$ reaction proceeds at a rate of 1300 s^{-1} , a result which, if correct, has important implications for chlorine radical chemistry in cloud water.



We have tried to observe a first order decay of $\text{Cl}_2^{\cdot -}$ under conditions of high Cl^- (0.1 M) and low pH (1.1). These experiments were carried out using extremely low $\text{Cl}_2^{\cdot -}$ concentrations (in the nanomolar range) to minimize contributions from the $\text{Cl}_2^{\cdot -}$ self reaction; the $[\text{S}_2\text{O}_8^{2-}]$ and $[\text{SO}_4^{\cdot -}]$ employed in our study are about three orders of magnitude lower than employed by McElroy.²⁸ Typical data are shown in Figure 10. At very low radical concentrations, we observe decay rates slower than 10 s^{-1} which decrease with decreasing laser power at constant $[\text{S}_2\text{O}_8^{2-}]$; these observations suggest that even the very slow decays we observe are not due to reaction (17), but instead were due to a radical-radical reaction. It is possible (or even likely) that if reaction (17) occurs, the product is a radical species which would rapidly react to regenerate $\text{Cl}_2^{\cdot -}$, i.e., OH, Cl, or $\text{HOCl}^{\cdot -}$. Experiments are currently in progress to examine this possibility.

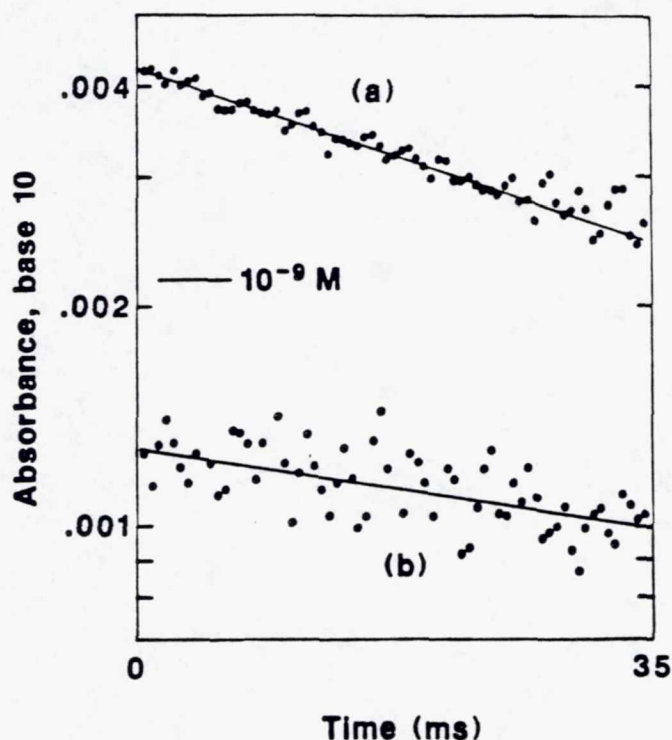


Fig. 10. $\text{Cl}_2^{\cdot -}$ temporal profiles observed following 248 nm laser flash photolysis of $10^{-5} \text{ M S}_2\text{O}_8^{2-}/0.1 \text{ M Cl}^-/0.08 \text{ M H}^+$. Higher laser power was employed to obtain (a). Best fit first order decay rates are (a) 15.8 s^{-1} and (b) 7.3 s^{-1} .

5. ACKNOWLEDGMENTS

The research described in this paper has been supported by the NASA Upper Atmosphere Research Program (grant NAGW-1001), the NSF Atmospheric Chemistry Program (grant ATM-9104807), the EPA Exploratory Research Program (grant R-816559), and the Georgia Tech Research Institute (internal grant E-8904-038).

6. REFERENCES

1. M. A. A. Clyne, P. B. Monkhouse, and L. W. Townsend, "Reactions of O(³P_J) Atoms with Halogens: The Rate Constants for the Elementary Reactions O + BrCl, O + Br₂, and O + Cl₂," *Int. J. Chem. Kinetics*, vol. VIII, pp. 425 - 449, May 1976.
2. see for example, C. J. Howard, "Kinetic Measurements Using Flow Tubes," *J. Phys. Chem.*, vol. 83, pp. 3 - 9, January 11, 1979.
3. A. R. Ravishankara, P. H. Wine, and J. M. Nicovich, "Pulsed Laser Photolysis Study of the Reaction Between O(³P) and HO₂," *J. Chem. Phys.*, vol. 78, pp. 6629 - 6639, June 1, 1983.
4. J. M. Nicovich and P. H. Wine, "Temperature Dependence of the O + HO₂ Rate Coefficient," *J. Phys. Chem.*, vol. 91, pp. 5118 - 5123, September 10, 1987.
5. J. M. Nicovich, P. H. Wine, and A. R. Ravishankara, "Pulsed Laser Photolysis Kinetics Study of the O(³P) + ClO Reaction," *J. Chem. Phys.*, vol. 89, pp. 5670 - 5679, November 1, 1988.
6. P. H. Wine and A. R. Ravishankara, "O₃ Photolysis at 248 nm and O(¹D₂) Quenching by H₂O, CH₄, H₂, and N₂O: O(³P_J) Yields," *Chem. Phys.*, vol. 69, pp. 365 - 373, August 1982.
7. P. H. Wine and A. R. Ravishankara, "Kinetics of O(¹D) Interactions with the Atmospheric Gases N₂, N₂O, H₂O, H₂, CO₂, and O₃," *Chem. Phys. Lett.*, vol. 77, pp. 103 - 109, January 1, 1981.
8. R. J. Donovan and D. Husain, "Electronically Excited Bromine Atoms Br(4²P_{1/2}): Part 2 - Spin Orbit Relaxation," *Trans. Far. Soc.*, vol. 62, pp. 2987 - 2993, October 1966.
9. J. M. Nicovich, K. D. Kreutter, and P. H. Wine, "Kinetics of the Reactions of Cl(²P_J) and Br(²P_{1/2}) with O₃," *Int. J. Chem. Kinetics*, vol. 22, pp. 399 - 414, March 1990.
10. J. M. Nicovich and P. H. Wine, "Kinetics of the Reactions of O(³P) and Cl(²P) with HBr and Br₂," *Int. J. Chem. Kinetics*, vol. 22, pp. 379 - 397, March 1990.
11. W. B. DeMore, S. P. Sander, D. M. Golden, M. J. Molina, R. F. Hampson, M. J. Kurylo, C. J. Howard, and A. R. Ravishankara, *Chemical Kinetics and Photochemical Data for Use in Stratospheric Modeling*, Evaluation No. 9, JPL Publication 90-1, Jet Propulsion Laboratory, January 1, 1990.
12. A. Wahner, A. R. Ravishankara, S. P. Sander, and R. R. Friedl, "Absorption Cross Section of BrO Between 312 and 385 nm at 298 and 223 K," *Chem. Phys. Lett.*, vol. 152, pp. 507 - 512, November 25, 1988.
13. P. H. Wine, J. R. Wells, and J. M. Nicovich, "Kinetics of the Reactions of F(²P) and Cl(²P) with HNO₃," *J. Phys. Chem.*, vol. 92, pp. 2223 - 2228, April 21, 1988.
14. E. P. Daykin and P. H. Wine, "Kinetics of the Reactions of IO Radicals with NO and NO₂," *J. Phys. Chem.*, vol. 94, pp. 4528 - 4535, May 31, 1990.
15. K. Y. Choo and M.-T. Leu, "Rate Constants for the Quenching of Metastable O₂(¹Σ_g⁺) Molecules," *Int. J. Chem. Kinetics*, vol. 17, pp. 1155 - 1167, November 1985.
16. J. A. Ganske, H. N. Berko, and B. J. Finlayson-Pitts, "Absorption Cross Sections for Gaseous ClNO₂ and Cl₂ at 298 K: Potential Organic Oxidant Source in the Marine Troposphere," *J. Geophys. Res.*, vol. 97, pp. 7651 - 7656, May 20, 1992.
17. O. J. Nielsen, H. W. Sidebottom, L. Nelson, O. Rattigan, J. J. Treacy, and D. J. O'Farrell, "Rate Constants for the Reactions of OH Radicals and Cl Atoms with Diethyl Sulfide, Di-n-propyl Sulfide, and Di-n-butyl Sulfide," *Int. J. Chem. Kinetics*, vol. 22, pp. 603 - 612, June 1990.
18. A. J. Hynes, P. H. Wine, and D. H. Semmes, "Kinetics and Mechanism of OH Reactions with Organic Sulfides," *J. Phys. Chem.*, vol. 90, pp. 4148 - 4156, August 14, 1986.

19. J. M. Nicovich, C. J. Shackelford, and P. H. Wine, "Kinetics and Thermochemistry of Reversible Adduct Formation in the Reaction of $\text{Cl}(^2\text{P}_{1/2})$ with CS_2 ," *J. Phys. Chem.*, vol. 94, pp. 2896 - 2903, April 5, 1990, and references therein.
20. S. N. Pandis and J. H. Seinfeld, "Sensitivity Analysis of a Chemical Mechanism for Aqueous-Phase Atmospheric Chemistry," *J. Geophys. Res.*, vol. 94, pp. 1105 - 1126, January 20, 1989, and references therein.
21. J. Lelieveld and P. J. Crutzen, "The Role of Clouds in Tropospheric Photochemistry," *J. Atmos. Chem.*, vol. 12, pp. 229 - 267, April 1991.
22. P. H. Wine, R. L. Mauldin III, and R. P. Thorn, "Kinetics and Spectroscopy of the NO_3 Radical in Aqueous Cerium Nitrate - Nitric Acid Solutions," *J. Phys. Chem.*, vol. 92, pp. 1156 - 1162, March 10, 1988.
23. Y. Tang, R. P. Thorn, R. L. Mauldin III, and P. H. Wine, "Kinetics and Spectroscopy of the SO_4^- Radical in Aqueous Solution," *J. Photochem. Photobiol., A: Chem.*, vol. 44, pp. 243 - 258, September 1988.
24. P. H. Wine, Y. Tang, R. P. Thorn, J. R. Wells, and D. D. Davis, "Kinetics of Aqueous Phase Reactions of the SO_4^- Radical with Potential Importance in Cloud Chemistry," *J. Geophys. Res.*, vol. 94, pp. 1085 - 1094, January 20, 1989.
25. M. Chin and P. H. Wine, "Laboratory Investigations of Free Radical Chemistry in Cloud Water," presented at the 203rd National ACS Meeting, San Francisco, CA, April 1992.
26. G. G. Jayson, B. J. Parsons, and A. J. Swallow, "Some Simple, Highly Reactive, Inorganic Chlorine Derivatives in Aqueous Solution," *J. Chem. Soc. Farad. Trans. 1*, vol. 69, pp. 1597 - 1607, September 1973.
27. U. K. Kläning and T. Wolff, "Laser Flash Photolysis of HClO , ClO^- , HBrO , and BrO^- in Aqueous Solution. Reactions of Cl^- and Br^- Atoms," *Ber. Bunsenges. Phys. Chem.*, vol. 89, pp. 243 - 245, March 1985.
28. W. J. McElroy, "A Laser Photolysis Study of the Reaction of SO_4^- with Cl^- and the Subsequent Decay of Cl_2^- in Aqueous Solution," *J. Phys. Chem.*, vol. 94, pp. 2435 - 2441, March 22, 1990.

NDB
5-10.1 58-25
026 126
18P.

ACS SYMPOSIUM SERIES **502**

073544

Isotope Effects in Gas-Phase Chemistry

Jack A. Kaye, EDITOR
National Aeronautics and Space Administration

Developed from a symposium sponsored
by the Division of Physical Chemistry
at the 201st National Meeting
of the American Chemical Society,
Atlanta, Georgia,
April 14-19, 1991



American Chemical Society, Washington, DC 1992

Chapter 7

Deuterium Substitution Used as a Tool for Investigating Mechanisms of Gas-Phase Free-Radical Reactions

P. H. Wine, A. J. Hynes, and J. M. Nicovich

Physical Sciences Laboratory, Georgia Tech Research Institute, Georgia
Institute of Technology, Atlanta, GA 30332

Results are presented and discussed for a number of gas phase free radical reactions where H/D isotope effects provide valuable mechanistic insights. The cases considered are (1) the reactions of OH, NO₃, and Cl with atmospheric reduced sulfur compounds, (2) the reactions of OH and OD with CH₃CN and CD₃CN, and (3) the reactions of alkyl radicals with HBr and DBr.

A major focus of modern chemical kinetics research is on understanding complex chemical systems of practical importance such as the atmosphere and fossil fuel combustion. In these applications, accurate information on reaction mechanisms (i.e., product identities and yields) as well as reaction rate coefficients is often critically important. Since detailed experimental kinetic and mechanistic information for every reaction of importance in a complex chemical system is often an unrealizable goal, it is highly desirable to develop a firm theoretical understanding of well studied reactions which can be extrapolated to prediction of unknown rate coefficients and product yields.

In recent years it has become apparent that many reactions of importance in atmospheric and combustion chemistry occur via complex mechanisms involving potential energy minima (i.e., weakly bound intermediates) along the reaction coordinate. The OH + CO reaction is one of the best characterized examples (1). While theoretical descriptions can sometimes be employed to rationalize experimental observations (1-3), a theoretical framework does not yet exist for predicting complex behavior. In this paper we discuss some experimental studies carried out in our laboratory over the last several years which were aimed at characterizing the kinetics and mechanisms of a number of complex chemical reactions of practical interest. Mechanistic details were deduced in part from studies of the

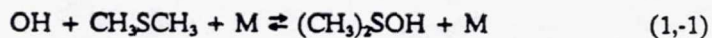
effects of temperature, pressure, and $[O_2]$ on reaction kinetics and from direct observation of reaction products. However, studies of H/D isotope effects were also employed as a tool for deducing reaction mechanisms; information obtained from the isotope effect studies is highlighted in the discussion.

The chemical processes we have chosen for discussion are (1) the reactions of OH, NO_3 , and Cl with atmospheric reduced sulfur compounds (2) the reactions of OH and OD with CH_3CN and CD_3CN , and (3) the reactions of alkyl radicals with HBr and DBr. The experimental methodology employed to investigate the above reactions involved coupling generation of reactant radicals by laser flash photolysis with time resolved detection of reactants and products by pulsed laser induced fluorescence (OH and OD), atomic resonance fluorescence (Cl and Br), and long path tunable dye laser absorption (NO_3).

The Reactions of OH, NO_3 , and Cl with Atmospheric Reduced Sulfur Compounds

Dimethylsulfide (CH_3SCH_3 , DMS) emissions into the atmosphere from the oceans are thought to account for a significant fraction of the global sulfur budget (4). It has been suggested that DMS oxidation in the marine atmosphere is an important pathway for production of cloud condensation nuclei and, therefore, that atmospheric DMS can play a major role in controlling the earth's radiation balance and climate (5). Hence, there currently exists a great deal of interest in understanding the detailed mechanism for oxidation of atmospheric DMS.

It is generally accepted that the OH radical is an important initiator of DMS oxidation in the marine atmosphere (4). Several years ago, we carried out a detailed study of the kinetics and mechanism of the OH + DMS reaction (6). We found that OH reacts with DMS via two distinct pathways, one of which is only operative in the presence of O_2 and one of which is operative in the absence or presence of O_2 (see Figure 1). The rate of the O_2 -dependent pathway increases with increasing $[O_2]$, increases dramatically with decreasing temperature, and shows no kinetic isotope effect, i.e., CH_3SCH_3 and CD_3SCD_3 react at the same rate. These observations indicate that the O_2 -dependent pathway involves formation of a weakly bound adduct which reacts with O_2 in competition with decomposition back to reactants.



The absence of a kinetic isotope effect strongly suggests that none of the three elementary steps in the above mechanism involve breaking a C-H bond.

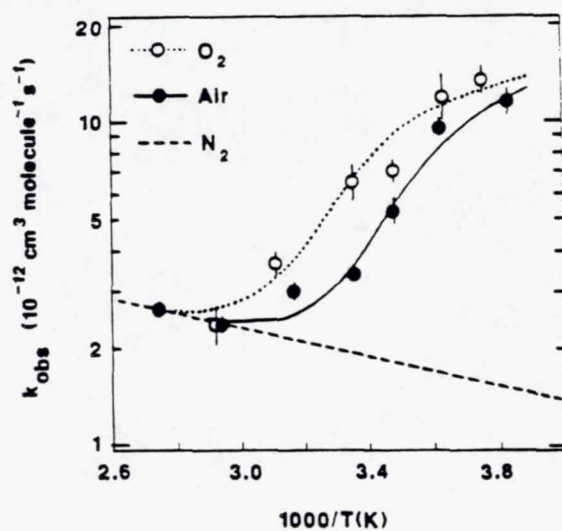
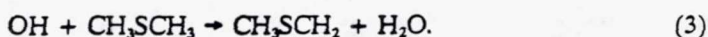


Figure 1. Arrhenius plots for the $\text{OH} + \text{CD}_3\text{SCD}_3$ reaction in 700 Torr N_2 , air, and O_2 . $k_{\text{obs}} \equiv$ the slope of a plot of the pseudo-first order OH decay rate versus the CD_3SCD_3 concentration under conditions where the adduct $(\text{CD}_3)_2\text{SOH}$ is removed much more rapidly than it is formed. (Reproduced from reference 62. Copyright 1987 American Chemical Society.)

The O_2 -independent channel for the OH + DMS reaction proceeds with a 298K rate coefficient of $4.4 \times 10^{-12} \text{ cm}^3\text{molecule}^{-1}\text{s}^{-1}$; in one atmosphere of air, the O_2 -independent channel is dominant at $T > 285\text{K}$ while the O_2 -dependent channel dominates at lower temperatures (6). We find that the rate of the O_2 -independent channel is pressure independent but increases slightly with increasing temperature (small positive activation energy). Furthermore, the O_2 -independent channel displays a significant kinetic isotope effect, $k_H/k_D \sim 2.3$ at 298K. Based upon the observed positive activation energy and significant isotope effect, we have postulated (6) that the O_2 -independent pathway is a direct hydrogen abstraction reaction, i.e., there is no potential energy minimum (corresponding to an OH-DMS adduct) on the potential energy surface connecting reactants with products.

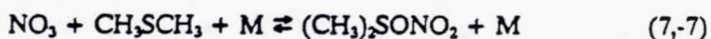
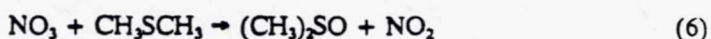
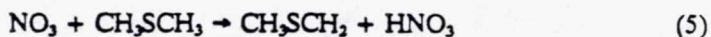


Interestingly, Domine et al. (7) have recently observed production of $\text{C}_2\text{H}_5 + \text{CH}_3\text{SOH}$ from the reaction of OH with $\text{C}_2\text{H}_5\text{SCH}_3$ at low pressure and in the absence of O_2 , although the branching ratio for production of $\text{C}_2\text{H}_5 + \text{CH}_3\text{SOH}$ remains rather uncertain. By analogy, Domine et al.'s results suggest that the O_2 -independent pathway in OH + DMS may involve cleavage of the relatively weak C-S bond rather than the C-H bond.



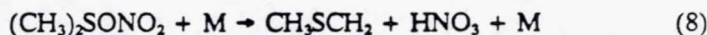
If the O_2 -independent pathway for OH + DMS is reaction 4 rather than reaction 3, then the H/D isotope effect we have observed (6) would, to our knowledge, be the largest secondary isotope effect known for a gas phase reaction. Clearly, direct determination of the product yields from the O_2 -independent channel of the OH + DMS reaction could have a major impact not only on our understanding of atmospheric sulfur oxidation, but also on our understanding of chemical reactivity in general and kinetic isotope effects in particular.

In coastal marine environments where NO_3 levels are relatively high, it is generally believed that NO_3 can compete with OH as an initiator of DMS oxidation (4). The 298K rate coefficient for the $\text{NO}_3 + \text{DMS}$ reaction is known to be about $1 \times 10^{-12} \text{ cm}^3\text{molecule}^{-1}\text{s}^{-1}$ (8-13) and a significant negative activation energy has been reported (12). The reaction of NO_3 with DMS could proceed via direct H or O atom transfer or via formation of long-lived adduct.



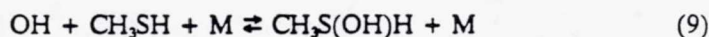
Attempts to detect NO_2 as a reaction product have been unsuccessful (9,12) suggesting that O atom transfer via either a direct mechanism or via adduct decomposition is unimportant. As pointed out by Atkinson et al. (8), the $\text{NO}_3 + \text{DMS}$ reaction is several orders of magnitude faster than the known rates of H-abstraction of, for example, relatively weakly bound aldehydic hydrogens by NO_3 ; this fact, coupled with the observed negative activation energy (12), strongly suggests that the $\text{NO}_3 + \text{DMS}$ reaction does not proceed via a direct H-abstraction pathway. By the process of elimination, it is generally accepted that the initial step in the $\text{NO}_3 + \text{DMS}$ reaction is adduct formation, i.e., reaction (7).

In a recent study of the kinetics of NO_3 reactions with organic sulfides (13), we observed a large kinetic isotope effect for the $\text{NO}_3 + \text{DMS}$ reaction; at 298K NO_3 reacts with CH_3SCH_3 a factor of 3.8 more rapidly than with CD_3SCD_3 . The observed isotope effect, coupled with the observation that at 298K $\text{C}_2\text{H}_5\text{SC}_2\text{H}_5$ reacts with NO_3 a factor of 3.7 more rapidly than does CH_3SCH_3 , clearly demonstrates that the adduct decomposes via a process which involves C-H bond cleavage. A very recent chamber study by Jensen et al. (14) confirms the magnitude of our reported isotope effect and reports quantitative observation of HNO_3 as a reaction product.

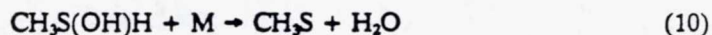


As we discuss elsewhere (13), the postulate that the $\text{NO}_3 + \text{DMS}$ reaction proceeds via reactions 7, -7, and 8 appears to be consistent with all available product data.

It is interesting to compare and contrast kinetic and mechanistic findings for the $\text{NO}_3 + \text{DMS}$ reaction, with those for the reaction of OH with CH_3SH . Like $\text{NO}_3 + \text{DMS}$, the $\text{OH} + \text{CH}_3\text{SH}$ reaction becomes faster with decreasing temperature (15-18), suggesting that the initial step in the mechanism is adduct formation.



Also, as appears to be the case for $\text{NO}_3 + \text{DMS}$, the $\text{OH} + \text{CH}_3\text{SH}$ reaction is known to give H-abstraction products with unit yield (19).



Hence, there are important similarities between the $\text{NO}_3 + \text{DMS}$ and $\text{OH} + \text{CH}_3\text{SH}$ reactions. However, there are also important differences. First, at 298K the $\text{OH} + \text{CH}_3\text{SH}$ reaction is about 30 times faster than the $\text{NO}_3 + \text{DMS}$ reaction. Secondly, while $\text{NO}_3 + \text{DMS}$ displays a large H/D kinetic isotope effect (see above), isotope effects in OH reactions with CH_3SH , CD_3SH , and CH_3SD are minimal (17,18). These reactivity differences can be rationalized by postulating that decomposition of $(\text{CH}_3)_2\text{SONO}_2$ to products competes relatively unfavorably with decomposition back to

reactants (i.e. $k_7 \gg k_8$), whereas decomposition of $\text{CH}_3\text{S(OH)H}$ to products is much faster than decomposition back to reactants (i.e. $k_9 \ll k_{10}$). Hence, the rate of the adduct \rightarrow product step, which should be sensitive to isotopic substitution, strongly influences the overall rate of the $\text{NO}_3 + \text{DMS}$ reaction but does not influence the overall rate of the $\text{OH} + \text{CH}_3\text{SH}$ reaction.

Recently in our laboratory we have investigated the kinetics of chlorine atom reactions with CH_3SH , CD_3SD , H_2S , and D_2S (20) as a function of temperature. There have been no previous reports of the temperature dependence of the $\text{Cl} + \text{CH}_3\text{SH}$ rate coefficient and no previous kinetics studies of Cl reactions with CD_3SD or D_2S . Nesbitt and Leone (21,22) have shown that, at 298K, the $\text{Cl} + \text{CH}_3\text{SH}$ reaction occurs at a gas kinetic rate ($k \sim 1.84 \times 10^{-10} \text{ cm}^3\text{molecule}^{-1}\text{s}^{-1}$) and that $k_{11}/k_{12} \sim 45$.



Several kinetics studies of the $\text{Cl} + \text{H}_2\text{S}$ reaction have been reported (21,23-27) with published 298K rate coefficients spanning the range $(4.0 - 10.5) \times 10^{-11} \text{ cm}^3\text{molecule}^{-1}\text{s}^{-1}$. Two temperature dependence studies (26,27) both conclude that the $\text{Cl} + \text{H}_2\text{S}$ rate coefficient is temperature independent. Internal state distributions in the HCl product of $\text{Cl} + \text{H}_2\text{S}$ and $\text{Cl} + \text{CH}_3\text{SH}$ (28,29) and the SH product of $\text{Cl} + \text{H}_2\text{S}$ (29) have also been reported.

Arrhenius plots for reactions of Cl with H_2S , D_2S , CH_3SH , and CD_3SD are shown in Figure 2. Arrhenius expressions derived from our data are as follows (units are $10^{-11} \text{ cm}^3\text{molecule}^{-1}\text{s}^{-1}$; errors are 2σ , precision only):

$$\text{Cl} + \text{H}_2\text{S}: \quad k = (3.60 \pm 0.26) \exp [(210 \pm 20)/T], \quad 202-430\text{K}$$

$$\text{Cl} + \text{D}_2\text{S}: \quad k = (1.65 \pm 0.27) \exp [(225 \pm 45)/T], \quad 204-431\text{K}$$

$$\text{Cl} + \text{CH}_3\text{SH}, \text{CD}_3\text{SD}: \quad k = (11.9 \pm 1.7) \exp [(151 \pm 38)/T], \quad 193-430\text{K}$$

Kinetic data for CH_3SH and CD_3SD were indistinguishable so one Arrhenius expression incorporating all data is presented. One important aspect of our results is that all reactions are characterized by small but well-defined negative activation energies, suggesting that long range attractive forces between S and Cl are important in defining the overall rate coefficient. Our interpretation of observed kinetic isotope effects follows the same arguments as employed above in the comparison of $\text{NO}_3 + \text{DMS}$ with $\text{OH} + \text{CH}_3\text{SH}$. In the case of the $\text{Cl} + \text{CH}_3\text{SH}$ reaction, adduct decomposition to products is apparently fast compared to adduct decomposition back to reactants whereas in the case of the $\text{Cl} + \text{H}_2\text{S}$ reaction the two adduct decomposition pathways occur at competitive rates. This argument seems

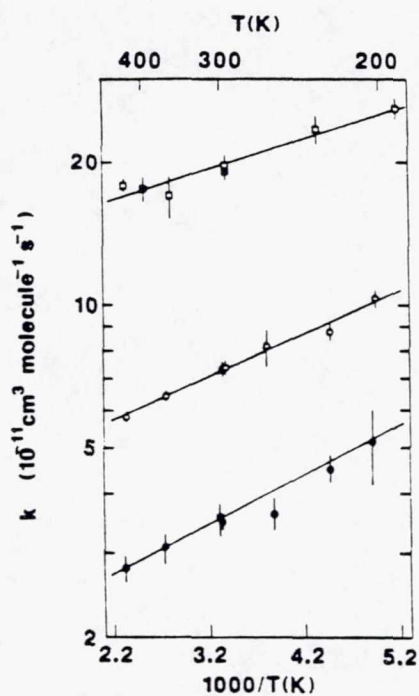


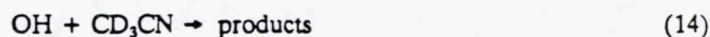
Figure 2. Arrhenius plots for the reactions of chlorine atoms with H_2S (\circ), D_2S (\bullet), CH_3SH (\square), and CD_3SD (\blacksquare). Error bars are 2σ and represent precision only. Solid lines are obtained from linear least squares analyses which yield the Arrhenius parameters given in the text.

reasonable since we expect H_2SCl to be a less strongly bound species than $\text{CH}_3\text{S}(\text{Cl})\text{H}$, thus making adduct decomposition back to reactants considerably more rapid for $\text{Cl} + \text{H}_2\text{S}$ than for $\text{Cl} + \text{CH}_3\text{SH}$. The relative stabilities of the adducts can be predicted based on the facts that a methyl group releases electron density to the sulfur atom more efficiently than does a hydrogen atom (30), and that the ionization potential of CH_3SH is about 1 eV lower than the ionization potential of H_2S (31), thus facilitating the formation of a more stable charge transfer complex in the $\text{Cl} + \text{CH}_3\text{SH}$ case.

The Reactions of OH and OD with CH_3CN and CD_3CN

Acetonitrile (CH_3CN) is present at significant levels in both the troposphere and the stratosphere, and has been implicated in stratospheric ion chemistry (32-35). Reaction with OH is generally thought to be a major atmospheric removal mechanism for acetonitrile (35). Early studies of the kinetics of the $\text{OH} + \text{CH}_3\text{CN}$ reaction demonstrated that $k(298\text{K}) \sim 2 \times 10^{-14} \text{ cm}^3\text{molecule}^{-1}\text{s}^{-1}$ and that $E_{\text{act}} \sim 2 \text{ kcal mole}^{-1}$ (36-41); it has generally been thought that reaction proceeds via a direct H-abstraction mechanism (40-42).

We recently carried out a detailed study of the hydroxyl reaction with acetonitrile which demonstrates that the reaction mechanism is considerably more complex than previously thought (43). The kinetics of the following four isotopic variants were investigated:

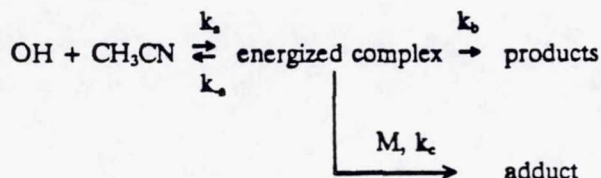


All four reactions were studied at 298K as a function of pressure and O_2 concentration, while reactions 13 and 14 were also studied as a function of temperature.

Experiments which employed N_2 buffer gas gave some results which appear inconsistent with the idea that reactions 13 - 16 occur via direct H (or D) abstraction pathways. First, rate coefficients for reactions 13 and 14 (but not reactions 15 and 16) increase with increasing pressure over the range 50 - 700 Torr; the largest increase, nearly a factor of two, is observed for reaction 14. Second, observed isotope effects on the (high pressure limit) 298K rate coefficients are not as would be expected for an H (or D)-abstraction mechanism. Measured 298K rate coefficients in units of $10^{-14} \text{ cm}^3\text{molecule}^{-1}\text{s}^{-1}$ are $k_{13} = 2.48 \pm 0.38$, $k_{14} = 2.16 \pm 0.11$, $k_{15} = 3.18 \pm 0.40$, and $k_{16} = 2.25 \pm 0.28$ (errors are 2σ). If the dominant reaction pathway is H (or D) abstraction we would expect reactions 13 and 15, which break C-H

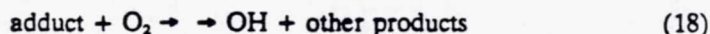
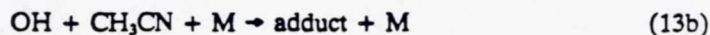
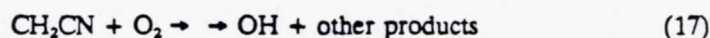
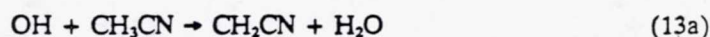
bonds, to be faster by a factor of two or more than reactions 14 and 16, which break C-D bonds. Observed differences in reactivity are quite small, although reaction 15 does appear to be somewhat faster than the other reactions.

The observed kinetics in the absence of O_2 can best be reconciled with a complex mechanism which proceeds via formation of an energized intermediate, i.e.



Such an energized intermediate could decompose to produce $\text{CH}_2\text{CN} + \text{H}_2\text{O}$ or other products, decompose back to reactants, or be collisionally stabilized at sufficiently high pressures. Hence, the reaction proceeds at a finite rate at low pressure but shows an enhancement in the rate as the pressure is increased. Such a mechanism is well documented for the important atmospheric reactions of OH with CO and HNO_3 (44) and has recently been observed in our laboratory for the Cl + DMS reaction (45). The pressure, temperature, and isotopic substitution dependences of the elementary rate coefficients k_1 , k_{-1} , k_2 , and k_c interact to produce the observed complex behavior.

Perhaps the most conclusive evidence that the OH + CH_3CN reaction proceeds, at least in part, via formation of an intermediate complex comes from experiments carried out in reaction mixtures containing O_2 . Observed OH temporal profiles in the presence of CH_3CN and O_2 are non-exponential and suggest that OH is regenerated via a reaction of O_2 with a product of reaction 13. Two possibilities are as follows:



In the mixed-isotope experiments, we observe that OD is regenerated from $\text{OD} + \text{CH}_3\text{CN} + \text{O}_2$ and that OH is regenerated from $\text{OH} + \text{CD}_3\text{CN} + \text{O}_2$; these findings conclusively demonstrate that an important channel for the hydroxyl + acetonitrile reaction involves formation of an adduct which lives long enough to react with O_2 under atmospheric conditions, and also places considerable constraints on possible adduct + O_2 reaction pathways. A

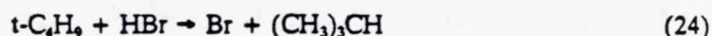
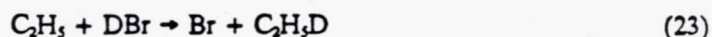
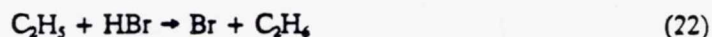
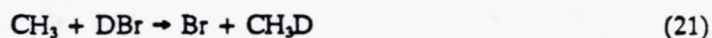
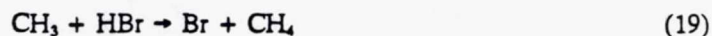
plausible set of elementary steps via which OH can be regenerated in the $\text{OH} + \text{CD}_3\text{CN} + \text{O}_2$ reaction is shown in Figure 3. The mechanism involves OH addition to the nitrogen atom, followed by O_2 addition to the cyano carbon atom, isomerization, and decomposition to $\text{D}_2\text{CO} + \text{DOCN} + \text{OH}$. Further studies are needed to establish whether or not OD as well as OH is generated from $\text{OH} + \text{CD}_3\text{CN} + \text{O}_2$ and whether or not OH as well as OD is generated from $\text{OD} + \text{CH}_3\text{CN} + \text{O}_2$. Further studies are also needed to directly detect end products of the adduct + O_2 reactions(s).

The Reactions of Alkyl Radicals with HBr and DBr

The thermochemistry and kinetics of alkyl radicals are subjects of considerable importance in many fields of chemistry. Accurate evaluation of alkyl radical heats of formation are required for determination of primary, secondary, and tertiary bond dissociation energies in hydrocarbons, for establishing rates of heat release in combustion, and for relating unknown "reverse" rate coefficients to known "forward" values. Kinetic data for numerous alkyl radical reactions are needed for modeling hydrocarbon combustion.

Recent direct kinetic studies (46-51), primarily by Gutman and coworkers (46-49), strongly suggest that alkyl + HX reactions have negative activation energies, a finding which seems counter-intuitive for apparently simple hydrogen abstraction reactions. It should be noted, however, that one recent direct study (52) reports much slower rate coefficients compared to other direct studies (46,48,50,51) and positive activation energies for the reactions of $t\text{-C}_4\text{H}_9$ with DBr and DI.

Motivated initially by the desire to obtain improved thermochemical data for sulfur-containing radicals of atmospheric interest, we developed a method for studying radical + HBr(DBr) reactions by observing the appearance kinetics of product bromine atoms (53). We have recently applied the same experimental approach to investigate the kinetics of the following reactions (54):



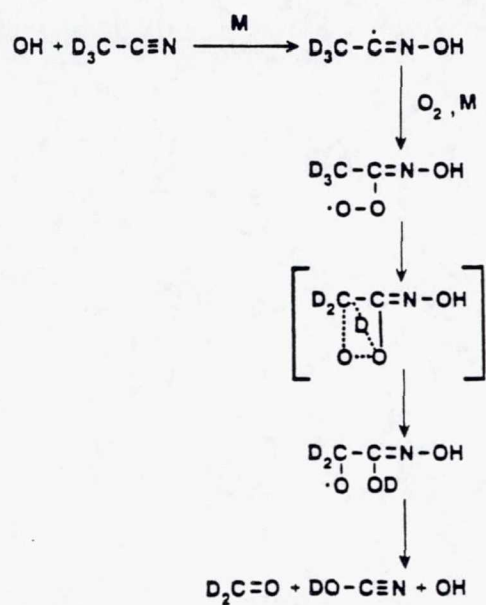


Figure 3. Plausible set of elementary steps for the reaction $\text{OH} + \text{CD}_3\text{CN} + \text{O}_2 \rightarrow \text{D}_2\text{CO} + \text{DOCN} + \text{OH}$. Adduct decomposition to products is shown as a single step; in reality, it probably occurs via two sequential steps with either D_2CO or OH coming off before the other. (Reproduced from reference 43. Copyright 1991 American Chemical Society.)

The isotope effect studies were motivated by a recent theoretical investigation of the $t\text{-C}_4\text{H}_9 + \text{HI}$, DI reactions (55) which suggests that negative activation energies for alkyl + HX reactions should be accompanied by inverse kinetic isotope effects, i.e., $k_H/k_D < 1$.

In Table I our results (54) are compared with other available direct kinetic data for reactions 19 - 25. The negative activation energies and fast rate coefficients for alkyl + HBr reactions reported by Gutman and coworkers (46,47,49) are confirmed in our study. In fact, the activation energies derived from our data are consistently a little lower, i.e., more negative, than those reported by Gutman and coworkers and the 298K rate coefficients obtained in our study are consistently more than a factor of two faster than those reported by Gutman and coworkers. Our 298K rate coefficient for the $t\text{-C}_4\text{H}_9 + \text{HBr}$ reaction exceeds the values reported by Russell et al. (46) and Richards et al. (50) by a factor of 2.7, but is in excellent agreement with the value reported by Seakins and Pilling (51); interestingly, the experimental technique employed by Seakins and Pilling was very similar to the technique employed in our study. Our 298K rate coefficient for the $t\text{-C}_4\text{H}_9 + \text{DBr}$ reaction exceeds the value reported by Richards et al. (50) by a factor of 2.7 and exceeds the value reported by Müller-Markgraf et al. (52) by more than two orders of magnitude. As discussed in some detail by Gutman (56), the probable source of error in the Müller-Markgraf et al. study (52) is neglect of heterogeneous loss of $t\text{-C}_4\text{H}_9$ in their data analysis.

Traditionally, hydrogen transfer reactions such as $\text{R} + \text{HX} \rightarrow \text{RH} + \text{X}$ have been thought of as "direct" metathesis reactions with a barrier along the reaction coordinate and a single transition state located at the potential energy maximum. Rationalization of observed negative activation energies for $\text{R} + \text{HX}$ reactions has centered around the postulate that product formation proceeds via formation of weakly bound $\text{R}\cdots\text{XH}$ complexes (45-48,55). As shown by Mozurkewich and Benson (57), if the transition state leading from reactants to complex (TS1) is loose and the transition state leading from complex to products is both tighter and lower in energy compared to TS1, then a negative activation energy for the overall reaction should be observed. McEwen and Golden (55) have carried out a two channel RRKM calculation that models the $t\text{-C}_4\text{H}_9 + \text{HI}(\text{DI})$ reactions as proceeding through a weakly bound complex; they were able to reproduce the kinetics results of Seetula et al. (48) for $t\text{-C}_4\text{H}_9 + \text{HI}$ assuming complex binding energies as low as 3 kcal mole⁻¹. Probably the most interesting aspect of McEwen and Golden's study is the fact that models which were capable of reproducing experimentally observed (48) $k(T)$ values for $t\text{-C}_4\text{H}_9 + \text{HI}$ also predicted an inverse kinetic isotope effect (KIE), i.e., $t\text{-C}_4\text{H}_9 + \text{DI}$ was predicted to be faster than $t\text{-C}_4\text{H}_9 + \text{HI}$. The predicted inverse KIE results from the fact that the transition state leading from complex to products becomes looser with lower vibrational frequencies associated with deuterium substitution. Contrary to McEwen and Golden's prediction for $t\text{-C}_4\text{H}_9 + \text{HI}$, we observe normal KIE's for CH_3 , C_2H_5 , and $t\text{-C}_4\text{H}_9$ reactions with HBr . Richards et al. (50) also observe a normal KIE for the $t\text{-C}_4\text{H}_9 +$

Table I. Comparison of our results (reference 54) with other direct determinations of alkyl + HBr(DBr) rate coefficients.^a

Reaction	Exptl Method ^b	Range of T	A ^c	-E/R ^c	k _t (298K) ^d	Reference
CH ₃ + HBr	LFP - PIMS	296 - 532	0.87	160 ± 110	1.49	47
	LFP - RF	257 - 422	1.36	233 ± 23	2.97	54
CD ₃ + HBr	LFP - IRE	298			4.7	60
	LFP - RF	297			3.35	54
CH ₃ + DBr	VLPP	608 - 1000	0.32	0 ± 500	0.32	61
	LFP - RF	267 - 429	1.07	130 ± 55	1.66	54
C ₂ H ₅ + HBr	LFP - PIMS	295 - 532	1.0	410 ± 110	3.96	47
	LFP - RF	259 - 427	1.33	539 ± 78	8.12	54
C ₂ H ₅ + DBr	LFP - RF	298 - 415	(0.92)	(580)	6.44	54
t-C ₄ H ₉ + HBr	LFP - PIMS	296 - 532	0.99	700 ± 110	10.4	46
	LFP - DLA	297			10	50
	LFP - RF	298			32	51
	LFP - RF	297 - 429	1.07	963 ± 152	27.1	54
t-C ₄ H ₉ + DBr	VLPP ^e	295 - 384	(8.3)	(-1180)	0.16	52
	LFP - DLA	297			8	50
	LFP - RF	298 - 415	(1.03)	(919)	22.5	54

a. Units are T, E/R: degrees K; A, k_t(298K): 10⁻¹² cm³molecule⁻¹s⁻¹.

b. LFP: laser flash photolysis; PIMS: photoionization mass spectrometry; RF: resonance fluorescence; IRE: infrared emission; VLPP: very low pressure pyrolysis; DLA: diode laser absorption; VLPP^e: very low pressure photolysis.

c. Parentheses indicate Arrhenius parameters which are based on experiments at only two temperatures.

d. Calculated from Arrhenius parameters when temperature dependent data were obtained. Error limits not quoted due to inconsistencies in methods used by different groups to arrive at uncertainties; most values of k_t(298K) have absolute accuracies in the 15-30% range.

HBr reaction. It does appear, however, that the magnitude of the KIE is reduced as the activation energy becomes more negative, i.e., the observed KIE is largest for $R = \text{CH}_3$ and smallest for $R = t\text{-C}_4\text{H}_9$. Chen et al. have recently calculated a potential energy surface for the $\text{CH}_3 + \text{HBr}$ reaction at the G1 level of theory and deduced the existence of a hydrogen bridged complex which is bound by $0.28 \text{ kcal mole}^{-1}$ and is formed without activation energy (58). They have also calculated rate coefficients for $\text{CH}_3 + \text{HBr}$, $\text{CH}_3 + \text{DBr}$, and $\text{CD}_3 + \text{HBr}$ from RRKM theory with corrections for tunneling evaluated using the Wigner method (59). Their calculated isotope effects agree quantitatively with our measured isotope effects, a result which lends strong support to the idea that the methyl-HBr complex is hydrogen-bridged rather than bromine-bridged.

Summary

Experimental kinetic data have been presented and discussed for a number of reactions where H/D isotope effects provide valuable mechanistic insights. For the reactions of atmospheric free radicals with reduced sulfur compounds, isotope effect studies provide information not only about C-H or S-H bond cleavage versus other reactive pathways but also on the relative rates of adduct decompositions back to reactants versus on to products. For the reaction of hydroxyl radicals with acetonitrile, isotope effect studies conclusively demonstrate the intermediacy of a long-lived adduct and also provide site-specific information which places important constraints on the detailed mechanism for hydroxyl generation from the adduct + O_2 reaction. For the $\text{CH}_3 + \text{HBr}$ reaction, comparison of observed and theoretical isotope effects supports the view that reaction proceeds via formation of a very weakly bound, hydrogen-bridged addition complex. In one case considered, namely the O_2 -independent channel for the $\text{OH} + \text{CH}_3\text{SCH}_3$ reaction, there exist potential problems in relating experimental observations (6,7) to existing prejudices concerning the nature of kinetic isotope effects.

Acknowledgments

Support for the work described in this paper has been provided by grants ATM-8217232, ATM-8600892, ATM-8802386, and ATM-9104807 from the National Science Foundation and grant NAGW-1001 from the National Aeronautics and Space Administration.

Literature Cited

1. Brunning, J.; Derbyshire, D. W.; Smith, I. W. M.; Williams, M. D., *JCS Farad. Trans.* 2 1988, 84, 105, and references therein.
2. Mozurkewich, M.; Lamb, J. J.; Benson, S. W. *J. Phys. Chem.* 1984, 88, 6435.

3. Lamb, J. J.; Mozurkewich, M.; Benson, S. W. *J. Phys. Chem.* **1984**, *88*, 6441.
4. see for example, Toon, O. B.; Kasting, J. F.; Turco, R. P.; Liu, M. S. *J. Geophys. Res.* **1987**, *92*, 943.
5. Charlson, R. J.; Lovelock, J. E.; Andreae, M. O.; Warren, S. G. *Nature* **1987**, *326*, 655.
6. Hynes, A. J.; Wine, P. H.; Semmes, D. H. *J. Phys. Chem.* **1986**, *90*, 4148.
7. Domine, F.; Ravishankara, A. R.; Howard, C. J. *J. Phys. Chem.*, in press
8. Atkinson, R.; Pitts, J. N., Jr.; Aschmann, S. M. *J. Phys. Chem.* **1984**, *88*, 1584.
9. Tyndall, G. S.; Burrows, J. P.; Schneider, W.; Moortgat, G. K. *Chem. Phys. Lett.* **1986**, *130*, 463.
10. Wallington, T. J.; Atkinson, R.; Winer, A. M.; Pitts, J. N., Jr. *J. Phys. Chem.* **1986**, *90*, 4640.
11. Wallington, T. J.; Atkinson, R.; Winer, A. M.; Pitts, J. N., Jr. *J. Phys. Chem.* **1986**, *90*, 5393.
12. Dlugokencky, E. J.; Howard, C. J. *J. Phys. Chem.* **1988**, *92*, 1188.
13. Daykin, E. P.; Wine, P. H. *Int. J. Chem. Kinet.* **1990**, *22*, 1083.
14. Jensen, N. R.; Hjorth, J.; Lohse, C.; Skov, H.; Restelli, G. *J. Atmos. Chem.*, in press.
15. Atkinson, R.; Perry, R. A.; Pitts, J. N., Jr. *J. Chem. Phys.* **1977**, *66*, 1578.
16. Wine, P. H.; Kreutter, K. D.; Gump, C. A.; Ravishankara, A. R. *J. Phys. Chem.* **1981**, *85*, 2660.
17. Wine, P. H.; Thompson, R. J.; Semmes, D. H. *Int. J. Chem. Kinet.* **1984**, *16*, 1623.
18. Hynes, A. J.; Wine, P. H. *J. Phys. Chem.* **1987**, *91*, 3672.
19. Tyndall, G. S.; Ravishankara, A. R. *J. Phys. Chem.* **1989**, *93*, 4707.
20. Nicovich, J. M.; van Dijk, C. A.; Kreutter, K. D.; Wine, P. H., to be published.
21. Nesbitt, D. J.; Leone, S. R. *J. Chem. Phys.* **1980**, *72*, 1722.
22. Nesbitt, D. J.; Leone, S. R. *J. Chem. Phys.* **1981**, *75*, 4949.
23. Braithewaite, M.; Leone, S. R. *J. Chem. Phys.* **1978**, *69*, 840.
24. Clyne, M. A. A.; Ono, Y. *Chem. Phys. Lett.* **1983**, *94*, 597.
25. Clyne, M. A. A.; MacRobert, A. J.; Murrels, T. P.; Stief, L. J. *JCS Farad. Trans. 2* **1984**, *80*, 877.
26. Nava, D. F.; Brobst, W. D.; Stief, L. J. *J. Phys. Chem.* **1985**, *89*, 4703.
27. Lu, E. C. C.; Iyer, R. S.; Rowland, F. S. *J. Phys. Chem.* **1986**, *90*, 1988.
28. Dill, B.; Heydtmann, H. *Chem. Phys.* **1978**, *35*, 161.
29. Agrawalla, B. S.; Setser, D. W. *J. Phys. Chem.* **1986**, *90*, 2450.
30. see for example, Morrison, R. T.; Boyd, R. N. *Organic Chemistry*, 2nd edition. Allyn and Bacon, Inc., Boston, MA, 1966.

31. Lias, S. G.; Bartmess, J. E.; Liebman, J. F.; Holmes, J. L.; Levin, R. D.; Mallard, W. G. *J. Phys. Chem. Ref. Data* **1988**, *17*, Supplement 1.
32. Arnold, F.; Böhringer, H.; Henschen, G. *Geophys. Res. Lett.* **1978**, *5*, 653.
33. Arijs, E.; Nevejans, D.; Ingels, J. *Nature* **1983**, *303*, 314.
34. Schlager, H.; Arnold, F. *Planet. Space Sci.* **1986**, *34*, 245.
35. Arijs, E.; Nevejans, D.; Ingels, J. *Int. J. Mass Spectrom. Ion Processes* **1987**, *81*, 15.
36. Harris, G. W.; Kleindienst, T. E.; Pitts, J. N., Jr. *Chem. Phys. Lett.* **1981**, *80*, 479.
37. Fritz, B.; Lorenz, K.; Steinert, W.; Zellner, R. in *Proceedings of the 2nd European Symposium on the Physico-Chemical Behavior of Atmospheric Pollutants*. Varsino, B., Angeletti, G., Eds. D. Reidel: Boston, MA, **1982**.
38. Zetsch, C.; Bunsekolloquium; Battelle Institut: Frankfurt, **1983**.
39. Kurylo, M. J.; Knable, G. L. *J. Phys. Chem.* **1984**, *88*, 3305.
40. Rhasa, D.; Diplomarbeit, Gottingen, FRG, **1983**.
41. Poulet, D.; Laverdet, G.; Jourdain, J. L.; LeBras, G. *J. Phys. Chem.* **1984**, *88*, 6259.
42. Atkinson, R. *J. Phys. Chem. Ref. Data Monograph* 1, **1989**.
43. Hynes, A. J.; Wine, P. H. *J. Phys. Chem.* **1991**, *95*, 1232.
44. DeMore, W. B.; Sander, S. P.; Golden, D. M.; Molina, M. J.; Hampson, R. F.; Kurylo, M. J.; Howard, C. J.; Ravishankara, A. R. *Chemical Kinetics and Photochemical Data for Use in Stratospheric Modeling*, Evaluation No. 9, JPL publication 90-1, **1990**, and references therein.
45. Nicovich, J. M.; Wang, S.; Stickel, R. E.; Wine, P. H., to be published.
46. Russell, J. J.; Seetula, J. A.; Timonen, R. S.; Gutman, D.; Nava, D. F. *J. Am. Chem. Soc.* **1988**, *110*, 3084.
47. Russell, J. J.; Seetula, J. A.; Gutman, D. *J. Am. Chem. Soc.* **1988**, *110*, 3092.
48. Seetula, J. A.; Russell, J. J.; Gutman, D. *J. Am. Chem. Soc.* **1990**, *112*, 1347.
49. Seetula, J. A.; Gutman, D. *J. Phys. Chem.* **1990**, *94*, 7529.
50. Richards, P. D.; Ryther, R. R.; Weitz, E. *J. Phys. Chem.* **1990**, *94*, 3663.
51. Seakins, P. W.; Pilling, M. J. *J. Phys. Chem.*, **1991**, *95*, 9874.
52. Müller-Markgraf, W.; Rossi, M. J.; Golden, D. M. *J. Am. Chem. Soc.* **1989**, *111*, 956.
53. Nicovich, J. M.; Kreutter, K. D.; van Dijk, C. A.; Wine, P. H. *J. Phys. Chem.*, in press.
54. Nicovich, J. M.; van Dijk, C. A.; Kreutter, K. D.; Wine, P. H. *J. Phys. Chem.*, **1991**, *95*, 9890.
55. McEwen, A. B.; Golden, D. M. *J. Mol. Struct.* **1990**, *224*, 357.
56. Gutman, D. *Acc. Chem. Res.* **1990**, *23*, 375.
57. Mozurkewich, M.; Benson, S. W. *J. Phys. Chem.* **1984**, *88*, 6429.

58. Chen, Y.; Tschuikow-Roux, E.; Rauk, A. *J. Phys. Chem.*, **1991**, *95*, 9832.
59. Chen, Y.; Rauk, A.; Tschuikow-Roux, E. *J. Phys. Chem.*, **1991**, *95*, 9900.
60. Donaldson, D. J.; Leone, S. R. *J. Phys. Chem.* **1986**, *90*, 936.
61. Gac, N. A.; Golden, D. M.; Benson, S. W. *J. Am. Chem. Soc.* **1969**, *91*, 309.
62. Hynes, A. J.; Wine, P. H. in *The Chemistry of Acid Rain. Sources and Atmospheric Processes*; Johnson, R. W.; Gordon, G. E., Eds.; American Chemical Society Symposium Series 349, Washington, DC, **1987**, pp. 133-141.

RECEIVED December 17, 1991

Reprinted from ACS Symposium Series No. 502

Isotope Effects in Gas-Phase Chemistry

Jack A. Kaye, Editor

Copyright © 1992 by the American Chemical Society

Reprinted by permission of the copyright owner

Kinetics of the Reactions of Alkyl Radicals with HBr and DBr

om IT
93A44528

J. M. Nicovich, C. A. van Dijk, K. D. Kreutter, and P. H. Wine*

Physical Sciences Laboratory, Georgia Tech Research Institute, Georgia Institute of Technology, Atlanta, Georgia 30332 (Received: June 10, 1991; In Final Form: July 23, 1991)

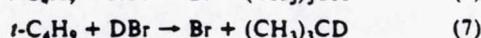
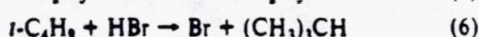
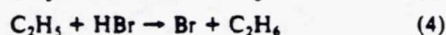
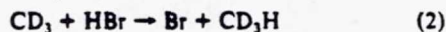
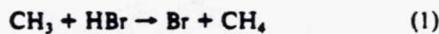
Time-resolved resonance fluorescence detection of Br atom appearance following laser flash photolysis of RI (R = CH₃, CD₃, C₂H₅, *t*-C₄H₉) or Cl₂/RH (R = CH₃, C₂H₅) has been employed to study the kinetics of the reactions CH₃ + HBr (1), CD₃ + HBr (2), CH₃ + DBr (3), C₂H₅ + HBr (4), C₂H₅ + DBr (5), *t*-C₄H₉ + HBr (6), and *t*-C₄H₉ + DBr (7) as a function of temperature (257–430 K) and pressure (10–300 Torr of N₂). The rates of all reactions are found to increase with decreasing temperature; i.e., activation energies are negative, and 298 K rate coefficients for reactions 1 and 3–7 are found to be significantly faster than previously thought. Arrhenius expressions for reactions 1, 3, 4, and 6 in units of 10⁻¹² cm³ molecule⁻¹ s⁻¹ are $k_1 = (1.36 \pm 0.10) \exp[(233 \pm 23)/T]$, $k_3 = (1.07 \pm 0.17) \exp[(130 \pm 55)/T]$, $k_4 = (1.33 \pm 0.33) \exp[(539 \pm 78)/T]$, and $k_6 = (1.07 \pm 0.34) \exp[(963 \pm 152)/T]$; errors are 2σ and represent precision only. Normal kinetic isotope effects are observed ($k_{HBr} > k_{DBr}$), although the ratio k_{HBr}/k_{DBr} decreases in magnitude with decreasing activation energy; i.e., k_{HBr}/k_{DBr} is largest for R = CH₃ and smallest for R = *t*-C₄H₉. Combining our results with the best available kinetic data for the reverse reactions (Br + RH) yields the following 298 K alkyl radical heats of formation in units of kcal mol⁻¹: CH₃, 35.3 ± 0.6; C₂H₅, 29.1 ± 0.6; *t*-C₄H₉, 12.1 ± 0.8; errors are 2σ and represent estimates of absolute accuracy.

Introduction

The thermochemistry and kinetics of alkyl radicals are subjects of considerable importance in many fields of chemistry. Accurate evaluation of alkyl radical heats of formation is required for determination of primary, secondary, and tertiary bond dissociation energies in hydrocarbons, for establishing rates of heat release in combustion, and for relating unknown "reverse" rate coefficients to known "forward" values. Kinetic data for numerous alkyl radical reactions are needed for modeling hydrocarbon combustion.

Despite the importance of alkyl radical kinetics and thermochemistry, and an extensive literature which dates back several decades, important discrepancies in the data base have persisted. For example, results from iodination and bromination studies have consistently yielded heats of formation for alkyl radicals that are 2–4 kcal mol⁻¹ lower than those obtained from studies of bond scission and recombination rates of simple alkanes and radicals.^{1–3} Recent direct kinetic studies,^{4–9} primarily by Gutman and co-workers,^{4–7} strongly suggest that alkyl + HX reactions have negative activation energies; while this finding seems counterintuitive for apparently simple hydrogen-transfer reactions, it can resolve the above-mentioned discrepancy in alkyl radical heats of formation since all earlier iodination and bromination studies were analyzed under the assumption that alkyl + HX reactions have small, positive activation energies. However, it should be noted that one recent direct study¹⁰ reports much slower rate coefficients (compared to other direct studies^{4,4,9}) and positive activation energies for the reactions of *t*-C₄H₉ with DBr and DI.

Motivated initially by the desire to obtain improved thermochemical data for sulfur-containing radicals of atmospheric interest, we developed a method for studying radical + HBr(DBr) reactions by observing the appearance kinetics of product bromine atoms.¹¹ In this paper we report the results of a series of experiments where time-resolved monitoring of bromine atom appearance was employed to investigate the kinetics of the following reactions:



The isotope effect studies have been motivated by a recent theoretical study of the *t*-C₄H₉ + HI, DI reactions,¹² which suggests that negative activation energies for alkyl + HX reactions should be accompanied by inverse kinetic isotope effects, i.e., $k_{HX}/k_{DX} < 1$.

Experimental Technique

The experimental approach involved coupling alkyl radical production by laser flash photolysis of suitable precursors with time-resolved detection of bromine atom appearance by resonance fluorescence spectroscopy. A schematic diagram of the apparatus, as configured for bromine atom detection, can be found elsewhere.¹³ A description of the experimental methodology is given below.

A Pyrex, jacketed reaction cell with an internal volume of 150 cm³ was used in all experiments. The cell was maintained at a constant temperature by circulating ethylene glycol ($T > 298$ K) or methanol ($T < 298$ K) from a thermostatically controlled bath through the outer jacket. A copper–constantan thermocouple with a stainless steel jacket was injected into the reaction zone through a vacuum seal, thus allowing measurement of the gas temperature under the precise pressure and flow rate conditions of the experiment.

Alkyl radicals were produced by 266-nm pulsed laser photolysis of RI/HBr/N₂ mixtures (R = CH₃, CD₃, C₂H₅, *t*-C₄H₉) or by 355-nm pulsed laser photolysis of Cl₂/RH/HBr/N₂ mixtures (R = CH₃, C₂H₅). Third or fourth harmonic radiation from a Quanta Ray Model DCR-2 Nd:YAG laser provided the photolytic ra-

(1) Tsang, W. *Int. J. Chem. Kinet.* 1978, 10, 821.(2) Tsang, W. *J. Am. Chem. Soc.* 1985, 107, 2872.(3) McMillen, D. F.; Golden, D. M. *Annu. Rev. Phys. Chem.* 1982, 33, 493.(4) Russell, J. J.; Seetula, J. A.; Timonen, R. S.; Gutman, D.; Nava, D. *J. Am. Chem. Soc.* 1988, 110, 3084.(5) Russell, J. J.; Seetula, J. A.; Gutman, D. *J. Am. Chem. Soc.* 1988, 110, 3092.(6) Seetula, J. A.; Russell, J. J.; Gutman, D. *J. Am. Chem. Soc.* 1990, 112, 1347.(7) Seetula, J. A.; Gutman, D. *J. Phys. Chem.* 1990, 94, 7529.(8) Richards, P. D.; Rytber, R. R.; Weitz, E. *J. Phys. Chem.* 1990, 94, 3663.(9) Seakins, P. W.; Pilling, M. J. *J. Phys. Chem.* 1991, 95, 9874.(10) Müller-Markgraf, W.; Rossi, M. J.; Golden, D. M. *J. Am. Chem. Soc.* 1989, 111, 956.(11) Nicovich, J. M.; Kreutter, K. D.; van Dijk, C. A.; Wine, P. H. *J. Phys. Chem.*, submitted for publication.(12) McEwen, A. B.; Golden, D. M. *J. Mol. Struct.* 1990, 224, 357.(13) Nicovich, J. M.; Shackelford, C. J.; Wine, P. H. *J. Photochem. Photobiol. A: Chem.* 1990, 51, 141.

* Author to whom correspondence should be addressed.

diation. The laser could deliver up to 3×10^{16} photons per pulse at 266 nm and up to 1×10^{17} photons per pulse at 355 nm; the maximum repetition rate was 10 Hz, and the pulse width was approximately 6 ns.

A bromine resonance lamp, situated perpendicular to the photolysis laser, excited resonance fluorescence in the photolytically produced atoms. The resonance lamp consisted of an electrodeless microwave discharge through about 1 Torr of a flowing mixture containing a trace of Br_2 in helium. The flows of a 0.2% Br_2 in helium mixture and pure helium into the lamp were controlled by separate needle valves, thus allowing the total pressure and Br_2 concentration to be adjusted for optimum signal-to-noise ratio. Radiation was coupled out of the lamp through a magnesium fluoride window and into the reaction cell through a magnesium fluoride lens. Before entering the reaction cell, the lamp output passed through a flowing gas filter containing 50 Torr-cm of methane in nitrogen. The methane filter prevented radiation at wavelengths shorter than 140 nm (including impurity emissions from excited oxygen, hydrogen, and nitrogen atoms) from entering the reaction cell but transmitted the strong bromine lines in the 140–160-nm region.

Fluorescence was collected by a magnesium fluoride lens on an axis orthogonal to both the photolysis laser beam and resonance lamp beam and was imaged onto the photocathode of a solar blind photomultiplier. Signals were processed by using photon counting techniques in conjunction with multichannel scaling. A large number of laser shots were typically averaged to obtain a bromine atom temporal profile with signal-to-noise ratio sufficient for quantitative kinetic analysis. It is worth noting that the resonance fluorescence detection scheme is sensitive to both ground state ($^2P_{3/2}$) and spin-orbit excited state ($^2P_{1/2}$) bromine atoms.

To avoid accumulation of photolysis or reaction products, all experiments were carried out under "slow flow" conditions. The linear flow rate through the reactor was in the range 2–10 cm s^{-1} , and the laser repetition rate was varied over the range 5–10 Hz (5 Hz typical). Hence, no volume element of the reaction mixture was subjected to more than a few laser shots. The alkyl iodides, ethane, Cl_2 , HBr, and DBr flowed into the reaction cell from bulbs (12-L volume) containing dilute mixtures in nitrogen while methane, hydrogen, and additional nitrogen were flowed directly from their storage cylinders. All gases except Cl_2 (see below) were premixed before entering the reactor. The concentrations of each component in the reaction mixture were determined from measurements of the appropriate mass flow rates and the total pressure. The concentrations of HBr and DBr were also determined by in situ UV photometry at 202.6 nm (Zn^+ line). A zinc hollow cathode lamp was employed as the light source for the photometric measurement, and a quarter meter monochromator was used to isolate the 202.6-nm line. The absorption cross sections needed to convert measured absorbances into concentrations were determined during the course of this investigation and were found to be $1.02 \times 10^{-18} \text{ cm}^2$ for HBr and $9.7 \times 10^{-19} \text{ cm}^2$ for DBr. The measured HBr cross section agrees well with values reported by Goodeve and Taylor¹⁴ and by Huebert and Martin¹⁵ but is ~20% higher than the value reported by Romand¹⁶ and ~20% lower than the value of Nee et al.¹⁷ Experimental results were found to be independent of whether the 2 m long absorption cell was positioned upstream or downstream relative to the reaction cell.

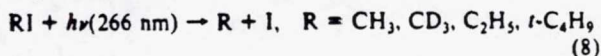
The gases used in this study had the following stated minimum purities: N_2 , 99.999%; H_2 , 99.999%; Cl_2 , 99.99%;¹⁸ CH_4 , 99.9995%; C_2H_6 , 99.99%; HBr, 99.8%;¹⁸ DBr, unstated chemical purity and 99 atom % D.¹⁸ Nitrogen, hydrogen, methane, and ethane were used as supplied, while Cl_2 , HBr, and DBr were purified by repeated freeze (77 K)–pump–thaw cycles. It is worth noting that the HBr and DBr gas samples taken directly from their storage cylinders contained significant (25–50%) levels of a

noncondensable impurity which was determined by weighing to be $\text{H}_2(\text{D}_2)$.

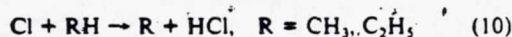
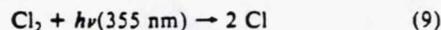
The liquids used in this study had the following stated minimum purities: CH_3I , 99.5%; CD_3I , unstated chemical purity and 99.5+ atom % D; $\text{C}_2\text{H}_5\text{I}$, 99%; *t*- $\text{C}_4\text{H}_9\text{I}$, 95%. All liquid samples were transferred under nitrogen into vials fitted with high-vacuum stopcocks and were subjected to repeated freeze (77 K)–pump–thaw cycles before being used to prepare gaseous RI/N_2 mixtures. When not in use, the vials were stored in the dark at 278 K.

Results and Discussion

In most experiments, alkyl radicals were generated by 266-nm laser flash photolysis of the appropriate alkyl iodide ($[\text{RI}]$ in the range $1\text{--}12 \times 10^{13} \text{ molecules cm}^{-3}$):

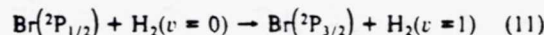


Reactions 1 and 4 were also studied using the following alternate alkyl production scheme:



When the alternate production scheme was applied, Cl_2 (concentration $\sim 1 \times 10^{13} \text{ molecules cm}^{-3}$) was injected into the gas flow just upstream from the reaction zone to suppress the heterogeneous dark reaction between Cl_2 and HBr.¹⁹ Also, RH was added to the reaction mixture in sufficient quantity that (a) production of alkyl radicals was essentially instantaneous on the time scale for the alkyl + HBr reaction and (b) nearly all Cl ($>95\%$) reacted with RH rather than with HBr. Observed kinetics were found to be independent of the choice of alkyl radical production scheme. As will be discussed in more detail below, the invariance of observed kinetics to the alkyl radical source rules out some potential sources of systematic error.

Reactions 1–5 are sufficiently exothermic that the bromine atom product could be formed in the spin-orbit excited state, $\text{Br}(^2P_{1/2})$. To ensure that relaxation of $\text{Br}(^2P_{1/2})$ was not rate-limiting in defining observed Br appearance rates, all experiments were carried out with 0.2–2 Torr of H_2 added to the reaction mixtures. The reaction



is known to be fast, with $k_{11} \sim 6 \times 10^{-12} \text{ cm}^3 \text{ molecule}^{-1} \text{ s}^{-1}$.²⁰

All experiments were carried out under pseudo-first-order conditions with HBr in large excess (typically a factor of 10^4) over the alkyl radical. Concentrations of photolytically generated radicals were typically in the range $5\text{--}10 \times 10^{10}/\text{cm}^3$, although this experimental parameter was varied over a wide range (factor of 20). Observed kinetics were found to be independent of both the alkyl iodide concentration and the concentration of photolytically generated radicals.

In the absence of side reactions that remove or produce Br, the observed temporal profile following the flash would be described by the relationship

$$S_t = k_2 C_1 (k_d - k_a)^{-1} [\exp(-k_a t) - \exp(-k_d t)] + C_2 \exp(-k_d t) \quad (I)$$

In eq I, S_t is the fluorescence signal level at time t (proportional to $[\text{Br}]_t$), k_a and k_d are the pseudo-first-order rate coefficients for Br appearance (k_a) and disappearance (k_d), and the parameters C_1 and C_2 are defined as follows:

$$C_1 = \alpha[\text{R}]_0 \quad (II)$$

$$C_2 = \alpha[\text{Br}]_0 \quad (III)$$

In the above equations $[\text{R}]_0$ and $[\text{Br}]_0$ are the alkyl and Br concentrations after photolysis and reaction 10 have gone to com-

(14) Goodeve, C. F.; Taylor, A. W. C. *Proc. R. Soc.* 1935, *A152*, 221.

(15) Huebert, B. J.; Martin, R. M. *J. Phys. Chem.* 1968, *72*, 3046.

(16) Romand, F. *Ann. Phys. (Paris)* 1948, *4*, 527.

(17) Nee, J. B.; Suto, M.; Lee, L. C. *J. Chem. Phys.* 1986, *85*, 4919.

(18) Stated purity of liquid phase in cylinder.

(19) Nicovich, J. M.; Wine, P. H. *Int. J. Chem. Kinet.* 1990, *22*, 379.

(20) Nesbitt, D. J.; Leone, S. R. *J. Chem. Phys.* 1980, *73*, 6182.

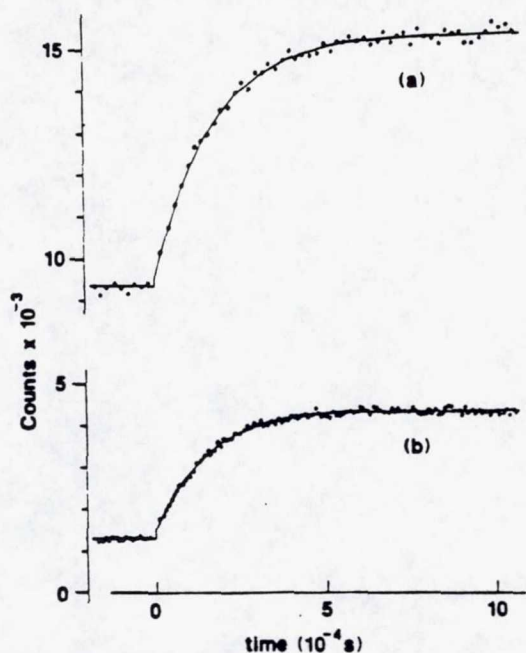


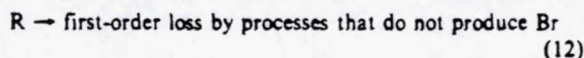
Figure 1. Typical Br atom temporal profiles. Reaction: $C_2H_3 + HBr$. C_2H_3 source: (a) $C_2H_3I + h\nu(266 \text{ nm})$, (b) $Cl_2/C_2H_4 + h\nu(355 \text{ nm})$. Experimental conditions: $T = 298 \text{ K}$; P (Torr) = (a) 100, (b) 50; photolyte concentrations in units of $10^{13} \text{ molecules cm}^{-3}$: (a) $[C_2H_3I] = 6.3$, (b) $[Cl_2] = 1.3$ and $[C_2H_4] = 160$; $[C_2H_3]_0$ ($10^{10} \text{ radicals cm}^{-3}$) = (a) 5, (b) 9; $[HBr]$ ($10^{14} \text{ molecules cm}^{-3}$) = (a) 5.45, (b) 5.64; number of laser shots averaged = (a) 5000, (b) 2000. Solid lines are obtained from nonlinear least-squares analyses which give the following best fit parameters: k_a (s^{-1}) = (a) 5470, (b) 6320; k_d (s^{-1}) = (a) 22, (b) 39; C_1 = (a) 5920, (b) 2950; C_2 = (a) 190, (b) 240.

pletion but before significant removal of alkyl radical has occurred, f is the fraction of alkyl radicals that are removed via a reaction which produces Br, and α is the proportionality constant which relates S_i to $[Br]_i$. For the reaction systems of interest, we expect that

$$k_a = k_i[HBr(DBr)] + k_{12} \quad (i = 1-7) \quad (\text{IV})$$

$$f = k_i[HBr(DBr)]/k_a \quad (i = 1-7) \quad (\text{V})$$

where k_{12} is the rate coefficient for the following reaction(s):



A nonlinear least-squares analysis of each experimental temporal profile was employed to determine k_a , k_d , C_1 , and C_2 . The bimolecular rate coefficients of interest, $k_i(P, T)$ were determined from the slopes of k_a vs $[HBr(DBr)]$ plots. Typical data are shown in Figures 1 and 2. It is worth pointing out that the accuracy with which k_a could be determined via the nonlinear least-squares fitting technique was quite good because it was always the case that $k_a \gg k_d$ and $C_1 \gg C_2$. Observation of Br temporal profiles that are well described by eq I, a linear dependence of k_a on $[HBr(DBr)]$, and invariance of k_a to variation in laser photon fluence and photolyte concentration suggest that the alkyl + $HBr(DBr)$ reaction and reaction 13 ($k_{13} = k_d$) are the only

Br \rightarrow first-order loss by diffusion from the detector field of view and reaction with background impurities (13)

processes that significantly affect the Br time history (once photolysis and Cl reaction with RH and HBr are complete). One potential interference that is not ruled out by the above observations is reaction of alkyl radicals with impurities which are either present in the HBr sample or produced via dark reactions of HBr with other components in the reaction mixture; impurity reactions are considered below when potential systematic errors are discussed.

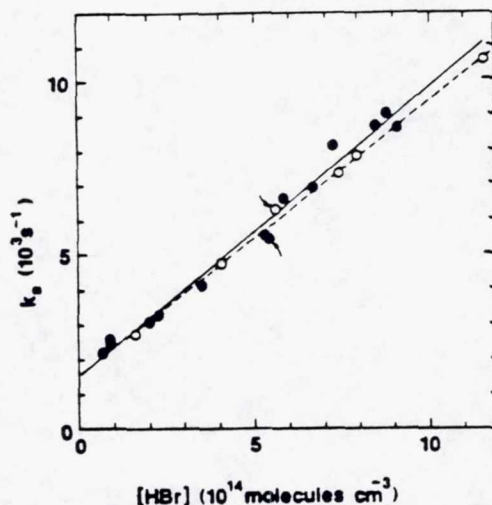
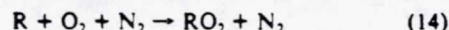


Figure 2. Typical plots of k_a vs $[HBr]$. Reaction: $C_2H_3 + HBr$. C_2H_3 source: (●) $C_2H_3I + h\nu(266 \text{ nm})$, (○) $Cl_2/C_2H_4 + h\nu(355 \text{ nm})$. Experimental conditions: $T = 298 \text{ K}$; P (Torr) = (●) 100, (○) 50. Solid and dashed lines are obtained from linear least-squares analyses of the solid and open circle data points, respectively, and give the following bimolecular rate coefficients in units of $10^{-12} \text{ cm}^3 \text{ molecule}^{-1} \text{ s}^{-1}$: (●) 8.24 ± 0.65 , (○) 7.81 ± 0.51 . Arrows indicate the two points obtained from the data shown in Figure 1.

One interesting aspect of the data in Figure 2 is the relatively large value for k_{12} , i.e., the relatively large intercept in the k_a vs $[HBr]$ plot. The observed values for k_{12} were typically larger than expected if background removal of alkyl radicals was due only to reaction with their photolytic precursors and to diffusion out of the detector field of view. At low $[HBr(DBr)]$, where $k_{12} > k_i[HBr(DBr)]$ ($i = 1-7$), fluorescence signal levels were considerably reduced; this indicates that the process responsible for background alkyl radical removal did not result in production of bromine atoms. The magnitude of k_{12} tended to increase with decreasing temperature and with increasing complexity of the alkyl radical, suggesting that a process responsible for significant background removal of alkyl radicals was reaction with O_2 :



The O_2 levels required to account for observed k_{12} values are around 0.01 Torr—significantly higher than expected O_2 impurity levels in the N_2 buffer gas. Hence, a small leak in the slow flow system is the probable source of O_2 . The presence of a reactive impurity at the levels encountered in our experiments is not expected to introduce systematic error into the kinetic measurements. However, when the condition $k_{12} \ll k_i[HBr(DBr)]$ is not met at least for the highest $HBr(DBr)$ concentrations employed in a particular rate coefficient determination, the precision of the derived value for $k_i(P, T)$ is reduced; the worst case in this regard was the k_7 measurement at $T = 415 \text{ K}$, where $k_{12}/k_7(\text{max}) \approx 0.28$ (Table I).

Kinetic data for reactions 1-7 are summarized in Table I, and Arrhenius plots for reactions 1, 3, 4, and 6 are shown in Figure 3. The solid lines in Figure 3 are obtained from linear least-squares analyses of the $\ln k_i(P, T)$ vs T^{-1} data; these analyses give the following Arrhenius expressions in units of $\text{cm}^3 \text{ molecule}^{-1} \text{ s}^{-1}$:

$$k_1 = (1.36 \pm 0.10) \times 10^{-12} \exp[(233 \pm 23)/T]$$

$$k_3 = (1.07 \pm 0.17) \times 10^{-12} \exp[(130 \pm 55)/T]$$

$$k_4 = (1.33 \pm 0.33) \times 10^{-12} \exp[(539 \pm 78)/T]$$

$$k_6 = (1.07 \pm 0.34) \times 10^{-12} \exp[(963 \pm 152)/T]$$

Errors in the above expressions are 2σ and represent precision only. As reported previously by Gutman and co-workers,⁴⁻⁷ we find that alkyl + $HBr(DBr)$ rate coefficients increase with decreasing

TABLE I: Summary of Kinetic Data^a

reaction (i) ^b	T	P ^c	no. of expts ^d	range of k ₂	range of k ₄	k ₁₂ ^e	k ₁ ^{f,g}
CH ₃ + HBr (1)	257	100	5	994-6420	4-12	186 ± 93	3.37 ± 0.08
	297	30 ^h	6	757-3950	36-87	158 ± 86	3.04 ± 0.10 ⁱ
	297	100	16	701-7740	3-68	99 ± 86	2.95 ± 0.12
	350	100	7	570-6760	9-25	55 ± 226	2.63 ± 0.13
	419	100	5	1240-4740	8-38	81 ± 338	2.34 ± 0.25
422	10	7	915-9920	80-152	377 ± 86	2.40 ± 0.07	
CD ₃ + HBr (2)	297	30	6	1370-6630	14-20	161 ± 71	3.33 ± 0.05
	297	300	5	1850-7320	15-25	167 ± 56	3.38 ± 0.04
CH ₃ + DBr (3)	267	100	7	651-6880	34-59	393 ± 128	1.71 ± 0.07
	298	100	18	1200-6130	35-87	440 ± 195	1.68 ± 0.10
	361	100	5	967-3510	43-56	183 ± 226	1.61 ± 0.16
	378	100	6	704-5210	32-50	191 ± 199	1.44 ± 0.09
	415	100	4	604-5090	38-54	152 ± 169	1.47 ± 0.08
	428	100	6	870-5100	39-48	243 ± 58	1.43 ± 0.03
	430	10	8	850-4630	76-124	545 ± 216	1.46 ± 0.11
C ₂ H ₅ + HBr (4)	259	30	6	3050-12900	8-20	1240 ± 420	10.4 ± 0.6
	297	30	5	2170-9350	20-30	734 ± 206	8.69 ± 0.33,
	298	50	6	2710-10600	32-43	↓580 ± 360	7.81 ± 0.51 ^h
	298	100	14	2180-8630	-5 to 22	1540 ± 370	8.24 ± 0.65
	348	30	4	1230-4710	25-51	675 ± 63	6.26 ± 0.15
	423	30	7	1120-4160	26-56	273 ± 231	5.06 ± 0.41
	427	10	6	1280-5670	122-193	512 ± 290	4.38 ± 0.38
C ₂ H ₅ + DBr (5)	298	100	5	3030-9080	56-72	1580 ± 420	6.44 ± 0.55
	415	100	5	1400-4740	36-48	687 ± 202	3.72 ± 0.28
<i>i</i> -C ₄ H ₉ + HBr (6)	297	30	11	3860-17500	-48 to 58	2560 ± 470	25.6 ± 1.3
	330	30	5	3670-15600	-32 to 32	1710 ± 390	21.4 ± 0.9
	378	30	6	2560-10700	2-50	1560 ± 300	14.1 ± 0.7
	428	30	7	1820-8110	38-92	1370 ± 290	10.1 ± 0.6
	429	10	5	3310-11300	216-311	1160 ± 140	9.60 ± 0.21
<i>i</i> -C ₄ H ₉ + DBr (7)	298	100	14	6290-27100	54-323	4610 ± 1610	22.5 ± 3.0
	415	100	5	3350-8140	70-99	2240 ± 318	9.43 ± 0.80

^aUnits are T (K); P (Torr); k₂, k₄, k₁₂ (s⁻¹); k₁ (10⁻¹² cm³ molecule⁻¹ s⁻¹). RI photolysis at 266 nm employed as alkyl source except where indicated. ^b(i) refers to reaction number in text. ^cN₂ buffer gas except where indicated. ^dExpt = measurement of a single Br temporal profile. ^eErrors are 2σ and represent precision only. ^fCl₂/CH₄ photolysis employed as CH₃ source; CH₄ used as buffer gas, i.e. [CH₄] ~ 9.6 × 10¹⁷ molecules cm⁻³. ^gCl₂/C₂H₆ photolysis employed as C₂H₅ source; [C₂H₆] ~ 1.6 × 10¹⁵ molecules cm⁻³.

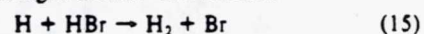
temperature, i.e., activation energies are negative. Pressure variations within the range 10-300 Torr of N₂ revealed no evidence of a pressure dependence for any of the reactions studied. On the basis of observed precision and consideration of possible systematic errors (see below), we estimate the absolute accuracy of each measured rate coefficient, k_i(T), to be ±20%.

Potential Systematic Errors. As discussed briefly above, a number of potential systematic errors in our kinetic measurements can be ruled out on the basis of the observed invariance of Br temporal profiles to variations in laser photon fluence, photolyte concentrations, and flow velocity through the reactor; these include contributions to Br kinetics from radical-radical side reactions, from radical-RI side reactions, or from reactions involving stable products which build up in concentration with successive laser flashes. In situ measurement of HBr(DBr) concentrations greatly reduces another potential source of systematic error.

It is well-known that UV photolysis of CH₃I produces vibrationally hot methyl radicals,²¹ and both ethyl and *tert*-butyl radicals are likely to be produced in excited vibrational states from RI photolysis. However, it is generally thought that under our experimental conditions relaxation to a thermalized vibrational distribution occurs much more rapidly than chemical reaction.^{7,22} Our experiments employing the Cl₂/RH source provide further evidence that we are, indeed, observing reactions of thermalized alkyl radicals. On the basis of the best available thermochemical data,²³ the Cl(²P_{3/2}) + CH₄ reaction is slightly endothermic and

the Cl + C₂H₆ reaction is only slightly exothermic; hence, these reactions cannot produce vibrationally hot alkyl radicals.

Another potential interference could have resulted if primary photolysis of RI or secondary photolysis of hot alkyl radicals led to generation of hydrogen atoms. The reaction



is thought to proceed with k₁₅(298 K) ~ 6 × 10⁻¹² cm³ molecule⁻¹ s⁻¹.²⁴ Hence, if the H atom concentration was significant compared to the alkyl radical concentration, we would systematically overestimate methyl radical reaction rates and systematically underestimate *tert*-butyl radical reactions rates. The experiments employing the Cl₂/RH source provide evidence that H atom production was not a problem in our CH₃ + HBr study. Insignificant H atom production is expected when 355-nm photolysis is employed and the only H precursors are RH and HBr. Furthermore, secondary photolysis of alkyl radicals does not seem possible because (a) the radicals are born with little internal energy and, therefore, cannot be excited via a single photon process at 355 nm and (b) nearly all alkyl radical formation is delayed in time until after the laser flash is over.

Another possible interference that must be addressed is the role of Br₂ impurity. Potential sources of Br₂ are impurity in the HBr sample, residual Br₂ (from Br recombination) not swept out of the reaction zone between laser flashes, and catalytic formation of Br₂ from heterogeneous reactions of HBr (presumably on the metal surfaces of valves and fittings). Since alkyl + Br₂ reactions are about an order of magnitude faster than the corresponding alkyl + HBr reactions,²⁵ the condition [Br₂] < 0.001 [HBr] must

(21) Suzuki, T.; Kanamori, H.; Hirota, E. *J. Chem. Phys.* 1991, 94, 6607, and references cited therein.

(22) Donaldson, D. J.; Leone, S. R. *J. Phys. Chem.* 1986, 90, 936.

(23) Atkinson, R.; Baulch, D. L.; Cox, R. A.; Hampson, R. F., Jr.; Kerr, J. A.; Troe, J. *J. Phys. Chem. Ref. Data* 1989, 18, 881.

(24) Umemoto, H.; Wada, Y.; Tsunashima, S.; Takayanagi, T.; Sato, S. *Chem. Phys. Lett.* 1990, 143, 333, and references cited therein.

TABLE II: Comparison of Our Results with Other Direct Determinations of k , ($i = 1-7$)^a

reaction (i)	exptl method ^b	range of T	A^c	$-E/R^c$	$k_A(298\text{ K})^d$	ref
CH ₃ + HBr (1)	LFP-PIMS	296-532	0.87	160 ± 110	1.49	5
	LFP-RF	257-422	1.36	233 ± 23	2.97	this work
CD ₃ + HBr (2)	LFP-IRE	298			4.7	22
	LFP-RF	297			3.35	this work
CH ₃ + DBr (3)	VLPP	608-1000	0.32	0 ± 500	0.32	41
	LFP-RF	267-429	1.07	130 ± 55	1.66	this work
C ₂ H ₅ + HBr (4)	LFP-PIMS	295-532	1.0	410 ± 110	3.96	5
	LFP-RF	259-427	1.33	529 ± 78	8.12	this work
C ₂ H ₅ + DBr (5)	LFP-RF	298-415	(0.92)	(580)	6.44	this work
<i>i</i> -C ₄ H ₉ + HBr (6)	LFP-PIMS	296-532	0.99	700 ± 110	10.4	4
	LFP-DLA	297			10	8
	LFP-RF	298			32	9
	LFP-RF	297-429	1.07	963 ± 152	27.1	this work
<i>i</i> -C ₄ H ₉ + DBr (7)	VLP Φ	295-384	(8.3)	(-1180)	0.16	10
	LFP-DLA	297			8	8
	LFP-RF	298-415	(1.03)	(919)	22.5	this work

^a Units are T , E/R , degrees K; A , $k_A(298\text{ K})$, $10^{-12}\text{ cm}^3\text{ molecule}^{-1}\text{ s}^{-1}$. The letter i refers to reaction numbers in the text. ^b LFP, laser flash photolysis; PIMS, photoionization mass spectrometry; RF, resonance fluorescence; IRE, infrared emission; VLPP, very low pressure pyrolysis; DLA, diode laser absorption; VLP Φ , very low pressure photolysis. ^c Parentheses indicate Arrhenius parameters based on experiments at only two temperatures. ^d Calculated from Arrhenius parameters when temperature-dependent data were obtained. Error limits not quoted due to inconsistencies in methods used by different groups to arrive at uncertainties; most values of $k_A(298\text{ K})$ have absolute accuracies in the 15-30% range.

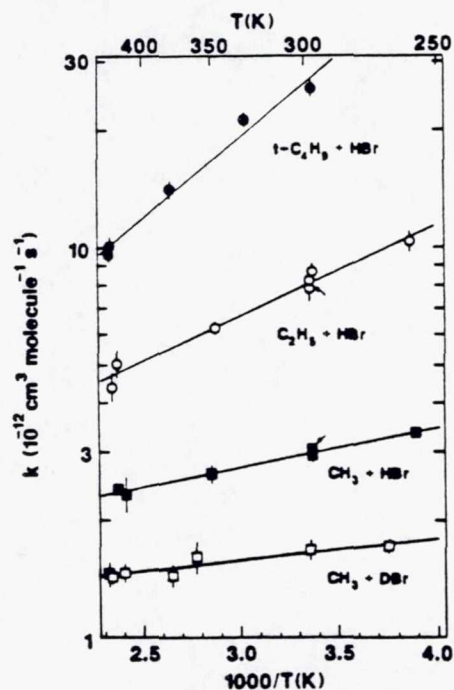


Figure 3. Arrhenius plots for the CH₃ + HBr(1), CD₃ + HBr(3), C₂H₅ + HBr(4), and *i*-C₄H₉ + HBr(6) reactions. Solid lines are obtained from linear least-squares analyses and yield the following Arrhenius expressions in units of $10^{-12}\text{ cm}^3\text{ molecule}^{-1}\text{ s}^{-1}$: $k_1 = 1.36\text{ exp}(233/T)$; $k_3 = 1.07\text{ exp}(130/T)$; $k_4 = 1.33\text{ exp}(539/T)$; $k_6 = 1.07\text{ exp}(963/T)$. Error bars represent 2σ , precision only. Arrows indicate the rate coefficients measured using the Cl₂/RH alkyl radical source.

be met before Br₂ interference can be considered negligible. Two experimental observations lead us to conclude that Br₂ levels were very low in our experiments. In one set of experiments the 2-m absorption cell was positioned in the slow flow system downstream from the reaction cell and employed to monitor Br₂ photometrically (at 404.7 nm) with typical RI/HBr/H₂/N₂ reaction mixtures flowing and the laser firing ($\lambda = 266\text{ nm}$). No absorption was observed (i.e., $I/I_0 > 0.997$) even at HBr levels as high as 10^{16}

molecules cm⁻³. Since the Br₂ absorption cross section at 404.7 nm is about $6 \times 10^{-19}\text{ cm}^2$,²⁶ these experiments suggest that $[\text{Br}_2] < 0.0025[\text{HBr}]$. A second set of observations which confirm that Br₂ levels were very low is the small values for C₂ obtained from the data analysis in all experiments. The experiments employing the Cl₂/RH photolysis source are particularly important in this regard because (a) the Br₂ absorption cross section at 355 nm ($8.4 \times 10^{-20}\text{ cm}^2$)²⁶ is considerably larger than at 266 nm and (b) it is known that BrCl and/or Br₂ can be generated from heterogeneous reaction between Cl₂ and HBr.¹⁹ Taking trace b in Figure 1 as an example, the laser fluence was about 3.5×10^{16} photons cm⁻², the peak signal corresponds to a Br concentration of about 9×10^{10} atoms cm⁻³, and the nonlinear least-squares analysis of the temporal profile gives $C_1/C_2 \sim 12$, i.e., the instantaneous bromine atom signal corresponds to about 7.5×10^9 atoms cm⁻³. The ethane and HBr concentrations were such that $\sim 3 \times 10^9$ atoms cm⁻³ of the instantaneous signal are attributable to the Cl + HBr reaction. Assuming all other "instantaneous" bromine atoms were generated from Br₂ photolysis implies that $[\text{Br}_2] \sim 3 \times 10^{11}$ molecules cm⁻³, i.e., $[\text{Br}_2] \leq 0.0014[\text{HBr}]$. We conclude from the above arguments that reaction with Br₂ accounted for no more than a few percent of observed alkyl reactivity.

As discussed above, the experiments that employed the Cl₂/RH alkyl radical source were of value for assessing the importance of several potential interferences. However, the use of Cl₂/RH photolysis for generating alkyl radicals introduces an additional chemistry complication which requires consideration, namely the reaction of alkyl radicals with Cl₂:



Rate coefficients for reaction 16 at 298 K are $2.1 \times 10^{-12}\text{ cm}^3\text{ molecule}^{-1}\text{ s}^{-1}$ for $\text{R} = \text{CH}_3$ and $1.85 \times 10^{-11}\text{ cm}^3\text{ molecule}^{-1}\text{ s}^{-1}$ for $\text{R} = \text{C}_2\text{H}_5$.²⁷ For $[\text{Cl}_2] \sim 1 \times 10^{13}$ molecules cm⁻³, as employed in our experiments, reaction with Cl₂ was a negligible alkyl removal mechanism in the experiments with $\text{R} = \text{CH}_3$ but did account for 2-7% of alkyl removal in the experiments with $\text{R} = \text{C}_2\text{H}_5$. However, the Cl atom product of reaction 16 reacts instantaneously (on the time scale for $\text{R} + \text{HBr}$ reaction) to regenerate R (yield >95%) or produce Br (yield <5%). We conclude from the above discussion that reaction 16 did not significantly alter observed Br temporal profiles.

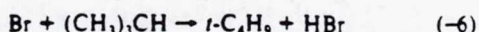
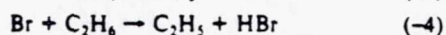
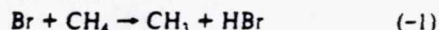
(25) Timonen, R. S.; Seetula, J. A.; Gutman, D. *J. Phys. Chem.* 1990, 94, 3005.

(26) Calvert, J. G.; Pitts, J. N., Jr. *Photochemistry*; Wiley, New York, 1966.

(27) Timonen, R. S.; Gutman, D. *J. Phys. Chem.* 1986, 90, 2987.

Comparison with Previous Work. Available kinetic data for alkyl radical reactions with HBr and DBr are summarized in Table II. The negative activation energies and fast rate coefficients for alkyl + HBr reactions reported by Gutman and co-workers^{4,5,7} are confirmed in our study. However, the activation energies derived from our data are consistently a little lower, i.e., more negative, than those reported by Gutman and co-workers, and the 298 K rate coefficients obtained in our study are consistently more than a factor of 2 faster than those reported by Gutman and co-workers. We observe "normal" kinetic isotope effects (i.e., R + HBr is faster than R + DBr) which decrease in magnitude with increasing complexity of the alkyl radical (and with decreasing activation energy). The 20% kinetic isotope effect we observe for *t*-C₄H₉ + HBr(DBr) at 298 K is an excellent agreement with the isotope effect observed by Richards et al.⁸ By far the most studied of the alkyl + HBr(DBr) reactions are those involving the *tert*-butyl radical. A majority of recent work, including our own, suggests that $k_6(298\text{ K}) \geq 1 \times 10^{-11} \text{ cm}^3 \text{ molecule}^{-1} \text{ s}^{-1}$ and $E_{\text{act}} < -1 \text{ kcal mol}^{-1}$.^{4,8,9} The exception is the very low pressure photolysis study of reaction 7 by Müller-Markgraf et al.,¹⁰ they report $k_7(295\text{ K}) = 1.5 \times 10^{-13} \text{ cm}^3 \text{ molecule}^{-1} \text{ s}^{-1}$ and a significant positive activation energy ($>2 \text{ kcal mol}^{-1}$). As discussed in some detail by Gutman,²⁸ the probable source of error in the Müller-Markgraf et al. study is neglect of heterogeneous loss of *t*-C₄H₉ in their data analysis. The only study of reactions 6 and 7 where kinetic data were obtained by monitoring the decay of *t*-C₄H₉ is the work of Russell et al.,⁴ who coupled time-resolved photoionization mass spectrometry with 193-nm laser flash photolysis of 4,4-dimethyl-1-pentene or 2,2,4,4-tetramethyl-3-pentanone; they obtained the results $k_6(298\text{ K}) = 1.04 \times 10^{-11} \text{ cm}^3 \text{ molecule}^{-1} \text{ s}^{-1}$ and $E_{\text{act}} = -1.4 \pm 0.2 \text{ kcal mol}^{-1}$. Subsequently, Richards et al.⁸ also generated *t*-C₄H₉ radicals by 193-nm laser flash photolysis of 4,4-dimethyl-1-pentene but obtained kinetic data by monitoring the appearance of the product (CH₃)₃CH using tunable diode laser spectroscopy as the monitoring technique; they found $k_6 = 1.0 \times 10^{-11} \text{ cm}^3 \text{ molecule}^{-1} \text{ s}^{-1}$, in excellent agreement with Russell et al. We find that $k_6(298\text{ K})$ is a factor of 2.7 faster than reported by Russell et al.⁴ and by Richards et al.⁸ and that $E_{\text{act}} = -1.9 \pm 0.3 \text{ kcal mol}^{-1}$, i.e., 0.5 kcal mol⁻¹ lower than reported by Russell et al. Seakins and Pilling⁹ have measured $k_6(298\text{ K})$ using 351-nm laser flash photolysis of azoisobutane as the *t*-C₄H₉ source and, as in our study, employing time-resolved resonance fluorescence monitoring of product bromine atoms as the kinetic probe; interestingly, they find $k_6(298\text{ K}) = (3.2 \pm 1.0) \times 10^{-11} \text{ cm}^3 \text{ molecule}^{-1} \text{ s}^{-1}$, in excellent agreement with our result. Any attempt to explain the difference between the rate coefficients reported in this study and those reported by Gutman and co-workers^{4,5,7} and by Richards et al.⁸ would be speculation on our part, since the alkyl + HBr(DBr) reactions appear to have been kinetically isolated from potential side reactions in all cases. Systematic error in determination of the HBr(DBr) concentration is one possibility. For example, Russell et al. report that HBr samples were not degassed prior to use,⁴ while we find that gas taken directly from the HBr storage cylinder can contain up to 50% H₂ impurity; hence, a large fraction of the gas flow that Russell et al. thought was HBr could have been unreactive H₂, thus leading to underestimation of the alkyl + HBr rate coefficients. Arguing against the above explanation, however, is the fact that Richards et al., who report that HBr and DBr samples were repeatedly degassed at 77 K prior to use,⁸ also obtained relatively slow rate coefficients for reactions 6 and 7.

Alkyl Radical Thermochemistry. Arrhenius parameters for reactions 1, 4, and 6 determined in this study can be combined with the best available Arrhenius parameters for the reverse (Br + RH) reactions to obtain entropies and enthalpies of reaction, using the "second-law method".



(28) Gutman, D. *Acc. Chem. Res.* 1990, 23, 375.

TABLE III: Arrhenius Parameters for k_{-1} , k_{-4} , and k_{-6} Used in the Thermochemical Calculations

reaction (no.)	$A^{a,b}$	$E/R^{a,c}$	range of T^c	ref
Br + CH ₄ (-1)	171 ± 85	8888 ± 220	298–621	29, 30
Br + C ₂ H ₆ (-4)	235 ± 112	6411 ± 180	476–621	29
Br + (CH ₃) ₃ CH (-6)	172 ± 30	3458 ± 90	298–623	4, 29

^aUnits are 10⁻¹² cm³ molecule⁻¹ s⁻¹. ^bUncertainties are estimates based on error bars reported in references. ^cUnits are degrees Kelvin.

TABLE IV: Thermochemical Parameters for the Reactions R + HBr → RH + Br, R = CH₃, C₂H₅, and *t*-C₄H₉

R	T, K	-ΔH, kcal mol ⁻¹		-ΔS, cal mol ⁻¹ deg ⁻¹	
		second law	third law	second law	third law
CH ₃	356	18.12 ± 0.48	17.56 ± 0.48	9.61 ± 1.23	7.96 ± 0.50
	298	17.97 ± 0.55	17.51 ± 0.41	9.05 ± 1.35	7.55 ± 0.50
C ₂ H ₅	403	13.81 ± 0.51	13.78 ± 0.68	10.28 ± 1.50	10.21 ± 1.20
	298	13.71 ± 0.60	13.70 ± 0.50	9.92 ± 1.75	9.91 ± 1.20
<i>t</i> -C ₄ H ₉	375	8.78 ± 0.48	9.23 ± 1.20	10.09 ± 1.40	11.27 ± 2.70
	298	8.67 ± 0.55	8.99 ± 0.95	9.69 ± 1.65	10.77 ± 2.70

The second-law method employs the following relationships to obtain thermochemical parameters for reaction *i*

$$\Delta H_i = E_i - E_{-i} \quad (\text{VI})$$

$$\Delta S_i = R \ln (A_i/A_{-i}) \quad (\text{VII})$$

where A_i and E_i are the A factor and activation energy for reaction *i*. The literature values for Arrhenius parameters for reactions -1, -4, and -6 which we have adopted are summarized in Table III. For k_{-4} , we adopt the recent direct determination of Seakins and Pilling.²⁹ For k_{-6} , we take the average of recent direct determinations by Seakins and Pilling²⁹ and by Russell et al.⁴ (which are in excellent agreement). We combine the Seakins and Pilling determination of k_{-4} with the temperature-dependent ratios k_{-4}/k_{17} and k_{-1}/k_{17} reported by Coomber and Whittle³⁰ to obtain an Arrhenius expression for k_{-1} .



Thermochemical parameters for reactions 1, 4, and 6 obtained from the second-law analysis are given in Table IV. The temperature in each case is defined as the arithmetic mean of the T^{-1} ranges employed in the determinations of k_i (this work) and k_{-i} (Table III). Values for ΔH at 298 K were computed using heat capacity corrections obtained from Burcat (CH₃),³¹ Chen et al. (C₂H₅),³² and Manion and Golden (*t*-C₄H₉);³³ the corrections calculated by Manion and Golden are based in large part on the experimental and theoretical studies of Pacansky and co-workers.^{34–37} Second-law values for ΔS at 298 K were computed from the relationship

$$\Delta G_{298} = \Delta H_{298} - T\Delta S_{298} = RT \ln K_{\text{eq}}(298\text{ K}) = RT \ln [k_{-i}(298\text{ K})/k_i(298\text{ K})] \quad (\text{VIII})$$

Values for $k_i(298\text{ K})$ were computed from the Arrhenius expressions reported in this paper, while values for $k_{-i}(298\text{ K})$ were computed from the Arrhenius expressions in Table III.

An alternate procedure for obtaining thermochemical parameters is the "third-law method" where the entropy change is

(29) Seakins, P. W. Dissertation, Oxford University, 1990. Seakins, P. W.; Pilling, M. J. Unpublished results.

(30) Coomber, J. W.; Whittle, E. *Trans. Faraday Soc.* 1966, 62, 1553.

(31) Burcat, A. In *Combustion Chemistry*; Gardiner, W. C., Jr., Ed.; Springer-Verlag: New York, 1984; pp 455–504.

(32) Chen, Y.; Rauk, A.; Tschuikow-Roux, E. *J. Chem. Phys.* 1990, 93, 1187.

(33) Manion, J. A.; Golden, D. M. Private communication.

(34) Pacansky, J.; Chang, J. S. *J. Chem. Phys.* 1981, 74, 5539.

(35) Schrader, B.; Pacansky, J.; Pfeiffer, U. *J. Phys. Chem.* 1984, 88, 4069.

(36) Pacansky, J.; Yoshimine, M. *J. Phys. Chem.* 1986, 90, 1980.

(37) Pacansky, J.; Koch, W.; Miller, M. D. *J. Am. Chem. Soc.* 1991, 113, 317.

TABLE V: Heats of Formation and R-H Bond Strengths^a

R	$\Delta H_{f,298}^{\circ}(\text{R})$	$D_{298}^{\circ}(\text{R-H})$
CH ₃	35.3 ± 0.5	105.3 ± 0.6
C ₂ H ₅	29.1 ± 0.5	101.3 ± 0.6
<i>t</i> -C ₄ H ₉	12.1 ± 0.7	96.4 ± 0.8

^aUnits are kcal mol⁻¹.

calculated using standard statistical mechanical methods³⁸ and employed in conjunction with experimental values for $K_{\text{eq}}(T)$ to obtain ΔH_T (using eq VIII). Absolute entropies as a function of temperature were obtained from Burcat³¹ except in the cases of C₂H₅^{32,39} and *t*-C₄H₉,³³ where updated entropy calculations are available. Third-law entropy changes for reactions 1, 4, and 6 are given in Table IV. Uncertainties in the third-law ΔS values are estimated on the basis of uncertainties in key structural parameters. The uncertainties in calculated entropy changes increase with increasing alkyl radical complexity, due in large part to uncertainties in the magnitudes of internal rotation barriers for C₂H₅³² and particularly for *t*-C₄H₉.^{2,36} In units of cal mol⁻¹ deg⁻¹, the 298 K entropies of CH₃, C₂H₅, and *t*-C₄H₉ used in our third-law determinations are 48.06, 58.98, and 75.70, respectively.

The enthalpy changes for reactions 1, 4, and 6 determined in this study can be combined with the accurately known heats of formation of Br, HBr, and RH^{23,31} to obtain alkyl radical heats of formation. Values for $\Delta H_{f,298}^{\circ}(\text{R})$ are given in Table V along with R-H bond strengths derived by combining the $\Delta H_{f,298}^{\circ}(\text{R})$ values with known heats of formation for RH and H.^{23,31} Simple averages of the second- and third-law enthalpies of reaction have been employed to obtain our reported values for $\Delta H_{f,298}^{\circ}(\text{R})$; this approach seems reasonable since (a) estimated uncertainties in the second- and third-law determinations are similar and (b) the second- and third-law values for $\Delta H_{298}^{\circ}(\text{reaction } i)$ agree to within a few tenths of a kilocalorie per mole in all three cases. The relatively low activation energies for reactions 4 and 6 reported in this study leads to heats of formation for C₂H₅ and *t*-C₄H₉ which are 0.4 and 0.5 kcal mol⁻¹ higher than those reported by Russell et al.,^{4,5} although our results agree with those of Russell et al. within combined uncertainties. As discussed briefly under Introduction, Tsang has critically reviewed the literature and, showing a preference for thermochemical data from bond scission and recombination studies of simple alkanes and radicals over thermochemical data from iodination and bromination studies, has recommended values for the heats of formation of a number of alkyl radicals including C₂H₅¹ and *t*-C₄H₉.² Our value for $\Delta H_{f,298}^{\circ}(\text{C}_2\text{H}_5)$ is 0.5 kcal mol⁻¹ larger than the value recommended by Tsang, although in agreement within combined uncertainties. Our value for $\Delta H_{f,298}^{\circ}(\textit{t}\text{-C}_4\text{H}_9)$ is 0.2 kcal mol⁻¹ smaller than the value recommended by Tsang under the assumption that all barriers to internal rotation are zero but 1.1 kcal mol⁻¹ larger than the value recommended by Tsang under the assumption that all internal rotation barriers are 2.4 kcal mol⁻¹; a recent ab initio calculation³⁶ predicts that the barriers to methyl rotation are 1.51 kcal mol⁻¹. The alkyl radical heats of formation reported in this study are significantly higher than those recommended by McMillen and Golden³ in a critical review which showed a preference for results from iodination and bromination studies over those from bond scission and recombination studies; as discussed in detail by Gutman and co-workers,^{4,5,28} the apparently incorrect assumption by McMillen and Golden of small positive activation energies for alkyl + HX reactions appears to completely account for the discrepancy. As discussed above, Müller-Markgraf et al.¹⁰ observe a significant positive activation energy for

reaction 7; hence, these authors derive a value for $\Delta H_{f,298}^{\circ}(\textit{t}\text{-C}_4\text{H}_9)$ which is 2.9 kcal mol⁻¹ lower than the value reported in this study.

Mechanism for Alkyl + HX Reactions. Traditionally, hydrogen-transfer reactions such as $\text{R} + \text{HX} \rightarrow \text{RH} + \text{X}$ have been thought of as "direct" metathesis reactions with a barrier along the reaction coordinate and a single transition state located at the potential energy maximum. Rationalization of observed negative activation energies for $\text{R} + \text{HX}$ reactions requires the postulate that reaction proceeds via formation of a weakly bound $\text{R}\cdots\text{X}\cdots\text{H}$ complex.^{4-6,12} As shown by Mozurkewich and Benson,⁴⁰ if the transition state leading from reactants to complex (TS1) is loose and the transition state leading from complex to products is both tighter and lower in energy compared to TS1, then a negative temperature dependence for the overall reaction should be observed. McEwen and Golden¹² have carried out a two-channel RRKM calculation that models the *t*-C₄H₉ + HI(DI) reactions as proceeding through a weakly bound complex; they were able to reproduce the kinetic results of Seetula et al.⁶ for *t*-C₄H₉ + HI with complex binding energies as low as 3 kcal mol⁻¹. One interesting aspect of McEwen and Golden's study is the fact that models which were capable of reproducing experimentally observed⁶ $k(T)$ values for *t*-C₄H₉ + HI also predicted an inverse kinetic isotope effect (KIE), i.e., $k_{\text{HI}} < k_{\text{DI}}$; the inverse KIE results from the fact that the transition state leading from complex to products becomes looser with the lower vibrational frequencies associated with deuterium substitution. Contrary to McEwen and Golden's predictions for *t*-C₄H₉ + HI, we observe normal KIEs for CH₃, C₂H₅, and *t*-C₄H₉ reactions with HBr, i.e., $k_{\text{HBr}} > k_{\text{DBr}}$. Richards et al.⁸ also observe a normal KIE for the *t*-C₄H₉ + HBr reaction. It does appear, however, that the magnitude of the KIE is reduced as the activation energy becomes more negative; i.e., the observed KIE is largest for R = CH₃ and smallest for R = *t*-C₄H₉. Further experimental and theoretical studies of alkyl + HX reaction dynamics are clearly needed before a detailed understanding of these complex chemical reactions will be forthcoming.

Acknowledgment. We thank P. W. Seakins and M. J. Pilling for making their results on Br + C₂H₅, Br + (CH₃)₃CH, and *t*-C₄H₉ + HBr available to us before publication and J. A. Manion and D. M. Golden for calculation of *t*-C₄H₉ thermodynamic functions. We also thank D. M. Golden and D. Gutman for several helpful discussions. This work was supported by Grants ATM-8802386 and ATM-9104807 from the National Science Foundation and Grant NAGW-1001 from the National Aeronautics and Space Administration.

Note Added in Proof. We have recently become aware of a theoretical study of the CH₃ + HBr reaction by Chen, Tschui-kow-Roux, and Rauk; two papers describing their study appear in this issue. These authors have calculated a potential energy surface for the CH₃ + HBr reaction at the G1 level of theory and deduced the existence of a hydrogen-bridged complex with C_{3v} symmetry which is bound by 0.28 kcal mol⁻¹ and is formed without activation energy. They have also calculated rate constants for CH₃ + HBr, CH₃ + DBr, and CD₃ + HBr from RRKM theory with corrections for tunneling evaluated using the Wigner method. Their calculated isotope effects agree quantitatively with those reported in this paper.

Registry No. ICH₃, 74-88-4; IC₂H₅, 75-03-6; *l*-C₄H₉, 558-17-8; Cl₂H, 7782-50-5; HCH₃, 74-82-8; HC₂H₅, 74-84-0; HBr, 10035-10-6; CH₃, 2229-07-4; C₂H₅, 2025-56-1; *t*-C₄H₉, 1605-73-8; H, 1333-74-0; D, 7782-39-0.

(38) See, for example: Knox, J. H. *Molecular Thermodynamics*; Wiley-Interscience: London, 1971.

(39) Brouard, M.; Lightfoot, P. D.; Pilling, M. J. *J. Phys. Chem.* **1986**, *90*, 445.

(40) Mozurkewich, M.; Benson, S. W. *J. Phys. Chem.* **1984**, *88*, 6429.

(41) Gac, N. A.; Golden, D. M.; Benson, S. W. *J. Am. Chem. Soc.* **1969**, *91*, 309.

Kinetics and Thermochemistry of the $\text{Br}(^2P_{3/2}) + \text{NO}_2$ Association Reaction

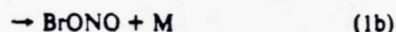
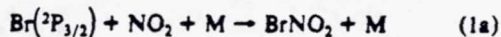
K. D. Kreutter, J. M. Nicovich, and P. H. Wine*

Physical Sciences Laboratory, Georgia Tech Research Institute, Georgia Institute of Technology,
Atlanta, Georgia 30332 (Received: October 12, 1990; In Final Form: December 17, 1990)

A laser flash photolysis-resonance fluorescence technique has been employed to study the kinetics of the $\text{Br}(^2P_{3/2}) + \text{NO}_2$ association reaction as a function of temperature (259–432 K), pressure (12.5–700 Torr), and buffer gas identity (He, Ar, H_2 , N_2 , CO_2 , CF_4 , SF_6). The reaction is found to be in the falloff regime between third and second order over the entire range of conditions investigated. At temperatures below 350 K, the association reaction is found to be irreversible on the time scale of the experiment (~30 ms). At higher temperatures reversible addition is observed, allowing equilibrium constants for BrNO_2 formation and dissociation to be determined. Second- and third-law analyses of the equilibrium data are in only fair agreement and lead to the following thermochemical parameters for the association reaction: $\Delta H^\circ_{298} = -19.6 \pm 1.7$ kcal mol⁻¹, $\Delta H^\circ_0 = -18.6 \pm 2.0$ kcal mol⁻¹, $\Delta S^\circ_{298} = -29.3 \pm 4.2$ cal mol⁻¹ K⁻¹; $\Delta H^\circ_{298}(\text{BrNO}_2) = 17.0 \pm 1.8$ kcal mol⁻¹ (uncertainties are 2 σ estimates of absolute accuracy). The value for ΔH°_0 determined in this study has been employed to calculate k_0^{SC} , the low-pressure third-order rate coefficient in the strong collision limit, by using the method of Troe; calculated values of k_0^{SC} are inconsistent with experimental results unless ΔH°_0 is assigned a value near the lower limit derived from analysis of the high-temperature approach to equilibrium data, i.e., $\Delta H^\circ_0 \approx -16.6$ kcal mol⁻¹. A potential source of systematic error in the calculation of both k_0^{SC} and the absolute entropy of BrNO_2 results from the complete lack of knowledge of the energies and degeneracies of the electronic states of BrNO_2 . The procedure developed by Troe and co-workers has been employed to extrapolate experimental falloff curves to the low- and high-pressure limits. Derived values for $k_0(\text{M}, 298\text{K})$ in units of 10^{-31} cm⁶ molecule⁻² s⁻¹ range from 2.75 for M = He to 6.54 for M = CO_2 ; 2 σ uncertainties are estimated to be $\pm 20\%$. Values for $k_0(\text{N}_2, T)$ in units of 10^{-31} cm⁶ molecule⁻² s⁻¹ are 5.73 at 259 K, 4.61 at 298 K, and 3.21 at 346 K; the observed temperature dependence for $k_0(\text{N}_2, T)$ is consistent with the theoretical temperature dependence for $\beta_0 k_0^{\text{SC}}$. Values for $k_w(T)$ in units of 10^{-11} cm³ molecule⁻¹ s⁻¹ are 2.86 at 259 K, 3.22 at 298 K, and 3.73 at 346 K; 2 σ uncertainties are estimated to be a factor of 2. Approximate falloff parameters in a convenient format for atmospheric modeling are also derived.

Introduction

The reactions of fluorine and chlorine atoms with NO_2 have been studied extensively in cryogenic matrices¹⁻³ and in the gas phase.⁴⁻¹¹ These studies have established the gas-phase kinetics of the F, Cl + NO_2 association reactions⁵⁻¹¹ and have demonstrated that both the nitrite (XONO) and the nitryl halide (XNO₂) isomers are produced.¹⁻⁴ Under atmospheric conditions, ClONO is the major product of the Cl + NO_2 reaction; the ClONO₂ yield is only about 0.2.⁴ Until very recently, the only information about the reaction



came from cryogenic matrix studies,^{12,13} which demonstrated that BrNO_2 is the dominant product, i.e., $k_{1a} \gg k_{1b}$; this observation has now been extended to the gas phase.¹⁴ Also, gas-phase BrNO_2 has recently been observed as a product of the heterogeneous reaction of N_2O_3 vapor with solid NaBr.¹⁵ Nitryl bromide could act as a reservoir for BrO_2 in the lower stratosphere, and it has recently been suggested¹⁶ that photolysis of BrNO_2 (formed via the $\text{N}_2\text{O}_3(\text{g}) + \text{NaBr}(\text{s})$ reaction) may initiate chain reactions that result in the recently observed ground-level arctic ozone hole.^{17,18} Hence, there currently exists a great deal of interest in understanding the reaction kinetics, photochemistry, and thermochemistry of nitryl bromide.

The only reported kinetics study of reaction 1 is the work of Mellouki et al.,¹⁹ who employed a discharge flow technique with EPR and mass spectrometric analysis to measure k_1 at 298 K in helium buffer gas over the pressure range 0.6–2.1 Torr; they report the low-pressure limit rate coefficient $k_{1,0}(\text{He}, 298\text{K}) = (3.7 \pm 0.7) \times 10^{-31}$ cm⁶ molecule⁻² s⁻¹.

In this paper, we report the results of an experimental study that employed the laser flash photolysis-resonance fluorescence technique to study the kinetics of reaction 1 over wide ranges of temperature (259–432 K), pressure (12.5–700 Torr), and buffer gas identity (N_2 , He, Ar, H_2 , CO_2 , CF_4 , SF_6). These data allow

accurate values for $k_1(P, T)$ to be obtained over the pressure-temperature regime of atmospheric interest and provide the first data that can be used to estimate (with a rather large uncertainty) $k_{1,0}$, the rate coefficient in the high-pressure limit. At temperatures above 350 K, bromine atom regeneration from BrNO_2 decomposition occurred on the experimental time scale for reaction 1, i.e., 10^{-5} – 10^{-2} s. Analysis of the resultant double-exponential decays has allowed the first determinations of both BrNO_2 unimolecular decomposition rate coefficients and the BrNO_2 heat of formation.

- (1) Smardzewski, R. R.; Fox, W. B. *J. Chem. Soc., Chem. Commun.* 1974, 241.
- (2) Smardzewski, R. R.; Fox, W. B. *J. Chem. Phys.* 1974, 60, 2980.
- (3) Tevault, D. E.; Smardzewski, R. R. *J. Chem. Phys.* 1977, 67, 3777.
- (4) Niki, H.; Makey, P. D.; Savage, D. M.; Breitenbach, L. P. *Chem. Phys. Lett.* 1978, 59, 78.
- (5) Fasano, D. M.; Nogar, N. S. *J. Chem. Phys.* 1983, 77, 6688.
- (6) Clyne, M. A. A.; White, I. F. Reported in: Watson, R. T. *J. Phys. Chem. Ref. Data* 1977, 6, 871.
- (7) Zahniser, M. S.; Chang, J. S.; Kaufman, F. *J. Chem. Phys.* 1977, 67, 997.
- (8) Lou, M. T. *Int. J. Chem. Kinet.* 1984, 16, 1311.
- (9) Glavas, S.; Heicklen, J. *J. Photochem.* 1985, 31, 21.
- (10) Mellouki, A.; Poulet, G.; LeBras, G. *J. Geophys. Res.* 1987, 92, 4217.
- (11) Ravishankara, A. R.; Smith, G. J.; Davis, D. D. *Int. J. Chem. Kinet.* 1988, 20, 811.
- (12) Tevault, D. E. *J. Phys. Chem.* 1979, 83, 2217.
- (13) Feuerhahn, M.; Minkwitz, R.; Engelhardt, U. *J. Mol. Spectrosc.* 1979, 77, 429.
- (14) Yarwood, G.; Niki, H., private communication.
- (15) Finlayson-Pitts, B. J.; Livingston, F. E.; Berko, H. N. *J. Phys. Chem.* 1989, 93, 4397.
- (16) Finlayson-Pitts, B. J.; Livingston, F. E.; Berko, H. N. *Nature* 1990, 343, 622.
- (17) Barrie, L. A.; Bottenheim, J. W.; Schnell, R. C.; Crutzen, P. J.; Rasmussen, R. A. *Nature* 1983, 334, 138.
- (18) Barrie, L. A.; den Hartog, G.; Bottenheim, J. E.; Landsberger, S. J. *Atmos. Chem.* 1990, 9, 101.
- (19) Mellouki, A.; Laverdet, G.; Jourdain, J. L.; Poulet, G. *Int. J. Chem. Kinet.* 1989, 21, 1161.

* To whom correspondence should be addressed.

Experimental Technique

A schematic diagram of the laser flash photolysis-resonance fluorescence apparatus, as configured for bromine atom detection, is shown elsewhere.²⁰ A description of the experimental methodology is given below.

A Pyrex-jacketed reaction cell with an internal volume of 150 cm³ was used in all experiments. The cell was maintained at a constant temperature by circulating ethylene glycol or methanol from a thermostatically controlled bath through the outer jacket. A copper-constantan thermocouple with a stainless steel jacket was injected into the reaction zone through a vacuum seal, thus allowing measurement of the gas temperature under the precise pressure and flow rate conditions of the experiment.

Bromine atoms were produced by 266-nm pulsed laser photolysis of CF₂Br₂/NO₂/M or Br₂/NO₂/M mixtures; a majority of experiments employed a CF₂Br₂ as the bromine atom precursor. Fourth harmonic radiation from a Quanta Ray Model DCR-2 Nd:YAG laser provided the photolytic light source. The laser could deliver up to 3 × 10¹⁶ photons/pulse at a repetition rate of up to 10 Hz; the pulse width was 6 ns.

A bromine resonance lamp, situated perpendicular to the photolysis laser, excited resonance fluorescence in the photolytically produced atoms. The resonance lamp consisted of an electrodeless microwave discharge through about 1 Torr of a flowing mixture containing a trace of Br₂ in helium. The flows of a 0.2% Br₂ in helium mixture and pure helium into the lamp were controlled by separate needle valves, thus allowing the total pressure and Br₂ concentration to be adjusted for optimum signal-to-noise ratio. Radiation was coupled out of the lamp through a magnesium fluoride window and into the reaction cell through a magnesium fluoride lens. Before entering the reaction cell, the lamp output passed through a flowing gas filter containing 50 Torr cm of methane in nitrogen. The methane filter prevented radiation at wavelengths shorter than 140 nm (including impurity emissions from excited oxygen, hydrogen, chlorine, and nitrogen atoms) from entering the reaction cell but transmitted the strong bromine lines in the 140–160-nm region.

Fluorescence was collected by a magnesium fluoride lens on an axis orthogonal to both the photolysis laser beam and the resonance lamp beam and was imaged onto the photocathode of a solar blind photomultiplier. Signals were processed by using photon-counting techniques in conjunction with multichannel scaling. For each bromine atom decay measured, signals from a large number of laser shots were averaged in order to obtain a well-defined temporal profile over (typically) three 1/e times of decay.

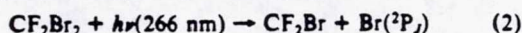
To avoid accumulation of photolysis or reaction products, all experiments were carried out under "slow flow" conditions. The linear flow rate through the reactor was in the range 1–3 cm s⁻¹, and the laser repetition rate was varied over the range 1–10 Hz (5 Hz typical). Hence, no volume element of the reaction mixture was subjected to more than a few laser shots. CF₂Br₂, Br₂, and NO₂ were flowed into the reaction cell from bulbs (12-L volume) containing dilute mixtures in buffer gas. The photolyte (CF₂Br₂ or Br₂) mixture, NO₂ mixture, buffer gas, and a small amount of hydrogen were premixed before entering the reactor. The concentrations of each component in the reaction mixture were determined from measurements of the appropriate mass flow rates and the total pressure. The concentration of NO₂ in the reaction mixture was also determined by in situ UV photometry at 366 nm. A mercury pen-ray lamp was employed as the light source for the photometric measurement, and an interference filter was used to isolate the three closely spaced Hg lines around 366 nm from other lamp emissions. For the lamp-filter combination employed, the "effective" NO₂ absorption cross section has been previously determined to be 5.75 × 10⁻¹⁹ cm²;²¹ experimental results were found to be independent of whether the NO₂ ab-

sorption cell was positioned upstream or downstream relative to the reaction cell.

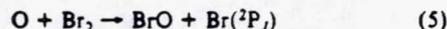
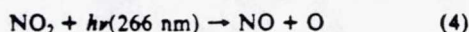
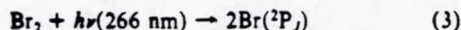
The gases used in this study had the following stated minimum purities: N₂, 99.999%; He, 99.999%; Ar, 99.999%; H₂, 99.999%; CO₂, 99.998%; SF₆, 99.99%; O₂, 99.99%; CF₄, 99.7%; NO, 99.0%. All gases except NO were used as supplied. The procedures employed to purify NO and synthesize pure NO₂ from the NO + O₂ reaction are described elsewhere.²² The liquids used in this study had the following stated minimum purities: CF₂Br₂, 99.0%; Br₂, 99.94%. Both CF₂Br₂ and Br₂ were transferred under nitrogen into vials fitted with high-vacuum stopcocks and were degassed repeatedly at 77 K before being used to prepare gaseous photolyte-buffer gas mixtures.

Results and Discussion

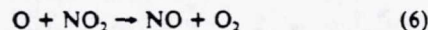
In a vast majority of experiments, bromine atoms were generated by laser flash photolysis of CF₂Br₂:



The CF₂Br₂ absorption cross section at 266 nm is 8 × 10⁻²⁰ cm² (T = 298 K)^{23,24} and the bromine atom yield is unity.²⁴ In a few experiments, the following alternative bromine atom production scheme was employed:

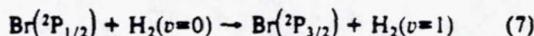


Absorption cross sections for Br₂ and NO₂ at 266 nm are ~2 × 10⁻²⁰²⁵ and 2.7 × 10⁻²⁰ cm²,²⁶ respectively. To minimize production of NO from the side reaction



rather large concentrations of CF₂Br₂ (or Br₂) and low laser powers were typically employed. Observed kinetics were independent of laser power and photolyte concentration over wide ranges; concentrations of photolytically produced bromine atoms ranged from 3 × 10¹⁰ to 30 × 10¹⁰ atoms cm⁻³. Observed kinetics were also found to be independent of whether reaction 2 or reactions 3–5 was employed as the bromine atom source.

To ensure rapid relaxation of bromine atoms in the spin-orbit excited ²P_{1/2} state, about 1 Torr of H₂ was added to the reaction mixture. The reaction



is known to be fast, with k₇ ≈ 6 × 10⁻¹² cm³ molecule⁻¹ s⁻¹.²⁷ Since the equilibrium concentration of Br(²P_{1/2}) is negligible over the temperature range of our study, all measured bromine atom temporal profiles should be considered as representative of removal of ground-state atoms, Br(²P_{3/2}); in the discussion that follows Br = Br(²P_{3/2}).

All experiments were carried out under pseudo-first-order conditions with NO₂ in large excess over Br. Hence, in the absence of side reactions that remove or produce Br, the Br temporal profile following the laser flash would be described by the relationship

$$\ln \{[\text{Br}]_0/[\text{Br}]_t\} = (k_1[\text{NO}_2] + k_2)t = k't \quad (1)$$

where k₂ is the rate coefficient for the process

Br → first-order loss by diffusion from the detector field of view and/or reaction with background impurities (8)

(22) Daykin, E. P.; Wine, P. H. *J. Phys. Chem.* **1990**, *94*, 4528.

(23) Molina, L. T.; Molina, L. J.; Rowland, F. S. *J. Phys. Chem.* **1982**, *86*, 2672.

(24) Ravishankara, A. R. *11th International Conference on Gas Kinetics*, Assisi, Italy, 1990; paper O-11.

(25) Calvert, J. G.; Pitts, J. N., Jr. *Photochemistry*; Wiley: New York, 1966; p 184.

(26) Schneider, W.; Moortgat, G. K.; Tyndall, G. S.; Burrows, J. P. *J. Photochem. Photobiol., A* **1987**, *40*, 195.

(27) Nesbitt, D. J.; Leone, S. R. *J. Chem. Phys.* **1980**, *73*, 6182.

(20) Nicovich, J. M.; Shackelford, C. J.; Wine, P. H. *J. Photochem. Photobiol.* **1990**, *51*, 141.

(21) Wine, P. H.; Kreutter, N. M.; Ravishankara, A. R. *J. Phys. Chem.* **1979**, *83*, 3191.

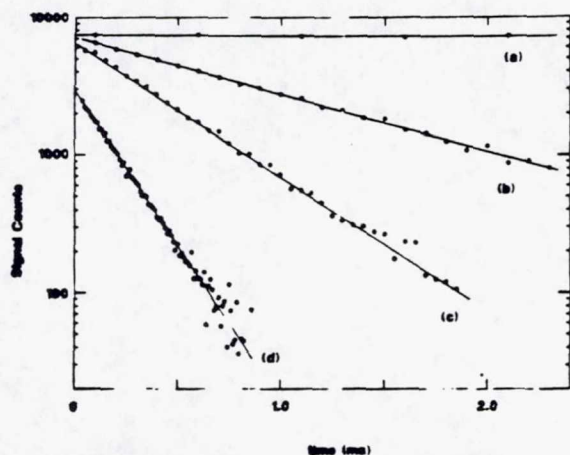


Figure 1. Typical Br($2P_{3/2}$) temporal profiles observed at $T < 350$ K. Experimental conditions: $T = 298$ K; $P = 100$ Torr; $M = N_2$; $[CF_2Br_2] = 2.0 \times 10^{13}$ molecules cm^{-3} ; $[Br]_0 = 6 \times 10^{10}$ atoms cm^{-3} ; $[NO_2]$ in units of 10^{15} molecules cm^{-3} (a) 0, (b) 0.886, (c) 1.97, (d) 4.69; number of laser shots averaged (a) 100, (b) 400, (c) 700, (d) 2001. Solid lines are obtained from least-squares analyses and give the following pseudo-first-order decay rates in units of s^{-1} : (a) 12, (b) 950, (c) 2250, (d) 5290.

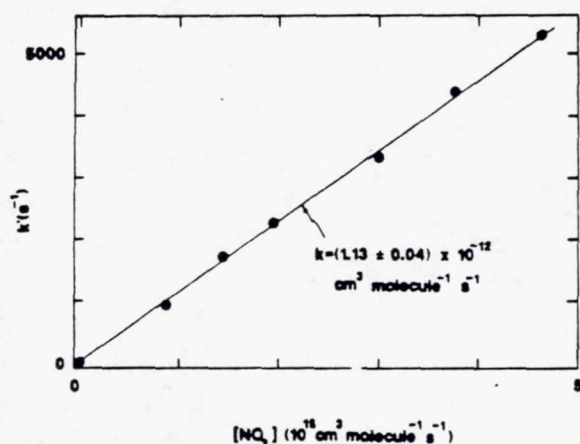


Figure 2. Typical plot of k' , the Br($2P_{3/2}$) pseudo-first-order decay rate, versus NO_2 concentration for data obtained at $T < 350$ K. Experimental conditions: $T = 298$ K; $P = 100$ Torr; $M = N_2$. The solid line is obtained from a linear least-squares analysis and gives the bimolecular rate coefficient shown in the figure.

The bimolecular rate coefficients of interest, $k_1([M], T)$ are determined from the slopes of k' versus $[NO_2]$ plots. Observation of Br temporal profiles that are exponential (i.e., obey eq I), a linear dependence of k' on $[NO_2]$, and invariance of k' to variation in laser photon fluence and photolyte concentration strongly suggest that reactions 1 and 8 are, indeed, the only processes that significantly affect the Br time history.

Kinetics at $T < 350$ K. For all experiments carried out at temperatures below 350 K, well-behaved pseudo-first-order kinetics were observed, i.e., Br temporal profiles obeyed eq I and k' increased linearly with increasing $[NO_2]$ but was independent of laser photon fluence and photolyte concentration. Typical data are shown in Figures 1 and 2. Measured bimolecular rate coefficients, $k_1([M], T)$, are summarized in Table I. Kinetics studies were restricted to $T \geq 259$ K because NO_2 dimerization became a problem at lower temperatures.²⁸

Parametrization of $k_1([N_2], T)$ for Atmospheric Modeling. For purposes of atmospheric modeling, it is convenient to generate a mathematical expression that can be used to compute $k_1([N_2], T)$ over the range of relevant temperatures and pressures (the effi-

TABLE I: Rate Coefficients for the Reaction $Br + NO_2 + M \rightarrow BrNO_2 + M$ Obtained under Experimental Conditions ($T < 350$ K) Where the Association Reaction Was Irreversible on the Time Scale for Br Decay^a

M	P, Torr	$k_1, 10^{-13} \text{ cm}^3 \text{ molecule}^{-1} \text{ s}^{-1}$		
		259 K	298 K	346 K
He	12.5		0.97 ± 0.02	
	25		1.92 ± 0.04	
Ar	12.5		1.26 ± 0.02	
	25		2.42 ± 0.03	
H ₂	12.5		1.92 ± 0.05	
	25		3.23 ± 0.08	
N ₂	12.5	2.36 ± 0.23	1.73 ± 0.15	1.07 ± 0.04
	25	4.83 ± 0.40	3.18 ± 0.10	1.98 ± 0.04
	50	8.24 ± 0.49	6.20 ± 0.27	3.66 ± 0.07
	100	15.4 ± 1.2	11.3 ± 0.4	6.72 ± 0.08
	200	26.5 ± 0.9	19.8 ± 1.4	12.3 ± 0.4
	400	42.7 ± 2.1	31.6 ± 1.6	22.8 ± 1.0
700	62.9 ± 4.3	48.6 ± 1.0	35.4 ± 1.6	
CO ₂	12.5		2.36 ± 0.10	
	25		4.52 ± 0.15	
CF ₄	12.5		2.27 ± 0.47	
	25		4.27 ± 0.08	
	50		7.93 ± 0.23	
	100		14.2 ± 0.5	
	200		26.6 ± 1.8	
SF ₆	400		44.1 ± 0.9	
	700		63.9 ± 3.5	
	12.5		2.06 ± 0.03	
	25		3.64 ± 0.26	

^a Errors are 2σ and represent precision only.

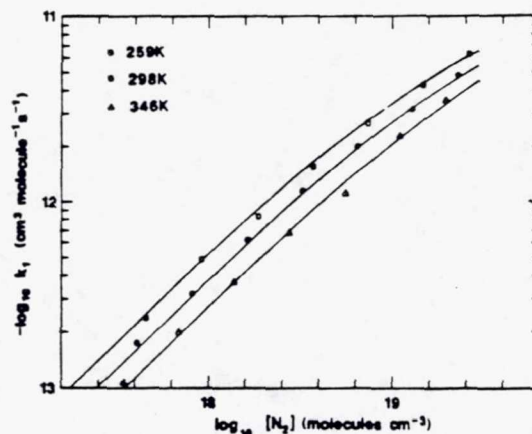


Figure 3. Best fits of the $k_1(N_2, T)$ versus pressure data to eq II. Squares, circles, and triangles are experimental data at different temperatures. Solid lines are calculated from eq II with $A = 4.24 \times 10^{-31} (T/300)^{-2.4} \text{ cm}^6 \text{ molecule}^{-2} \text{ s}^{-1}$ and $B = 2.66 \times 10^{-11} (T/300)^{0.0} \text{ cm}^3 \text{ molecule}^{-1} \text{ s}^{-1}$.

ciency of O_2 as a third body is generally very similar to that of N_2). The expression generally used for this purpose is²⁹

$$k_1([N_2], T) = \{A/[1 + (A/B)]\}0.6^{1 + \ln(A/B)^{1/2}} \quad (\text{II})$$

where

$$A = k_{1,0}(T)[N_2] = k_{1,0}(300\text{K})(T/300)^{-n} \quad (\text{III})$$

$$B = k_{1,\infty}(T) = k_{1,\infty}(300\text{K})(T/300)^{-m} \quad (\text{IV})$$

In the above expressions, $k_{1,0}$ and $k_{1,\infty}$ are approximations to the low- and high-pressure limit rate coefficients for reaction 1. Fitting our measured values of $k_1([N_2], T)$ to eq II gives the following parameters:

(29) See, for example: DeMore, W. B.; Sander, S. P.; Golden, D. M.; Molina, M. J.; Hampson, R. F.; Kurylo, M. J.; Howard, C. J.; Ravishankara, A. R. *Chemical Kinetics and Photochemical Data for Use in Stratospheric Modeling*; Evaluation no. 9, Jet Propulsion Laboratory publication 90-1, 1990.

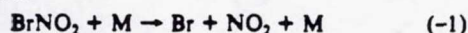
(28) Blend, H. J. *Chem. Phys.* 1970, 53, 4497.

$$A = 4.24 \times 10^{-31} (T/300)^{-2.4} \text{ cm}^6 \text{ molecule}^{-2} \text{ s}^{-1}$$

$$B = 2.66 \times 10^{-11} (T/300)^{0.0} \text{ cm}^3 \text{ molecule}^{-1} \text{ s}^{-1}$$

Falloff curves calculated by substituting the above parameters into eq II are compared with measured rate coefficients in Figure 3; the parametrization represents the experimental data very well.

Kinetics at $T > 350$ K. At temperatures above 350 K, bromine atom regeneration due to a secondary reaction became evident. Observed Br temporal profiles were independent of laser fluence and CF₂Br₂ concentration but varied as a function of [NO₂] and [M] in the manner expected if unimolecular decomposition of BrNO₂ was the source of regenerated Br. Assuming that BrNO₂ regeneration was occurring, the relevant kinetic scheme controlling Br removal includes not only reactions 1 and 8 but also the additional reactions



BrNO₂ →

first-order loss by processes that do not regenerate Br atoms (9)

Assuming that all processes affecting Br and BrNO₂ concentrations are first order, the rate equations for reactions 1, -1, 8, and 9 can be solved analytically:

$$[\text{Br}]_t / [\text{Br}]_0 = \frac{(Q + \lambda_1) \exp(\lambda_1 t) - (Q + \lambda_2) \exp(\lambda_2 t)}{(\lambda_1 - \lambda_2)} \quad (\text{V})$$

where

$$\lambda_1 = 0.5[(a^2 - 4b)^{1/2} - a] \quad (\text{VI})$$

$$\lambda_2 = -0.5[(a^2 - 4b)^{1/2} + a] \quad (\text{VII})$$

$$Q = k_{-1} + k_9 \quad (\text{VIII})$$

$$a = Q + k_8 + k_1[\text{NO}_2] = -(\lambda_1 + \lambda_2) \quad (\text{IX})$$

$$b = k_8 Q + k_9 k_1[\text{NO}_2] = \lambda_1 \lambda_2 \quad (\text{X})$$

Observed temporal profiles for Br atoms were fit to the double-exponential eq V by using a nonlinear least-squares method to obtain values for λ_1 , λ_2 , and Q for each decay. The background Br atom loss rate in the absence of NO₂ (k_9) was directly measured at each temperature and pressure; k_9 ranged from 10 to 90 s⁻¹. Rearrangement of the above equations shows that the fit parameters λ_1 , λ_2 , and Q can be related to the rate coefficients of interest as follows:

$$k_1 = -(Q + k_2 + \lambda_1 + \lambda_2) / [\text{NO}_2] \quad (\text{XI})$$

$$k_9 = (\lambda_1 \lambda_2 - k_2 Q) / k_1 [\text{NO}_2] \quad (\text{XII})$$

$$k_{-1} = Q - k_9 \quad (\text{XIII})$$

Typical Br atom temporal profiles observed in the high-temperature experiments are shown in Figure 4 along with best fits to eq V. The results for all high-temperature experiments are summarized in Table II. The equilibrium constants, K_p , given in Table II are computed from the relationship

$$K_p = k_1 / k_{-1} RT = K_c / RT \quad (\text{XIV})$$

It is worth noting that values for k_1 ([N₂], T) obtained from the least-squares analyses are consistent with those expected based on extrapolation of data from $T < 350$ K. We believe that reported values for k_1 , even at high temperature where Br regeneration is fast, are accurate to within $\pm 20\%$. Absolute uncertainties in reported values for k_{-1} are somewhat more difficult to assess. Inspection of Table II shows that the precision in multiple determinations of k_{-1} at a particular temperature and pressure (for varying [NO₂]) is quite good, even at low T and low P , where k_9 contributes about as much as k_{-1} to the parameter Q . An inherent assumption in our analysis is that the only significant BrNO₂ loss process that results in Br atom production is reaction -1; as long as this assumption is correct (it almost certainly is), we believe the absolute accuracy of our reported k_{-1} values is $\pm 30\%$ over the full range of temperature and pressure investigated.

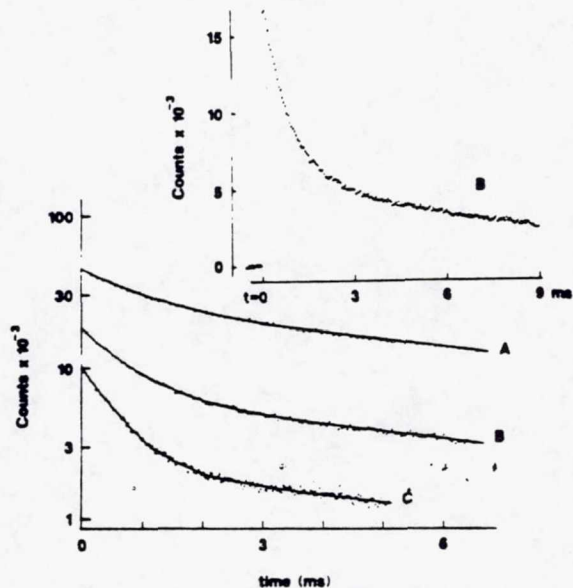


Figure 4. Typical Br(²P_{3/2}) temporal profiles observed at $T > 350$ K. Experimental conditions: $T = 411$ K; $P = 50$ Torr; $M = \text{N}_2$; $[\text{CF}_2\text{Br}_2] = (2.2\text{--}2.8) \times 10^{13}$ molecules cm^{-3} ; $[\text{Br}]_0 = (6\text{--}8) \times 10^{10}$ atoms cm^{-3} ; $[\text{NO}_2]$ in units of 10^{15} molecules cm^{-3} (A) 2.22, (B) 4.01, (C) 7.09; number of laser shots averaged (A) 3000, (B) 3000, (C) 5000. Solid lines are obtained from nonlinear least-squares fits to eq V. Best-fit parameters in units of s⁻¹ are $-\lambda_1 =$ (A) 83.8, (B) 107, (C) 115, $-\lambda_2 =$ (A) 837, (B) 1280, (C) 1830; $Q =$ (A) 462, (B) 525, (C) 500. The inset shows trace B with the signal counts displayed on a linear scale.

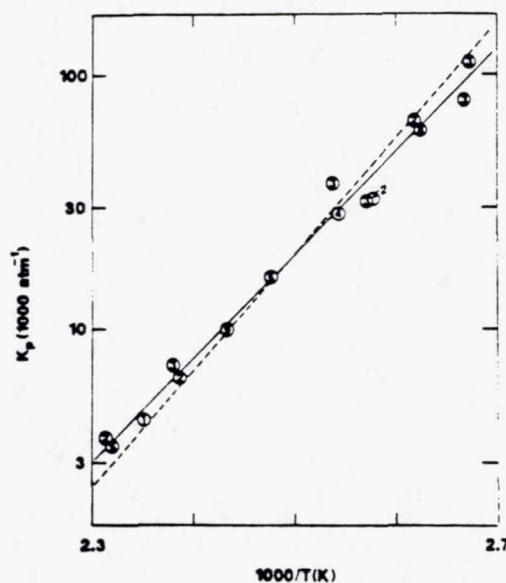


Figure 5. van't Hoff plot for the reaction $\text{Br} + \text{NO}_2 \rightleftharpoons \text{BrNO}_2$. The small numbers inside the data points indicate the number of individual experiments that were averaged to obtain the particular point. The solid line is obtained from a weighted least-squares analysis and gives the second-law thermochemical parameters $\Delta H_{401} = -18.64 \pm 0.56$ kcal mol^{-1} (slope) and $\Delta S_{401} = -26.94 \pm 1.40$ cal $\text{mol}^{-1} \text{ deg}^{-1}$ (intercept). The dotted line is obtained from a third-law analysis with K_p at 401 K assigned the value obtained by interpolation using the second-law method; third-law thermochemical parameters are $\Delta H_{401} = -20.77$ kcal mol^{-1} and $\Delta S_{401} = -32.24$ cal $\text{mol}^{-1} \text{ deg}^{-1}$.

BrNO₂ Thermochemistry. A van't Hoff plot for the equilibrium defined by reactions 1 and -1 is shown in Figure 5. Since

$$\ln K_p = (\Delta S/R) - (\Delta H/RT) \quad (\text{XV})$$

the enthalpy change associated with reaction 1 is obtained from the slope of the van't Hoff plot while the entropy change is ob-

TABLE II: Results of the $\text{Br} + \text{NO}_2 + \text{N}_2 \rightarrow \text{BrNO}_2 + \text{N}_2$ Approach-to-Equilibrium Experiments^a

T	P	concn			Q	- λ_1	- λ_2	k_3	k_9	k_1	k_{-1}	K_p
		CF_2Br_2	Br_{res}	NO_2								
374	200	30	0.10	505	273	108	694	54	126	9.39	146	126 000
		30	0.09	1140	323	127	1390	54	139	9.95	184	106 000
		30	0.10	3290	261	76.9	3450	54	78	9.76	183	105 000
375	50	24	0.08	346	117	43.2	214	39	46	2.93	71	80 800
		24	0.08	1560	163	85.0	553	39	93	2.80	70	79 500
		24	0.08	2270	152	76.6	754	39	81	2.82	71	77 700
381	100	16	0.09	1250	200	42.3	792	21	48	4.93	152	62 400
		46	0.25	2530	222	55.4	1450	21	60	4.97	162	59 100
		15	0.03	2600	219	52.1	1480	21	56	4.96	163	58 600
		5	0.03	2660	285	82.9	1560	21	92	5.01	193	50 000
		16	0.09	2740	240	63.6	1500	21	69	4.77	170	54 000
381	400	16	0.08	4100	232	60.2	2250	21	64	5.01	169	57 200
		20	0.09	987	602	90.3	2040	40	180	15.3	422	69 800
		20	0.09	2670	444	130	4740	40	197	16.2	439	71 200
382	25	15	0.09	1420	64	28.3	262	43	25	1.30	39	64 000
		23	0.06	3450	96	52.9	598	43	54	1.48	42	67 100
388	50	23	0.09	1270	168	51.5	477	30	59	2.60	109	45 100
		23	0.07	2490	204	73.3	804	30	82	2.58	121	40 200
389	200	29	0.09	790	556	146	1110	72	194	7.93	362	41 400
		29	0.09	1720	581	165	1980	72	191	8.68	390	42 000
		29	0.09	2550	513	135	2650	72	183	8.72	389	42 300
393	100	18	0.05	594	372	62.1	584	33	100	4.05	273	27 700
		213	0.07	1820	379	78.7	1130	33	96	4.40	283	29 000
		18	0.06	2370	399	85.4	1420	33	101	4.52	298	28 300
		21	0.07	3340	393	82.2	1860	33	92	4.57	301	28 400
394	400	26	0.07	768	1060	186	2300	86	251	17.5	805	40 600
		127	0.07	784	1150	180	2390	86	248	17.0	904	31 000
		43	0.12	1740	1050	199	3820	86	232	16.7	817	38 000
404	50	22	0.07	1250	341	68.3	583	33	103	2.22	238	17 000
		22	0.07	2780	337	78.2	888	33	98	2.14	239	13 900
		22	0.07	4380	481	144	1380	33	181	2.30	300	16 300
411	50	22	0.07	2220	462	83.8	837	32	130	1.92	332	10 300
		22	0.06	4010	525	107	1280	32	144	2.07	380	9 740
		28	0.08	7090	500	115	1830	32	137	2.00	362	9 840
411	100	25	0.08	1330	866	94.4	1260	25	209	3.53	657	9 600
		26	0.09	2430	866	117	1670	25	193	3.70	673	9 800
		26	0.09	5150	820	132	2580	25	171	3.63	649	9 980
412	200	33	0.11	1460	1770	188	2720	43	396	7.63	1380	9 880
		24	0.10	3660	1400	197	3770	43	271	6.90	1130	10 900
		33	0.12	5590	1600	281	5490	43	357	7.37	1250	10 500
419	50	38	0.10	4050	637	119	1290	47	170	1.80	467	6 750
		38	0.10	6620	772	166	1940	47	222	1.94	549	6 180
420	200	38	0.10	4620	1960	311	4560	90	441	6.11	1520	7 010
		38	0.10	7480	2060	346	6970	90	431	6.89	1630	7 380
		38	0.10	10400	1960	356	8400	90	419	6.42	1540	7 310
425	100	34	0.10	5370	1590	197	3130	25	336	3.20	1250	4 420
431	50	39	0.09	4940	1060	156	1740	44	286	1.60	777	3 500
		39	0.09	6030	1120	172	2020	40	288	1.72	827	3 540
431	100	44	0.09	7870	1980	265	4230	34	425	3.15	1560	3 440
		44	0.09	12200	2020	323	5540	34	452	3.11	1570	3 380
		44	0.10	16100	2030	379	6820	34	490	3.19	1540	3 530
432	25	42	0.09	5280	562	129	981	79	174	0.89	388	3 890
		42	0.09	5960	656	142	1170	79	198	0.98	458	3 630

^a Units are as follows: T, K; P, Torr; concentrations, $10^{12}/\text{cm}^3$; Q, λ_1 , λ_2 , k_3 , k_9 , k_1 , k_{-1} , K_p , atm^{-1} .

tained from the intercept (solid line in Figure 5). At 401 K, the midpoint of the experimental $1/T$ range, this "second-law method" yields the results $\Delta H_{401} = -18.64 \pm 0.56 \text{ kcal mol}^{-1}$ and $\Delta S_{401} = -26.94 \pm 1.40 \text{ cal mol}^{-1} \text{ K}^{-1}$, where the errors are 2σ and represent precision only.

In addition to the second-law analysis described above, we also carried out a third-law analysis, where the experimental value for K_p at 401 K was employed in conjunction with a calculated entropy change to determine ΔH_{401} . To calculate the absolute entropy of BrNO_2 , we employed the vibrational frequencies reported in the above-mentioned matrix isolation studies^{12,13} and tabulated by Jacox.³⁰ On the basis of reported structural parameters for FNO_2 , ClNO_2 , FNO , ClNO , and BrNO ,³¹ we assumed that

BrNO_2 is planar with an N-Br bond length of 2.1 Å, N-O bond lengths of 1.2 Å, and an O-N-O bond angle of 125° ; these estimates are expected to be reasonably accurate. In the absence of information about BrNO_2 electronic states, we assumed that the electronic contribution to the BrNO_2 entropy is zero, i.e., a singlet ground state with no low-lying excited states. All parameters used in the calculation of the entropy change for reaction 1 are summarized in Table III.

The entropy change calculated from the third-law analysis, $\Delta S_{401} = -32.24 \text{ cal mol}^{-1} \text{ K}^{-1}$, differs substantially from the entropy change obtained from the second-law analysis (see above); hence, the value for ΔH_{401} obtained from the third-law analysis, $\Delta H_{401} = -20.77 \text{ kcal mol}^{-1}$, differs by 2.13 kcal mol^{-1} from the value obtained from the second-law analysis. The major source of uncertainty in the calculation of ΔS appears to be in the electronic contribution to the BrNO_2 entropy. For example, if the ground electronic state of BrNO_2 were assumed to be a triplet rather than a singlet, the difference between the second- and third-law en-

(30) Jacox, M. E. *J. Phys. Chem. Ref. Data* 1984, 13, 945.

(31) Harmony, M. D.; Laurie, V. W.; Kuczkowski, R. L.; Schwendeman, R. H.; Ramsay, D. A.; Lovas, F. J.; Lafferty, W. J.; Maki, A. G. *J. Phys. Chem. Ref. Data* 1979, 8, 619 and references therein.

TABLE III: Molecular Parameters Used in Calculations of ΔS and $k_{1,0}^{SC}$

species	ν , cm ⁻¹	g_0^e	g_1^e	E_1^e , cm ⁻¹	I , amu Å ²	Lennard-Jones params		ref
						σ , Å	ϵ/k , K	
BrNO ₂	402	1	-	=	183.3 ^c	4.35 ^d	341 ^d	30-32
	196				36.3			
	574				219.6			
	784							
	1289							
NO ₂	1660	2	2	~14500	40.8			45, 46
	757							
	1358							
	1665							
Br		4	2	3685				47
He						2.55	10	48
Ar						3.47	114	49
H ₂						2.83	60	48
N ₂						3.61	91.5	50
CO ₂						3.94	201	49
CF ₄						4.49	167	49
SF ₆						5.20	212	49

^a g_0, g_1 = degeneracies of the ground and first excited electronic states, respectively. ^b E_1 = energy difference between the ground and first excited electronic states. ^cBrNO₂ structure estimated based on information for ClNO₂, ClONO₂, and BrNO from ref 31 (see text). ^dEstimated based on parameters for ClNO₂ and BrONO₂ given in ref 32.

properties would be reduced from 5.30 to 3.12 cal mol⁻¹ K⁻¹. Until the source of the difference between the second- and third-law results is better understood, it seems most prudent to report the average of the two values and adjust error limits so as to encompass all reasonable possibilities. Using this approach, we report $\Delta H_{401}^\circ = -19.7 \pm 1.7$ kcal mol⁻¹ and $\Delta S_{401}^\circ = 29.6 \pm 4.2$ cal mol⁻¹ K⁻¹, where the errors are 2 σ estimates of absolute accuracy.

The parameters in Table III have been employed to correct the above enthalpies and entropies to 298 and 0 K values. We obtain the following results: $\Delta H_{298}^\circ = -19.6 \pm 1.7$ kcal mol⁻¹, $\Delta H_{00}^\circ = -18.6 \pm 2.0$ kcal mol⁻¹ (the Br-NO₂ bond dissociation energy), $\Delta S_{298}^\circ = -29.3 \pm 4.2$ cal mol⁻¹ K⁻¹. In conjunction with known heats of formation for Br and NO₂,²⁹ our value for ΔH_{298}° leads to the result of $\Delta H_f^\circ(\text{BrNO}_2) = 17.0 \pm 1.8$ kcal mol⁻¹. Uncertainties in the above thermochemical parameters are 2 σ and include both precision and estimates of systematic errors.

Comparison of Theoretical $k_{1,0}^{SC}$ with Experiment. Since reaction 1 appears to be a barrierless process, our experimental value for $-\Delta H_{00}^\circ$ can be equated with E_0 , the critical energy for BrNO₂ dissociation. Hence, our experimental value for ΔH_{00}° can be employed to calculate $k_{1,0}^{SC}$, the low-pressure limit value for k_1 in the "strong collision" limit, which is related to $k_{1,0}$ via the relationship

$$k_{1,0} = \beta_c k_{1,0}^{SC} \quad (\text{XVI})$$

where β_c is the collisional efficiency ($0 < \beta_c < 1$). For collisions of an energized adduct with N₂ at 298 K, $\beta_c \sim 0.3$ is typical.³² On the basis of analytical solutions of the master equation for an exponential collision model, it has been shown³³ that the temperature dependence of β_c can be approximated by the expression

$$\beta_c(1 - \beta_c^{1/2})^{-1} \approx -(\Delta E)(F_E kT)^{-1} \quad (\text{XVII})$$

where (ΔE) is the average energy removed from the energized adduct per collision and F_E is given by the expression³²

$$F_E \approx \sum_{v=0}^{s-1} \frac{(s-1)!}{(s-1-v)!} \left(\frac{RT}{E_0 + \alpha(E_0)E_z} \right)^v \quad (\text{XVIII})$$

where s is the number of adduct vibrational degrees of freedom, $\alpha(E_0)$ is the Whitten-Rabinovich parameter,³⁴ and E_z is the adduct zero-point energy; for BrNO₂ $s = 6$, $E_0 \sim 18.6$ kcal mol⁻¹ (as determined in this study), $\alpha(E_0) = 0.949$, and $E_z = 7.441$ kcal mol⁻¹. We have employed eq XVII to calculate the temperature

TABLE IV: Comparison of Theoretical and Experimental Low-Pressure Third-Order Rate Coefficients $k_{1,0}(N_2, T)^a$

E_0 , kcal mol ⁻¹	$\beta_c k_{1,0}^{SC}, 10^{-31}$ cm ⁶ molecule ⁻² s ⁻¹		
	259 K	298 K	346 K
16.6	5.38	3.87	2.59
18.6	0.723	0.516	0.363
20.6	0.093	0.067	0.047
exptl $k_{1,0}$	5.73	4.61	3.21

^a $\beta_c(N_2, 298\text{K})$ assumed to be 0.3; temperature dependence of β_c calculated from eq XVII with (ΔE) assumed to be temperature independent.

dependence of β_c under the assumption that (ΔE) is temperature independent.

The methodology employed to calculate $k_{1,0}^{SC}$ was developed by Troe,^{33,35} the relevant equations are summarized in a "user-friendly" form by Patrick and Golden.³² Values for $k_{1,0}^{SC}$ have been calculated for N₂ buffer gas at the three experimental temperatures 259, 298, and 346 K and for three choices of ΔH_{00}° spanning the range of values consistent with our "approach to equilibrium" experiments, i.e., $-\Delta H_{00}^\circ = 18.6 \pm 2.0$ kcal mol⁻¹. To facilitate comparison of calculated $k_{1,0}^{SC}$ values with experimental $k_{1,0}$ values, we assume that $\beta_c = 0.3$ at 298 K and calculate the temperature dependence of β_c as described above. The procedure employed to extrapolate from our experimental pressure range to the low-pressure limit is described in the next section; because experiments were carried out at pressures not far removed from the low-pressure limit, this extrapolation is expected to be quite accurate.

Experimental and theoretical results are compared in Table IV. The experimental temperature dependence for $k_{1,0}$ agrees reasonably well with the calculated temperature dependence for $\beta_c k_{1,0}^{SC}$. However, the magnitude of calculated values for $\beta_c k_{1,0}^{SC}$ is inconsistent with experiment when $-\Delta H_{00}^\circ$ is assigned a value of 18.6 kcal mol⁻¹, the average of our second- and third-law determinations. Only when $-\Delta H_{00}^\circ$ is assigned our experimental lower limit value of 16.6 kcal mol⁻¹ does the magnitude of $k_{1,0}^{SC}$ fall in the range expected based on eq XVI.

The above comparison of theory with experiment can be interpreted as favoring our second-law determination of the enthalpy change over our third-law determination. However, alternative explanations also exist. For example, Smith has discussed the potential role of electronically excited states in recombination reactions.³⁶ In the low-pressure regime, Smith finds that the role

(32) Patrick, R.; Golden, D. M. *Int. J. Chem. Kinet.* 1983, 15, 1189.

(33) Troe, J. *J. Chem. Phys.* 1977, 66, 4745.

(34) Robinson, P. J.; Holbrook, K. A. *Unimolecular Reactions*; Wiley: London, 1972.

(35) Troe, J. *J. Chem. Phys.* 1977, 66, 4758.

(36) Smith, I. W. M. *Int. J. Chem. Kinet.* 1984, 16, 423.

of bound excited states falls rapidly as the size of the system increases due to the much steeper increase of state density with internal energy for molecules with more degrees of freedom. For a four-atom system such as BrNO_2 , reaction on an excited-state potential energy surface could contribute to $k_{1,0}$ if a bound, very low lying excited state existed. The existence of a reaction channel leading to formation of the BrONO isomer is another potential complication. Only the BrNO_2 isomer is observed when Br and NO_2 are codeposited into argon matrices at ~ 10 K,^{12,13} although near-ultraviolet photolysis of matrix isolated BrNO_2 does result in isomerization to BrONO .¹² Recently, Yarwood and Niki¹⁴ carried out a study where reaction products were monitored by FTIR spectroscopy during UV photolysis of Br_2/NO_2 /air mixtures; they observed BrNO_2 as a reaction product but did not observe BrONO even though (by analogy with ClONO) the 1725-cm^{-1} band of BrONO should have a strong Q branch and, therefore, be relatively easy to detect.¹⁴ Hence, the available evidence argues against the existence of a significant channel for BrONO formation.

Extrapolation of Experimental Results To Obtain $k_{1,0}$ and $k_{1,\infty}$
Under all experimental conditions employed in this study, reaction 1 is found to be in the "falloff" region between third and second order. Troe and co-workers^{33,35,37-40} have shown that bimolecular rate coefficient versus pressure curves (i.e., falloff curves) for addition reactions can be approximated by the three-parameter equation

$$k([M], T) = k_{\infty}(T) F_{\text{LH}} F([M], T) \quad (\text{XIX})$$

where F_{LH} is the Lindemann-Hinshelwood factor:

$$F_{\text{LH}} = C/(1 + C) \quad (\text{XX})$$

$$C = k_0(M, T)[M]/k_{\infty}(T) \quad (\text{XXI})$$

and $F([M], T)$ is a parameter that characterizes the broadening of the falloff curve due to the energy dependence of the rate coefficient for the decomposition of the energized adduct. $F([M], T)$ is the product of strong collision and weak collision broadening factors:

$$F([M], T) = F^{\text{SC}}([M], T) F^{\text{WC}}([M], T) \quad (\text{XXII})$$

Both the strong collision and weak collision broadening factors are parametrized as a pressure-independent parameter raised to a pressure-dependent power:

$$F^{\text{SC}}([M], T) = F^{\text{SC}}_c(T)^{x([M], T)} \quad (\text{XXIII})$$

$$F^{\text{WC}}([M], T) = F^{\text{WC}}_c(M, T)^{y([M], T)} \quad (\text{XXIV})$$

$$x([M], T) = \{1 + [(\log C - 0.12)/(N^{\text{SC}} + \delta D)]^2\}^{-1} \quad (\text{XXV})$$

$$N^{\text{SC}} = 0.75 - 1.27 \log F^{\text{SC}}_c(T)$$

$$D = 0.1 + 0.6 \log F^{\text{SC}}_c(T)$$

$$\delta = +1 \text{ if } C > 1, \quad \delta = -1 \text{ if } C < 1$$

$$y([M], T) = \{1 + [D/(N^{\text{WC}} - dD)]^2\}^{-1} \quad (\text{XXVI})$$

$$N^{\text{WC}} = 0.7 + 0.3S_K - 0.25 \log \beta_c$$

$$D = \log C + 0.085S_K - 0.17 \log \beta_c$$

$$d = -0.2 - 0.12 \log \beta_c$$

where the parameter S_K in equation XXVI is defined below. F^{SC}_c can be estimated from structural information about the adduct (Table III),^{37,38} whereas estimation of F^{WC}_c requires knowledge

of the efficiency of energy transfer between the energized adduct and the buffer gas.

Values for F^{SC}_c have been determined by Luther and Troe^{38,39} in tabular form as a function of the reduced Kassel integral parameters S_K and B_K . S_K is given by the relationship

$$S_K = S_{\text{eff}} + (E_{\infty} - E_0)/RT \quad (\text{XXVII})$$

where E_{∞} is the Arrhenius activation energy for unimolecular decomposition of the adduct in the high-pressure limit (an ill-defined parameter) and S_{eff} is the effective number of transition-state oscillators. S_{eff} can be estimated from the vibrational partition function of the adduct molecule:

$$S_{\text{eff}} \approx -T^{-1} d \ln Q_{\text{vib}}/dT^{-1} = \sum_{i=1}^S (h\nu_i/kT) [\exp(h\nu_i/kT) - 1]^{-1} \quad (\text{XXVIII})$$

The parameter B_K is approximated by

$$B_K \approx B'(S_K - 1)/(s - 1) \quad (\text{XXIX})$$

where

$$B' = [E_0 + a(E_0)E_{\infty}]/(RT)^{-1} \quad (\text{XXX})$$

Although the value of E_{∞} is highly uncertain, for a barrierless process such as reaction 1, the relationship $1 < S_K - S_{\text{eff}} < 2$ is usually obeyed.^{38,39} Comparison of preliminary fits of the experimental data to eq XIX suggest that the values of $F^{\text{SC}}_c(T)$ calculated with $S_K - S_{\text{eff}}$ set equal to 2 are more appropriate for modeling the falloff behavior of reaction 1 than are $F^{\text{SC}}_c(T)$ values calculated for lower values of $S_K - S_{\text{eff}}$ ($F^{\text{SC}}_c(T)$ decreases with increasing $S_K - S_{\text{eff}}$ and with increasing T). Hence, our falloff analysis assumes that $S_K - S_{\text{eff}} = 2$.

To a good approximation, $F^{\text{WC}}_c(M, T)$ can be calculated from the expression³⁴

$$F^{\text{WC}}_c(M, T) = \beta_c(M, T)^{0.14} \quad (\text{XXXI})$$

To apply eq XXXI, we fix $\beta_c(\text{N}_2, 298\text{K})$ at a typical value of 0.3,³² employ eq XVII (with ΔE assumed temperature independent) to calculate $\beta_c(\text{N}_2, T)$, and employ equation XXXII to calculate $\beta_c(M, 298\text{K})$:

$$\frac{\beta_c(M, 298\text{K})}{\beta_c(\text{N}_2, 298\text{K})} = \frac{k_0(M, 298\text{K})Z_{\text{LJ}}(\text{N}_2, 298\text{K})}{k_0(\text{N}_2, 298\text{K})Z_{\text{LJ}}(M, 298\text{K})} \quad (\text{XXXII})$$

In eq XXXII, $Z_{\text{LJ}}(M, T)$ is the Lennard-Jones collision frequency for BrNO_2 -M encounters; it was calculated from the Lennard-Jones parameters in Table III by using a relationship given elsewhere.³² Equation XXXII requires knowledge of $k_0(M, T)$ in order to compute $\beta_c(M, T)$, which is then used to calculate $k_0(M, T)$. Clearly, an iterative procedure must be employed in order to arrive at internally consistent values for $\beta_c(M, T)$ and $k_0(M, T)$. However, because the low end of our experimental pressure range is very close to the low-pressure limit, nearly exact initial estimates of $k_0(M, 298\text{K})/k_0(\text{N}_2, 298\text{K})$ could be made.

Using calculated values for $F^{\text{SC}}_c(T)$ (with $S_K - S_{\text{eff}}$ set equal to 2), we have determined the parameters $k_{1,0}(M, T)$, $k_{1,\infty}(T)$, and $F^{\text{WC}}_c(M, T)$ by fitting our data to eq XIX using a least-squares method subject to the constraints that (1) $k_{\infty}(T)$ must be independent of buffer gas identity, (2) $\beta_c(\text{N}_2, 298\text{K}) = 0.3$, and (3) eqs XVII (with ΔE assumed temperature independent), XXXI, and XXXII must be obeyed. Falloff parameters obtained from the analysis are given in Table V. Best-fit falloff curves for N_2 buffer gas at 259 and 346 K, and for CF_4 , N_2 , and He buffer gases at 298 K are plotted and compared with experimental rate coefficients in Figures 6 and 7. Because all experimental data were obtained in the low-pressure half of the falloff curves, i.e., where $k_{1,0}[M] < k_{1,\infty}$, and because the extrapolated value for $k_{1,0}$ is much less sensitive to the choice of F_c than is the extrapolated value for $k_{1,\infty}$, the absolute accuracy of our $k_{1,0}(M, T)$ values is quite good—we estimate the uncertainties to be $\pm 20\%$. On the other hand, the absolute accuracy of $k_{1,\infty}(T)$ is estimated to be no better than a factor of 2, although the derived small positive activation energy for $k_{1,\infty}(T)$ is probably correct as long as reaction

(37) Troe, J. *J. Phys. Chem.* 1979, 83, 114.

(38) Luther, K.; Troe, J. *Int. Symp. Combust. Proc.* 1978, 17, 535.

(39) Troe, J. *Ber. Bunsen-Ges. Phys. Chem.* 1983, 87, 161.

(40) Gilbert, R. G.; Luther, K.; Troe, J. *Ber. Bunsen-Ges. Phys. Chem.* 1983, 87, 169.

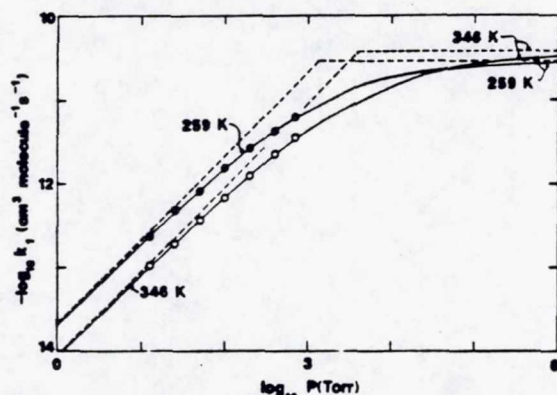


Figure 6. Falloff curves for $M = \text{N}_2$ at 259 and 346 K. Closed circles are 259 K data, and open circles are 346 K data. Solid lines are calculated from the parameters in Table V. Dotted lines show the low- and high-pressure limits.

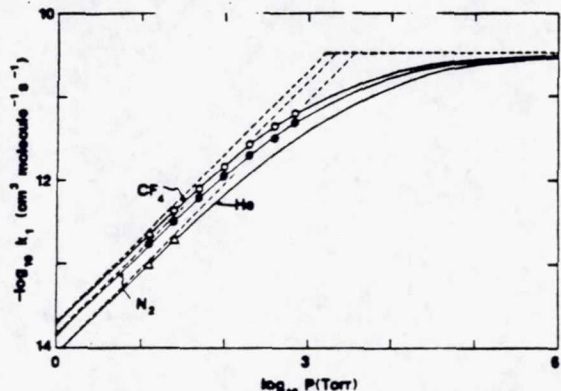
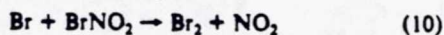


Figure 7. Falloff curves for $M = \text{He}$, N_2 , and CF_4 at 298 K. Closed circles are N_2 data, open circles are CF_4 data, and open triangles are He data. Solid lines are calculated from the parameters in Table V. Dotted lines show the low- and high-pressure limits.

proceeds predominantly on the ground electronic state surface. Smith has shown that recombination into even weakly bound excited electronic states of the adduct, particularly states with high electronic degeneracies, can grossly affect the shape of the falloff curve near the high-pressure limit.³⁶ The falloff analysis described above is based on the assumption that excited electronic states of BrNO_2 play no role in the association process. As discussed above, comparison of thermochemical parameters obtained from second- and third-law analyses as well as comparison of theoretical values for $k_{1,0}$ ^{3C} with experiment lead to the suspicion that excited electronic states of BrNO_2 may indeed be important. Rate coefficient measurements of k_1 at high pressure along with *ab initio* calculations that characterize all low-lying bound electronic states of BrNO_2 are needed before the high-pressure behavior of $k_1(T)$ can be considered well characterized.

Comparison with Previous Work. The only published study of $\text{Br} + \text{NO}_2$ kinetics with which to compare our results is the recent low-pressure study of Mellouki et al.¹⁹ These authors employed a discharge flow technique with EPR and mass spectrometric diagnostics to study reaction 1 at 298 K in helium buffer gas at pressures of 0.6–2.1 Torr. The bimolecular rate coefficients reported by Mellouki et al. are considerably faster than predicted based on extrapolation of our results to lower pressure. Mellouki et al. corrected their rate coefficients downward to account for Br removal via the fast secondary reaction



and to account for Br removal by reaction 1 with NO_2 as the third body (both of these interferences were negligible under our experimental conditions) to obtain the termolecular rate coefficient $k_{1,0}(\text{He}, 298\text{K}) = (3.7 \pm 0.7) \times 10^{-31} \text{ cm}^6 \text{ molecule}^{-2} \text{ s}^{-1}$. We find

TABLE V: Falloff Parameters

param	M	T, K		
		259	298	346
F _c	He		0.484	
	Ar		0.534	
	H ₂		0.485	
	N ₂	0.589	0.545	0.504
	CO ₂		0.571	
	CF ₄		0.576	
k _{1,0} ^a	SF ₆		0.562	
	He		2.75	
	Ar		3.46	
	H ₂		5.20	
	N ₂	5.73	4.61	3.21
	CO ₂		6.54	
k _{1,0} ^b	CF ₄		5.76	
	SF ₆		5.62	
		2.86	3.22	3.73

^aUnits are $10^{-31} \text{ cm}^6 \text{ molecule}^{-2} \text{ s}^{-1}$. ^bUnits are $10^{-11} \text{ cm}^3 \text{ molecule}^{-1} \text{ s}^{-1}$.

TABLE VI: Bond Strengths of XNO₂ Species, X = F, Cl, Br, I

X	$-\Delta H_{298}^\circ$, kcal mol ⁻¹	ref
F	52.9 ^a	32
Cl	33.9	29
Br	19.6 ± 1.7	this work
I	19.1 ± 1.0	41, 44

^aEnthalpy change for the reaction $\text{X} + \text{NO}_2 \rightarrow \text{XNO}_2$. ^bEstimate; no experimental data available.

that $k_{1,0}(\text{He}, 298\text{K}) = (2.75 \pm 0.55) \times 10^{-31} \text{ cm}^6 \text{ molecule}^{-2} \text{ s}^{-1}$.

Comparison of kinetic data for the homologous series of $\text{X} + \text{NO}_2$ reactions is of limited instructional value because the $\text{F} + \text{NO}_2$ and $\text{Cl} + \text{NO}_2$ reactions are thought to proceed primarily via channels that lead to the XONO product,^{1-5,8,32} whereas the $\text{Br} + \text{NO}_2$ reaction seems to form exclusively the BrNO_2 isomer.¹²⁻¹⁴ No information is available concerning the isomer(s) that is (are) formed from the $\text{I} + \text{NO}_2$ reaction. Reported $k_0(M, T)$ values for the $\text{F} + \text{NO}_2$ ⁴ and $\text{Cl} + \text{NO}_2$ ⁶⁻¹¹ reactions are faster by factors of 2–5 than the corresponding $k_{1,0}(M, T)$ values reported in this study and by Mellouki et al.¹⁹ The $\text{I} + \text{NO}_2$ reaction follows the same trend: i.e. reported values of $k_0(M, T)$ for $\text{I} + \text{NO}_2$ ^{19,41-43} are slower than the corresponding $\text{Br} + \text{NO}_2$ rate coefficients. All reported studies of $\text{F} + \text{NO}_2$ and $\text{Cl} + \text{NO}_2$ kinetics except one relative rate study by Glavas and Heicklen⁹ have been restricted to pressures (≤ 200 Torr of N_2) where only slight deviations from low-pressure limit behavior were observed. Estimates of $k_\infty(298\text{K})$ for both $\text{F} + \text{NO}_2$ ^{5,29,32} and $\text{Cl} + \text{NO}_2$ ^{29,32} have been obtained by using very approximate extrapolation procedures; the resulting $k_\infty(298\text{K})$ values are $\sim 3 \times 10^{-11} \text{ cm}^3 \text{ molecule}^{-1} \text{ s}^{-1}$ for $\text{F} + \text{NO}_2$ and $\sim 1 \times 10^{-10} \text{ cm}^3 \text{ molecule}^{-1} \text{ s}^{-1}$ for $\text{Cl} + \text{NO}_2$. Although these values for k_∞ can be employed to compute rate coefficients over the atmospheric pressure regime, their absolute uncertainties are huge—probably a factor of 5 or greater. The best known k_∞ value in the $\text{X} + \text{NO}_2$ series is for the $\text{I} + \text{NO}_2$ reaction. van den Bergh and Troe have studied the NO_2 -catalyzed recombination of iodine atoms at 320–450 K and 1–200 atm of helium.⁴¹ From analysis of their data they obtained $k_\infty(298\text{K}) \approx 6.6 \times 10^{-11} \text{ cm}^3 \text{ molecule}^{-1} \text{ s}^{-1}$, about a factor of 2 faster than our extrapolated value for $k_{1,0}(298\text{K})$; in van den Bergh and Troe's experiment, the high-pressure limit was not reached even at a pressure of 200 atm. It is worth noting that we actually obtained slightly better fits to our data when F_c values somewhat smaller than those summarized in Table V were employed; the $k_{1,0}$ values associated with these lower F_c values are higher than those summarized in Table V and in better agreement with the high-pressure $\text{I} + \text{NO}_2$ results of van den Bergh and Troe.⁴¹ We did not employ

(41) van den Bergh, H.; Troe, J. *J. Chem. Phys.* 1976, 64, 736.

(42) van den Bergh, H.; Benoit-Guyot, N.; Troe, J. *Int. J. Chem. Kinet.* 1977, 9, 223.

(43) Buben, S. N.; Larin, I. K.; Messineva, N. A.; Trofimova, E. M. *XIth International Conference on Gas Kinetics*, Assisi, Italy, 1990; paper A-22.

the lower F_c values in our falloff analysis because they can only be rationalized if $S_k - S_{\text{eff}}$ is assumed to be larger than the "normal" upper limit value of 2. As mentioned above, the "true" value for $k_{1,\infty}$ (298 K) remains uncertain by at least a factor of 2.

Heats of reaction for the $X + \text{NO}_2 \rightarrow \text{XNO}_2$ reactions are summarized in Table VI. While the X-NO₂ bond strengths decrease monotonically in the order $F > \text{Cl} > \text{Br}$, the BrNO₂ bond strength determined in this study is identical within experimental uncertainty to the INO₂ dissociation energy determined by Troe and co-workers.^{41,44} It should be noted that the potential contribution of an IONO species to the iodine recombination experiments has yet to be adequately addressed.

Summary

The kinetics of the $\text{Br}(^2P_{3/2}) + \text{NO}_2$ association reaction have been investigated as a function of temperature (259–432 K), pressure (12.5–700 Torr), and bath gas identity (He, Ar, H₂, N₂, CO₂, CF₄, SF₆). At temperatures below 350 K, the association reaction is irreversible on the (~30 ms) time scale of the experiment. The 21 rate coefficients obtained with N₂ as the buffer gas were fit to the expression recommended by the NASA panel for chemical kinetics and photochemical data evaluation for use in parametrizing the pressure and temperature dependences of association reaction rate coefficients for atmospheric modeling purposes;²⁹ the best-fit parameters are $A = 4.24 \times 10^{-31}(T/300)^{-2.4} \text{ cm}^6 \text{ molecule}^{-2} \text{ s}^{-1}$ ($\sim k_{1,0}$) and $B = 2.66 \times 10^{-11}(T/300)^{0.0} \text{ cm}^3 \text{ molecule}^{-1} \text{ s}^{-1}$ ($\sim k_{1,\infty}$).

At temperatures above 350 K, reversible addition has been observed. Rate coefficients for BrNO₂ formation and decomposition have been determined over the temperature range 374–432 K. Second- and third-law analyses of the data yields somewhat

different thermochemical parameters. The major uncertainty in the calculated third-law entropy change appears to be the electronic entropy of BrNO₂. Averaging the second- and third-law results and choosing error limits to encompass all reasonable possibilities, we report the following thermochemical parameters for reaction 1: $\Delta H^\circ_{298} = -19.6 \pm 1.7 \text{ kcal mol}^{-1}$, $\Delta H^\circ_0 = -18.6 \pm 2.0 \text{ kcal mol}^{-1}$, $\Delta S^\circ_{298} = -29.3 \pm 4.2 \text{ cal mol}^{-1} \text{ K}^{-1}$, $\Delta H^\circ_{298}(\text{BrNO}_2) = 17.0 \pm 1.8 \text{ kcal mol}^{-1}$ (uncertainties are 2σ estimates of absolute accuracy).

Our experimental value for ΔH°_0 has been employed to calculate $k_{1,0}^{\text{SC}}$, the low-pressure limit rate coefficient in the strong collision limit, using the method of Troe.^{33,35} Calculated values for $k_{1,0}^{\text{SC}}$ are inconsistent with experimental results unless $-\Delta H^\circ_0$ is assigned a value near the lower limit derived from the high-temperature data, i.e., 16.6 kcal mol⁻¹. Systematic errors in the calculations could result from the assumptions that (a) reaction occurs entirely on the ground electronic state potential energy surface and (b) formation of the BrONO isomer is unimportant; experimental data are available that suggest that assumption b is valid,¹²⁻¹⁴ but no information is available to validate assumption a.

The procedure developed by Troe and co-workers^{33,35,37-40} has been employed to extrapolate experimental falloff curves to the low- and high-pressure limits. Derived values for $k_{1,0}(M, 298 \text{ K})$ in units of $10^{-31} \text{ cm}^6 \text{ molecule}^{-2} \text{ s}^{-1}$ range from 2.75 for $M = \text{He}$ to 6.54 for $M = \text{CO}_2$. Values for $k_{1,0}(N_2, T)$ in units of $10^{-31} \text{ cm}^6 \text{ molecule}^{-2} \text{ s}^{-1}$ are 5.73 at 259 K, 4.61 at 298 K, and 3.21 at 346 K; the temperature dependence of $k_{1,0}(N_2, T)$ is consistent with the theoretical temperature dependence for $\beta_c k_{1,0}^{\text{SC}}$. Values for $k_{1,\infty}(T)$ in units of $10^{-11} \text{ cm}^3 \text{ molecule}^{-1} \text{ s}^{-1}$ are 2.86 at 259 K, 3.22 at 298 K, and 3.73 at 346 K. Uncertainties in derived values for $k_{1,0}$ are estimated to be $\pm 20\%$, whereas uncertainties in derived values of $k_{1,\infty}(T)$ are considerably larger—a factor of 2 or more; however, the derived small positive activation energy for $k_{1,\infty}(T)$ is probably correct. Experimental data up to pressures of several hundred atmospheres and ab initio calculations that characterize the low-lying bound electronic states of BrNO₂ are needed before the magnitude of $k_{1,\infty}$ can be considered well established.

Acknowledgment. We thank Drs. G. Yarwood and H. Niki for communicating their unpublished results to us. This work was supported by NSF Grant ATM-88-02386 and NASA Grant NAGW-1001.

(44) Hippler, H.; Luther, K.; Teitelbaum, H.; Troe, J. *Int. J. Chem. Kinet.* **1977**, *9*, 917.

(45) Danis, F.; Caralp, F.; Masanet, J.; Lesclaux, R. *Chem. Phys. Lett.* **1990**, *167*, 450.

(46) Herzberg, G. *Molecular Spectra and Molecular Structure. III. Electronic Spectra and Electronic Structure of Polyatomic Molecules*; Van Nostrand Reinhold: New York, 1966.

(47) Donovan, R. J.; Husain, D. *Chem. Rev.* **1970**, *70*, 489.

(48) Hippler, H.; Troe, J.; Wendelken, H. *J. J. Chem. Phys.* **1983**, *78*, 6709.

(49) Mouris, F. M.; Rummens, F. H. A. *Can. J. Chem.* **1977**, *55*, 3007.

(50) Reid, R. C.; Sherwood, T. K. *Properties of Gases and Liquids*; McGraw-Hill: New York, 1958.

NDB
 510-25
 026128
 7P.
 273548

Thermochemistry and kinetics of the Cl+O₂ association reaction

J.M. Nicovich, K.D. Kreutter, C.J. Shackelford and P.H. Wine

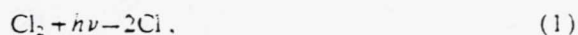
Physical Sciences Laboratory, Georgia Tech Research Institute, Georgia Institute of Technology, Atlanta, GA 30332, USA

Received 28 January 1991; in final form 8 February 1991

Laser flash photolysis of Cl₂/O₂ mixtures has been employed in conjunction with Cl(²P_{3/2}) detection by time-resolved resonance fluorescence spectroscopy to investigate equilibration kinetics for the reactions Cl+O₂+O₂=ClOO+O₂ at temperatures of 181–200 K and O₂ pressures of 1.5–40 Torr. The third-order rate coefficient for the association reaction at 186.5±5.5 K is (8.9±2.9)×10⁻³³ cm⁶ molecule⁻² s⁻¹ and the equilibrium constant (*K_p*) at 185.4 K is 18.9 atm⁻¹ (factor of 1.7 uncertainty). A third law analysis of our data leads to a value for the Cl–OO bond dissociation energy of 4.76±0.49 kcal mol⁻¹.

1. Introduction

The existence of the ClOO radical was first postulated by Porter and Wright [1] to explain ClO production following flash photolysis of Cl₂/O₂ mixtures.



Subsequent flash photolysis work by Burns and Norrish [2] supports the above mechanism. An early thermochemical estimate by Benson and Buss [3] suggested that ClOO is a very weakly bound species with a bond dissociation energy, *D*₀⁰(Cl–OO), of 8±2 kcal mol⁻¹. The only kinetic information for reaction (2) comes from a flash photolysis study by Nicholas and Norrish [4]; these investigators measured temporal profiles for ClO appearance following flash photolysis of Cl₂/O₂ mixtures, and modified their results using the mechanism suggested by Porter and Wright [1] (see above), to obtain the rate coefficient *k*₂(298 K)=1.7×10⁻³³ cm⁶ molecule⁻² s⁻¹ in N₂+O₂ bath gas.

The ClOO radical was first observed directly by ESR spectroscopy in cryogenic matrices [5], although subsequent work [6–9] was needed to correct the misassigned spectrum as being due to ClOO rather than ClO. The first infrared spectroscopic observation of ClOO was reported by Arkell and Schwager [10], who found the fundamental vibrational frequencies to be 1441, 407, and 373 cm⁻¹. Arkell and Schwager produced ClOO by photolysis of Cl₂/O₂ and OClO cryogenic matrices. Direct observation of ClOO in the gas phase was first reported by Johnston et al. [11]; these authors employed molecular modulation spectroscopy to observe both the ultraviolet and infrared spectra of ClOO, and to obtain kinetic information about reactions (3) and (4). More recent flash photolysis [12], molecular modulation [13], and theoretical [14–16] studies provide additional information concerning the branching ratio for reaction (3) as well as ClOO thermochemistry, structure, and excited electronic state energies. An evaluation of all published information leads to a recommended equilibrium constant for Cl+O₂=ClOO of 2.3×10⁻²⁵ exp(3000/*T*) cm³ molecule⁻¹, and a recommended third-order rate coefficient for reaction (2) of 2.0×10⁻³³ × (*T*/300)^{-1.4} cm⁶ molecule⁻² s⁻¹ [17].

While ClOO plays an important role in laboratory studies of ClO_x chemistry, it has not been considered an important species in atmospheric chemistry. However, interest in the potential role of ClOO in

the chemistry of the lower stratosphere has increased dramatically in recent years with the realization that increasing levels of ClO_x in the atmosphere are largely responsible for the antarctic ozone hole [18]. In the wintertime antarctic lower stratosphere, heterogeneous reactions in polar stratospheric clouds (PSCs) can convert the reservoir species HCl and ClONO_2 into the photochemically more labile species Cl_2 and HOCl [19,20]. As a result, high levels of ClO are produced at the expense of HCl and ClONO_2 , and catalytic odd oxygen destruction cycles involving the $\text{ClO} + \text{ClO}$ [21] and $\text{BrO} + \text{ClO}$ [22] rate-limiting reactions become very rapid; both of these cycles involve ClOO as an intermediate. Also, it has recently been suggested that OCIO photo-isomerization to ClOO may be an important mechanism for odd oxygen destruction under antarctic springtime conditions [23], although the quantum yield for photo-isomerization may be too low for this process to be of atmospheric importance [24]. Under the low temperature, high pressure conditions which exist in the springtime antarctic lower stratosphere, the currently recommended equilibrium constant [17] (see above) suggests that equilibrium ClOO levels exceed levels of Cl atoms. Hence, ClOO could play an important role in antarctic stratospheric chemistry if its reactions with key species occur sufficiently rapidly.

In this study we report a series of kinetics experiments aimed at directly measuring k_2 and k_{-2} , and, therefore, the equilibrium constant ($\equiv k_2/k_{-2}$). Our results suggest that both the association and dissociation reactions are faster, and that the $\text{Cl}-\text{OO}$ bond is about 1 kcal mol^{-1} weaker, than previously thought.

2. Experimental technique

All experiments involved coupling laser flash photolysis of Cl_2/O_2 mixtures with Cl atom detection by time-resolved resonance fluorescence spectroscopy. A complete description of the experimental technique can be found elsewhere [25]. Chlorine atoms were monitored using the closely spaced $^2\text{D}_{5/2,3/2}-^2\text{P}_{3/2}$ doublet at 118.9 nm; these transitions are in accidental coincidence with a "window" in the O_2 absorption spectrum.

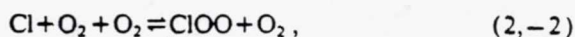
The gases used in this study had the following

stated minimum purities: O_2 , 99.99%; Cl_2 , 99.99%. Oxygen was used as supplied while chlorine was degassed at 77 K before use.

3. Results and discussion

In all experiments, $\text{Cl}(^2\text{P}_J)$ was produced by 355 nm pulsed laser photolysis of Cl_2 . Both theoretical [26] and experimental [27] information suggests that photolysis of Cl_2 around 355 nm produces almost exclusively ground state chlorine atoms, $\text{Cl}(^2\text{P}_{3/2})$; the fraction of photolytically generated atoms in the $^2\text{P}_{1/2}$ spin-orbit excited state is probably less than the equilibrium fraction, which is only 6×10^{-4} at a typical experimental temperature of 190 K. Reported rate coefficients for quenching of $\text{Cl}(^2\text{P}_{1/2})$ by O_2 in units of $10^{-13} \text{ cm}^3 \text{ molecule}^{-1} \text{ s}^{-1}$ are 210 ± 50 [28], 230 ± 30 [29], 1.7 ± 0.4 [30], and 1.3 ± 0.3 [31]. Based on observed reaction times (see table 1) it appears that $\text{Cl}(^2\text{P}_{1/2})$ deactivation was faster than chemical reaction of $\text{Cl}(^2\text{P}_J)$ under our experimental conditions, though only by factors of three to six if the slower literature values for the deactivation rate [30,31] are correct. The above discussion suggests that although the fraction of Cl atoms in the $^2\text{P}_{1/2}$ state could have varied somewhat over the experimental time scale for Cl decay, this fraction was so small at all reaction times that observed reactivity can be attributed entirely to $\text{Cl}(^2\text{P}_{3/2})$. Furthermore, negligible systematic error is introduced by the assumption that the observed temporal evolution of the $\text{Cl}(^2\text{P}_{3/2})$ fluorescence signal is identical to the temporal evolution of the total chlorine atom population.

When Cl_2/O_2 mixtures are subjected to 355 nm laser flash photolysis and experimental conditions are maintained where radical-radical reactions are unimportant, i.e. low radical concentrations and short reaction times, the Cl atom temporal profile should be controlled by the following reactions:



Cl —loss by diffusion from the detector field

of view and reaction with background

impurities, (5)

Table 1
Results of the $\text{Cl} + \text{O}_2 + \text{O}_2 = \text{ClOO} + \text{O}_2$ approach-to-equilibrium experiments

T (K)	p_{O_2} (Torr)	Concentrations (10^{11} cm^{-3})		Q (s^{-1})	$-\lambda_1$ (s^{-1})	$-\lambda_2$ (s^{-1})	k_6 (s^{-1})	k_2 (10^{-15} cm^3 molecule $^{-1} \text{ s}^{-1}$)	k_{-2} (s^{-1})	K_p (atm^{-1})
		Cl_2	$\text{Cl}_{t=0}$							
181	15	91	5.1	11800	118	18800	231	8.62	11600	30.2
182	20	140	7.0	18400	112	29600	212	10.2	18200	22.6
182	40	240	11	22200	154	69400	202	22.8	22000	41.7
183	20	330	9.9	18900	183	30300	399	10.2	18500	22.2
183	20	330	9.9	17000	175	26800	385	9.47	16600	22.9
183	20	330	9.9	18800	295	29800	700	10.7	18100	23.7
183	30	140	6.6	33400	235	58200	479	15.8	32900	19.3
183	30	110	3.3	24000	-49	52500	-134	17.4	24200	28.9
183	40	270	8.1	25800	116	74800	151	23.3	25600	36.4
183	40	240	11	24900	138	59300	201	16.7	24700	27.1
185	20	1800	8.3	17100	95	24300	84	6.77	17100	15.7
185	30	350	9.7	33200	191	54600	361	13.6	32900	16.5
185	30	840	11	33900	309	52400	721	11.9	33200	14.2
187	30	1500	7.6	30100	151	55100	211	16.3	29900	21.4
187	30	450	13	30300	154	46900	287	10.6	30000	13.9
187	40	290	9.8	41700	171	73500	289	15.5	41400	14.7
189	20	2000	11	27000	130	34300	239	7.18	26700	10.4
189	30	1900	11	39700	175	56200	352	10.9	39300	10.7
190	40	1600	9.6	41300	157	72800	230	15.5	41100	14.6
191	20	2300	9.4	45500	151	58100	333	12.6	45100	10.7
191	25	950	8.6	36700	110	48100	298	9.27	36400	9.80
191	30	1300	11	35600	151	53100	255	11.6	35400	12.6
191	30	2000	10	43500	117	63400	153	13.0	43300	11.5
192	25	1500	9.5	49300	95	62700	261	10.8	49000	8.45
192	30	350	9.8	54630	132	74000	279	13.0	54400	9.12
192	30	2100	11	42700	215	68800	435	16.9	42300	15.3
200	30	1000	4.2	33200	-5	46800	-214	9.10	33400	9.99
200	40	1600	7.7	57500	200	86900	434	15.4	57100	9.89

$\text{ClOO} \rightarrow$ loss by processes that do not generate Cl .

(6)

$$a = Q + k_5 + k_2[\text{O}_2] = -(\lambda_1 - \lambda_2), \quad (11)$$

$$b = k_5 Q + k_6 k_2[\text{O}_2] = \lambda_1 \lambda_2. \quad (12)$$

The rate equations for the above scheme can be solved analytically as long as all Cl and ClOO loss processes are first order

$$[\text{Cl}]_t / [\text{Cl}]_0 = \{ (Q + \lambda_1) \exp(\lambda_1 t) - (Q + \lambda_2) \exp(\lambda_2 t) \} / (\lambda_1 - \lambda_2), \quad (7)$$

where

$$\lambda_1 = 0.5 \{ (a^2 - 4b)^{1/2} - a \}, \quad (8)$$

$$\lambda_2 = -0.5 \{ (a^2 - 4b)^{1/2} + a \}, \quad (9)$$

$$Q = k_{-2} + k_6, \quad (10)$$

A double-exponential decay is predicted. Good quality experimental data can be fit to eq. (7) to obtain values for three parameters λ_1 , λ_2 , and Q . Values for k_5 can be estimated based on measurements in N_2 and O_2 buffer gases at temperatures ($> 250 \text{ K}$) where equilibrium ClOO levels are negligible and on low temperature measurements in N_2 buffer gas; over the range of temperatures (181–200 K) and O_2 pressures (15–40 Torr) investigated, estimated values for k_5 range from 50 to 100 s^{-1} . The elementary rate coefficients k_2 , k_{-2} , and k_6 can be obtained from the fit parameters using the following relationships:

$$k_2 = -(\lambda_1 + \lambda_2 + k_5 + Q) / [\text{O}_2], \quad (13)$$

$$k_6 = (\lambda_1 \lambda_2 - k_5 Q) / k_2 [\text{O}_2], \quad (14)$$

$$k_{-2} = Q - k_6. \quad (15)$$

It should be noted that the parameter Q represents the sum of all first-order ClOO removal processes. Therefore, eqs. (10) and (15) require the assumption that the only important ClOO loss process that regenerates Cl atoms is reaction (-2); for the chemical system of interest, this assumption should be valid.

When mixtures containing 0.17–4.5 mTorr Cl_2 and 15–40 Torr O_2 were subjected to 355 nm laser flash photolysis, the expected double-exponential decays were observable, but only at very low temperatures, i.e. $T \leq 200$ K. A typical Cl temporal profile, observed at $T = 182$ K and $p \approx p_{\text{O}_2} = 20$ Torr, is shown in fig. 1. The solid line in fig. 1 represents the best fit of the data to eq. (7) while the dashed line represents the Cl temporal profile expected based on an evaluation of previously published results [17]; clearly, the approach of laser-flash generated Cl into equilibrium with ClOO is much faster than expected based on previous work while the equilibrium concentration ratio $[\text{Cl}]/[\text{ClOO}]$ is much higher than

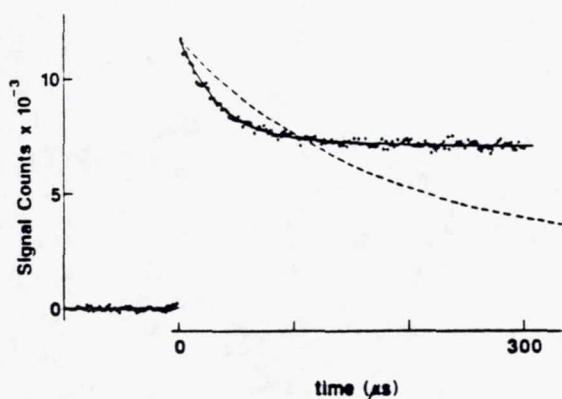


Fig. 1. Typical Cl temporal profile observed following 355 nm pulsed laser photolysis of Cl_2/O_2 mixtures. The laser fired at time $t = 0$. Experimental conditions: $T = 182$ K, $p = 20$ Torr, $[\text{Cl}_2] = 1.4 \times 10^{13}$ molecules cm^{-3} , $[\text{Cl}]_0 = 7 \times 10^{11}$ atoms cm^{-3} , 10000 laser shots averaged. The solid line is obtained from a non-linear least squares analysis that yields the following best fit parameters: $Q = 18400$ s^{-1} , $\lambda_1 = -112$ s^{-1} , and $\lambda_2 = -29600$ s^{-1} . The dashed line is calculated from the evaluated values for k_2 and K_c given in ref. [17].

expected. These differences between observed and expected kinetic behavior (fig. 1) made this study experimentally much more difficult than we had anticipated. An experimental problem (the viscosity of the 50% methanol–50% ethanol cooling fluid) limited the accessible temperature regime to $T > 180$ K. The requirement that relatively large O_2 concentrations be employed in order to drive the equilibrium to significant ClOO production resulted in sensitivity problems, as did the short multichannel scaler dwell times which were required to observe the very rapid equilibration process. The above problems severely limited the range of temperatures and oxygen pressures where quantitative data could be obtained.

Summarized in table 1 are results derived from analyses of 28 Cl atom temporal profiles obtained under experimental conditions where double-exponential decays were observed. The equilibrium constants, K_p , given in table 1 were computed from the relationship

$$K_p = K_c / RT = k_2 / k_{-2} RT. \quad (16)$$

Non-linear least squares analyses were employed to extract values for λ_1 , λ_2 , Q , and the extrapolated signal level at $t = 0$ from the experimental temporal profiles. Values for k_2 , k_{-2} , k_6 , and K_p were then calculated as described above.

Values for k_2 obtained from the 26 experiments at $181 \leq T \leq 192$ K are plotted as a function of O_2 concentration in fig. 2 (although k_2 is expected to increase with decreasing temperature, it should change very little over the relatively narrow temperature range 181–192 K). The spread in the data results from the fact that, under the conditions of our experiments, reaction (-2) typically contributed significantly to the rate of approach into equilibrium ($= k_2[\text{O}_2] + k_{-2}$); hence, uncertainties in individual k_2 determinations are rather large. The solid line in fig. 2 is obtained from a linear least squares analysis of the k_2 versus $[\text{O}_2]$ data. As expected for a three atom system like $\text{Cl} + \text{O}_2$, the data are well represented by a straight line passing through the origin (the standard deviation of the intercept is ten times larger than the absolute value of the intercept), thus indicating that reaction (2) is in its low pressure termolecular limit under our experimental conditions. The termolecular rate coefficient, k_2^{III} , can be evaluated in two different ways. From the slope of the

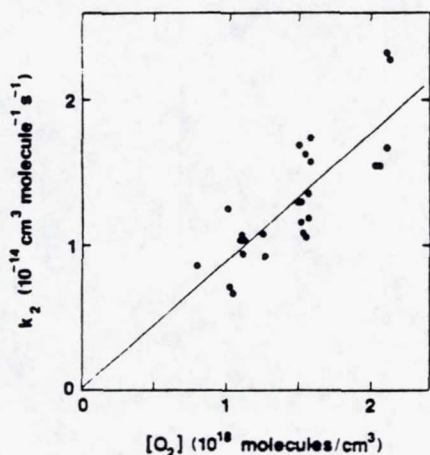


Fig. 2. Plot of k_2 versus $[O_2]$ for all data obtained at temperatures between 181 and 192 K. The solid line is obtained from a linear least squares analysis and gives the termolecular rate coefficient: $k_2^{\text{III}} \pm 2\sigma = (8.8 \pm 2.5) \times 10^{-33} \text{ cm}^6 \text{ molecule}^{-2} \text{ s}^{-1}$.

plot in fig. 2 we obtain $k_2^{\text{III}} \pm 2\sigma = (8.8 \pm 2.5) \times 10^{-33} \text{ cm}^6 \text{ molecule}^{-2} \text{ s}^{-1}$. Alternatively, by simply averaging the 26 values of $k_2/[O_2]$, we obtain $k_2^{\text{III}} \pm 2\sigma = (9.0 \pm 3.3) \times 10^{-33} \text{ cm}^6 \text{ molecule}^{-2} \text{ s}^{-1}$. Since we do not prefer one method of analysis over the other, and since we believe that systematic errors are small compared to uncertainties resulting from precision, we report the rate coefficient

$$k_2^{\text{III}} = (8.9 \pm 2.9) \times 10^{-33} \text{ cm}^6 \text{ molecule}^{-2} \text{ s}^{-1}$$

$$\text{at } T = 186.5 \pm 5.5 \text{ K,}$$

where the uncertainty is 2σ and represents absolute accuracy.

A van 't Hoff plot for the equilibrium defined by reactions (2) and (-2) is shown in fig. 3. Since

$$\ln K_p = \Delta S/R - \Delta H/RT, \quad (17)$$

the enthalpy change associated with reaction (2) can, in principle, be determined from the slope of the van 't Hoff plot while the entropy change can, in principle, be determined from the intercept. However, because our experiments were limited to a rather narrow temperature range, this "second law" analysis gives rather imprecise results. The solid line in fig. 3 is obtained from a linear least squares analysis of the $\ln K_p$ versus $1/T$ data with all data points in-

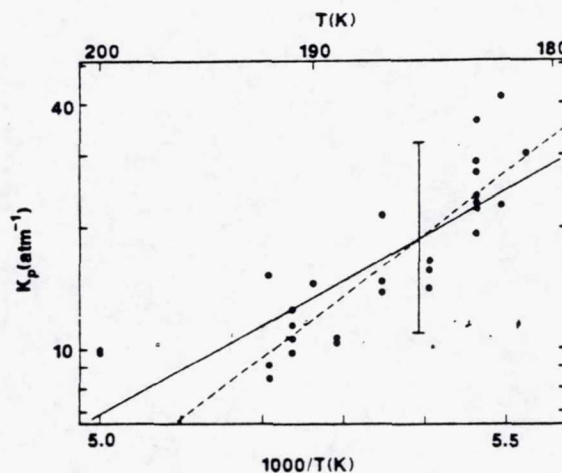


Fig. 3. Van 't Hoff plot for the equilibrium $\text{Cl} + \text{O}_2 = \text{ClOO}$. The solid line is obtained from a linear least squares analysis which includes all data; it gives the result $\Delta H = -5.15 \pm 1.41 \text{ kcal mol}^{-1}$ and $\Delta S = -21.94 \pm 7.51 \text{ cal mol}^{-1} \text{ deg}^{-1}$ (errors are 2σ). The dashed line is obtained from a linear least squares analysis which excludes the two data points at $T = 200 \text{ K}$; it gives the result $\Delta H = -7.00 \pm 1.63 \text{ kcal mol}^{-1}$ and $\Delta S = -31.92 \pm 8.74 \text{ cal mol}^{-1} \text{ deg}^{-1}$ (errors are 2σ). The error bar represents the estimated 2σ uncertainty in K_p at 185.4 K.

cluded; it yields the results $\Delta H_{190}^0 = -5.15 \pm 1.41 \text{ kcal mol}^{-1}$ and $\Delta S_{190}^0 = -21.94 \pm 7.51 \text{ cal mol}^{-1} \text{ deg}^{-1}$. The dashed line in fig. 3 is obtained from a similar analysis with the two experiments at 200 K excluded (the equilibrium constants measured at 200 K have particularly large uncertainties); it yields the results $\Delta H_{186}^0 = -7.00 \pm 1.63 \text{ kcal mol}^{-1}$ and $\Delta S_{186}^0 = -31.92 \pm 8.74 \text{ cal mol}^{-1} \text{ deg}^{-1}$. Errors in the above thermochemical parameters are 2σ and represent precision only.

A potentially more accurate approach for obtaining ClOO thermochemical parameters is the "third law" method, where the measured equilibrium constant at a particular temperature is employed in conjunction with a calculated entropy change to determine ΔH . At 185.4 K, the temperature where the solid and dashed lines in fig. 3 cross, our experiments indicate that $K_p = 18.9 \text{ atm}^{-1}$; the estimated 2σ uncertainty in K_p (185.4 K) is a factor of 1.7 (see error bar in fig. 3). While high resolution spectroscopic data for ClOO are not available, reasonable structural parameters can be deduced from the estimates

of Arkell and Schwager [10] and from the SCF-MO calculations of Hinchliffe [15]. We assume a Cl-O bond length of 1.835 Å, an O-O bond length of 1.31 Å, and a Cl-O-O bond angle of 112.5°. The vibrational frequencies for ClOO, 373, 407, and 1441 cm^{-1} , are taken from infrared measurements in cryogenic matrices [10]; only the high frequency vibration, which does not contribute to the entropy at $T < 300$ K, has been observed in the gas phase [11]. Ab initio calculations suggest that ClOO has a doublet ground state with no excited doublet or quartet states low enough in energy to contribute to the ClOO entropy at $T < 300$ K [16]. Using the above information, we calculate $S_{185.4}^0(\text{ClOO}) = 59.52 \pm 1.09$ cal mol^{-1} deg^{-1} and $\Delta S_{185.4}^0$ (reaction (2)) = -23.18 ± 1.09 cal mol^{-1} deg^{-1} . The uncertainty in $S^0(\text{ClOO})$ is 2σ and is based on the following estimated uncertainties in the ClOO structural parameters and low frequency vibrations: O-O bond length, ± 0.12 Å; Cl-O bond length, ± 0.05 Å; bond angle, $\pm 5^\circ$; each of the two low frequency vibrations, ± 100 cm^{-1} . It is worth noting that the value we calculate for $S_{298}^0(\text{ClOO})$, 64.50 cal mol^{-1} deg^{-1} , is 1.50 cal mol^{-1} deg^{-1} larger than the value reported by Johnston et al. [11]. If we use the same ClOO bond angle and bond lengths in our calculation as Johnston et al. used in their calculation (those suggested by Arkell and Schwager [10]), the two results differ by almost exactly $R \ln 2$, i.e. the electronic contribution to the ClOO entropy.

Using our experimental value for K_p at 185.4 K and our calculated value for $\Delta S_{185.4}^0$, we compute from eq. (17) the enthalpy change $\Delta H_{185.4}^0$ (reaction (2)) = -5.38 ± 0.41 kcal mol^{-1} . Making the appropriate heat capacity corrections, one obtains the results ΔH_{298}^0 (reaction (2)) = -5.56 ± 0.47 kcal mol^{-1} and $-\Delta H_0^0$ (reaction (2)) = 4.76 ± 0.49 kcal mol^{-1} (\equiv the Cl-OO bond dissociation energy). In conjunction with known heats of formation for Cl and O₂ [32], our value for ΔH_{298}^0 (reaction (2)) leads to a value of 23.4 ± 0.5 kcal mol^{-1} for the ClOO heat of formation at 298 K; previous work has led to a recommended ClOO heat of formation of 22.5 ± 1 kcal mol^{-1} [17].

Literature data with which we can compare our results are sparse. The only published measurement of k_2 was reported over twenty years ago by Nicholas and Norrish [4]. Their experiment involved flash

photolysis of Cl₂/O₂/N₂ mixtures. Complex analysis of the time-resolved production of ClO, measured by photographic recording of absorption in the UV region, was employed to extract a value for k_2 . Nicholas and Norrish reported $k_2^{\text{III}} = (1.7 \pm 0.3) \times 10^{-33}$ cm^6 molecule^{-2} s^{-1} at 298 K in N₂+O₂ buffer gas, a factor of 5.2 slower than the value for k_2^{III} determined in this study at 186.5 ± 5.5 K in O₂ buffer gas. If both determinations of k_2^{III} are correct, and if N₂ and O₂ are assumed to be equally efficient at stabilizing the ClOO adduct, then the activation energy for reaction (2) is -1.6 kcal mol^{-1} , i.e. somewhat smaller than one would "guesstimate" [17] but within the range of reasonable values. There are no quantitative kinetic data for reaction (-2) in the literature, though values for k_{-2}^{II} have been estimated by several groups [11-13] using measured equilibrium constants in conjunction with the value for k_2^{III} reported by Nicholas and Norrish [4]; these estimates range from $(2.55-4.67) \times 10^{-13}$ cm^3 molecule^{-1} s^{-1} at 298 K. Our data give $k_{-2}^{\text{II}} = 1.8 \times 10^{-14}$ cm^3 molecule^{-1} s^{-1} at 185 K. Assuming that the activation energy for reaction (2) is -1 ± 1 kcal mol^{-1} and using our measured enthalpy of reaction of -5.47 ± 0.44 kcal mol^{-1} (averaged over the range 180-300 K), we estimate the activation energy for reaction (-2) to be 6.5 ± 1.4 kcal mol^{-1} . This leads to a best estimate for k_{-2}^{II} (298 K) of 1.4×10^{-11} cm^3 molecule^{-1} s^{-1} , i.e. 30-55 times faster than previous estimates [11-13]. In a recent study of ClOOCl photochemistry, Molina et al. also report evidence that ClOO decomposition is faster than previously thought [33].

Published values for K_p (298 K) are based on analyses of ClOO and ClO temporal behavior in molecular modulation [11,13] and flash photolysis [12] studies. In all cases, complex kinetic behavior had to be modeled to extract rate parameters and equilibrium constants. Radical-radical processes such as reactions (3) and (4) were important in these studies [11-13] and greatly complicated the kinetic analyses. Reported values for K_p (298 K) range from 0.090 to 0.165 atm^{-1} . Using the thermochemical parameters determined in this study in conjunction with eq. (17), we calculate K_p (298 K) = 0.071 atm^{-1} , somewhat lower than the literature values [11-13].

After our preliminary results were reported [34], two other groups undertook investigations of the Cl,

O₂, ClOO equilibrium [35,36]. Both groups employed time-resolved UV absorption to monitor ClOO following flash photolytic generation of Cl in the presence of O₂. Neither study obtained kinetic data for reactions (2) and (-2). However, because O₂ concentrations up to 1 atm [35] or 100 atm [36] could be employed, equilibrium constants could be determined at temperatures up to 250 K in one study [35] and up to 300 K in the other study [36]. Reported enthalpy changes for reaction (2) are -5.1 kcal mol⁻¹ at 215 K [35] and -5.53 kcal mol⁻¹ at 240 K [36], i.e. in excellent agreement with the enthalpy change reported in this study. All three recent determinations suggest that the ClOO bond strength is weaker by 1.0-1.3 kcal mol⁻¹ than previously thought [17].

Acknowledgement

This work was supported by the NASA Upper Atmosphere Research Program through grant No. NAGW-1001. We thank R.L. Mauldin III, J.B. Burkholder, and A.R. Ravishankara for communicating their results to us prior to publication and for several helpful discussions.

References

- [1] G. Porter and F.J. Wright, *J. Phys. Chem.* 14 (1953) 23.
- [2] G. Burns and R.G.W. Norrish, *Proc. Roy. Soc. A* 271 (1963) 289.
- [3] S.W. Benson and J.H. Buss, *J. Chem. Phys.* 27 (1957) 1382.
- [4] J.E. Nicholas and R.G.W. Norrish, *Proc. Roy. Soc. A* 307 (1968) 391.
- [5] P.W. Atkins, J.A. Brivati, N. Keen, M.C.R. Symons and P.A. Trevalion, *J. Chem. Soc.* (1962) 4785.
- [6] R.S. Eachus, P.R. Edwards, S. Subramanian and M.C.R. Symons, *Chem. Commun.* (1967) 1036.
- [7] J.L. Byberg, *J. Chem. Phys.* 47 (1967) 861.
- [8] R.S. Eachus, P.R. Edwards, S. Subramanian and M.C.R. Symons, *J. Chem. Soc. A* (1968) 1704.
- [9] F.J. Adrian, E.L. Cochran and V.A. Bowers, *J. Chem. Phys.* 56 (1972) 6251.
- [10] A. Arkell and I. Schwager, *J. Am. Chem. Soc.* 89 (1967) 5999.
- [11] H.S. Johnston, E.D. Morris Jr. and J. Van den Bogaerde, *J. Am. Chem. Soc.* 91 (1969) 7712.
- [12] R.D. Ashford, N. Basco and J.E. Hunt, *Intern. J. Chem. Kinetics* 10 (1978) 1233.
- [13] R.A. Cox, R.G. Derwent, A.E.J. Eggleton and H.J. Reid, *J. Chem. Soc. Faraday Trans. I* 75 (1978) 1648.
- [14] J.L. Gole, *J. Phys. Chem.* 84 (1980) 1333.
- [15] A. Hinchliffe, *J. Mol. Struct.* 64 (1980) 117.
- [16] J.A. Jafri, B.H. Lengsfeld III, C.W. Bauschlicher Jr. and J.H. Phillips, *J. Chem. Phys.* 83 (1985) 1693.
- [17] W.B. DeMore, M.J. Molina, S.P. Sander, D.M. Golden, R.F. Hampson, M.J. Kurylo, C.J. Howard and A.R. Ravishankara, JPL publication 87-41, Jet Propulsion Laboratory, California Institute of Technology, Pasadena, CA (1987).
- [18] M.B. McElroy, R.J. Salawitch and S.C. Wofsy, *Planet. Space Sci.* 36 (1988) 73.
- [19] M.J. Molina, T.-L. Tso, L.T. Molina and F.C.-Y. Wang, *Science* 238 (1987) 1253.
- [20] M.A. Tolbert, M.J. Rossi, R. Malhotra and D.M. Golden, *Science* 238 (1987) 1258.
- [21] L.T. Molina and M.J. Molina, *J. Phys. Chem.* 91 (1986) 433.
- [22] M.B. McElroy, R.J. Salawitch, S.C. Wofsy and J.A. Logan, *Nature* 321 (1986) 759.
- [23] V. Vaida, S. Solomon, E.C. Richard, E. Rühl and A. Jefferson, *Nature* 342 (1989) 405.
- [24] W.G. Lawrence, K.C. Clemitshaw and V.A. Apkarian, *J. Geophys. Res.* 95 (1990) 18591.
- [25] J.M. Nicovich, C.J. Shackelford and P.H. Wine, *J. Phys. Chem.* 94 (1990) 2896.
- [26] R.S. Mulliken, *Phys. Rev.* 57 (1940) 500.
- [27] G.E. Busch, R.T. Mahoney, R.I. Morse and K.R. Wilson, *J. Chem. Phys.* 51 (1969) 449.
- [28] I.S. Fletcher and D. Husain, *Chem. Phys. Letters* 49 (1977) 516.
- [29] R.H. Clark and D. Husain, *J. Chem. Soc. Faraday Trans. II* 80 (1984) 97.
- [30] S.A. Chasnikov, A.I. Chichinin and L.N. Krasnoperov, Tenth International Symposium on Gas Kinetics, Swansea, UK (1988) paper No. 38.
- [31] S.A. Sotnichenko, V.Ch. Bokun and A.I. Nadkhin, *Chem. Phys. Letters* 153 (1988) 560.
- [32] R. Atkinson, D.L. Baulch, R.A. Cox, R.F. Hampson Jr., J.A. Kerr and J. Troe, *J. Phys. Chem. Ref. Data* 18 (1989) 881.
- [33] M.J. Molina, A.J. Colussi, L.T. Molina, R.N. Schindler and T.-L. Tso, *Chem. Phys. Letters* 173 (1990) 310.
- [34] A preliminary report of this study was presented at the XVIIIth Informal Conference on Photochemistry, Santa Monica, CA (January, 1989).
- [35] R.L. Mauldin III, J.B. Burkholder and A.R. Ravishankara, to be published.
- [36] H. Hippler, R. Rahn, N. Seitzinger, M. Siefke and J. Troe, to be published.

NDB
511-25
026129
91
273550

K-10.1

Reprinted from *The Journal of Physical Chemistry*, 1991, 95.
Copyright © 1991 by the American Chemical Society and reprinted by permission of the copyright owner.

Kinetics and Mechanism of the Reaction of Hydroxyl Radicals with Acetonitrile under Atmospheric Conditions

A. J. Hynes* and P. H. Wine

Physical Sciences Laboratory, Georgia Tech Research Institute, Georgia Institute of Technology, Atlanta, Georgia 30332 (Received: March 16, 1990; In Final Form: August 21, 1990)

The pulsed laser photolysis-pulsed laser induced fluorescence technique has been employed to determine absolute rate coefficients for the reaction $\text{OH} + \text{CH}_3\text{CN}$ (1) and its isotopic variants, $\text{OH} + \text{CD}_3\text{CN}$ (2), $\text{OD} + \text{CH}_3\text{CN}$ (3), and $\text{OD} + \text{CD}_3\text{CN}$ (4). Reactions 1 and 2 were studied as a function of pressure and temperature in N_2 , N_2/O_2 , and He buffer gases. In the absence of O_2 all four reactions displayed well-behaved kinetics with exponential OH decays and pseudo-first-order rate constants which were proportional to substrate concentration. Data obtained in N_2 over the range 50–700 Torr at 298 K are consistent with k_1 showing a small pressure dependence. The Arrhenius expression obtained by averaging data at all pressures is $k_1(T) = (1.1^{+0.5}_{-0.3}) \times 10^{-12} \exp[(-1130 \pm 90)/T] \text{ cm}^3 \text{ molecule}^{-1} \text{ s}^{-1}$. The kinetics of reaction 2 are found to be pressure dependent with k_2 (298 K) increasing from $(1.21 \pm 0.12) \times 10^{-14}$ to $(2.16 \pm 0.11) \times 10^{-14} \text{ cm}^3 \text{ molecule}^{-1} \text{ s}^{-1}$ over the pressure range 50–700 Torr of N_2 at 298 K. Data at pressures >600 Torr give $k_2(T) = (9.4^{+13.4}_{-3.0}) \times 10^{-13} \exp[(-1180 \pm 250)/T] \text{ cm}^3 \text{ molecule}^{-1} \text{ s}^{-1}$. The rates of reactions 3 and 4 are found to be independent of pressure over the range 50–700 Torr of N_2 with 298 K rate coefficients given by $k_3 = (3.18 \pm 0.40) \times 10^{-14} \text{ cm}^3 \text{ molecule}^{-1} \text{ s}^{-1}$ and $k_4 = (2.25 \pm 0.28) \times 10^{-14} \text{ cm}^3 \text{ molecule}^{-1} \text{ s}^{-1}$. In the presence of O_2 each reaction shows complex (non-pseudo-first-order) kinetic behavior and/or an apparent decrease in the observed rate constant with increasing $[\text{O}_2]$, indicating the presence of significant OH or OD regeneration. Observation of regeneration of OH in (2) and OD in (3) is indicative of a reaction channel which proceeds via addition followed by reaction of the adduct, or one of its decomposition products, with O_2 . The observed OH and OD decay profiles have been modeled by using a simple mechanistic scheme to extract kinetic information about the adduct reactions with O_2 and branching ratios for OH regeneration. A plausible mechanism for OH regeneration in (2) involves OH addition to the nitrogen atom followed by O_2 addition to the cyano carbon atom, isomerization, and decomposition to $\text{D}_2\text{CO} + \text{DOCN} + \text{OH}$. Our results suggest that the $\text{OH} + \text{CH}_3\text{CN}$ reaction occurs via a complex mechanism involving both bimolecular and termolecular pathways, analogous to the mechanisms for the important atmospheric reactions of OH with CO and HNO_3 .

Introduction

It is now generally accepted that acetonitrile (CH_3CN) is present at ppt levels in the stratosphere.¹ Attempts to understand the role of acetonitrile in stratospheric positive ion chemistry² and its contribution to the stratospheric NO_x budget³ require a detailed

understanding of its atmospheric sources, emission rates, and oxidation mechanism. Acetonitrile was first proposed as a com-

(1) Schlager, H.; Arnold, F. *Planet. Space Sci.* 1986, 34, 245.

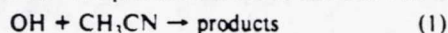
(2) Arijis, E.; Nevejans, D.; Ingels, Int. *J. Mass Spectrom. Ion Processes* 1987, 81, 15.

(3) "Atmospheric Ozone 1985." WMO-Report No. 16, Vol. 1, World Meteorological Organization, Geneva, 1985.

* Author to whom correspondence should be addressed.

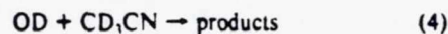
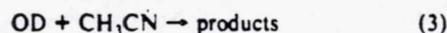
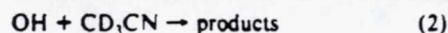
ponent of stratospheric positive cluster ions by Arnold et al.,⁴ who used a rocket-borne ion mass spectrometer to identify cluster ions of the type $H^+X_n(H_2O)_m$, where $X = \text{mass } 41$, $l = 1, 2$, and $n = 0, 1, 2, 3$. These ions have been termed non-proton hydrates (NPH)⁵ to distinguish them from proton hydrates (PH) of the form $H^+(H_2O)_n$ which had been predicted to be present in the stratosphere⁶ and were also observed experimentally. Subsequent experiments using balloon-borne mass spectrometers⁷ determined ion concentration profiles in the 25–40-km region and, although the identification of X as CH_3CN remained circumstantial, were used to infer stratospheric mixing ratios for neutral CH_3CN ⁷ and even for the OH radical.⁷ The first definitive identification of X as CH_3CN came from field and laboratory measurements of Schlager and Arnold,¹ who used electric-field-induced collisional activation to fragment the NPH clusters and produce mass 15, identified as CH_3^+ , as a product. The totally unexpected observation of NPH and inferred free CH_3CN mixing ratios in the ppt range has led to a number of efforts to identify the source of the CH_3CN and model its atmospheric profiles.⁸ While it now appears that the only significant sources of CH_3CN involve emission at the Earth's surface,⁸ modeling efforts have been hampered by the paucity of data on emission rates, tropospheric concentration profiles, and atmospheric degradation processes. Three major deficiencies identified by Arijis et al.² in a recent review of stratospheric positive ion measurements and acetonitrile detection are (a) accurate measurements of rate constants for the atmospheric reactions of CH_3CN , in particular with OH, (b) a detailed study of the emission sources of CH_3CN , and (c) a better knowledge of atmospheric eddy diffusion processes.

This work addresses the first of the above-mentioned data requirements, the rate and mechanism of reaction 1 under atmospheric conditions. Six previous studies of reaction 1 have



employed the flash photolysis–resonance fluorescence^{9–13} and discharge flow–EPR¹⁴ techniques. While the most recent studies are in reasonable agreement on the 298 K rate constant at pressures in excess of 50 Torr Ar,^{10–13} there are considerable discrepancies in observed temperature and pressure dependencies. There has been no investigation of the effects of isotopic substitution on reaction 1. Furthermore, since all studies of reaction 1 have been performed in either Ar or He buffer gases, the effects of N_2 and O_2 on the rate constant and hence the effective value for the rate constant under atmospheric conditions have not been delineated.

In this work we have employed a pulsed laser photolysis–pulsed laser induced fluorescence (PLP–PLIF) technique to study reaction 1 as a function of pressure and temperature in N_2 , N_2/O_2 , and He buffer gases. Studies of the isotopic variants, reactions 2, 3, and 4, have been performed in an attempt to shed light on the detailed reaction mechanism. Our results are inconsistent with



(4) Arnold, F.; Böhlinger, H.; Henschen, G. *Geophys. Res. Lett.* **1978**, *5*, 653.

(5) Arijis, E.; Ingels, J.; Nevejans, D. *Nature* **1978**, *271*, 642.

(6) Mohnen, V. A. *Pure Appl. Geophys.* **1971**, *84*, 114.

(7) Arijis, E.; Nevejans, D.; Ingels, J. *Nature* **1983**, *303*, 314, and references therein.

(8) Arijis, E.; Brasscur, G. *J. Geophys. Res.* **1986**, *91*, 4003.

(9) Harris, G. W.; Kleindienst, T. E.; Pitts, J. N., Jr. *Chem. Phys. Lett.* **1981**, *80*, 479.

(10) Fritz, B.; Lorenz, K.; Steinert, W.; Zellner, R. In *Proceedings of the 2nd European Symposium on the Physico-Chemical Behaviour of Atmospheric Pollutants*; Varsino, B.; Angeletti, G., Eds.; D. Reidel: Boston, MA, **1982**; p 192.

(11) Zetzsch, C. *Bunsekolloquium*; Battelle Institut: Frankfurt, **1983**.

(12) Kurylo, M. J.; Knable, G. L. *J. Phys. Chem.* **1984**, *88*, 3305.

(13) Rhasa, D.; Zellner, R. Unpublished work. Rhasa, D. Diplomarbeit, Göttingen, FRG, **1983**.

(14) Poulet, D.; Laverdet, G.; Jourdain, J. L.; Le Bras, G. *J. Phys. Chem.* **1984**, *88*, 6259.

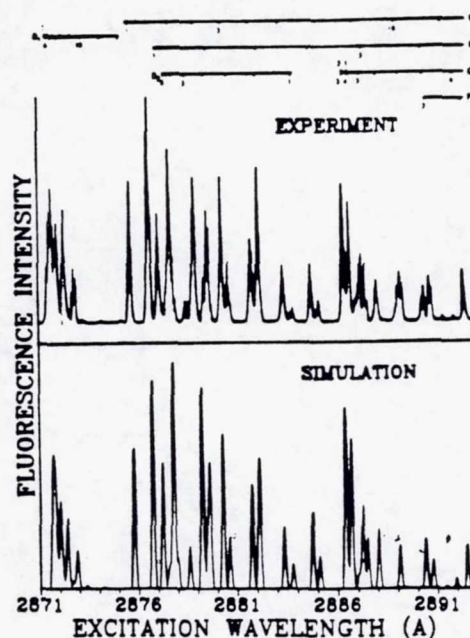


Figure 1. Experimental and simulated laser excitation spectrum of the OD $A^2\Sigma^+-X^2\Pi(1-0)$ transition.

the view that reaction 1 is pressure independent and proceeds exclusively via a direct hydrogen abstraction mechanism.

Experimental Section

The PLP–PLIF apparatus has been described in detail elsewhere.¹⁵ Modifications and a brief review of its operation are given below. Three different reaction cells were used, with most of the experiments being performed in a Pyrex cell which had an internal diameter of 4 cm and a length of 50 cm. Two side arms, 4 cm i.d. and 14 cm long, which terminated in Brewster angle windows were attached to the center of the cell. The photolysis laser passed through these side arms across the direction of gas flow while the probe laser passed along the length of the cell. Fluorescence was detected through a third side arm, 4 cm i.d. and 5 cm long, perpendicular to the photolysis and probe beams. The central 25 cm length of the cell was jacketed to permit the flow of heating or cooling fluid from a thermostated bath. Detailed descriptions of the other two reaction cells, which were constructed of Pyrex and brass, are given elsewhere.^{15,16} A copper–constantan thermocouple with a stainless steel jacket was inserted into the reaction zone through a vacuum seal, allowing measurement of the gas temperature under the precise pressure and flow conditions of the experiment.

OH and OD were produced by the pulsed laser photolysis of H_2O_2 , HNO_3 , or DNO_3 using the 193-nm (ArF) and 248-nm (KrF) outputs from an excimer laser or the 266-nm fourth harmonic output from a Nd:YAG laser. Pulsed laser induced fluorescence using a Nd:YAG laser pumped, frequency-doubled dye laser was used for OH(D) detection. Excitation was via the Q_{11} line of the $A^2\Sigma^+-X^2\Pi(1-0)$ transition at ≈ 282 nm for OH and ≈ 287 nm for OD. All kinetic studies were performed with a line-narrowing etalon in the dye laser cavity giving an estimated line width of 0.1 cm^{-1} at 280 nm. The laser could be reproducibly scanned on and off the OH(D) line by pressure tuning using N_2 gas. Fluorescence in the 0–0 and 1–0 bands was detected by an EMI 9813QB photomultiplier after passing through collection optics and filters to discriminate against Rayleigh scattering and Raman scattering from N_2 and/or O_2 . The photomultiplier output

(15) Hynes, A. J.; Wine, P. H.; Semmes, D. H. *J. Phys. Chem.* **1986**, *90*, 4148.

(16) Hynes, A. J.; Wine, P. H.; Ravishankara, A. R. *J. Geophys. Res.* **1986**, *91*, 11815.

was appropriately terminated and fed to a 100-MHz waveform analyser to obtain the peak voltage averaged for (typically) 100 laser shots. To ensure that we were, in fact, producing and monitoring OD, a laser excitation spectrum of the A-X(1-0) band was obtained by scanning the un narrowed dye laser. In this case the photomultiplier output was processed by a boxcar averager and the output digitized and stored in a small computer. The excitation spectrum was assigned by comparison with a simulated spectrum of the six main branches calculated from the term energies of Clync et al.¹⁷ Intensities were calculated for a 300 K Boltzman population distribution by using the formula of Earls¹⁸ and convoluting over the laser bandwidth. The experimental and simulated spectra, shown in Figure 1, are in good agreement and confirm that we were producing and monitoring OD.

Kinetic information was obtained by varying the delay between the photolysis and probe lasers using a digital delay generator. Signal was collected for 15–20 delays, varying from 0 to 20 ms, in order to map out an OH(D) decay profile over three $1/e$ times.

In order to avoid the accumulation of photolysis or reaction products all experiments were carried out under "slow flow" conditions with the linear flow rate through the reactor varied between 1 and 5 cm s⁻¹. In a typical experiment the flows were set in the absence of CH₃CN to give the desired pressure. A CH₃CN/N₂ mixture was then added incrementally to the flow and a range of pseudo-first-order rate constants measured. The throttle valves in the flow system were not adjusted to keep the pressure constant during this process and hence there was some variation in total pressure over the course of an experiment. Bulbs containing ≈5% acetonitrile in N₂ were prepared manometrically and the concentration of acetonitrile in the reaction mixture was calculated from flow rates and reactor total pressure. The flow rates and total pressure were measured by using calibrated mass flow meters and a capacitance manometer. The response of the mass flow meter which measured the mixture containing CH₃CN was corrected for its presence by calibrating with CH₃CN/N₂ and CH₃CN/He mixtures. For a 5% CH₃CN/N₂ mixture the correction was 7%, and for the 6% CH₃CN/He mixture used in the two sets of He buffer experiments the correction was 17%. These corrections were somewhat larger than the 5% and 12% corrections calculated by using a formula supplied by the manufacturer.¹⁹

In order to assess the possibility of complications arising from isotopic exchange between H₂O₂ and CD₃CN the infrared spectra of CH₃CN, CD₃CN, and CD₃CN/H₂O₂ mixtures were measured. For the CD₃CN/H₂O₂ mixtures, no evidence for isotopic exchange was observed on a time scale of 15 min.

Chemicals. The pure gases used in this study had the following stated minimum purities: N₂, 99.999%; O₂, 99.99%. Air was zero grade, <1 ppm total hydrocarbons. H₂O₂ (90%) was obtained from FMC Corp.; it was further concentrated and purified by bubbling buffer gas through the sample for several days before use in experiments. HNO₃ (70% in H₂O) was used in a 50/50 mixture with H₂SO₄ (95%); both were Fisher AR grade. DNO₃ (99 atom % D, 70% solution in D₂O) and D₂SO₄ (99 atom % D) were obtained from ICN Biomedicals. CH₃CN, UV grade (>99.9%) was obtained from Burdick & Jackson. CD₃CN (>99.9% chemical purity and 99 atom % D) was obtained from Aldrich. Acetonitrile samples were degassed and purified by trap to trap distillation before use.

Results and Discussion

Experiments in the Absence of Oxygen. All experiments were performed under pseudo-first-order conditions with [CH₃CN] ≫ [OH]. Typical initial OH concentrations were 1 × 10¹¹ to 3 × 10¹² molecules cm⁻³ while CH₃CN concentrations were in the range 1 × 10¹⁵ to 3 × 10¹⁷ molecules cm⁻³. Under these conditions

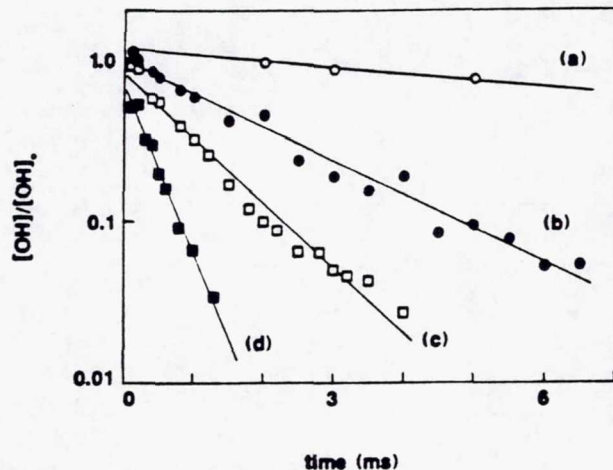
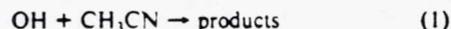
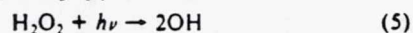


Figure 2. Typical OH temporal profiles for reaction 1. Experimental conditions: 298 K, 587–623 Torr of N₂, [OH]₀ ≈ 2 × 10¹² molecules cm⁻³. CH₃CN concentrations in units of 10¹⁶ molecules cm⁻³ were (a) 0, (b) 1.39, (c) 4.03, (d) 9.39. Solid lines are obtained from linear least-squares analyses and give the pseudo-first-order rate constants (a) 64 ± 5 s⁻¹, (b) 478 ± 39 s⁻¹, (c) 916 ± 76 s⁻¹, (d) 2386 ± 173 s⁻¹ (errors are 2σ). The plots have been displaced vertically for clarity.

we expect the temporal profile of OH to be governed by the following reactions (for H₂O₂ precursor):



OH → loss by diffusion, reaction with H₂O₂,

and reaction with background impurities (6)

Since [CH₃CN] ≫ [OH]₀, observed OH decays were expected to follow simple first-order kinetics:

$$\ln ([\text{OH}]_0/[\text{OH}]_t) = (k_1[\text{CH}_3\text{CN}] + k_d)t = k't \quad (1)$$

The bimolecular rate constant, k_1 , is determined from the slope of a k' vs [CH₃CN] plot. Observation of OH temporal profiles which are exponential, a linear dependence of k' on [CH₃CN] and invariance of k' to variations in laser photolysis energy would serve to confirm the above mechanism. Factor of 5 variations in laser photolysis energy were carried out under a variety of experimental conditions and found to have no effect on observed kinetics; these observations confirmed that radical-radical side reactions had a negligible effect on OH kinetics.

OH decay profiles obtained at different CH₃CN concentrations in 600 ± 20 Torr of N₂ are shown in Figure 2. Some scatter and curvature is evident in this data which results from instabilities in the photolysis or probe laser. This scatter, which was particularly prevalent for high-pressure data where the signal to noise ratio was low, is reflected in the rather low precision of some of the rate constants obtained, particularly for k_1 . However, there were no systematic deviations from exponential behavior for any OH and OD decays in the absence of oxygen. Figure 6d, for example, shows an OH decay in 450 Torr of N₂; this decay, which was measured on a day the system was particularly stable, shows excellent linearity for greater than 4 $1/e$ times.

All decays were analyzed for at least three $1/e$ times; typical 2σ errors in measured decay rates were <10% although at high pressures 2σ errors as large as 15% were obtained. Figure 3 shows plots of k' vs acetonitrile concentration observed in studies employing N₂ buffer gas at high pressure. The results of all studies in the absence of O₂ are summarized in Tables I–III; quoted errors in tables are 2σ and represent precision only. A plot of the 298 K rate constants for reactions 1 and 2 as a function of pressure is shown in Figure 4. To avoid congestion on the plot, the data are shown with 1σ error bars. The data for k_2 show a clear pressure dependence, increasing by almost a factor of 2 over the pressure range 40–700 Torr. The pressure dependence is confirmed by the results at higher temperature which show a trend

(17) Clync, M. A. A.; Coxon, J. A.; Woon Fat, A. R. *J. Mol. Spectrosc.* 1973, 46, 146.

(18) Earls, L. T. *Phys. Rev.* 1935, 48, 423.

(19) MKS Instruments, Inc., Burlington, MA.

TABLE I: Summary of Kinetic Data for OH + CH₃CN

T, K	photolysis wavelength, ^a nm	press., ^b Torr	k', 10 ⁻¹⁴ cm ³ molecule ⁻¹ s ⁻¹
388	266	40-50	5.94 ± 0.20
377	266	600-680	6.11 ± 0.69
370.5	266	550-650	5.71 ± 0.52
366.5	266	45-55	5.07 ± 0.19
352.5	266	46-60	4.71 ± 0.24
345.5	248	120-150	5.40 ± 0.7
338.5	266	50-60	3.61 ± 0.91
336	266	580-660	3.68 ± 0.50
318	248	660-700	3.15 ± 0.13
318	248	112-142	3.30 ± 0.55
298	266	600-700	2.81 ± 0.28
298	193 ⁽¹⁾	587-623	2.43 ± 0.22
298	248	580-630 ⁽²⁾	2.15 ± 0.35
298	248	520-570	2.56 ± 0.22
298	248	246-294	2.64 ± 0.22
298	248	149-171	2.47 ± 0.23
298	266	130-160	2.41 ± 0.58
298	248	78-98	2.37 ± 0.12
298	266	46-60	2.17 ± 0.22
298	248	30-40 ⁽²⁾	2.22 ± 0.12
278	248	180-235	2.30 ± 0.13
274.5	248	600-700	1.88 ± 0.24
274.5	248	100-120	1.84 ± 0.18
273	248	625-721	1.99 ± 0.13
256.5	248	550-600	1.46 ± 0.09
256.5	248	100-130	1.38 ± 0.08

^a Photolytic precursor was H₂O₂ except for (1) when HNO₃ was used. ^b Buffer gas was N₂ except for (2) He. ^c Errors are 2σ.

TABLE II: Summary of Kinetic Data for OH + CD₃CN

T, K	photolysis wavelength, ^a nm	press., ^b Torr	k', 10 ⁻¹⁴ cm ³ molecule ⁻¹ s ⁻¹
379	266	50-66	2.88 ± 0.16
358.5	266	600-680	3.64 ± 0.51
345.5	248	130-170	2.18 ± 0.11
340	266	43-55	1.82 ± 0.29
335	266	580-676	2.59 ± 0.23
298	248	666-692	2.16 ± 0.11
298	248	330-360	1.90 ± 0.09
298	248	154-183	1.51 ± 0.14
298	193 ⁽¹⁾	137-154	1.51 ± 0.22
298	248	40-70	1.43 ± 0.07
298	266	40-55	1.21 ± 0.12
276	248	40-60	1.11 ± 0.07
275	248	600-700	1.26 ± 0.13
275	248	100-120	1.46 ± 0.13
257	248	40-60	0.95 ± 0.06
256	248	550-600	0.94 ± 0.041
256	248	50-60	0.865 ± 0.094

^a Photolytic precursor was H₂O₂ except for (1) when HNO₃ was used. ^b Buffer gas was N₂. ^c Errors are 2σ.

TABLE III: Summary of Kinetic Data for Reactions 3 and 4

photolysis wavelength, ^a nm	press., ^b Torr	k', 10 ⁻¹⁴ cm ³ molecule ⁻¹ s ⁻¹
OD + CH ₃ CN		
266	490-550	3.17 ± 0.44
193	200-250	3.10 ± 0.52
248	47-55	3.00 ± 0.19
248	45-55	3.46 ± 0.44
OD + CD ₃ CN		
266	500-560	2.32 ± 0.63
266	500-550	2.34 ± 0.41
266	59-69	2.04 ± 0.26
266	46-50	2.31 ± 0.06

^a Photolytic precursor was DNO₃. ^b Buffer gas was N₂. ^c Errors are 2σ.

of increasing pressure dependence with increasing temperature. The situation for reaction 1 is rather less clear because the precision of the data is not as good as for reaction 2. The data for N₂ is

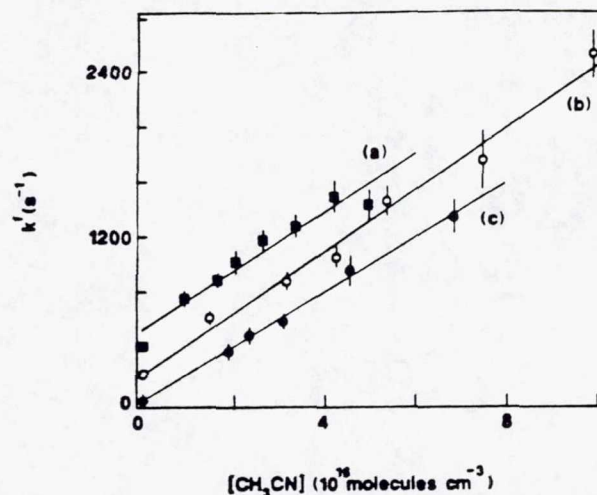


Figure 3. Typical k' vs reactant concentration plots. Experimental conditions: 298 K, N₂ buffer. (a) OD + CD₃CN, 500-550 Torr. (b) OH + CH₃CN, 587-623 Torr. (c) OH + CD₃CN, 666-692 Torr. Solid lines were obtained from linear least-squares analyses and give the following bimolecular rate constants in units of 10⁻¹⁴ cm³ molecule⁻¹ s⁻¹: (a) 2.34 ± 0.41, (b) 2.43 ± 0.22, (c) 2.16 ± 0.11 (errors are 2σ and represent precision only). The plots have been displaced vertically for clarity.

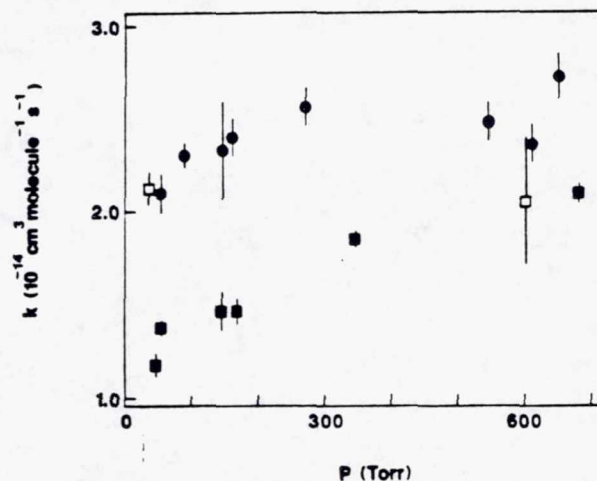


Figure 4. Pressure dependence of reactions 1 and 2 at 298 K. (●) OH + CH₃CN, N₂ buffer; (□) OH + CH₃CN, He buffer; (■) OH + CD₃CN, N₂ buffer.

consistent with k_1 showing a small pressure dependence. However, the data would also be consistent with a pressure-independent k_1 value of $(2.48 \pm 0.38) \times 10^{-14}$ cm³ molecule⁻¹ s⁻¹. The data in He, which consist of one high- and one low-pressure series of experiments, are pressure independent over the range 30-600 Torr. For reactions 3 and 4, within the precision of the limited data set which encompasses two high- and two low-pressure rate constants for each reaction, the data suggests that k_3 and k_4 are independent of pressure over the range 50-700 Torr. The temperature dependence of k_1 is plotted in Arrhenius form in Figure 5 along with the temperature dependence of k_2 at high pressure (i.e., $P > 600$ Torr). For reaction 1 all data were weighted equally in the calculation of the expression

$$k_1(T) = (1.1^{+0.5}) \times 10^{-12} \exp[(-1130 \pm 90)/T] \text{ cm}^3 \text{ molecule}^{-1} \text{ s}^{-1}$$

For reaction 2 the data at $T > 298$ K confirm the observed pressure dependence at 298 K; these data suggest that the high-pressure limit is approached at progressively lower pressures as the temperature decreases. The observed pressure dependences suggest that, over the temperature range of our experiments, k_2 is close to its high-pressure limit at nitrogen pressures of 600 Torr

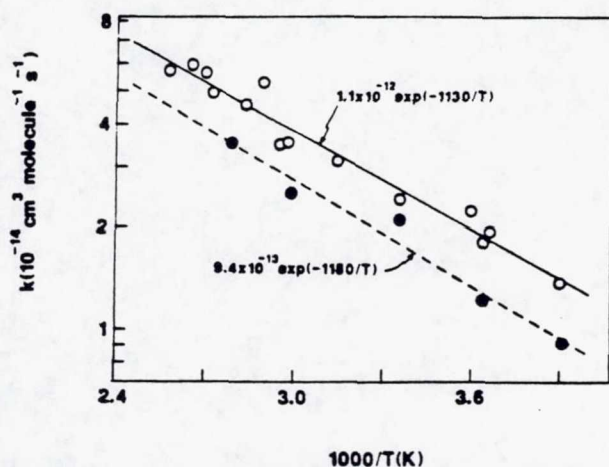


Figure 5. Arrhenius plots. (—○—) OH + CH₃CN; (—●—) OH + CD₃CN. *P* > 600 Torr. Solid and dashed lines are obtained from least-squares analyses. *A* factors are in units of cm³ molecule⁻¹ s⁻¹.

TABLE IV: Summary of Arrhenius Parameters and 298 K Rate Constants for Reactions 1-4^a

reaction	<i>A</i> ^b	<i>E</i> / <i>R</i> , K	<i>k</i> (298 K) ^c
OII + CH ₃ CN	1.1 ^{+0.1} _{-0.1}	1104 ± 118	2.48 ± 0.38
OII + CD ₃ CN	0.96 ^{+0.1} _{-0.1}	1175 ± 243	2.16 ± 0.11 ^d
OD + CH ₃ CN			3.18 ± 0.40
OD + CD ₃ CN			2.25 ± 0.28

^aErrors are 2σ. ^bUnits are 10¹² cm³ molecule⁻¹ s⁻¹. ^cUnits are 10⁻¹⁴ cm³ molecule⁻¹ s⁻¹. ^dAt ≈ 680 Torr.

TABLE V: On-Line and Off-Line Signals Observed during OH Regeneration^a

	signal + background, mV	background, mV
on OH line	2372 ± 490	917 ± 43
off OII line	903 ± 78	918 ± 45

^aThe voltages are the means ± 1σ of 5 × 100 shot averages.

or greater. The data for *P* > 600 Torr give the Arrhenius expression

$$k_2(T) = (9.4^{+1.3}_{-0.4}) \times 10^{-13} \exp\{(-1180 \pm 250)/T\} \text{ cm}^3 \text{ molecule}^{-1} \text{ s}^{-1}$$

Measured 298 K rate constants are summarized in Table IV together with the Arrhenius expressions for reactions 1 and 2. The mechanistic implications of these results are discussed below.

Experiments in the Presence of Oxygen. Although determination of the effective rate constant for reaction 1 in air was a central objective of the present work, initial experiments gave indications of severe complications from secondary chemistry when oxygen was present in the reaction mixture. This took the form of nonexponential decays with the apparent regeneration of OH radicals. A set of typical OH temporal profiles, with [CH₃CN] constant and varying amounts of O₂ present, is shown in Figure 6. To ensure that the deviations from exponential behavior were due to OH regeneration and not to the detection of a second species, the dye laser was pressure scanned off the OH line and the signal monitored. Table V shows the results of such an experiment for curve b of Figure 6 obtained by scanning ≈ 0.1 nm off line at a delay of 1.5 ms; the reported voltages are the means ± 1σ of five 100 shot averages. This and a number of similar experiments clearly demonstrated that OH regeneration was occurring and suggested that a product of reaction 1 was reacting with O₂ to regenerate OH. Two possible routes to OH regeneration could involve the reaction of O₂ with the methylcyano radical, CH₃CN, or its decomposition products, or with an OH adduct or its decomposition products.

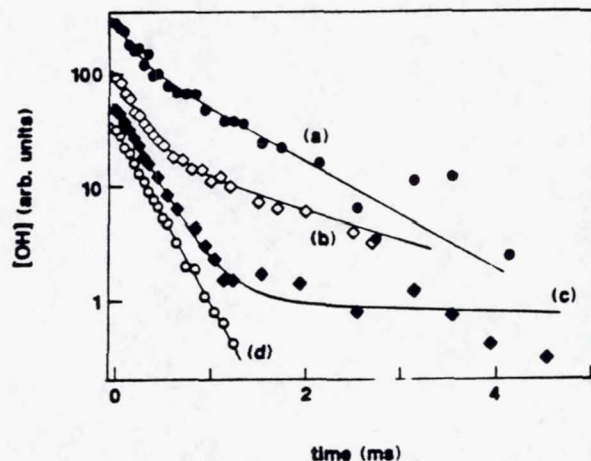
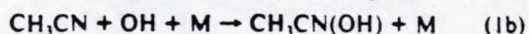
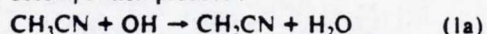


Figure 6. OH temporal profiles for reaction 1 in N₂ and N₂/O₂ mixtures. Experimental conditions: 298 K; 450 Torr total pressure, [CH₃CN] = 1.5 × 10¹⁷ molecules cm⁻³, [OH]₀ ≈ 5 × 10¹¹ molecules cm⁻³, buffer gas: (a) 50/50 N₂/O₂, (b) air, (c) 2% O₂ in N₂, (d) N₂. Solid lines are obtained from the simulations described in the text. The plots have been displaced vertically for clarity.

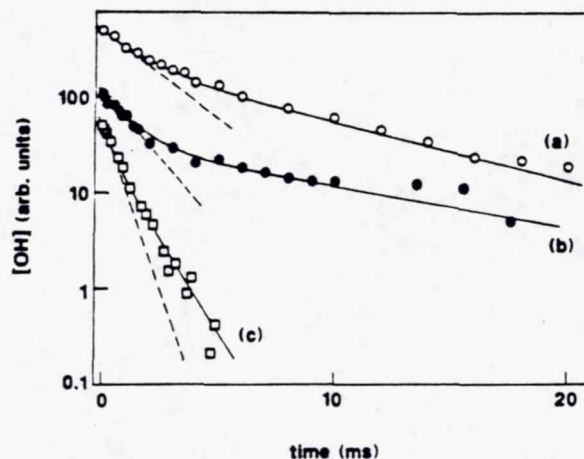


Figure 7. OH(D) temporal profiles in N₂/O₂ mixtures. (a) OD + CD₃CN, 298 K, 50 Torr total pressure, 50/50 N₂/O₂; (b) OH + CD₃CN, 256 K, 110 Torr total pressure, air; (c) OD + CH₃CN, 298 K, 270 Torr total pressure, 50/50 N₂/O₂. Solid lines are obtained from the simulations described in the text. Dashed lines represent behavior observed in N₂. The plots have been displaced vertically for clarity.

In order to attempt to distinguish between regeneration from the products of (1a) or (1b), we examined reaction 2 in the presence of O₂. Trace b in Figure 7 shows an OH temporal profile for reaction 2 in 100 Torr of air at 256 K together with the temporal profile which would be expected from the rate constant measured in N₂. Again the deviation from exponential behavior and the presence of OH regeneration is clear. Similar results were obtained in a number of experiments at 300 K. In this case the interpretation of the data is relatively unambiguous since any CD₃CN formed in reaction 2 cannot react with O₂ to regenerate OH. Either massive isotope exchange between CD₃CN and H₂O₂ must have taken place or OH regeneration must have occurred via a process which involves an OH adduct. The former explanation can be rejected on two counts. First, as noted above, IR spectra of mixtures of CD₃CN and H₂O₂ showed no indications of isotopic exchange taking place. Second, since the concentrations of CD₃CN and H₂O₂ were 7.1 and 0.003 × 10¹⁶ molecules cm⁻³, respectively, significant isotopic exchange would have affected only a small fraction of the CD₃CN while totally depleting the OH photolytic precursor. A very limited amount of data on reactions 3 and 4 in the presence of O₂ buffer gas was also obtained and is discussed below.

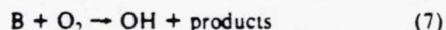
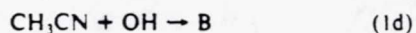
TABLE VI: Best-Fit Parameters in OH Regeneration Simulations^a

reaction	simulation parameters			measd rate in N ₂ k ₁ ^b	[CH ₃ CN], 10 ¹⁶ molecules cm ⁻³	[O ₂], Torr	press., Torr	T, K	no. of expts
	k _{1c} ^b	k _{1d} ^b	k ₆₊₇ ^c						
OH + CH ₃ CN (i = 1)	1.25	1.25	5 ± 4	2.5	4.9-11.2	120	600	298	3
	1.25	1.25	5 ± 4	2.5	15.0	0.9-225	450	298	3
	1.0	0.7	5 ± 4	2.5	4.0-10.7	40	200	298	2
	0.7	0.7	5	1.38	7.1	23	114	256	1
OH + CD ₃ CN (i = 2)	0.85	0.65	5 ± 4	1.5	1.4-7.3	28	140	298	3
	0.55	0.35	5	0.9	7.1	22	110	256	1
OD + CH ₃ CN (i = 3)	2.25	0.85	5	3.2	4.6	135	270	298	1
OD + CD ₃ CN (i = 4)	1.1	1.1	5	2.2	1.6	25	50	298	1

^a Best fits were obtained by visual comparison of experimental and simulated decay profiles. Errors were estimated from the scatter in the experimental data and simulation parameters. ^b Units are 10⁻¹⁴ cm³ molecule⁻¹ s⁻¹. ^c Units are 10⁻¹⁶ cm³ molecule⁻¹ s⁻¹.

Modeling the Regeneration Process. In order to examine the plausibility of the above mechanism we have modeled some of our O₂ data using a GEAR program²⁰ to numerically integrate the rate equations.

The simulations of reaction 1 in the presence of O₂ involved a simple four-reaction kinetic scheme which consisted of two reactive channels, (1c) and (1d), background losses, (6), and a regeneration step, (7), which involves the reaction of a product of (1d) with O₂ to produce OH.

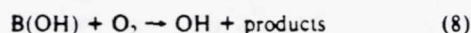
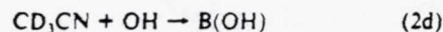


In this scheme, which clearly oversimplifies the actual reaction mechanism, A represents the unidentified products of all reactive channels which do not lead to OH regeneration, and k_{1c} represents the sum of the rates of those processes. Similarly reaction 1d, which may be a single or multistep process, produces an intermediate B, which reacts with O₂ to regenerate OH. While A and B may represent multiple products of (1c) and (1d), this scheme does not preclude A and B in fact being the same species. For instance, if the reaction proceeded solely by adduct formation followed by adduct reaction with O₂ then A and B would both represent the adduct. Those channels which led to OH regeneration would be represented by (1d), and those which did not would be represented by (1c).

Initially the sum k_{1c} + k_{1d} was taken as the value of k₁ obtained in N₂ buffer. k₆ was determined experimentally, and the branching ratio between (1c) and (1d) as well as the value of k₇ were varied to produce the best fit to the experimental data. The fitting process was qualitative with best fits being obtained by visual comparison of the simulated and experimental data. While the values of the branching ratio and k₇ couple to some extent, the fits are very sensitive to the upper limit of the branching ratio k_{1c}/k_{1d}. Figure 6 shows simulations obtained with k_{1c} + k_{1d} = 1.25 × 10⁻¹⁴ cm³ molecule⁻¹ s⁻¹ and k₇ = 5 × 10⁻¹⁶ cm³ molecule⁻¹ s⁻¹; these simulations are able to reproduce the observed OH decay profiles at a single [CH₃CN] as the O₂ partial pressure is varied from 0.9 to 225 Torr at 450 Torr total pressure. Table VI shows the values of the "best fit" parameters for nine experiments in which OH regeneration was observed including one experiment at 256 K. All of the experimental profiles, with the exception of two experiments in 200 Torr of air at 298 K, are reproduced well with k_{1c} = k_{1d} = k₁/2; for these two experiments the value of k_{1d} was reduced slightly to give the best fits. For all the experiments a value of k₇ = (5 ± 4) × 10⁻¹⁶ cm³ molecule⁻¹ s⁻¹ was able to reproduce the observed profiles. The success of this simple kinetic scheme indicates that our data is consistent with reaction 1 proceeding by either of two channels with approximately equal probability. One of these channels leads eventually to the regeneration of OH and the process involves a rate-determining step in which O₂ reacts with an unknown intermediate with a bimo-

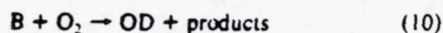
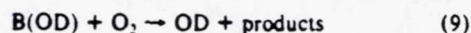
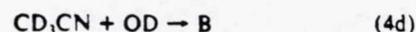
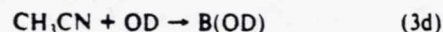
lecular rate coefficient of (5 ± 4) × 10⁻¹⁶ cm³ molecule⁻¹ s⁻¹.

As noted above, for reaction 1, either an abstraction or an addition channel could lead to OH regeneration. An abstraction channel could lead to OH regeneration if the methyl cyano radical, or one of its decomposition products, reacted with O₂. It is not possible, therefore, to identify the rate constants k_{1c} and k_{1d} with specific channels. For reaction 2 the situation is less ambiguous since any methylcyano-d₃ (or its decomposition products) produced cannot react with O₂ to regenerate OH. Any OD produced in such a reaction would not be observed by LIF when the laser was tuned to an OH transition. In this case observation of OH regeneration provides almost conclusive evidence for the presence of an addition channel. As was noted above, OH regeneration was observed for reaction 2 in the presence of O₂. Simulations were again performed using a kinetic scheme analogous to the one used for reaction 1.



Four experiments at 298 K in 140 Torr of air and one experiment at 256 K in 100 Torr of air were analyzed and the results are summarized in Table VI. The fit to the 256 K experiment with k_{2c} = 5.5 × 10⁻¹⁵ cm³ molecule⁻¹ s⁻¹, k_{2d} = 3.5 × 10⁻¹⁵ cm³ molecule⁻¹ s⁻¹, and k₈ = 5 × 10⁻¹⁶ cm³ molecule⁻¹ s⁻¹ is shown in Figure 7 together with the decay profile which would be expected in N₂. Again the data is consistent with the reaction proceeding via two channels one of which leads to OH regeneration, and again the rate-determining step in the regeneration process proceeds with a bimolecular rate coefficient of (5 ± 4) × 10⁻¹⁶ cm³ molecule⁻¹ s⁻¹.

OD regeneration was observed for reactions 3 and 4 in the presence of O₂. Two observed decay profiles along with simulated profiles and decays which would be expected based on rates measured in N₂ are shown in Figure 7; the rate constants used in the simulation are included in Table VI.



Reactions 9 and 10 are the analogous OD regeneration steps. Reaction 4 shows similar behavior to reactions 1 and 2; however, for reaction 3 the degree of OD regeneration is less pronounced although still evident when compared with the decay profile expected from the rate constant measured in N₂.

Overall, the above simulations indicate that the observed OH(D) regeneration profiles obtained under a variety of conditions can be simulated by using a simple four-step kinetic scheme. One channel leads to OH(D) regeneration and the initial step in the regeneration process appears to involve an addition step to produce

(20) McKinney, R. J.; Weigert, F. J. GEAR: Gear Algorithm Integration of Chemical Kinetics Equations; QCMP #022, Department of Chemistry, Indiana University, Bloomington, IN.

an OH(D)/acetonitrile adduct. The adduct, or one of its decomposition products, reacts with O₂ to regenerate OH(D) at a rate of $(5 \pm 4) \times 10^{-16} \text{ cm}^3 \text{ molecule}^{-1} \text{ s}^{-1}$. A second channel or channels lead to the formation of products other than OH. By themselves the simulations give no added information on this channel since, in terms of the generated OH profiles, all of the possible mechanisms are kinetically equivalent. The observed kinetic isotope effects and pressure dependencies, however, have considerable mechanistic implications for this channel and these are discussed below.

Reversible Adduct Formation. Since the observed pressure dependence of reaction 2 and the observation of OH regeneration in reaction 2 and OD regeneration in reaction 3 provide strong evidence for an addition channel, we investigated the possibility that reversible adduct formation was occurring. Such behavior might manifest itself in several ways. If the forward addition step is proceeding at a rate that is faster than the overall rate of reaction, but sufficiently slow that it is resolvable by the (≈ 100 ns) time resolution of this experiment, then nonexponential decays would be observed. An initial fast decay into equilibrium would be followed by a slower decay due to chemical reaction. In cases in which the adduct reacts with oxygen, the presence of oxygen results in an increase in the observed rate of reaction and a tendency toward exponential decay with increasing [O₂]. At the highest CH₃CN concentrations used, we saw no deviation from exponential behavior in N₂ buffer. In O₂, although we saw OH regeneration, the initial slopes of the decays were consistent with the reaction rate measured by N₂.

If reversible adduct formation took place on a very fast time scale (i.e., < 100 ns), then although we would be unable to temporally resolve the decay into equilibrium, we should be able to detect its presence by monitoring the OH fluorescence signal immediately after photolysis in the presence and absence of CH₃CN. Since decay due to reaction is negligible, any decrease in the OH signal must be due to the fact that some OH has been tied up in adduct formation. We performed such experiments for reactions 1 and 2 in 600–700 Torr of N₂ buffer. Under these conditions the only significant deactivation processes for OH A²Σ⁺ are fluorescence and collisional quenching by N₂ and CH₃CN; the rates of these processes have the following magnitudes for a mixture of 5 Torr of CH₃CN in 600 Torr of N₂.^{21,22}

$$k_Q(\text{N}_2) \approx 8 \times 10^8 \text{ s}^{-1}$$

$$k_Q(\text{CH}_3\text{CN}) \approx 5 \times 10^7 \text{ s}^{-1} \text{ (guesstimate)}$$

$$k_F \approx 1.5 \times 10^6 \text{ s}^{-1}$$

The quenching rate for CH₃CN does not appear to have been determined directly so the CH₃CN quenching rate was calculated assuming $k_Q = 3 \times 10^{-10} \text{ cm}^3 \text{ molecule}^{-1} \text{ s}^{-1}$ from comparison with known quenching rates.²² It can be seen that quenching by N₂ is the dominant deactivation process for OH A²Σ⁺ even assuming the very fast quenching rate for CH₃CN. Under these conditions the Stern–Volmer equation for fluorescence quenching

$$I_F/I_{F,0} = k_F/(k_F + k_Q[M]) \quad (\text{II})$$

reduces to

$$I_F(P_1)/I_F(P_2) = P_2/P_1 \quad (\text{III})$$

where $I_F(P_i)$ is the fluorescence intensity at pressure P_i .

In these experiments the OH signal was measured in the absence of CH₃CN and then a CH₃CN/N₂ mixture was added without adjusting the throttle valve. Hence the pressure increased, but the concentration of the OH precursor and the photolytically generated OH remained approximately the same. In the absence of any adduct formation we would therefore expect the OH signal to decrease in inverse proportion to the pressure increase. Table

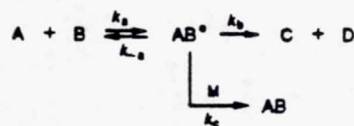
TABLE VII: Effects of CH₃CN Addition on the Pressure Dependence of OH Fluorescence Intensity

reaction	$P_{\text{N}_2/\text{CH}_3\text{CN}}/P_{\text{N}_2}$	$[\text{CH}_3\text{CN}]$, molecules cm ⁻³	$P_{\text{N}_2/\text{CH}_3\text{CN}}$, Torr	$I_{\text{F,N}_2}/I_{\text{F,N}_2/\text{CH}_3\text{CN}}$
OH + CH ₃ CN	1.15	1.56×10^{17}	720	1.16
OH + CD ₃ CN	1.08	1.25×10^{17}	680	1.07

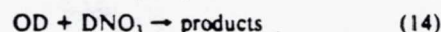
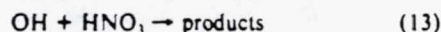
VII shows the OH signal and total pressure ratios for reactions 1 and 2 taken 300 ns after the photolysis pulse. The OH signal is seen to be inversely proportional to the total pressure, demonstrating the absence of any rapid reversible adduct formation.

Mechanistic Implications. While the consensus view of reaction 1 is that it proceeds via a direct abstraction mechanism,^{12,14,23} three aspects of our data are clearly inconsistent with such a mechanism being the dominant reaction pathway. First, if the reaction proceeded only via direct abstraction we would expect the observed isotope dependencies to be quite different. The rates of reactions 1 and 3 would be similar, as would the rates of reactions 2 and 4, with small differences being due to a secondary isotope effect. The primary isotope effect would result in reactions 2 and 4, which break C–D bonds, being slower than reactions 1 and 3, which break C–H bonds. In fact, the rates of (1) and (4) are similar with those of (2) and (3) showing deviations. Second, we would not expect to see a pressure dependence for any of the reactions. Third, we would expect to see identical kinetic behavior in N₂ and oxygen-containing buffer gases for reactions 2 and 4, since in these cases any secondary chemistry involving the methylcyano radical and O₂ could not regenerate the radical which is being monitored.

The observed behavior can be reconciled with a complex reaction mechanism which proceeds via the formation of an energized intermediate, i.e.



Such an energized intermediate could decompose to produce CH₃CN and H₂O, decompose back to reactants, or at sufficiently high pressures be collisionally stabilized. Hence the reaction proceeds at a finite rate at low pressure but shows an enhancement in the rate as the pressure is increased. Such mechanisms have been invoked²⁴ to explain observations on reactions such as OH + CO and OH + HNO₃, which display complex kinetic behavior such as negative temperature dependencies, pressure effects, and curved Arrhenius plots.



The pressure, temperature, and isotope dependencies of the elementary steps k_a , k_{-a} , k_b , and k_c interact to produce complex behavior in the observed rate constant. For instance, reaction 11 is pressure dependent in N₂ at room temperature, increasing from a low-pressure rate of $1.5 \times 10^{-13} \text{ cm}^3 \text{ molecule}^{-1} \text{ s}^{-1}$ to $2.3 \times 10^{-13} \text{ cm}^3 \text{ molecule}^{-1} \text{ s}^{-1}$ in 760 Torr of N₂;¹⁶ no significant rate enhancement is observed in He at pressures up to 1 atm.²⁵ The rate of reaction 12 increases from the low-pressure limit of $0.5 \times 10^{-13} \text{ cm}^3 \text{ molecule}^{-1} \text{ s}^{-1}$ to $1.7 \times 10^{-13} \text{ cm}^3 \text{ molecule}^{-1} \text{ s}^{-1}$ in 760 Torr of N₂ and a significant pressure effect is observed in He.²⁶ Larson, et al.²⁷ have performed two-channel RRKM calculations for reaction 11 and are able to reproduce the observed pressure and temperature dependencies. Brunning et al. have

(23) Atkinson, R. *J. Phys. Chem. Ref. Data Monograph* 1, 1989.

(24) Mozurkewich, M.; Benson, S. W. *J. Chem. Phys.* 1984, 88, 6429, 6435, and 6441.

(25) Paraskevopoulos, G.; Irwin, R. S. *J. Chem. Phys.* 1984, 80, 259.

(26) Paraskevopoulos, G.; Irwin, R. S. *Chem. Phys. Lett.* 1982, 93, 138.

(27) Larson, C. W.; Steward, P. H.; Golden, D. M. *Int. J. Chem. Kinet.* 1988, 20, 27.

(21) Burris, J.; Butler, J. J.; McGee, T. J.; Heaps, W. S. *Chem. Phys.* 1988, 124, 251.

(22) Copeland, R. A.; Dyer, M. J.; Crosley, D. R. *J. Phys. Chem.* 1985, 82, 4022.

directly measured the formation rates of the HOCO and DOCO complexes in reactions 11 and 12.²⁸ They have constructed a detailed model which is able to reproduce the observed pressure, temperature, and isotope effects. Among the points noted in their study was the importance of including angular momentum effects since the rate of dissociation of the HOCO complex to H + CO₂ decreases with increasing *J*. Calculations on reaction 13 predict that it should show a small pressure dependence, while the rate of reaction 14 is predicted to be faster and to show a much larger pressure dependence.²⁴ Recent careful experimental work indicates that *k*₁₃ is weakly pressure dependent.^{29,30} Reaction 14 also appears to show a pressure dependence at room temperature; interestingly, *k*₁₄ is found to be a factor of 14 slower than *k*₁₃,³¹ in contradiction to the theoretical prediction that *k*₁₄ > *k*₁₃.²⁴

There are interesting parallels in some aspects of the behavior of reactions 1-4 and 11-14. Perhaps the most important point is that the behavior of reactions which proceed via such complexes is very different from third-order reactions. Detailed models with accurate structures for the complex and the transition states leading to complex and product formation are required in order to understand observed pressure, temperature, and isotope dependencies. While our data set is too limited to draw any firm conclusions, the observed pressure and isotope effects are consistent with a complex mechanism. As we noted above, a direct abstraction channel should exhibit a significant isotope effect and no pressure dependence. In a study of the reaction of OH with dimethyl sulfide, (CH₃)₂S, we observed this type of behavior.¹⁵ An abstraction channel is observed which is pressure independent, shows a positive activation energy, and shows a significant isotope effect. A reversible addition channel becomes evident when oxygen is added to the system because the adduct reacts with oxygen rather than decomposing back to reactants; hence, the observed reaction rate increases. This increase shows no isotope dependence, implying that both the addition rate and the rate of the adduct reaction with oxygen show no isotope dependence. The similarities between the rates of reactions 1, 4, and 2 at high pressure would argue against the presence of a major direct abstraction channel. Clearly, the definitive establishment of such a mechanism requires much further work including studies of the rate at low pressure and over a much wider temperature range, and also product identification studies.

Our data provides a limited amount of information on the mechanism of OH regeneration. As we have noted above, the initial step must involve the formation of an adduct followed by reaction of the adduct, or one of its decomposition products, with O₂. While it is not possible to directly distinguish between these processes, it is possible to place a lower limit on the adduct decomposition rate which would be necessary if reaction of an adduct decomposition product with O₂ were the rate-determining step in OH regeneration. This rate will be pressure dependent. However, for the 298 K, 450 Torr data for reaction 1, simulations of the experimentally observed decay profiles indicate that the adduct decomposition rate would have to be greater than 10⁴ s⁻¹ for reaction of an adduct decomposition product with O₂ to be the rate-determining step. Considering the likely strength of chemical bonds in the adduct, it seems unlikely that it would decompose to products other than OH + CH₃CN on such a fast time scale. Hence direct reaction of the adduct with O₂ is probably the rate-determining step in regeneration.

One possible reaction path (written for reaction 2) which is energetically feasible and results in OH regeneration via an adduct + O₂ reaction is



$$\Delta H \sim -62 - \Delta H_{\text{add}} \text{ kcal mol}^{-1}$$

(28) Brunning, J.; Derbyshire, D. W.; Smith, I. W. M.; Williams, M. D. *J. Chem. Soc., Faraday Trans. 2* 1988, **84**, 105.

(29) Margitan, J. J.; Watson, R. T. *J. Phys. Chem.* 1982, **86**, 3819.

(30) Stachnik, R. A.; Molina, L. T.; Molina, L. J. *J. Phys. Chem.* 1986, **90**, 2777.

(31) Bossard, A. R.; Paraskevopoulos, G.; Singleton, D. L. *Chem. Phys. Lett.* 1987, **134**, 583.

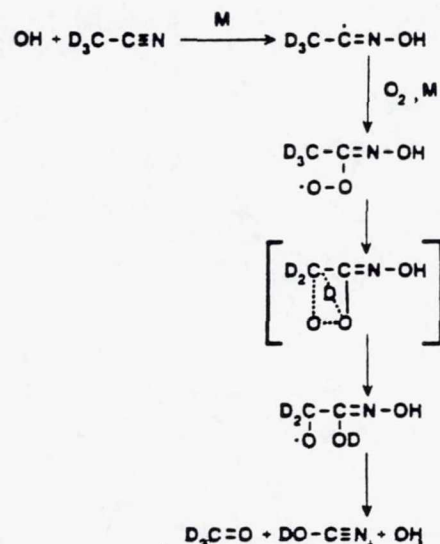


Figure 8. Plausible set of elementary steps for the reaction of OH + CD₃CN + O₂ → D₂CO + DOCN + OH. Adduct decomposition to products is shown as a single step; in reality, it probably occurs via two sequential steps with either D₂CO or OH coming off before the other.

TABLE VIII: Summary of Reported Rate Constants for Reaction 1

A ^a	E/R, K	k(298 K) ^b	technique ^c	ref
0.586	755	4.94 ± 0.6	FP-RF	9
		2.4 ± 0.3	FP-RF	10
		1.9 ± 0.2	FP-RF	11
0.628	1031	1.94 ± 0.37	FP-RF	12
		2.1 ± 0.3	DF-EPR	14
<i>d</i>	<i>d</i>	2.63 ± 0.5	FP-RF	13
1.1	1104	2.58 ± 0.38	PLP-PLIF	this work

^aUnits are 10⁻¹² cm³ molecule⁻¹ s⁻¹. ^bUnits are 10⁻¹⁴ cm³ molecule⁻¹ s⁻¹. ^cFP, flash photolysis; RF, resonance fluorescence; DF, discharge flow; EPR, electron paramagnetic resonance; PLP, pulsed laser photolysis; PLIF, pulse laser induced fluorescence. ^dTemperature dependence given by $k(T) = \exp((7.8 \pm 0.9)T/1000) - (33.7 \pm 0.4)$.

where Δ*H*_{add} is the enthalpy change for the OH + CD₃CN addition reaction. A plausible set of elementary steps via which reaction 15 could proceed is shown in Figure 8. The mechanism assumes that OH adds to the nitrogen atom in acetonitrile, thus creating a carbon-centered radical. Interestingly, attempts to construct a plausible mechanism for reaction 15 based on initial addition of OH to the cyano carbon atom were unsuccessful because the regenerated hydroxyl radical was deuterated.

One set of experiments which we have not carried out is determination of both the OH and OD yields for reactions 2 and 3 in the presence of O₂. Such experiments would be of interest for further constraining the reaction mechanism. If hydrogen-deuterium exchange within the adduct is efficient, or if OH addition to the nitrogen atom and to the cyano carbon atom occur at similar rates, then production of both OH and OD would be expected.

Comparison with Previous Work. Four studies of reaction 1 have been published^{9,10,12,14} and the results of two other studies^{11,13} are available and have been included in recent evaluations.^{23,32} There have been no previous reported studies of reactions 2-4. Table VIII summarizes the available data. Our results are in good agreement with the study of Kurylo and Knable¹² and with all room temperature results with the exception of the data of Harris et al.⁹ As has been noted previously,^{12,23} it appears that the data of Harris et al. were erroneously high due to the presence of impurities or secondary chemistry. Rhasa and Zellner¹³ have

(32) DeMore, W. B.; Molina, M. J.; Sander, S. P.; Golden, D. M.; Hampson, R. F.; Kurylo, M. J.; Howard, C. J.; Ravishankara, A. R. "Chemical Kinetics and Photochemical Data for Use in Stratospheric Modeling"; JPL publication 87-41, 1987.

reported non-Arrhenius behavior over the range 296–520 K and expressed their data in terms of a two-parameter fit. However, over most of the temperature range of their study, Rhasa and Zellner's results agree, within the combined uncertainties, with this work and that of Kurylo and Knable.¹² Poulet et al.¹⁴ measured k_1 at room temperature and at 393 K using the discharge-flow technique in 1 Torr of He; their room temperature results are in good agreement with the flash photolysis results, excluding those of Harris et al.⁹ However, their 393 K result is in good agreement with that of Harris et al. Poulet et al.'s data, if fit to a simple Arrhenius expression, would result in an activation energy that is considerably higher than was measured in other studies.

Of the studies of reaction 1 at room temperature only Zetzsch¹¹ has observed a significant pressure effect. In Ar buffer he observed a decrease from 2×10^{-14} to 0.8×10^{-14} cm³ molecule⁻¹ s⁻¹ over the pressure range 100–5 Torr. Rhasa and Zellner saw a small decrease in k_1 at 10 Torr in He¹³ and Kurylo and Knable saw no pressure dependence over the range 20–50 Torr in Ar and SF₆ buffers.¹² Finally, as noted above, Poulet et al.¹⁴ measured a room temperature value of k_1 in agreement with the average of the lower room temperature flash photolysis results and concluded that there is no pressure dependence. In a recent evaluation of reaction 1, Atkinson²³ also concludes that the reaction proceeds mainly via abstraction, citing the lack of a pressure dependence and the fact that the OH + R-CN rate constant increases by a factor of 4–10 in going from acetonitrile to propionitrile.

Our results appear to be incompatible with reaction 1 proceeding primarily by simple abstraction, and our analysis of the OH regeneration data is consistent with the pressure-dependent channel accounting for 50% of the branching ratio, in good agreement with the results of Zetzsch. The majority of the other available data would appear to contradict this view. However, a number of possible problems can be identified in the other studies. The 1 Torr discharge-flow study of Poulet et al.¹⁴ while in apparent agreement with the room temperature high-pressure limits obtained in the flash photolysis studies (excluding that of Harris et al.) is a factor of 1.8 greater at 393 K. Atkinson²³ cites the increase in the rate of reaction in going from acetonitrile to propionitrile as evidence of the reaction proceeding by abstraction, since such an enhancement might be expected due to the presence of more weakly bound secondary hydrogens. However, this rate increase is based on the study of Harris et al.⁹ and, since their measurement of k_1 appears to be too high, it seems questionable to rely on other data from the same study for mechanistic interpretation without an independent verification. The failure of both Kurylo and Knable and Rhasa and Zellner to observe a pressure dependence is rather more difficult to explain. Rhasa and Zellner were attempting to reproduce the results of Zetzsch and rationalize their failure to observe a pressure effect as being possibly due to impurities. This would require an impurity reaction which shows an inverse pressure dependence which exactly cancels the pressure dependence of reaction 1—an unlikely possibility.

Implications for Atmospheric Chemistry. The agreement between this work and that of Kurylo and Knable over an extended temperature range greatly decreases the uncertainty in k_1 over

the temperature and pressure range appropriate for most of the troposphere. Additionally, our results in N₂ and N₂/O₂ buffer gases indicate that while the mechanism of reaction 1 is the subject of considerable uncertainty, its effective rate under lower atmospheric conditions is well established. However, the unresolved question of the pressure dependence and reaction mechanism has important implications for modeling the upper troposphere and stratosphere. If reaction 1 proceeds via a pressure-dependent, complex mechanism, then a simple Arrhenius expression may not be appropriate for extrapolation to lower stratospheric temperatures. The most recent modeling calculations of CH₃CN profiles² considered the effects of both the Harris et al. and Kurylo and Knable Arrhenius expressions for the rate of reaction 1. The Kurylo and Knable expression gives the best fit to the observed profiles above 20 km but predicts rather lower ground level mixing ratios than reported observations.³³ The model also predicts that the only significant loss mechanism for CH₃CN below 40 km is reaction 1. Since a large body of data on CH₃CN concentration profiles above 20 km exists, the establishment of accurate ground level mixing ratios should place significant constraints on model calculations; it also potentially offers an alternate approach for calculation of OH profiles.

Summary

We have employed the PLP-PLIF technique to study the kinetics of reaction 1 over the temperature range 256–379 K and pressure range 50–700 Torr in N₂, N₂/O₂, Ar, and He buffer gases. Our results, which are in good agreement with a previous flash photolysis-resonance fluorescence study in 50 Torr of Ar,¹² greatly decrease the uncertainty in the rate of reaction 1 for use in atmospheric modeling calculations. Our studies of the isotopic variants of reaction 1 together with the observation of complex kinetics in the presence of O₂, indicate that the reaction cannot proceed only via a direct hydrogen abstraction mechanism. Our results are consistent with reaction proceeding via the formation of a complex intermediate which can dissociate to reactants or products, or be collisionally stabilized. The thermalized adduct does not appear to redissociate to OH; however, it, or one of its dissociation products, reacts with O₂ to regenerate OH with a rate constant of $(5 \pm 4) \times 10^{-16}$ cm³ molecule⁻¹ s⁻¹. The unresolved question of the pressure dependence of reaction 1 at low temperature could be important for constraining models of stratospheric CH₃CN profiles and also for using these measured profiles to determine OH profiles.

Acknowledgment. This work was supported by the National Science Foundation through grant no. ATM-88-02386 and the National Aeronautics and Space Administration through grant no. NAGW-1001. We thank Dr. C. Zetzsch, Dr. R. Zellner, and Dr. D. Rhasa for communicating their results to us prior to publication.

Registry No. OH^{*}, 3352-57-6; H₃CCN, 75-05-8; O₂, 7782-44-7; D, 7782-39-0.

(33) Snider, J. R.; Dawson, G. A. *Geophys. Res. Lett.* **1984**, *11*, 241.

NDB
K-10-1 512-25
026130
6P.
073551

A competitive kinetics study of the reaction of Cl with CS₂ in air at 298 K

Timothy J. Wallington, Jean M. Andino, Alan R. Potts
Research Staff, Ford Motor Company, Dearborn, P.O. Box 2053, MI 48121-2053, USA

and

Paul H. Wine
Physical Sciences Laboratory, Georgia Tech Research Institute, Georgia Institute of Technology, Atlanta, GA 30332, USA

Received 6 September 1990; in final form 4 October 1990

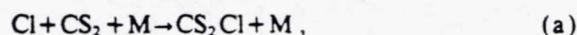
The relative rate technique has been used to investigate the kinetics of the reaction of Cl atoms with carbon disulfide, CS₂, at 700 Torr total pressure of air at 298 K. The decay rate of CS₂ was measured relative to CH₄, CH₃Cl and CHF₂Cl. For experiments using CH₄ and CH₃Cl references, the decay rate of CS₂ was dependent on the ratio of the concentration of the reference to that of CS₂. We ascribe this behavior to the generation of OH radicals in the system leading to complicated secondary chemistry. From experiments using CHF₂Cl we are able to assign an upper limit of 4×10^{-15} cm³ molecule⁻¹ s⁻¹ for the overall reaction, Cl + CS₂ → products.

1. Introduction

The gas-phase reaction of Cl atoms with organic species represents an important loss process for Cl atoms and organic compounds in the upper atmosphere [1,2]. Additionally, Cl atom attack provides a useful laboratory method for studying the kinetics and mechanisms by which organics are oxidized (see for example refs. [3,4]). Despite the importance of such reactions, there are significant uncertainties and inconsistencies in the kinetic data base for Cl atom reactions.

Carbon disulfide, CS₂, is an important biogenic sulfur compound which has been identified as a trace component of the atmosphere [5]. The reaction of Cl atoms with CS₂ has been the subject of two recent studies. In the first study of this reaction, Martin et al. [6] used a relative rate technique at 150–760 Torr total pressure of N₂/O₂ mixtures at 293 K. In their study, Martin et al. [6] monitored the decay of CS₂ relative to CH₄ and CH₃Cl in the presence of Cl atoms, and observed that the kinetics of this reaction varied as a function of both pressure and molecular

oxygen concentration. These observations were interpreted in terms of a three-step mechanism with Cl atoms adding to CS₂ to form a weakly bound adduct which either dissociates to reform the reactants, or reacts with O₂ to form products



In 760 Torr of synthetic air, Martin et al. [6] report an effective rate constant for the reaction of Cl with CS₂,



$$k_1 = 8 \times 10^{-14} \text{ cm}^3 \text{ molecule}^{-1} \text{ s}^{-1}.$$

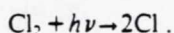
In the second study of the Cl + CS₂ reaction, Nicovich et al. [7] employed an absolute technique (pulsed laser photolysis time-resolved fluorescence) to study the kinetics of Cl atom loss in the presence of CS₂. Experiments were performed over the temperature range 193–293 K and pressures up to 300 Torr of air. Nicovich et al. [7] confirmed that the

reaction of Cl with CS₂ proceeds via reversible adduct formation as proposed by Martin et al. [6]. Although no evidence for the occurrence of reaction (c) was observed by Nicovich et al. [7], their data do not preclude the occurrence of reaction (1) with an overall rate, $k_1 = 8 \times 10^{-14} \text{ cm}^3 \text{ molecule}^{-1} \text{ s}^{-1}$ in 760 Torr of air at 298 K (as reported by Martin et al. [6]), provided that the CS₂Cl + O₂ reaction occurs via a channel which regenerates chlorine atoms.

To further our understanding of the kinetics and mechanism of reaction (1) in particular, and of chlorine atmospheric chemistry in general, we have reinvestigated the kinetics of the reaction of Cl atoms with CS₂. Experiments were conducted using the relative rate technique at 700 Torr total pressure of synthetic air and $295 \pm 2 \text{ K}$.

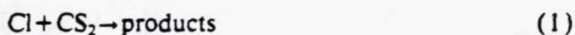
2. Experimental

The apparatus and experimental techniques employed in this work have been described previously [8,9], and are only briefly discussed here. The apparatus consists of a Mattson Instruments Inc. Sirius 100 FT-IR spectrometer interfaced to a 140 l, 2 m long evacuable pyrex chamber ($S/V = 0.14 \text{ cm}^{-1}$). The pyrex chamber was surrounded by 22 UV fluorescent lamps which were used to generate chlorine atoms by the photolysis of molecular chlorine.

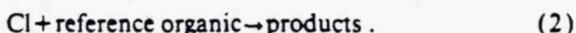


White type multiple reflection optics were mounted in the reaction chamber; the path length used in the present study was 26.6 m. The spectrometer was operated at a resolution of 0.25 cm^{-1} . Infrared spectra were derived from 16 co-added interferograms.

Reaction mixtures consisting of CS₂, a reference organic (CH₄, CH₃Cl, or CHF₂Cl) and chlorine, diluted in synthetic air, were admitted to the reaction chamber. In the presence of atomic chlorine, CS₂ and the reference organic decay via



and



Providing that the CS₂ and reference organic are lost solely by reactions (1) and (2), and that neither is

reformed in any process, it can be shown that

$$\ln \frac{[\text{CS}_2]_{t_0}}{[\text{CS}_2]_t} = \frac{k_1}{k_2} \ln \frac{[\text{reference}]_{t_0}}{[\text{reference}]_t}, \quad (1)$$

where $[\text{CS}_2]_{t_0}$ and $[\text{reference}]_{t_0}$, and $[\text{CS}_2]_t$ and $[\text{reference}]_t$ are the concentrations of CS₂ and reference organic at times t_0 and t , respectively, and k_1 and k_2 are the rate constants of reactions (1) and (2), respectively.

To test for loss processes in addition to reactions (1) and (2), mixtures of chlorine with both organics were prepared and allowed to stand in the dark. In all cases, the reaction of the organic species with chlorine, in the absence of ultraviolet light, was of negligible importance over the time periods used in this work. Additionally, to test for the possible photolysis of the organics used in the present work, mixtures of the reactants in synthetic air in the absence of molecular chlorine were irradiated using the output of all the blacklamps surrounding the chamber for 10 min. No photolysis (< 2%) of any of the reactants was observed. This observation is consistent with the fact that CH₄, CH₃Cl and CHF₂Cl do not absorb in the spectral region where the blacklamp emission is most intense (350–390 nm) and CS₂ absorption in this region is weak [10,11].

The decay of the CS₂ and reference organics were measured using their characteristic absorptions in the infrared over the following wavelength ranges (in cm^{-1}): CS₂, 1500–1575; CH₄, 1225–1400 and 2900–3100; CH₃Cl, 1300–1400; CHF₂Cl, 1000–1200. Initial concentrations of the gas mixtures were: CS₂, 1.5–4.4 mTorr; CH₄, 6.7–28 mTorr; CH₃Cl, 14–66 mTorr; CHF₂Cl, 3.4–4.4 mTorr; Cl₂, 70–110 mTorr. All reagents were purchased from commercial vendors at purities of > 99% and used without further purification. Experiments were performed at room temperature, $298 \pm 2 \text{ K}$, and 700 Torr total pressure of synthetic air.

3. Results

Figs. 1 and 2 show plots of $\ln([\text{CS}_2]_{t_0}/[\text{CS}_2]_t)$ versus $\ln([\text{reference}]_{t_0}/[\text{reference}]_t)$ for the references CH₄ and CH₃Cl, respectively. As seen from figs. 1 and 2, we observe nonlinear decay plots for experiments using either CH₄ or CH₃Cl as references

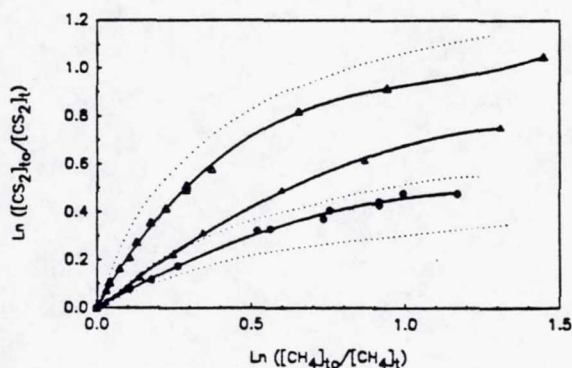


Fig. 1. Plot of $\ln([CS_2]_0/[CS_2]_t)$ versus $\ln([CH_4]_0/[CH_4]_t)$ for initial concentration ratios $[CH_4]/[CS_2]$: 1.7, (●); 3.5, (▲); 19, (Δ). Solid lines represent second- or third-order fit to the data to aid in visual inspection of the data trend. Dotted lines represent predicted behavior using chemical mechanism given in table 1, corresponding to each data set.

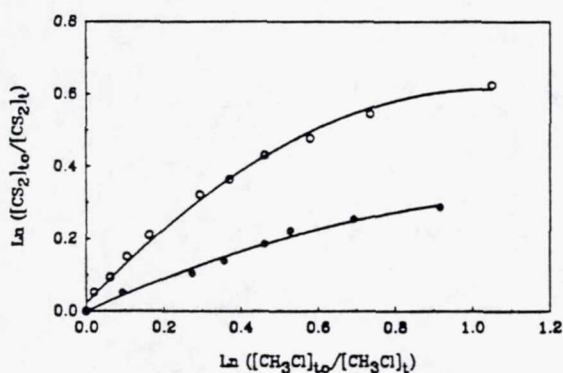


Fig. 2. Plot of $\ln([CS_2]_0/[CS_2]_t)$ versus $\ln([CH_3Cl]_0/[CH_3Cl]_t)$ for initial concentration ratios $[CH_3Cl]/[CS_2]$ = 24, (○) and 5.0, (●). Solid lines represent a second-order fit to the data to aid in visual inspection of the data trend.

with the initial values of the slope k_1/k_2 being dependent upon the initial concentration ratio [reference]/ $[CS_2]$, where [reference] = $[CH_4]$ or $[CH_3Cl]$.

The curvature shown in figs. 1 and 2 indicates that the assumptions implicit in the derivation of eq. (1) are not valid, i.e. either there are processes which reform the reactants in our chamber, or there are loss processes for the reactants in addition to reaction with Cl atoms, or both. With the exception of decomposition of the CS_2Cl adduct, there are no processes that could regenerate either CS_2 , CH_4 or CH_3Cl

in our system. Under our experimental conditions, the lifetime of the CS_2Cl adduct is less than 1 μs [7] compared to the typical time scale of 10–100 s for our experiments. Thus, decomposition of the CS_2Cl adduct will not affect our kinetic plots. It seems likely that the origin of the curvature observed in figs. 1 and 2 lies in the existence of significant loss processes for the reactants other than reaction with Cl atoms. It is our hypothesis that these loss processes involve reactions with OH radicals.

The reaction of Cl atoms with methane in air yields methyl peroxy radicals, CH_3O_2 , which in turn are known to undergo self reaction to produce a variety of products (CH_3O , $HCHO$ and CH_3OH). Methoxy radicals, CH_3O , formed from the self-reaction of CH_3O_2 , react with O_2 to produce HO_2 radicals which in turn are known to react rapidly with CH_3O_2 radicals to yield methyl hydroperoxide [12]. It has recently been demonstrated that Cl atoms react rapidly with methyl hydroperoxide with a rate constant of $k = 5.7 \times 10^{-11} \text{ cm}^3 \text{ molecule}^{-1} \text{ s}^{-1}$ [13]. This rate constant is some 570 times greater than that of reaction of Cl atoms with CH_4 . Hence, methyl hydroperoxide formed in our chamber will rapidly be consumed by Cl atoms. By analogy to the reaction of OH radicals with CH_3OOH , the reaction of Cl atoms with CH_3OOH is expected to lead to the generation of OH radicals [14,15]. Hydroxyl radicals may also be produced by the reaction of Cl atoms with HO_2 radicals [16].

Hydroxyl radicals, if generated in a mixture of CH_4 and CS_2 will preferentially react with the CS_2 as the rate constant for the reaction of OH with CS_2 is 180 times larger than that with CH_4 . As CS_2 and CH_4 are consumed a number of products, such as $HCHO$, SO_2 , and HCl , build up and compete with CS_2 for the available OH radicals. The result of hydroxyl radical formation in our chamber will be a fast initial CS_2 decay rate followed by a slow CS_2 loss rate at high conversions, consistent with the nonlinear decay plots observed.

To test the above hypothesis, we have modelled the chemistry occurring in the chamber following irradiation of $CH_4/CS_2/Cl_2/air$ mixtures using the Acuchem [17] kinetic modelling program and the chemical mechanism given in table 1.

The results of the modelling calculations are shown by the dotted lines in fig. 1. It should be noted that

Table 1
Reaction mechanism

Reaction	Rate constant ^{a)}	Ref.
Cl+CH ₄ →CH ₃ +HCl	1.0 × 10 ⁻¹³	[16]
CH ₃ +O ₂ +M→CH ₃ O ₂ +M	1.1 × 10 ⁻¹²	[16]
CH ₃ O ₂ +CH ₃ O ₂ →CH ₃ O+CH ₃ O+O ₂	1.3 × 10 ⁻¹³	[18]
CH ₃ O ₂ +CH ₃ O ₂ →HCHO +CH ₃ OH+O ₂	2.1 × 10 ⁻¹³	[18]
CH ₃ O+O ₂ →HCHO+HO ₂	1.9 × 10 ⁻¹⁵	[18]
CH ₃ O ₂ +HO ₂ →CH ₃ OOH+O ₂	4.5 × 10 ⁻¹²	[12]
Cl+HCHO→HCO+HCl	7.3 × 10 ⁻¹¹	[16]
HCO+O ₂ →HO ₂ +CO	5.5 × 10 ⁻¹²	[16]
Cl+CH ₃ OH→CH ₂ OH+HCl	4.5 × 10 ⁻¹¹	[19]
CH ₂ OH+O ₂ →HCHO+HO ₂	9.6 × 10 ⁻¹²	[16]
HO ₂ +HO ₂ →H ₂ O ₂ +O ₂	3.0 × 10 ⁻¹²	[16]
Cl+H ₂ O ₂ →HO ₂ +HCl	4.1 × 10 ⁻¹³	[16]
CH ₃ OOH+Cl→CH ₃ O ₂ +HCl	2.85 × 10 ⁻¹¹	[13] ^{b)}
CH ₃ OOH+Cl→CH ₂ OOH+HCl	2.85 × 10 ⁻¹¹	[13] ^{b)}
CH ₃ OOH→HCHO+OH	1 × 10 ⁶	c)
OH+CS ₂ →COS+SO ₂	1.5 × 10 ⁻¹²	[20]
OH+SO ₂ →products	8.6 × 10 ⁻¹³	[16]
OH+CO→HO ₂ +CO ₂	2.3 × 10 ⁻¹³	[16]
OH+HCHO→H ₂ O+HCO	9.8 × 10 ⁻¹²	[21]
OH+CH ₄ →CH ₃ +H ₂ O	8.4 × 10 ⁻¹⁵	[21]
OH+CH ₃ OOH→CH ₃ O ₂ +H ₂ O	3.7 × 10 ⁻¹²	[15]
OH+CH ₃ OOH→CH ₂ OOH+H ₂ O	1.8 × 10 ⁻¹²	[15]
OH+HO ₂ →H ₂ O+O ₂	1.0 × 10 ⁻¹⁰	[16]
OH+HCl→H ₂ O+Cl	8.0 × 10 ⁻¹³	[16]
OH+H ₂ O ₂ →H ₂ O+HO ₂	1.7 × 10 ⁻¹²	[16]
Cl+HO ₂ →HCl+O ₂	3.2 × 10 ⁻¹¹	[16]
Cl+HO ₂ →OH+ClO	9.1 × 10 ⁻¹²	[16]
OH+ClO→HO ₂ +Cl	1.7 × 10 ⁻¹¹	[16]
ClO+HO ₂ →HOCl+O ₂	5.0 × 10 ⁻¹²	[16]

^{a)} Units in cm³ molecule⁻¹ s⁻¹.

^{b)} Equal importance arbitrarily given to the two possible channels.

^{c)} Estimated. units in s⁻¹.

the chemical mechanism shown in table 1 does not include any reaction of Cl with CS₂. The sole loss process of CS₂ in this chemical model is via reaction with OH radicals which are produced from the reaction of Cl atoms with methyl hydroperoxide and/or HO₂ radicals as discussed above. There is no available data concerning the branching ratio of the reaction of Cl with CH₃OOH, and thus we have arbitrarily assigned equal importance to the two possible channels. The kinetic data given in table 1 has been taken from the literature. No attempt has been made to fit the experimental data points by adjustment of any of the kinetic parameters. Instead, we have simply used our starting conditions in the

model. From fig. 1, it can be seen that the model predictions are in qualitative agreement with our observations with large initial slopes which decrease with increasing consumption of the reactants. Quantitatively, the model predicts initial slopes, k_1/k_2 , which are within 20% of those observed. As seen from fig. 1, at reactant conversions greater than 50%, the model prediction deviates significantly from our observations. At such high conversions, the chemistry in the chamber is complicated by the presence of large amounts of products. The qualitative agreement between the model given in table 1 and our experimental observations shows that it is possible to explain a large fraction, if not all, of the observed CS₂ loss in the CS₂/CH₄/Cl₂/air experiments as caused by OH attack.

As seen from table 1, in addition to hydroxyl radicals, there are a number of other transient radical species formed following the irradiation of CS₂/CH₄/Cl₂/air mixtures. These species include CH₃, CH₃O₂, CH₃O, HO₂ and HCO. None of these radicals are expected to react significantly with either CH₄ or CS₂. Reaction with molecular oxygen (present at a concentration of 140 Torr) is the exclusive fate of CH₃, CH₃O and HCO. Neither CH₃O₂ nor HO₂ radicals react with methane. No evidence for the reaction of HO₂ with CS₂ was observed in the recent study by Lovejoy et al. [22] enabling calculation of an upper limit of $k < 4 \times 10^{-16}$ cm³ molecule⁻¹ s⁻¹ for the rate constant of this reaction. Finally we are not aware of any literature data to suggest that there is any reaction between CH₃O₂ and CS₂.

The major source of OH radicals in our model was reaction of chlorine atoms with CH₃OOH. Reaction of chlorine with HO₂ was of minor importance accounting for less than 25% of the OH radical source.

We have not modelled the CH₃Cl/CS₂/Cl₂/air system as there is insufficient kinetic and mechanistic data available. However, in the light of the curved plots, and dependence of the initial rate on the CH₃Cl concentration shown in fig. 2, it seems likely that analogous effects are present in this system also.

Given the complexity of the CH₄/CS₂ and CH₃Cl/CS₂ systems, we decided to conduct relative rate experiments of the reaction of Cl atoms with CS₂ using a reference organic which possessed only one hydrogen atom thereby precluding generation of OH rad-

icals in the system. We chose to use freon-22 (CHF_2Cl) as the reference. Results are shown in fig. 3. Within our experimental uncertainties, there is no evidence for curvature of this data plot. Linear least squares analysis of the data given in fig. 3 yields a value of 1.05 ± 0.05 for the rate constant ratio $k(\text{Cl} + \text{CS}_2)/k(\text{Cl} + \text{CHF}_2\text{Cl})$. Additionally, we measured the reactivity of Cl atoms towards CHF_2Cl relative to CH_4 in 700 Torr of nitrogen diluent; these results are also displayed in fig. 3. From these latter experiments we are able to define an upper limit of $k(\text{Cl} + \text{CHF}_2\text{Cl})/k(\text{Cl} + \text{CH}_4) < 0.04$. Using the literature value of $k(\text{Cl} + \text{CH}_4) = 1.0 \times 10^{-13} \text{ cm}^3 \text{ molecule}^{-1} \text{ s}^{-1}$ [16], we are then able to calculate an upper limit to the rate constant of the overall reaction of Cl with CS_2 in 700 Torr of air at 295 K of $4 \times 10^{-15} \text{ cm}^3 \text{ molecule}^{-1} \text{ s}^{-1}$.

To further compare the present work with that of Martin et al., we conducted a study of the products of the Cl atom initiated oxidation of CS_2 . In our experiments, 3 mTorr of CS_2 together with 30 mTorr of Cl_2 were admitted into the chamber and diluted with N_2/O_2 mixtures to a total pressure of 700 Torr. The O_2 partial pressures used were 10, 150, and 700 Torr. Upon irradiation, CS_2 was observed to decay slowly. The observed products were, in order of importance, HCl, CO, CO_2 , SO_2 , and COS. Additionally, at the lowest oxygen concentration used, COCl_2 and SOCl_2 were detected as minor products. The major sulfur containing product observed was SO_2 with a yield (in terms of sulfur balance) of $50 \pm 20\%$

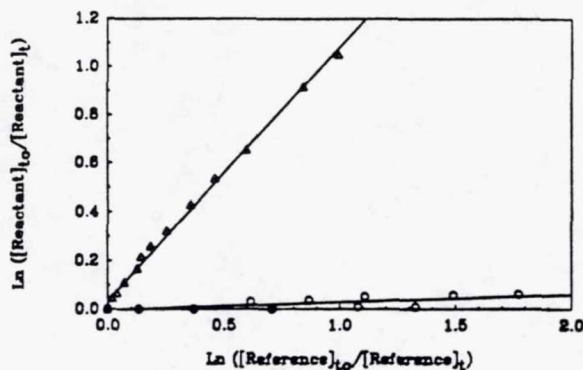


Fig. 3. Plot of $\ln([\text{reactant}]_t/[\text{reactant}]_0)$ versus $\ln([\text{reference}]_t/[\text{reference}]_0)$ for experiments using CS_2 as reactant and CHF_2Cl as reference (Δ) and CHF_2Cl as reactant and CH_4 as reference (\circ).

(somewhat lower than the 70–82% yield reported by Martin et al.). Within our experimental errors, we observed no dependence of the SO_2 yield on O_2 partial pressure. Consistent with the observation of Martin et al., we observed the COS yield to increase by a factor of 4 on increasing the O_2 partial pressure from 10 to 700 Torr.

In terms of understanding the mechanism by which CS_2 is oxidized following the irradiation of $\text{CS}_2/\text{Cl}_2/\text{O}_2$ mixtures, the most significant observation in our product study was that of large amounts of HCl, CO and CO_2 products. In the present work the HCl yield and the sum of the CO and CO_2 yields were larger than the observed loss of CS_2 by factors of 9–15 and 3–8, respectively. Martin et al. observed HCl as a product in their system but, in marked contrast to our observations, did not report any CO or CO_2 .

The HCl product in our experiments results from the reaction of Cl atoms with hydrogen containing compounds present either as impurities in the diluent gases used or on the walls of our reactor. In either case, a likely result of such reactions is the generation of OH radicals. Clearly, a detailed comparison between our product yields and those reported by Martin et al. is not justified at the present time.

4. Discussion

We have established an upper limit to the rate constant of the overall reaction of Cl with CS_2 in 700 Torr of air at 295 K of $k_1 < 4 \times 10^{-15} \text{ cm}^3 \text{ molecule}^{-1} \text{ s}^{-1}$, reaction (1).

This value is consistent with the upper limit of $k_1^* < 5 \times 10^{-15} \text{ cm}^3 \text{ molecule}^{-1} \text{ s}^{-1}$, reported by Nicovich et al. [7] for 300 Torr of air, where k_1^* is defined as the overall rate constant for reaction (1) via all channels for which the adduct reaction with O_2 does not regenerate chlorine atoms. In contrast, our value is at least 20 times lower than that reported by Martin et al. [6] who used a relative technique almost identical to our own. As discussed above, we observe nonlinear decay plots when using CH_4 or CH_3Cl as references. It is interesting to note that Martin et al. [6] did not also observe such nonlinear behavior. Instead, these workers report linear behavior. It is of interest to compare the initial slope, k_1/k_2 , from our data in fig. 1 using initial concen-

tration ratios, $[\text{CH}_4]/[\text{CS}_2]$, of 1.7 and 3.5, i.e. those which most closely match the ratio of approximately 2 used by Martin et al. Linear least squares analysis of our data corresponding to CH_4 loss of less than 30% yields a rate constant ratio of ≈ 0.8 which is indistinguishable, within the experimental errors, with the value of 0.9 reported by Martin et al.

Under the conditions of our experiments, the CS_2Cl concentration was very small compared to the concentrations of Cl atoms and CS_2 ; hence, the steady state approximation to the mechanism consisting of reactions (a), (b) and (c) leads to the expression

$$k_1 = k_a X[\text{O}_2]/(1 + X[\text{O}_2]), \quad (\text{II})$$

where

$$X = k_c/k_b. \quad (\text{III})$$

Nicovich et al. [7] have shown that at room temperature and atmospheric pressure, $k_a \approx 2 \times 10^{-11} \text{ cm}^3 \text{ molecule}^{-1} \text{ s}^{-1}$ and $k_b \approx 2 \times 10^6 \text{ s}^{-1}$. Substituting these values into eq. (II) along with the value $k_1 < 4 \times 10^{-15} \text{ cm}^3 \text{ molecule}^{-1} \text{ s}^{-1}$ determined in this study leads to the following upper limit for the adduct + O_2 rate constant: $k_c < 8 \times 10^{-17} \text{ cm}^3 \text{ molecule}^{-1} \text{ s}^{-1}$.

From the viewpoint of atmospheric chemistry, the present work provides an upper limit to the overall rate constant for the reaction of Cl with CS_2 measured under simulated atmospheric conditions. This upper limit is at least two orders of magnitude less than the corresponding rate constant for OH radical attack. As the atmospheric levels of Cl atoms are 1–2 orders of magnitude less than that of OH [23], reaction with Cl atoms represents a negligible sink for CS_2 in the earth's atmosphere.

Acknowledgement

One of the authors (PHW) acknowledges support from NSF grant ATM-88-02386 and NASA grant NAGW-1001.

References

- [1] W.L. Chameides and R.J. Cicerone, *J. Geophys. Res.* 83 (1978) 947.
- [2] D. Cronn and E. Robinson, *Geophys. Res. Letters* 6 (1979) 641.
- [3] R.A. Cox and G.S. Tyndall, *J. Chem. Soc. Faraday II* 76 (1980) 153.
- [4] H. Niki, P.D. Maker, C.M. Savage and L.P. Breitenbach, *J. Phys. Chem.* 85 (1981) 877.
- [5] V.P. Aneja and W.J. Cooper, in: *ACS Symp. Ser.* 393. *Biogenic sulfur in the environment*, eds. E.S. Saltzman and W.J. Cooper (Am. Chem. Soc., Washington, 1989).
- [6] D. Martin, I. Barnes and K.H. Becker, *Chem. Phys. Letters* 140 (1987) 195.
- [7] J.M. Nicovich, C.J. Shackelford and P.H. Wine, *J. Phys. Chem.* 94 (1990) 2896.
- [8] T.J. Wallington and S.M. Japar, *J. Atmos. Chem.* 10 (1989) 399.
- [9] T.J. Wallington, C.A. Gierczak, J.C. Ball and S.M. Japar, *Intern. J. Chem. Kinetics* 21 (1989) 1077.
- [10] P.H. Wine, W.L. Chameides and A.R. Ravishankara, *Geophys. Res. Letters* 5 (1981) 543.
- [11] B.M.R. Jones, R.A. Cox and S.A. Penkett, *J. Atmos. Chem.* 1 (1983) 65.
- [12] T.J. Wallington and S.M. Japar, *Chem. Phys. Letters* 167 (1990) 513.
- [13] T.J. Wallington, J.M. Andino, J.C. Ball and S.M. Japar, *J. Atmos. Chem.* 10 (1990) 301.
- [14] H. Niki, P.D. Maker, C.M. Savage and L.P. Breitenbach, *J. Phys. Chem.* 87 (1983) 2190.
- [15] G.L. Vaghjiani and A.R. Ravishankara, *J. Phys. Chem.* 93 (1983) 1948.
- [16] W.B. DeMore, M.J. Molina, S.P. Sander, R.F. Hampson, M.J. Kurylo, D.M. Golden, C.J. Howard and A.R. Ravishankara, *NASA-JPL Publication No.* 87-41 (1987).
- [17] W. Braun, J.T. Herron and D.K. Kahaner, *Intern. J. Chem. Kinetics* 20 (1988) 51.
- [18] R. Atkinson, D.L. Baulch, R.A. Cox, R.F. Hampson and J.A. Kerr, *J. Phys. Chem. Ref. Data* 18 (1989) 811.
- [19] T.J. Wallington, L.M. Skewes, W.O. Siegl, C.H. Wu and S.M. Japar, *Intern. J. Chem. Kinetics* 20 (1988) 867.
- [20] A.J. Hynes, P.H. Wine and J.M. Nicovich, *J. Phys. Chem.* 92 (1988) 3846.
- [21] R. Atkinson, *J. Phys. Chem. Ref. Data, Monograph* 1 (1989).
- [22] E.J. Lovejoy, T.P. Murrells, A.R. Ravishankara and C.J. Howard, *J. Phys. Chem.* 94 (1990) 2386.
- [23] H.B. Singh and J.F. Kasting, *J. Atmos. Chem.* 7 (1988) 261.

ND3

K-10.1

S13-25
026131
8P.

273552

Reprinted from *The Journal of Physical Chemistry*, 1990, 94.
Copyright © 1990 by the American Chemical Society and reprinted by permission of the copyright owner.

Kinetics of the Reactions of IO Radicals with NO and NO₂

E. P. Daykin and P. H. Wine*

*Molecular Sciences Branch, Georgia Tech Research Institute, Georgia Institute of Technology,
Atlanta, Georgia 30332 (Received: October 6, 1989; In Final Form: January 17, 1990)*

A laser flash photolysis-long path absorption technique has been employed to study the kinetics of the reactions of IO radicals with NO and NO₂ as a function of temperature and pressure. The IO + NO rate coefficient is independent of pressure over the range 40–200 Torr of N₂, and its temperature dependence over the range 242–359 K is adequately described by the Arrhenius expression $k_1 = (6.9 \pm 1.7) \times 10^{-12} \exp[(328 \pm 71)/T] \text{ cm}^3 \text{ molecule}^{-1} \text{ s}^{-1}$ (errors are 2 σ , precision only). These Arrhenius parameters are similar to those determined previously for the ClO + NO and BrO + NO reactions. The IO + NO₂ association reaction is found to be in the falloff regime over the temperature and pressure ranges investigated (254–354 K and 40–750 Torr of N₂). Assuming $F_c = 0.4$ independent of temperature, a physically reasonable set of falloff parameters which adequately describe the data are $k_0 = 7.7 \times 10^{-31} (T/300)^{-2.0} \text{ cm}^6 \text{ molecule}^{-2} \text{ s}^{-1}$ and $k_\infty = 1.55 \times 10^{-11} \text{ cm}^3 \text{ molecule}^{-1} \text{ s}^{-1}$ independent of temperature. The IO + NO₂ rate coefficients determined in this study are about a factor of 2 faster than those reported in the only previous study of this reaction.

Introduction

The potential role of iodine in tropospheric photochemistry has received considerable attention in recent years. It has been suggested that IO_x chemistry can result in catalytic destruction of tropospheric ozone as well as perturbation of the tropospheric cycles of H₂O₂, NO_x, and sulfur.^{1–3} Iodine can potentially play a more important role in tropospheric photochemistry than other halogens for two reasons. First, unlike a majority of fluorine, chlorine, and bromine atom precursors, most iodine atom precursors of atmospheric importance are photosensitive at wave-

lengths (>300 nm) which penetrate to the earth's surface. Second, reactions of hydrogen-containing species with iodine atoms to form the reservoir species HI are, in general, endothermic and do not occur at atmospheric temperatures. (The I + HO₂ reaction is

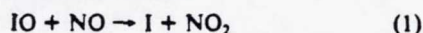
- (1) Chameides, W. L.; Davis, D. D. *J. Geophys. Res.* **1980**, *85*, 7383.
- (2) Jenkin, M. E.; Cox, R. A.; Candeland, D. E. *J. Atmos. Chem.* **1985**, *2*, 359.
- (3) Barnes, I.; Becker, K. H.; Martin, D.; Carlier, P.; Mouvier, G.; Jourdain, J. L.; Laverdet, G.; LeBras, G. In *Biogenic Sulfur in the Environment*; Saltzman, E. S., Cooper, W. J., Eds.; ACS Symposium Series 393; American Chemical Society: Washington, DC, 1989; pp 464–475, and references therein.

* Author to whom correspondence should be addressed.

a potentially important exception.)

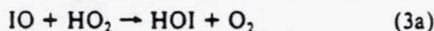
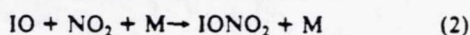
Volatilization of CH₃I from the oceans is thought to be an important source of tropospheric iodine.⁴⁻⁶ The reaction of O₃ with iodide in surface ocean waters may also result in volatilization of significant fluxes of I₂ and HOI into the atmosphere.^{7,8} In addition, radioactive iodine atoms, generated as a fission product of uranium fuels, represent a potentially harmful airborne emission from nuclear power installations.⁹

In the atmosphere, photodissociation of precursor molecules such as CH₃I, I₂, and HOI produces I atoms, which react with O₃ on a time scale of approximately 1 s¹⁰⁻¹² to produce the IO radical. Hence, IO is an important intermediate in tropospheric IO_x chemistry. Recycling of IO back to I atoms occurs primarily by photodissociation and the reaction



Data have been presented in the literature³ which suggest that the reaction of IO with CH₃SCH₃ (dimethyl sulfide) may be an important mechanism for recycling IO back to I in the marine boundary layer as well as an important sink for CH₃SCH₃. However, recent work in our laboratory suggests that the IO + CH₃SCH₃ reaction is much slower than previously thought.¹³

In addition to undergoing reactions that regenerate iodine atoms, IO radicals can react to form reservoir species:



Reaction 2 appears to be the more important of the reservoir-forming reactions except under conditions of extremely low NO_x.¹² Depending upon the (unknown) rates at which IONO₂ photodissociates and thermally dissociates, it is possible that IONO₂ is the predominant IO_x species in the atmosphere.

It is clear from the above discussion that accurate kinetic data for reactions 1 and 2 are required in order to successfully model tropospheric IO_x chemistry. Two studies of the kinetics of reaction 1 have appeared in the literature,^{14,15} both of which were restricted to T = 298 K; the reported values for k₁(298 K) differ by a factor of 1.7. The only reported study of the kinetics of reaction 2¹¹ covered a limited range of temperature and pressure and was carried out under conditions where a significant fraction of IO removal was due to heterogeneous reaction on the reactor walls and to the IO self-reaction. Hence, additional studies of the kinetics of reactions 1 and 2 are needed.

We have employed a laser flash photolysis-long path absorption technique to investigate the kinetics of reactions 1 and 2 as a function of temperature and pressure. Our results are reported in this paper.

Experimental Section

The kinetics of reactions 1 and 2 were investigated by monitoring the temporal profile of IO following 351-nm laser flash photolysis of I₂/NO₂/NO/N₂ mixtures. The laser flash photolysis-long path absorption apparatus was similar to one we employed recently to investigate the reactions of F and Cl atoms with

HNO₃.¹⁶ A schematic of the apparatus and descriptions of the reaction cell and temperature measurement techniques can be found elsewhere.¹⁶ The major apparatus modification required for the present study was replacement of the CW tunable dye laser used for NO₃ detection¹⁶ with a broad-band IO probe. An Osram XBO150W/S 150-W xenon arc lamp was employed as the probe light source. The lamp was housed in a PTI A100 housing and powered by a PTI LPS200X power supply.

The XeF laser (Lambda Physik EMG 200) photolysis beam was expanded by means of cylindrical lenses to be 12 cm wide and 2 cm high as it traversed the reactor. The xenon arc lamp beam was multipassed through the reactor at right angles to the photolysis beam by using modified White cell optics;¹⁷ 42-62 passes were employed, giving absorption path lengths in the range 500-750 cm. Output radiation from the multipass cell was focused onto the entrance slit of a 0.22-m monochromator (SPEX 1681) adjusted to transmit radiation at 427 nm, the peak of the strong, diffuse (due to excited-state predissociation) 4-0 band of the IO A²Π ← X²Π system.^{18,19} Reflective losses in the multipass system were minimized by using White cell mirrors coated for high reflectivity around 427 nm (Virgo Optics, HR-427-0) and reaction cell windows coated for maximum transmission around 427 nm (Virgo Optics, M-2-427-0). As a trade-off between light throughput and resolution, the monochromator slit widths were set at 200 μm (resolution 0.72 nm fwhm). Radiation exiting the monochromator was detected by a photomultiplier (Hamamatsu R928), the time-dependent output from which was monitored by a signal averager with 1.5-μs time resolution and 10-bit voltage resolution (Nicolet 370). The results of 32-512 laser shots were averaged to obtain data with suitable signal-to-noise ratio for quantitative kinetic analysis. Digitized voltage versus time data were transferred to a small computer (Beltron Turbo/XT) for storage and analysis.

In order to avoid accumulation of reaction or photolysis products, all experiments were carried out under "slow flow" conditions. The linear flow rate through the reaction cell was typically 2 cm s⁻¹, and the excimer laser repetition rate was 0.15 Hz. Hence, the gas mixture in the photolysis zone was replenished between laser shots. NO and NO₂ were flowed into the reaction cell from 12-L bulbs containing dilute mixtures in nitrogen (NO) or zero grade air (NO₂). Preparation of the NO₂ bulb with air as the diluent gas prevented conversion of NO₂ to NO during storage. An I₂/N₂ flow was generated by passing N₂ through a tube containing iodine crystals. To prevent condensation of IO_x species on the antireflection coated reaction cell windows, a four-port gas input/output system was employed.¹⁶ The NO mixture, NO₂ mixture, and 85-90% of the N₂ buffer gas entered the reactor through an outer port while the I₂/N₂ mixture entered through the corresponding inner port. The remaining 10-15% of the N₂ buffer gas entered the reactor through the opposite outer port. The concentrations of each component in the reaction mixture were determined from measurements of the appropriate mass flow rates and the total pressure. In addition, the concentrations of NO₂ and I₂ were measured in situ in the slow flow system by UV-vis photometry using separate absorption cells plumbed in series with the reaction cell. The three closely spaced mercury lines around 366 nm were employed for NO₂ detection. With the combination of an Hg pen-ray lamp light source and the band-pass filter employed to isolate the 366-nm lines, the effective NO₂ absorption cross section is known to be 5.75 × 10⁻¹⁹ cm².²⁰ Determination of the I₂ concentration was accomplished using 488-nm radiation from an argon ion laser as the light source and correcting the measured absorbance for the NO₂ contribution. Absorption cross sections for I₂ and NO₂ at 488 nm were taken

(4) Lovelock, J. E.; Maggs, R. J.; Wade, R. J. *Nature (London)* 1973, 241, 194.

(5) Zafriou, O. C. *J. Geophys. Res.* 1974, 79, 2730.

(6) Rasmussen, R. A.; Khalil, M. A. K.; Gunawardena, R.; Hoyt, S. D. *J. Geophys. Res.* 1982, 87, 3086.

(7) Garland, J. A.; Curtis, H. J. *J. Geophys. Res.* 1981, 86, 3186.

(8) Thompson, A. M.; Zafriou, O. C. *J. Geophys. Res.* 1983, 88, 6696.

(9) Chamberlain, A. C.; Eggleton, A. E. J.; Megaw, W. J.; Morris, J. B. *Discuss. Faraday Soc.* 1960, 30, 1.

(10) Clyne, M. A. A.; Cruse, H. W. *Trans. Faraday Soc.* 1970, 66, 2227.

(11) Jenkin, M. E.; Cox, R. A. *J. Phys. Chem.* 1985, 89, 192.

(12) Sander, S. P. *J. Phys. Chem.* 1986, 90, 2194.

(13) Daykin, E. P.; Wine, P. H. Presented at the Second International Conference on Chemical Kinetics, Gaithersburg, MD, 1989; manuscript in preparation.

(14) Ray, G. W.; Watson, R. T. *J. Phys. Chem.* 1981, 85, 2955.

(15) Inoue, G.; Suzuki, M.; Washida, N. *J. Chem. Phys.* 1983, 79, 4730.

(16) Wine, P. H.; Wells, J. R.; Nicovich, J. M. *J. Phys. Chem.* 1988, 92, 2223.

(17) White, J. U. *J. Opt. Soc. Am.* 1942, 32, 285.

(18) Coleman, E. H.; Gaydon, A. G.; Vaidya, W. M. *Nature (London)* 1948, 162, 108.

(19) Durie, R. A.; Ramsay, D. A. *Can. J. Phys.* 1958, 36, 35.

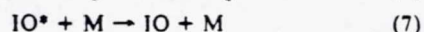
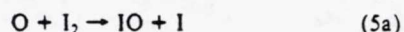
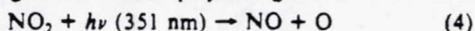
(20) Wine, P. H.; Kreutter, N. M.; Ravishankara, A. R. *J. Phys. Chem.* 1979, 83, 3191.

to be $1.64 \times 10^{-18.21}$ and $2.68 \times 10^{-19} \text{ cm}^2$,²² respectively. The fraction of NO in the NO/N₂ bulb was checked at the end of each set of experiments by diluting the bulb with O₂, allowing sufficient time for quantitative conversion of NO to NO₂, and then measuring the NO₂ photometrically.

The gases used in this study were obtained from Matheson and had the following stated minimum purities: N₂, 99.999%; O₂, 99.99%; NO, 99.0%. Air was ultra zero grade with total hydrocarbons less than 0.1 ppm. N₂, O₂, and air were used as supplied. Purification of NO involved passage over ascarite and degassing at 77 K. NO₂ was prepared by mixing 1 part NO with 3 parts O₂ at a total pressure of 1000 Torr and allowing the mixture to react overnight. The resulting NO₂/O₂ mixture was pumped through a liquid nitrogen trap where the NO₂ was frozen out and the O₂ pumped away. The lack of any blue color in the trapped white solid indicated complete conversion of NO to NO₂. Iodine crystals were obtained from Aldrich and had a stated minimum purity of 99.999%; they were used without further purification. Iodine was admitted to the reactor by diverting a small fraction of the main buffer gas flow through a flow meter and needle valve, then through the tube containing I₂ crystals, and finally into the reactor. An ice-water bath was employed to keep the I₂ crystals at a constant temperature of 273 K, thus avoiding drifts in the I₂ concentration during the course of experiments.

Results and Discussion

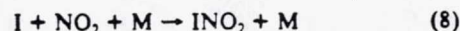
The following scheme was employed to generate IO radicals:



In the above reaction scheme, IO* represents vibrationally excited IO; our detection method is not sensitive to IO*. In preliminary experiments, a mixture containing $1 \times 10^{15} \text{ NO}_2 \text{ cm}^{-3}$, $1 \times 10^{15} \text{ I}_2 \text{ cm}^{-3}$, and 20 Torr of N₂ was photolyzed and the appearance rate of 427-nm absorption was observed. Based on the literature value for k_5 ,¹⁴ an IO risetime of about 7 μs was expected; the observed risetime was about 30 μs . However, the IO appearance rate increased with increasing pressure, suggesting that reaction 7 was the rate-limiting IO production step. In all experiments used to determine k_1 and k_2 , the IO appearance rate was at least a factor of 5 faster than the IO decay rate. Reaction 5 is known to be 14 times faster than reaction 6,^{14,23} so it was not difficult to establish experimental conditions where most photolytically generated oxygen atoms reacted with I₂ rather than with NO₂.

For the optical path lengths (13–20 m) traversed by the probe beam through the reaction cell and the NO₂ concentrations employed (up to $3.05 \times 10^{15} \text{ molecules cm}^{-3}$), a large fraction of the probe radiation was absorbed by NO₂. Hence, destruction of NO₂ by reactions 4 and 6 led to a noticeable difference between the (base line) signal levels before and after the laser fired in experiments where NO₂ was photolyzed in the absence of I₂. In the presence of I₂, the magnitude of the rapid base-line shift upon firing the laser was reduced somewhat due to the occurrence of reaction 5 in competition with reaction 6. However, the IO generated by reaction 5 decayed via processes that either generated NO₂ (IO + NO) or converted NO₂ to IONO₂, a species whose absorption cross section at 427 nm is not known. Sander and Watson²⁴ have shown that if an elementary reaction results in an absorbance change due to removal of an absorbing excess reagent

and/or formation of an absorbing product, the correct decay rate is obtained from the first-order decay of the overall absorbance by using the signal level at $t \rightarrow \infty$ as the base line. All of our kinetic data were analyzed in this manner. The only potential complication due to absorption of probe radiation by species other than IO which may have caused a problem in our kinetic analysis is the reaction of iodine atoms generated via reaction 5 with NO₂, i.e.



The kinetics of reaction 8 have been characterized^{25,26} and an IONO₂ absorption spectrum has been searched for unsuccessfully,²⁵ leading van den Bergh and Troe²⁵ to conclude that $\sigma(\text{INO}_2) < \sigma(\text{NO}_2)$ over the wavelength range 250–600 nm; their results suggest that absorption by IONO₂ had a negligible effect on our experiments. We did notice, however, that the difference between the base line before the laser fired and the base line after IO had decayed away was typically smaller than predicted based on calculation of the amount of NO₂ destroyed. Apparently, IONO₂ has a significant absorption cross section at 427 nm.

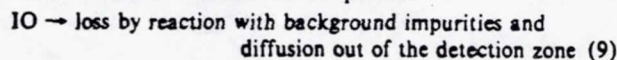
To ensure that we were detecting the IO radical, the spectrum of the absorbing species was mapped out over the wavelength range transmitted through the White cell (414–446 nm). The 5–0, 4–0, 3–0, and 2–0 bands of IO^{18,19} were observed; no transient absorption was observed at wavelengths between the IO bands although, as discussed above, small base-line shifts do occur due to NO₂ removal and (probably) due to IONO₂ formation. The apparent IO absorption cross section at the peak of the 4–0 band was estimated based on the measured laser fluence, the measured NO₂ and I₂ concentrations, and the known rate coefficients for reactions 5 and 6.^{14,23} A cross section of $(1.8 \pm 0.3) \times 10^{-17} \text{ cm}^2$ was obtained. At high resolution, the peak absorption cross section for the 4–0 band is $3.1 \times 10^{-17} \text{ cm}^2$.^{12,27} Our measured cross section is in the range expected based on the known high-resolution cross section, the known bandwidth,²⁷ and our monochromator resolution of 0.72 nm.

Results obtained for reactions 1 and 2 are discussed separately below.

The IO + NO Reaction. Reaction mixtures employed to study reaction 1 contained 35 mTorr of NO₂, 0–14 mTorr of NO, 30–63 mTorr of I₂, and 40–200 Torr of N₂ buffer gas. As mentioned above, a small amount of O₂ (typically about 0.5 Torr) was also present in the reaction mixture because the NO₂ storage bulb contained air rather than N₂ as the diluent gas. Concentrations of IO radicals generated via reactions 4–7 were in the range $(1.7\text{--}4.3) \times 10^{12} \text{ molecules cm}^{-3}$. In nearly all experiments, IO removal was dominated by reactions 1 and 2, so the data could be analyzed assuming pseudo-first-order kinetics:

$$\ln \left\{ \frac{[\text{IO}]_t}{[\text{IO}]_0} \right\} = \ln \left\{ \frac{S_t/S_{t'}}{S_t/S_{t''}} \right\} \\ = (k_1[\text{NO}] + k_2[\text{NO}_2] + k_9)t \equiv k't \quad (1)$$

In eq 1, t' represents a time shortly after the laser fired when IO production was complete but little or not IO decay had occurred, t'' represents a time after IO removal had gone to completion but before NO₂, IONO₂, and IONO₂ destroyed or produced as a result of the laser flash diffused or flowed out of the detection volume, S_t represents the signal level at time t , and k_9 represents the first-order rate coefficient for the process



Under the conditions of our experiments $k_2[\text{NO}_2] \gg k_9$. The only significant interference in the study of reaction 1 was from the fast reaction



$$k_{10} = 1.7 \times 10^{-12} \exp(1020/T) \text{ cm}^3 \text{ molecule}^{-1} \text{ s}^{-1} \quad (12)$$

(21) Tellinghuisen, J. *J. Chem. Phys.* **1973**, *58*, 2821.

(22) Schneider, W.; Moortgat, G. K.; Tyndall, G. S.; Burrows, J. P. *J. Photochem. Photobiol.*, **A** **1987**, *40*, 195.

(23) DeMore, W. B.; Molina, M. J.; Sander, S. P.; Golden, D. M.; Hampson, R. F.; Kurylo, M. J.; Howard, C. J.; Ravishankara, A. R. *Chemical Kinetics and Photochemical Data for Use in Stratospheric Modeling*. Evaluation No. 8, JPL Publication No. 87-41, 1987.

(24) Sander, S. P.; Watson, R. T. *J. Phys. Chem.* **1960**, *64*, 1664.

(25) van den Bergh, H.; Troe, J. *J. Chem. Phys.* **1975**, *64*, 736.

(26) van den Bergh, H.; Benoit-Guyot, N.; Troe, J. *Int. J. Chem. Kinet.* **1977**, *9*, 223.

(27) Stickel, R. E.; Hynes, A. J.; Bradshaw, J. D.; Chameides, W. L.; Davis, D. D. *J. Phys. Chem.* **1988**, *92*, 1862.

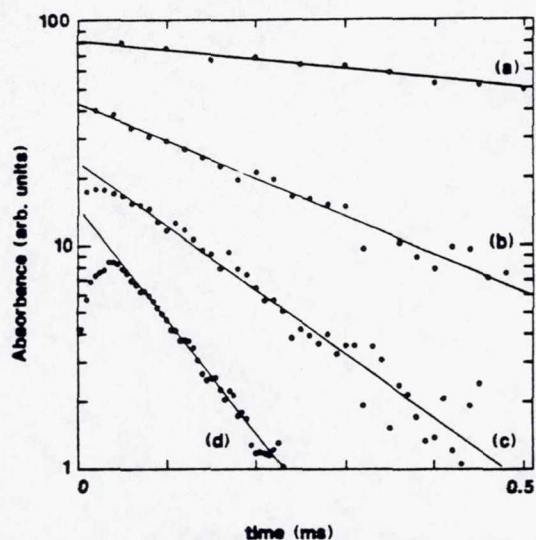


Figure 1. Typical IO temporal profiles observed in the study of the IO + NO reaction. Experimental conditions: $T = 273$ K; $P = 40$ Torr of N_2 ; electronic time constant = $16 \mu\text{s}$; absorption path length ~ 552 cm; $[I_2] = 1.2 \times 10^{15}$ molecules cm^{-3} ; $[\text{NO}_2] = 9.5 \times 10^{14}$ molecules cm^{-3} ; $[\text{NO}]$ in units of 10^{14} molecules cm^{-3} = (a) 0.028, (b) 1.30, (c) 2.47, and (d) 4.80. Number of laser shots averaged = (a) 128, (b) 320, (c) 384, and (d) 320. Solid lines are obtained from linear least-squares analyses and give the following pseudo-first-order decay rates (units are s^{-1}): (a) 992, (b) 3900, (c) 6610, (d) 11800. For the sake of clarity, temporal profiles are shifted on the absorbance scale; peak percent absorption was (a) 2.7, (b) 2.0, (c) 1.8, and (d) 1.7.

While the contribution of reaction 10 was negligible in most experiments, it was significant at short times after the laser flash in experiments where NO levels were low. Temporal profiles measured under such conditions were corrected for the contribution from reaction 10 as follows: The experimental temporal profile was analyzed under the (incorrect) assumption that the decay was exponential to obtain a best-fit first-order decay rate, k'_{exp} . The temporal profile was also simulated by numerical integration of the rate equations assuming that the only important IO loss processes were reactions 1, 2, and 10; the simulations employed our preliminary values for k_1 and k_2 along with the literature value for k_{10} . A best-fit first-order decay rate, k'_{sim} , was obtained by analyzing the simulated temporal profile over the same time interval as was employed to obtain k'_{exp} . The "real" first-order decay rate, k' , was then obtained from the relationship

$$k' = k'_{\text{exp}} k'_{0,\text{sim}} / k'_{\text{sim}} \quad (\text{II})$$

where $k'_{0,\text{sim}}$ is the simulated first-order decay rate with k_{10} set equal to zero. Flash-generated NO also contributed to IO removal in experiments where the reaction mixture initially contained no NO or relatively small concentrations of NO. The concentration of flash-generated NO, $[\text{NO}]_f$, was estimated from the relationship

$$[\text{NO}]_f = [\text{IO}]_r + 2k_6[\text{NO}_2] / (k_5[I_2] + k_6[\text{NO}_2]) \quad (\text{III})$$

and was added to the preflash NO concentration to determine the appropriate NO level for kinetic analysis. It should be noted that the effects of reaction 10 and flash-generated NO on our determinations of $k_1(T)$ are very small—values of $k_1(T)$ obtained by using corrected decay rates and NO concentrations differ by less than 2% from values obtained when the above corrections are ignored.

To measure $k_1(T)$, pseudo-first-order IO decay rates were measured as a function of $[\text{NO}]$ at constant $[\text{NO}_2]$. Typical results are shown in Figures 1 and 2. As predicted by eq 1, observed IO decays were exponential and plots of k' versus $[\text{NO}]$ were linear; the desired bimolecular rate coefficients, $k_1(T)$, were obtained from the slopes of the k' versus $[\text{NO}]$ plots. Measured rate coefficients are given along with other pertinent information in Table I. Uncertainties given in Table I for $k_1(T)$ values are 2σ and represent precision only. Taking into account possible

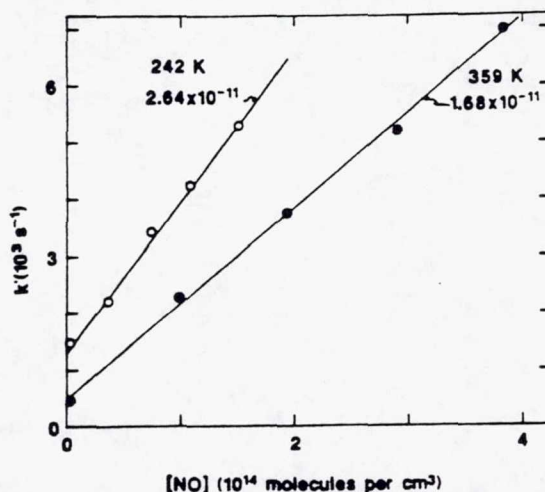


Figure 2. Plots of k' versus $[\text{NO}]$ for data obtained at the temperature extremes of the IO + NO study. Solid lines are obtained from linear least-squares analyses and give the rate coefficients shown in the figure (units are $\text{cm}^3 \text{molecule}^{-1} \text{s}^{-1}$).

TABLE I: Kinetic Data for the Reaction IO + NO \rightarrow I + NO₂

T, K	P, Torr	concentration, 10^{12} molecules cm^{-3}				k', s^{-1}	$10^{11} k_1, \text{cm}^3 \text{molecule}^{-1} \text{s}^{-1}$
		I_2	NO_2	IO_r	NO		
242	40	900	1130	2.1	2.2	1480 ^a	
				1.9	35.3	2210	
				1.7	74.6	3440	
				1.8	108	4250	
				1.8	150	5330	
				2.64 ± 0.15			
273	40	1200	950	2.8	2.9	967 ^a	
				2.1	130	3900	
				1.9	247	6610	
				1.7	372	8400	
				1.7	480	11800	
				2.19 ± 0.25			
298	40	1100	940	3.4	3.6	748 ^a	
				2.3	59.0	1960	
				2.5	106	2820	
				2.3	189	5130	
				2.3	280	6580	
				2.17 ± 0.22			
298	200	1500	1050	4.3	4.5	1780 ^a	
				4.1	112	3830	
				4.1	213	6160	
				3.4	309	8530	
				3.4	407	10400	
				2.19 ± 0.12			
328	40	900	1020	3.1	3.4	496 ^a	
				3.0	83.6	1530	
				2.9	127	2760	
				2.5	209	4930	
				2.5	313	6010	
				1.91 ± 0.38			
359	40	1700	1100	3.2	3.3	475 ^a	
				2.7	98.8	2290	
				2.6	193	3770	
				2.3	291	5220	
				2.0	383	7000	
				1.68 ± 0.09			

^a Errors are 2σ and represent precision only. ^b Corrected downward by $\leq 2.7\%$ to account for contribution from the IO + IO reaction.

systematic errors (primarily in the determination of the NO concentration), we estimate the absolute uncertainty in any measured $k_1(T)$ to be $\pm 20\%$ except at 328 K where unusually poor precision limits the absolute accuracy to $\pm 25\%$.

Our results demonstrate that $k_1(298 \text{ K})$ is independent of pressure over the range 40–200 Torr and that $k_1(T)$ increases with decreasing temperature. An Arrhenius plot for reaction 1 is shown in Figure 3. A weighted linear least-squares analysis of the $\ln k_1$ versus T^{-1} data gives the Arrhenius expression

$$k_1(T) = (6.9 \pm 1.7) \times 10^{-12} \exp[(328 \pm 71)/T] \text{ cm}^3 \text{molecule}^{-1} \text{s}^{-1}$$

where uncertainties are 2σ and represent precision only.

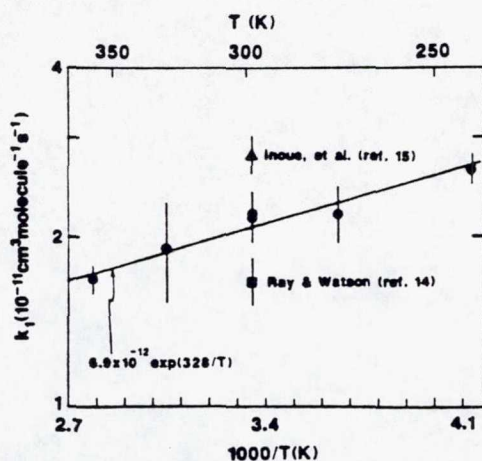


Figure 3. Arrhenius plot for the reaction $\text{IO} + \text{NO} \rightarrow \text{I} + \text{NO}_2$. Filled circles are our data at $P = 40$ Torr, and open circle is our data at $P = 200$ Torr. The solid line is obtained from a weighted linear least-squares analysis and gives the Arrhenius expression shown in the figure (units are $\text{cm}^3 \text{ molecule}^{-1} \text{ s}^{-1}$).

The kinetics of reaction 1 have been studied previously only at 298 K. For the sake of comparison, the two previous determinations of $k_1(298 \text{ K})$ are plotted along with our data in Figure 3. Ray and Watson¹⁴ employed the discharge flow-mass spectrometry technique to study reaction 1 using the $\text{O} + \text{I}_2$ reaction as the IO source; they obtained the result $k_1(298 \text{ K}) = (1.67 \pm 0.16) \times 10^{-11} \text{ cm}^3 \text{ molecule}^{-1} \text{ s}^{-1}$. Inoue et al.,¹⁵ as part of a study which reported the first observation of IO laser-induced fluorescence, used a laser flash photolysis-pulsed laser induced fluorescence technique to study reaction 1 using the $\text{O}(^1\text{D}) + \text{HI}$ reaction as the IO source; these investigators obtained the result $k_1(298 \text{ K}) = (2.8 \pm 0.2) \times 10^{-11} \text{ cm}^3 \text{ molecule}^{-1} \text{ s}^{-1}$. The value for $k_2(298 \text{ K})$ determined in this study is intermediate between those reported previously. The small negative activation energy observed for reaction 1 (Figure 3) is consistent with the temperature dependence observed previously for the $\text{ClO} + \text{NO}$ ^{24,29} and $\text{BrO} + \text{NO}$ ^{30,31} reactions and is typical of radical-radical reactions that proceed on a potential energy surface with a minimum along the reaction coordinate (corresponding in this case to IONO which, to our knowledge, has never been observed but should be a bound species).

The IO + NO₂ Reaction. Reaction mixtures employed to study reaction 2 contained 22–68 mTorr of I₂, 6–94 mTorr of NO₂, and 40–750 Torr of N₂ buffer gas. As mentioned above, a small amount of O₂ was also present in the reaction mixture because the NO₂ storage bulb contained air rather than N₂ as the diluent gas; typically $[\text{O}_2] \sim 10[\text{NO}_2]$. Concentrations of IO radicals generated via reactions 4–7 were in the range $(0.6\text{--}5.0) \times 10^{12} \text{ molecules cm}^{-3}$. The method of data analysis was similar to that described above for the IO + NO reaction except, in the case of reaction 2, all measured IO temporal profiles were corrected for contributions from IO reaction with itself (usually very minor) and with flash-generated NO. The magnitude of the required corrections increased with increasing laser fluence. For a constant laser fluence, the corrections were largest at low pressure since the IO + NO₂ reaction rate is pressure dependent while the IO + NO reaction rate is pressure independent. A typical IO temporal profile observed in 40 Torr of N₂ at 298 K is shown in Figure 4 while uncorrected and corrected k' versus $[\text{NO}_2]$ plots for the 40 Torr (N₂), 298 K data are shown in Figure 5. At 254 K, the low-temperature extreme of our study, a small fraction of NO₂ was tied up as N₂O₄ ($[\text{NO}_2] \geq 37[\text{N}_2\text{O}_4]$ in all experiments).

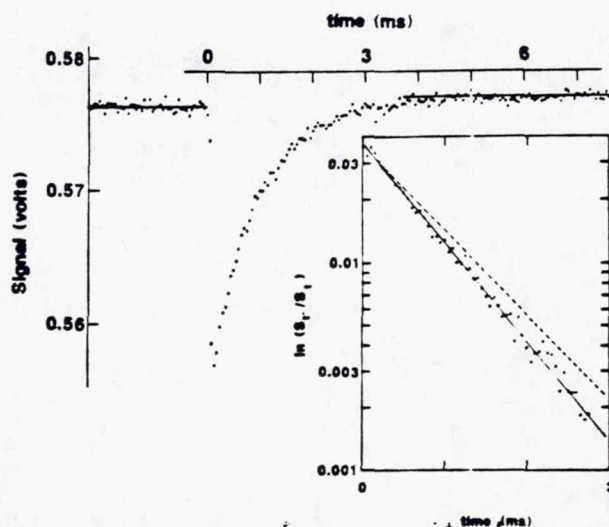


Figure 4. Typical IO temporal profile observed in the study of the IO + NO₂ reaction at $P = 40$ Torr and $T = 298 \text{ K}$. $[\text{NO}_2] = 1.59 \times 10^{15} \text{ molecules cm}^{-3}$; $[\text{I}_2] = 1.6 \times 10^{15} \text{ molecules cm}^{-3}$; electronic time constant = 16 μs ; absorption path length $\sim 552 \text{ cm}$; 256 laser shots averaged. Note that the base line after IO decay is higher than the pretrigger base line by 0.00073 V, the equivalent of 0.13% absorption. The inset is a plot of $\ln(I_0/I)$ versus time for the same data with absorbances calculated by using the base line obtained after IO decayed away. The solid line in the inset is obtained from a linear least-squares analysis and gives the decay rate $k' = 1100 \text{ s}^{-1}$. The dashed line in the inset is the decay rate corrected for IO reaction with itself and with flash-generated NO ($k'_{\text{corr}} = 950 \text{ s}^{-1}$).

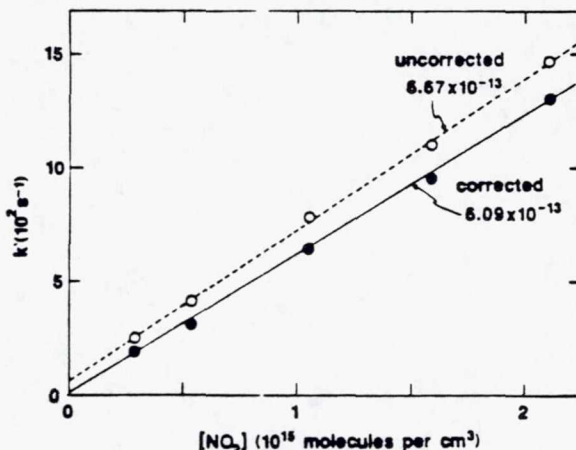


Figure 5. Plot of k' versus $[\text{NO}_2]$ for data obtained at 298 K in 40 Torr of N₂. Open circles are uncorrected for IO reaction with itself and with flash-generated NO while filled circles are corrected for these processes. Solid and dashed lines are obtained from linear least-squares analyses and give the rate coefficients shown in the figure (units are $\text{cm}^3 \text{ molecule}^{-1} \text{ s}^{-1}$).

Kinetic analyses employed the reasonable assumption that N₂O₄ is much less reactive toward IO than NO₂ is.

Measured bimolecular rate coefficients $k_2([\text{M}], T)$ are summarized along with other pertinent information in Table II. Uncertainties given in Table II for $k_2([\text{M}], T)$ values are 2 σ and represent precision only. Small systematic errors are possible in the NO₂ concentration determination and due to the assumption that absorption of 427-nm radiation by IONO₂ had a totally negligible effect on the $k_2([\text{M}], T)$ determinations. We estimate the accuracy of any measured $k_2([\text{M}], T)$ to be $\pm 20\%$.

Our results demonstrate that reaction 2 is in the "falloff" regime between third- and second-order kinetics over the temperature and pressure ranges investigated. Troe and co-workers^{32–35} have

(28) Leu, M. T.; DeMore, W. B. *J. Phys. Chem.* **1978**, *82*, 2049.
 (29) Lee, Y.-P.; Stimpfle, R. M.; Perry, R. A.; Mucha, J. A.; Evenson, K. M.; Jennings, D. A.; Howard, C. J. *Int. J. Chem. Kinet.* **1982**, *14*, 711.
 (30) Leu, M. T. *Chem. Phys. Lett.* **1979**, *61*, 275.
 (31) Watson, R. T.; Sander, S. P.; Yung, Y. L. *J. Phys. Chem.* **1979**, *83*, 2936.

(32) Luther, K.; Troe, J. *Symp. (Int.) Combust., [Proc.]* **1978**, *17*, 535.

TABLE II: Summary of Kinetic Data for the Reaction IO + NO₂ + N₂ → IONO₂ + N₂

T, K	no. of expts ^a	concentration ^b				range of k', s ⁻¹		10 ¹³ k ₂ , ^d cm ³ molecule ⁻¹ s ⁻¹	
		N ₂	I ₂	NO ₂	[NO ₂]/[O] ₀	uncorrected	corrected ^c	uncorrected	corrected ^c
254	7	3240	0.8	0.23-1.54	290-880	406-2700	370-2530	17.1 ± 0.7	16.5 ± 0.6
254	4	19400	0.8	0.50-1.64	310	2230-6900	2110-6660	40.5 ± 3.6	39.3 ± 3.4
275	6	3240	1.3	0.52-2.51	280-1200	782-3840	688-3460	15.2 ± 0.8	14.2 ± 0.8
275	4	19400	1.3	0.58-2.15	310	2060-8050	1980-7780	37.5 ± 2.8	36.3 ± 2.7
298	5	1300	1.6	0.29-2.11	340	250-1470	192-1300	6.67 ± 0.25	6.09 ± 0.22
298	5	3240	1.8	0.35-2.21	410	454-2620	392-2440	11.6 ± 0.7	11.0 ± 0.7
298	6	6480	2.0	0.35-2.15	410-560	719-4110	681-3940	18.6 ± 0.7	18.1 ± 0.7
298	7	13000	2.0	0.26-3.05	260-340	692-8080	651-7740	25.8 ± 0.5	25.0 ± 0.5
298	7	19400	1.3	0.30-2.50	320-1000	921-8860	883-8580	35.1 ± 2.3	34.1 ± 2.2
298	5	24300	0.7	0.35-1.89	390	1170-6910	1140-6770	37.1 ± 1.0	36.4 ± 0.9
320	4	3240	1.0	0.52-1.84	440	570-1580	456-1470	8.21 ± 0.32	7.74 ± 0.30
320	4	19400	0.6	0.40-1.60	250	963-3700	901-3540	22.6 ± 2.5	21.9 ± 2.4
354	4	3240	1.7	0.45-1.74	390	361-1180	332-1100	6.60 ± 0.95	6.22 ± 0.90
354	4	19400	0.6	0.72-2.09	390	1450-3980	1400-3830	18.3 ± 2.6	17.7 ± 2.5

^a Experiment = measurement of one IO temporal profile. ^b Units are 10¹⁵ molecules cm⁻³. ^c Corrected for contributions from the IO + IO and IO + NO reactions. ^d Errors are 2σ and represent precision only.

shown that bimolecular rate coefficient versus pressure curves (i.e., falloff curves) for association reactions can be approximated by the three-parameter equation

$$k([M], T) = k_{\infty}(T)F_{LH}F([M], T) \quad (IV)$$

where F_{LH} is the Lindeman-Hinshelwood factor

$$F_{LH} = X/(1 + X) \quad (V)$$

$$X = k_0([M], T)[M]/k_{\infty}(T) \quad (VI)$$

In the above equations, $k_0([M], T)$ is the rate coefficient in the low-pressure third-order limit, $k_{\infty}(T)$ is the rate coefficient in the high-pressure second-order limit, and $F([M], T)$ is the parameter which characterizes the broadening of the falloff curve due to the energy dependence of the rate coefficient for decomposition of the energized adduct. $F([M], T)$ can be calculated from the spectroscopic and thermodynamic properties of the adduct. Examples of studies where detailed analyses of falloff behavior have been carried out include our study of the OH + SO₂ reaction³⁶ and Sander et al.'s study of the BrO + NO₂ reaction.³⁷ The use of theoretical and experimental information to evaluate falloff parameters for a number of atmospherically important reactions has been discussed by Patrick and Golden.³⁸

For the relatively low temperatures employed in our study, eq IV can be approximated as follows:³³

$$k([M], T) = k_{\infty}(T)F_{LH}F_c(T)^y \quad (VII)$$

$$y = [1 + \{\log X / (0.75 - 1.27 \log F_c(T))\}^2]^{-1} \quad (VIII)$$

where $F_c(T)$ is the value of $F([M], T)$ at the center of the falloff curve, i.e., at the pressure where $k_0[M] = k_{\infty}$. As pointed out by Jenkin and Cox¹¹ in the only previous study of reaction 2, accurate determination of $F_c(T)$ is not possible due to a lack of spectroscopic and thermodynamic data for IONO₂. Furthermore, for a three-parameter expression like eq VII, good fits to experimental data can be obtained for a wide range of parameter values. For the above reasons, Jenkin and Cox¹¹ adopted a value of 0.4 for F_c based on the detailed analysis of Sander et al.³⁷ for the related BrO + NO₂ reaction. Use of $F_c(298 \text{ K}) = 0.4$ in our calculations seems physically reasonable and facilitates comparison of derived falloff parameters with those reported by Jenkin and Cox.¹¹ Theoretically, $F_c(T)$ is expected to increase with decreasing tem-

TABLE III: Comparison of Measured IO + NO₂ + N₂ Rate Coefficients with Those Obtained from "Best Fit" Falloff Parameters

T, K	10 ⁻¹⁸ [M], molecules cm ⁻³	10 ¹³ k ₂ , cm ³ molecule ⁻¹ s ⁻¹			
		exptl ^a	A ^b	B ^b	C ^b
254	3.24	16.5 ± 0.6	18.0	18.9	17.8
254	19.4	39.3 ± 3.4	42.6	47.7	43.0
275	3.24	14.2 ± 0.8	14.9	15.0	14.2
275	19.4	36.3 ± 2.7	37.7	39.5	35.8
298	1.30	6.09 ± 0.22	5.91	5.91	5.95
298	3.24	11.0 ± 0.7	11.6	11.6	11.1
298	6.48	18.1 ± 0.7	17.9	17.9	16.7
298	13.0	25.0 ± 0.5	26.3	26.3	24.0
298	19.4	34.1 ± 2.2	32.4	32.4	29.3
298	24.3	36.4 ± 0.9	36.3	36.3	32.7
320	3.24	7.74 ± 0.30	8.77	9.08	8.80
320	19.4	21.9 ± 2.4	27.8	27.1	24.5
354	3.24	6.22 ± 0.90	5.45	6.25	6.12
354	19.4	17.7 ± 2.5	21.1	20.8	18.8

^a Errors are 2σ and represent precision only. ^b F_c assumed to be 0.4 independent of temperature (see text for rationale). A: $k_0(298 \text{ K})$ and $k_{\infty}(298 \text{ K})$ obtained by fitting 298 K data only; n and m obtained by fitting data at $T = 298 \text{ K}$. Results: $k_0 = 7.3 \times 10^{-31}(T/300)^{-0.5} \text{ cm}^6 \text{ molecule}^{-2} \text{ s}^{-1}$; $k_{\infty} = 1.78 \times 10^{-11}(T/300)^{+2.5} \text{ cm}^3 \text{ molecule}^{-1} \text{ s}^{-1}$. B: $k_0(298 \text{ K})$ and $k_{\infty}(298 \text{ K})$ obtained by fitting 298 K data only; n obtained by fitting data at $T \neq 298 \text{ K}$ with m fixed at 0. Results: $k_0 = 7.3 \times 10^{-31}(T/300)^{-0.9} \text{ cm}^6 \text{ molecule}^{-2} \text{ s}^{-1}$; $k_{\infty} = 1.78 \times 10^{-11} \text{ cm}^3 \text{ molecule}^{-1} \text{ s}^{-1}$. C: $k_0(300 \text{ K})$, k_{∞} , and n obtained by fitting all data with m fixed at 0. Results: $k_0 = 8.1 \times 10^{-31}(T/300)^{-0.5} \text{ cm}^6 \text{ molecule}^{-2} \text{ s}^{-1}$; $k_{\infty} = 1.31 \times 10^{-11} \text{ cm}^3 \text{ molecule}^{-1} \text{ s}^{-1}$.

perature.³⁶ However, the temperature dependence of $F_c(T)$ is relatively weak and is usually ignored when parametrizing the temperature and pressure dependences of atmospheric association reactions.^{23,38,39} Hence, we take $F_c(T)$ for reaction 2 to be 0.4 independent of temperature. In keeping with the usual representation,^{23,38,39} the temperature dependences of k_0 and k_{∞} are parametrized as follows:

$$k_0(T) = k_0(300 \text{ K})(T/300)^{-m} \quad (IX)$$

$$k_{\infty}(T) = k_{\infty}(300 \text{ K})(T/300)^{-n} \quad (X)$$

Values for $k_0(300 \text{ K})$, $k_{\infty}(300 \text{ K})$, n , and m obtained from various fits of our data to eq VII are summarized in Table III while values for $k_2([M], 298 \text{ K})$ measured in this study are plotted in Figure 6. The best fit of our 298 K data only to eq VII gives the results $k_0(298 \text{ K}) = 7.6 \times 10^{-31} \text{ cm}^6 \text{ molecule}^{-2} \text{ s}^{-1}$ and $k_{\infty}(298 \text{ K}) = 1.78 \times 10^{-11} \text{ cm}^3 \text{ molecule}^{-1} \text{ s}^{-1}$. The falloff curve calculated from these parameters is shown in Figure 6 as is the "currently recommended"³⁹ falloff curve. The current recommendation, $k_0(298 \text{ K}) = 3.5 \times 10^{-31} \text{ cm}^6 \text{ molecule}^{-2} \text{ s}^{-1}$ and $k_{\infty} = 1.6 \times 10^{-11}$

(39) Atkinson, R.; Baulch, D. L.; Cox, R. A.; Hampson, Jr., R. F.; Kerr, J. A.; Troe, J. J. *Phys. Chem. Ref. Data* 1989, 18, 881.

(33) Troe, J. J. *Phys. Chem.* 1979, 83, 114.
 (34) Troe, J. *Ber. Bunsen-Ges. Phys. Chem.* 1983, 87, 161.
 (35) Gilbert, R. G.; Luther, K.; Troe, J. *Ber. Bunsen-Ges. Phys. Chem.* 1983, 87, 169.
 (36) Wine, P. H.; Thompson, R. J.; Ravishankara, A. R.; Semmes, D. H.; Gump, C. A.; Torabi, A.; Nicovich, J. M. *J. Phys. Chem.* 1984, 88, 2095.
 (37) Sander, S. P.; Ray, G. W.; Watson, R. T. *J. Phys. Chem.* 1981, 85, 199.
 (38) Patrick, R.; Golden, D. M. *Int. J. Chem. Kinet.* 1983, 15, 1189.

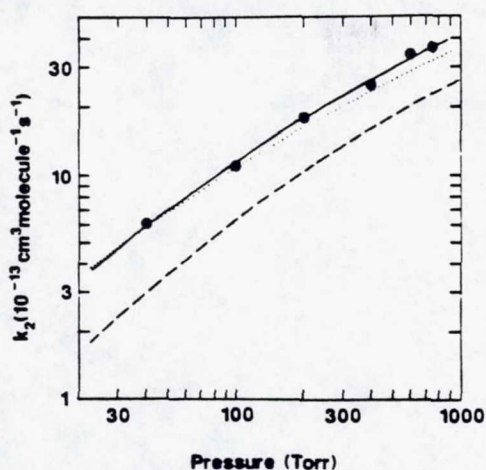


Figure 6. Comparison of our experimental 298 K falloff curve for the IO + NO₂ reaction with the current recommendation of the IUPAC panel³⁹ which is based on the 277 K study by Jenkin and Cox¹¹ and assumed temperature dependences for k_0 and k_∞ . Solid circles are our experimental data. Solid line is best fit to the data with F_c fixed at 0.4; best-fit parameters are $k_0 = 7.6 \times 10^{-31} \text{ cm}^6 \text{ molecule}^{-2} \text{ s}^{-1}$ and $k_\infty = 1.78 \times 10^{-11} \text{ cm}^3 \text{ molecule}^{-1} \text{ s}^{-1}$. Dotted line is obtained from the best fit to all data over the temperature range 254–354 K with F_c fixed at 0.4 and k_∞ forced to be temperature independent; the best-fit parameters are $k_0 = 8.4 \times 10^{-31} \text{ cm}^6 \text{ molecule}^{-2} \text{ s}^{-1}$ and $k_\infty = 1.31 \times 10^{-11} \text{ cm}^3 \text{ molecule}^{-1} \text{ s}^{-1}$. Dashed line is the current IUPAC panel recommendation: $k_0 = 3.5 \times 10^{-31} \text{ cm}^6 \text{ molecule}^{-2} \text{ s}^{-1}$ and $k_\infty = 1.6 \times 10^{-11} \text{ cm}^3 \text{ molecule}^{-1} \text{ s}^{-1}$.

$\text{cm}^3 \text{ molecule}^{-1} \text{ s}^{-1}$, is based on the values for $k_2([M], 277 \text{ K})$ reported by Jenkin and Cox¹¹ and the assumed temperature dependence parameters $n = 3$ and $m = 0$. When $k_0(298 \text{ K})$ and $k_\infty(298 \text{ K})$ were fixed at the values obtained by fitting the 298 K data only and data at $T \neq 298 \text{ K}$ were used to obtain n and m , a negative value for m gave the best fit. Since it does not seem physically realistic for k_∞ to increase with increasing temperature, this result is probably indicative of a small systematic error in the temperature dependence data. As an alternative fitting procedure, we fixed m at zero and varied only n ; the result was $n = 4.9$. Finally, we fit the entire set of data with m fixed at zero to obtain values for $k_0(300 \text{ K})$, k_∞ , and n ; the results were $k_0(300 \text{ K}) = 8.1 \times 10^{-31} \text{ cm}^6 \text{ molecule}^{-2} \text{ s}^{-1}$, $k_\infty = 1.31 \times 10^{-11} \text{ cm}^3 \text{ molecule}^{-1} \text{ s}^{-1}$, and $n = 5.1$. For comparison, the falloff curve obtained by fixing m at zero and varying $k_0(300 \text{ K})$, k_∞ , and n independently is shown in Figure 6 along with the curve obtained as the best fit to the 298 K data only. Rate coefficients calculated by using all sets of falloff parameters are compared with experimental results in Table III.

As a good, physically reasonable representation of our data, we take the average of the two fits with m fixed at zero, i.e., B and C in Table III, and report the following falloff parameters for reaction 2:

$$k_0 = 7.7 \times 10^{-31} (T/300)^{-5.0} \text{ cm}^6 \text{ molecule}^{-2} \text{ s}^{-1}$$

$$k_\infty = 1.55 \times 10^{-11} \text{ cm}^3 \text{ molecule}^{-1} \text{ s}^{-1}$$

$$F_c = 0.4$$

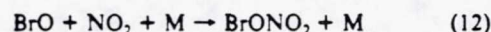
The above values for k_0 and k_∞ should not be considered true low- and high-pressure-limit rate coefficients. They are physically reasonable values which can be used to reproduce our measured values for $k_2([M], T)$ rather well (Table III). Over the ranges of temperature and pressure employed in our experiments, reaction 2 was rather far removed from both the low- and high-pressure limits; hence, uncertainties in both k_0 and k_∞ are substantial. Variation of F_c has a rather small effect on the best-fit k_0 but dramatically changes the best-fit k_∞ . For this reason, we feel that our reported value for $k_0(\text{N}_2, 298 \text{ K})$ probably is within $\pm 25\%$ of the true value while our reported value for $k_\infty(298 \text{ K})$ may deviate from the true value by as much as a factor of 2. Uncertainties

increase at temperatures far removed from 298 K.

The temperature dependence for k_0 derived from our data is rather large. The current NASA panel evaluation,²³ for example, considers 36 association reactions of atmospheric importance (but no IO reactions); recommended values for n range from 0 to 4.3. Two points should be made regarding the value $n \approx 5$ obtained in this study. First, no data were obtained at pressures close to the low-pressure limit, so the uncertainties in derived values for $k_0(300 \text{ K})$ and n are significant. Second, IO may be a species which exhibits large temperature coefficients for association reactions. For example, the association channel for the IO self-reaction is known to have an unusually large negative activation energy.¹²

As can be seen from examination of Figure 6, the rate coefficients $k_2([M], T)$ reported in this study are about a factor of 2 faster than those reported previously by Jenkin and Cox,¹¹ who employed a molecular modulation technique to study reaction 2 over the pressure ranges 35–404 Torr at 277 K and 24–101 Torr at 303 K. The study of Jenkin and Cox had two problems which may have resulted in inaccurate values for $k_2([M], T)$. Firstly, even at the highest NO₂ levels employed, extrapolated background IO removal rates (presumably due to heterogeneous processes) were about as fast as the apparent rate of IO removal by NO₂. Secondly, a second-order component was observed in their IO decays which increased markedly in importance with increasing pressure. Jenkin and Cox attributed the second-order component to the IO self-reaction. The recent study of the IO self-reaction by Sander¹² found a much smaller pressure-dependent component and much larger pressure-independent component to k_{10} than reported by Jenkin and Cox.¹¹ Thus, the procedure used by Jenkin and Cox to extract values for $k_2([M], T)$ from their observed mixed first- and second-order decays must be considered suspect.

It is of interest to compare the IO + NO₂ rate coefficients obtained in this study with reported measurements of $k_{11}([M], T)$ ^{40–50} and $k_{12}([M], T)$.^{37,51,52}



At 298 K, the high-pressure-limit rate coefficients are roughly equal for all three reactions, but the low-pressure-limit rate coefficients increase in the order ClO < BrO < IO. Hence, at atmospheric pressures $k_2 > k_{12} > k_{11}$.

It is now generally accepted that the yields of products other than ClONO₂ from reaction 11 are negligible.^{47,49,53} However, DeMore et al.²³ point out that "even though isomer formation seems to have been ruled out for the ClO + NO₂ reaction (i.e. the isomer stability is too low to make a significant contribution to the measured rate constant), this does not eliminate the possibility that BrO + NO₂ leads to more than one stable compound. In fact, if the measured low pressure limit rate constant for BrO + NO₂ is accepted, it can only be theoretically reconciled with

(40) Zahniser, M. S.; Chang, J. S.; Kaufman, F. *J. Chem. Phys.* 1977, 67, 997.

(41) Birks, J. W.; Shoemaker, B.; Leck, T. J.; Borders, R. A.; Hart, L. J. *J. Chem. Phys.* 1977, 66, 4591.

(42) Leu, M. T.; Lin, C. E.; DeMore, W. B. *J. Phys. Chem.* 1977, 81, 190.

(43) Knauth, H. D. *Ber. Bunsen-Ges. Phys. Chem.* 1978, 82, 212.

(44) Molina, M. J.; Molina, M. T.; Iriwata, T. *J. Phys. Chem.* 1980, 84, 3100.

(45) Cox, R. A.; Lewis, R. J. *J. Chem. Soc., Faraday Trans. 1* 1979, 75, 2649.

(46) Dasch, W.; Sternberg, H.; Schindler, R. N. *Ber. Bunsen-Ges. Phys. Chem.* 1981, 85, 611.

(47) Cox, R. A.; Burrows, J. P.; Coker, G. B. *Int. J. Chem. Kinet.* 1984, 16, 445.

(48) Handwerk, V.; Zellner, R. *Ber. Bunsen-Ges. Phys. Chem.* 1984, 88, 405.

(49) Burrows, J. P.; Griffiths, D. W. T.; Moortgat, G. K.; Tyndall, G. S. *J. Phys. Chem.* 1985, 89, 266.

(50) Wallington, T. J.; Cox, R. A. *J. Chem. Soc., Faraday Trans. 2* 1966, 82, 275.

(51) Danis, F.; Caralp, F.; Masanel, J.; Lesclaux, R. *Chem. Phys. Lett.*, in press.

(52) Thorn, R. P.; Daykin, E. P.; Wine, P. H. To be published.

(53) Margitan, J. J. *J. Geophys. Res.* 1983, 88, 5416.

a single isomer, BrONO_2 , which would have a 6–7 kcal mole⁻¹ stronger bond than ClONO_2 . This would fix the heat of formation of BrONO_2 to be the same as ClONO_2 , an unlikely possibility." A similar situation exists when comparing the measured low-pressure limit rate coefficient for $\text{IO} + \text{NO}_2$ with that for $\text{ClO} + \text{NO}_2$. Clearly, the thermochemistry of XONO_2 ($\text{X} = \text{Br}, \text{I}$) requires further investigation, as does the possible formation of

isomers such as OXNO_2 , XOONO , or OXONO .

Acknowledgment. This work was supported through Grant ATM-88-02386 from the National Science Foundation and Grant NAGW-1001 from the National Aeronautics and Space Administration.

Registry No. IO, 14696-98-1; NO, 10102-43-9; NO_2 , 10102-44-0.

K-10.1

NDB
314-25
026132
16P.
273554

Kinetics of the Reactions of $\text{Cl}(^2P_J)$ and $\text{Br}(^2P_{3/2})$ with O_3

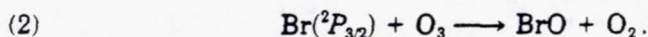
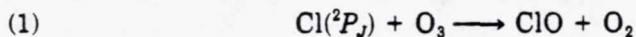
J. M. NICOVICH, K. D. KREUTTER, and P. H. WINE

Molecular Sciences Branch, Georgia Tech Research Institute, Georgia Institute of Technology, Atlanta, Georgia 30332

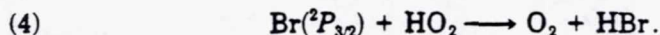
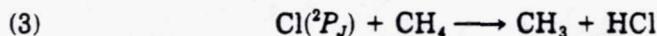
Abstract

A laser flash photolysis-resonance fluorescence technique has been employed to study the kinetics of the important stratospheric reactions $\text{Cl}(^2P_J) + \text{O}_3 \rightarrow \text{ClO} + \text{O}_2$ and $\text{Br}(^2P_{3/2}) + \text{O}_3 \rightarrow \text{BrO} + \text{O}_2$ as a function of temperature. The temperature dependence observed for the $\text{Cl}(^2P_J) + \text{O}_3$ reaction is nonArrhenius, but can be adequately described by the following two Arrhenius expressions (units are $\text{cm}^3 \text{ molecule}^{-1} \text{ s}^{-1}$, errors are 2σ and represent precision only): $k_1(T) = (1.19 \pm 0.21) \times 10^{-11} \exp[(-33 \pm 37)/T]$ for $T = 189\text{--}269\text{ K}$ and $k_1(T) = (2.49 \pm 0.38) \times 10^{-11} \exp[(-233 \pm 46)/T]$ for $T = 269\text{--}385\text{ K}$. At temperatures below 230 K, the rate coefficients determined in this study are faster than any reported previously. Incorporation of our values for $k_1(T)$ into stratospheric models would increase calculated ClO levels and decrease calculated HCl levels; hence the calculated efficiency of ClO_x catalyzed ozone destruction would increase. The temperature dependence observed for the $\text{Br}(^2P_{3/2}) + \text{O}_3$ reaction is adequately described by the following Arrhenius expression (units are $\text{cm}^3 \text{ molecule}^{-1} \text{ s}^{-1}$, errors are 2σ and represent precision only): $k_2(T) = (1.50 \pm 0.16) \times 10^{-11} \exp[(-775 \pm 30)/T]$ for $T = 195\text{--}392\text{ K}$. While not in quantitative agreement with Arrhenius parameters reported in most previous studies, our results almost exactly reproduce the average of all earlier studies and, therefore, will not affect the choice of $k_2(T)$ for use in modeling stratospheric BrO_x chemistry.

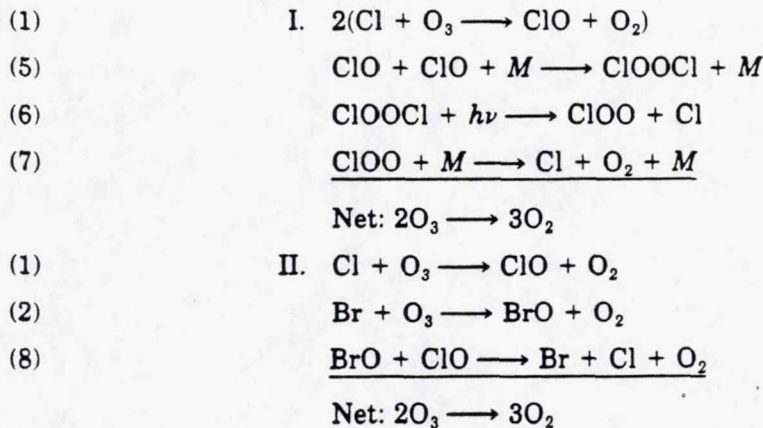
Catalytic cycles involving ClO_x and BrO_x species play an important role in stratospheric chemistry [1,2]. In most catalytic destruction cycles involving ClO_x and BrO_x , ozone is destroyed by the reactions



Although recycling of halogen monoxide radicals back to halogen atoms is rate-limiting under conditions which typically exist in the stratosphere, quantitative characterization of the kinetics of reactions (1) and (2) is nonetheless important because catalytic efficiencies are influenced by the competition between reactions (1) and (2) and reservoir-forming reactions such as



In recent years, two catalytic cycles involving ClO_x and BrO_x species have been implicated in the formation of the antarctic ozone hole [3,4]:



In the wintertime antarctic lower stratosphere, heterogeneous reactions in polar stratospheric clouds (PSCs) can convert the reservoir species HCl and ClONO₂ into the photolytically labile species Cl₂ and HOCl [5,6], which photolyze rapidly in springtime to generate chlorine atoms. In this manner, high levels of ClO are produced at the expense of HCl and ClONO₂. Reactions on PSCs may also result in production of BrO from HBr and BrONO₂ although, since BrO is thought to predominate over the reservoir species in the "normal" stratosphere [7], the effect of heterogeneous reactions on BrO_x chemistry is expected to be much smaller than the effect on ClO chemistry. Under the NO_x free conditions typical of the antarctic ozone hole, conversion of XO to X (X = Cl or Br) via reaction with NO ceases to occur, so reactions (5) and (8) become the principal mechanisms for cycling XO back to X. Hence, a photochemical steady state is established where the rates of reactions (1) and (2) become comparable to the rates of reactions (5) and (8).

A number of kinetics studies of both reaction (1) [8–14] and reaction (2) [14–19] are reported in the literature. At 298 K, there is excellent agreement between the various studies, such that the estimated uncertainties in $k_1(298 \text{ K})$ and $k_2(298 \text{ K})$ are only $\pm 15\%$ and $\pm 20\%$, respectively [20]. However, there is considerable scatter in reported activation energies for both reactions, leading to substantial uncertainties in both k_1 and k_2 at temperatures typical of the lower stratosphere. In this article we report the results of temperature dependent kinetics studies of reactions (1) and (2) over the temperature ranges 189–385 K and 195–392 K, respectively; particular attention was focused on obtaining accurate kinetic data near the low temperature end of the ranges studied. We find that extrapolation of previously reported Arrhenius expressions for $k_2(T)$ to lower temperature predicts rate coefficients in reasonable agreement with our measurements. However, the temperature dependence for k_1 observed in our study is quite different from any reported previously. Our measured value for $k_1(190\text{K})$ is significantly faster than would be predicted based on extrapolation of earlier measurements of $k_1(T)$.

Experimental Technique

The laser flash photolysis-resonance fluorescence apparatus used in this study was similar to one which we have employed previously in a number

of studies of chlorine atom kinetics [21–25] and one study of bromine atom kinetics [26]. Important features of the apparatus are described below.

A pyrex, jacketed reaction cell with an internal volume of 150 cm³ was used in all experiments. The cell was maintained at a constant temperature by circulating ethylene glycol or a 1:1 methanol-ethanol mixture from a thermostated bath through the outer jacket. A copper-constantan thermocouple with a stainless steel jacket could be injected into the reaction zone through a vacuum seal, thus allowing measurement of the gas temperature under the precise pressure and flow rate conditions of the experiment. Temperature variation within the reaction volume (i.e., the volume from which fluorescence could be detected) was less than 1 K at both the high and low temperature extremes of the study.

In most experiments halogen atoms (*X*) were produced by 355 nm pulsed laser photolysis of *X*₂. Third harmonic radiation from either a Quanta Ray model DCR-2 or a Quantel model 481-A Nd:YAG laser provided the photolytic light source. These lasers could deliver up to 1×10^{17} photons per pulse at a repetition rate of up to 10 Hz; pulsewidths were about 6 ns. In some experiments chlorine atoms were produced by 193 nm pulsed laser photolysis of CF₂Cl₂. A Lambda Physik model EMG-200 ArF excimer laser was used as the photolytic light source. The excimer laser could deliver up to 4×10^{17} 193 nm photons per pulse at a repetition rate of up to 10 Hz; the laser pulsewidth was about 15 ns.

An atomic resonance lamp, situated perpendicular to the photolysis laser, excited resonance fluorescence in the photolytically produced atoms. The resonance lamp consisted of an electrodeless microwave discharge through about one torr of a flowing mixture containing a trace of *X*₂ in He. The flows of a 0.1% *X*₂ in He mixture and pure He into the lamp were controlled by separate needle valves, thus allowing the total pressure and *X*₂ concentration to be adjusted for optimum signal-to-noise. Radiation was coupled out of the lamp through a magnesium fluoride window and into the reaction cell through a magnesium fluoride lens. Before entering the reaction cell the lamp output passed through a flowing gas filter. For detection of bromine atoms, the filter gas was 50 torr-cm CH₄ in N₂; this filter prevented radiation at wavelengths shorter than 139 nm (including impurity emissions from excited O, H, Cl, and N atoms) from entering the reaction cell, but transmitted the strong Br lines in the 140–160 nm region. For detection of chlorine atoms, the filter gas was normally 3 torr-cm N₂O in N₂; this filter blocked virtually all O atom impurity emissions at 130–131 nm while transmitting the chlorine lines in the 135–140 nm wavelength region. In some experiments, N₂ or dry air were used as the chlorine lamp filter. The only chlorine atom resonance lines transmitted through 760 torr-cm of air are the ²D_{5/2,3/2} – ²P_{3/2} doublet at 118.9 nm [27]. For both chlorine and bromine, fluorescence intensities were found to vary linearly with atom concentration up to levels several times higher than any employed in kinetics experiments ($[Br]_0 \leq 6 \times 10^{11}$ per cm³ and $[Cl]_0 \leq 8 \times 10^{11}$ per cm³ in all experiments).

Fluorescence was collected by a magnesium fluoride lens on an axis orthogonal to both the photolysis laser beam and the resonance lamp beam, and imaged onto the photocathode of a solar blind photomultiplier. The region between the reaction cell and the photomultiplier was purged with N₂. For detection of chlorine atoms in conjunction with N₂O/N₂ or pure N₂

lamp filters, a calcium fluoride window was placed between the reaction cell and the photomultiplier to prevent detection of emissions at wavelengths shorter than 125 nm (Lyman- α emission, for example). Signals were processed using photon counting techniques in conjunction with multi-channel scaling. For each halogen atom decay measured, signals from a large number of laser shots were averaged in order to obtain a well-defined temporal profile over (typically) three $1/e$ lifetimes of decay. The multi-channel analyzer sweep was triggered prior to the photolysis laser in order to allow a pre-trigger baseline to be obtained.

In order to avoid the accumulation of photolysis or reaction products, all experiments were carried out under "slow flow" conditions. The linear flow rate through the reactor was 2–3 cm s⁻¹ while the laser repetition rate was varied over the range 1–10 Hz. Even at the highest repetition rate employed, no volume element of the reaction mixture was subjected to more than a few laser shots. Cl₂, CF₂Cl₂, Br₂, and O₃ were flowed into the reaction cell from 12 liter bulbs containing dilute mixtures in nitrogen buffer gas. Hydrogen and nitrogen were flowed directly from their high pressure storage tanks. In most experiments, all components of the reaction mixtures were premixed before entering the reaction cell. As a check for the possible occurrence of heterogeneous reactions between X₂ and O₃, some experiments were carried out in a configuration where X₂ was injected into the reaction cell through a 1/8 inch O.D. teflon tube positioned such that X₂ mixed with other components in the reaction mixture about 2 cm upstream from the reaction zone. Concentrations of each component in the reaction mixtures were determined from measurements of the appropriate mass flow rates and the total pressure. The O₃ concentration was also measured *in situ* in the slow flow system by UV photometry at 253.7 nm using a 2-meter long absorption cell; the O₃ absorption cross section required to convert measured absorbances to concentrations was taken to be 1.146×10^{-17} cm² [28–31]. In most Cl + O₃ experiments the absorption cell was positioned downstream from the reaction cell. However, to check for O₃ loss in the flow system, some experiments were carried out with the absorption cell positioned upstream from the reactor. The Br + O₃ experiments employed two absorption cells, one upstream and one downstream from the reactor.

The stable, pure gases used in this study had the following stated minimum purities: N₂, 99.999%; Cl₂, 99.99%; CF₂Cl₂, 99.0%; O₂, 99.99%; H₂, 99.999%. Nitrogen, oxygen, and hydrogen were used as supplied while chlorine and CF₂Cl₂ were degassed repeatedly at 77 K before use. Bromine was Fisher ACS reagent grade with a maximum impurity level of 0.06%; it was transferred into a vial fitted with a high vacuum stopcock, then degassed repeatedly at 77 K before use. Ozone was prepared in a commercial ozonator using UHP oxygen. It was collected and stored on silica gel at 195 K, and degassed at 77 K before use.

Results and Discussion

To study the kinetics of reactions (1) and (2) it is desirable to establish experimental conditions where the X(²P_J) temporal profile is governed entirely by the following processes:

- (9) $RX + h\nu \longrightarrow R + X(^2P_J)$
 (i) $X(^2P_J) + O_3 \longrightarrow XO + O_2 \quad i = 1 \text{ or } 2$
 (10) $X(^2P_J) \longrightarrow$ first order loss by diffusion from the
 detector field of view or reaction
 with background impurities

Then, since $[O_3] \gg [X(^2P_J)]$, simple first-order kinetics are obeyed:

$$(1) \quad \ln\{[X(^2P_J)]_0/[X(^2P_J)]_t\} = (k_i[O_3] + k_{10})t = k't.$$

The bimolecular rate coefficients, $k_i(T)$, are determined from the slopes of k' vs. $[O_3]$ plots. Observations of $X(^2P_J)$ temporal profiles which are exponential (i.e., obey equation 1), a linear dependence of k' on $[O_3]$, and invariance of k' to variations in laser photon fluence and RX concentration strongly suggests that reactions (i), (9), and (10) are the only processes which affect the $X(^2P_J)$ time history. Typical $[Br(^2P_{3/2})]$ temporal profiles and k' vs. $[O_3]$ plots for data from our study of reaction (2) are shown in Figures 1 and 2. Results for reactions (1) and (2) are discussed separately below.

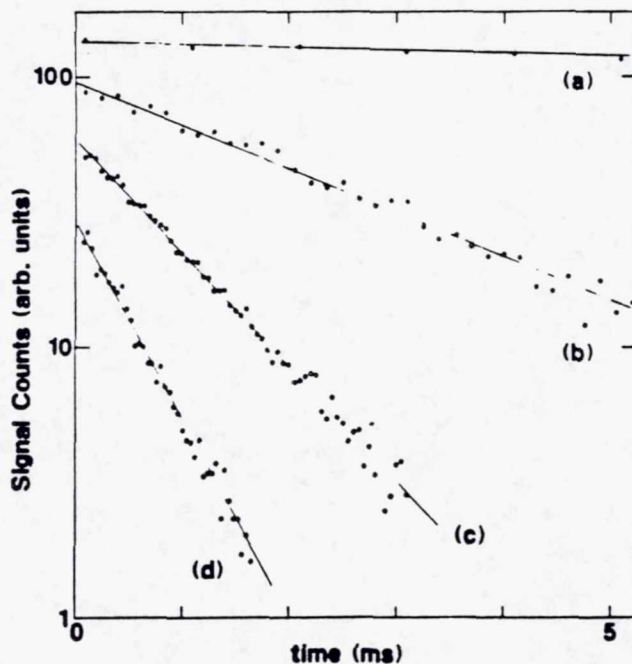


Figure 1. Typical halogen atom temporal profiles. Reaction: $Br(^2P_{3/2}) + O_3 \longrightarrow BrO + O_2$. Experimental conditions: $T = 201 \text{ K}$; $P = 150 \text{ torr}$; $[Br_2] = 3.8 \times 10^{13} \text{ molecules per cm}^3$; laser fluence = 11 mjoules per cm^2 ; $[O_3]$ in units of $10^{15} \text{ molecules per cm}^3 =$ (a) 0, (b) 1.04, (c) 3.29, (d) 5.43; number of laser shots averaged = (a) 64, (b) 128, (c) 926, (d) 1100. Solid lines are obtained from least squares analyses and give the following pseudo-first order decay rates in units of s^{-1} : (a) 25, (b) 376, (c) 979, (d) 1700.

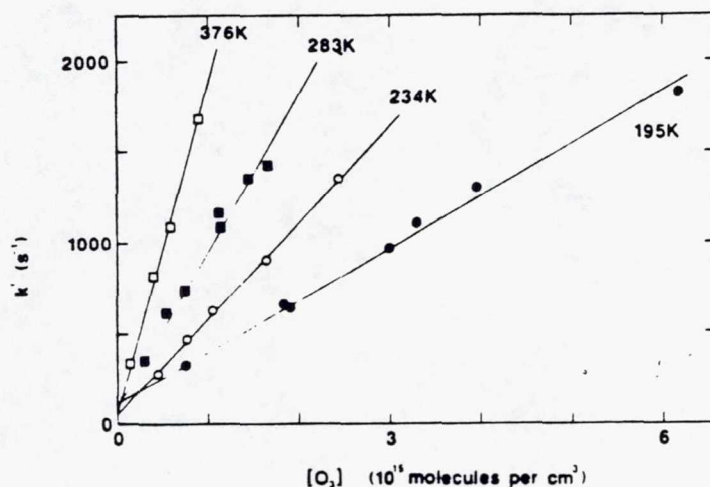


Figure 2. Typical plots of k' , the pseudo-first order halogen atom decay rate, as a function of ozone concentration. Reaction: $\text{Br}(^2P_{1/2}) + \text{O}_3 \rightarrow \text{BrO} + \text{O}_2$. For the sake of clarity, data points obtained with $[\text{O}_3] = 0$ are not shown. Solid lines are obtained from linear least squares analyses and give the following bimolecular rate coefficients in units of $10^{-13} \text{ cm}^3 \text{ molecule}^{-1} \text{ s}^{-1}$ (errors are 2σ , precision only): 195 K, 2.89 ± 0.19 ; 234 K, 5.41 ± 0.18 ; 283 K, 8.64 ± 0.93 ; 376 K, 18.1 ± 1.2 .

A. The Cl + O₃ Reaction

Most experiments in our study of reaction (1) employed 355 nm photolysis of Cl₂ as the Cl(²P_J) source. Ozone in its ground vibrational state is totally transparent at 355 nm [32]. The N₂ levels employed were sufficiently high that relaxation of atoms in the ²P_{1/2} spin-orbit excited state was expected to be much more rapid than the rate of chemical removal of Cl(²P_J) [33, 34]. Hence, all measured chlorine atom temporal profiles should be considered as representative of the removal of an equilibrium mixture of Cl(²P_{3/2}) and Cl(²P_{1/2}). As an experimental check on the above argument, some experiments were carried out with CF₂Cl₂, a species which deactivates Cl(²P_{1/2}) at a gas kinetic rate [35], added to the Cl₂/O₃/N₂ photolysis mixtures. Addition of 2×10^{15} CF₂Cl₂ per cm³ had no effect on the observed kinetics of reaction (1). Over the temperature range investigated (189–385 K), the equilibrium fraction of chlorine atoms in the ²P_{1/2} state ranges from 0.0012 to 0.037.

A total of about 300 Cl(²P_J) temporal profiles were measured under a wide variety of experimental conditions. The results used to obtain values for $k_1(T)$ are summarized in Table I. All experiments were consistent with equation 1, i.e., all decays were exponential and, in a given set of experiments, k' increased linearly with increasing ozone concentration. The observed kinetics were unaffected by significant variations in laser repetition rate, Cl₂ concentration, the concentration of photolytically produced atoms, and the distance in the flow system over which Cl₂ and O₃ were allowed to interact before entering the reaction zone. In preliminary experiments (not summarized in Table I) it was established that ozone was not lost during

TABLE I. Summary of kinetic data for the reaction $\text{Cl}(^2P_j) + \text{O}_3 \rightarrow \text{ClO} + \text{O}_2$ ^a

T/K	P/Torr	Cl Precursor (conc. $\times 10^{11} \text{ cm}^{-3}$)	[Cl] (10^{11} cm^{-3})	N ^c	k_{obs}^d (s^{-1})	$10^3 k_{\text{obs}} \pm 2\sigma$ ($\text{cm}^3 \text{ molecule}^{-1} \text{ s}^{-1}$)	Notes
189	30	Cl ₂ 7	5	5	3410	9.66 ± 0.29	
189	30	Cl ₂ 7	5	4	2760	9.83 ± 0.28	d
192	50	Cl ₂ 7	4	5	1680	8.98 ± 0.60	
193	30	Cl ₂ 6	3	9	4570	10.3 ± 0.4	e
193	30	Cl ₂ 18	3	5	2980	10.0 ± 0.6	
194	60	Cl ₂ 4	1.2	4	3980	11.2 ± 0.6	
196	200	Cl ₂ 1	3	9	1600	10.6 ± 0.8	f
198	200	Cl ₂ 8	8	13	10100	9.9 ± 0.91	f,g
199	150	Cl ₂ 14	3	5	2600	9.95 ± 0.16	g
204	30	CF ₂ Cl ₂ 80	0.4-2	8	2300	10.1 ± 1.5	
207	200	Cl ₂ 11	3	7	1560	9.56 ± 0.93	f
210	30	CF ₂ Cl ₂ 90	1.4	10	2510	9.98 ± 0.47	
215	200	Cl ₂ 6	2	6	1960	11.1 ± 1.2	f
215	150	Cl ₂ 13	3	6	3360	10.4 ± 0.7	g
217	200	Cl ₂ 0.3-2	2	18	2020	10.3 ± 0.8	f
220	30	Cl ₂ 5	5	4	2260	9.90 ± 0.20	
220	30	Cl ₂ 5	5	4	2320	10.1 ± 0.1	d
228	150	Cl ₂ 15	3	4	2730	10.3 ± 0.2	g
235	50	Cl ₂ 15	6	9	1690	10.2 ± 0.4	f
236	150	Cl ₂ 5	5	4	2020	10.0 ± 0.4	
248	200	Cl ₂ 2	4	5	1690	10.6 ± 1.0	f
249	200	Cl ₂ 10	3	7	1860	10.3 ± 0.7	f
251	200	Cl ₂ 2.5	5	7	1960	10.6 ± 0.7	f
262	50	Cl ₂ 12	6	8	1900	10.6 ± 0.4	
263	150	Cl ₂ 11	2	8	2360	10.3 ± 0.7	
284	300	Cl ₂ 7	4	4	1430	10.9 ± 0.8	
295	150	Cl ₂ 4	4	7	3060	11.4 ± 0.5	d
295	30	CF ₂ Cl ₂ 90	0.4-2	8	1870	11.3 ± 0.4	
298	30	CF ₂ Cl ₂ 90	0.3-0.9	7	2670	11.2 ± 0.8	
298	100	Cl ₂ 2	2	6	5940	11.1 ± 0.3	g
300	200	Cl ₂ 8	4.8	9	1290	11.8 ± 0.8	
342	200	Cl ₂ 1.5	3	7	1960	12.9 ± 0.6	f
385	200	Cl ₂ 2	4	7	1520	13.7 ± 0.6	f

^a Unless otherwise indicated, the purge gas between the resonance lamp and reactor was a dilute $\text{N}_2\text{O}/\text{N}_2$ mixture and the gas flows were combined in a mixing chamber upstream from the reactor. The linear flow rate through the reactor was $2\text{--}3 \text{ cm s}^{-1}$ in all experiments and the laser repetition rate was varied over the range $1\text{--}10 \text{ Hz}$. Nitrogen was used as the buffer gas in all experiments. The background $\text{Cl}(^2P_j)$ decay rate was typically 35 s^{-1} .

^b Photolysis wavelengths were 355 nm for Cl_2 and 193 nm for CF_2Cl_2 .

^c N = number of individual pseudo-first order decay rates measured.

^d $2 \times 10^{15} \text{ CF}_2\text{Cl}_2$ per cm^3 added to reaction mixture to facilitate equilibration of the $\text{Cl}(^2P_j)$ spin-orbit states.

^e Volume between resonance lamp and reactor purged with dry air.

^f Cl_2 injected into O_3/N_2 flow just upstream from the reaction zone.

^g Volume between resonance lamp and reactor purged with N_2 .

traversal through the flow system, i.e., ozone concentrations measured upstream and downstream from the reaction zone were identical. The observed kinetics were also found to be independent of the $\text{Cl}(^2P_j)$ photolytic source reaction (355 nm photolysis of Cl_2 or 193 nm photolysis CF_2Cl_2) and independent of whether $\text{N}_2\text{O}/\text{N}_2$, N_2 , or dry air was purged through the

volume between the resonance lamp and the reactor; these variations suggest that reactions and/or inadvertent detection of interfering radicals, such as $O(^3P_j)$ for example, did not result in systematic errors in our measurements.

The results in Table I show that k_1 is independent of pressure and only weakly dependent on temperature. An Arrhenius plot for reaction (1) is shown in Figure 3. Despite the rather small variation of k_1 as a function of temperature, the $\ln k_1$ vs. T^{-1} plot is clearly nonlinear, i.e., the activation energy for reaction (1) is larger at higher temperature. Arrhenius parameters can be used to describe the temperature dependence of k_1 if two separate temperature regimes are considered:

$$k_1(T) = (1.19 \pm 0.21) \times 10^{-11} \exp[(-33 \pm 37)/T] \quad 189 \text{ K} \leq T \leq 263 \text{ K}$$

$$k_1(T) = (2.49 \pm 0.38) \times 10^{-11} \exp[(-233 \pm 46)/T] \quad 262 \text{ K} \leq T \leq 385 \text{ K}$$

Units in the above expressions are $\text{cm}^3 \text{ molecule}^{-1} \text{ s}^{-1}$ and errors are 2σ , precision only. The absolute uncertainty (2σ) in $k_1(T)$ calculated from the above expressions is estimated to be $\pm 15\%$ independent of temperature. This error estimate is based on the precision of our rate coefficients (Table I), estimates of possible systematic errors (primarily in the ozone concentration determination), and the ability of the above Arrhenius expressions to reproduce the experimental data; the precision of the derived A-factors and activation energies suggest uncertainties in $k_1(T)$ values which we believe to be unrealistically high. It should be noted that data at $T = 262 \text{ K}$ and

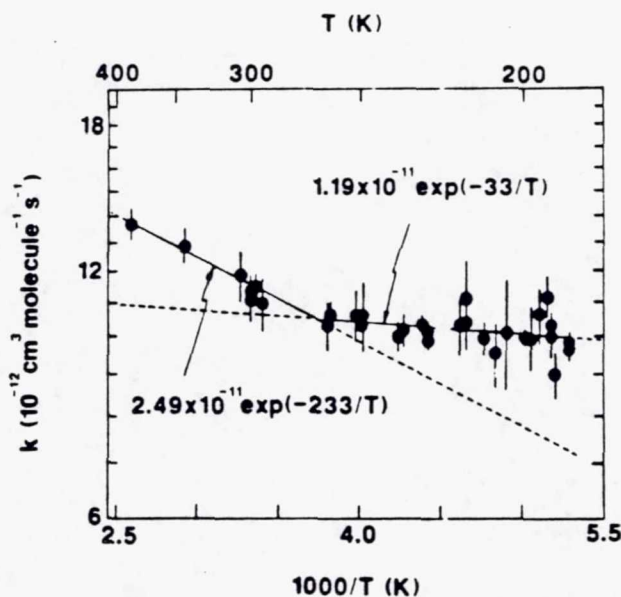


Figure 3. Arrhenius plot for the reaction $\text{Cl}(^2P_j) + \text{O}_3 \rightarrow \text{ClO} + \text{O}_2$. Solid lines are obtained from unweighted least squares analyses of data over the temperature ranges 189–263 K and 262–385 K.

263 K were used to obtain both of the above Arrhenius expressions; the values of k_1 (262.5 K) predicted by the two expressions differ by 2.5%. The two expressions give exactly equal rate coefficients at $T = 269$ K, so this would be the best temperature to switch from use of one expression to the other.

Our rate coefficient determinations for reaction (1) are compared with those reported by other investigators in Table II. Error estimates are not included in the Table because comparing reported errors from different labs can often be misleading. For a majority of the studies summarized in Table I, 2σ error limits appear to be around 15–20% for $k_1(T)$ at any temperature within the range investigated. The discharge flow-mass spectrometry studies of Clyne and Watson [8] and Leu and DeMore [12] required an absolute calibration for the unstable species $\text{Cl}(^2P_J)$; the error limits in these studies are about $\pm 30\%$. The rate coefficients reported by Clyne and Nip [9] also have error limits of about $\pm 30\%$ due to somewhat larger scatter in the data than was observed in other studies. With the exception of the faster rate coefficient reported by Clyne and Watson [8] and the somewhat slower rate coefficient reported by Kurylo and Braun [11], reported values for $k_1(298 \text{ K})$ fall within the narrow range $(1.22 \pm 0.08) \times 10^{-11} \text{ cm}^3 \text{ molecule}^{-1} \text{ s}^{-1}$. It is interesting to note, however, that the three studies which employed flash photolysis techniques (this work along with refs. [11] and [13]) obtained the three lowest reported values for $k_1(298 \text{ K})$, suggesting the presence of a small but significant systematic error in either the flash photolysis method or the discharge flow method. The source of such an error is not readily identifiable, although it is possible that some studies could have been affected by $\text{Cl}(^2P_J)$ or O_3 removal and/or re-

TABLE II. Comparison of our results for the reaction $\text{Cl}(^2P_J) + \text{O}_3 \rightarrow \text{ClO} + \text{O}_2$ with results reported by other investigators.

Investigators	Technique ^a	Range of T:K	$k_1 \cdot 10^{-12} \text{ cm}^3 \text{ molecule}^{-1} \text{ s}^{-1}$, b,c		
			298K	230K	190K
Clyne & Watson [8]	DF-MS	298	18.5		
Clyne & Nip [9]	DF-RA	221-629	12.7	6.4	5.7*
Zahniser, et al. [10]	DF-RF	210-360	12.2	10.3	8.8*
Kurylo & Braun [11]	FP-RF	213-298	10.1	7.4	5.7*
Leu & DeMore [12]	DF-MS	295	13		
Watson, et al. [13]	FP-RF	220-350	11.6	8.7	6.7*
Toohy, et al. [14]	DF-RF	298	13		
This Work	LFP-RF	189-385	11.4	10.3	10.0
NASA Panel [20]			12.1	9.4	7.4
IUPAC Panel [41]			11.4	8.8	7.0

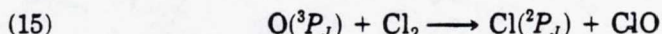
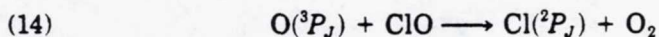
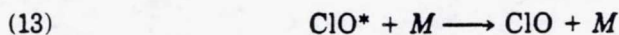
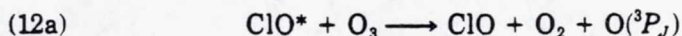
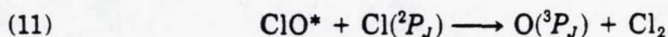
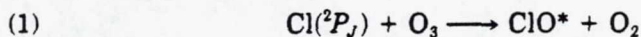
^a DF: discharge flow; FP: flash photolysis; LFP: laser flash photolysis; MS: mass spectrometry; RA: resonance absorption; RF: resonance fluorescence.

^b Where T -dependent data is reported, rate coefficients are calculated from Arrhenius expressions.

^c Error estimates are discussed in the text.

* Obtained by extrapolation of more than a factor of 1.1 in $1/T$.

generation resulting from reactions of the vibrationally excited ClO (ClO*) produced in reaction (1) [36]:



It has been observed experimentally that reaction (1) can lead to production of O(³P_J) [37–40], and reaction (11) has been identified as a probable O(³P_J) source under conditions of high [Cl(²P_J)] [38–40]. We have shown previously [39] that O(³P_J) production via the above chemistry is greatly suppressed at high N₂ pressures, presumably because reaction (13) becomes dominant over reactions (11) and (12). Hence, our observation that $k_1(T)$ is independent of pressure over the range 30–300 torr N₂ strongly suggests that the above chemistry did not affect our measurements.

While reported values for $k_1(298 \text{ K})$ are in quite good agreement, the scatter in reported and/or extrapolated rate coefficients increases with decreasing temperature. At temperatures below 230 K, the values for $k_1(T)$ reported in this study are higher than any reported previously. As shown in Table I, our measured value of $10.0 \times 10^{-12} \text{ cm}^3 \text{ molecule}^{-1} \text{ s}^{-1}$ for $k_1(190 \text{ K})$ is a factor of 1.4 faster than current "recommendations" [20,41], and agrees within combined error limits only with the (extrapolated) result of the discharge flow study of Zahniser et al. [10].

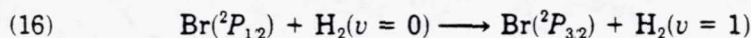
Incorporation of our results into models of stratospheric chemistry would increase the steady state fraction of ClO_x existing as ClO and reduce the fraction existing as the unreactive reservoir HCl; hence, model calculations aimed at reproducing ClO measurement data would predict higher ClO levels if our values for $k_1(T)$ were used in place of currently recommended values [20,41]. Our values for $k_1(T)$ would increase the calculated efficiency of chlorine catalyzed ozone destruction in modeling studies where ClO levels are calculated from analysis of production and loss terms. However, in some calculations of chlorine catalyzed ozone depletion, attempts are made to reproduce observed ClO levels by adjusting the total available inorganic chlorine; predictions from these models should be relatively insensitive to changes in $k_1(T)$.

Toohy et al. [14] have recently shown that rate coefficients for the reactions of O₃ with Br, Cl, F, O, and N atoms and OH radicals correlate with the electron affinities of the radicals, a correlation which leads these authors to suggest that X + O₃ reactions proceed through early transition states dominated by transfer of electron density from the highest occupied molecular orbital of ozone to the singly occupied molecular orbital of the radical. A semi-empirical ClO₃ potential energy surface has been constructed by Farantos and Murrell [42] which also suggests an early transition state for the collinear collision (Cl—O bond distance about 2.5 Å).

Farantos and Murrell [42] found no evidence for long-lived complex formation along the collinear pathway, but it does not appear that the possibility of energetically favorable insertion pathways was examined in detail by these authors. One possible explanation for the nonArrhenius temperature dependence observed in our study of reaction (1) is that a weak minimum exists in the potential energy surface for $\text{Cl}(^2P_J)$ insertion into an O—O bond of ozone, thus permitting formation of a long-lived OCIOO^* complex whose decomposition to $\text{ClO} + \text{O}_2$ makes a significant contribution to the overall reaction rate at low temperatures. However, a matrix isolation study of reaction (1) failed to observe evidence for any ClO_3 isomers [43]. As suggested by Toohey et al. [14], *ab-initio* studies of $X + \text{O}_3$ reaction dynamics would certainly be a worthwhile endeavor.

B. The $\text{Br} + \text{O}_3$ Reaction

In our study of reaction (2), 355 nm photolysis of Br_2 was employed as the $\text{Br}(^2P_J)$ source. Both theoretical [44] and experimental [45] information suggest that virtually all bromine atoms are produced in the $^2P_{3/2}$ ground state. To insure rapid relaxation of any photolytically generated $\text{Br}(^2P_{1/2})$, about 2 torr of H_2 was added to the reaction mixture. The reaction



is known to be fast, with $k_{16} \approx 6 \times 10^{-12} \text{ cm}^3 \text{ molecule}^{-1} \text{ s}^{-1}$ [46]. Since the equilibrium concentration of $\text{Br}(^2P_{1/2})$ is negligible over the temperature regime of our study, all measured bromine atom temporal profiles should be considered as representative of removal of ground state atoms, $\text{Br}(^2P_{3/2})$.

A total of about 250 $\text{Br}(^2P_{3/2})$ temporal profiles were measured under a wide variety of experimental conditions. The results used to determine values for $k_2(T)$ are summarized in Table III. All experiments summarized in Table III were consistent with equation I, i.e., all decays were exponential and, in a given set of experiments, k' increased linearly with increasing ozone concentration. The observed kinetics were unaffected by significant variations in Br_2 concentration, the concentration of photolytically produced atoms, and the distance in the flow system over which Br_2 and O_3 were allowed to interact before entering the reaction zone. In all experiments summarized in Table III, ozone concentrations were measured both upstream and downstream of the reaction cell; no evidence for ozone loss in the flow system was observed except at 392 K where the downstream ozone concentration was typically 10% lower than the upstream concentration, even when $\text{O}(^3P_J)$ production was minimized (see below). At 392 K, the ozone concentration in the reaction zone was taken to be the average of the upstream and downstream concentrations.

In preliminary experiments (not summarized in Table III), nonexponential decays were observed at high temperatures and under conditions where the ratio $[\text{O}_3]/[\text{Br}_2]$ was relatively high. The observed deviation from the prediction of equation I is attributed to $\text{Br}(^2P_{3/2})$ regeneration via the following mechanism:

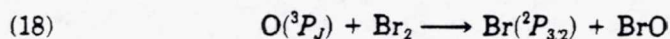
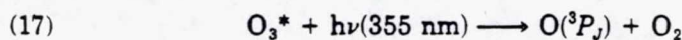


TABLE III. Summary of kinetic data for the reaction $\text{Br}(^2P_{3/2}) + \text{O}_3 \rightarrow \text{BrO} + \text{O}_2$.^a

T(K)	P(Torr)	$[\text{Br}_2](10^{11} \text{ cm}^{-3})$	$[\text{Br}](10^{11} \text{ cm}^{-3})$	N	$k_{\text{meas}}(s^{-1})$	$10^{11} k_2 \pm 2\sigma$ ($\text{cm}^3 \text{ molecule}^{-1} \text{ s}^{-1}$)
195	150	2.7	0.6-2	9	1830	2.89 ± 0.19
201	150	4	1.2	10	1410	3.15 ± 0.28
223	150	2.4	0.9-1.7	6	1290	4.81 ± 0.13
224	150	4	1.0	9	1970	4.82 ± 0.40
232	150	2.5	0.8-1.3	6	511	4.99 ± 0.80
234	150	4	1.4	6	1350	5.41 ± 0.18
246	150	2.6	0.8-2	8	999	6.59 ± 0.36
248	150	4	1.0	5	853	6.38 ± 0.36
262	150	4	1.5	5	1170	8.11 ± 0.40
283	150	3.7	0.9-2	8	1420	8.64 ± 0.93
298	30	5	1.6	5	1080	10.2 ± 0.6
298	100	4-14	2-6	13	2270	11.3 ± 0.7
298	150	3-11	1.5	9	1460	11.3 ± 0.7
298	150	2-10	0.8-3	6	1220	10.9 ± 0.7
298	150	4	1.6	8	1840	11.0 ± 0.3
298	300	4	1.6	6	888	11.3 ± 0.7
328	150	1.3-5	0.6-2	13	2150	14.4 ± 0.5
347	150	2-6	1-3	8	1390	14.7 ± 0.7
352	150	4-9	1.3-3	6	1440	17.8 ± 1.1
365	150	4	1.6	7	2460	18.0 ± 1.0
376	150	5	2	5	1680	18.1 ± 1.2
386	150	14	4	7	1920	20.8 ± 0.9
392	150	13-39	4	6	1670	22.6 ± 0.8

^aThe purge gas between the resonance lamp and reactor was 5% CH_4 in N_2 . The linear flow rate through the reactor was 2-3 cm s^{-1} and the laser repetition rate was 1 Hz in all experiments. Nitrogen was used as the buffer gas in all experiments. The background $\text{Br}(^2P_{3/2})$ decay rate was typically 30 s^{-1} . The photolysis wavelength was 355 nm.

^bN = number of individual pseudo-first order decay rates measured.

Reaction (18) is quite fast, i.e., k_{18} ca. $2 \times 10^{-11} \text{ cm}^3 \text{ molecule}^{-1} \text{ s}^{-1}$, with little or no temperature dependence [19,47,48]. As mentioned above, ozone in its ground vibrational level is totally transparent at 355 nm [32]. However, near the high temperature extreme of our study (i.e., $T > 380 \text{ K}$), excited vibrational levels from which 355 nm absorption can occur [32] become sufficiently populated to cause the above interference. To avoid $\text{Br}(^2P_{3/2})$ regeneration, our experiments at 386 K and 392 K employed much higher Br_2 levels than normal but relatively low laser powers, such that the concentration of photolytically generated $\text{Br}(^2P_{3/2})$ was much greater than the concentration of photolytically generated $\text{O}(^3P_J)$. The only deleterious effect of these experimental conditions was to increase the background count rate due to photodissociation of Br_2 by the resonance lamp and detection of the resultant $\text{Br}(^2P_{3/2})$; this two-photon process could be minimized by operating the resonance lamp at a relatively low power level, though some signal counts were sacrificed in the process.

An Arrhenius plot for reaction (2) is shown in Figure 4. A linear least squares analysis of the $\ln k_2$ vs. T^{-1} plot gives the following Arrhenius expression in units of $\text{cm}^3 \text{ molecule}^{-1} \text{ s}^{-1}$:

$$k_2(T) = (1.50 \pm 0.16) \times 10^{-11} \exp[-(775 \pm 30)/T].$$

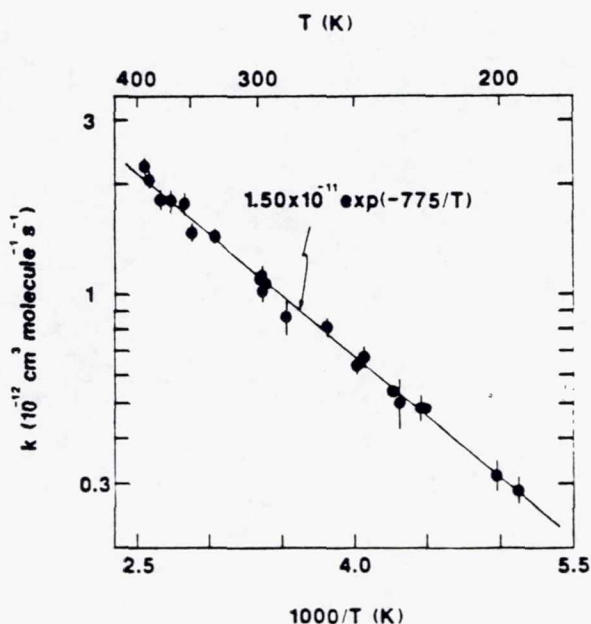


Figure 4. Arrhenius plot for the reaction $\text{Br}(^2P_{3/2}) + \text{O}_3 \rightarrow \text{BrO} + \text{O}_2$. Solid line is obtained from an unweighted least squares analysis.

Uncertainties in the above expression are 2σ and represent precision only. The absolute uncertainty in $k_2(T)$ calculated from the above expression is estimated to be $\pm 15\%$ except at 392 K where a small potential contribution from reactions (17) and (18) along with greater uncertainty in the O_3 concentration raise the estimated uncertainty in $k_2(392 \text{ K})$ to $\pm 25\%$.

Our rate coefficient determinations for reaction (2) are compared with those reported by other investigators in Table IV. As was the case for reaction (1), 2σ error limits in most previous determinations of $k_2(T)$ appear to be in the 20–30% range, although Leu and DeMore [16] report an uncertainty of $\pm 40\%$ for their lowest temperature (224 K) rate coefficient. Activation energies determined from the six temperature dependent studies of reaction (2) span the range 1.20–1.94 kcal mol⁻¹ with the discharge flow studies of Leu and DeMore [16] and Toohey et al. [14] at the high end, the flash photolysis and discharge flow studies of Michael and co-workers [17,18] at the low end, and our study along with the study of Dodonov et al. [19] in the middle. While our results are in quantitative agreement only with those of Dodonov et al., they rather fortuitously are in almost exact agreement with current panel recommendations for $k_2(T)$, which are obtained by averaging all previous results except the results of Dodonov et al. [20,41]! Hence, the values for $k_2(T)$ currently being employed to model stratospheric chemistry are in exact agreement with our measurements. It should be noted that the excellent agreement of our Arrhenius parameters with those reported by Dodonov et al., may be somewhat fortuitous since our study spans a range of $1/T$ more than four times larger than the range spanned by Dodonov et al.'s study.

TABLE IV. Comparison of our results for the reaction $\text{Br}(^2P_{3/2}) + \text{O}_3 \rightarrow \text{BrO} + \text{O}_2$ with results reported by other investigators.

Investigators	Technique ^a	Range of T (K)	$k_2(10^{-13} \text{ cm}^3 \text{ molecule}^{-1} \text{ s}^{-1})$, b,c		
			298K	230K	190K
Clyne & Watson [15]	DF-MS	298	12		
Leu & DeMore [16]	DF-MS	224-422	12.5	4.8	1.9*
Michael, et al [17]	FP-RF	200-360	10.2	5.6	3.2
Michael & Payne [18]	DF-RF	234-360	10.4	5.4	2.9*
Dodonov, et al [19]	DFL-MS	281-337	10.9	4.9*	2.3*
Toohy, et al [14]	DF-RF	248-418	13.6	5.4	2.3*
This Work	LFP-RF	195-392	11.1	5.2	2.5
NASA Panel [20]			11.6	5.2	2.5
ILPAC Panel [41]			11.6	5.2	2.5

^a DF: discharge flow; FP: flash photolysis; DFL: diffusion flame; LFP: laser flash photolysis; MS: mass spectrometry; RF: resonance fluorescence.

^b Where T -dependent data is reported, rate coefficients are calculated from Arrhenius expressions.

^c Error estimates are discussed in the text.

* Obtained by extrapolation of more than a factor of 1.1 in $1/T$.

Examination of Table IV shows that values for $k_2(230 \text{ K})$ and $k_2(190 \text{ K})$ calculated using various reported Arrhenius expressions agree quite well; the differences between the results of various studies are greatest at higher temperatures. Both studies of Michael and co-workers were carried out under less than ideal conditions and could be subject to systematic errors. Their flash photolysis study [17] was hampered by $\text{Br}(^2P_{3/2})$ regeneration which was attributed to the reaction of photolytically generated $\text{O}(^3P_j)$ with BrO , while their discharge flow study [18] was hampered by a severe wall loss problem. The studies where relatively large activation energies were measured [14,16] are harder to find fault with, particularly the study of Toohy et al. [14] which appears to have been done very carefully.

Summary

A laser flash photolysis-resonance fluorescence technique has been employed to study the kinetics of the reactions of $\text{Cl}(^2P_j)$ and $\text{Br}(^2P_{3/2})$ with O_3 , with particular emphasis on characterization of the rate coefficients at low temperature. Our observed temperature dependence for the $\text{Cl}(^2P_j) + \text{O}_3$ rate coefficient is non-Arrhenius, but can be adequately described by the following two Arrhenius expressions (units are $\text{cm}^3 \text{ molecule}^{-1} \text{ s}^{-1}$): $k_1(T) = 1.19 \times 10^{-11} \exp(-33/T)$ for $T = 189-269 \text{ K}$ and $k_1(T) = 2.49 \times 10^{-11} \exp(-233/T)$ for $T = 269-385 \text{ K}$. At lower stratospheric temperatures, the rate coefficients determined in this study are faster than any reported previously. Incorporation of our results into stratospheric models would lead to an increase in calculated ClO levels and a decrease in calculated HCl levels; hence, the calculated efficiency of ClO_2 catalyzed ozone

destruction would increase. For the $\text{Br}(^2P_{3/2}) + \text{O}_3$ reaction, we obtain the result $k_2(T) = 1.50 \times 10^{-11} \exp(-775/T) \text{ cm}^3 \text{ molecule}^{-1} \text{ s}^{-1}$ for $T = 195\text{--}392 \text{ K}$. While not in quantitative agreement with Arrhenius parameters reported in most previous studies, our results almost exactly reproduce the average of all earlier studies and, therefore, will not affect the choice of $k_2(T)$ for use in modeling stratospheric BrO_x chemistry.

Acknowledgment

This work was supported by the National Aeronautics and Space Administration through grant no. NAGW-1001.

Bibliography

- [1] M. J. Molina and F. S. Rowland, *Nature*, **249**, 810 (1974).
- [2] S. C. Wofsy, M. B. McElroy, and Y. L. Yung, *Geophys. Res. Lett.*, **2**, 215 (1975).
- [3] L. T. Molina and M. J. Molina, *J. Phys. Chem.*, **91**, 433 (1986).
- [4] M. B. McElroy, R. J. Salawitch, S. C. Wofsy, and J. A. Logan, *Nature*, **321**, 759 (1986).
- [5] M. J. Molina, T.-L. Tso, L. T. Molina, and F. C.-Y. Wang, *Science*, **238**, 1253 (1987).
- [6] M. A. Tolbert, M. J. Rossi, R. Malhotra, and D. M. Golden, *Science*, **238**, 1258 (1987).
- [7] Y. L. Yung, J. P. Pinto, R. T. Watson, and S. P. Sander, *J. Atmos. Sci.*, **37**, 339 (1980).
- [8] M. A. A. Clyne and R. T. Watson, *J. Chem. Soc. Far. Trans. I*, **70**, 2250 (1974).
- [9] M. A. A. Clyne and W. S. Nip, *J. Chem. Soc. Far. Trans. II*, **72**, 838 (1976).
- [10] M. S. Zahniser, F. Kaufman, and J. G. Anderson, *Chem. Phys. Lett.*, **37**, 226 (1976).
- [11] M. J. Kurylo and W. Braun, *Chem. Phys. Lett.*, **37**, 232 (1976).
- [12] M. T. Leu and W. B. DeMore, *Chem. Phys. Lett.*, **41**, 121 (1976).
- [13] R. T. Watson, G. Machado, S. Fischer, and D. D. Davis, *J. Chem. Phys.*, **65**, 2126 (1976).
- [14] D. W. Toohey, W. H. Brune, and J. G. Anderson, *Int. J. Chem. Kinet.*, **20**, 131 (1988).
- [15] M. A. A. Clyne and R. T. Watson, *J. Chem. Soc. Far. Trans. I*, **71**, 336 (1975).
- [16] M. T. Leu and W. B. DeMore, *Chem. Phys. Lett.*, **48**, 317 (1977).
- [17] J. V. Michael, J. H. Lee, W. A. Payne, and L. J. Stief, *J. Chem. Phys.*, **68**, 4093 (1978).
- [18] J. V. Michael and W. A. Payne, *Int. J. Chem. Kinet.*, **11**, 799 (1979).
- [19] A. F. Dodonov, V. V. Zelenov, and V. L. Tal'roze, *Kinet. Katal. (USSR)*, **22**, 245 (1981).
- [20] W. B. DeMore, M. J. Molina, S. P. Sander, D. M. Golden, R. F. Hampson, M. J. Kurylo, C. J. Howard, and A. R. Ravishankara, *Chemical Kinetics and Photochemical Data for Use in Stratospheric Modeling*, Evaluation No. 8, JPL publication 87-41, 1987.
- [21] A. R. Ravishankara and P. H. Wine, *J. Chem. Phys.*, **72**, 25 (1980).
- [22] P. H. Wine, D. H. Semmes, and A. R. Ravishankara, *Chem. Phys. Lett.*, **90**, 128 (1982).
- [23] P. H. Wine and D. H. Semmes, *J. Phys. Chem.*, **87**, 3572 (1983).
- [24] P. H. Wine, J. R. Wells, and J. M. Nicovich, *J. Phys. Chem.*, **92**, 2223 (1988).
- [25] J. M. Nicovich, C. J. Shackelford, and P. H. Wine, *J. Phys. Chem.*, in press.
- [26] J. M. Nicovich, C. J. Shackelford, and P. H. Wine, *J. Photochem. Photobiol., A: Chem.*, in press.
- [27] J. G. Anderson, H. J. Grassl, R. E. Shetter, and J. J. Margitan, *J. Geophys. Res.*, **85**, 2869 (1980).
- [28] A. G. Hearn, *Proc. Phys. Soc.*, **78**, 932 (1961).
- [29] K. Mauersberger, J. Barnes, D. Hanson, and J. Morton, *Geophys. Res. Lett.*, **13**, 671 (1986).
- [30] L. T. Molina and M. J. Molina, *J. Geophys. Res.*, **91**, 14501 (1986).
- [31] K. Yoshino, D. E. Freeman, J. R. Esmond, and W. H. Parkinson, *Planet. Space Sci.*, **36**, 395 (1988).
- [32] J. W. Simons, R. J. Paur, H. A. Webster III, and E. J. Bair, *J. Chem. Phys.*, **59**, 1203 (1973).
- [33] R. H. Clark and D. Husain, *J. Chem. Soc. Farad. Trans. II*, **80**, 97 (1984).
- [34] S. A. Sotnichenko, V. Ch. Bokun, and A. I. Nadkin, *Chem. Phys. Lett.*, **153**, 560 (1988).
- [35] R. H. Clark and D. Husain, *J. Photochem.*, **21**, 93 (1983).
- [36] W. D. McGrath and R. G. W. Norrish, *Z. Phys. Chem.*, **15**, 245 (1958).

- [37] J. W. Vanderzanden and J. W. Birks, *Chem. Phys. Lett.*, **88**, 109 (1982).
- [38] K. Y. Choo and M. T. Leu, *J. Phys. Chem.*, **89**, 4832 (1985).
- [39] J. M. Nicovich, P. H. Wine, and A. R. Ravishankara, *J. Chem. Phys.*, **89**, 5670 (1988).
- [40] J. B. Burkholder, P. D. Hammer, C. J. Howard, and A. Goldman, *J. Geophys. Res.*, **94**, 2225 (1989).
- [41] R. Atkinson, D. L. Baulch, R. A. Cox, R. F. Hampson, J. A. Kerr, and J. Troe, *J. Phys. Chem. Ref. Data*, **18**, 881 (1989).
- [42] S. C. Farantos and J. N. Murrell, *Int. J. Quant. Chem.*, **14**, 659 (1978).
- [43] R. O. Carter, III and L. Andrews, *J. Phys. Chem.*, **85**, 2351 (1981).
- [44] R. S. Mulliken, *Phys. Rev.*, **46**, 549 (1934); *J. Chem. Phys.*, **4**, 620 (1936); *Phys. Rev.*, **57**, 500 (1940).
- [45] R. J. Oldman, R. K. Sander, and K. R. Wilson, *J. Chem. Phys.*, **63**, 4252 (1975).
- [46] D. J. Nesbitt and S. R. Leone, *J. Chem. Phys.*, **73**, 6182 (1980).
- [47] M. A. A. Clyne, P. B. Monkhouse, and L. W. Townsend, *Int. J. Chem. Kinet.*, **8**, 425 (1976).
- [48] J. M. Nicovich and P. H. Wine, *Int. J. Chem. Kinet.*, **22**, 379 (1990).

Received July 6, 1989

Accepted October 5, 1989

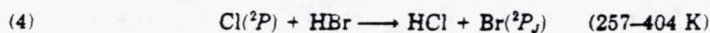
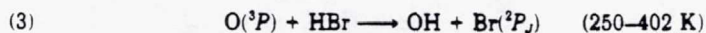
Kinetics of the Reactions of $O(^3P)$ and $Cl(^2P)$ with HBr and Br_2

J. M. NICOVICH and P. H. WINE

Molecular Sciences Branch, Georgia Tech Research Institute, Georgia Institute of Technology,
Atlanta, Georgia 30332

Abstract

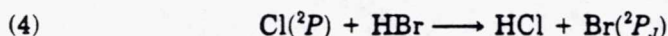
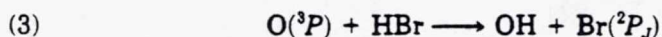
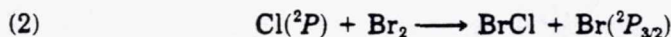
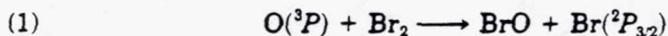
A laser flash photolysis-resonance fluorescence technique has been employed to study the kinetics of reactions (1)–(4) as a function of temperature.



In all cases, the concentration of the excess reagent, i.e., HBr or Br_2 , was measured *in situ* in the slow flow system by UV-visible photometry. Heterogeneous dark reactions between XBr ($X = H$ or Br) and the photolytic precursors for $Cl(^2P)$ and $O(^3P)$ (Cl_2 and O_3 , respectively) were avoided by injecting minimal amounts of precursor into the reaction mixture immediately upstream from the reaction zone. The following Arrhenius expressions summarize our results (errors are 2σ and represent precision only, units are $cm^3 \text{ molecule}^{-1} s^{-1}$): $k_1 = (1.76 \pm 0.80) \times 10^{-11} \exp[(40 \pm 100)/T]$; $k_2 = (2.40 \pm 1.25) \times 10^{-10} \exp[-(144 \pm 176)/T]$; $k_3 = (5.11 \pm 2.82) \times 10^{-12} \exp[-(1450 \pm 160)/T]$; $k_4 = (2.25 \pm 0.56) \times 10^{-11} \exp[-(400 \pm 80)/T]$. The consistency (or lack thereof) of our results with those reported in previous kinetics and dynamics studies of reactions (1)–(4) is discussed.

Introduction

The increasing levels of anthropogenic bromine compounds in the earth's atmosphere has led to concerns over the contribution of these species to the catalytic destruction of stratospheric ozone [1]. To support studies of bromine chemistry directly relevant to the chemistry of the atmosphere, the kinetics of reactions (1)–(4) have been studied as a function of temperature.



While not of direct atmospheric importance, reactions (1)–(4) often occur in laboratory systems designed to obtain kinetic data for other reactions of atmospheric interest. For example, reaction (1) is a commonly employed laboratory source of BrO , the predominant BrO_x species in the stratosphere [2].

International Journal of Chemical Kinetics, Vol. 22, 379–397 (1990)

© 1990 John Wiley & Sons, Inc.

CCC 0538-8066/90/040379-20\$04.00

K-10.1 NDB
5/5-25
026133
273556
19p.

Based on literature values for deactivation of spin-orbit excited $\text{Cl}(^2P_{1,2})$ by N_2 (k_8 ca. $5 \times 10^{-13} \text{ cm}^3 \text{ molecule}^{-1} \text{ s}^{-1}$ [66,67]), it appears that experimental conditions were always such that $k_8[\text{N}_2] \gg k_2[\text{Br}_2]$ or $k_4[\text{HBr}]$. Hence, all measured chlorine atom temporal profiles should be considered as representative of the removal of an equilibrium mixture of $\text{Cl}(^2P_{3,2})$ and $\text{Cl}(^2P_{1,2})$. Third harmonic radiation from a Nd:YAG laser served as the photolytic light source for chlorine atom production. The laser could deliver up to 1×10^{17} photons per pulse at a repetition rate of up to 10 Hz; the pulse-width was 6 ns.

An atomic resonance lamp, situated perpendicular to the photolysis laser, excited resonance fluorescence in the photolytically produced atoms. The resonance lamp consisted of an electrodeless microwave discharge through about one torr of a flowing mixture containing a trace of O_2 or Cl_2 in He. The flows of a 0.1% O_2 or Cl_2 in He mixture and pure He into the lamp were controlled by separate needle valves, thus allowing the total pressure and O_2 or Cl_2 concentration to be adjusted for optimum signal-to-noise. Radiation was coupled out of the lamp through a magnesium fluoride window and into the reaction cell through a magnesium fluoride lens. Before entering the reaction cell, the lamp output passed through a flowing gas filter. For $\text{O}(^3P)$ detection, the gas filter was 0.1 cm-atm O_2 in N_2 ; this filter prevented lamp emissions in the 135–165 nm region from entering the reactor. For $\text{Cl}(^2P)$ detection, the gas filter was 0.004 cm-atm N_2O in N_2 ; this filter absorbed all impurity emissions from the oxygen triplet at 130–131 nm while only slightly attenuating the chlorine lines in the 135–140 nm region, and also provided some attenuation of impurity emissions in the 140–150 nm region.

Fluorescence was collected by a magnesium fluoride lens on an axis orthogonal to both the photolysis laser beam and the resonance lamp beam, and imaged onto the photocathode of solar blind photomultiplier. The region between the reaction cell and the photomultiplier was purged with N_2 . A calcium fluoride window was placed between the reaction cell and the photomultiplier to prevent detection of emissions at wavelengths shorter than 125 nm (Lyman- α emission, for example). Signals were processed using photon counting techniques in conjunction with multichannel scaling. For each atom decay measured, signals from a large number of laser shots were averaged to obtain a well-defined temporal profile over (typically) three $1/e$ lifetimes of decay. The multichannel analyzer sweep was triggered prior to the photolysis laser in order to allow a pre-trigger baseline to be obtained.

In order to avoid accumulation of photolysis or reaction products, all experiments were carried out under "slow flow" conditions. The linear flow rate through the reactor was typically 5 cm s^{-1} and the laser repetition rate was $\leq 5 \text{ Hz}$. Hence, no volume element of the reaction mixture was subjected to more than one or two laser shots. The photolytic precursors O_3 and Cl_2 and the stable reactants Br_2 and HBr were flowed into the reaction cell from 12 liter bulbs containing dilute mixtures in nitrogen buffer gas. The stable reactant flow was pre-mixed with additional nitrogen before entering the reaction cell. Since heterogeneous reactions of the photolytic precursors with the stable reactants were a problem in these studies, in

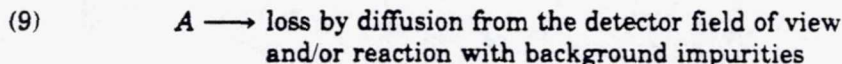
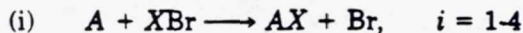
most experiments the photolytic precursors were not pre-mixed with other components of the reaction mixture upstream from the reaction cell; instead, they were injected into the reaction cell through a $\frac{1}{8}$ inch O.D. teflon tube positioned such that the photolyte mixed with other components about 1 to 5 cm upstream from the reaction zone.

Concentrations of each component in the reaction mixtures were determined from measurements of the appropriate mass flow rates and the total pressure. The concentrations of HBr and Br₂ were also measured *in situ* in the slow flow system by UV photometry. The 184.9 nm emission from an Hg pen ray lamp was employed as the light source for monitoring HBr. Absorption cells were 20 cm long in the study of reaction (3) and 216 cm long in the study of reaction (4). After passing through the absorption cell, the 184.9 nm radiation was isolated for detection using a $\frac{3}{4}$ meter monochromator-bandpass filter combination. The HBr absorption cross section at 184.9 nm was taken to be 2.36×10^{-18} cm² [68,69]. A multipass White cell arrangement was employed to monitor Br₂. Radiation from a xenon arc lamp was multipassed through a 35 cm absorption cell 42 times giving an absorption pathlength of 14.7 meters. A $\frac{1}{4}$ meter monochromator in conjunction with dielectric coated White cell mirrors and narrow-band anti-reflection coated absorption cell windows isolated radiation at the monitoring wavelength, 415.8 nm. The Br₂ absorption cross section at 415.8 nm was taken to be 5.87×10^{-19} cm² [70]; measurements carried out during the course of our study confirmed that this cross section is correct. To ensure that the reactant concentration was not changing during transit through the flow system, all four reactions were studied with the absorption cell positioned both upstream and downstream from the reaction cell; in the upstream position, of course, a small correction was required for dilution upon injection of the photolyte into the mixture.

The gases used in this study had the following stated minimum purities: N₂, 99.999%; He, 99.999%; Cl₂, 99.99%; HBr, 99.8%. Nitrogen and helium were used as supplied while Cl₂ and HBr were degassed repeatedly at 77 K before use. Bromine was Fischer ACS reagent grade with a maximum impurity level of 0.06%; it was transferred into a vial fitted with a high vacuum stopcock, then degassed repeatedly at 77 K before use. Ozone was prepared in a commercial ozonator using UHP oxygen (99.99%). It was collected and stored on silica gel at 195 K, and degassed at 77 K before use.

Results and Discussion

All experiments were carried out under pseudo-first order conditions with HBr or Br₂ in large excess over O(³P) or Cl(²P). Hence, in the absence of secondary reactions which enhance or deplete the atom concentration, the atom temporal profile is dominated by the reactions



where A = O or Cl and X = Br or H. Integration of the rate equations for the above scheme yields the simple relationship

$$(I) \quad \ln\{[A]_0/[A]_t\} = (k_1[XBr] + k_9)t = k't.$$

The bimolecular rate coefficients, k_1 , are determined from the slopes of k' vs. $[XBr]$ plots.

For all four reactions studied, atom temporal profiles were found to be exponential (i.e., obeyed eq. (I)) and to increase linearly with increasing XBr concentration. Observed pseudo-first order decay rates were found to be independent of laser photon fluence and photolytic precursor concentration in all cases. The above set of observations strongly supports the contention that reactions (i) and (9) are the only processes which affected the post-flash atom time histories in our studies of reactions (1)–(4). Results for reactions (1)–(4) are discussed separately below.

$O(^3P) + Br_2$

Results from our study of reaction (1) are summarized in Table I. The rate coefficient k_1 is found to be virtually independent of temperature over the range 255–350 K. Typical $O(^3P)$ temporal profiles are shown in Figure 1 while k' vs. $[Br_2]$ plots for data taken at 255 K and 350 K are shown in Figure 2. A linear least squares analysis of the $\ln k_1$ vs. T^{-1} data gives the Arrhenius expression.

$$k_1(T) = (1.76 \pm 0.80) \times 10^{-11} \exp[(40 \pm 100)/T] \text{ cm}^3 \text{ molecule}^{-1} \text{ s}^{-1}.$$

The temperature independent rate coefficient $k_1 = (2.03 \pm 0.12) \times 10^{-11} \text{ cm}^3 \text{ molecule}^{-1} \text{ s}^{-1}$ is an equally good representation of our results. Errors in the above expressions are 2σ and represent precision only. We estimate the absolute uncertainty (2σ) in $k_1(T)$ at any temperature within the range of our study to be $\pm 15\%$.

There have been a limited number of previous studies of the thermal rate coefficient for reaction (1). In a study by Clyne and coworkers [40], k_1 was measured at room temperature in a discharge flow system using resonance fluorescence to follow oxygen atom loss and, in separate experiments, bromine atom production. At lower stoichiometries these workers found

TABLE I. Kinetic data for the reaction of $O(^3P)$ with Br_2 .^{a,b}

T	P	$[O_3]$	$[O(^3P)]_0$	N^c	k'_{max}	k_1^d
255	100	250	4.8	8	11900	2.01 ± 0.07
278	100	300	5.0	6	8720	1.97 ± 0.05
296	100	240	4.5	8	8910	2.14 ± 0.10
298	30	100	2.0	7	9120	1.99 ± 0.16
298	100	90–260	0.7–3.4	19	10300	2.11 ± 0.07
298	300	900	10	6	10000	2.08 ± 0.09
350	100	160	2.0	7	8550	1.91 ± 0.07

^aUnits are as follows: T (K); P (torr); $[O_3]$, $[O(^3P)]_0$ (10^{11} per cm^3); k'_{max} (s^{-1}); k_1 ($10^{-11} \text{ cm}^3 \text{ molecule}^{-1} \text{ s}^{-1}$).

^bAll experiments were done with N_2 buffer gas. The linear flow rate was varied from 3 cm s^{-1} to 15 cm s^{-1} (5 cm s^{-1} typical). The laser repetition rate was varied from 1 Hz (typical) to 2.5 Hz. The $O(^3P)$ loss rate in the absence of Br_2 was typically 100 s^{-1} .

^c N = number of pseudo first order decays measured.

^dError is 2σ and represents precision only.

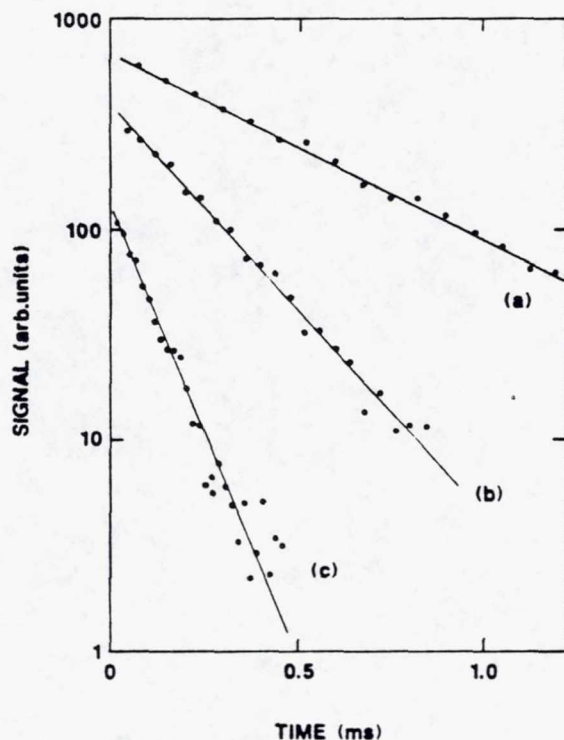
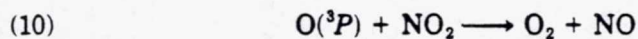


Figure 1. Typical $O(^3P)$ temporal profiles obtained in our study of the $O(^3P) + Br_2$ reaction. Experimental conditions: $T = 298$ K; $P = 300$ torr; $[O_2] = 9.0 \times 10^{13}$ molecules per cm^3 ; $[O(^3P)]_0$ ca. 5×10^{11} atoms per cm^3 ; $[Br_2]$ in units of 10^{14} molecules per $cm^3 =$ (a) 1.04, (b) 2.05, (c) 4.86; number of laser shots averaged = (a) 150, (b) 250, (c) 500. Solid lines are obtained from least squares analyses and give the following pseudo-first order decay rates in units of s^{-1} : (a) 1930, (b) 4400, (c) 10000.

that secondary chemistry due to the BrO produced from reaction (1) (i.e., the $BrO + O$ reaction) was suppressed by adding excess NO. A value of $(1.4 \pm 0.2) \times 10^{-11} \text{ cm}^3 \text{ molecule}^{-1} \text{ s}^{-1}$ was reported; the currently recommended value for k_1 [71] is based on this result. Clyne et al. [40] also discussed previous studies of reaction (1) carried out in Clyne's laboratory [38,39]. The experiments of Clyne and Cruse [38], also performed in a discharge flow system with resonance fluorescence detection of $O(^3P)$, were carried out in excess NO but with $[Br_2]_0$ ca. $[O]_0$. Therefore, Clyne et al. concluded that the reaction



was a complication in the Clyne and Cruse study and proposed that the earlier result should be lowered to $(1.2 \pm 0.4) \times 10^{-11} \text{ cm}^3 \text{ molecule}^{-1} \text{ s}^{-1}$ from the originally reported $1.74 \times 10^{-11} \text{ cm}^3 \text{ molecule}^{-1} \text{ s}^{-1}$. Also discussed by Clyne et al. is the work of Cruse [39]. Using techniques similar to Clyne et al., the study of Cruse apparently yielded a value of $(2.1 \pm 0.4) \times 10^{-11} \text{ cm}^3 \text{ molecule}^{-1} \text{ s}^{-1}$ for k_1 . This is again the composite result of both $O(^3P)$ disappearance and $Br(^2P)$ appearance measurements. As a weighted

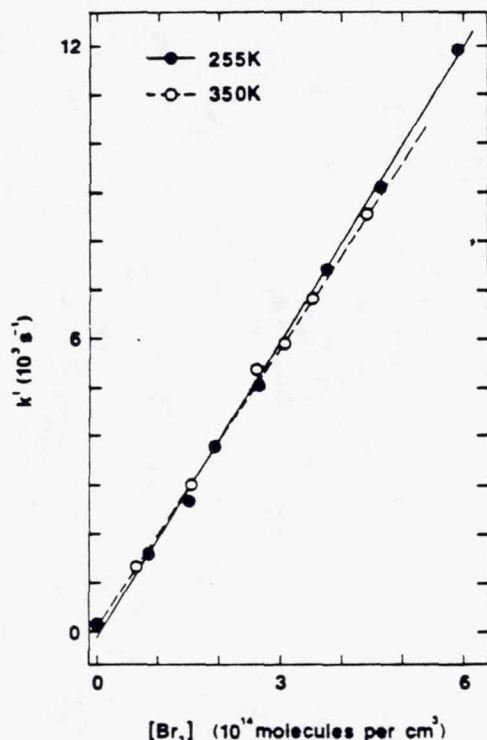
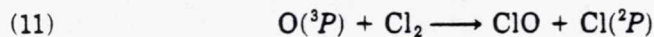


Figure 2. Plots of k' vs. $[\text{Br}_2]$ for data obtained at the temperature extremes of our $\text{O}(^3P) + \text{Br}_2$ study. Lines are obtained from linear least squares analyses and give the rate coefficients 2.01 ± 0.07 at 255 K and 1.91 ± 0.07 at 350 K in units of $10^{-11} \text{ cm}^3 \text{ molecule}^{-1} \text{ s}^{-1}$; errors are 2σ and represent precision only.

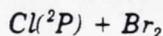
average of all three studies, Clyne et al. [40] offer $k_1 = (1.65 \pm 0.30) \times 10^{-11} \text{ cm}^3 \text{ molecule}^{-1} \text{ s}^{-1}$ at 298 K.

There have been two studies of the temperature dependence of k_1 reported in the literature. Moin et al. [41] measured $k_1(T)$ relative to $k_{11}(T)$



over the temperature range 306 K to 425 K. These investigators report $k_1(T)/k_{11}(T) = (3.98_{-2.81}^{+9.51}) \exp[(1300 \pm 45)/T]$. Using our recently reported [60] Arrhenius expression for reaction (11), $k_{11}(T) = (7.4 \pm 2.4) \times 10^{-12} \exp[-(1650 \pm 100)/T] \text{ cm}^3 \text{ molecule}^{-1} \text{ s}^{-1}$, in conjunction with the $k_1(T)/k_{11}(T)$ ratios reported by Moin et al. [41] leads to the result $k_1(T) = (3.0_{-2.3}^{+7.2} \times 10^{-11}) \exp[-(350 \pm 150)/T] \text{ cm}^3 \text{ molecule}^{-1} \text{ s}^{-1}$. Dodonov et al. [42], have also measured $k_1(T)$ over the temperature range 246–431 K using a diffusional flame method. These investigators obtained the result $k_1(T) = 4.6 \times 10^{-11} \exp[-(210 \pm 75)/T] \text{ cm}^3 \text{ molecule}^{-1} \text{ s}^{-1}$. The results of Dodonov et al. are in fair agreement with our results particularly at temperatures below 298 K. The error limits reported by Moin et al. are so large that quantitative comparison with their study is a pointless exercise; their results do suggest values for $k_1(T)$ of the same order of magnitude as do our results.

Both experimental and theoretical studies of the dynamics of reaction (1) have appeared in the literature. Reactive scattering experiments at low translational energies (1–3 kcal mol⁻¹) [3,4] indicate a long lived collision complex while higher energy (15–40 kcal mol⁻¹) scattering experiments [5,6] are more compatible with a complex that is short lived compared to a rotational period. An RRKM model [7] suggests that the long lived complex mechanism may adequately describe the scattering experiments. The same RRKM model has been used to calculate a thermal rate coefficient for reaction (1) [8]. Good agreement is obtained only when a barrier of approximately 1 kcal mol⁻¹ is introduced into the entrance channel. While this activation energy is consistent with a roughly estimated value that has appeared in the literature [72], and is reasonably close to that observed by Moin et al. [41], it is not compatible with the lack of a significant temperature dependence observed in our study.



In order to study reaction (2) with *in situ* measurement of the Br₂ concentration, it was necessary to observe pseudo-first order decay rates approaching 10⁵ s⁻¹, i.e., more than an order of magnitude faster than is customarily employed in flash photolysis-resonance fluorescence studies. Typical Cl(²P) temporal profiles observed in our study of reaction (2) are shown in Figure 3, while a summary of the data is compiled in Table II. The rate coefficient k_2 is found to be virtually independent of temperature over the range 298–401 K. A linear least squares analysis of the ln k_2 vs. T^{-1} data gives the Arrhenius expression

$$k_2(T) = (2.40 \pm 1.25) \times 10^{-10} \exp[-(144 \pm 176)/T] \text{ cm}^3 \text{ molecule}^{-1} \text{ s}^{-1}.$$

The temperature independent rate coefficient $k_2 = (1.58 \pm 0.22) \times 10^{-10}$ cm³ molecule⁻¹ s⁻¹ is an equally good representation of our results. Errors in the above expressions are 2σ and represent precision only. We estimate the absolute uncertainty (2σ) in $k_2(T)$ at any temperature within the range of our study to be ±20%.

There have been two previous studies of k_2 . Both studies were performed in the same laboratory using a discharge flow-resonance fluorescence system at low pressures. In the earlier study Clyne and Cruse [43] reported $k_2(298 \text{ K}) = (1.20 \pm 0.15) \times 10^{-10}$ cm³ molecule⁻¹ s⁻¹. In the later work Bemand and Clyne [44] measured $k_2(298 \text{ K}) = (1.9 \pm 0.2) \times 10^{-10}$ cm³ molecule⁻¹ s⁻¹. The average of these two studies is in good agreement with our result. Given the rapidity of reaction (2) it is not surprising that there is no significant activation energy.

There have been several molecular beam studies of the dynamics of reaction (2). As summarized by Valentini et al. [9] the lack of a significant dependence of the total cross section on collision energy indicates a lack of any energy barrier. This conclusion is also supported by the forwardly peaked center of mass angular distributions of the product BrCl which are independent of total collision energy. The total cross sections quoted in the molecular beam studies, 1–20 Å² for $E_{\text{trans}} = 2.0$ kcal/mol⁻¹ [10–12], 4–33 Å² for $E_{\text{trans}} = 6.8$ kcal/mol⁻¹ [9], and 5–42 Å² for $E_{\text{trans}} = 14.7$ kcal/mol⁻¹ [9] are less than an estimated hard sphere cross section (ca. 48 Å²) [73]. For the

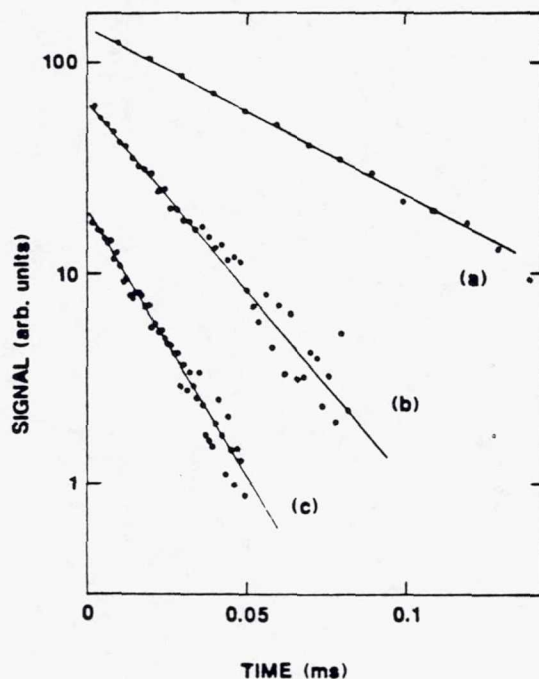


Figure 3. Typical $\text{Cl}(^2P)$ temporal profiles obtained in our study of the $\text{Cl}(^2P) + \text{Br}_2$ reaction. Experimental conditions: $T = 327 \text{ K}$; $P = 100 \text{ torr}$; $[\text{Cl}_2] = 1.9 \times 10^{13}$ molecules per cm^3 ; $[\text{Cl}(^2P)]_0$ ca. 3×10^{11} atoms per cm^3 ; $[\text{Br}_2]$ in units of 10^{14} molecules per $\text{cm}^3 =$ (a) 1.04, (b) 2.58, (c) 3.65; number of laser shots averaged = (a) 1024, (b) 2048, (c) 8192. Solid lines are obtained from least squares analyses and give the following pseudo-first order decay rates in units of s^{-1} : (a) 18400, (b) 41600, (c) 59400.

sake of comparison, if our value for the thermal rate coefficient is divided by the mean relative velocity at 298 K a "cross section" of 34 \AA^2 is derived.

$\text{O}(^3P) + \text{HBr}$

Results from our study of reaction (3) are summarized in Table III and plots of k' vs. $[\text{HBr}]$ at a series of temperatures are shown in Figure 4. An

TABLE II. Kinetic data for the reaction of $\text{Cl}(^2P)$ with Br_2 .^{a,b}

T	P	$[\text{Cl}_2]$	$[\text{Cl}(^2P)]_0$	N^c	k'_{max}	k_2^d
298	100	130–630	1.3–5.3	55	66000	1.49 ± 0.10
327	100	190	3.0	6	59200	1.60 ± 0.05
349	100	200	1.5	5	56300	1.49 ± 0.17
401	100	220	3.4	6	59900	1.72 ± 0.11

^aUnits are as follows: T (K); P (torr); $[\text{Cl}_2]$, $[\text{Cl}(^2P)]_0$ (10^{11} per cm^3); k'_{max} (s^{-1}); k_2 ($10^{-10} \text{ cm}^3 \text{ molecule}^{-1} \text{ s}^{-1}$).

^bAll experiments were done with N_2 buffer gas at $\approx 5 \text{ cm s}^{-1}$ linear flow rate and 1 Hz laser repetition rate. The loss rate of $\text{Cl}(^2P)$ in the absence of Br_2 was typically 120 s^{-1} .

^c N = number of pseudo first order decays measured.

^dError is 2σ and represents precision only.

TABLE III. Kinetic data for the reaction of $O(^3P)$ with HBr .^{a,b}

T	P	$[O_3]$	$[O(^3P)]_0$	N^c	k'_{max}	k_3^d
250	100	76-130	6.0-10	7	1410	1.65 ± 0.09
272	100	38	2.0	7	1130	2.55 ± 0.09
298	30	40	3.0	5	1040	3.56 ± 0.15
298	100	80-230	5.0-12	11	1710	3.65 ± 0.15
298	100	40	3.0	6	1040	3.51 ± 0.16
298	300	340	20	6	1120	3.51 ± 0.26
345	100	40-80	3.2-7.0	10	1340	7.12 ± 0.53
402	100	30-130	2.0-12	17	1660	15.2 ± 1.4

^a Units are as follows: T (K); P (torr); $[O_3]$, $[O(^3P)]_0$ (10^{11} per cm^3); k'_{max} (s^{-1}); k_3 (10^{-14} cm^3 molecule $^{-1}$ s^{-1}).

^b All experiments were done with N_2 buffer gas at 5 cm s^{-1} linear flow rate. The laser repetition rate was varied from 1 Hz (typical) to 5 Hz. The typical $O(^3P)$ loss rate in the absence of HBr was 80 s^{-1} .

^c N = number of pseudo first order decays measured.

^d Error is 2σ and represents precision only.

Arrhenius plot for reaction (3) is shown in Figure 5. A linear least squares analysis of the $\ln k_3$ vs. T^{-1} data gives the Arrhenius expression

$$k_3(T) = (5.11 \pm 2.82) \times 10^{-12} \exp[-(1450 \pm 160)/T] \text{ cm}^3 \text{ molecule}^{-1} \text{ s}^{-1}.$$

Errors in the above expression are 2σ and represent precision only. We estimate the absolute uncertainty (2σ) in $k_3(T)$ at any temperature within the range of our study (250-402 K) to be $\pm 15\%$.

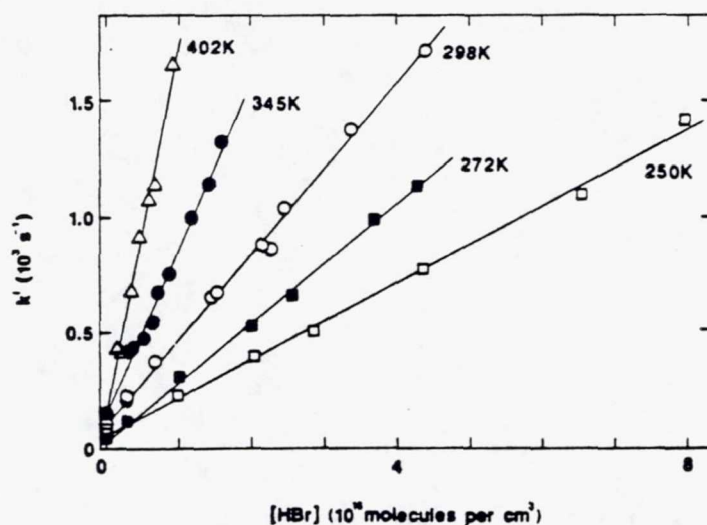


Figure 4. Plots of k' vs. $[HBr]$ for data from our study of the $O(^3P) + HBr$ reaction at 100 torr total pressure. Lines are obtained from linear least squares analyses and give the following rate coefficients in units of 10^{-14} cm^3 molecule $^{-1}$ s^{-1} : 1.65 ± 0.09 at 250 K, 2.55 ± 0.09 at 272 K, 3.65 ± 0.15 at 298 K, 7.12 ± 0.53 at 345 K, and 15.2 ± 1.4 at 402 K; errors are 2σ and represent precision only.

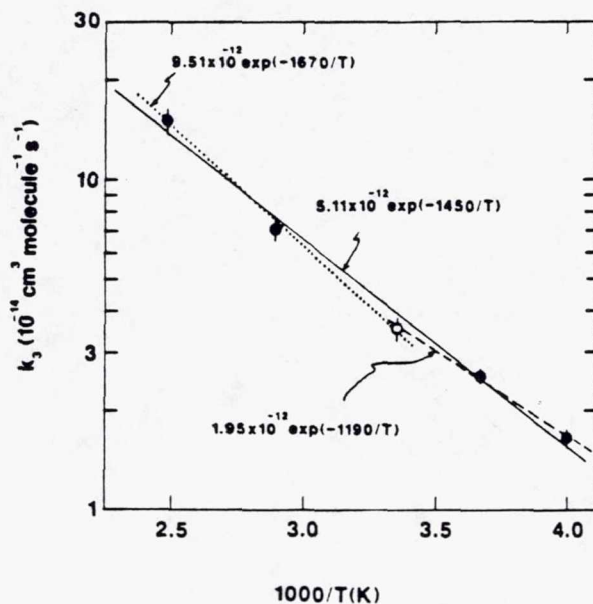


Figure 5. Arrhenius plot for the reaction of $O(^3P)$ with HBr . Solid line is obtained from a least squares analysis of all data. Dashed line is obtained from a least squares analysis of all data at $T \leq 298$ K. Dotted line is obtained from a least squares analysis of all data at $T \geq 298$ K. The data point at 298 K (open circle) actually represents the average of four separate $k_3(298$ K) determinations (see Table III for individual rate coefficients).

The kinetics of reaction (3) have been studied by four other groups over the combined temperature range 221–554 K [47–50]; their results are compared with ours in Table IV. The agreement among all studies is excellent, especially considering the diversity of experimental methods employed. Broida et al. [17] recently reported very good agreement between the experi-

TABLE IV. Comparison of results obtained from kinetics studies of the $O(^3P) + HBr$ reaction.

Investigators	Technique ^a	Range of T^b	A^c	E/R^b	$k_3(298K)^c$
Takacs & Glass [47]	DF-ESR	289			4.4
Brown & Smith [48]	DF-CL	267–430	400	1360	4.2
Singleton & Cvetanovic [49]	MM-CL	298–554	1340	1810	3.52
Nava et al. [50]	FP-RF	221–455	673	1540	3.37
		298–455	1100	1720	
Broida et al. [17]	QTC	200–550	530	1410	3.9
		300–550	795	1590	
This Work	LFP-RF	250–402	511	1450	3.55
		298–402	951	1670	

^aDF = discharge flow; ESR = electron spin resonance; CL = chemiluminescence; MM = molecular modulation; FP = flash photolysis; RF = resonance fluorescence; QTC = quasi-classical trajectory calculation; LFP = laser flash photolysis.

^bUnits are degrees Kelvin.

^cUnits are 10^{-14} cm^3 molecule⁻¹ s⁻¹.

mental results [47–50] and their own quasiclassical trajectory calculations which were carried out on a London-Eyring-Polanyi-Sato semiempirical potential energy surface. McKendrick et al. [15] have used the same potential energy surface to calculate the energy partitioning in the products of reaction (4), and have obtained good agreement with their experimental product state distributions. It is interesting to note that the theoretical results of Broida et al. predict slightly nonArrhenius behavior for reaction (3) over the temperature range of our study. Both our results and the results of Nava et al. [50] seem to show a slight trend toward increasing activation energy with increasing temperature, as predicted by Broida et al.'s calculations. For example, the rate coefficients we have measured at $T \leq 298$ K suggest an activation energy of 2.36 ± 0.36 kcal mol⁻¹ while the rate coefficients we have measured at $T \geq 298$ K suggest an activation energy of 3.32 ± 0.37 kcal mol⁻¹ (errors are 2σ and represent precision only).

$\text{Cl}(^2P) + \text{HBr}$

Results from our study of reaction (4) are summarized in Table V and plots of k' vs. $[\text{HBr}]$ at the temperature extremes of our study are shown in Figure 6. An Arrhenius plot for reaction (4) is shown in Figure 7. A linear least squares analysis of the $\ln k_4$ vs. T^{-1} data gives the Arrhenius expression

$$k_4(T) = (2.25 \pm 0.56) \times 10^{-11} \exp[-(400 \pm 80)/T] \text{ cm}^3 \text{ molecule}^{-1} \text{ s}^{-1}.$$

TABLE V. Kinetic data for the reaction of $\text{Cl}(^2P)$ with HBr .^{a,b}

T	P	$[\text{Cl}_2]$	$[\text{Cl}(^2P)]_0$	N^c	k'_{max}	k_4^d
257	100	110–470	0.6–2.7	10	9800	5.06 ± 0.35
260	100	120	1.2	7	8160	4.96 ± 0.19
272	100	160	1.1	6	8290	5.15 ± 0.13
294	100	100	1.1	11	7960	5.39 ± 0.34
298	30	170	1.6	5	6780	5.37 ± 0.31
298	100	60–230	0.3–3.6	13	8230	5.55 ± 0.28
298	100	170	2.7	6	11400	5.64 ± 0.23
298	100	200	1.6	7	7600	5.63 ± 0.23
298	300	200	2.0	5	7850	5.84 ± 0.20
304	100	100	1.0	8	8710	5.90 ± 0.34
319	100	190	1.9	6	7280	5.94 ± 0.37
320	100	90	1.0	7	7580	6.12 ± 0.20
347	100	200	1.7	6	7760	7.14 ± 0.36
372	100	180	1.5	6	10900	8.27 ± 0.43
404	100	210	2.0	14	8720	8.56 ± 0.46

^a Units are as follows: T (K); P (torr); $[\text{Cl}_2]$, $[\text{Cl}(^2P)]_0$ (10^{11} per cm^3); k'_{max} (s^{-1}); k_4 (10^{-12} cm^3 molecule⁻¹ s^{-1}).

^b All experiments were done with N_2 buffer gas at a flow rate of ≈ 5 cm s^{-1} . The laser repetition rate was typically 1 Hz, although this was varied up to 5 Hz. The typical $\text{Cl}(^2P)$ loss rate in the absence of HBr was 180 s^{-1} .

^c N = number of pseudo first order decays measured.

^d Error is 2σ and represents precision only.

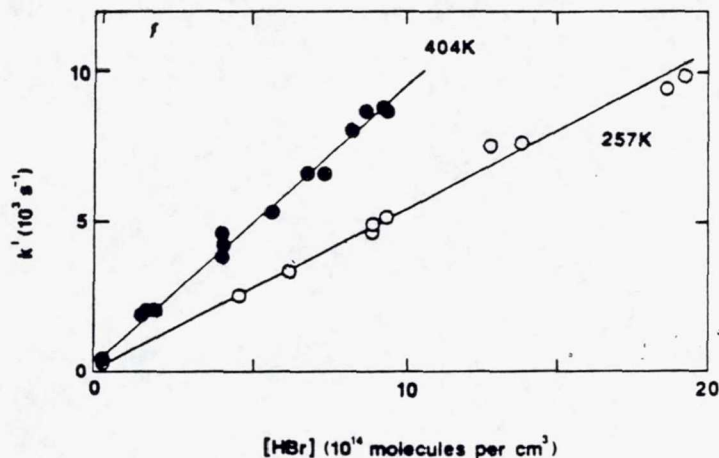


Figure 6. Plots of k' vs. $[HBr]$ for data obtained at the temperature extremes of our $Cl(^2P) + HBr$ study. Lines are obtained from linear least squares analyses and give the rate coefficients 5.04 ± 0.35 at 257 K and 8.56 ± 0.47 at 404 K in units of $10^{-12} \text{ cm}^3 \text{ molecule}^{-1} \text{ s}^{-1}$; errors are 2σ and represent precision only.

Errors in the above expression are 2σ and represent precision only. As we discuss below, heterogeneous dark reaction between Cl_2 and HBr was a problem in this study. For this reason, the absolute uncertainty (2σ) in $k_4(T)$ at any temperature within the range of our study (257–404 K) is relatively large, and is estimated to be $\pm 25\%$.

Systematic variations in experimental parameters during the course of our investigation demonstrated that it was imperative to inject the $Cl(^2P)$

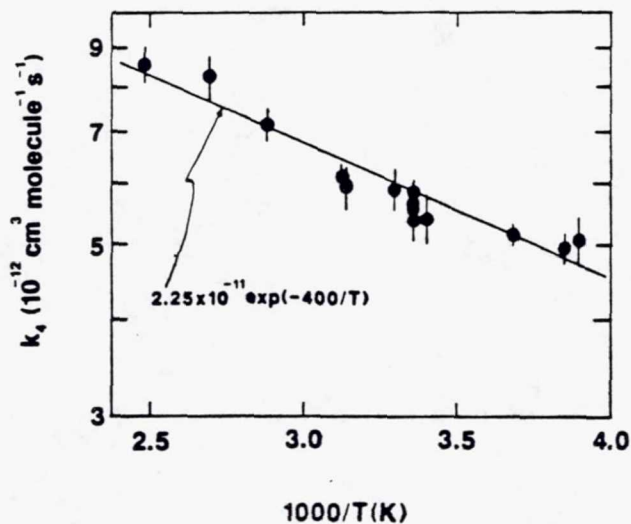
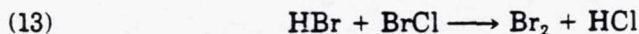
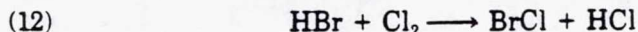
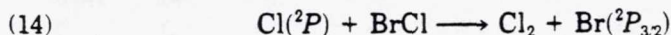


Figure 7. Arrhenius plot for the reaction of $Cl(^2P)$ with HBr . The solid line is obtained from a linear least squares analysis.

precursor (Cl_2) into the reaction mixture close to the reaction zone. As the contact time between Cl_2 and HBr in the flow system was increased, the observed $\text{Cl}(^2P)$ decay rate increased. When relatively large Cl_2 concentrations were employed, a decrease in the HBr concentration (measured downstream from the mixing point) was observed. This phenomenon has been observed previously [35] and appears to be attributable to the reactions



Wen and Noyes [74] have estimated upper limits for the homogeneous gas phase rate coefficients k_{12} and k_{13} to be $1.3 \times 10^{-21} \text{ cm}^3 \text{ molecule}^{-1} \text{ s}^{-1}$ and $2.5 \times 10^{-20} \text{ cm}^3 \text{ molecule}^{-1} \text{ s}^{-1}$ respectively, but have observed that reactions (12) and (13) are surface catalyzed. As shown in this study, the reaction of $\text{Cl}(^2P)$ with Br_2 is very fast. The reaction



is also quite fast, with k_{14} ca. $1.5 \times 10^{-11} \text{ cm}^3 \text{ molecule}^{-1} \text{ s}^{-1}$ [43].

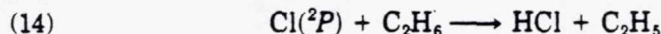
The results reported in Table V were all obtained under experimental conditions where we believe the interference from reactions (12) and (13) was negligible. The following observations support this contention:

(1) For Cl_2 concentrations of $1\text{--}7 \times 10^{13}$ molecules per cm^3 , k' was found to increase linearly as a function of HBr concentration (over the range 0 to 1.5×10^{15} molecules per cm^3) while the resonance fluorescence signal strength was independent of the quantity $[\text{HBr}]/f[\text{Cl}_2]_0$ (f = laser fluence and $[\text{Cl}_2]_0$ = molecular chlorine concentration calculated assuming no loss due to dark reaction); this suggests negligible loss of Cl_2 via dark reaction.

(2) The average of k' values at $[\text{HBr}] = 0$ calculated from linear least squares analyses of the k' vs. $[\text{HBr}]$ data was ca. 60 s^{-1} higher than the directly measured background $\text{Cl}(^2P)$ decay rate. If the observed increase is attributed entirely to production of Br_2 via reactions (12) and (13) then, based on our measured values for $k_2(T)$, about 3×10^{11} Br_2 per cm^3 are generated (apparently) by a dark reaction which occurs when small amounts of HBr are added to the reaction cell but "saturates" and does not become faster with increasing $[\text{HBr}]$. For the range of Cl_2 and HBr concentrations used to obtain the data in Table V, production of 3×10^{11} Br_2 per cm^3 would be accompanied by a drop in $[\text{Cl}_2]$ of ca. 1% and a negligible change in $[\text{HBr}]$.

(3) For $[\text{Cl}_2] \leq 7 \times 10^{13}$ molecules per cm^3 and for Cl_2 injection into the flow near the reaction zone, measured rate coefficients, $k_4(T)$, were found to be independent of Cl_2 concentration and injector position. In these experiments the injector position was varied over the range 1 to 5 cm upstream from the reaction zone, corresponding to a pre-flash contact time between Cl_2 and HBr of 0.2 to 1.0 seconds.

There have been several previous investigations of the kinetics of reaction (4). Moore and coworkers [33–35] studied reaction (4) by observing the time-resolved infrared emission from vibrationally excited HCl product. Rubin and Persky [45] measured $k_4(T)$ relative to reaction (14) in a discharge flow system.



Lamb et al. [46] studied reaction (4) using the very low pressure reactor (VLPR) technique. Using an apparatus similar to that employed by Moore and coworkers [33–35], Nesbitt and Leone [36] reported a value for k_4 (298K) from their study of the Cl_2/HBr laser initiated chain reaction. More recently, Dolson and Leone [37], also using an infrared chemiluminescence (IRCL) technique but with improved wavelength resolution, re-investigated the Cl_2/HBr laser-initiated chain reaction and, in the process, re-measured $k_4(T)$. Several theoretical calculations of k_4 are also reported in the literature [21–23,32]. Our results are compared with all previous studies of the kinetics of reaction (4) in Table VI.

It can be seen from inspection of Table VI that significant discrepancies exist in measured values for $k_4(298\text{ K})$ and in measured activation energies for reaction (4). Dolson and Leone [37] suggest that in all earlier IRCL studies [33–36], where the infrared emission was poorly resolved, $k_4(T)$ may have been underestimated due to vibrational cascading into the levels being detected. Dolson and Leone demonstrated that improper accounting for vibrational cascading could lead to the nonArrhenius temperature dependence reported by Mei and Moore [35]. The relatively fast rate coefficient reported by Dolson and Leone agrees well with the competitive

TABLE VI. Comparison of results obtained from kinetics studies of the $\text{Cl}(^2P) + \text{HBr}$ reaction.

Investigators	Technique ^a	Range of T^b	A^c	E/R^b	$k_4(298\text{ K})^c$
Wodarczyk & Moore [34]	LFP-IRCL	295			7.6 ^d
Bergmann & Moore [33]	LFP-IRCL	295			7.4 ^d
Mei & Moore [35]	LFP-IRCL	218–402	40 ^e	460 ^e	8.5 ^f
Nesbitt & Leone [36]	LFP-IRCL	298			7.9
Rubin & Persky [45]	DF-MS-CK	222–504	41 ^g	411 ^g	10.3 ^f
Lamb et al. [46]	VLPR-MS	267–333	3.4	0	3.4
Dolson & Leone [37]	LFP-IRCL	298			10.2
Douglas et al. [21]	CTC	h	h	360	h
Brown et al. [23]	QTC	298			50 ⁱ
Smith [22]	CTC	300–1000	j	j	4.7 ^k
Broida & Persky [32]	QTC	220–500	34 ^m	410 ^m	8.1
This Work	LFP-RF	257–404	22.5	400	4.9 ^f

^aLFP = laser flash photolysis; IRCL = infrared chemiluminescence; DF = discharge flow; MS = mass spectrometry; CK = competitive kinetics; VLPR = very low pressure reactor; RF = resonance fluorescence; QTC = quasi-classical trajectory calculation; CTC = classical trajectory calculation.

^bUnits are degrees Kelvin.

^cUnits are $10^{-12}\text{ cm}^3\text{ molecule}^{-1}\text{ s}^{-1}$.

^d $T = 295\text{ K}$.

^eFor 218–298 K data only; nonArrhenius behavior observed at $T > 298\text{ K}$.

^fCalculated from Arrhenius parameters.

^gCalculated assuming the following Arrhenius expression for the $\text{Cl} + \text{C}_2\text{H}_6$ reference reaction [71,75]: $k = 7.7 \times 10^{-11} \exp(-90/T)\text{ cm}^3\text{ molecule}^{-1}\text{ s}^{-1}$.

^hActivation energy reported but temperature range and absolute rate coefficients not given.

ⁱAssuming units in ref. [23] were meant to be $\text{cm}^3\text{ mol}^{-1}\text{ s}^{-1}$.

^j $k(1000\text{ K}) = 8.9k(300\text{ K})$.

^k $T = 300\text{ K}$.

^mArrhenius fit to rate coefficients calculated at 220 K, 300 K, and 500 K. Slightly non-Arrhenius behavior actually computed with 220 K and 300 K results giving E/R ca. 300 K while 300 K and 500 K results give E/R ca. 500 K.

kinetics result of Rubin and Persky [45], when the currently recommended Arrhenius expression for $k_4(T)$ [71,75] is used to put the Rubin and Persky result on an absolute scale. The VLPR study of Lamb et al. [36] employed much different experimental conditions than all other studies of reaction (4) (i.e., 5 mtorr total pressure, $[\text{Cl}]$ ca. $[\text{HBr}]$ ca. 5×10^{11} per cm^3); these investigators report a value for $k_4(298 \text{ K})$ which is about a factor of three lower than the values reported by Dolson and Leone and by Rubin and Persky, and observe no temperature dependence for k_4 over the range 267–333 K. Lamb et al. present mass balance data which suggests no problem with wall reactions. These authors also present an entropy calculation for reaction (4) which suggests an A -factor of $6 \times 10^{-12} \text{ cm}^3 \text{ molecule}^{-1} \text{ s}^{-1}$, significantly smaller than other experimental determinations (including ours). It is well established that a significant fraction of the HCl product of reaction (4) is formed in the second excited vibrational level [19,37]. Under the conditions employed by Lamb et al., it is possible that occurrence of the slightly exothermic back reaction



could have resulted in underestimation of k_4 . All other experimental studies employed conditions where $[\text{HBr}] \gg [\text{Cl}(^2P)]$ and, therefore, would not have been influenced by reaction (15).

The calculated rate coefficient reported by Brown et al. [23] appears to have been printed incorrectly in ref. [23] since the authors claim good agreement with the early experimental work of Wodarczyk and Moore [24] even though the value for $k_4(298 \text{ K})$ which appears in their article, $30.2 \times 10^{12} \text{ cm}^3 \text{ molecule}^{-1} \text{ s}^{-1}$ [23], is absurd. Rubin and Persky [34] suggest that Brown et al.'s rate coefficient is actually in units of $\text{cm}^3 \text{ mol}^{-1} \text{ s}^{-1}$; dividing Brown et al.'s reported value by Avogadro's number gives $k_4(298 \text{ K}) = 5.0 \times 10^{-11} \text{ cm}^3 \text{ molecule}^{-1} \text{ s}^{-1}$, much faster than all experimental values. Smith [22] has carried out a classical trajectory study of reaction (4) and reports $k_4(300 \text{ K}) = (4.7 \pm 0.8) \times 10^{-12} \text{ cm}^3 \text{ molecule}^{-1} \text{ s}^{-1}$, in excellent agreement with our result. A quasi classical trajectory calculation of $k_4(T)$ was recently reported by Broida and Persky [32]; their result, $k_4(300 \text{ K}) = 8.1 \times 10^{-12} \text{ cm}^3 \text{ molecule}^{-1} \text{ s}^{-1}$, is intermediate between our experimental value and the experimental values reported by Dolson and Leone [37] and by Rubin and Persky [45]. Comparison of experimental and theoretical values for k_4 at ambient temperature is probably not very meaningful since the potential energy surfaces used in the trajectory calculations [22,32] were adjusted to give reasonable agreement with experimental values for $k_4(298 \text{ K})$.

The activation energy for reaction (4) obtained in our study, $0.8 \text{ kcal mol}^{-1}$, agrees well with the activation energy reported by Rubin and Persky [45] and with the low temperature activation energy reported by Mei and Moore [35], but is in poor agreement with the result E_{act} ca. 0 reported by Lamb et al. [46]. Smith [22] has calculated k_4 at 300 K and 1000 K and finds that k_4 increases by a factor of 8.9 between these two temperatures. Assumption of a linear $\ln k_4(T)$ vs. T^{-1} dependence between 300 K and 1000 K would lead to an activation energy of $1.9 \text{ kcal mol}^{-1}$ from Smith's calculated rate coefficients, considerably larger than all experimental values (obtained from data at $T < 504 \text{ K}$). It is possible that E_{act} in-

creases with increasing T between 500 K and 1000 K. In fact, the rate coefficients calculated by Broida and Persky [32] at 220 K, 300 K, and 500 K suggest just such a trend, increasing E_{act} with increasing T . Both the magnitude and the temperature dependence of E_{act} calculated by Broida and Persky are consistent with our results. However, the scatter in our data prevents us from stating conclusively that we observe nonArrhenius behavior.

Summary

The laser flash photolysis-resonance fluorescence technique has been employed along with *in situ* monitoring of the excess reagent to study the temperature dependence of the thermal rate coefficients for reactions (1)–(4). The rate coefficient for reaction (1) has been found to be $(2.03 \pm 0.30) \times 10^{-11} \text{ cm}^3 \text{ molecule}^{-1} \text{ s}^{-1}$ independent of temperature over the range 255–350 K, in reasonable though not quantitative agreement with previous work [38–42] and about 40% faster than the currently recommended [71] value. The first temperature dependence study of the kinetics of reaction (2) is reported. We find that $k_2 = (1.58 \pm 0.36) \times 10^{-10} \text{ cm}^3 \text{ molecule}^{-1} \text{ s}^{-1}$ independent of temperature; our value for $k_2(298 \text{ K})$ agrees reasonably well with the rate coefficients reported previously by Clyne and coworkers [43,44]. Reaction (3) was studied over the temperature range 250 K to 402 K. As predicted by a recent theoretical study [17], our data are suggestive of a slightly nonArrhenius temperature dependence; best fit activation energies over various temperature ranges are $2.36 \pm 0.32 \text{ kcal mol}^{-1}$ for $250 \text{ K} < T < 298 \text{ K}$, $3.32 \pm 0.37 \text{ kcal mol}^{-1}$ for $298 \text{ K} < T < 402 \text{ K}$, and $2.88 \pm 0.32 \text{ kcal mol}^{-1}$ for $250 \text{ K} < T < 402 \text{ K}$. Values for $k_3(T)$ obtained in our study agree well with those reported previously [47–50]. Our results for reaction (4) are adequately described by the Arrhenius expression $k_4(T) = 2.25 \times 10^{-11} \exp(-400/T)$ for $257 \text{ K} \leq T \leq 404 \text{ K}$ although an activation energy which increases slightly with increasing temperature would also be consistent with our data. Due to problems with a heterogeneous dark reaction between HBr and Cl_2 the absolute uncertainty (2σ) in $k_4(T)$ at any temperature within the range studied is relatively high, and is estimated to be $\pm 25\%$. The values for $k_4(T)$ reported in this study are in rather poor agreement with all previously reported experimental rate coefficients [33–37,45,46].

Acknowledgment

This work was supported by the National Aeronautics and Space Administration through grant NAGW-1001. The authors would like to acknowledge K.D. Kruetter and C.J. Shackelford for assisting with some of the experiments.

Bibliography

- [1] S. C. Wofsy, M. B. McElroy, and Y. L. Yung, *Geophys. Res. Lett.*, **2**, 215 (1975).
- [2] Y. L. Yung, J. P. Pinto, R. T. Watson, and S. P. Sander, *J. Atmos. Sci.*, **37**, 339 (1980).
- [3] D. D. Parrish and D. R. Herschbach, *J. Am. Chem. Soc.*, **95**, 6133 (1973).

- [4] D. St. A. G. Radlein, J. C. Whitehead, and R. Grice, *Mol. Phys.*, **29**, 1813 (1975).
- [5] D. P. Fernie, D. J. Smith, A. Durkin, and R. Grice, *Mol. Phys.*, **46**, 41 (1982).
- [6] N. C. Firth, N. W. Keane, D. J. Smith, and R. Grice, *Laser Chem.*, **9**, 265 (1988).
- [7] P. A. Elofson, K. Rynsfors, and L. Holmid, *Chem. Phys.*, **118**, 1 (1987).
- [8] K. Rynsfors, L. Holmid, and P. A. Elofson, *Chem. Phys.*, **118**, 417 (1987).
- [9] J. J. Valentini, Y. T. Lee, and D. J. Auerbach, *J. Chem. Phys.*, **67**, 4866 (1977).
- [10] N. C. Blais and J. B. Cross, *J. Chem. Phys.*, **52**, 3580 (1970).
- [11] Y. T. Lee, J. D. McDonald, P. R. LeBreton, and D. R. Herschbach, *J. Chem. Phys.*, **49**, 2447 (1968).
- [12] Y. T. Lee, J. D. McDonald, P. R. LeBreton, and D. R. Herschbach, *J. Chem. Phys.*, **51**, 455 (1969).
- [13] D. Beck, F. Engelke, and H. J. Loesch, *Ber. Bunsenges. Phys. Chem.*, **72**, 1105 (1968).
- [14] H. J. Loesch and D. Beck, *Ber. Bunsenges. Phys. Chem.*, **75**, 736 (1971).
- [15] K. G. McKendrick, D. J. Rakestraw, R. Zhang, and R. N. Zare, *J. Phys. Chem.*, **92**, 5530 (1988).
- [16] J. E. Spencer and G. P. Glass, *Int. J. Chem. Kinet.*, **11**, 97 (1977).
- [17] M. Broida, M. Tamir, and A. Persky, *Chem. Phys.*, **110**, 83 (1986).
- [18] A. Persky and H. Kornweitz, *Chem. Phys.*, **133**, 415 (1989).
- [19] D. H. Maylotte, J. C. Polanyi, and K. B. Woodall, *J. Chem. Phys.*, **57**, 1547 (1972).
- [20] M. Baer, *J. Chem. Phys.*, **62**, 305 (1975).
- [21] D. J. Douglas, J. C. Polanyi, and J. J. Sloan, *Chem. Phys.*, **13**, 15 (1976).
- [22] I. W. M. Smith, *Chem. Phys.*, **20**, 437 (1977).
- [23] J. C. Brown, H. E. Bass, and D. L. Thompson, *J. Phys. Chem.*, **81**, 479 (1977).
- [24] J. A. Kaye and A. Kuppermann, *Chem. Phys. Lett.*, **92**, 574 (1982).
- [25] M. A. Wickramaaratchi and D. W. Setser, *J. Phys. Chem.*, **87**, 64 (1983).
- [26] N. Abusalbi, D. J. Kouri, V. Lopez, V. Babamov, and R. A. Marcus, *Chem. Phys. Lett.*, **103**, 458 (1984).
- [27] V. Lopez, V. K. Babamov, and R. A. Marcus, *J. Chem. Phys.*, **81**, 3962 (1984).
- [28] B. C. Garrett, N. Abusalbi, D. J. Kouri, and D. G. Truhlar, *J. Chem. Phys.*, **83**, 2252 (1985).
- [29] C. Lim and D. G. Truhlar, *J. Phys. Chem.*, **89**, 5 (1985).
- [30] C. Lim and D. G. Truhlar, *J. Phys. Chem.*, **90**, 2616 (1986).
- [31] H. Teitelbaum, *J. Chem. Soc. Farad. Trans. II*, **84**, 1889 (1988).
- [32] M. Broida and A. Persky, *Chem. Phys.*, **133**, 405 (1989).
- [33] K. Bergmann and C. B. Moore, *J. Chem. Phys.*, **63**, 643 (1975).
- [34] F. J. Wodarczyk and C. B. Moore, *Chem. Phys. Lett.*, **26**, 484 (1974).
- [35] C.-C. Mei and C. B. Moore, *J. Chem. Phys.*, **67**, 3936 (1977).
- [36] D. J. Nesbitt and S. R. Leone, *J. Chem. Phys.*, **75**, 4949 (1981).
- [37] D. A. Dolson and S. R. Leone, *J. Phys. Chem.*, **91**, 3543 (1987).
- [38] M. A. A. Clyne and H. W. Cruse, *Trans. Far. Soc.*, **67**, 2869 (1971).
- [39] H. W. Cruse, *Dissertation*, Queen Mary College, London University, 1971.
- [40] M. A. A. Clyne, P. B. Monkhouse, and L. W. Townsend, *Int. J. Chem. Kinet.*, **8**, 425 (1976).
- [41] F. B. Moin, Ya. P. Yurkevich, and V. M. Drogobyt'skii, *Doklady Akad. Nauk SSSR*, **226**, 866 (1975).
- [42] A. F. Dodonov, V. V. Zelenov, and V. L. Tal'roze, *Kinet. Katal. (USSR)*, **22**, 245 (1981).
- [43] M. A. A. Clyne and H. W. Cruse, *J. Chem. Soc. Far. Trans. II*, **68**, 1377 (1972).
- [44] P. P. Bemand and M. A. A. Clyne, *J. Chem. Soc. Far. Trans. II*, **71**, 1132 (1975).
- [45] R. Rubin and A. Persky, *J. Chem. Phys.*, **79**, 4310 (1983).
- [46] J. J. Lamb, O. Kondo, and S. W. Benson, *J. Phys. Chem.*, **90**, 841 (1986).
- [47] G. A. Takacs and G. P. Glass, *J. Phys. Chem.*, **77**, 1182 (1973).
- [48] R. D. H. Brown and I. W. M. Smith, *Int. J. Chem. Kinet.*, **7**, 301 (1975).
- [49] D. L. Singleton and R. J. Cvetanovic, *Can. J. Chem.*, **56**, 2934 (1978).
- [50] D. F. Nava, S. R. Bosco, and L. J. Stief, *J. Chem. Phys.*, **78**, 2443 (1983).
- [51] A. R. Ravishankara and P. H. Wine, *J. Chem. Phys.*, **72**, 25 (1980).
- [52] P. H. Wine, D. H. Semmes, and A. R. Ravishankara, *Chem. Phys. Lett.*, **90**, 128 (1982).
- [53] P. H. Wine and D. H. Semmes, *J. Phys. Chem.*, **87**, 3572 (1983).
- [54] P. H. Wine, J. R. Wells, and J. M. Nicovich, *J. Phys. Chem.*, **92**, 2223 (1988).
- [55] J. M. Nicovich, C. J. Shackelford, and P. H. Wine, *J. Phys. Chem.*, in press.
- [56] P. H. Wine and A. R. Ravishankara, *Chem. Phys. Lett.*, **77**, 103 (1981).

- [57] P. H. Wine and A. R. Ravishankara, *Chem. Phys. Lett.*, **69**, 365 (1982).
- [58] P. H. Wine and A. R. Ravishankara, *Chem. Phys. Lett.*, **96**, 129 (1983).
- [59] P. H. Wine, J. M. Nicovich, R. J. Thompson, and A. R. Ravishankara, *J. Phys. Chem.*, **87**, 3948 (1983).
- [60] P. H. Wine, J. M. Nicovich, and A. R. Ravishankara, *J. Phys. Chem.*, **89**, 3914 (1985).
- [61] P. H. Wine, J. R. Wells, and A. R. Ravishankara, *J. Chem. Phys.*, **84**, 1349 (1986).
- [62] A. R. Ravishankara, P. H. Wine, C. A. Smith, P. E. Barbone, and A. Torabi, *J. Geophys. Res.*, **91**, 5355 (1986).
- [63] J. C. Brock and R. T. Watson, *Chem. Phys. Lett.*, **71**, 371 (1980).
- [64] G. E. Streit, C. J. Howard, A. L. Schmeltekopf, J. A. Davidson, and H. I. Schiff, *J. Chem. Phys.*, **65**, 4761 (1976).
- [65] S. T. Amimoto, A. P. Force, R. G. Gulotty, Jr., and J. R. Wiesenfeld, *J. Chem. Phys.*, **71**, 3640 (1979).
- [66] R. H. Clark and D. Husain, *J. Chem. Soc. Far. Trans. II*, **80**, 97 (1984).
- [67] S. A. Sotnichenko, V. Ch. Bokun, and A. I. Nadkin, *Chem. Phys. Lett.*, **153**, 560 (1988).
- [68] C. F. Goodeve and A. W. C. Taylor, *Proc. Roy. Soc. London Ser. A*, **152**, 221 (1935).
- [69] A. R. Ravishankara, P. H. Wine, and A. O. Langford, *Chem. Phys. Lett.*, **63**, 479 (1979).
- [70] J. G. Calvert and J. N. Pitts, Jr., *Photochemistry*, Wiley, New York, 1966.
- [71] R. Atkinson, D. L. Baulch, R. A. Cox, R. F. Hampson, Jr., J. A. Kerr, and J. Troe, *J. Phys. Chem. Ref. Data*, **18**, 881 (1989).
- [72] R. H. Krech, G. J. Diebold, and D. L. McFadden, *J. Am. Chem. Soc.*, **99**, 4605 (1977).
- [73] H. O. Hirschfelder, C. F. Curtiss, and R. B. Bird, *Molecular Theory of Gases and Liquids*, Wiley, New York, 1954.
- [74] W. Y. Wen and R. M. Noyes, *Int. J. Chem. Kinet.*, **6**, 29 (1974).
- [75] W. B. DeMore, M. J. Molina, S. P. Sander, D. M. Golden, R. F. Hampson, M. J. Kurylo, C. J. Howard, and A. R. Ravishankara, *Chemical Kinetics and Photochemical Data For Use in Stratospheric Modeling*, JPL Publication 87-41, 1987.

Received July 25, 1989

Accepted October 6, 1989

NDB
S16-25

K-10-1
026134
073558
8P.

Kinetics and Thermochemistry of Reversible Adduct Formation in the Reaction of $\text{Cl}(^2P_J)$ with CS_2

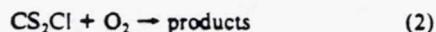
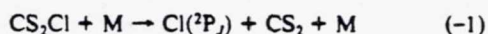
J. M. Nicovich, C. J. Shackelford,[†] and P. H. Wine*

Molecular Sciences Branch, Georgia Tech Research Institute, Georgia Institute of Technology, Atlanta, Georgia 30332 (Received: May 15, 1989; In Final Form: November 8, 1989)

Reversible adduct formation in the reaction of $\text{Cl}(^2P_J)$ with CS_2 has been observed over the temperature range 193–258 K by use of time-resolved resonance fluorescence spectroscopy to follow the decay of pulsed-laser-generated $\text{Cl}(^2P_J)$ into equilibrium with CS_2Cl . Rate coefficients for CS_2Cl formation and decomposition have been determined as a function of temperature and pressure; hence, the equilibrium constant has been determined as a function of temperature. A second-law analysis of the temperature dependence of K_p and heat capacity corrections calculated with use of an assumed CS_2Cl structure yields the following thermodynamic parameters for the association reaction: $\Delta H_{f,298}^\circ = -10.5 \pm 0.5 \text{ kcal mol}^{-1}$, $\Delta H^\circ_0 = -9.5 \pm 0.7 \text{ kcal mol}^{-1}$, $\Delta S^\circ_{298} = -26.8 \pm 2.4 \text{ cal mol}^{-1} \text{ deg}^{-1}$, and $\Delta H_{f,298}(\text{CS}_2\text{Cl}) = 46.4 \pm 0.6 \text{ kcal mol}^{-1}$. The resonance fluorescence detection scheme has been adapted to allow detection of $\text{Cl}(^2P_J)$ in the presence of large concentrations of O_2 , thus allowing the $\text{CS}_2\text{Cl} + \text{O}_2$ reaction to be investigated. We find that the rate coefficient for $\text{CS}_2\text{Cl} + \text{O}_2$ reaction via all channels that do not generate $\text{Cl}(^2P_J)$ is $< 2.5 \times 10^{-16} \text{ cm}^3 \text{ molecule}^{-1} \text{ s}^{-1}$ at 293 K and 300-Torr total pressure and that the total rate coefficient is $< 2 \times 10^{-15} \text{ cm}^3 \text{ molecule}^{-1} \text{ s}^{-1}$ at 230 K and 30-Torr total pressure. Evidence for reversible adduct formation in the reaction of $\text{Cl}(^2P_J)$ with COS was sought but not observed, even at temperatures as low as 194 K.

Introduction

It is now well established that the reaction of OH radicals with CS_2 in air proceeds via a complex three-step mechanism involving formation of a weakly bound adduct that reacts with O_2 to form products in competition with unimolecular decomposition back to reactants.^{1–4} Recently, Martin et al.⁵ reported results from a steady-state-photolysis-competitive-kinetics-end-product analysis study that suggest that chlorine atoms react with CS_2 via a similar mechanism



In this study, we report direct kinetic observations that test the above mechanism and allow determination of rate coefficients for reactions 1, -1, and 2 as well as the CS_2Cl heat of formation. A few experiments that examine the related reactions of $\text{Cl}(^2P_J)$ with COS are also reported.

Experimental Technique

The laser flash photolysis-resonance fluorescence apparatus used in this study was similar to one we have employed previously in a number of studies of chlorine atom kinetics.^{6–9} Some modifications were required in order to facilitate $\text{Cl}(^2P_J)$ detection in the presence of relatively large concentrations of O_2 . Important features of the apparatus are described below.

A Pyrex, jacketed reaction cell with an internal volume of $\sim 150 \text{ cm}^3$ was used in most experiments,¹⁰ while a newly constructed Pyrex, jacketed cell with a similar internal volume was used in a few experiments with O_2 buffer gas. The new reaction cell was specifically designed to minimize the path of fluorescence excitation radiation and emitted fluorescence through O_2 ; a schematic of the new cell is shown in Figure 1. Both cells could be

maintained at a constant temperature by circulating ethylene glycol or 50% methanol/50% ethanol from a thermostated bath through the outer jacket. A copper-constantan thermocouple with a stainless steel jacket was injected into the reaction zone through a vacuum seal, thus allowing measurement of the gas temperature under the precise pressure and flow rate conditions of the experiment.

$\text{Cl}(^2P_J)$ was produced by 355-nm pulsed laser photolysis (third harmonic, Nd:YAG laser) of Cl_2 ; the laser pulse width was 6 ns. The laser was typically operated at a fluence of 5–10 mJ/pulse and a repetition rate of 2 Hz, although 50 mJ/pulse at a repetition rate of 10 Hz was attainable.

A chlorine resonance lamp, situated perpendicular to the photolysis laser, excited resonance fluorescence in the photolytically produced atoms. The resonance lamp consisted of an electrodeless microwave discharge through about 1 Torr of a flowing mixture containing a trace of Cl_2 in He. The flows of a 0.1% Cl_2 in He mixture and pure He into the lamp were controlled by separate needle valves, thus allowing the total pressure and Cl_2 concentration to be adjusted for optimum signal-to-noise ratio. Radiation was coupled out of the lamp through a magnesium fluoride window and into the reaction cell through a magnesium fluoride lens. Before entering the reaction cell, the lamp output passed through a flowing gas filter. For detection of chlorine atoms in N_2 buffer gas, the filter gas was normally a dilute $\text{N}_2\text{O}/\text{N}_2$ mixture; the N_2O level was adjusted to attenuate virtually all oxygen atom impurity emissions from the lamp (130–131 nm) while transmitting the

(1) Jones, B. M. R.; Burrows, J. P.; Cox, R. A.; Penkett, S. A. *Chem. Phys. Lett.* 1982, 88, 372.

(2) Barnes, I.; Becker, K. H.; Fink, E. H.; Reiner, A.; Zabel, F.; Niki, H. *Int. J. Chem. Kinet.* 1983, 15, 631.

(3) Hynes, A. J.; Wine, P. H.; Nicovich, J. M. *J. Phys. Chem.* 1988, 92, 3846.

(4) Murrells, T. P.; Lovejoy, E. R.; Ravishankara, A. R. *J. Phys. Chem.*, in press.

(5) Martin, D.; Barnes, I.; Becker, K. H. *Chem. Phys. Lett.* 1987, 140, 195.

(6) Ravishankara, A. R.; Wine, P. H. *J. Chem. Phys.* 1980, 72, 25.

(7) Wine, P. H.; Semmes, D. H.; Ravishankara, A. R. *Chem. Phys. Lett.* 1982, 90, 128.

(8) Wine, P. H.; Semmes, D. H. *J. Phys. Chem.* 1983, 87, 3572.

(9) Wine, P. H.; Wells, J. R.; Nicovich, J. M. *J. Phys. Chem.* 1988, 92, 2223.

(10) Wine, P. H.; Kreutter, N. M.; Ravishankara, A. R. *J. Phys. Chem.* 1979, 83, 3191.

* Author to whom correspondence should be addressed.

[†] Present address: School of Physics, Georgia Institute of Technology, Atlanta, GA 30332.

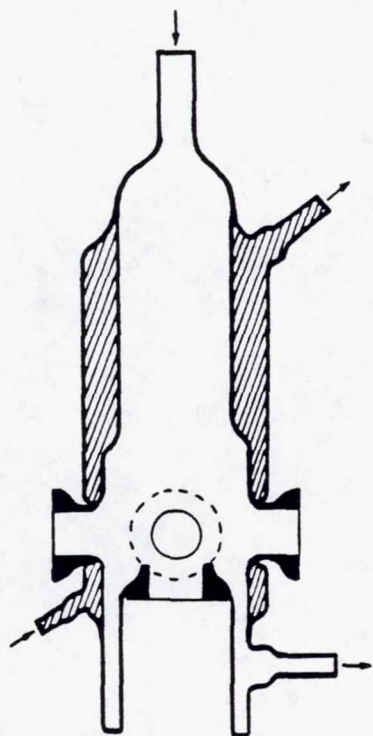


Figure 1. Diagram of reaction cell designed to minimize the path length of $\text{Cl}(^2\text{P}_j)$ resonance radiation through an absorbing gas in the reaction mixture. The bottom port is used for fluorescence detection.

chlorine lines in the 135–140-nm region.

Fluorescence was collected by a magnesium fluoride lens on an axis orthogonal to both the photolysis laser beam and the resonance lamp beam and imaged onto the photocathode of a solar-blind photomultiplier. The region between the reaction cell and the photomultiplier was purged with N_2 . For detection of chlorine atoms in N_2 buffer gas, a calcium fluoride window was placed between the reaction cell and photomultiplier to prevent lamp emissions at wavelengths shorter than 125 nm (Lyman- α emission for example) from reaching the photomultiplier. Signals were processed by photon-counting techniques in conjunction with multichannel scaling. The multichannel analyzer sweep was triggered prior to the laser Q switch to allow a pretrigger base line to be obtained.

In order to avoid the accumulation of photolysis or reaction products, all experiments were carried out under "slow-flow" conditions. The linear flow rate through the reactor was (typically) 3 cm s^{-1} , and the laser repetition rate was (typically) 2 Hz. Hence, no volume element of the reaction mixture was subjected to more than a few laser shots. CS_2 , COS , O_3 , and Cl_2 were flowed into the reaction cell from 12-L bulbs containing dilute mixtures in nitrogen, air, or oxygen buffer gas. The reactant mixture, chlorine mixture, and additional buffer gas were premixed before entering the reactor. The concentrations of each component in the reaction mixture were determined from measurements of the appropriate mass flow rates and the total pressure. Concentrations of CS_2 , COS , and O_3 were also measured in situ in the slow-flow system by UV photometry. Monitoring wavelengths, light sources, absorption path lengths, and absorption cross sections relevant to the photometric measurements are summarized in Table I.

The pure gases used in this study had the following stated minimum purities: N_2 , 99.999%; O_2 , 99.99%; Cl_2 , 99.99%; COS , 97.5%. Air was ultra zero grade with total hydrocarbons less than 0.1 ppm. Nitrogen, oxygen, and air were used as supplied. Chlorine was degassed at 77 K before use. The COS sample was purified by degassing at 77 K after passage over ascarite.¹¹ Carbon disulfide was Aldrich Gold Label with a stated purity of

TABLE I: Parameters Relevant to in Situ Monitoring of CS_2 , COS , and O_3

species	λ , nm	$10^{20}\sigma$, cm^2	path length, cm
CS_2	312.6, 313.2 ^a	7.08	115, 216
CS_2	213.9 ^b	340	15.1, 115
COS	228.8 ^c	27.0	115
O_3	253.7 ^a	1150	216

^aLight source: Hg pen ray lamp. ^bLight source: Zn hollow cathode lamp. ^cLight source: Cd pen ray lamp.

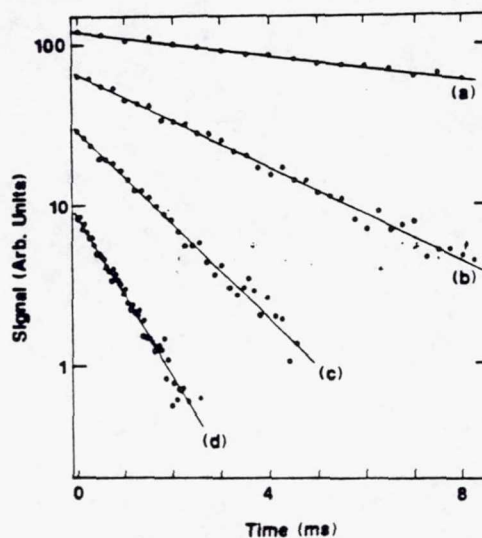


Figure 2. Typical $\text{Cl}(^2\text{P}_j)$ temporal profiles observed following pulsed laser photolysis of Cl_2/O_3 mixtures in 300 Torr of air at 293 K. In all experiments shown in the figure, $[\text{Cl}_2] = 1.0 \times 10^{14} \text{ molecules/cm}^3$ and $[\text{Cl}(^2\text{P}_j)]_0 = 1.0 \times 10^{12} \text{ atoms/cm}^3$. $[\text{O}_3]$ ($10^{13} \text{ molecules/cm}^3$) = (a) 0, (b) 1.81, (c) 5.19, and (d) 9.68. Number of laser shots averaged = (a) 500, (b) 1000, (c) 1500, (d) 4000. Solid lines are obtained from least-squares analyses and give the following pseudo-first-order decay rates (s^{-1}): (a) 83, (b) 336, (c) 679, and (d) 1160.

99+%. Before use, the liquid CS_2 sample was transferred under nitrogen atmosphere into a vial fitted with a high-vacuum stopcock, degassed at 77 K, and then purified by trap-to-trap distillation (210–77 K). Ozone was prepared in a commercial ozonator with UHP oxygen. It was collected and stored on silica gel at 195 K and degassed at 77 K before use.

One aspect of this work that differs from all previous studies of chlorine atom kinetics in our laboratory is the use of time-resolved resonance fluorescence spectroscopy as a $\text{Cl}(^2\text{P}_j)$ detection technique in the presence of large levels of oxygen. An accidental overlap of the 118.9-nm chlorine doublet ($^2\text{D}_{5/2,3/2} \rightarrow ^2\text{P}_{3/2}$ transitions) with a "window" in the O_2 absorption spectrum makes such an experiment feasible. A 1 atm-cm amount of air completely absorbs all lines of the $^2\text{D} \rightarrow ^2\text{P}$, $^2\text{P} \rightarrow ^2\text{P}$, and $^4\text{P} \rightarrow ^2\text{P}$ chlorine multiplets except the 118.9-nm doublet, which is only attenuated by about a factor of 2.¹² Use of 118.9 nm as the resonant wavelength for $\text{Cl}(^2\text{P}_j)$ detection requires that all optics in the detection train be magnesium fluoride or lithium fluoride; hence, no filter for Lyman- α radiation could be employed. In most experiments, the filter cell between the resonance lamp and the reactor was flushed with N_2 , i.e., most of the lamp output was absorbed by O_2 in the reactor (but far removed from the region where the photolysis beam and probe beam crossed). As a check, some experiments were carried out with N_2 replaced by dry air as the filter gas. Observed kinetics were independent of this variation—only signal strengths were affected.

To test the integrity of our scheme for studying chlorine atom kinetics in the presence of O_2 , the well-studied $\text{Cl} + \text{O}_3$ reaction was investigated at 293 K in 300-Torr air. Typical pseudo-

(11) Friedl, R. R. Dissertation, Harvard University, 1984.

(12) Anderson, J. G.; Grassl, H. J.; Shetter, R. E.; Margitan, J. J. *J. Geophys. Res.* 1980, 85, 2869.

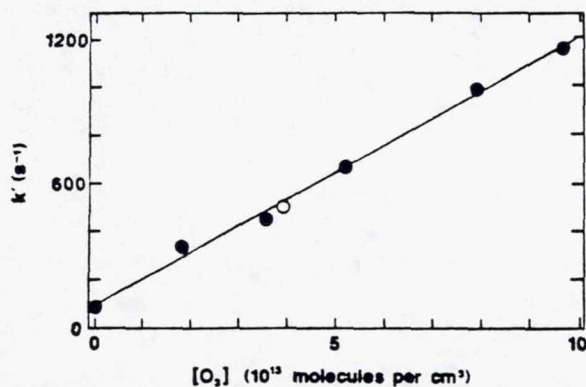
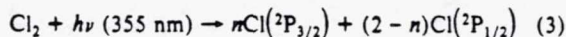


Figure 3. Plot of the pseudo-first-order chlorine atom decay rate, k' , as a function of the O_3 concentration. Experimental conditions: $T = 293$ K, $P = 300$ Torr of air, $[Cl_2] = 1.0 \times 10^{14}$ molecules/cm³, $[Cl(^2P_J)] = 1.0 \times 10^{12}$ (●) or 4.0×10^{11} (○) atoms/cm³. The solid line is obtained from a linear least-squares analysis and gives the bimolecular rate coefficient $(1.12 \pm 0.08) \times 10^{-11}$ cm³ molecule⁻¹ s⁻¹ where the uncertainty is 2σ and represents precision only.

first-order $Cl(^2P_J)$ decays observed in the $Cl + O_3$ experiment are shown in Figure 2; the photolytically produced chlorine atom concentration in all four experiments shown in Figure 2 was 1.0×10^{12} atoms/cm³. A plot of the pseudo-first-order chlorine atom decay rate as a function of the ozone concentration is shown in Figure 3. The slope of this plot gives a bimolecular rate coefficient of $(1.12 \pm 0.08) \times 10^{-11}$ cm³ molecule⁻¹ s⁻¹ where the uncertainty is 2σ and represents precision only. Agreement with the literature value¹³ of 1.16×10^{-11} cm³ molecule⁻¹ s⁻¹ is excellent. The results shown in Figures 2 and 3 clearly demonstrate that time-resolved resonance fluorescence spectroscopy is a viable detection scheme for flash photolysis studies of chlorine atom kinetics in the presence of large levels of O_2 .

Results and Discussion

As mentioned above, $Cl(^2P_J)$ was produced by 355-nm pulsed laser photolysis of Cl_2 .



Reported rate coefficients for quenching of the spin-orbit excited state, $Cl(^2P_{1/2})$, by N_2 and O_2 are in the range $(4.0\text{--}6.5) \times 10^{-13}$ cm³ molecule⁻¹ s⁻¹ and $(1.3\text{--}230) \times 10^{-13}$ cm³ molecule⁻¹ s⁻¹, respectively.^{14,15} Hence, for the N_2 , O_2 , and CS_2 levels employed in this study (Table II), relaxation of $Cl(^2P_{1/2})$ was greater than 10 times more rapid than chemical removal of $Cl(^2P_J)$, and all measured $Cl(^2P_J)$ temporal profiles can be considered as representative of the removal of an equilibrium mixture of $Cl(^2P_{1/2})$ and $Cl(^2P_{3/2})$. The equilibrium fraction of chlorine atoms in the $^2P_{1/2}$ state ranges from 0.0013 at 190 K to 0.015 at 300 K.

The CS_2 absorption cross section at 355 nm is very small ($< 1 \times 10^{-21}$ cm²).¹⁶ In the presence of O_2 buffer gas, electronically excited CS_2 can react with O_2 to produce $CS + SO_2$; the quantum yield for chemical reaction is thought to be a few percent.¹⁷ Under the conditions of our experiments with O_2 buffer gas, CS produced via the above mechanism was about 100 times lower in concentration than $Cl(^2P_J)$ produced via Cl_2 photolysis. Hence, side reactions involving CS that produce or destroy $Cl(^2P_J)$ could not

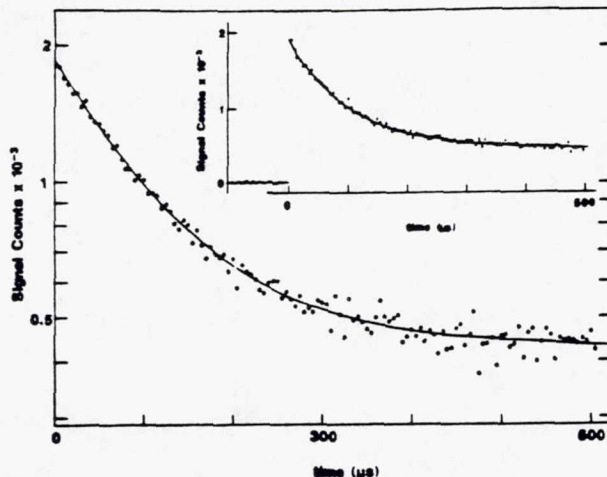
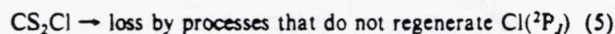
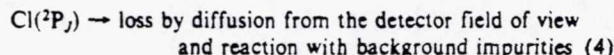
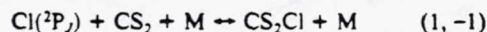


Figure 4. Typical $Cl(^2P_J)$ temporal profile observed following pulsed laser photolysis of $Cl_2/CS_2/N_2$ mixtures at temperatures below 260 K. The laser fired at time = 0. Experimental conditions: $T = 222$ K, $P = 30$ Torr, $[CS_2] = 2.70 \times 10^{15}$ molecules/cm³, $[Cl_2] = 4.8 \times 10^{13}$ molecules/cm³, $[Cl(^2P_J)]_0 = 4.1 \times 10^{11}$ atoms/cm³, 1050 laser shots averaged. The solid line is obtained from a nonlinear least-squares analysis that yields the following best fit parameters: $Q = 2370$ s⁻¹, $\lambda_1 = -87$ s⁻¹, $\lambda_2 = -9440$ s⁻¹. The inset shows the same data plotted on a linear rather than a logarithmic scale.

have been a significant interference in any of our experiments.

If the mechanism for the $Cl + CS_2$ reaction proposed by Martin et al.⁵ is correct, then, in the absence of O_2 , the $Cl(^2P_J)$ temporal profile should be controlled by the following reactions:



There appear to be no energetically allowed bimolecular channels for the $Cl + CS_2$ reaction. The rate equations for the above scheme can be solved analytically as long as all $Cl(^2P_J)$ and CS_2Cl loss processes are first order:

$$\frac{[Cl(^2P_J)]_t}{[Cl(^2P_J)]_0} = \frac{(Q + \lambda_1) \exp(\lambda_1 t) - (Q + \lambda_2) \exp(\lambda_2 t)}{\lambda_1 - \lambda_2} \quad (I)$$

where

$$\lambda_1 = 0.5((\alpha^2 - 4\beta)^{1/2} - \alpha) \quad (II)$$

$$\lambda_2 = -0.5((\alpha^2 - 4\beta)^{1/2} + \alpha) \quad (III)$$

$$Q = k_{-1} + k_5 \quad (IV)$$

$$\alpha = Q + k_4 + k_1[CS_2] = -(\lambda_1 + \lambda_2) \quad (V)$$

$$\beta = k_4 Q + k_1 k_5 [CS_2] = \lambda_1 \lambda_2 \quad (VI)$$

A double-exponential decay is predicted. Good-quality experimental data could be fit to eq I to obtain values for the three parameters λ_1 , λ_2 , and Q . Since k_4 is directly measured, the other elementary rate coefficients can be obtained as follows:

$$k_1 = -(\lambda_1 + \lambda_2 + k_4 + Q)/[CS_2] \quad (VII)$$

$$k_5 = (\lambda_1 \lambda_2 - k_4 Q)/k_1 [CS_2] \quad (VIII)$$

$$k_{-1} = Q - k_5 \quad (IX)$$

It should be noted that the parameter Q represents the sum of all first-order CS_2Cl removal processes. Therefore, eqs IV and IX require the assumption that the only CS_2Cl removal process that regenerates chlorine atoms is reaction -1.

When $Cl_2/CS_2/N_2$ mixtures at 298 K were subjected to 355-nm laser flash photolysis, the double-exponential decays predicted in the above analysis were not observed. However, at temperatures

(13) DeMore, W. B.; Molina, M. J.; Sander, S. P.; Golden, D. M.; Hampson, R. F.; Kurylo, M. J.; Howard, C. J.; Ravishankara, A. R. *Chemical Kinetics and Photochemical Data for Use in Stratospheric Modeling*; JPL Publication No. 87-41; Jet Propulsion Laboratory: Pasadena, CA, 1987.

(14) Clark, R. H.; Hussain, D. J. *Chem. Soc., Faraday Trans. 2* 1984, 80, 97.

(15) Sotnichenko, S. A.; Bokun, V. Ch.; Nadkhin, A. I. *Chem. Phys. Lett.* 1988, 153, 560.

(16) Rabalais, J. W.; McDonald, J. M.; Scherr, V.; McGlynn, S. P. *Chem. Rev.* 1971, 71, 73.

(17) Jones, B. M. R.; Cox, R. A.; Penkett, S. A. *J. Atmos. Chem.* 1983, 1, 65.

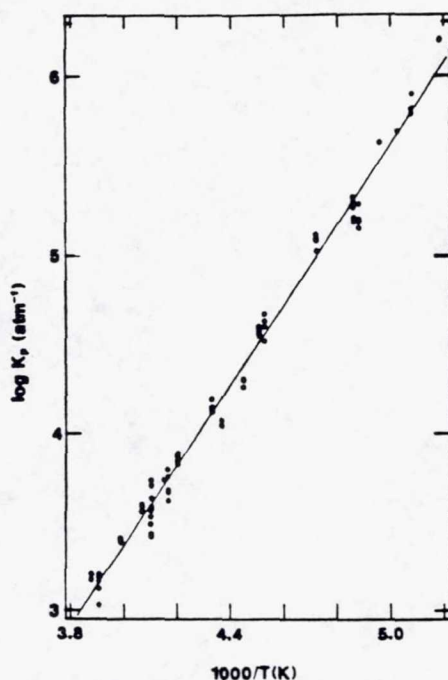


Figure 5. van't Hoff plot for the equilibrium $\text{Cl}(^2P_J) + \text{CS}_2 \rightleftharpoons \text{CS}_2\text{Cl}$. The solid line is obtained from a linear least-squares analysis; its slope gives $\Delta H^\circ = -10.34 \pm 0.23 \text{ kcal mol}^{-1}$, and its intercept gives $\Delta S^\circ = -25.94 \pm 1.02 \text{ cal mol}^{-1} \text{ deg}^{-1}$ where the uncertainties are 2σ and represent precision only.

below 260 K, double-exponential decays became readily observable. A typical $\text{Cl}(^2P_J)$ temporal profile, observed at $T = 222 \text{ K}$, $P = 30 \text{ Torr}$, $[\text{CS}_2] = 2.70 \times 10^{15} \text{ molecules/cm}^3$, is shown in Figure 4. A total of 85 temporal profiles were measured at temperatures, pressures, and CS_2 levels where double-exponential decays were observed; the results obtained from analysis of these temporal profiles are summarized in Table II. The equilibrium constants, K_p , given in Table II were computed from the relationship

$$K_p = K_c/RT = k_1/k_{-1}RT \quad (\text{X})$$

Nonlinear least-squares analyses were employed to extract values for λ_1 , λ_2 , Q , and the extrapolated signal level at $t = 0$ from the experimental temporal profiles. Values for k_1 , k_{-1} , and K_p were then calculated.

A van't Hoff plot for the equilibrium defined by reactions 1 and -1 is shown in Figure 5. Since

$$\ln K_p = (\Delta S^\circ/R) - (\Delta H^\circ/RT) \quad (\text{XI})$$

the enthalpy change associated with reaction 1 is obtained from the slope of the van't Hoff plot while the entropy change is obtained from the intercept. At 221 K, the midpoint of the experimental $1/T$ range, this "second-law method" yields the results $\Delta H^\circ = -10.34 \pm 0.23 \text{ kcal mol}^{-1}$ and $\Delta S^\circ = -25.94 \pm 1.02 \text{ cal mol}^{-1} \text{ deg}^{-1}$, where the errors are 2σ and represent precision only. Considering potential systematic errors (in the $[\text{CS}_2]$ and temperature measurements, for example), we estimate the accuracies of the ΔH° and ΔS° determinations to be $\pm 4\%$ and $\pm 8\%$, respectively.

Since no structural information or vibrational frequencies are available for CS_2Cl , it is not possible to accurately calculate an entropy change for reaction 1. However, to see if our second-law value for ΔS° is reasonable, we have carried out an entropy calculation using an assumed, reasonable structure. We assume that Cl binds to the carbon atom to form a planar ClCS_2 species. The C-S bond lengths are taken to be 1.55 Å (identical with that in CS_2), the C-Cl bond length is taken to be 2.0 Å, and the S-C-S bond angle is assumed to be 150°. The set of assumed vibrational frequencies are given in Table III. At 221 K, the calculation gives $S(\text{ClCS}_2) = 65.0 \text{ cal mol}^{-1} \text{ deg}^{-1}$ and $\Delta S^\circ = -26.0 \text{ cal mol}^{-1}$

deg^{-1} , i.e., the calculated ΔS° agrees with the experimental value within $0.06 \text{ cal mol}^{-1} \text{ deg}^{-1}$. While the degree of agreement is clearly fortuitous, we can conclude that our experimental value for ΔS° is reasonable. Using our assumed structural parameters and vibrational frequencies to calculate heat capacity corrections leads to the following thermodynamic parameters: $\Delta H^\circ_{298} = -10.5 \pm 0.5 \text{ kcal mol}^{-1}$, $\Delta H^\circ_0 = -9.5 \pm 0.7 \text{ kcal mol}^{-1}$, $\Delta S^\circ_{298} = -26.8 \pm 2.4 \text{ cal mol}^{-1} \text{ deg}^{-1}$. In conjunction with known heats of formation for $\text{Cl}(^2P_J)$ and CS_2^{13} , our value for ΔH°_{298} leads to the result $\Delta H_{1,298}(\text{ClCS}_2) = 46.4 \pm 0.6 \text{ kcal mol}^{-1}$. Uncertainties in the above thermodynamic parameters are 2σ and include both precision and estimates of systematic errors.

Examination of the experimental results at $T = 205, 206, 229, 231, 240, 244,$ and 256 K (Table II) shows an apparent tendency for K_p to vary systematically as a function of pressure. One possible explanation for such results is nonthermalization of the energized CS_2Cl adduct before dissociation. However, if adduct decomposition occurred from highly vibrationally excited levels, then the apparent value for k_{-1} would be larger than the real value and $K_p (=k_1/k_{-1}RT)$ would be underestimated. Then, if reactions 1 and -1 were in the fall-off regime such that the adduct relaxation rate increased more rapidly with pressure than did k_1 and k_{-1} , K_p would appear to increase with increasing pressure. In fact, the opposite trend is observed (Table II). It appears, therefore, that the tendency for measured values for K_p to decrease with increasing pressure is due not to incomplete thermalization of CS_2Cl but rather to small systematic errors in the experimental or data analysis procedures. At low temperature and pressure, k_{-1} is difficult to determine accurately because reaction 5 can make a significant contribution to CS_2Cl removal. At high temperature and pressure, the rate of decay into equilibrium becomes very fast and difficult to measure accurately; also, a small error (less than 1 μs) in defining the exact time that the laser fires can lead to significant errors in K_p under high-temperature, high-pressure conditions. Another possible systematic error that could explain the observed dependence of K_p on pressure would be a pressure-dependent error in the temperature measurement. Needless to say, we are aware of the above-mentioned sources of error and have tried our best to minimize them.

To assess the possible affect of pressure-dependent systematic errors on the accuracy of our results, we have carried out two additional second-law analyses, one on the 54 experiments carried out at 30-Torr total pressure and another on the 31 experiments carried out at 60–600-Torr total pressure. The 30-Torr data give $\Delta H^\circ_{221 \text{ K}} = -10.41 \pm 0.14 \text{ kcal mol}^{-1}$ and $\Delta S^\circ_{221 \text{ K}} = -26.00 \pm 0.64 \text{ cal mol}^{-1} \text{ deg}^{-1}$ while the high-pressure data give $\Delta H^\circ_{225 \text{ K}} = -10.15 \pm 0.26 \text{ kcal mol}^{-1}$ and $\Delta S^\circ_{225 \text{ K}} = -25.49 \pm 1.14 \text{ cal mol}^{-1} \text{ deg}^{-1}$ (errors are 2σ , precision only). We conclude that pressure-dependent systematic errors have a virtually negligible influence on the accuracy of reported thermodynamic parameters.

Our direct observation of equilibrium kinetics confirms that the $\text{Cl}(^2P_J) + \text{CS}_2$ reaction proceeds via reversible adduct formation as proposed by Martin et al.⁵ Removal of CS_2 in Martin et al.'s steady-state-photolysis experiments is proposed to result from the fact that CS_2Cl can react with O_2 in competition with reaction -1. To investigate this possibility, we studied the kinetics of $\text{Cl}(^2P_J)$ removal as a function of CS_2 concentration in 300 Torr of N_2 and 300 Torr of air at the same temperature (293 K) as employed by Martin et al.⁵ In 300 Torr of N_2 , nonexponential $\text{Cl}(^2P_J)$ decays were observed with the decay rate at short times after the laser flash, being faster than the decay rate at longer times. In 300 Torr of air, $\text{Cl}(^2P_J)$ decays were nearly exponential. A likely explanation for the nonexponential decays observed in N_2 and, to a lesser extent, in air, is given below. Plots of k' versus $[\text{CS}_2]$ for the data obtained in N_2 and air are shown in Figure 6, where k' is the fast component of the observed decays (first 5–10 ms after the laser flash). Defining the apparent rate coefficient, k_{app} , to be the slope of the plot of k' versus $[\text{CS}_2]$, we find that $k_{\text{app}} \sim 1.4 \times 10^{-14} \text{ cm}^3 \text{ molecule}^{-1} \text{ s}^{-1}$ in both N_2 and air.

Since there are no energetically feasible bimolecular channels for the $\text{Cl}(^2P_J) + \text{CS}_2$ reaction, the apparent reactivity must be

TABLE II: Results of the $\text{Cl}(^2P_{1/2}) + \text{CS}_2 + \text{N}_2 \leftrightarrow \text{CS}_2\text{Cl} + \text{N}_2$ "Approach-to-Equilibrium" Experiments^a

T	P	concentrations			Q	$-\lambda_1$	$-\lambda_2$	k_2	k_1	k_{-1}	K_p
		Cl_2	$\text{Cl}_{1,0}$	CS_2							
193	30	88	0.60	324	202	101	1490	104	4.10	97	1600
193	30	88	0.60	628	179	76	2890	77	4.33	103	1610
197	30	84	0.63	180	230	67	800	75	3.34	155	802
197	30	84	0.63	353	262	75	1350	82	3.20	180	662
197	30	84	0.63	371	328	85	1740	93	3.94	235	625
199	30	84	0.63	713	329	73	2740	77	3.44	252	503
201	30	84	0.63	103	355	65	3870	67	3.44	288	437
205	80	42	0.35	416	1630	124	4380	158	6.75	1470	164
205	80	57	0.47	835	1500	120	7630	139	7.45	1360	195
205	80	42	0.35	992	1890	150	9520	170	7.78	1720	161
205	80	42	0.35	1710	1890	143	14700	154	7.55	1730	156
205	80	42	0.35	1920	2180	231	16800	253	7.72	1930	143
206	30	32	0.36	346	580	69	1550	88	2.91	492	211
206	30	32	0.36	574	604	65	2350	76	3.11	528	210
206	30	32	0.36	1260	622	57	4760	61	3.31	561	210
206	30	32	0.36	3340	669	38	12400	38	3.51	631	198
206	220	70	0.69	467	3540	168	11500	221	17.3	3320	186
206	220	70	0.69	1430	4110	207	29500	233	17.9	3870	164
206	600	91	0.89	353	8860	251	24600	362	45.0	8500	189
206	600	91	0.89	1140	9330	211	54800	244	40.0	9080	157
206	600	91	0.89	2080	9340	387	94400	422	41.1	8920	164
212	30	53	0.33	356	828	73	1750	110	2.73	718	132
212	30	53	0.33	647	954	90	2850	119	3.04	835	126
212	30	53	0.33	1250	970	92	4760	108	3.09	862	124
212	30	53	0.33	2690	1060	123	8600	135	2.84	922	107
221	30	32	0.29	743	3550	392	5090	990	2.57	2540	33.6
221	30	32	0.29	1500	2300	102	6160	146	2.63	2150	40.6
221	30	86	0.86	1720	1840	136	5870	173	2.40	1670	47.7
221	30	32	0.29	3170	2140	79	10600	94	2.67	2050	43.3
222	30	34	0.31	574	2450	68	3920	131	2.62	2320	37.4
222	30	48	0.41	640	2040	75	3480	126	2.31	1920	39.8
222	30	48	0.41	1080	2350	90	5140	132	2.64	2210	39.4
222	30	48	0.41	1750	2370	96	6870	126	2.61	2250	38.4
222	30	34	0.31	2300	2730	80	9230	102	2.85	2630	35.7
222	30	48	0.41	2700	2370	87	9440	103	2.64	2270	38.4
222	30	34	0.31	3990	2350	62	12400	70	2.55	2280	36.9
222	30	34	0.31	7470	3060	14	27200	154	3.24	2910	36.8
225	100	50	0.42	683	9990	116	14000	288	6.03	9700	20.3
225	100	50	0.42	1130	10200	128	16900	251	6.03	9920	19.8
225	100	50	0.42	2540	11700	160	29200	234	6.96	11400	19.9
225	100	50	0.42	5280	12500	237	47800	297	6.64	12200	18.1
229	300	67	0.62	2220	41300	228	72600	452	14.2	40800	11.1
229	300	67	0.62	5970	46800	446	148000	623	17.1	46100	11.8
231	30	17	0.14	1770	4470	44	7700	59	1.83	4400	13.2
231	30	17	0.14	3300	5110	85	12300	122	2.19	4990	14.0
231	30	17	0.14	4210	5020	130	15000	178	2.40	4840	15.7
231	30	17	0.14	8370	5330	114	23300	137	2.16	5160	13.3
231	30	17	0.14	12400	5130	77	31000	86	2.09	5040	13.2
238	30	37	0.26	2620	8040	75	13100	141	1.96	7900	7.65
238	30	37	0.26	4800	8420	96	17400	154	1.87	8270	7.01
238	30	37	0.26	8230	9230	205	24900	303	1.93	8920	6.67
238	30	37	0.26	10800	8680	34	31500	35	2.11	8650	7.54
240	30	62	0.44	4040	8580	61	15600	105	1.75	8480	6.30
240	30	62	0.44	8160	10900	269	26500	432	1.94	10400	5.69
240	100	55	0.50	3100	32200	99	45700	220	4.37	32000	4.19
240	100	55	0.50	4500	30800	71	52400	104	4.80	30700	4.79
240	100	55	0.50	9780	32600	35	82400	26	5.10	32500	4.79
240	100	55	0.50	12900	32500	242	96000	340	4.94	32100	4.70
241	300	160	1.4	13500	57400	480	194000	660	10.1	56800	5.44
244	30	56	0.45	4250	13100	132	20800	288	1.83	12800	4.29
244	30	56	0.45	5540	13800	156	23100	328	1.69	13500	3.76
244	30	56	0.45	7520	12900	208	28500	343	2.12	12600	5.06
244	60	84	0.86	5210	24800	202	40000	470	2.95	24300	3.66
244	60	84	0.86	10500	24700	350	56900	588	3.09	24200	3.85
244	60	84	0.86	14200	24200	316	66600	475	3.00	23800	3.80
244	120	87	0.80	6290	48800	287	82700	635	5.42	48200	3.38
244	120	87	0.80	11500	49200	357	116000	587	5.83	48600	3.61
244	240	110	0.87	3990	82800	225	112000	656	7.36	82100	2.70
244	240	120	0.98	5150	82600	291	119000	873	7.12	81700	2.62
244	40	110	0.87	9180	98200	333	190000	613	9.98	97600	3.08
246	30	33	0.30	2550	12400	56	16400	117	1.58	12200	3.85
246	30	58	0.56	5970	14600	159	25800	295	1.89	14300	3.97
246	30	33	0.30	6220	14200	86	25500	147	1.83	14000	3.88
246	30	33	0.30	9630	15100	162	32600	270	1.82	14800	3.66
251	30	44	0.25	2690	14500	48	17700	108	1.20	14400	2.44

TABLE II (Continued)

T	P	concentrations			Q	-λ ₁	-λ ₂	k ₃	k ₁	k ₋₁	K _p
		Cl ₂	Cl ₁₌₀	CS ₂							
251	30	44	0.25	5210	20700	139	29500	377	1.72	20300	2.47
251	30	44	0.25	10300	19400	119	36600	212	1.69	19100	2.58
251	30	44	0.25	14800	22600	430	50700	737	1.93	21900	2.58
256	30	54	0.50	3640	23900	44	28700	147	1.31	23700	1.59
256	30	65	0.60	9560	24700	131	36400	354	1.24	24300	1.46
256	30	65	0.60	17400	26400	325	50300	650	1.39	25700	1.55
256	100	100	1.1	7970	105000	141	137000	536	3.94	105000	1.08
256	100	100	1.1	13500	74000	93	120000	205	3.41	73800	1.33
258	30	72	0.51	8560	26100	163	37400	465	1.34	25600	1.49
258	30	72	0.51	15300	25100	128	46300	243	1.39	24800	1.60

* Units: T, K; P, Torr; concentrations, 10¹²/cm³; Q, λ₁, λ₂, k₋₁, k₃, s⁻¹; k₁, 10⁻¹³ cm³ molecule⁻¹ s⁻¹; K_p, 10³ atm⁻¹.

TABLE III: Assumed Vibrational Frequencies for CClCS₂

vibrational mode	ν, cm ⁻¹	vibrational mode	ν, cm ⁻¹
symmetric stretch	650	asymmetric stretch	1530
scissor	400	CS ₂ wag	(350)
C-Cl stretch	(500)	out-of-plane deformation	(500)

* Values in parentheses are more uncertain.

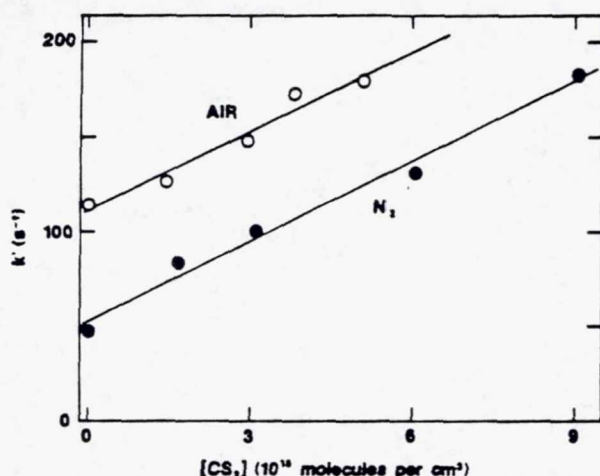
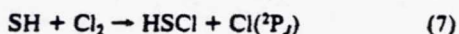


Figure 6. Plots of pseudo-first-order chlorine atom decay rates, k' , as a function of the CS₂ concentration. Experimental conditions: $T = 293$ K, $P = 300$ Torr, $[Cl_2] \approx 1.5 \times 10^{14}$ molecules/cm³, $[Cl(^2P_J)]_0 \approx 1.0 \times 10^{12}$ atoms/cm³. The solid lines are obtained from linear least-squares analyses and give the apparent bimolecular rate coefficients $(1.40 \pm 0.33) \times 10^{-14}$ cm³ molecule⁻¹ s⁻¹ (air) and $(1.41 \pm 0.20) \times 10^{-14}$ cm³ molecule⁻¹ s⁻¹ (N₂) where the uncertainties are 2σ and represent precision only.

due to an impurity in the CS₂ sample. Unfortunately, we were not able to obtain an analysis of the distilled CS₂ sample. However, one likely impurity whose presence would explain the observed nonexponential Cl(²P_J) decays is H₂S. Laser flash photolysis of Cl₂/H₂S mixtures is known to initiate a chain reaction:¹⁸

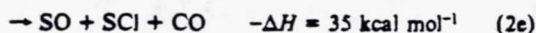
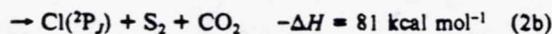


The rate coefficients for reactions 6 and 7 at 298 K are known to be 7.3×10^{-11} and 1.4×10^{-12} cm³ molecule⁻¹ s⁻¹, respectively.¹⁸ An H₂S impurity level of 0.02–0.03% would completely account for the measured k_{app} , while the occurrence of reaction 7 would account for the observation of nonexponential Cl(²P_J) decays (all data shown in Figure 6 were obtained with $[Cl_2] = 1.5 \times 10^{14}$ molecules/cm³ and $[Cl]_0 \approx 1 \times 10^{12}$ atoms/cm³). The larger intercept in the k' versus $[CS_2]$ plot for the data obtained in air (Figure 6) suggests that the background chlorine atom decay rate in air is larger than in nitrogen. The "less nonexponential" decays

observed in air reflect the fact that a larger fraction of chlorine atoms were removed by nonchain processes in the air experiments (due to the faster background chlorine atom decay rate in air). It is also possible that O₂ or an impurity in the air sample scavenged SH effectively in competition with reaction 7. It should be noted that the rate coefficient for the SH + O₂ reaction is thought to be very slow.¹⁹

If, as suggested above, reactions 6 and 7 can influence observed Cl(²P_J) temporal profiles, then two assumptions made in analyzing the "approach-to-equilibrium" data (Table II) need to be reevaluated. First, it was assumed that k_4 was independent of CS₂ concentration. Also, the derivation of eq 1 assumes that radical species other than Cl(²P_J) and CS₂Cl (SH, for example) exert a negligible influence on observed chlorine atom temporal profiles. To test the validity of the above assumptions, we carried out computer simulations of a number of typical approach-to-equilibrium experiments with and without reactions 6 and 7 included in the mechanism. The rate coefficient k_6 was assumed to be independent of temperature while k_7 was assigned an A factor of 1×10^{-11} cm³ molecule⁻¹ s⁻¹, leading to an assumed activation energy of 1.16 kcal mol⁻¹. Because Cl₂ concentrations in the approach-to-equilibrium experiments were generally rather low (Table II), and because large CS₂ concentrations were employed only in experiments where the approach to equilibrium was very fast, the influence of reactions 6 and 7 on the approach-to-equilibrium data was found to be negligible under all experimental conditions employed.

The results shown in Figure 6 would seem to suggest that the effective rate coefficient, k_{eff} , for reaction of Cl(²P_J) with CS₂ via reactions 1, -1, and 2 in 300 Torr of air at 293 K is very slow. However, it should be kept in mind that our experiment is "blind" to channels for reaction 2 which result in Cl(²P_J) regeneration:



With k_{eff}^* defined to be the effective rate coefficient for reaction of Cl(²P_J) with CS₂ via reactions 1, -1, and those channels of reaction 2 that do not produce Cl(²P_J), i.e., channels 2a, 2d, 2e, and 2f, the data in Figure 6 show that $k_{eff}^* < 5 \times 10^{-15}$ cm³ molecule⁻¹ s⁻¹. By comparison, Martin et al.,³ whose experiment was sensitive to the total rate coefficient for reaction 2 independent of whether or not Cl(²P_J) is produced, report values for k_{eff} in units of 10⁻¹⁵ cm³ molecule⁻¹ s⁻¹ of 49 ± 16 , 68 ± 12 , and 70 ± 30 in 50 Torr of O₂ + 710 Torr of N₂, 100 Torr of O₂ + 660 Torr of

(18) Nesbitt, D. J.; Leone, S. R. *J. Chem. Phys.* 1980, 72, 1722.

(19) Stachnik, R. A.; Molina, M. J. *J. Phys. Chem.* 1987, 91, 4603.

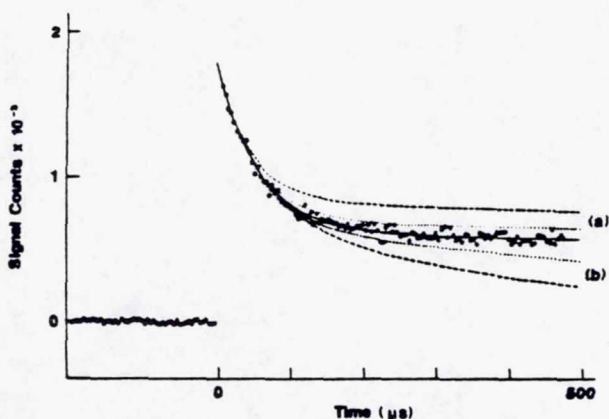


Figure 7. $\text{Cl}(^2\text{P}_j)$ temporal profile observed following pulsed laser photolysis of 4.5×10^{13} Cl_2 molecules/ cm^3 + 4.64×10^{15} CS_2 molecules/ cm^3 in 30 Torr of O_2 at 230 K. $[\text{Cl}(^2\text{P}_j)]_0 \sim 7 \times 10^{11}$ atoms/ cm^3 , 30 000 laser shots averaged. The laser fired at time = 0. The solid line is obtained from a nonlinear least-squares analysis that yields the following best fit parameters: $K = 6630 \text{ s}^{-1}$, $\lambda_1 = -242 \text{ s}^{-1}$, $\lambda_2 = -18100 \text{ s}^{-1}$. The dashed lines are obtained from simulations that use the best fit values for k_1 , k_{-1} , and k_3 and assume that $k_2 \neq 0$, but rather that (a) $k_2 = 3 \times 10^{-15} \text{ cm}^3 \text{ molecule}^{-1} \text{ s}^{-1}$, $k_{2A} = 0$ or (b) $k_2 = k_{2A} = 3 \times 10^{-15} \text{ cm}^3 \text{ molecule}^{-1} \text{ s}^{-1}$. Similarly, the dotted lines are obtained from simulations that assume that (a) $k_2 = 1 \times 10^{-15} \text{ cm}^3 \text{ molecule}^{-1} \text{ s}^{-1}$, $k_{2A} = 0$ or (b) $k_2 = k_{2A} = 1 \times 10^{-15} \text{ cm}^3 \text{ molecule}^{-1} \text{ s}^{-1}$.

N_2 , and 150 Torr of O_2 + 150 Torr of N_2 , respectively (errors are 2 σ).

Clearly, one possible explanation for the fact that Martin et al.⁵ report values for k_{eff} that are much larger than our value for k_{eff} is that reaction 2 proceeds via channels that produce $\text{Cl}(^2\text{P}_j)$, i.e., channels 2b, 2c, and/or 2g. To further investigate this possibility, we conducted some experiments using O_2 buffer gas under experimental conditions (low temperature and pressure) where the double-exponential decays predicted by equation 1 would be observable unless the $\text{CS}_2\text{Cl} + \text{O}_2$ reaction was fast. A typical $\text{Cl}(^2\text{P}_j)$ temporal profile observed in these experiments is shown in Figure 7. The data were first analyzed with use of I-IX, i.e., assuming $k_2 = 0$. Both k_1 and k_{-1} were found to be about 25% faster at 230 K in 30 Torr of O_2 than at 230 K in 30 Torr of N_2 , suggesting that O_2 is a little more efficient than N_2 as a third body. However, the equilibrium constant obtained from analysis of the O_2 data, $K_p \sim 13000 \text{ atm}^{-1}$, is in excellent agreement with the equilibrium constants determined from experiments in N_2 at 229 and 231 K (see Table II)—a result that strongly suggests that the $\text{CS}_2\text{Cl} + \text{O}_2$ reaction is slow. If reaction 2 proceeded via a channel that does not produce $\text{Cl}(^2\text{P}_j)$, the slow component in the decay shown in Figure 7 would be much faster than was observed. On the other hand, if reaction 2 proceeded via a channel that regenerated $\text{Cl}(^2\text{P}_j)$, the steady-state $\text{Cl}(^2\text{P}_j)$ concentration at long times after the laser flash would be larger than the concentration expected from the equilibrium between reactions 1 and -1; hence, the above analysis would have given an erroneously small value for K_p .

To put a quantitative upper limit on k_2 , we expand the mechanism used to derive equations I-VI to include reaction 2. Equations I, II, III, and V remain unchanged while eqs IV and VI are modified as follows:

$$Q = k_{-1} + k_3 + k_2[\text{O}_2] \quad (\text{IV}')$$

$$\beta = k_4Q + k_1[\text{CS}_2](k_5 + k_{2A}[\text{O}_2]) \quad (\text{VI}')$$

In the above equations, k_{2A} represents all channels of reaction 2 that do not produce $\text{Cl}(^2\text{P}_j)$

$$k_{2A} = k_{2a} + k_{2d} + k_{2e} + k_{2f} = k_2 - k_{2b} - k_{2c} - k_{2g} \quad (\text{XII})$$

The $\text{Cl}(^2\text{P}_j)$ temporal profiles observed in 30 Torr of O_2 at 230 K were simulated with equations I-III, IV', V, and VI'. Values assumed for k_1 , k_{-1} , and k_3 were those obtained from a nonlinear least-squares analysis with k_2 set equal to zero (solid line in Figure

7). The objective was to determine minimum values for k_{2A} and $k_2 - k_{2A}$, which were clearly inconsistent with our data. As shown in Figure 7, if either k_{2A} or $k_2 - k_{2A}$ is assumed to be $1 \times 10^{-15} \text{ cm}^3 \text{ molecule}^{-1} \text{ s}^{-1}$ or greater, a noticeably different $\text{Cl}(^2\text{P}_j)$ temporal profile is predicted. Further simulations showed that it is not possible to reproduce the experimental data by assuming values for k_{2A} and/or $k_2 - k_{2A}$ larger than $1 \times 10^{-15} \text{ cm}^3 \text{ molecule}^{-1} \text{ s}^{-1}$ and varying k_1 , k_{-1} , and/or k_3 to optimize the fit. It appears that the slow $\text{Cl}(^2\text{P}_j)$ decay rate and "correct" equilibrium $\text{Cl}(^2\text{P}_j)$ concentration observed at long times after the laser flash can only be explained by postulating a very slow rate for reaction 2. We feel that our data support an upper limit of $2 \times 10^{-15} \text{ cm}^3 \text{ molecule}^{-1} \text{ s}^{-1}$ for k_2 at 230 K in 30 Torr of O_2 .

Under the conditions of Martin et al.'s experiments (293 K, 760 Torr of air, 5 ppm CS_2),⁵ the CS_2Cl concentration was very small compared to the concentrations of $\text{Cl}(^2\text{P}_j)$ and CS_2 ; hence, the steady-state approximation can be applied to CS_2Cl . Application of the steady-state approximation to the mechanism consisting of reactions 1, -1, 4, 5, and 2 leads to the expression

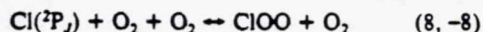
$$k_{\text{eff}} = k_1X[\text{O}_2]/(1 + X[\text{O}_2]) \quad (\text{XIII})$$

where

$$X = k_2/k_{-1} \quad (\text{XIV})$$

Although long extrapolations are required, our data can be used to estimate values for k_1 and k_{-1} at 293 K and 760-Torr total pressure, the conditions of most of Martin et al.'s competitive kinetics experiments.⁵ With an accuracy of about a factor of 2, we estimate $k_1 \sim 2 \times 10^{-11} \text{ cm}^3 \text{ molecule}^{-1} \text{ s}^{-1}$ and $k_{-1} \sim 2 \times 10^6 \text{ s}^{-1}$ under these conditions. Substituting our estimates for k_1 and k_{-1} along with Martin et al.'s measured value for k_{eff} in 760 Torr of air ($8.3 \times 10^{-14} \text{ cm}^3 \text{ molecule}^{-1} \text{ s}^{-1}$) into eq XIII leads to a value of $k_2 \sim 2 \times 10^{-15} \text{ cm}^3 \text{ molecule}^{-1} \text{ s}^{-1}$ —not inconsistent with our 230 K, 30 Torr of O_2 upper limit of $2 \times 10^{-15} \text{ cm}^3 \text{ molecule}^{-1} \text{ s}^{-1}$ (it is, of course, possible that k_2 increases with increasing temperature or pressure). Hence, although we observe no positive evidence for a reaction between CS_2Cl and O_2 , our data do not preclude the occurrence of reaction 2 with a rate coefficient (on the order of $10^{-15} \text{ cm}^3 \text{ molecule}^{-1} \text{ s}^{-1}$) consistent with the steady-state-kinetics observations of Martin et al.,⁵ provided that reaction 2 occurs by a channel that regenerates $\text{Cl}(^2\text{P}_j)$. As discussed above, the data in Figure 6 suggest that $k_{\text{eff}} < 5 \times 10^{-15} \text{ cm}^3 \text{ molecule}^{-1} \text{ s}^{-1}$ at 293 K and 300-Torr total pressure. Considering this result in conjunction with eq XIII leads to $k_{2A} < 2.5 \times 10^{-16} \text{ cm}^3 \text{ molecule}^{-1} \text{ s}^{-1}$ at $T = 293 \text{ K}$ and $P = 300 \text{ Torr}$.

Direct observation of the approach to equilibrium in O_2 buffer gas at temperatures below 230 K could potentially allow very slow values for k_2 (i.e., $< 10^{-15} \text{ cm}^3 \text{ molecule}^{-1} \text{ s}^{-1}$) to be determined. However, interpretation of such experiments is complicated by the occurrence of another rapid equilibrium



Recent work in our laboratory²⁰ has established that the equilibrium concentration of ClOO in 30 Torr of O_2 is negligible at temperatures of 230 K and above.

It is interesting to compare the kinetic and thermodynamic data reported in this paper for the CS_2Cl adduct with analogous results reported elsewhere^{3,4} for the CS_2OH adduct. The enthalpy changes for the $\text{Cl} + \text{CS}_2$ and $\text{OH} + \text{CS}_2$ association reactions at 298 K are both around 10–11 kcal mol^{-1} , but the entropy change associated with the $\text{Cl} + \text{CS}_2$ reaction, $\Delta S^\circ_{298} = -26.8 \text{ cal mol}^{-1} \text{ deg}^{-1}$, appears to be somewhat larger than the entropy change associated with the $\text{OH} + \text{CS}_2$ reaction (analysis of our K_p versus $1/T$ data³ gives $\Delta S^\circ_{298} \sim 22 \pm 3 \text{ cal mol}^{-1} \text{ deg}^{-1}$ while Murrells et al.⁴ report $\Delta S^\circ_{298} \sim 24 \pm 4 \text{ cal mol}^{-1} \text{ deg}^{-1}$). Hence, at a given temperature, K_p is about a factor of 3 larger for the $\text{OH} + \text{CS}_2$ equilibrium than for the $\text{Cl} + \text{CS}_2$ equilibrium. At $T = 256\text{--}258$

(20) Nicovich, J. M.; Kreutter, K. D.; Shackelford, C. J.; Wine, P. H. To be published.

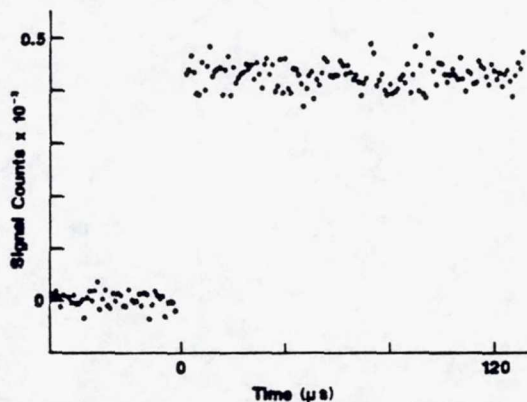


Figure 8. $\text{Cl}(^2P_J)$ temporal profile observed following pulsed laser photolysis of 3.0×10^{13} Cl_2 molecules/ cm^3 + 5.5×10^{15} COS molecules/ cm^3 in 30 Torr of N_2 at 194 K. $[\text{Cl}(^2P_J)]_0 \sim 2 \times 10^{11}$ atoms/ cm^3 , 2500 laser shots averaged. The laser fired at time = 0.

K and P = 75 Torr of N_2 , a temperature and pressure regime where experimental kinetic data are available for both the $\text{Cl} + \text{CS}_2$ and $\text{OH} + \text{CS}_2$ reactions, we find that adduct formation proceeds about 2.5 times more rapidly for $\text{Cl} + \text{CS}_2$ ($k \sim 2.5 \times 10^{-12}$ cm^3 molecule $^{-1}$ s $^{-1}$) than for $\text{OH} + \text{CS}_2$ ($k \sim 1.0 \times 10^{-12}$ cm^3 molecule $^{-1}$ s $^{-1}$) while the adduct lifetime toward unimolecular decomposition back to reactants is about 7.5 times shorter for CS_2Cl ($\tau \sim 16$ μs) than for CS_2OH ($\tau \sim 120$ μs). CS_2OH is at least 1 order of magnitude more reactive with O_2 than is CS_2Cl , a reasonable finding considering that the CS_2OH reaction with O_2 appears to involve breaking of the O-H bond.²¹

In addition to the studies of CS_2Cl formation and removal described above, we also searched for evidence of reversible adduct formation in the $\text{Cl} + \text{COS}$ system. As typified by the $\text{Cl}(^2P_J)$ temporal profile shown in Figure 8, no evidence for formation of a COSCl adduct was observed. Each data point in Figure 8 represents 1 μs of time. Since the COS concentration was 5.5×10^{15} molecules/ cm^3 , in order for a decay of $\text{Cl}(^2P_J)$ into equilibrium to be too rapid for observation, the $\text{Cl}(^2P_J) + \text{COS}$ rate coefficient would have to be unrealistically fast, i.e., close to 10^{-10} cm^3 molecule $^{-1}$ s $^{-1}$ at a pressure (30 Torr of N_2) expected to be far removed from the high-pressure limit. It seems safe to assume, therefore, that the absence of a fast component in the

$\text{Cl}(^2P_J)$ decay implies that $[\text{COSCl}]_{\text{eq}} < 0.1[\text{Cl}(^2P_J)]_{\text{eq}}$ at 194 K and $[\text{COS}] = 5.5 \times 10^{15}$ molecules/ cm^3 . Hence, $K_c < 1.8 \times 10^{-17}$ cm^3 /molecule and $K_p < 680$ atm $^{-1}$. Our data suggest that either (a) a significant barrier exists in the entrance channel that prevents $\text{Cl}(^2P_J)$ addition to COS or (b) the species COSCl is very weakly bound. Since no barrier to addition is observed for the similar $\text{Cl}(^2P_J) + \text{CS}_2$ reaction, the latter of the above possibilities seems more reasonable. In either case, COSCl should not be an important species in atmospheric chemistry. It is worth noting that Wahner and Ravishankara,²² in a study of the similar $\text{OH} + \text{COS}$ reaction, also found no evidence for adduct formation.

Summary

Reversible adduct formation in the reaction of $\text{Cl}(^2P_J)$ with CS_2 has been observed via direct monitoring of the decay of pulsed-laser-generated $\text{Cl}(^2P_J)$ into equilibrium with time-resolved resonance fluorescence spectroscopy as the detection technique. Rate coefficients for CS_2Cl formation and decomposition have been determined as a function of temperature and pressure; hence, the equilibrium constant has been determined as a function of temperature. A second-law analysis of the temperature dependence of K_p and heat capacity corrections calculated with an assumed CS_2Cl structure yields the following thermodynamic parameters for the association reaction: $\Delta H_{298}^\circ = -10.5 \pm 0.5$ kcal mol $^{-1}$, $\Delta H_0^\circ = -9.5 \pm 0.7$ kcal mol $^{-1}$, $\Delta S_{298}^\circ = -26.8 \pm 2.4$ cal mol $^{-1}$ deg $^{-1}$, and $\Delta H_{f,298}(\text{CS}_2\text{Cl}) = 46.4 \pm 0.6$ kcal mol $^{-1}$.

The resonance fluorescence detection scheme has been adapted to allow detection of $\text{Cl}(^2P_J)$ in the presence of large concentrations of O_2 , thus allowing the reaction of CS_2Cl with O_2 to be investigated. Our results demonstrate that k_{2A} , the rate coefficient for the $\text{CS}_2\text{Cl} + \text{O}_2$ reaction via all channels that do not regenerate $\text{Cl}(^2P_J)$, is less than 2.5×10^{-16} cm^3 molecule $^{-1}$ s $^{-1}$ at 293 K and 300-Torr total pressure. Another series of experiments places an upper limit of 2×10^{-15} cm^3 molecule $^{-1}$ s $^{-1}$ on the total rate coefficient k_2 at 230 K and 30-Torr total pressure.

Evidence for reversible adduct formation in the reaction of $\text{Cl}(^2P_J)$ with COS was sought but not observed, even at temperatures as low as 194 K, suggesting either that a barrier exists in the $\text{Cl} + \text{COS}$ entrance channel or that COSCl is a very weakly bound species.

Acknowledgment. This work was supported by Grant No. ATM-88-02386 from the National Science Foundation and Grant No. NAGW-1001 from the National Aeronautics and Space Administration.

(21) Lovejoy, E. R.; Murrells, T. P.; Ravishankara, A. R.; Howard, C. J. *J. Phys. Chem.*, in press.

(22) Wahner, A.; Ravishankara, A. R. *J. Geophys. Res.* 1987, 92, 2189.

Kinetics and thermochemistry of ClCO formation from the Cl + CO association reaction

J. M. Nicovich, K. D. Kreutter, and P. H. Wine

Molecular Sciences Branch, Georgia Tech Research Institute, Georgia Institute of Technology, Atlanta, Georgia 30332

(Received 7 November 1989; accepted 19 December 1989)

Laser flash photolysis of Cl₂/CO/M mixtures (M = N₂, CO, Ar, CO₂) has been employed in conjunction with Cl(²P_J) detection by time-resolved resonance fluorescence spectroscopy to investigate equilibration kinetics in the reactions Cl(²P_J) + CO → ClCO as a function of temperature (185–260 K) and pressure (14–200 Torr). The association and dissociation reactions are found to be in the low-pressure limit over the range of experimental conditions investigated. In N₂ and/or CO buffer gases, the temperature dependences of the ClCO formation and dissociation reaction rate constants are described by the Arrhenius expressions $k_1 = (1.05 \pm 0.36) \times 10^{-34} \exp[(810 \pm 70)/T] \text{ cm}^6 \text{ molecule}^{-2} \text{ s}^{-1}$ and $k_{-1} = (4.1 \pm 3.1) \times 10^{-10} \exp[(-2960 \pm 160)/T] \text{ cm}^3 \text{ molecule}^{-1} \text{ s}^{-1}$ (errors are 2σ). Second- and third-law analyses of the temperature dependence of the equilibrium constant (k_1/k_{-1}) lead to the following thermodynamic parameters for the association reaction: $\Delta H_{298}^0 = -7.7 \pm 0.6 \text{ kcal mol}^{-1}$, $\Delta H_0^0 = -6.9 \pm 0.7 \text{ kcal mol}^{-1}$, $\Delta S_{298}^0 = -23.8 \pm 2.0 \text{ cal mole}^{-1} \text{ K}^{-1}$, $\Delta H_{f,298}^0(\text{ClCO}) = 5.2 \pm 0.6 \text{ kcal mol}^{-1}$ (errors are 2σ). The results reported in this study significantly reduce the uncertainties in all reported kinetic and thermodynamic parameters.

INTRODUCTION

The chloroformyl radical (ClCO) has been of interest to photochemists for many years. Bodenstein, Lenher, and Wagner¹ first postulated the existence of ClCO as an intermediate in the photocatalyzed production of phosgene (Cl₂CO) from Cl₂/CO mixtures. Models of the CO₂-rich atmosphere of Venus have included the chemistry of chloroformyl radicals.² ClCO may also play a role in the chemistry of the Earth's atmosphere. For instance, photooxidation of CCl₄ can lead to ClCO production via a Cl₂CO reservoir.

Information concerning the kinetics and thermochemistry of the Cl + CO association reaction is rather sparse:



The only study of the kinetics of reaction (R1) was carried out by Clark, Clyne, and Stedman³ over 20 years ago. These authors employed a discharge flow reactor to measure k_1 at 195 and 300 K in argon buffer gas. Reported values for the ClCO bond dissociation energy are based on indirect experimental information^{4,5} and *ab initio* theory,⁶ and range from 3.5 to 7.1 kcal mol⁻¹.

In this paper we report direct observations of the decay of pulsed-laser-generated chlorine atoms into equilibrium with ClCO. These experiments allow determination of k_1 and k_{-1} as functions of temperature and pressure, and the equilibrium constant (k_1/k_{-1}) as a function of temperature. Second- and third-law methods are employed to evaluate the ClCO entropy, heat of formation, and bond dissociation energy.

EXPERIMENTAL SECTION

The apparatus employed in this study was similar to those used in this laboratory in several previous studies of

chlorine atom kinetics.⁷⁻¹² The salient features of the apparatus and technique are described below.

A Pyrex reaction cell with an internal volume of 150 cm³ was used in all experiments. A 1:1 methanol/ethanol mixture from a thermostated bath was circulated through an outer jacket of the reactor to control the experimental temperature. The temperature of the gas mixture under the exact pressure and flow rate conditions of the experiment was measured with a retractable copper-Constantan thermocouple.

Chlorine atoms were produced by 355 nm pulsed laser photolysis of Cl₂ using third-harmonic radiation from a Quanta Ray model DCR-2 Nd:YAG laser. Cl atom fluorescence was excited by radiation from a cw atomic resonance lamp, which consisted of an electrodeless, microwave-powered discharge through a few Torr of a flowing Cl₂/He mixture. Radiation was coupled out of the lamp through a MgF₂ window and into the cell through a MgF₂ lens. The resonance lamp radiation intersected the photolysis laser beam at 90° near the center of the reaction cell. A flowing gas filter between the resonance lamp and reaction cell blocked extraneous emissions from the lamp. The gas filter was either 3 Torr cm N₂O or 150 Torr cm O₂. The N₂O filter blocked O atom impurity emissions at 130–131 nm while transmitting the 134–140 nm Cl resonance lines. The O₂ filter blocked virtually all emissions from the lamp except the ²D_{5/2,3/2}-²P_{3/2} Cl doublet at 118.9 nm (Ref. 13) and the hydrogen Lyman-α line at 121.6 nm.

Fluorescence was collected by a MgF₂ lens on an axis orthogonal to both the photolysis laser beam and the resonance lamp radiation, and imaged onto the photocathode of a solar blind photomultiplier. The region between the reaction cell and the photomultiplier was purged with N₂. Whenever N₂O filtered the resonance lamp, a CaF₂ window was

NDR
K-10.1 57-25
026135
273559
G.P.

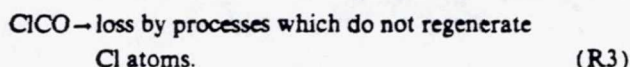
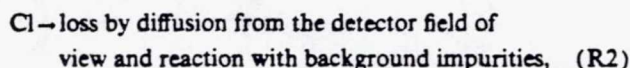
placed between the reaction cell and the photomultiplier to prevent detection of radiation at wavelengths shorter than 125 nm (Lyman- α , for instance). Signals were processed using photon counting techniques in conjunction with multi-channel scaling. For each chlorine atom decay profile measured, between 200 and 34 000 laser shots were averaged to obtain a well-defined temporal profile. The multichannel scaler sweep was triggered before the laser pulse to permit determination of the (constant) background signal level.

In order to avoid the accumulation of photolysis or reaction products, all experiments were carried out under slow flow conditions. The linear flow rate through the reactor was typically 3 cm s^{-1} while the laser repetition rate was varied from 1 to 10 Hz (5 Hz typical). Hence, no volume element of the reaction mixture was subjected to more than two or three laser shots. Cl_2 was leaked from a 12 liter Pyrex bulb containing a dilute ($\sim 10\%$) mixture of Cl_2 in N_2 , while the other reagents flowed directly from high-pressure storage tanks. The CO was passed through a Pyrex trap maintained at 77 K before mixing with other gases immediately upstream of the reaction cell; this procedure removed reactive, photosensitive metal carbonyls from the CO flow. The concentrations of each component in the reaction mixtures were determined from measurement of individual flows using calibrated electronic mass flow meters. The reagent gases had the following stated minimum purities: N_2 , 99.999%; Cl_2 , 99.99%; O_2 , 99.99%; CO_2 , 99.99%; Ar, 99.999%; CO, 99.99%. The Cl_2 we repeatedly degassed at 77 K before dilution. The other gases were used as supplied.

RESULTS AND DISCUSSION

All experiments were carried out under pseudo-first-order conditions with $[\text{CO}] \gg [\text{Cl}]_0$ (the concentration of Cl atoms immediately following the laser pulse). Reaction mixtures contained $(1.0\text{--}18) \times 10^{13}$ molecules cm^{-3} Cl_2 while $[\text{Cl}]_0$ varied from $(2.0\text{--}10) \times 10^{11}$ atoms cm^{-3} . Experiments were performed over the temperature range 185–260 K, and the total pressure was varied from 14 to 200 Torr by diluting the gas mixture with the appropriate partial pressure of an unreactive buffer gas (N_2 , CO_2 , or Ar).

In these experiments the fate of Cl atoms is controlled by the following reactions:



The rate equations for reactions (R1), (R-1), (R2), and (R3) can be solved analytically:

$$[\text{Cl}]_t / [\text{Cl}]_0 = [(Q + \lambda_1) \exp(\lambda_1 t) - (Q + \lambda_2) \exp(\lambda_2 t)] / (\lambda_1 - \lambda_2), \quad (1)$$

where

$$\lambda_1 = 0.5[(A^2 - 4B)^{1/2} - A], \quad (2)$$

$$\lambda_2 = -0.5[A^2 - 4B]^{1/2} + A, \quad (3)$$

$$Q = k_{-1} + k_3, \quad (4)$$

$$A = Q + k_2 + k_1[\text{CO}], \quad (5)$$

$$B = k_2 Q + k_3 k_1[\text{CO}]. \quad (6)$$

The observed temporal profiles for Cl atoms were fit to the double-exponential equation (1) using a nonlinear least-squares method to obtain values for λ_1 , λ_2 , and Q for each decay. The background Cl atom loss rate in the absence of CO (k_2) was directly measured at each temperature and pressure. k_2 ranged from 10 to 40 s^{-1} except for the experiments in CO_2 buffer gas, where k_2 was approximately 600 s^{-1} due to reaction of $\text{Cl}(^2P)$ with an impurity in the CO_2 . Using the identities

$$\lambda_1 + \lambda_2 = -A, \quad (7)$$

$$\lambda_1 \lambda_2 = B, \quad (8)$$

the fit parameters λ_1 , λ_2 , and Q can be directly related to the rate coefficients of interest via

$$k_1 = -(Q + k_2 + \lambda_1 + \lambda_2) / [\text{CO}], \quad (9)$$

$$k_3 = (\lambda_1 \lambda_2 - k_2 Q) / k_1 [\text{CO}], \quad (10)$$

$$k_{-1} = Q - k_3. \quad (11)$$

Typical observed Cl atom temporal profiles are shown in Fig. 1. The results for all experiments are presented in Table I. The results exhibit no systematic dependence upon

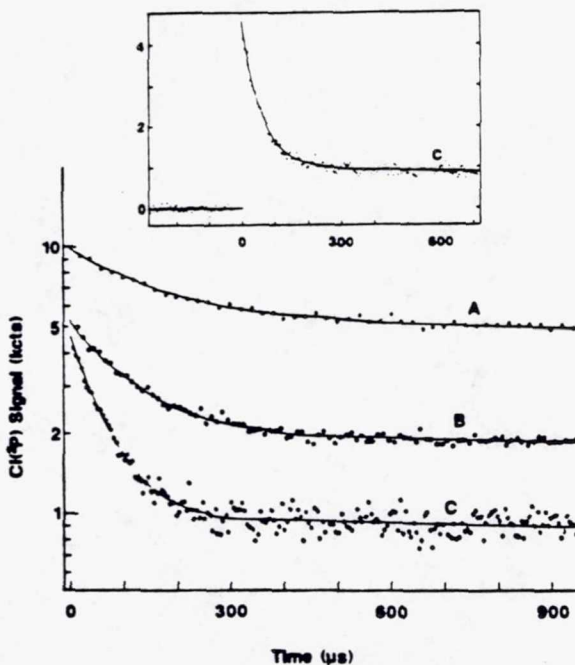


FIG. 1. $\text{Cl}(^2P)$ temporal profiles in the presence of varying amounts of CO at 100 Torr total pressure (N_2 diluent) and 227 K. For all experiments $[\text{Cl}_2] = 3.1 \times 10^{13}$ molecules cm^{-3} and $[\text{Cl}]_0 = 5.2 \times 10^{11}$ atoms cm^{-3} . The carbon monoxide concentrations for each experiment in units of 10^{17} molecules cm^{-3} are A: 1.90, B: 3.72, and C: 8.08. The number of laser shots averaged for each experiment are A: 4000, B: 4000, and C: 10 000. The values for the biexponential parameters (see text) for A, B, and C, respectively, are $-\lambda_1 = 67.1, 81.9, \text{ and } 107$; $-\lambda_2 = 5790, 9180, \text{ and } 16\,500$; and $Q = 3110, 3470, \text{ and } 3590$; units are s^{-1} . The inset shows decay C with the signal counts displayed on a linear scale.

TABLE I. Summary of kinetic and equilibrium measurements.

T(K)/M	[Cl ₂] ^a	[Cl] ₀ ^a	[CO] ^b	[M] ^b	k ₁ ^c	k ₋₁ ^d	k ₂ ^e	K _p ^f
260/N ₂ ,CO	150	4.4	18.6	111	1.86	40.2	317	13.1
	150	4.4	111	111	2.03	44.3	126	12.9
	150	4.4	201	201	2.20	52.2	247	11.9
242/N ₂ ,CO	220	5.5	79.4	79.4	3.11	25.1	101	37.6
	1800	4.2	83.4	83.4	3.12	28.9	132	32.7
	160	4.1	120	120	3.62	26.3	497	41.7
	160	4.4	159	159	3.17	24.3	181	39.6
	160	4.1	199	199	2.93	22.8	133	39.0
227/N ₂ ,CO	310	5.2	19.0	425	3.39	7.01	129	156
	310	5.2	37.2	425	3.63	7.84	123	150
	310	5.2	37.2	425	3.63	8.01	145	147
	310	5.2	80.8	425	3.79	8.14	133	151
226/N ₂ , CO	140	3.8	19.2	128	3.52	8.91	78.0	128
	230	3.7	54.2	128	4.02	11.0	84.4	119
	220	3.1	108	128	3.82	11.4	53.4	109
216/CO ₂	140	3.0	13.9	67.2	17.8	6.51	191	929
215/CO ₂	180	4.6	6.70	61.2	14.7	8.74	21.4	576
	180	4.6	9.73	63.5	14.6	7.90	43.7	632
	180	4.6	13.5	66.5	16.1	7.02	139	785
	180	4.6	15.9	69.3	16.4	8.14	59.7	689
212/Ar	220	5.0	6.04	137	3.19	1.72	90.8	642
	220	5.0	7.66	137	3.33	1.81	89.9	637
	220	5.0	10.1	137	3.34	1.76	89.0	657
	220	5.0	18.7	137	3.57	2.04	111	606
209/N ₂	100	3.1	3.50	924	6.72	17.4	113	1350
	100	3.1	5.27	924	5.93	18.5	184	1120
	100	3.1	8.10	924	5.81	17.5	142	1170
	100	3.1	8.24	924	6.14	17.7	128	1210
	100	3.1	11.1	924	5.32	16.5	122	1130
208/N ₂	130	4.1	5.30	139	5.19	2.45	88.8	749
	130	4.1	8.54	139	5.55	2.46	89.4	796
	130	4.1	11.2	139	5.47	2.31	73.2	836
	130	4.1	18.0	139	5.54	2.82	97.0	694
206/N ₂	210	4.3	3.85	141	4.86	2.15	95.6	807
	210	4.3	6.45	141	4.97	2.43	70.0	730
	200	5.8	15.8	141	5.87	2.09	113	1000
197/N ₂	140	5.9	3.34	147	6.86	1.06	64.1	2410
	140	5.9	6.57	147	6.61	1.02	54.8	2410
	140	5.9	9.85	147	6.43	1.19	93.9	2010
	140	5.9	19.0	147	6.38	1.15	94.5	2060
187/N ₂	110	3.2	16.7	155	7.16	0.789	81.6	3560
	310	2.9	16.9	155	7.12	0.708	73.6	3940
	1000	10	17.1	155	7.07	0.712	81.2	3890
	1000	2.9	17.2	155	7.23	0.726	95.5	3910
185/N ₂	110	4.4	5.55	130	7.41	0.554	96.7	5310
	110	4.0	5.34	193	9.03	0.391	98.3	9160
	110	4.0	10.5	193	8.92	0.647	175	5470
	100	4.0	10.6	261	10.0	0.561	169	7070
	130	4.4	6.64	397	9.52	0.430	190	8780
	130	4.4	13.3	397	8.53	0.570	224	5940
	170	5.2	8.20	522	8.54	0.448	89.1	7570
	110	3.7	5.47	1040	6.32	0.331	179	7570
	110	3.7	12.9	1040	7.27	0.411	9.5	7020

^aUnits are 10¹¹ molecules (atoms) cm⁻³.

^bUnits are 10¹⁶ molecules (atoms) cm⁻³; [M] = total number density.

^cUnits are 10⁻³³ cm⁶ molecules⁻² s⁻¹.

^dUnits are 10⁻¹⁶ cm³ molecules⁻¹ s⁻¹.

^eUnits are s⁻¹.

^fUnits are atm⁻¹.

variations in [CO], [Cl₂], [Cl]₀, or laser repetition rate. It was also found that measured values for the termolecular rate coefficient k₁ and the bimolecular rate coefficient k₋₁

were independent of total bath gas pressure over a wide range, indicating that reactions (R1) and (R-1) are in the low-pressure limit up to approximately 200 Torr. An Arr-

henius plot for reaction (R1) is shown in Fig. 2. A linear least-squares analysis of $\ln k_1$ vs T^{-1} for all data taken in N_2 and/or CO buffer gases yields

$$k_1 = (1.05 \pm 0.36) \times 10^{-34} \exp[(810 \pm 70)/T]$$

in units of $\text{cm}^6 \text{ molecule}^{-2} \text{ s}^{-1}$. Similar analysis of the results for the reverse process (k_{-1}) gives

$$k_{-1} = (4.1 \pm 3.1) \times 10^{-10} \exp[-(2960 \pm 160)/T]$$

$\text{cm}^3 \text{ molecule}^{-1} \text{ s}^{-1}$. Panel recommendations of kinetic data for use in modeling atmospheric chemistry parametrize the temperature dependence of association rate constants using the relationship $k(T) = k(300 \text{ K})(T/300)^{-n}$;^{14,15} analysis of our measurements of k_1 in this form yields the expression

$$k_1 = (1.31 \pm 0.15) \times 10^{-33} (T/300)^{-3.8 \pm 0.3}$$

$\text{cm}^6 \text{ molecule}^{-2} \text{ s}^{-1}$. A van't Hoff plot for the equilibrium defined by reactions (R1) and (R-1) is shown in Fig. 3. A linear least-squares analysis of the $\ln K_p$ vs T^{-1} data yields the result

$$\begin{aligned} \ln K_p (\text{atm}^{-1}) &= -\Delta H/RT + \Delta S/R \\ &= (7830 \pm 420)/RT - (24.5 \pm 2.0)/R, \end{aligned}$$

where R is the universal gas constant in units of $\text{cal mol}^{-1} \text{ K}^{-1}$. Errors in the above expressions are 2σ and represent precision only. We believe that systematic errors associated with, for example, the measurement of T , P , and $[\text{CO}]$ are small and do not increase the above uncertainties significantly.

At higher temperatures relatively large concentrations

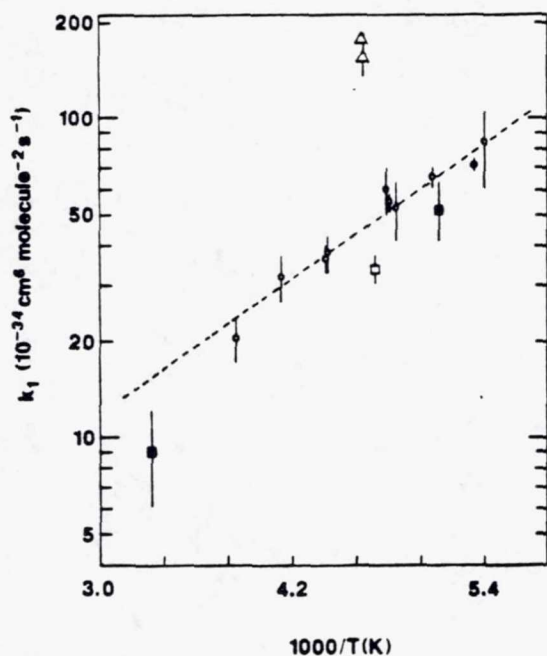


FIG. 2. The termolecular rate coefficient for the formation of ClCO (k_1) as a function of T^{-1} . Buffer gases: Δ , CO_2 ; \circ , N_2/CO ; \square , Ar; \blacksquare , Ar (Ref. 3). At each temperature the average value of k_1 is shown with 2σ error bars, precision only. The dashed line is a best fit of the CO and N_2 data to the Arrhenius form.

of CO were necessary to drive the system into equilibrium. Therefore most of the experiments at 242 and 260 K were carried out in nearly pure CO. Over the entire temperature range studied, the fractional CO concentration (X_{CO}) varied from 0.005 to 1.0. At a given temperature, the invariance of k_1 and k_{-1} with X_{CO} indicates that N_2 and CO have essentially the same efficiencies as third-body colliders for these reactions. The experiments carried out in CO_2 and Ar result in values of K_p very near the N_2/CO results but with different values for the individual rate constants. A comparison of k_1 and k_{-1} for the various buffer gases at $T = 214 \pm 2 \text{ K}$ gives the following relative collision efficiencies for stabilization of the energized ClCO adduct:

$$\beta(\text{CO}_2) : \beta(\text{CO}/\text{N}_2) : \beta(\text{Ar}) = 3.2 : 1.0 : 0.8.$$

The relative collision efficiencies for two buffer gases M_1 and M_2 are computed from the relationship¹⁶

$$\beta(M_1)/\beta(M_2) = k_1(M_1)Z_{LJ}(M_2)/k_1(M_2)Z_{LJ}(M_1), \quad (12)$$

where Z_{LJ} is the Lennard-Jones collision frequency for ClCO-M collisions. It should be noted that the results given in Table I and Figs. 2 and 3 for experiments performed with CO_2 and Ar diluent gas have been corrected for the contribution of CO to the total bath gas concentration.

In Figs. 2 and 3 the results of this study are compared to previous kinetics and equilibrium studies of reactions (R1) and (R-1). From a photochemical study of the formation of Cl_2CO from Cl_2/CO mixtures over the temperature range 298–328 K, Burns and Dainton⁴ report the following expression for the equilibrium constant: $K_c = 10^{-2.806} \exp(6310/RT)$ liter mol^{-1} . When extrapolated to near 300 K, our re-

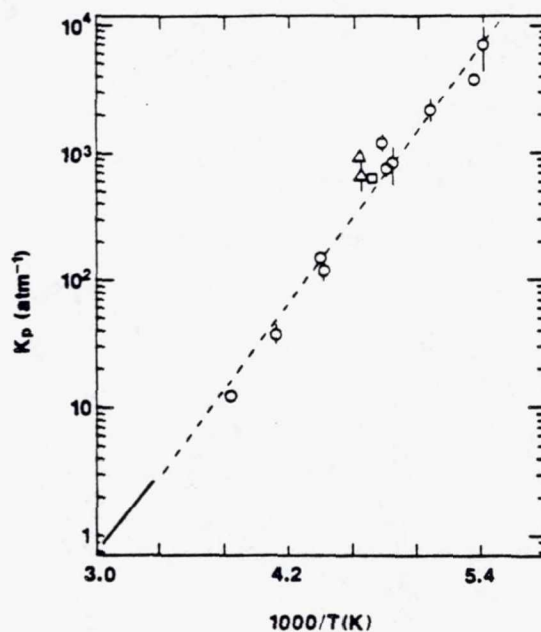


FIG. 3. The equilibrium constant (K_p) for reactions (R1) and (R-1) as a function of T^{-1} . Buffer gases: Δ , CO_2 ; \circ , N_2/CO ; \square , Ar. At each temperature the average value of K_p is shown with 2σ error bars, precision only. The dashed line is a best fit to the van't Hoff form. The solid line represents the data of Burns and Dainton (Ref. 4).

sults for K_p agree quite well with the Burns and Dainton measurement. The narrow temperature range of the Burns and Dainton study makes comparison at lower temperatures risky. The measurements of the forward rate coefficient by Clark, Clyne, and Stedman³ were carried out at low pressure (< 3 Torr) in Ar at 195 and 300 K with Cl atoms in excess over CO. At 195 K these authors report that the kinetics in their discharge flow system were controlled by reaction (R1) followed by the faster process



At higher temperatures decomposition of the ClCO apparently was a complication, competing with reaction (R4). Clark, Clyne, and Stedman report an activation energy for reaction (R1) of approximately -2 kcal mol⁻¹, which is in reasonable agreement with our observed activation energy in N₂/CO. In argon at 214 K our result is virtually identical to the value of k_1 derived by interpolation of the results of Clark, Clyne, and Stedman.

The infrared spectrum of ClCO has been observed by Jacox and Milligan in an argon matrix at 14 K.¹⁷ These investigators assigned bands at 1880, 570, and 281 cm⁻¹ to the chloroformyl radical. The ClCO radical has also been the subject of two theoretical investigations. Self-consistent-field, molecular-orbital calculations have been carried out by Hinchcliffe.¹⁸ An optimized geometry for an *sp* basis set gave a Cl-C-O bond angle of 134° with $r_{\text{C-Cl}} = 178$ pm and $r_{\text{C-O}} = 129$ pm. More recently, Francisco and Goldstein⁶ have reported the results of *ab initio* molecular-orbital calculations. These workers arrived at a slightly different equilibrium geometry with $r_{\text{C-Cl}} = 179$ pm, $r_{\text{C-O}} = 118$ pm, and bond angle = 128.9°. The two geometries derived theoretically are quite similar to the configuration originally estimated by Jacox and Milligan ($r_{\text{C-Cl}} = 175$ pm, $r_{\text{C-O}} = 118$ pm, and 120° < bond angle < 134°). The results of Francisco and Goldstein's calculations indicate that the bent ²A' electronic state is more stable than the linear ²Σ⁺ electronic state by 1.0 kcal mol⁻¹. Francisco and Goldstein's results also allow comparison of calculated vibrational frequencies and intensities with the experimental results of Jacox and Milligan. The calculated frequency of the ClCO bend is much larger, 384 cm⁻¹ compared to 281 cm⁻¹, and the calculated intensity relatively weaker than the frequency and intensity as assigned by Jacox and Milligan. Therefore, Francisco and Goldstein suggest reassignment of the lowest-energy fundamental vibration to a weaker absorption observed by Jacox and Milligan at 333 cm⁻¹.

Despite the above-mentioned uncertainties in the structure and properties of the ClCO radical, it is possible to make a reasonably accurate calculation of the ClCO entropy. A value for the entropy of ClCO at 298 K of 63.4 ± 0.3 cal mol⁻¹ K⁻¹ has been derived using standard statistical mechanical methods.¹⁹ The vibrational frequency assignments of Jacox and Milligan were assumed along with a low-lying excited electronic state 1000 cal mol⁻¹ above the ground state. The uncertainty in the entropy is based upon variation in the calculated value of S^0 over the range of proposed geometries, choice of bending frequency, and allowance for a low-lying electronic state in the range 300–6000 cal mol⁻¹

above the ground state. The value of ΔS_{298}^0 for reaction (1a) is therefore -23.3 ± 0.3 cal mol⁻¹ K⁻¹. Using calculated entropies at each experimental temperature and our measured values of $K_p(T)$, the heat of reaction (1a) at each temperature was calculated. Each value of $\Delta H_T(\text{rxn})$ was then adjusted to ΔH_{298}^0 using calculated changes in heat capacity for the reaction. An average "third-law" value of $\Delta H_{298}^0(\text{rxn}) = -7.53 \pm 0.60$ kcal mol⁻¹ was thus derived. The third-law values of ΔH_{298}^0 and ΔS_{298}^0 can be compared to the same quantities given by the slope and intercept of the van't Hoff plot, i.e., the second-law method. Taking the slope of the van't Hoff plot (Fig. 3) and correcting to the standard temperature gives $\Delta H_{298}^0(\text{rxn}) = -7.95 \pm 0.45$ kcal mol⁻¹. The intercept of the van't Hoff plot gives $\Delta S_{298}^0 = 24.5 \pm 2.0$ cal mol⁻¹ K⁻¹. A consensus value of -7.7 ± 0.6 kcal mol⁻¹ is adopted for $\Delta H_{298}^0(\text{rxn})$ along with an average value of -23.8 ± 2.0 cal mol⁻¹ K⁻¹ for $\Delta S_{298}^0(\text{rxn})$. Using known heats of formation for Cl and CO (Ref. 14) leads to a value of -5.2 ± 0.6 kcal mol⁻¹ for $\Delta H_{f,298}^0(\text{ClCO})$; the currently recommended value for $\Delta H_{f,298}^0(\text{ClCO})$ is -4.1 kcal mol⁻¹.¹⁴ The calculated enthalpy functions were used to correct to absolute zero giving $\Delta H_0^0(\text{rxn}) = -6.9 \pm 0.7$ kcal mol⁻¹ (identically equal to the Cl-CO bond dissociation energy) and $\Delta H_{f,0}^0(\text{ClCO}) = -5.6 \pm 0.7$ kcal mol⁻¹.

The previous measurement of the equilibrium constant by Burns and Dainton⁴ also yields an estimate of the heat of reaction (R1). After first converting the results of these workers from an equilibrium constant expression in concentration units to K_p in units of atm⁻¹, a value of $\Delta H_{298}^0(\text{rxn}) = -7.1$ kcal mol⁻¹ is derived. Due to the limited temperature range covered by Burns and Dainton's study, there should be a rather large error bar associated with the enthalpy value of these researchers. Our results agree quite well with those of Burns and Dainton but are more precise and are based on more direct experimental information. Additional information on the thermochemistry of ClCO has been reported by Walker and Prophet.⁵ The heat of formation of gas phase ClCO at 298 K was deduced from a measurement of the heat of formation of liquid oxalyl chloride (C₂Cl₂O₂, a stable dimeric form of ClCO) and an estimate of the C-C bond strength in C₂Cl₂O₂. Our value for $\Delta H_{f,298}^0(\text{ClCO})$ agrees quite well with Walker and Prophet's estimate of -4.0 ± 3.0 kcal mol⁻¹ although the precision of the value obtained in this study is considerably improved. In the theoretical study by Francisco and Goldstein⁶ a value for the bond dissociation energy of ClCO at 298 K of 3.5 kcal mol⁻¹ (approximately one-half of our experimental value) is reported. Francisco and Goldstein's results also indicate that there should be no potential-energy barrier for the formation of ClCO from reaction (1). The substantial "negative" activation energy observed in our study and in the study of Clark, Clyne, and Stedman³ confirm the lack of an energy barrier.

SUMMARY

Using time-resolved resonance fluorescence spectroscopy to detect pulsed-laser-generated Cl(²P) in the presence of CO, the kinetics of the formation and decomposition of

CICO radicals have been directly measured over the temperature range 185–260 K and the pressure range 14–200 Torr. Both second- and third-law methods have been employed to evaluate the enthalpy and entropy of reaction, with good agreement obtained between the two methods. The results reported herein represent the first direct study of the kinetics and equilibrium of the Cl + CO reaction over a wide temperature range and, therefore, significantly improve the quality of the database for CICO kinetics and thermochemistry.

ACKNOWLEDGMENTS

This work was supported by Grant No. NAGW-1001 from the National Aeronautics and Space Administration.

¹M. Bodenstein, S. Lenher, and C. Wagner, *Z. Phys. Chem. Abt. B3*, 429 (1929).

²Y. L. Yung and W. B. DeMore, *Icarus* **51**, 199 (1982).

³T. C. Clark, M. A. A. Clyne, and D. H. Stedman, *Trans. Faraday Soc.* **62**, 3354 (1966).

⁴W. G. Burns and F. S. Dainton, *Trans. Faraday Soc.* **48**, 39 (1952).

⁵L. C. Walker and H. Prophet, *Trans. Faraday Soc.* **63**, 879 (1967).

⁶J. S. Francisco and A. N. Goldstein, *Chem. Phys.* **128**, 367 (1988).

⁷A. R. Ravishankara and P. H. Wine, *J. Chem. Phys.* **72**, 25 (1980).

⁸P. H. Wine, D. H. Semmes, and A. R. Ravishankara, *Chem. Phys. Lett.* **90**, 128 (1982).

⁹P. H. Wine and D. H. Semmes, *J. Phys. Chem.* **87**, 3572 (1983).

¹⁰P. H. Wine, J. R. Wells, and J. M. Nicovich, *J. Phys. Chem.* **92**, 2223 (1988).

¹¹J. M. Nicovich, C. J. Shackelford, and P. H. Wine, *J. Phys. Chem.* (in press).

¹²J. M. Nicovich, K. D. Kreutter, and P. H. Wine, *Int. J. Chem. Kinet.* (in press).

¹³J. G. Anderson, H. J. Grassl, R. E. Shetter, and J. J. Margitan, *J. Geophys. Res.* **85**, 2869 (1980).

¹⁴R. Atkinson, D. L. Baulch, R. A. Cox, R. F. Hampson, Jr., J. A. Kerr, and J. Troe, *J. Phys. Chem. Ref. Data* **18**, 881 (1989).

¹⁵W. B. DeMore, M. J. Molina, S. P. Sander, D. M. Golden, R. F. Hampson, M. J. Kurylo, C. J. Howard, and A. R. Ravishankara, Evaluation No. 8, Jet Propulsion Laboratory Publication No. 87-41 (1987).

¹⁶J. Troe, *J. Chem. Phys.* **66**, 4758 (1977).

¹⁷M. E. Jacox and D. E. Milligan, *J. Chem. Phys.* **43**, 866 (1965).

¹⁸A. Hinchcliffe, *J. Mol. Struct.* **64**, 117 (1980).

¹⁹See, for example, J. H. Knox, *Molecular Thermodynamics* (Wiley-Interscience, London, 1971).

NDB

518-25
026136

K-10.1

273560

KINETICS OF THE Br₂-CH₃CHO PHOTOCHEMICAL CHAIN REACTION

13P.

J. M. NICOVICH, C. J. SHACKELFORD[†] and P. H. WINE

Molecular Sciences Branch, Georgia Tech Research Institute, Georgia Institute of Technology, Atlanta, GA 30332 (U.S.A.)

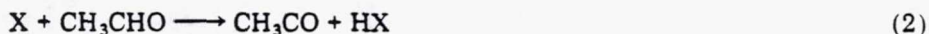
(Received February 21, 1989; in revised form August 16, 1989)

Summary

Time-resolved resonance fluorescence spectroscopy was employed in conjunction with laser flash photolysis of Br₂ to study the kinetics of the two elementary steps in the photochemical chain reaction $n\text{Br}_2 + n\text{CH}_3\text{CHO} + h\nu \rightarrow n\text{CH}_3\text{CBrO} + n\text{HBr}$. In the temperature range 255 - 400 K, the rate coefficient for the reaction $\text{Br}(^2\text{P}_{3/2}) + \text{CH}_3\text{CHO} \rightarrow \text{CH}_3\text{CO} + \text{HBr}$ is given by the Arrhenius expression $k_6(T) = (1.51 \pm 0.20) \times 10^{-11} \exp\{-(364 \pm 41)/T\}$ cm³ molecule⁻¹ s⁻¹. At 298 K, the reaction $\text{CH}_3\text{CO} + \text{Br}_2 \rightarrow \text{CH}_3\text{CBrO} + \text{Br}$ proceeds at a near gas kinetic rate, $k_7(298 \text{ K}) = (1.08 \pm 0.38) \times 10^{-10}$ cm³ molecule⁻¹ s⁻¹.

1. Introduction

The reaction of ground state halogen atoms with acetaldehyde is a useful laboratory source of the acetyl radical, a precursor to the important atmospheric species peroxyacetylnitrate (PAN)



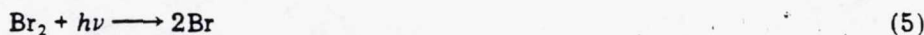
(PAN)

Niki *et al.* [1] have shown that quantitative conversion of acetaldehyde to PAN is facilitated when bromine is employed as the initiating halogen species instead of the more commonly used chlorine molecule. A major advantage of

[†]Present address: School of Physics, Georgia Institute of Technology, Atlanta, GA 30332, U.S.A.

the bromine system is that Br_2 can be photolyzed at wavelengths where neither CH_3CHO nor NO_2 are photochemically active, thus avoiding numerous complicating side reactions involving CH_3CHO and NO_2 photofragments. Another advantage of the bromine system is that only abstraction of the aldehydic hydrogen is energetically allowed, whereas in the chlorine system abstraction of a methyl hydrogen is also possible.

In the absence of oxygen, photolysis of Br_2 is known to initiate a chain reaction [1]



Niki *et al.* [1] demonstrated the occurrence of reaction (7) through Fourier transform IR (FTIR) spectroscopic observation of CH_3CBrO production. They also measured the ratio k_6/k_8 at 298 K



Combining their result with the literature value k_8 (298 K) = 1.08×10^{-12} $\text{cm}^3 \text{ molecule}^{-1} \text{ s}^{-1}$ [2], Niki *et al.* reported k_6 (298 K) = 3.7×10^{-12} $\text{cm}^3 \text{ molecule}^{-1} \text{ s}^{-1}$. One absolute measurement of k_6 (300 K) has also been reported. Islam *et al.* [3], using the very low pressure reactor (VLPR) technique, obtained the result k_6 (300 K) = 3.5×10^{-12} $\text{cm}^3 \text{ molecule}^{-1} \text{ s}^{-1}$, in excellent agreement with the findings of Niki *et al.*

We have employed pulsed laser photolysis of Br_2 in conjunction with time-resolved detection of $\text{Br}(^2\text{P}_{3/2})$ by resonance fluorescence spectroscopy to carry out the first temperature-dependent study of reaction (6) and the first determination of k_7 . Our results are reported in this paper.

2. Experimental technique

The experimental apparatus used was similar to that employed previously in our laboratory to study chlorine atom kinetics [4-6]. A schematic diagram of the apparatus is shown in Fig. 1 and a brief description is given below.

A Pyrex jacketed reaction cell with an internal volume of 150 cm^3 was used in all experiments. The cell was maintained at a constant temperature by circulating ethylene glycol or methanol from a thermostatically controlled bath through the outer jacket. A copper-constantan thermocouple with a stainless steel jacket was injected into the reaction zone through a vacuum seal, thus allowing measurement of the gas temperature under the precise pressure and flow rate conditions of the experiment.

$\text{Br}(^2\text{P}_j)$ was produced by 355 nm pulsed laser photolysis of Br_2 . Third harmonic radiation from a Quanta Ray model DCR-2 Nd:YAG laser provided the photolytic light source. The laser could deliver up to 1×10^{17} photons pulse^{-1} at a repetition rate of up to 10 Hz; the pulse width was 6 ns.

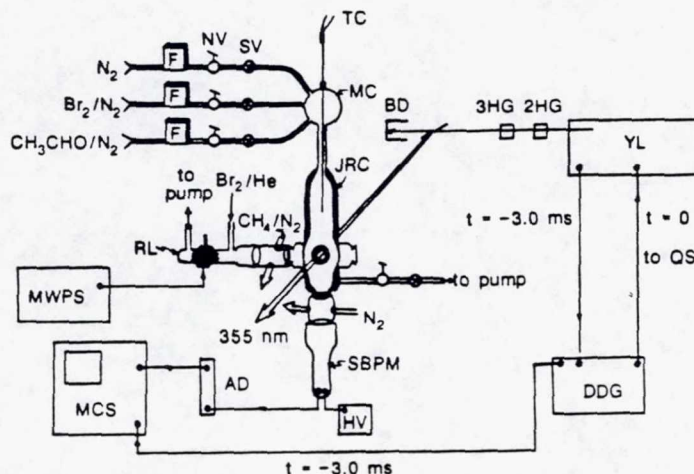


Fig. 1. Schematic diagram of the apparatus: AD, amplifier discriminator; BD, beam dump; DDG, digital delay generator; F, flow meter; HV, high voltage; JRC, jacketed reaction cell; MC, mixing chamber; MCS, multichannel scalar; MWPS, microwave power supply; NV, needle valve; QS, Q switch; SBPM, solar blind photomultiplier; SV, shut-off valve; TC, thermocouple; YL, Nd:YAG laser; 2HG, second harmonic generator; 3HG, third harmonic generator.

A bromine resonance lamp, situated perpendicular to the photolysis laser, excited resonance fluorescence in the photolytically produced atoms. The resonance lamp consisted of an electrodeless microwave discharge through about 1 Torr of a flowing mixture containing a trace of Br_2 in helium. The flows of a 0.2% Br_2 in helium mixture and pure helium into the lamp were controlled by separate needle valves, thus allowing the total pressure and Br_2 concentration to be adjusted for optimum signal-to-noise ratio. Radiation was coupled out of the lamp through a magnesium fluoride window and into the reaction cell through a magnesium fluoride lens. Before entering the reaction cell the lamp output passed through a flowing gas filter containing 50 Torr cm of methane in nitrogen. The methane filter prevented radiation at wavelengths shorter than 140 nm (including impurity emissions from excited oxygen, hydrogen, chlorine and nitrogen atoms) from entering the reaction cell, but transmitted the strong bromine lines in the 140 - 160 nm region.

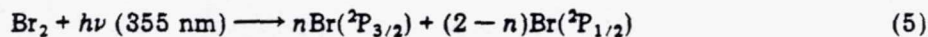
Fluorescence was collected by a magnesium fluoride lens on an axis orthogonal to both the photolysis laser beam and resonance lamp beam and was imaged onto the photocathode of a solar blind photomultiplier. Signals were processed using photon counting techniques conjunction with multichannel scaling. For each bromine atom decay measured, signals from a large number of laser shots were averaged in order to obtain a well-defined temporal profile over at least two $1/e$ times of decay.

To avoid the accumulation of photolysis or reaction products, all experiments were carried out under "slow flow" conditions. The linear flow rate through the reactor was (typically) 3 cm s^{-1} and the laser repetition rate was (typically) 5 Hz. Hence no volume element of the reaction mixture was subjected to more than a few laser shots. Acetaldehyde and bromine flowed into the reaction cell from bulbs (12 l) containing dilute mixtures in nitrogen. The acetaldehyde mixture, bromine mixture and additional nitrogen were pre-mixed before entering the reactor. The concentrations of each component in the reaction mixture were determined from measurements of the appropriate mass flow rates and the total pressure. The fractions of acetaldehyde and bromine in the bulb mixtures were checked frequently by UV photometry using atomic mercury lines as the absorption light sources. The monitoring wavelength for acetaldehyde was 253.7 nm and the monitoring wavelength for bromine was 404.7 nm. Absorption cross-sections were measured during the course of this investigation; they were found to be $1.46 \times 10^{-20} \text{ cm}^2$ for acetaldehyde at 253.7 nm and $5.85 \times 10^{-19} \text{ cm}^2$ for bromine at 404.7 nm, in good agreement with literature values [7].

The nitrogen used in this study had a stated minimum purity of 99.999% (UHP grade). The bromine used was Fisher ACS reagent grade with a maximum impurity level of 0.06%. Acetaldehyde was obtained from Aldrich and had a stated purity of 99%. Both bromine and acetaldehyde were transferred under nitrogen into vials fitted with high vacuum stopcocks, and were then degassed repeatedly at 77 K before being used to prepare reactant-nitrogen mixtures.

3. Results and discussion

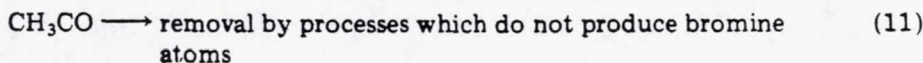
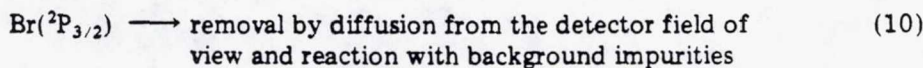
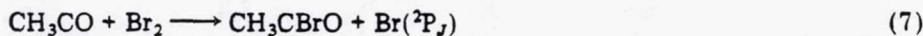
All experiments were carried out under pseudo-first-order conditions with CH_3CHO and Br_2 in large excess over bromine atoms. Reaction mixtures contained 0 - 0.05 Torr of CH_3CHO , 1×10^{-5} - 5×10^{-4} Torr of Br_2 and 150 Torr of N_2 buffer gas. The nitrogen level was sufficient to facilitate rapid deactivation of bromine atoms in the electronically excited spin-orbit state



The rate coefficient for reaction (9) is $2.5 \times 10^{-15} \text{ cm}^3 \text{ molecule}^{-1} \text{ s}^{-1}$ [8]. Both theoretical [9] and experimental [10] information suggests that the parameter n in eqn. (5) has a value near 2, *i.e.* little or no $\text{Br}({}^2\text{P}_{1/2})$ is produced when Br_2 is photolyzed in the near UV.

We expect the decay of $\text{Br}({}^2\text{P}_{3/2})$ to be controlled by the following reactions





The rate equations for the reaction scheme (6), (7), (10) and (11) can be solved analytically

$$[\text{Br}]_t/[\text{Br}]_0 = \{(K + \lambda_1) \exp(\lambda_1 t) - (K + \lambda_2) \exp(\lambda_2 t)\}/(\lambda_1 - \lambda_2) \quad (12)$$

where

$$\lambda_1 = 0.5\{(\alpha^2 - 4\beta)^{1/2} - \alpha\} \quad (13)$$

$$\lambda_2 = -0.5\{(\alpha^2 - 4\beta)^{1/2} + \alpha\} \quad (14)$$

$$K = k_7[\text{Br}_2] + k_{11} \quad (15)$$

$$\alpha = K + k_{10} + k_6[\text{CH}_3\text{CHO}] \quad (16)$$

$$\beta = k_{10}K + k_{11}k_6[\text{CH}_3\text{CHO}] \quad (17)$$

The observed temporal profiles can be fitted to the predicted double-exponential functional form (eqn. (12)) to obtain values for λ_1 , λ_2 and K . The rate coefficient k_{10} was directly measured to be $35 \pm 7 \text{ s}^{-1}$ in all experiments (assuming negligible contribution to k_{10} from impurities in the $\text{CH}_3\text{CHO-N}_2$ mixture). Therefore recognizing that

$$\lambda_1 + \lambda_2 = -\alpha \quad (18)$$

and

$$\lambda_1\lambda_2 = \beta \quad (19)$$

we obtain the following relationships for the rate coefficients k_6 , k_7 and k_{11}

$$k_6 = -A/[\text{CH}_3\text{CHO}] \quad (20)$$

$$k_7 = (K - k_{11})/[\text{Br}_2] \quad (21)$$

$$k_{11} = (k_{10}K - \lambda_1\lambda_2)/A \quad (22)$$

$$A = K + k_{10} + \lambda_1 + \lambda_2 \quad (23)$$

A typical $\text{Br}(^2\text{P}_{3/2})$ temporal profile observed under conditions of relatively high $[\text{Br}_2]$ is shown in Fig. 2, and the results obtained from the analysis of a number of temporal profiles are summarized in Table 1. Uncertainties in the parameters λ_1 , λ_2 and K obtained from non-linear least-squares analyses of the observed double-exponential decays are difficult to evaluate quantitatively. However, for data of the quality shown in Fig. 2 (which is typical of all experiments summarized in Table 1), we believe that a reasonable estimate of the 2σ uncertainties of all three parameters is $\pm 15\%$.

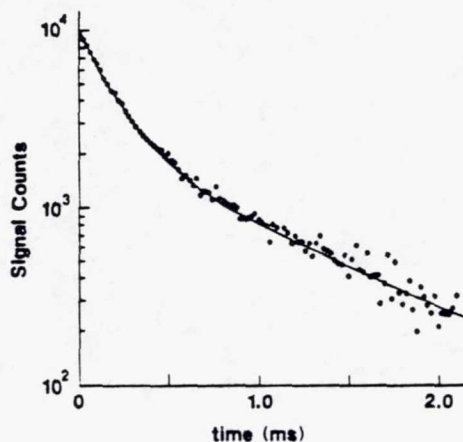


Fig. 2. Typical $\text{Br}(^2\text{P}_{3/2})$ temporal profile observed under conditions of relatively high $[\text{Br}_2]$. Experimental conditions: 150 Torr N_2 ; 298 K; 1.09×10^{15} CH_3CHO cm^{-3} ; 8.94×10^{12} Br_2 cm^{-3} ; 1.7×10^{11} Br atoms cm^{-3} at $t = 0$; 2048 laser shots averaged. The full line is obtained from a non-linear least-squares fit to eqn. (12). Best fit parameters: $\lambda_1 = -1040$ s^{-1} ; $\lambda_2 = -5430$ s^{-1} ; $K = 2040$ s^{-1} .

When the two time constants λ_1 and λ_2 differ by less than a factor of five, the uncertainties in all three parameters increase in magnitude.

A simple average of the k_6 (298 K) values obtained from all 17 experiments summarized in Table 1 is $(4.05 \pm 0.76) \times 10^{-12}$ cm^3 molecule^{-1} s^{-1} (error is 2σ , precision only), which is in good agreement with the literature values of 3.7×10^{-12} cm^3 molecule^{-1} s^{-1} [1] and 3.5×10^{-12} cm^3 molecule^{-1} s^{-1} [3]. It should be noted, however, that the most accurate measurements of k_6 are expected to be obtained under conditions of very low $[\text{Br}_2]$ since, under these conditions, the effect of reactions (7) and (11) on the $\text{Br}(^2\text{P}_{3/2})$ temporal profile is minimized. The experiments at very low Br_2 concentrations are discussed below.

Inspection of Table 1 shows that k_{11} (298 K) appears to increase with increasing $[\text{Br}_2]$. This result, which was unexpected, indicates that CH_3CO radicals react with Br_2 or an impurity in the Br_2 flow via a process which does not produce bromine atoms. A plot of k_{11} (298 K) vs. $[\text{Br}_2]$ is shown in Fig. 3. Although somewhat scattered, the data are reasonably well represented by a straight line with an intercept of 648 ± 230 s^{-1} and a slope of $(6.4 \pm 2.5) \times 10^{-11}$ cm^3 molecule^{-1} s^{-1} (errors are 2σ , precision only). The rather large background CH_3CO decay rate of 648 s^{-1} is probably due, in large part, to the reaction



The 298 K rate coefficient for reaction (3) is known to be 2×10^{-12} cm^3 molecule^{-1} s^{-1} [11]. Hence a background O_2 level of 10 mTorr, i.e. 0.007%, in the slow flow system would completely account for CH_3CO removal with

TABLE 1

Summary of results obtained at relatively high Br₂ concentrations^a

[CH ₃ CHO] (10 ¹¹ molecules cm ⁻³)	[Br ₂] (10 ¹¹ molecules cm ⁻³)	[Br] ₀ (10 ¹¹ molecules cm ⁻³)	K (s ⁻¹)	-λ ₁ (s ⁻¹)	-λ ₂ (s ⁻¹)	k ₁₁ (s ⁻¹)	k ₆ (10 ⁻¹² cm ³ molecule ⁻¹ s ⁻¹)	k ₇ (10 ⁻¹² cm ³ molecule ⁻¹ s ⁻¹)
5230	95.1	0.65	2780	937	4360	1610	4.74	123
5150	93.5	2.2	2200	873	3480	1400	4.11	86
5060	90.1	0.19	2210	831	3860	1280	4.82	103
5270	145	0.31	2960	732	4410	1460	4.07	104
5470	150	2.6	2880	739	4270	1460	3.84	95
8290	88.1	0.15	2430	1150	4900	1550	4.32	100
10800	40.7	0.78	1190	826	5290	884	4.53	76
10700	89.4	1.7	2040	1040	5430	1270	4.11	86
10700	89.7	0.92	2250	1090	5720	1360	4.23	99
7330	22.3	0.79	1050	757	3200	831	3.91	98
7330	44.5	0.72	1150	588	3340	700	3.75	100
7280	77.6	0.26	2020	716	4140	1030	3.85	127
7320	121	0.42	2430	680	4330	1120	3.48	108
3700	44.9	0.68	1320	537	2190	820	3.72	111
3660	121	0.44	2850	461	3810	1190	3.80	137
3700	22.3	0.77	860	520	1710	641	3.62	97
3670	79.1	0.26	2280	502	3260	1070	3.96	153

^aT = 298 K in all experiments.

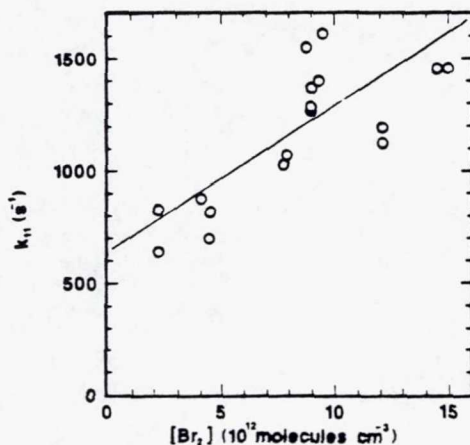


Fig. 3. Plot of k_{11} vs. $[\text{Br}_2]$ for the results summarized in Table 1. The full line is obtained from an unweighted linear least-squares analysis.

the Br_2 flow off. The process which causes k_{11} to increase when Br_2 is added cannot be identified with any degree of confidence.

The values of k_7 (298 K) obtained from eqn. (21) and summarized in Table 1 do not appear to vary systematically as a function of either the CH_3CHO concentration or the Br_2 concentration. A simple average of the k_7 (298 K) values obtained from all 17 experiments is $(1.06 \pm 0.39) \times 10^{-10} \text{ cm}^3 \text{ molecule}^{-1} \text{ s}^{-1}$ where the error is 2σ and represents precision only. Alternatively, k_7 can be evaluated from the slope of a plot of $K - k_{11}$ vs. $[\text{Br}_2]$ (Fig. 4). An unweighted linear least-squares analysis of the data plotted in Fig. 4 gives the result k_7 (298 K) $\pm 2\sigma = (1.08 \pm 0.22) \times 10^{-10} \text{ cm}^3 \text{ molecule}^{-1} \text{ s}^{-1}$. The improved precision of the second method for determining k_7 results from the fact that data at high $[\text{Br}_2]$, where $K - k_{11}$ is relatively large and therefore more accurately determined, are effectively given a higher weight in determining the $K - k_{11}$ vs. $[\text{Br}_2]$ slope, whereas all points are weighted equally in the simple average. Hence the "slope" method of analysis is preferred. We estimate the absolute accuracy of our k_7 (298 K) determination to be $\pm 35\%$ and, therefore, report the rate coefficient

$$k_7(298 \text{ K}) = (1.08 \pm 0.38) \times 10^{-10} \text{ cm}^3 \text{ molecule}^{-1} \text{ s}^{-1}$$

It should be noted that the only important mechanistic assumption required to extract the above value for $k_7(T)$ from the data analysis is that reaction (7) is the only process which regenerates bromine atoms. For the chemical system of interest here, this assumption appears to be justified.

Typical $\text{Br}(^2\text{P}_{3/2})$ temporal profiles observed under conditions of relatively low $[\text{Br}_2]$ are shown in Fig. 5. The decays are exponential. However, simulations employing eqn. (12) in conjunction with the rate coefficients determined in the high $[\text{Br}_2]$ experiments demonstrate that, over the range of Br_2 and CH_3CHO concentrations employed, the observed temporal

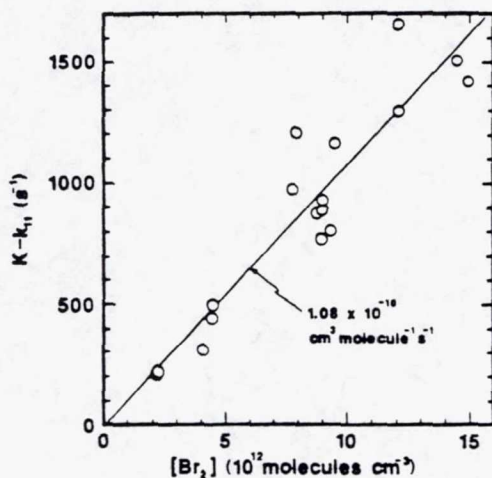


Fig. 4. Plot of $K - k_{11}$ vs. $[Br_2]$ for the results summarized in Table 1. The full line is obtained from an unweighted linear least-squares analysis and gives the bimolecular rate coefficient k_7 .

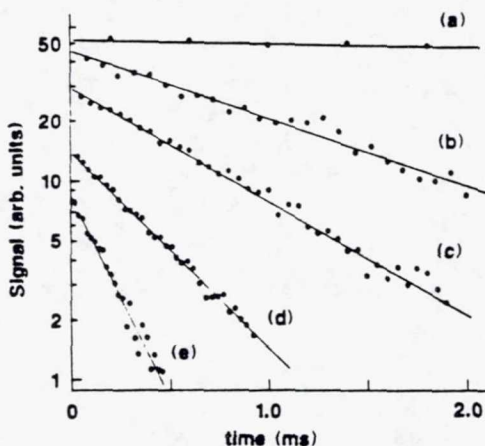


Fig. 5. Typical $Br(2P_{3/2})$ temporal profiles observed under conditions of relatively low $[Br_2]$ ($1 \times 10^{12} \text{ cm}^{-3}$ or less). $P = 150 \text{ Torr N}_2$; $T = 255 \text{ K}$. $[CH_3CHO]$ in units of $10^{14} \text{ molecules cm}^{-3}$: (a) 0; (b) 2.25; (c) 3.80; (d) 6.63; (e) 13.4. Full lines are obtained from linear least-squares analyses and give the following pseudo-first-order rate coefficients: (a) 40 s^{-1} ; (b) 781 s^{-1} ; (c) 1310 s^{-1} ; (d) 2260 s^{-1} ; (e) 4690 s^{-1} .

profiles should be slightly non-exponential due to bromine atom regeneration via reaction (7). To analyze the experimental data, we obtained an uncorrected pseudo-first-order decay rate k' by carrying out a linear least-squares analysis of the first two $1/e$ times of decay (i.e. down to $[Br]_t/[Br]_0 = 0.135$); we then corrected k' using the ratio of the simulated decay

rate with the Br_2 concentration set equal to zero to the simulated decay rate for the Br_2 concentration employed in the experiment. The simulated decay rates were obtained from linear least-squares analyses of the simulated $\ln [\text{Br}]_t$ vs. t data for the first two $1/e$ times of decay. For simulations at temperatures other than 298 K, it was assumed that the nearly gas kinetic k_7 value was independent of temperature. Two scenarios were adopted for the temperature dependence of k_{11} . One set of simulations was carried out with k_{11} assumed to be independent of temperature. A second set of simulations assumed that the $[\text{Br}_2]$ -independent component of k_{11} , which was speculated to be due primarily to the addition reaction (3), varied according to the expression $k(T) = k(298 \text{ K})(T/298)^{-4}$; the $[\text{Br}_2]$ -dependent component of k_{11} , which was very small under the conditions of the low $[\text{Br}_2]$ experiments, was assumed to be independent of temperature.

The results of the "low $[\text{Br}_2]$ " experiments are summarized in Table 2. The rate coefficients $k_6(T)$ reported in Table 2 were obtained from linear least-squares analyses of plots of k' , the pseudo-first-order $\text{Br}(^2\text{P}_{3/2})$ decay rate, vs. CH_3CHO concentration. As can be seen from inspection of Table 2, although correction for $\text{Br}(^2\text{P}_{3/2})$ regeneration raised individual k' values by factors ranging from 1.03 to 1.21, corrected $k_6(T)$ values were only about 4% larger than the uncorrected values. The magnitudes of the corrections to $k_6(T)$ did not depend strongly on temperature, and were virtually independent of the temperature dependence adopted for $k_{11}(T)$. It should be noted that the method used to obtain a corrected value for $k_6(T)$ required an initial estimate of $k_6(T)$. However, this estimate could be made quite accurately because the required corrections were so small. For this reason, it was not necessary to employ an iterative procedure to obtain accurate correction factors.

The rate coefficients $k_6(T)$ determined in this study are listed in Table 2 and plotted in Arrhenius form in Fig. 6. An unweighted linear least-squares analysis of the $\ln k_6$ vs. T^{-1} data gives the Arrhenius expression ($255 \text{ K} \leq T \leq 400 \text{ K}$)

$$k_6(T) = (1.51 \pm 0.20) \times 10^{-11} \exp\{-(364 \pm 41)/T\} \text{ cm}^3 \text{ molecule}^{-1} \text{ s}^{-1}$$

where the errors are 2σ and represent precision only. The above Arrhenius parameters seem reasonable. The A factor is typical of that found for a direct atom-molecule hydrogen abstraction reaction and the trend for bromine atom reactions with formaldehyde and acetaldehyde is similar to the trends observed for other radical-aldehyde reactions, i.e. similar A factors but larger activation energies for the formaldehyde reaction than for the acetaldehyde reaction [12].

From the above Arrhenius expression we obtain $k_6(298 \text{ K}) = 4.45 \times 10^{-12} \text{ cm}^3 \text{ molecule}^{-1} \text{ s}^{-1}$ — about 25% faster than the two literature values [1, 3]. We estimate the uncertainty in our $k_6(298 \text{ K})$ value to be $\pm 15\%$ (2σ). Niki *et al.* [1] report a 2σ uncertainty of $\pm 6\%$ for the ratio k_6/k_8 , whereas the uncertainty in k_8 is estimated to be $\pm 30\%$ [12]. Hence our result agrees well with that of Niki *et al.* considering the combined uncertainties of the

TABLE 2

Summary of results obtained at relatively low Br₂ concentrations^a

T (K)	[Br ₂] (10 ¹¹ molecules cm ⁻³)	[CH ₃ CHO] (10 ¹¹ molecules cm ⁻³)	k' (s ⁻¹) ^c			k ₆ ± 2σ ^b (10 ⁻¹² cm ³ molecule ⁻¹ s ⁻¹)
			A	B	C	
255	10.3	0	40	40	40	A: 3.45 ± 0.06
	5.13	2250	781	841	820	B: 3.59 ± 0.07
	10.0	3800	1310	1470	1420	C: 3.59 ± 0.06
	6.11	4890	1660	1760	1730	
	10.2	6630	2260	2450	2410	
	10.3	12000	4100	4320	4300	
	9.59	13400	4690	4890	4870	
298	8.72	0	34	34	34	A: 4.27 ± 0.24
	4.70	2920	1230	1300	1300	B: 4.40 ± 0.33
	8.08	2990	1310	1440	1440	C: 4.40 ± 0.33
	4.69	6040	2530	2620	2620	
	8.66	6100	2710	2890	2890	
	8.02	8020	3630	3800	3800	
	8.00	10500	4400	4540	4540	
298	7.29	0	32	32	32	A: 4.44 ± 0.30
	6.90	2070	880	968	968	B: 4.61 ± 0.24
	6.89	3530	1410	1510	1510	C: 4.61 ± 0.24
	6.52	4680	2010	2130	2130	
	6.51	5470	2390	2510	2510	
	6.51	6980	3140	3270	3270	
345	9.18	0	41	41	41	A: 4.96 ± 0.17
	8.84	1350	724	829	872	B: 5.23 ± 0.24
	9.00	2250	1190	1340	1370	C: 5.23 ± 0.32
	9.10	3950	1950	2120	2140	
	8.66	5840	2970	3140	3160	
400	6.82	0	29	29	29	A: 5.87 ± 0.26
	6.78	1050	605	675	734	B: 6.08 ± 0.26
	6.54	1620	956	1040	1090	C: 6.06 ± 0.28
	6.48	2730	1570	1680	1700	
	6.15	3360	2060	2170	2200	
	6.43	4180	2380	2490	2520	
	6.33	5410	3220	3350	3360	

^a[Br]₀ was in the range (1.4 - 3.5) × 10¹⁰ atoms cm⁻³ in all experiments.^bErrors represent precision only.^cA, uncorrected for bromine atom regeneration via the CH₃CO + Br₂ reaction; B, corrected for bromine atom regeneration via the CH₃CO + Br₂ reaction assuming that k₁₁ is independent of temperature; C, corrected for bromine atom regeneration via the CH₃CO + Br₂ reaction assuming that the [Br₂]-independent component of k₁₁ has a T⁻⁴ temperature dependence (see text for rationale).

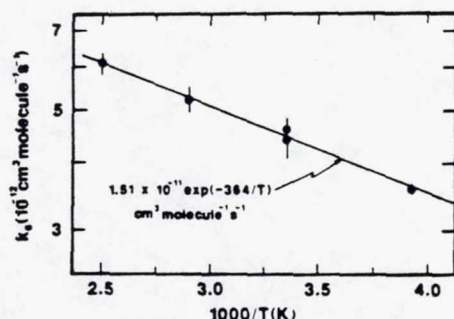


Fig. 6. Arrhenius plot for the reaction $\text{Br}(^2P_{3/2}) + \text{CH}_3\text{CHO} \rightarrow \text{CH}_3\text{CO} + \text{HBr}$. The full line is obtained from an unweighted linear least-squares analysis.

two studies. Islam *et al.* [3] carried out a VLPR study of the kinetics of reaction (6) and obtained the result $k_6(300 \text{ K}) \pm 2\sigma = (3.5 \pm 1.0) \times 10^{-12} \text{ cm}^3 \text{ molecule}^{-1} \text{ s}^{-1}$, again in agreement with our result within the combined uncertainties of the studies. Islam *et al.* observed upward curvature in their plots of $[\text{Br}]_0/[\text{Br}]$ vs. $[\text{CH}_3\text{CHO}]$ which they considered to be insignificant due to the relatively large uncertainty associated with the data points at high values of $[\text{Br}]_0/[\text{Br}]$. Islam *et al.* generated bromine atoms by passing a Br_2 -He mixture through a microwave discharge. Incomplete dissociation of Br_2 in the discharge would have resulted in the observed upward curvature of the $[\text{Br}]_0/[\text{Br}]$ vs. $[\text{CH}_3\text{CHO}]$ plot, because reaction (7) would have represented a more important bromine atom regeneration step at low $[\text{CH}_3\text{CHO}]$ than at high $[\text{CH}_3\text{CHO}]$. If Br_2 was present in the reactor of Islam *et al.*, it is clear that they would have underestimated k_6 .

Barnes *et al.* [13] have recently published the results of a competitive kinetics investigation of bromine atom reactions with a series of alkanes, alkenes and alkynes. These workers used the reactions of bromine atoms with CH_3CHO and 2-methylpropane as their reference reactions. The results of Niki *et al.* [1] and Islam *et al.* [3] were used to obtain an absolute value for k_6 , and the recent results of Russell *et al.* [14] were used to obtain an absolute value for the Br-2-methylpropane rate coefficient. As a consistency check, Barnes *et al.* studied the Br-propyne reaction using both CH_3CHO and 2-methylpropane as competitors. Their Br-propyne rate coefficient was 33% faster when referenced to 2-methylpropane than when referenced to CH_3CHO ; if our value for $k_6(T)$ was used, this would reduce the difference to less than 10%.

Acknowledgments

This work was supported by the U.S. Environmental Protection Agency through Grant R814527 and by the National Aeronautics and Space Administration through Grant NAGW-1001.

References

- 1 H. Niki, P. D. Maker, C. M. Savage and L. P. Breitenbach, *Int. J. Chem. Kinet.*, **17** (1985) 525.
- 2 D. F. Nava, J. V. Michael and L. J. Stief, *J. Phys. Chem.*, **85** (1981) 1896.
- 3 T. S. A. Islam, R. M. Marshall and S. W. Benson, *Int. J. Chem. Kinet.*, **16** (1984) 1161.
- 4 A. R. Ravishankara and P. H. Wine, *J. Chem. Phys.*, **72** (1980) 25.
- 5 P. H. Wine, D. H. Semmes and A. R. Ravishankara, *Chem. Phys. Lett.*, **90** (1982) 128.
- 6 P. H. Wine and D. H. Semmes, *J. Phys. Chem.*, **87** (1983) 3572.
- 7 J. G. Calvert and J. N. Pitts, Jr., *Photochemistry*, Wiley, New York, 1966.
- 8 R. J. Donovan and D. Husain, *Trans. Faraday Soc.*, **62** (1966) 2987.
- 9 R. S. Mulliken, *Phys. Rev.*, **46** (1934) 549; *J. Chem. Phys.*, **4** (1936) 620; *Phys. Rev.*, **57** (1940) 500.
- 10 R. J. Oldman, R. K. Sander and K. R. Wilson, *J. Chem. Phys.*, **63** (1975) 4252.
- 11 C. E. McDade, T. M. Lenhardt and K. D. Bayes, *J. Photochem.*, **20** (1982) 1.
- 12 W. B. DeMore, M. J. Molina, S. P. Sander, D. M. Golden, R. F. Hampson, M. J. Kurylo, C. J. Howard and A. R. Ravishankara, Chemical kinetics and photochemical data for use in stratospheric modeling, Evaluation number 8, *JPL Publ. 87-41*, 1987 and references cited therein.
- 13 I. Barnes, V. Bastian, K. H. Becker, R. Overath and Z. Tong, *Int. J. Chem. Kinet.*, **21** (1989) 499.
- 14 J. J. Russell, J. A. Seetula, R. S. Timonen, D. Gutman and D. F. Nava, *J. Am. Chem. Soc.*, **110** (1988) 3084.

MIT

89A-6396

Pulsed laser photolysis kinetics study of the O(³P) + ClO reaction

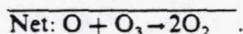
J. M. Nicovich, P. H. Wine,^{a)} and A. R. Ravishankara^{b)}
Molecular Sciences Branch, Georgia Tech Research Institute, Georgia Institute of Technology, Atlanta, Georgia 30332

(Received 23 June 1988; accepted 21 July 1988)

A pulsed laser photolysis technique has been employed to study the kinetics of the important stratospheric reaction $O + ClO \xrightarrow{k_1} Cl + O_2$ in N_2 buffer gas over the temperature and pressure ranges 231–367 K and 25–500 Torr. 351 nm pulsed laser photolysis of $Cl_2/O_3/N_2$ mixtures produced Cl atoms in excess over O_3 . After a delay sufficient for the reaction $Cl + O_3 \rightarrow ClO + O_2$ to go to completion, a small fraction of the ClO was photolyzed at 266 nm to produce O(³P). The decay of O(³P) in the presence of an excess, known concentration of ClO was then followed by time-resolved resonance fluorescence spectroscopy. We find that k_1 is independent of pressure, but that $k_1(T)$ increases with decreasing temperature. Our results suggest that the Arrhenius expression $k_1(T) = (1.55 \pm 0.33) \times 10^{-11} \exp\{(263 \pm 60)/T\}$ $cm^3 \text{ molecule}^{-1} s^{-1}$ is appropriate for modeling stratospheric chemistry. Errors in the Arrhenius expression are 2σ and represent precision only. The absolute accuracy of k_1 at any temperature within the range studied is estimated to be $\pm 20\%$. Our results agree with other recent measurements of k_1 at 298 K but give significantly faster rate coefficients at stratospheric temperatures. A few measurements of the rate coefficient for the reaction $ClO + ClO \xrightarrow{k_2} \text{products}$ were also carried out. These measurements were necessary to assess the time dependence of [ClO].

INTRODUCTION

The reaction of ground state oxygen atoms O(³P) with ClO radicals is the rate determining step in the dominant catalytic cycle via which chlorine atoms destroy odd oxygen in the middle stratosphere:



The primary source of stratospheric chlorine atoms is the photolysis of anthropogenic chlorofluorocarbons.

Seven measurements of k_1 (298 K) are reported in the literature.¹⁻⁷ There is agreement among the five most recent studies that $k_1(298 \text{ K})$ lies in the range $3.5\text{--}4.2 \times 10^{-11} \text{ cm}^3 \text{ molecule}^{-1} \text{ s}^{-1}$. The activation energy for reaction (1) is known to be small,²⁻⁷ but its value is not as well defined as would be desirable for such an important stratospheric reaction. In fact, it is not clear if $k_1(T)$ increases or decreases with decreasing temperature. In addition to the abovementioned studies of reaction (1) at atmospheric temperatures, one high temperature (1250 K) shock tube measurement of k_1 has been reported,⁸ as has one theoretical calculation of $k_1(T)$ over the temperature range 220–1000 K.⁹

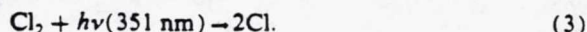
Because predictions of chlorine catalyzed ozone loss are very sensitive to the value of $k_1(T)$ used in model calculations, it is important that this rate coefficient be determined with high precision at stratospheric temperatures. Studies

employing a variety of experimental techniques are desirable in order to uncover possible systematic errors. All previous studies of reaction (1) at ambient and subambient temperatures¹⁻⁷ employed discharge flow systems which were limited to total pressures of 10 Torr or less. It is interesting to note that reaction (1) occurs on a potential energy surface with a minimum along the reaction coordinate, i.e., the intermediate complex ClOO is a bound species whose ground state correlates with O(³P) + ClO($X^2\pi$).¹⁰ Reactions which occur on potential energy surfaces of this type often exhibit negative activation energies and pressure dependent rates.

We have recently developed a pulsed laser photolysis method for carrying out direct kinetics studies of radical-radical reactions at pressures up to 1 atm, and applied this method to study the temperature and pressure dependences of the O + HO₂ reaction.^{11,12} Using an extension of the technique employed in the O + HO₂ investigations, we have studied the kinetics of reaction (1) in N_2 buffer gas over the temperature and pressure ranges 231–367 K and 25–200 Torr. Our results, which include observation of a significant negative activation energy, are reported in this paper.

EXPERIMENTAL

A schematic of the apparatus appears in Fig. 1. The two radical species were created via a scheme involving two separate photolysis lasers. Under "slow flow" conditions, a gas mixture containing Cl_2 and O_3 in a large excess of N_2 buffer gas was first subjected to photolysis by a XeF excimer laser,



^{a)} Author to whom correspondence should be addressed.

^{b)} Present address: Aeronomy Laboratory, National Oceanic and Atmospheric Administration, 325 Broadway, Boulder, CO 80303.

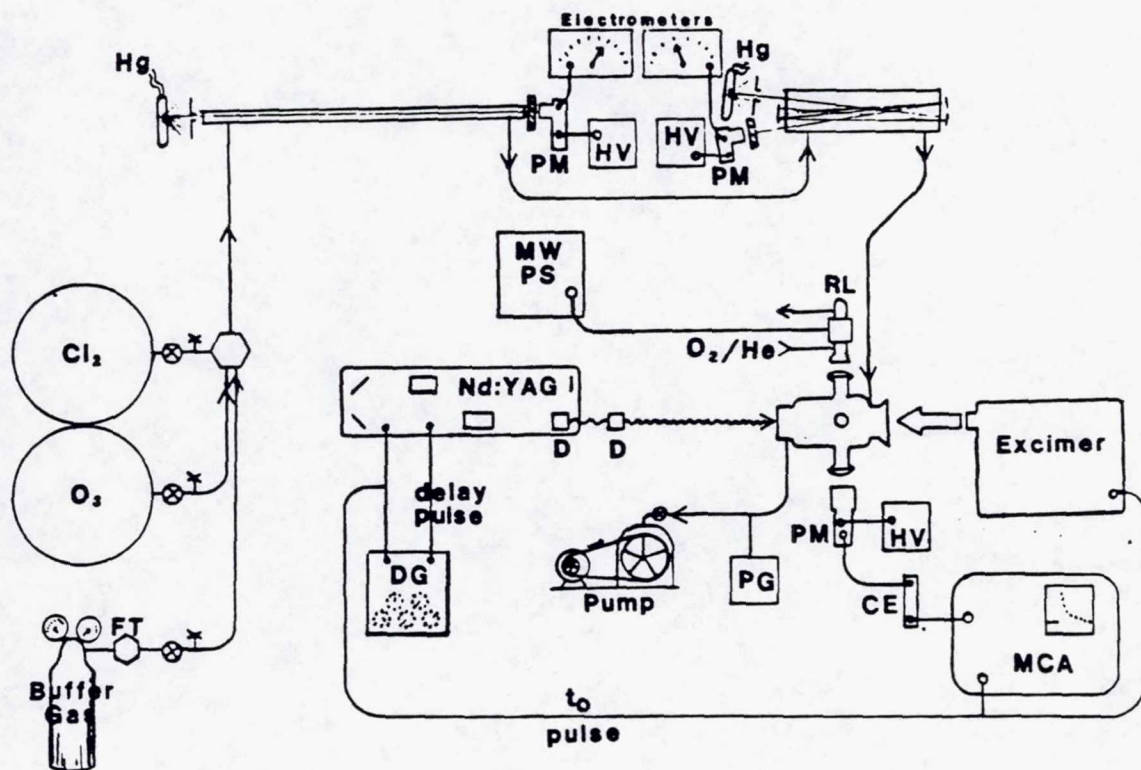
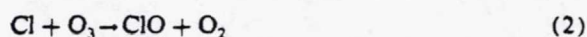
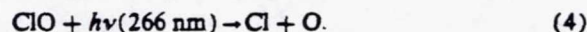


FIG. 1. Schematic diagram of the experimental apparatus. The abbreviations used are as follows: FT—flow transducer; Hg—mercury pen-ray lamp; PM—photomultiplier tube; HV—high voltage power supply; MWPS—microwave power supply; RL—resonance lamp; DG—delay generator; PG—pressure gauge; MCA—multichannel analyzer; D—doubling crystal; CE—counting electronics. For the sake of clarity, the resonance lamp and photomultiplier tube are shown facing each other when, in fact, they were mounted at 90° to each other and perpendicular to the direction of the laser beams.

The combination of the excimer laser fluence and $[Cl_2]$ was always large enough for the condition $[Cl]_0 > [O_3]_0$ to hold. During a predetermined delay period, t_d , the reaction



was allowed to go to completion. At this time the ozone in the reaction cell had effectively been titrated by Cl atoms and the initial value of $[O_3]_0$ could be related to $[ClO]_{t_d}$. At the end of this delay a second laser pulse, the fourth harmonic of the fundamental wavelength from a Nd:YAG laser, photolyzed a small fraction of the ClO,



The decay of oxygen atoms in the presence of excess ClO was followed by monitoring the time dependence of fluorescence signal which was continuously excited by a microwave discharge resonance lamp. The lamp was operated with a low pressure of helium (< 1 Torr) containing a small fraction of O_2 .

The ozone storage bulb contained a mixture of 1% to 2% O_3 in nitrogen, while the Cl_2 was stored neat. These species were leaked through needle valves into the main gas flow. Ozone in the gas flow was measured in a 35.0 cm absorption cell that was placed within a multipass optical arrangement. Using modified White cell optics, 30 passes of

the 254 nm Hg line from a pen-ray lamp were sent through the absorption cell for an effective path length of 10.50 m. The chlorine was measured in a 216 cm absorption cell using a single pass of the 366 nm Hg line, also from a pen-ray lamp. Both atomic lines were isolated using suitable bandpass filters. Typically, the absorption cells were upstream from the reaction cells, although in a few experiments the Cl_2 and O_3 were measured after the flow exited the reaction cell. Because Cl_2 absorbance at 254 nm was not totally negligible [$\sigma = 1.6 \times 10^{-21} \text{ cm}^2$ (Ref. 13)], the reference light intensity for the $[O_3]$ determination was always measured with Cl_2 flowing. The Cl_2 absorption cross section at 366 nm and the O_3 absorption cross section at 254 nm were taken to be $1.01 \times 10^{-19} \text{ cm}^2$ (Ref. 13) and $1.147 \times 10^{-17} \text{ cm}^2$ (Ref. 14), respectively.

The Pyrex reaction cell measured 16 cm along its longer axis and had an internal diameter of 4 cm. The two laser beams counterpropagated along the longer axis. Around the middle of the cell were four 1.5 cm diameter side arms, each perpendicular to the long axis of the cell and at 90° to each other. The resonance lamp radiation entered the cell through one of the side arms and the fluorescence signal was collected through a neighboring arm. The central portion of the cell was surrounded by a jacket through which thermostated liquids were flowed to control the temperature of the

gas mixture inside the reactor. The gas mixture entered the cell through several ports very near the window at one end of the long axis and exited the cell through similar ports near the opposite window. Because the chemistry initiated by the excimer laser beam completely titrated one component (O_3) of the gas mixture within much of the cell volume, the cell was designed to have minimum total volume and low dead space, i.e., gas flowed through all volume elements of the cell at approximately equal rates. The typical linear flow rate through the cell was 14 cm s^{-1} and the repetition rate of the two laser sequence was usually 0.4 Hz. Therefore, the gas mixture within the entire volume of the reaction cell was replenished between excimer laser pulses. The temperature of the gas mixture was measured by replacing one of the end windows with an acrylic flange through which a copper-constantan thermocouple could be inserted. The errors in the reported temperatures are estimated to be no more than $\pm 1.0 \text{ K}$ at the extreme temperatures and less at intermediate temperatures.

Oxygen resonance lamp radiation was focused into the reaction zone by a 2 in. focal length MgF_2 lens. The reaction zone was viewed by a solar blind photomultiplier tube through a similar lens. The volumes between the resonance lamp and the reaction cell, and between the reaction cell and the photomultiplier tube were purged with a mixture of 1% O_2 in nitrogen. This excluded room air and also acted as a filter of extraneous emissions from the resonance lamp. A CaF_2 window between the cell and the photomultiplier tube eliminated the possibility of hydrogen atom detection. Fluorescence signals were accumulated using photon counting techniques in conjunction with multichannel scaling. Each sweep of the analyzer was triggered simultaneously with the excimer laser. From 50 to 500 flashes were averaged to obtain sufficient signal-to-noise ratio for quantitative kinetic analysis.

The total pressure in the flow system was measured with a capacitance manometer. Due to the necessarily fast flow rate and the small (4.0 mm i.d.) tubing connecting the various components of the flow system, there were measurable pressure gradients between the absorption cells and the reaction cell. Quantitative adjustments were made for these gradients in the calculation of the Cl_2 and O_3 concentrations in the reaction cell under each set of conditions. The magnitude of the adjustment was largest at the lowest pressure (15% at 25 Torr) and negligible at the highest (1% at 200 Torr). The nitrogen buffer gas comprised at least 94% of the mixture for all experiments and its flow rate was monitored using a calibrated electronic mass flowmeter.

The concentration of ClO, the excess species in this technique, was derived from the concentration of ozone as measured "in situ." Therefore, it was not necessary to have an absolute calibration of the photolysis laser fluences. However, it was important to know that following the excimer laser pulse the condition $[Cl] > [O_3]$ held throughout the reaction zone. Therefore, the excimer laser fluence was measured in each experiment. As will be discussed below, it was also important to monitor the 266 nm laser fluence. Both of these quantities were determined using a photodiode-based calibrated radiometer. With the front optic of the excimer

laser approximately 2 m from the center of the reaction cell, the beam was rectangular in cross section and measured 2.0 by 4.0 cm. When measured through a 0.5 cm diameter aperture, the fluence peaked at the center of the beam and dropped off by 10% per 0.5 cm distance from the center in both the vertical and horizontal directions. The beam from the Nd:YAG laser was aligned at the center of the volume irradiated by the excimer laser. It was estimated to be $0.4 \pm 0.1 \text{ cm}$ in diameter.

The reagent purities and sources were as follows: N_2 (99.999%, Spectra Gases, Inc.); Cl_2 (99.9%, Matheson Gas Products, Inc.); O_2 (99.99%, Spectra Gases, Inc.). Ozone was prepared in a commercial ozonator using UHP oxygen. It was stored at 195 K on silica gel and degassed at 77 K before use. The other gases were used without further purification.

RESULTS

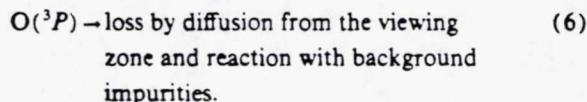
In the absence of competing reactions that either deplete or enhance the ground state oxygen atom [$O(^3P)$] concentration, the temporal behavior of [$O(^3P)$] following the 266 nm laser pulse can be described by the relationship

$$\ln\{[O(^3P)]_t/[O(^3P)]_{t_d}\} = -(k_1[ClO] + k'_d)(t - t_d) \\ = -k'(t - t_d), \quad (I)$$

where

$$k'_d = k_5[Cl_2] + k_6. \quad (II)$$

In Eq. (II), k_5 and k_6 are the rate coefficients for the following processes:



A typical experimental $O(^3P)$ temporal profile is shown in Fig. 2. Unexpectedly, a significant buildup and decay of $O(^3P)$ occurred before the 266 nm laser fired; possible sources of this $O(^3P)$ and its implications for our study of reaction (1) are discussed below. It should be noted that the vertical axis in Fig. 2 has units of concentration. To construct Fig. 2, the fluorescence signal before the 266 nm laser fired was scaled to account for the fact that the 351 nm laser photolyzed the entire field of view of the detection system, while the 266 nm laser photolyzed only 15% of the detector viewing zone. The size of the viewing zone was estimated by placing a series of apertures in front of the 351 nm beam and noting the variation of fluorescence signal strength with beam size.

Typical decays of $O(^3P)$ generated by the 266 nm laser pulse are shown in Fig. 3. At each temperature and pressure a minimum of five and an average of eight experiments were performed at various values of $[O_3]_0$. Because the Nd:YAG laser fluence was measured in each experiment, the amount of ClO lost via 266 nm photolysis could be quantified. The expression

$$[ClO]_{t_d} = [O_3]_0 - [O(^3P)]_{t_d} \quad (III)$$

was used to calculate the ClO concentration under the as-

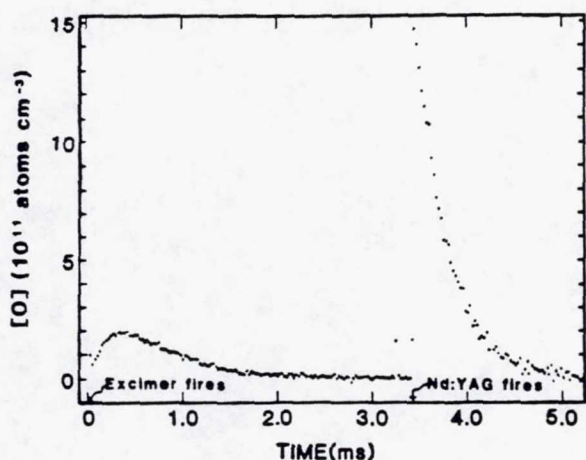


FIG. 2. An experimental O atom temporal profile obtained under the following conditions: $[Cl_2] = 1.40 \times 10^{16}$ molecules cm^{-3} ; $[O_3]_0 = 7.27 \times 10^{13}$ molecules cm^{-3} ; $[Cl]_0 = 1.82 \times 10^{14}$ molecules cm^{-3} ; Total pressure = 25 Torr; temperature = 298 K; MCA dwell time = 25 μs .

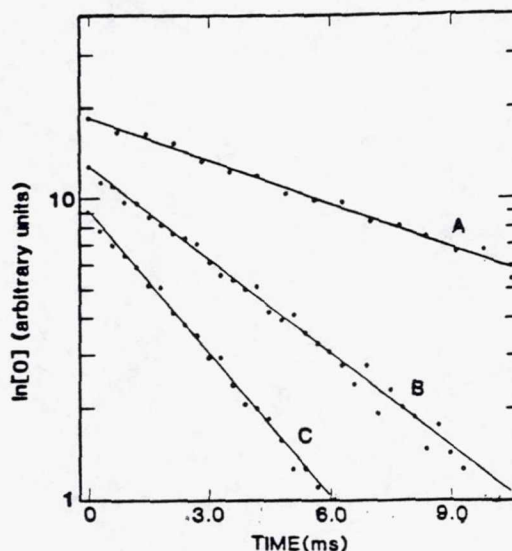


FIG. 3. Typical O atom temporal profiles. These experiments were carried out under the following conditions (all concentrations expressed in molecules cm^{-3}): 25 Torr total pressure; $T = 298$ K; $[Cl_2] = 9.8 \times 10^{15}$; $[O_3]_0 = 1.73 \times 10^{13}$ (A), 5.15×10^{13} (B), 8.76×10^{13} (C); and $[Cl]_0 = 1.10 \times 10^{14}$ (A); 1.66×10^{14} (B); 2.29×10^{14} (C).

sumption that no loss of ClO occurred during the delay between photolysis laser pulses. The ratio $[O(^3P)]/[ClO]$ immediately following the 266 nm laser pulse was determined for each experiment, and was typically in the range 0.01–0.04. Hence, it was appropriate to correct each measured decay rate for slight deviations from pseudo-first-order conditions. These corrections were derived from computer simulations of reactions (1), (5), and (6) under the range of experimental conditions employed. Best fit values for each decay rate (k') were obtained from linear regression analyses of the experimental data over at least $2 1/e$ times. Each value of k' was then increased by 2% or less using the appropriate non-pseudo-first-order correction. Representative plots of $[ClO]$ vs k' are shown in Fig. 4. These data were subjected to linear least squares analyses to give values for k_1 . The results are presented in Table I. Note the separate columns for k_1 (uncorrected) and k_1 (corrected). The former represents the best fit to the data when k' was not corrected for non-pseudo-first-order behavior and $[ClO]$ was set equal to $[O_3]_0$ less the amount photolyzed to produce $[O(^3P)]$. The latter k_1 values include the small non-pseudo-first-order correction to k' and additional corrections to $[ClO]$ discussed below.

The absorption cross section used to calculate the amount of ClO photolyzed by the Nd:YAG laser was estimated experimentally. The signal level immediately after the Nd:YAG laser fired was directly proportional to the concentration of oxygen atoms. If the Nd:YAG laser was not preceded by a pulse from the excimer laser, then the photolyte was O_3 . If all the O_3 had been converted to ClO via reaction with Cl atoms created in the 351 nm excimer pulse, then the signal was due to ClO photolysis. Therefore, in back-to-back experiments with constant $[Cl_2]$, $[O_3]$ and 266 nm fluence, the ratio of $O(^3P)$ signal with and without 351 nm photolysis should be identical to the ratio of the ClO and O_3 absorption

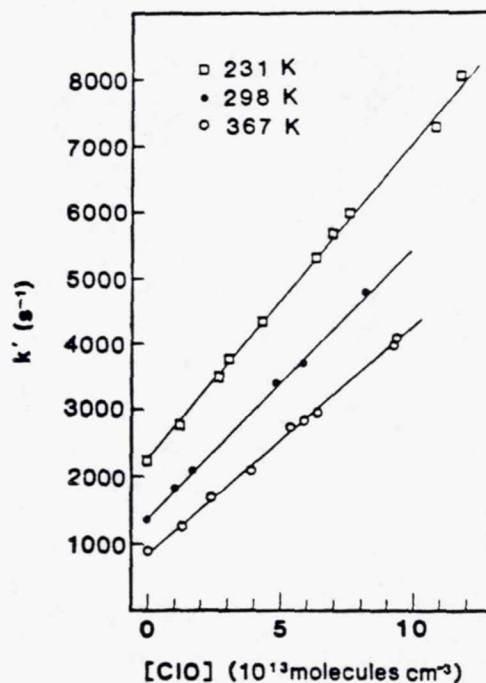


FIG. 4. A k' vs $[ClO]$ plot of typical data taken at 25 Torr total pressure of N_2 and at three temperatures. Note that the 298 and 231 K data have been displaced upward by 1000 and 2000 s^{-1} , respectively. Solid lines are obtained from linear least squares analyses and give the following rate coefficients (in units of $10^{-11} cm^3 molecule^{-1} s^{-1}$): 4.99 at 231 K, 4.07 at 298 K, 3.44 at 367 K.

TABLE I. Summary of k_1 determinations.^a

Temperature (K)	Pressure (Torr)	$k_1 \times 10^{11}$ (uncorrected) ^b (cm ³ molecule ⁻¹ s ⁻¹)	$k_1 \times 10^{11}$ (corrected) (cm ³ molecule ⁻¹ s ⁻¹)
231	25	4.64 ± 0.16	4.99 ± 0.17
238	25	4.25 ± 0.43	4.47 ± 0.43
252	200	3.10 ± 0.22	3.97 ± 0.30
255	25	4.15 ± 0.20	4.42 ± 0.20
255	200	3.25 ± 0.20	3.95 ± 0.32
257	25	3.86 ± 0.15	4.10 ± 0.11
257	25	4.30 ± 0.15	4.47 ± 0.19
275	25	3.94 ± 0.17	4.10 ± 0.16
298	25	3.55 ± 0.21	3.84 ± 0.14
298	25	3.47 ± 0.25	3.59 ± 0.25
298	25	3.51 ± 0.14	3.62 ± 0.13
298	25	3.87 ± 0.36	3.93 ± 0.36
298	25	3.89 ± 0.15	4.07 ± 0.17
298	50	3.91 ± 0.23	4.07 ± 0.24
298	50	3.62 ± 0.15	3.98 ± 0.18
298	50	3.70 ± 0.12	3.91 ± 0.11 ^c
298	50	3.53 ± 0.19	3.76 ± 0.14
298	50	3.76 ± 0.16	3.98 ± 0.14
298	100	3.73 ± 0.68	3.97 ± 0.67
298	200	3.39 ± 0.27	3.73 ± 0.24
298	200	3.39 ± 0.28	3.71 ± 0.32
298	200	3.55 ± 0.12	3.76 ± 0.13
298	500	3.18 ± 0.16	4.03 ± 0.20
338	25	3.16 ± 0.60	3.26 ± 0.12
359	200	2.99 ± 0.14	3.09 ± 0.15
360	25	2.89 ± 0.13	2.96 ± 0.12
367	25	3.35 ± 0.13	3.44 ± 0.13

^a Errors are 2σ and represent precision only.

^b Uncorrected values have not been adjusted for non-pseudo-first-order conditions and [ClO] loss by reaction (5). See the text for details.

^c Carried out with 283 nm photolysis of ClO, under "reversed" and "normal" flow conditions.

cross sections at the Nd:YAG laser wavelength [the O(¹D) product of O₃ photolysis is rapidly quenched to O(³P) by N₂]. This experiment resulted in a value of 0.35 for the signal ratio. If $\sigma_{266}(\text{O}_3)$ is taken to be 9.0×10^{-18} cm² (Ref. 13) then $\sigma_{266}(\text{ClO})$ is $\sim 3.1 \times 10^{-18}$ cm². This is somewhat lower than the low resolution cross section at this wavelength that is reported in the literature.¹⁵ However, we carried out the identical signal level comparison near 283 nm, a wavelength where the high resolution cross section has been characterized.¹⁶ Using a frequency doubled, Nd:YAG pumped tunable dye laser the rotational structure in the ClO spectrum was reproduced by observing the resonance fluorescence signal as the wavelength was scanned. At 282.95 nm, the peaks of the R(19.5) and P(16.5) lines of the $A^2\Pi_{3/2} - X^2\Pi_{3/2}$ 9-0 band, we observed a factor of 1.65 ± 0.20 more fluorescence signal when the excimer laser photolyzed Cl₂ than when the excimer laser beam was blocked. Based on the dye laser linewidth employed and the literature values for the ozone and ClO cross sections, we expected a ratio of 1.80 ± 0.40 . This result confirms our value for $\sigma_{266}(\text{ClO})$.

As mentioned above, the delay between the two laser pulses t_d , was adjusted to be long enough for reaction (2) to go to completion. The value of the Cl + O₃ rate constant is reasonably well known¹³ so an appropriate delay time could be calculated. As a check the delay time was varied until a constant signal and decay rate were observed, indicating that

all the O₃ had been converted to ClO. The majority of experiments were carried out with delay periods of either 3.4 or 6.4 ms.

The temporal behavior of ClO could be monitored by following both the O(³P) signal level produced by 266 nm photolysis and the measured value of k' . For some conditions (lower temperature, higher pressures) it was observed that ClO was decreasing on the time scale of the delay between the two lasers. The disappearance of ClO is probably due to self-reaction, a process that has not been completely characterized.¹⁷ In order to make a correction for the amount of ClO lost during the delay between laser pulses and also during the O atom decay, a series of experiments were carried out in which the delay time was varied at fixed [O₃], [Cl₂], and laser fluences.

For the process



the time dependence of [ClO] is described by the relationship

$$2k_7 t = [\text{ClO}]_t^{-1} - [\text{ClO}]_0^{-1} \quad (IV)$$

If we define k_7 to be the second-order rate coefficient for ClO removal under our experimental conditions, then plotting $[\text{ClO}]_t^{-1}$ vs t should yield a straight line of slope $2k_7$ and intercept equivalent to $[\text{ClO}]_0^{-1}$. The absolute concen-

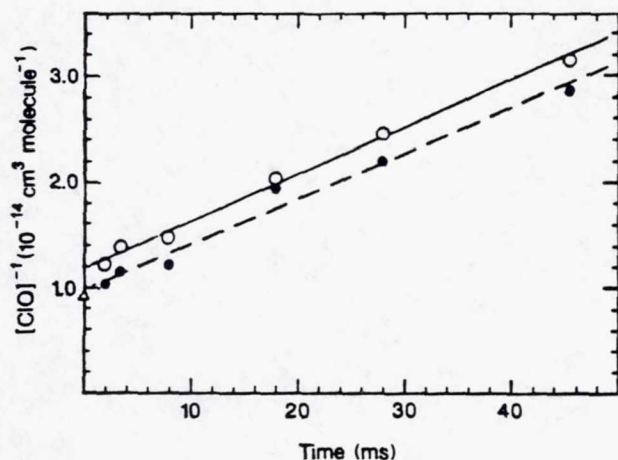
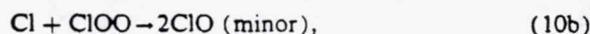
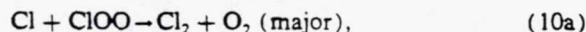
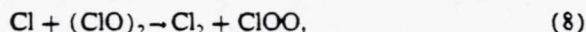
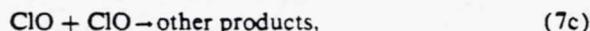
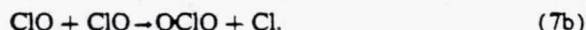
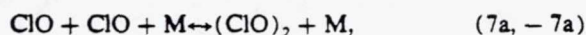


FIG. 5. A plot of $[\text{ClO}]^{-1}$ vs delay time. The open circles are based on ClO concentrations calculated from the O atom decay at each delay and the closed circles are based upon the fluorescence signal immediately following the 266 nm laser pulse. The triangular point on the abscissa represents $[\text{O}_3]_0^{-1}$. Experimental conditions: $T = 252 \text{ K}$; $P = 200 \text{ Torr}$.

tration of ClO needed to determine k_7 was deduced in two manners. In the first method, Eq. (I) was rearranged to calculate $[\text{ClO}]$. Here k_1 was taken from fixed delay experiments at the same experimental temperature and pressure. k_7 was determined from Eq. (IV). Then the values for $[\text{ClO}]$ in the fixed delay experiments were adjusted to account for the loss of ClO during the delay. This procedure was iterated until constant values of k_1 and k_7 were obtained. The second method involved relating the signal level immediately following the 266 nm laser pulse to the value of $[\text{ClO}]$. The signal calibration could be arrived at by two procedures. When enough data was available under the same experimental conditions, a $[\text{ClO}]$ vs signal calibration curve was constructed. Otherwise, signal vs delay time was plotted and extrapolated to time zero and that signal level normalized to $[\text{O}_3]_0$. This normalization factor was then used to put

the signal level at each delay time on an absolute concentration scale. Because of the reciprocal relation in Eq. (IV), the value of k_7 is quite sensitive to the scaling factor used in setting the value of $[\text{ClO}]$. Also the signal level is quite dependent on the operating conditions of the resonance lamp. Therefore, the values of k_7 determined from the first method are more precise. However, when using k' as a measure of $[\text{ClO}]$, we assume that O atoms are removed only by reaction with ClO and Cl_2 ; this assumption appears to be justified. A typical plot of $[\text{ClO}]^{-1}$ vs t appears in Fig. 5. The end results of a number of such experiments appear in Table II. These results are presented only as a measure of the phenomenological loss rate of ClO in our system, not as a definitive measurement of k_7 .

Hayman *et al.*¹⁷ report 298 K values for k_7 which are substantially faster than the values for k_7 (298 K, P) we have determined. However, our 255 K results appear to agree reasonably well with Hayman *et al.*'s low temperature values for k_7 . According to Hayman *et al.*,¹⁷ reaction (7) has an important branch to form a weakly bound dimer which can either decompose or react rapidly with chlorine atoms. The relevant reaction scheme is given below:



Hayman *et al.*¹⁷ obtained their kinetic data from a molecular modulation study. They observed much smaller apparent values for k_7 during the lights-off cycle (no chlorine atoms present) than during the lights-on cycle (large concentration of chlorine atoms present). Hence, a plausible explanation for the difference between our k_7 (298 K) determinations and the k_7 (298 K) values reported by Hayman *et al.*¹⁷

TABLE II. Summary of k_7 determinations.

$T(\text{K})$	$P(\text{Torr})$	$10^{-14}[\text{Cl}]_0^a$	$10^{-13}[\text{O}_3]^a$	No. of experiments	Range of t_d (ms)	$10^{13}k_7^{b,c}$
252	200	4.0–4.8	10.4	6	1.5–45	2.27 ± 0.18
255	25	4.0–5.1	9.8	6	3.0–45	0.47 ± 0.19
255	200	3.4–4.7	12.2	8	3.0–50	2.47 ± 0.18
298	16	1.7–2.5	7.3	7	1.5–60	0.17 ± 0.12
298	50	4.3–7.8	13.0	6	5.0–60	0.40 ± 0.09
298	50	2.2–5.2	8.3	8	1.5–60	0.36 ± 0.09
298	200	1.9–4.6	9.7	12	1.5–60	1.12 ± 0.11
298	200	2.6–3.9	6.15	6	1.5–60	0.92 ± 0.18
298	500	3.2–3.4	11.8	6	2.0–45	1.63 ± 0.17
298	500	3.7–4.0	5.9	5	1.5–35	2.94 ± 0.63
359	200	2.0–2.5	9.3	5	3.0–45	0.38 ± 0.15

^a Units are molecules per cm^3 .

^b Units are $\text{cm}^3 \text{ molecule}^{-1} \text{ s}^{-1}$.

^c Errors are 2σ , precision only.

TABLE III. Correction factors for loss of ClO via reaction (7) as a function of temperature, pressure, [O₃]₀ and [Cl]₀/[O₃]₀.

[O ₃] ₀	[Cl] ₀ /[O ₃] ₀ ^a	255 K		298 K			363 K	
		25 Torr	200 Torr	25 Torr ^b	200 Torr	500 Torr	25 Torr	200 Torr
2.0 × 10 ¹³	10	0.993	0.970	0.996	0.986	0.970	0.997	0.994
2.0 × 10 ¹³	5	0.961	0.943	0.976	0.968	0.956	0.987	0.984
6.0 × 10 ¹³	6	0.983	0.918	0.990	0.962	0.919	0.992	0.985
6.0 × 10 ¹³	2	0.930	0.887	0.952	0.933	0.901	0.969	0.964
1.2 × 10 ¹⁴	5	0.965	0.845	0.979	0.926	0.849	0.984	0.970
1.2 × 10 ¹⁴	2	0.964	0.864	0.979	0.934	0.877	0.985	0.973

^a Typical range of values for [Cl]₀/[O₃]₀ employed in *k*₇ determinations.

^b *k*₇ determined by interpolation to be 3 × 10⁻¹⁴ cm³ molecule⁻¹ s⁻¹.

is that *k*_{-7a} (298 K) was substantially faster than *k*₈ [Cl] under our experimental conditions, thus facilitating ClO regeneration by dimer decomposition; this is, of course, a favorable situation for measurement of *k*₇ but would result in systematic underestimation of *k*₇. No clear variation of *k*₇ with [Cl] is evident in our data, although our experiments spanned a rather narrow range of chlorine atom concentrations (Table II).

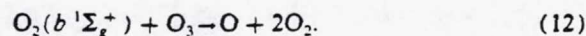
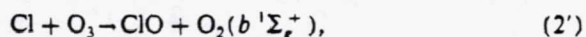
In order to make appropriate corrections for the loss of ClO during the delay between laser pulses, a reaction system consisting of reactions (2) and (7) was modeled under a variety of initial conditions using literature values for *k*₂(*T*)¹³ and setting *k*₇ = *k*₇. From these calculations a set of correction factors (*F*) could be derived:

$$F_{t_d} = [\text{ClO}]_{t_d}/[\text{O}_3]_0 \quad (\text{V})$$

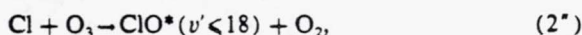
Values of *F*_{*t*_d} at *t*_d = 3.4 ms are given in Table III as a function of temperature, pressure, [O₃]₀, and [Cl]₀/[O₃]₀. Note that the maximum correction is made for the highest value of [ClO] for a given experiment; also, the longer the delay used in an experiment the larger the correction applied. For a few experimental conditions where *k*₇ was great enough (i.e., high pressure, low temperature) a correction was made to the observed *k*' for loss of ClO during the decay itself; this correction never exceeded 1.4%.

As a further check on the consistency of our experiments, the rate coefficient for reaction (1) was determined at 298 K in 50 Torr N₂ using 283 nm photolysis of ClO rather than 266 nm photolysis. The additional photolysis wavelength was provided by the frequency doubled, Nd:YAG pumped tunable dye laser. Also, to ensure that neither O₃ nor Cl₂ were being lost in the flow system, a measurement of *k*₁ (298 K) was carried out with the two absorption cells plumbed downstream from the reaction cell rather than in the "normal" upstream position. Neither of these variations in experimental parameters affected the observed kinetics.

As mentioned above, a significant O atom signal was generated subsequent to the excimer laser pulse (Fig. 2). Leu⁴ and Vanderzanden and Birks¹⁸ have observed O atoms from the reaction of chlorine atoms with ozone. The following chemistry was proposed to explain their observations:



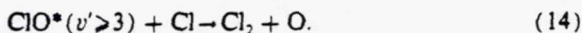
Subsequently, Choo and Leu¹⁹ monitored O₂(*b*¹Σ_g⁺) directly by observing its near infrared emission and put an upper limit of ~0.05% on the O₂(*b*¹Σ_g⁺) yield from reaction (2). Such a yield is much too small to account for the observed levels of O(³P) produced in the Cl + O₃ studies.^{4,18} Choo and Leu have suggested that the O atoms may be generated by reactions of vibrationally excited ClO formed in reaction (2), i.e.,



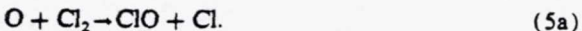
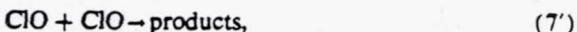
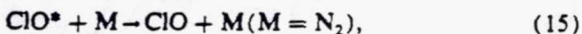
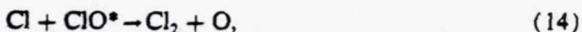
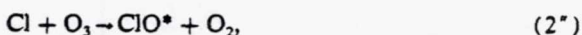
followed by



or



In our system Cl atoms are in excess over O₃ and, therefore, in excess over the ClO created in reaction (2). Also, the occurrence of reaction (14) results in loss of two ClO molecules which otherwise would have been present at *t*_d while the occurrence of reaction (13) results in loss of only one ClO molecule. Hence, reaction (14) would potentially have the larger effect on the ClO concentration in our experiments. To examine the potential role of reaction (14) in consuming ClO, we simulated the system chemistry using a Gear routine to solve the rate equations numerically. The following scheme was modeled:



Although reactions (2'') and (14) may have other channels, this scheme was devised to have the greatest impact on the [ClO] at the end of the reaction period; therefore, only the branches that deplete ClO were used. It should be noted that a large dependence of the extraneous O(³P) signal on the total pressure in the system was observed. This observation would be consistent with quenching of either ClO* or O₂(*b*¹Σ_g⁺) by N₂. *k*₁ and *k*₅ are known, and the other rate coefficients were adjusted to reproduce the magnitude and

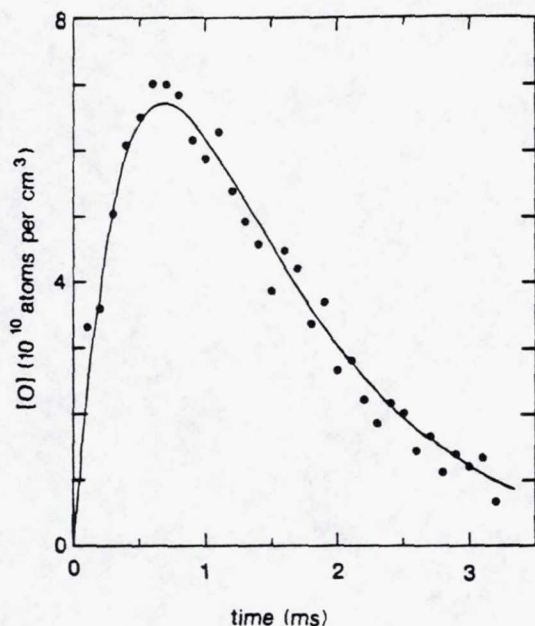


FIG. 6. Comparison of oxygen atom temporal profile immediately following 351 nm laser pulse to computer simulation of reaction scheme discussed in the text. Experimental conditions are as follows: $T = 298$ K; $[O_3]_0 = 1.65 \times 10^{13}$ molecules cm^{-3} ; $[Cl_2] = 1.42 \times 10^{16}$ molecules cm^{-3} ; $[Cl]_0 = 1.81 \times 10^{14}$ molecules cm^{-3} ; pressure = 25 Torr. The reaction rate coefficients used in the simulation are: $k_1 = 3.66 \times 10^{-11}$; $k_2 = 1.18 \times 10^{-11}$; $k_3 = 2.91 \times 10^{-14}$; $k_7 = 3.0 \times 10^{-14}$; $k_{13} = 2.0 \times 10^{-11}$; $k_{14} = 5.8 \times 10^{-13}$. All rate coefficients are in units of cm^3 molecule $^{-1}$ s $^{-1}$.

temporal behavior of the O atom signal observed. Typical results are shown in Fig. 6. It was found that the above reaction scheme lead to no more than a 2% perturbation in the concentration of ClO. Of course there is no direct proof that the assumed reaction scheme is correct. However, it is the worst case of the suggested possibilities and any corrections would be quite small. Since the mechanism for O atom formation following the excimer laser pulse is not well understood, the effect of this chemistry on the ClO concentration was not taken into account in the determination of "corrected" values for k_1 (Table I).

The combination of Cl_2 photolysis, $Cl + O_3$ reaction, and ClO photolysis could result in some heating of the gas in the reaction zone. Calculations which assume worst case conditions, i.e., $P = 25$ Torr N_2 , $[Cl]_0 = 6 \times 10^{14}$ molecules per cm^3 , $[O_3]_0 = 1 \times 10^{14}$ molecules per cm^3 , $[O]_0 = 2 \times 10^{12}$ atoms per cm^3 , and all excess energy dissipated as heat show that laser heating of the reaction zone could not have exceeded 2 K in any experiment. This potential systematic error is negligibly small so it was not incorporated into the data analysis.

As discussed above, several corrections were made to either the observed k' values or in the calculation of $[ClO]$ from $[O_3]_0$. For clarity this set of corrections is reiterated:

(a) A quantitative correction was made in k' for non-pseudo-first-order conditions during the O atom decay. In only a few cases did this exceed a 1% adjustment.

(b) $[ClO]$ was corrected for the amount of ClO lost to photolysis at 266 nm. This correction was dependent upon knowledge of the laser fluence, which was monitored in every experiment using a calibrated radiometer, and on our estimated value of $\sigma_{266}(ClO)$. Because there was only a small adjustment to $[ClO]$ (on the average 3%) the final results were not very sensitive to this correction. For example, in an experiment where the fraction of ClO photolyzed was above the average, an increase in $\sigma_{266}(ClO)$ of a factor of 2 was found to change the final value of k_1 by only 4%.

(c) Using the loss rate of ClO determined in the same system, a correction was made to $[ClO]$ for the ClO that undergoes self-reaction (or other loss processes) during the delay time between laser firings. The largest corrections were made at higher pressures, lower temperatures, and in long delay experiments. Because the simulation of the production and loss of ClO was sensitive to the errors in our measurements of k_7 , this correction has a rather large uncertainty.

(d) A few decays were corrected for ClO loss during the decay itself; however, this correction was insignificant under most experimental conditions.

(e) It was concluded that of the known possibilities for the source of O atoms prior to ClO photolysis, none could have had more than a 2% effect on $[ClO]_0$; no corrections were made for this chemistry.

Even though there were several corrections made in order to reach a final value for k_1 at each temperature and pressure, the magnitudes of the corrections were small in most cases (see Table I), the corrections could be quantitatively applied, and in general, the results are self-consistent. An Arrhenius plot of our data appears in Fig. 7. An unweighted least squares analysis of all data yields the expression

$$k_1(T) = (1.68 \pm 0.31) \times 10^{-11} \exp\{(241 \pm 53)/T\} \text{ cm}^3 \text{ molecule}^{-1} \text{ s}^{-1}, \quad (\text{VI})$$

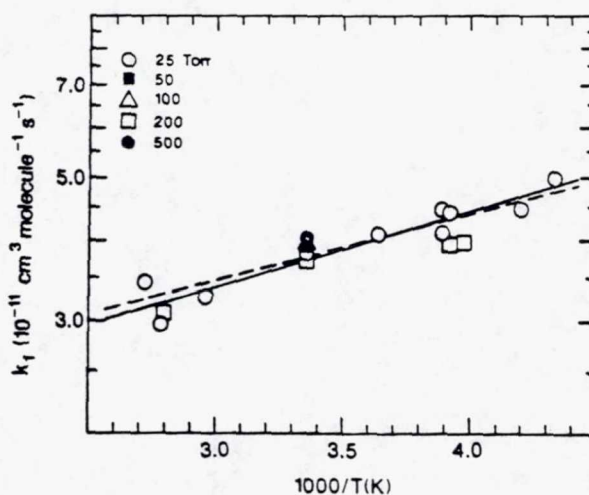


FIG. 7. Arrhenius plot of our results for $k_1(T,P)$. The dashed line represents an unweighted least squares analysis of the 25 Torr data only while the solid line includes all data.

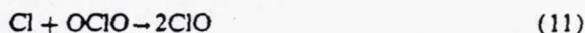
where the errors represent 2σ , precision only, and $\sigma_A \equiv A\sigma_{\ln A}$. For the 25 Torr data only, the expression

$$k_1(T) = (1.55 \pm 0.33) \times 10^{-11} \exp\{(263 \pm 60)/T\} \text{ cm}^3 \text{ molecule}^{-1} \text{ s}^{-1} \quad (\text{VII})$$

is obtained from an unweighted least squares analysis. The difference between the Arrhenius expression obtained from the 25 Torr data and that obtained from the complete data set is primarily due to the slightly lower rate coefficients obtained at high pressure (200 Torr) and low temperature (252–255 K). These rate coefficients required rather large corrections for contributions from reaction (7) and, therefore, are more likely to be in error than rate coefficients obtained at higher temperatures and/or lower pressures. For this reason, we believe the Arrhenius expression obtained from the 25 Torr data only should be preferred. The absolute accuracy of k_1 at any temperature within the range studied is estimated to be $\pm 20\%$.

DISCUSSION

In all prior investigations, reaction (1) was studied by flow tube techniques at pressures less than 10 Torr. The results of all studies are summarized in Table IV. In the earliest study Bemand *et al.*,¹ measured k_1 (298 K) using resonance fluorescence to monitor O(³P) in excess ClO. The ClO was produced by the reaction



assuming a stoichiometric factor of 2. These workers reported k_1 (298 K) = $(5.3 \pm 0.8) \times 10^{-11} \text{ cm}^3 \text{ molecule}^{-1} \text{ s}^{-1}$. They also measured the rate coefficient by following the decay of ClO mass spectrometrically in excess oxygen atoms and obtained the result $(5.7 \pm 2.3) \times 10^{-11} \text{ cm}^3 \text{ molecule}^{-1} \text{ s}^{-1}$. In a subsequent study in the same laboratory Clyne and Nip² measured the temperature dependence of k_1 . Again, O(³P) was monitored by resonance fluorescence in

excess ClO, the latter species being generated via reaction (2). The room temperature rate coefficient was in good agreement with their previous study. They report a significant activation energy and quote the Arrhenius expression $k_1(T) = (1.07 \pm 0.30) \times 10^{-10} \exp\{-(224 \pm 76)/T\} \text{ cm}^3 \text{ molecule}^{-1} \text{ s}^{-1}$.

Zahniser and Kaufman³ measured the temperature dependence of the ratio k_1/k_2 . Using a value of k_2 measured directly in the same system these workers report $k_1(T) = (3.38 \pm 0.50) \times 10^{-11} \exp\{(75 \pm 40)/T\} \text{ cm}^3 \text{ molecule}^{-1} \text{ s}^{-1}$.

The next reported investigation of $k_1(T)$ was performed by Leu⁴ using resonance fluorescence detection of O(³P) in excess ClO. ClO radicals were produced using three different source reactions in order to validate stoichiometric assumptions necessary to arrive at ClO concentration levels. Reactions (2), (11), and



were the three sources used at room temperature. Reaction (2) was used at all other temperatures. Leu's value for k_1 (298 K) is lower than the previously reported values and he measured a small positive activation energy with $k_1(T) = (5.0 \pm 1.0) \times 10^{-11} \exp\{-(96 \pm 20)/T\} \text{ cm}^3 \text{ molecule}^{-1} \text{ s}^{-1}$. The use of reaction (2) as the only ClO source in all experiments at $T \neq 298 \text{ K}$ could result in a systematic error in Leu's reported temperature dependence. At the low pressures employed in Leu's study, the ClO* + Cl reaction may have competed favorably with ClO* deactivation, thus leading to overestimation of [ClO]. Since the ratio of k_{14}/k_{15} may be temperature dependent, such an effect could have been more important at one end of the investigated temperature range than at the other end. It should be emphasized that while the abovementioned systematic error in Leu's [ClO] determination is possible, there currently exists insufficient information concerning ClO* chemistry to prove or disprove this conjecture.

TABLE IV. Comparison of measurements of k_1 .

Investigators	Reference	Experimental method ^{a,b}	Temperature range (K)	Pressure range (Torr)	k_1 ($10^{-11} \text{ cm}^3 \text{ molecule}^{-1} \text{ s}^{-1}$) ^c		
					210 K	250 K	298 K
Bemand, Clyne, and Watson	1	DF-RF(O)	298	~1.0	5.3 ± 0.8
	1	DF-MS(ClO)	298	0.75	5.7 ± 2.3
Clyne and Nip	2	DF-RF(O)	220–426	0.90	3.68	4.37	5.05
Zahniser and Kaufman	3	DF-RF(Cl) ^d	220–298	2.0–4.0	4.83	4.56	4.35
Leu	4	DF-RF(O)	236–422	1.0–3.5	3.17	3.41	3.62
Schwab, Toohey, Brune, and Anderson	5	DF-LMR(ClO)	252–347	0.8–2.0	3.50	3.50	3.50
		DF-RF(O)					
Ongstad and Birks	6	DF-CL(O) ^e	220–387	2.3	4.14	3.85	3.61
Margitan	7	DF-LFP-RF(O)	241–298	10	4.20	4.20	4.20
Nicovich, Wine, and Ravishankara	This work	LFP-RF(O)	231–367	25–500	5.29	4.41	3.77
				25	5.42	4.44	3.75

^aDF—discharge flow; RF—resonance fluorescence; MS—mass spectrometry; LMR—laser magnetic resonance; CL—chemiluminescence; LFP—laser flash photolysis.

^bThe monitored species is given in parentheses.

^cCalculated from reported Arrhenius expressions.

^d $k(\text{O} + \text{ClO})$ measured relative to $k(\text{Cl} + \text{O}_2)$.

^eNO added to produce chemiluminescence via $\text{O} + \text{NO} + \text{M} \rightarrow \text{NO}_2^* \rightarrow h\nu + \text{NO}_2$.

Schwab *et al.*⁵ employed an experimental apparatus in which both reactants [ClO by laser magnetic resonance and O(³P) by resonance fluorescence] and one product (Cl atoms by resonance fluorescence) could be monitored. [Interestingly, this is the only O + ClO study where ClO was directly measured in the reaction zone.] Again, a somewhat lower value was measured [$k_1(298 \text{ K}) = (3.5 \pm 0.5) \times 10^{-11} \text{ cm}^3 \text{ molecule}^{-1} \text{ s}^{-1}$] and these workers observed essentially no temperature dependence for k_1 .

Ongstad and Birks⁶ measured $k_1(T)$ in a discharge flow system using the same three sources of ClO as Leu.⁴ O(³P) was followed via the chemiluminescence from NO₂ generated by reacting the oxygen atoms with NO added to the detection region of their flow tube. These workers measured $k_1(T)$ directly and also relative to the reaction



In a successive measurement scheme $k_{17}(T)$ was also measured. The relative measurements yielded somewhat higher values, presumably due to nonpure source gases (Cl₂O, ClO₂, O₃) or other channels for the source reactions. Ongstad and Birks measured a value for $k_1(298 \text{ K})$ that agrees with the other more recent studies and a small "negative activation energy." They reported the expression $k_1(T) = (2.61 \pm 0.60) \times 10^{-11} \exp\{(97 \pm 64)/T\} \text{ cm}^3 \text{ molecule}^{-1} \text{ s}^{-1}$.

The only other study of k_1 at or near room temperature reported in the literature was by Margitan.⁷ ClO radicals were generated in a flow tube via reaction (16). Downstream from this source O(³P) was created by laser photolysis of the ClO and followed by resonance fluorescence. The ClO concentration was measured directly in the flow by absorption. However, large corrections (up to 20%) had to be made for ClO loss between the ClO detection region and the O(³P) detection region. Margitan used literature values for k_7 to make these corrections. Given the recent advances in our understanding of reaction (7),¹⁷ a large uncertainty must be associated with the magnitude of Margitan's correction for ClO loss via the self-reaction. His results are also very dependent on the value chosen for the ClO absorption cross section. Margitan reports that E/R lies within the range $\pm 200 \text{ K}$ and $k_1(298 \text{ K}) = (4.2 \pm 0.8) \times 10^{-11} \text{ cm}^3 \text{ molecule}^{-1} \text{ s}^{-1}$.

As seen by the comparison in Table IV, there is very little difference between the value of $k_1(298 \text{ K})$ from our experiments and from any of the other recent studies. However, at the lower temperatures typical of the middle stratosphere our results indicate significantly faster values for $k_1(T)$ than any of the other recent investigations (see Table

IV). Hence, model calculations which employ our expression for $k_1(T)$ would predict somewhat larger ozone depletion due to chlorofluorocarbon injection than calculations which take $k_1(T)$ from previously available data.

SUMMARY

We have measured k_1 as a function of temperature and pressure. Our results indicate a lack of any pressure dependence at 298 K over the range 25 to 500 Torr. Although our 298 K rate coefficient agrees well with previous studies, our observation of an activation energy that is more negative than any previously reported leads to a significant difference between our result and other recent measurements at temperatures relevant to stratospheric chemistry.

ACKNOWLEDGMENTS

We thank M. McQuaid for carrying out some of the computer simulations. This work was supported by the fluorocarbon program panel of the Chemical Manufacturer's Association (Contract No. FC-84-499) and by the National Aeronautics and Space Administration (Grant No. NAGW-1001).

- ¹P. P. Bemand, M. A. A. Clyne, and R. T. Watson, *J. Chem. Soc. Faraday Trans. 1* **69**, 1356 (1973).
- ²M. A. A. Clyne and W. S. Nip, *J. Chem. Soc. Faraday Trans. 1* **72**, 2211 (1976).
- ³M. S. Zahniser and F. Kaufman, *J. Chem. Phys.* **66**, 3673 (1977).
- ⁴M. T. Leu, *J. Phys. Chem.* **88**, 1394 (1984).
- ⁵J. J. Schwab, D. W. Toobey, W. H. Brune, and J. G. Anderson, *J. Geophys. Res.* **89**, 9581 (1984).
- ⁶(a) A. P. Ongstad and J. W. Birks, *J. Chem. Phys.* **81**, 3922 (1984); (b) **85**, 3359 (1986).
- ⁷J. J. Margitan, *J. Phys. Chem.* **88**, 3639 (1984).
- ⁸C. Park, *J. Phys. Chem.* **80**, 565 (1976).
- ⁹R. L. Jaffee, *Chem. Phys.* **40**, 185 (1979).
- ¹⁰J. L. Gole, *J. Phys. Chem.* **84**, 1333 (1980).
- ¹¹A. R. Ravishankara, P. H. Wine, and J. M. Nicovich, *J. Chem. Phys.* **78**, 6629 (1983).
- ¹²J. M. Nicovich and P. H. Wine, *J. Phys. Chem.* **91**, 5118 (1987).
- ¹³W. B. Demore, M. J. Molina, S. P. Sander, D. M. Golden, R. F. Hampson, M. J. Kurylo, C. J. Howard, and A. R. Ravishankara, *JPL Publication* 87-41, 1987.
- ¹⁴(a) A. G. Hearn, *Proc. Phys. Soc.* **78**, 932 (1961). (b) L. T. Molina and M. J. Molina, *J. Geophys. Res.* **91**, 14501 (1986). (c) K. Mauersberger, J. Barnes, D. Hanson, and J. Morton, *Geophys. Res. Lett.* **13**, 671 (1986).
- ¹⁵M. Mandelman and R. W. Nicholls, *J. Quant. Spectrosc. Radiat. Transfer* **17**, 483 (1977).
- ¹⁶P. H. Wine, A. R. Ravishankara, D. L. Philen, D. D. Davis, and R. T. Watson, *Chem. Phys. Lett.* **50**, 101 (1977).
- ¹⁷G. D. Hayman, J. M. Davies, and R. A. Cox, *Geophys. Res. Lett.* **13**, 1347 (1986).
- ¹⁸J. W. Vanderzanden and J. W. Birks, *Chem. Phys. Lett.* **88**, 109 (1982).
- ¹⁹K. Y. Choo and M. T. Leu, *J. Phys. Chem.* **89**, 4832 (1985).

NDB

519-25

026137

273562

5P.

Reprinted from The Journal of Physical Chemistry, 1988, 92, 2223.
 Copyright © 1988 by the American Chemical Society and reprinted by permission of the copyright owner.

Kinetics of the Reactions of F(²P) and Cl(²P) with HNO₃

P. H. Wine,* J. R. Wells,[†] and J. M. Nicovich

Molecular Sciences Branch, Georgia Tech Research Institute, Georgia Institute of Technology, Atlanta, Georgia 30332 (Received: August 10, 1987; In Final Form: November 19, 1987)

The kinetics of the reactions of HNO₃ with fluorine (*k*₁) and chlorine (*k*₂) atoms have been studied by using a time-resolved long-path laser absorption technique to monitor the appearance of product NO₃ radicals following 351-nm pulsed laser photolysis of X₂/HNO₃/He mixtures (X = F, Cl). Absolute rate coefficients for the F(²P) + HNO₃ reaction have been determined over the temperature range 260–373 K. Between 260 and 320 K, the data are adequately represented by the Arrhenius expression $k_1(T) = (6.0 \pm 2.6) \times 10^{-12} \exp[(400 \pm 120)/T] \text{ cm}^3 \text{ molecule}^{-1} \text{ s}^{-1}$. Between 335 and 373 K, the rate coefficient is found to be $(2.0 \pm 0.3) \times 10^{-11} \text{ cm}^3 \text{ molecule}^{-1} \text{ s}^{-1}$ independent of temperature. The observed temperature dependence suggests that reaction proceeds via competing direct abstraction and complex pathways. No NO₃ production was observed in the experiments with X = Cl, thus establishing that $k_2(298\text{K}) < 2 \times 10^{-16} \text{ cm}^3 \text{ molecule}^{-1} \text{ s}^{-1}$. The Cl(²P) + HNO₃ reaction was also investigated by using a pulsed laser photolysis–resonance fluorescence technique to monitor the decay of Cl(²P). Upper limit values for *k*₂ obtained from these experiments, in units of 10⁻¹⁶ cm³ molecule⁻¹ s⁻¹, are 13 at 298 K and 10 at 400 K.

Introduction

The nitrate radical (NO₃) is a key reactive intermediate in the atmosphere. Motivated primarily by the need to quantitatively understand its role in atmospheric chemistry, numerous studies of NO₃ kinetics, photochemistry, and spectroscopy have been reported in the literature. A number of these studies employed the reaction



as the nitrate radical source.^{1–12} Despite its widespread use as an NO₃ source in both fast flow^{1–9} and flash photolysis^{10–12} studies, the first room temperature measurement of *k*₁ has only recently been reported,⁹ and the temperature dependence of *k*₁ has not been investigated. In this paper we report a determination of the absolute rate coefficient for reaction 1 as a function of temperature over the range 260–373 K. We also report new results on the related reaction



There have been several previous studies of reaction 2, but reported

values for *k*₂(298K) span a range of more than 3 orders of magnitude.^{13–18}

- (1) Nelson, H. H.; Pasternack, L.; McDonald, J. R. *J. Phys. Chem.* **1983**, *87*, 1286.
- (2) Nelson, H. H.; Pasternack, L.; McDonald, J. R. *J. Chem. Phys.* **1983**, *79*, 4279.
- (3) Ravishankara, A. R.; Wine, P. H. *Chem. Phys. Lett.* **1983**, *101*, 73.
- (4) Smith, C. A.; Ravishankara, A. R.; Wine, P. H. *J. Phys. Chem.* **1985**, *89*, 1423.
- (5) Ravishankara, A. R.; Mauldin III, R. L. *J. Phys. Chem.* **1985**, *89*, 3144.
- (6) Ravishankara, A. R.; Mauldin III, R. L. *J. Geophys. Res.* **1986**, *91*, 8709.
- (7) Sander, S. P. *J. Phys. Chem.* **1986**, *90*, 4135.
- (8) Friedl, R. R.; Sander, S. P. *J. Phys. Chem.* **1987**, *91*, 2721.
- (9) Mellouki, A.; LeBras, G.; Poulet, G. *J. Phys. Chem.* **1987**, *91*, 5760.
- (10) Wallington, T. J.; Atkinson, R.; Winer, A. M.; Pitts, Jr., J. N. *J. Phys. Chem.* **1986**, *90*, 4640.
- (11) Wallington, T. J.; Atkinson, R.; Winer, A. M.; Pitts, Jr., J. N. *J. Phys. Chem.* **1986**, *90*, 5393.
- (12) Wallington, T. J.; Atkinson, R.; Winer, A. M.; Pitts, Jr., J. N. *Int. J. Chem. Kinet.* **1987**, *19*, 243.
- (13) Leu, M.-T.; DeMore, W. B. *Chem. Phys. Lett.* **1976**, *41*, 121.
- (14) Poulet, G.; LeBras, G.; Combournieu, J. *J. Chem. Phys.* **1978**, *69*, 767.
- (15) Clark, R. H.; Hussain, D.; Jezquel, J. Y. *J. Photochem.* **1982**, *18*, 39.
- (16) Kurylo, M. J.; Murphy, J. L.; Knable, G. L. *Chem. Phys. Lett.* **1983**, *94*, 281.

* Author to whom correspondence should be addressed.

[†] Present address: Department of Chemistry, Northwestern University, Evanston, IL 60201.

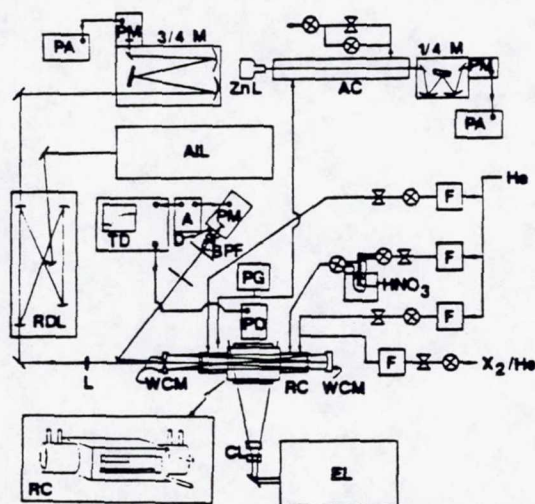


Figure 1. Schematic of the pulsed laser photolysis-long-path laser absorption apparatus: A, amplifier; AC, absorption cell; AIL, argon ion laser; BPF, band-pass filter; CL, cylindrical lenses; D, diffuser; EL, excimer laser; F, flowmeter; L, lens; PA, picoammeter; PD, photodiode; PG, pressure gauge; PM, photomultiplier; RC, reaction cell; RDL, ring dye laser; TD, transient digitizer; WCM, White cell mirror; ZnL, zinc hollow cathode lamp; 1/4 M, 1/4-m monochromator; 3/4 M, 3/4-m monochromator; \times , needle valve; \bullet , shut-off valve.

Experimental Section

The kinetics of reactions 1 and 2 were investigated by monitoring the temporal profile of the product NO_3 following 351-nm pulsed laser photolysis of X_2 ($\text{X} = \text{F}, \text{Cl}$). The pulsed laser photolysis-long-path laser absorption (PLP-LPLA) apparatus employed for these measurements was a modified version of one which we used previously to study NO_3 production from the reaction of hydroxyl radicals with nitric acid;¹⁹ the modified apparatus is described below. Reaction 2 was also investigated by monitoring the decay of $\text{Cl}(\text{P})$ by using time-resolved resonance fluorescence detection. The pulsed laser photolysis-resonance fluorescence apparatus was virtually identical with one we have employed previously to study the kinetics of several chlorine atom reactions;²⁰⁻²² details of its operation can be found elsewhere.²⁰⁻²²

A drawing of the reaction cell used in the PLP-LPLA experiments is shown in Figure 1. The main body of the cell was black anodized aluminum; its outside dimensions were 18 cm \times 10 cm \times 8 cm and its internal volume was 560 cm^3 . To minimize heterogeneous reactions, all internal surfaces were overcoated with halocarbon wax. The main body could be heated or cooled by flowing a suitable fluid through a series of channels in its top and bottom. PVDF [poly(vinylidene fluoride)] extensions were fitted to either end of the cell's main body. Gases were flowed in and out through these extensions. The total length of the cell, including extensions, was 33 cm, and the total internal volume was 920 cm^3 .

A schematic of the PLP-LPLA apparatus is shown in Figure 1. The excimer laser photolysis beam was expanded by using two cylindrical lenses to be 13 cm wide and 2.5 cm high as it traversed the reactor. A CW ring dye laser beam, tuned to the peak of the strong NO_3 absorption band at 662 nm, was multipassed through the reactor at right angles to the photolysis beam by using modified White cell optics;²³ 140 passes were typically employed, giving an absorption path length of 1820 cm. The dye laser line width

(0.2 Å) was narrow compared to the width of the totally diffuse²⁴ absorption band. Reflective losses were minimized in the multipass system by using dielectric coated White cell mirrors and antireflection (AR) coated reaction cell windows. The output beam from the multipass system was reflected through two apertures, a narrow band-pass filter, and a diffuser onto the photocathode of a red-sensitive photomultiplier. The time-dependent photomultiplier output was amplified and then monitored by a transient digitizer-signal averager with 8-bit voltage resolution. The results of 16-256 photolysis laser shots were averaged to obtain data with suitable signal-to-noise ratio for quantitative kinetic analysis. Digitized voltage versus time data were transferred to a small computer for storage and analysis. The time resolution of the detection system was limited by the transit time of the multipass beam and was $\sim 0.25 \mu\text{s}$. To minimize noise in the long-path absorption monitoring system, all components were mounted on a vibrationally isolated optical table.

In order to avoid accumulation of reaction or photolysis products, all experiments were carried out under "slow flow" conditions. The linear flow rate through the reaction cell was typically 2 cm s^{-1} , and the excimer laser repetition rate was 0.15 Hz. Hence, the gas mixture in the photolysis zone was replenished every 1-2 laser shots. The fraction of nitric acid in the reaction mixture was determined directly in the slow flow system by UV photometry at either 202.6 nm (Zn⁺ line) or 213.9 nm (Zn line). Absorption cross sections used to convert measured absorbances to HNO_3 concentrations were $4.16 \times 10^{-18} \text{ cm}^2$ at 202.6 nm and $4.70 \times 10^{-19} \text{ cm}^2$ at 213.9 nm; these cross sections were measured during the course of the investigation and are in good agreement with literature values.²⁵⁻²⁷ The reaction mixture flowed through the 150-cm absorption cell after exiting the reactor.

Because nitric acid vapor can damage the antireflection coating on the reactor windows, a four-port gas input/output system was employed (Figure 1). X_2 and 85-90% of the He buffer gas entered the reactor through an outer port while a dilute HNO_3/He mixture entered through the corresponding inner port. The remaining 10-15% of the He buffer gas entered the reactor through the opposite outer port, and the gas mixture exited the reactor through the corresponding inner port. UV absorption measurements ($\lambda = 185.0 \text{ nm}$, $\sigma = 1.63 \times 10^{-17} \text{ cm}^2$)²⁶ along the path traversed by the excimer laser beam, i.e., across the direction of flow, demonstrated that (1) the nitric acid concentration was uniform across the reaction zone and (2) the HNO_3 dilution factor between the reaction zone and the 150-cm absorption cell (typically a factor of 1.1) agreed with the dilution factor obtained from mass-flow measurements.

Measurement of the temperature in the reaction zone was achieved by replacing one of the AR coated probe beam entrance windows with a Plexiglass plate fitted with a cajon fitting through which a jacketed copper-constantan thermocouple could be inserted. Hence, the temperature could be measured under the precise pressure and flow conditions of the experiment. Preliminary tests at both low and high temperatures showed that the measured temperature was constant within $\pm 0.5^\circ\text{C}$ throughout the volume of intersection of the probe beam with the photolysis beam.

The gases used in this study had the following stated minimum purities: He, 99.999%; Cl_2 , 99.9%; F_2 , 98.0%. Helium and a 5% F_2 in He mixture were used without purification. Cl_2 was degassed repeatedly at 77 K; dilute Cl_2/He mixtures were then prepared manometrically in 12-L bulbs for use in experiments. Anhydrous HNO_3 was admitted to the reactor by diverting a small fraction of the main buffer gas flow through a needle valve, then through a bubbler containing a mixture of 1 part reagent grade HNO_3 (70% in H_2O) and 2 parts reagent grade H_2SO_4 , and then to the reactor. A temperature-controlled bath maintained the bubbler temperature at 250 K during storage and at $\sim 280 \text{ K}$ during

(17) Zagogianni, H.; Mellouki, A.; Poulet, G. C. R. Acad. Sci., Ser. 2 1987, 304, 573.

(18) Cantrell, C. A.; Davidson, J. A.; Sbetter, R. E.; Anderson, B. A.; Calvert, J. G. J. Phys. Chem. 1987, 91, 6017.

(19) Ravishankara, A. R.; Eisele, F. L.; Wine, P. H. J. Phys. Chem. 1982, 86, 1854.

(20) Ravishankara, A. R.; Wine, P. H. J. Chem. Phys. 1980, 72, 25.

(21) Wine, P. H.; Semmes, D. H.; Ravishankara, A. R. Chem. Phys. Lett. 1982, 90, 128.

(22) Wine, P. H.; Semmes, D. H. J. Phys. Chem. 1983, 87, 3572.

(23) White, J. U. J. Opt. Soc. Am. 1942, 32, 285.

(24) Marinelli, W. J.; Swanson, D. M.; Johnston, H. S. J. Chem. Phys. 1962, 76, 1984.

(25) Molina, L. T.; Molina, M. J. J. Photochem. 1981, 15, 97.

(26) Biau, F. J. Photochem. 1973, 2, 139.

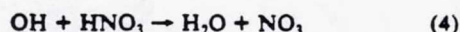
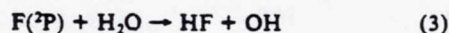
(27) Johnston, H. S.; Graham, R. J. Phys. Chem. 1973, 77, 62.

TABLE I: Kinetic Data for the F + HNO₃ Reaction

T, K	no. of expt ^a	concn. molecules/cm ³			range of <i>k'</i> , 10 ⁴ s ⁻¹	10 ¹¹ <i>k</i> ₁ , ^c cm ³ molecule ⁻¹ s ⁻¹
		F ₂ × 10 ¹⁶	NO ₃ (max) × 10 ^{12b}	HNO ₃ × 10 ¹⁵		
260	5	1.5–6.3	1.5–7.2	0.75–5.03	1.93–14.3	2.86 ± 0.17
273	6	3.2–3.8	2.0–2.6	0.98–13.1	2.43–32.0	2.45 ± 0.06
275	5	2.9	4.0–5.0	0.83–6.79	2.20–17.0	2.62 ± 0.34
296	4	2.8	2.7–3.0	1.12–6.60	2.64–15.3	2.30 ± 0.19
298	6	1.0–3.4	0.8–4.5	0.44–4.28	1.48–10.7	2.36 ± 0.10
320	4	2.6–2.8	2.3–3.2	1.21–10.4	2.97–22.3	2.08 ± 0.06
335	8	1.7–3.5	1.2–3.1	0.75–5.13	2.15–10.8	1.94 ± 0.22
350	7	2.5–2.7	1.8–2.3	0.69–11.6	1.60–24.1	2.00 ± 0.08
373	4	2.8–4.0	1.7–2.5	0.65–5.45	1.34–11.1	2.01 ± 0.07

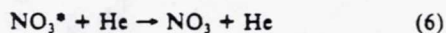
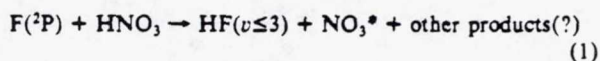
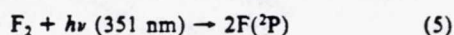
^a Experiment = determination of one pseudo-first-order NO₃ appearance rate. ^b Calculated based on an assumed absorption cross section of 1.8 × 10⁻¹⁷ cm², independent of temperature. ^c Errors are 2σ and refer to precision only.

experiments. The use of anhydrous HNO₃ eliminates the potential side reactions

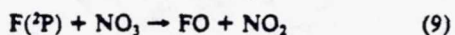


Results and Discussion

The F + HNO₃ Reaction. Reaction mixtures employed to study reaction 1 contained 0.3–1.7 Torr of F₂, 0.009–0.37 Torr of HNO₃, and 150 Torr of helium. The relevant reaction scheme¹⁵ is



In the above reaction scheme NO₃^{*} represents vibrationally excited NO₃; our detection method is not sensitive to NO₃^{*}. In a recent study²⁴ we showed that NO₃^{*} produced from 248-nm photolysis of N₂O₃ is deactivated by helium with an effective rate coefficient of 2.7 × 10⁻¹³ cm³ molecule⁻¹ s⁻¹. Hence, under our experimental conditions, reaction 6 proceeds with a pseudo-first-order rate coefficient (*k*₆' = *k*₆[He]) of 1.3 × 10⁶ s⁻¹. Measured pseudo-first-order NO₃ appearance rate coefficients (*k*_a) ranged from 4 to 100 times slower than *k*₆'. We conclude that cascade from undetected excited vibrational levels into the ground vibrational level did not interfere with our determination of *k*₁. Another potential interference is the fast secondary reaction



To avoid this potential complication, all experiments were carried out under conditions where [HNO₃]/[F]₀ was greater than 150. Variation of the F₂ concentration by a factor of 4 at constant laser fluence did not affect the observed kinetics nor did variation of the laser fluence by a factor of 3 at constant [F₂].

Under our experimental conditions, the NO₃ appearance rate was always more than 2500 times faster than the background NO₃ decay rate (*k*₇ ~ 5 s⁻¹). Hence, the appearance of NO₃ could be analyzed as a single exponential rise:

$$[\text{NO}_3]_t / [\text{NO}_3]_{\text{max}} = 1 - \exp(-k_a t) \quad (1)$$

where

$$k_a = k_1[\text{HNO}_3] + k_8 \quad (11)$$

and [NO₃]_{max} = the NO₃ concentration after all fluorine atoms had reacted away, but before any significant decay of NO₃ had occurred. Assuming NO₃ absorption obeys Beer's law, the above

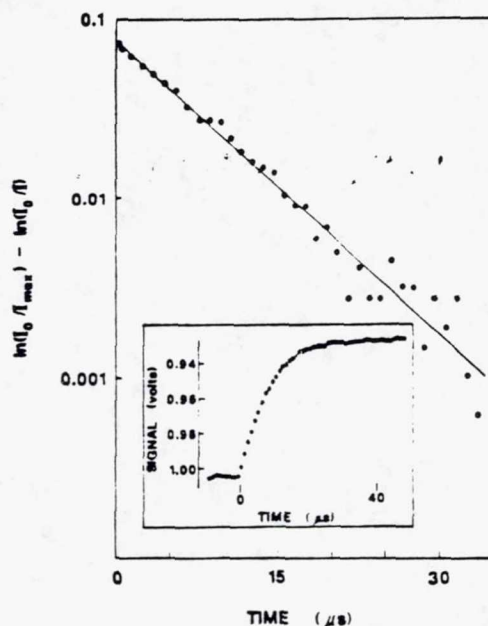


Figure 2. Typical NO₃ appearance temporal profile observed following 351-nm pulsed laser photolysis of F₂/HNO₃/He mixtures. Experimental conditions: T = 350 K, P = 150 Torr, [HNO₃] = 5.95 × 10¹⁵ molecules/cm³, [F₂] = 2.7 × 10¹⁶ molecules/cm³, laser photon fluence = 3.0 mJ/cm², 64 laser shots averaged. The solid line is obtained from a linear least-squares analysis and gives the pseudo-first-order NO₃ appearance rate *k*_a = (1.26 ± 0.06) × 10⁵ s⁻¹ (error is 2σ, precision only).

equations predict that a plot of ln [ln (I₀/I_{max}) - ln (I₀/I)] versus *t* should be linear with slope = -*k*_a, and that a plot of *k*_a versus [HNO₃] should be linear with slope = *k*₁ (I₀ = the probe beam intensity before the photolysis laser fired and I_{max} = the probe beam intensity in the presence of [NO₃]_{max}). Typical experimental results are shown in Figures 2 and 3. The predicted linear dependences were observed in all cases. These observations, along with the above-mentioned invariance of the observed kinetics to variations in [F₂] and laser photon fluence, strongly suggest that the NO₃ temporal profile was governed entirely by reactions 1 and 5–7. Reaction of F(²P) with NO₂ impurity in the nitric acid sample could not have been important unless impurity levels reached several percent; UV photometry at 366 nm confirmed that NO₂ levels in the nitric acid samples were always less than 0.5%.

Our experimental data for reaction 1 are summarized in Table I. Errors quoted for individual *k*₁ determinations are 2σ and refer only to the precision of the *k*_a versus [HNO₃] data. The absolute accuracy of the results is limited by precision, uncertainties in the determination of the nitric acid concentration, and other unidentified systematic errors which we believe to be negligible. We estimate that the absolute accuracy of a typical *k*₁ determination is ±15%.

Our experimental results are plotted in Arrhenius form in Figure 4. The ln *k*₁ versus 1/*T* plot is nonlinear. Over the temperature

(28) Ravishankara, A. R.; Wine, P. H.; Smith, C. A.; Barbone, P. E.; Torabi, A. *J. Geophys. Res.* 1986, 91, 5355.

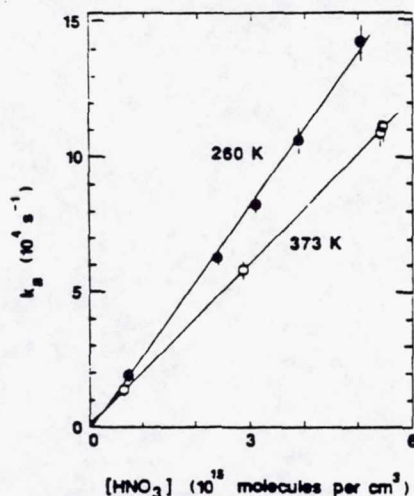


Figure 3. Typical plots of k_2 versus $[\text{HNO}_3]$ observed in the $\text{F}(^2\text{P}) + \text{HNO}_3$ study. Solid lines are obtained from linear least-squares analyses and give the bimolecular rate coefficients listed in Table I.

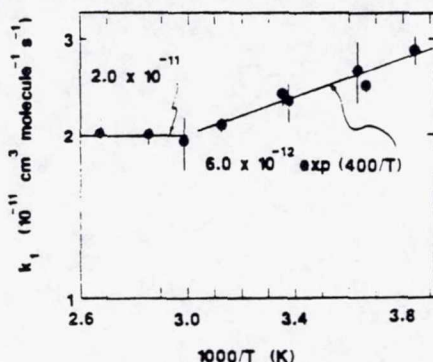


Figure 4. Arrhenius plot for the reaction $\text{F}(^2\text{P}) + \text{HNO}_3 \rightarrow \text{products}$. range 260–320 K, the data are well represented by the expression (units are $\text{cm}^3 \text{ molecule}^{-1} \text{ s}^{-1}$)

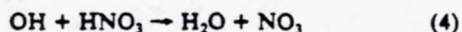
$$k_1(T) = (6.0 \pm 2.6) \times 10^{-12} \exp[(400 \pm 120)/T], \quad 260 \text{ K} \leq T \leq 320 \text{ K} \quad (\text{III})$$

Uncertainties in the above expression are 2σ and represent only the precision of the $\ln k_1$ versus $1/T$ fit. Over the temperature range 335–373 K, our data support the temperature-independent rate coefficient (in units of $\text{cm}^3 \text{ molecule}^{-1} \text{ s}^{-1}$)

$$k_1(T) = (2.0 \pm 0.3) \times 10^{-11}, \quad 335 \text{ K} \leq T \leq 373 \text{ K} \quad (\text{IV})$$

The quoted error in expression IV represents our estimate of the 2σ absolute uncertainty in $k_1(T)$.

The only published value of k_1 with which to compare our results is the very recent 298 K measurement of Mellouki et al.⁹ These authors employed the discharge flow-EPR technique with HNO_3 in about 10-fold excess over F atoms and obtained the result $k_1(298\text{K}) = (2.7 \pm 0.5) \times 10^{-11} \text{ cm}^3 \text{ molecule}^{-1} \text{ s}^{-1}$, in excellent agreement with our 298 K value of $(2.3 \pm 0.3) \times 10^{-11} \text{ cm}^3 \text{ molecule}^{-1} \text{ s}^{-1}$. The non-Arrhenius temperature dependence we have observed is similar to the temperature dependence reported by a number of investigators^{29–32} for the related (although much slower) reaction



A plausible explanation for the observed temperature dependence is that the overall reaction proceeds via two distinct pathways:

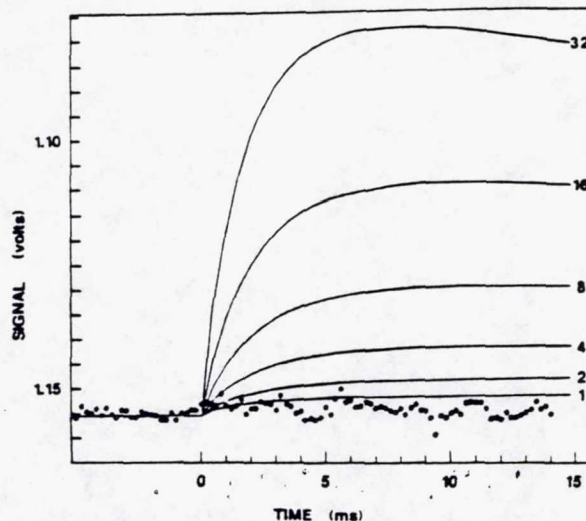
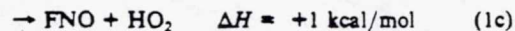
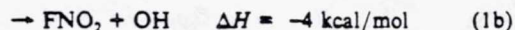
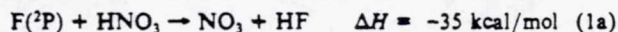


Figure 5. Typical 662-nm absorbance temporal profile observed following pulsed laser photolysis of $\text{Cl}_2/\text{HNO}_3/\text{He}$ mixtures. Experimental conditions: $T = 298 \text{ K}$, $P = 80 \text{ Torr}$, $[\text{HNO}_3] = 5.3 \times 10^{16} \text{ molecules/cm}^3$, $[\text{Cl}_2] = 9.1 \times 10^{15} \text{ molecules/cm}^3$, laser photon fluence = 1.2 mJ/cm^2 , 256 laser shots averaged. Solid lines are obtained from computer simulations as described in the text. Each simulation employed a different value for k_2 ; values for k_2 in units of $10^{-16} \text{ cm}^3 \text{ molecule}^{-1} \text{ s}^{-1}$ are given in the figure.

a direct abstraction route with the zero or positive activation energy and a route involving formation of an intermediate complex followed by rearrangement and dissociation to products. The complex route would be expected to show a negative activation energy.

In addition to channel 1a, two other sets of products are energetically accessible via a complex reaction pathway:



Comparison of $[\text{F}]_0$ (calculated from measurements of $[\text{F}_2]$ and laser fluence, and the known F_2 absorption cross section at the photolysis wavelength³³) with $[\text{NO}_3]_{\text{max}}$ (calculated from the estimated path length and an assumed absorption cross section of $1.8 \times 10^{-17} \text{ cm}^2$ at 662 nm) indicates that reaction 1a is the major channel over the entire temperature range of our study. However, uncertainties in the magnitude of the NO_3 cross section⁷ and the temperature dependences of both the NO_3 ^{6,7,18} and F_2 cross sections prevent quantitative determination of the NO_3 yield.

The occurrence of reaction 1b as a minor channel represents a potential kinetic complication in our study because reaction 4 would result in conversion of OH to NO_3 . However, since k_4 (298K) is about 200 times slower than k_1 (298K),³⁵ the occurrence of reactions 1b and 4 would lead to readily observable nonexponential NO_3 appearance temporal profiles; such nonexponential temporal profiles were not observed. As a further check for the possible occurrence of reaction 1b, a few experiments were carried out where sufficient CO was added to the reaction mixture to scavenge more than 90% of any OH produced. In back-to-back experiments with and without added CO, no change in $[\text{NO}_3]_{\text{max}}$ was observed. On the basis of the above observations, we are able to conclude that, at 298 K, $k_{1b}/k_1 < 0.02$.

The $\text{Cl} + \text{HNO}_3$ Reaction. Reaction 2 was studied by two different experimental methods. The first was identical with the

(29) Kurylo, M. J.; Cornett, K. D.; Murphy, J. L. *J. Geophys. Res.* 1982, 87, 3081.

(30) Margitan, J. J.; Watson, R. T. *J. Phys. Chem.* 1982, 86, 3819.

(31) Devolder, P.; Carlier, M.; Pauwels, J. F.; Sobet, L. R. *Chem. Phys. Lett.* 1984, 111, 94.

(32) ... P. S.; Howard, C. J. *Int. J. Chem. Kinet.* 1985, 17, 17.

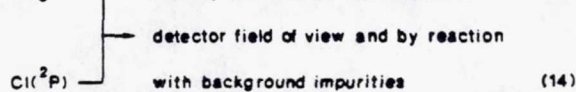
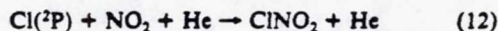
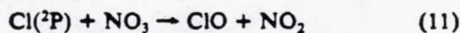
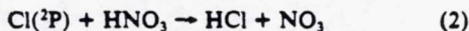
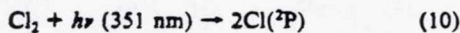
(33) Steunenberg, R. K.; Vogel, R. C. *J. Am. Chem. Soc.* 1956, 78, 901.

(34) Deleted in proof.

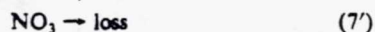
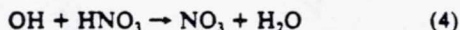
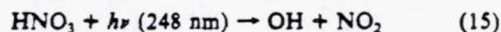
(35) DeMore, W. B.; Margitan, J. J.; Molina, M. J.; Watson, R. T.; Golden, D. M.; Hampson, R. F.; Kurylo, M. J.; Howard, C. J.; Ravishankara, A. R. *Chemical Kinetics and Photochemical Data for Use in Stratospheric Modeling*; JPL Publication 85-37; Jet Propulsion Laboratory: Pasadena, CA, 1985.

approach used to study reaction 1 but with Cl₂ replacing F₂ as the photolyte (PLP-LPLA technique). In the other experimental approach, the decay of Cl(²P) was monitored by time-resolved resonance fluorescence following 355-nm pulsed laser photolysis of Cl₂/HNO₃/He mixtures (PLP-RF technique).

The PLP-LPLA study of reaction 2 employed reaction mixtures containing 0.6–2.5 Torr of HNO₃, 0.2–1.5 Torr of Cl₂, and 80 Torr of helium. No evidence for NO₃ production was observed. Typical data are shown in Figure 5. Also shown in Figure 5 are the results of a series of numerical simulations of the NO₃ absorbance temporal profile. The following mechanism was assumed for the simulations:



Values for k_{11} , k_{12} , and k_{13} were taken from the literature.^{35–38} In units of cm³ molecule⁻¹ s⁻¹, the rate coefficients used in the simulations were $k_{11} = 5.5 \times 10^{-11}$, $k_{12} = 2.0 \times 10^{-12}$, and $k_{13} = 6.2 \times 10^{-13}$. The Cl(²P) concentration was calculated from the measured laser photon fluence and Cl₂ concentration by assuming a quantum yield of 2 for Cl(²P) production; for the data shown in Figure 5, [Cl(²P)]₀ = 7.1 × 10¹² molecules/cm³. The background Cl(²P) loss rate was set at 100 s⁻¹, an upper limit value based on PLP-RF measurements of Cl(²P) decay rates and the geometry of the PLP-LPLA reactor—a geometry that minimizes the rate of diffusion and/or flow out of the detector field of view. The NO₃ decay rate was determined by photolyzing the reaction mixture at 248 nm, a wavelength where HNO₃ rather than Cl₂ is the dominant absorber:



For the reaction mixture used to obtain the data shown in Figure 5, we obtained the result $k_7 = 8.0 \pm 0.7 \text{ s}^{-1}$. The value for k_7 was used in conjunction with the literature value for k_{13} to establish an upper limit NO₂ concentration (for the reaction mixture used to obtain the data shown in Figure 5, [NO₂] ≤ 1.8 × 10¹³ molecules/cm³). Since the upper limit NO₂ concentrations were used in the simulations, k_7 was set equal to zero. The results of the simulations are very insensitive to k_{13} and k_7 as long as $k_{13}[\text{NO}_2] + k_7 < 25 \text{ s}^{-1}$.

The results shown in Figure 5 support the conclusion that $k_2(298\text{K}) < 2 \times 10^{-16} \text{ cm}^3 \text{ molecule}^{-1} \text{ s}^{-1}$. Experiments over a range of values of [HNO₃], [Cl₂], and laser fluence all showed no evidence for NO₃ production from reaction 2, and simulations led to upper limit values for k_2 similar to that obtained from Figure 5. We feel that the reported upper limit is conservative because (1) values for k_{14} and [NO₂] used in the simulations are upper limits and (2) even the simulation with k_2 equal to $1 \times 10^{-16} \text{ cm}^3 \text{ molecule}^{-1} \text{ s}^{-1}$ predicts more absorbance than was actually observed (Figure 5).

The PLP-RF experiments employed reaction mixtures containing 0.1–1 mTorr of Cl₂, 0–0.41 Torr of HNO₃, and 25 Torr of helium. The relatively low total pressure served to minimize

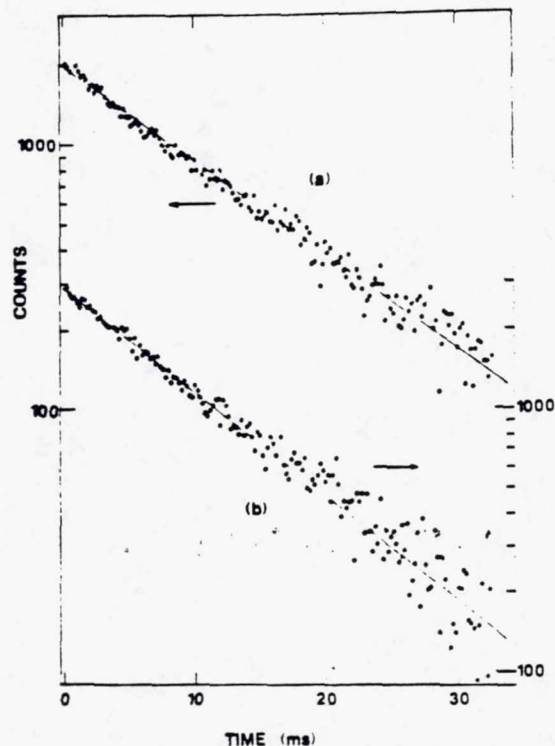


Figure 6. Typical Cl(²P) temporal profiles observed following 355-nm pulsed laser photolysis of Cl₂/HNO₃/He mixtures. Experimental conditions: $T = 298 \text{ K}$; $P = 25 \text{ Torr}$; [HNO₃] in units of 10¹⁵ molecules/cm³ = (a) 0, (b) 12.5; [Cl₂] = 1.0×10^{13} molecules/cm³ in both experiments; [Cl]₀ = 8×10^{10} molecules/cm³ in both experiments; number of laser shots averaged = (a) 16, (b) 1536. Solid lines are obtained from least-squares analyses and give the following pseudo-first-order decay rates: (a) $82 \pm 2 \text{ s}^{-1}$ and (b) $91 \pm 3 \text{ s}^{-1}$; errors are 2σ and represent precision only.

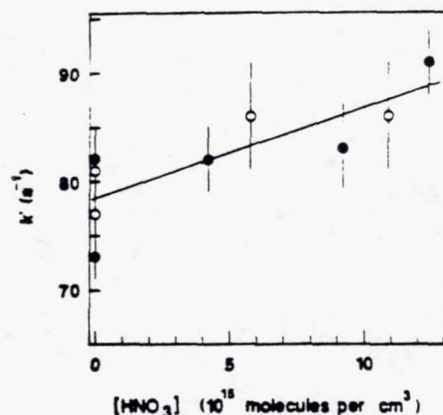


Figure 7. Plot of the pseudo-first-order Cl(²P) decay rate versus nitric acid concentration. O: [Cl]₀ = 4×10^{10} molecules/cm³; ●: [Cl]₀ = 8×10^{10} molecules/cm³. The solid line is obtained from a linear least-squares analysis and gives the bimolecular rate coefficient $(8.3 \pm 4.5) \times 10^{-16} \text{ cm}^3 \text{ molecule}^{-1} \text{ s}^{-1}$, where the uncertainty is 2σ and represents precision only.

the interference from reaction 12. Initial chlorine atom concentrations were always less than 1×10^{11} per cm³, so radical-radical side reactions were relatively unimportant. Some typical Cl(²P) temporal profiles observed in 298 K experiments are shown in Figure 6. A plot of the pseudo-first-order Cl(²P) decay rate as a function of the HNO₃ concentration is shown in Figure 7. A linear least-squares analysis of the data in Figure 7 gives the bimolecular rate coefficient $k \pm 2\sigma = (8.3 \pm 4.5) \times 10^{-16} \text{ cm}^3 \text{ molecule}^{-1} \text{ s}^{-1}$. This rate coefficient can only be considered an upper limit for k_2 since, for example, an NO₂ impurity level of 0.1% in the nitric acid sample would account for the entire ob-

(36) Cox, R. A.; Fowles, M.; Moulton, D.; Wayne, R. P. *J. Phys. Chem.* 1987, 91, 3361.

(37) Leu, M.-T. *Int. J. Chem. Kinet.* 1984, 16, 1311.

(38) Kircher, C. C.; Margitan, J. J.; Sander, S. P. *J. Phys. Chem.* 1984, 88, 4370.

TABLE II: Comparison of Our Kinetic Data for the Cl + HNO₃ Reaction with Those Reported by Other Investigators

investig- ators	exptl tech. ^a	monitored species	k ₂ (298K) ^b	k ₂ (400K) ^b	ref
Leu and DeMore	DF-MS	HNO ₃ ^c	68 ± 34		13
Poulet et al.	DF-MS	HNO ₃ ^c	<0.2 ^d	2.6 ^e	14
Clark et al.	FP-RA	Cl	340 ± 160		15
Kurylo et al.	FP-RF	Cl	167 ^{f,g}		16
Zagogianni et al.	DF-EPR	Cl	<5		17
Cantrell et al.	CK	HNO ₃ , CH ₄	<33		18
this work	FTIR	CINO ₂	<1.6 ^h		
	PLP-LPLA	NO ₃	<2		
	PLP-RF	Cl	<13 ⁱ	<10	

^aDF, discharge flow; MS, mass spectrometry; FP, flash photolysis; RA, resonance absorption; RF, resonance fluorescence; EPR, electron paramagnetic resonance; CK, competitive kinetics; FTIR, Fourier transform infrared spectroscopy; PLP, pulsed laser photolysis; LPLA, long-path laser absorption. ^bUnits are 10⁻¹⁶ cm³ molecule⁻¹ s⁻¹. ^cMonitored HNO₃ with Cl in excess; [Cl] obtained via titration with NOCl. ^dEstimated by authors based on extrapolation of data obtained over the temperature range 439–633 K. ^eCalculated from Arrhenius expression obtained from data at 439 K < T < 633 K. ^fBased on measured upper limit for the NO₃ + HCl rate coefficient and thermodynamic data. ^gLeast-squares slope of k' versus [HNO₃] plot plus 2σ.

served increase in k' with added nitric acid.

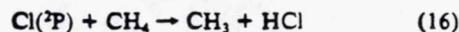
In addition to the 298 K experiments discussed above, we also investigated reaction 2 at T = 400 K using the PLP-RF technique. At 400 K, background Cl(²P) decays were found to be nonexponential. Over the first half-life the measured decay rate was ~150 s⁻¹, while at longer time after the laser pulse the decay rate dropped to ~115 s⁻¹. The reason for the observed nonexponential behavior is not clear. However, experiments with 3, 5, 7, and 9 × 10¹⁵ HNO₃/cm³ added to the reaction mixture demonstrated that neither the fast component nor the slow component of the Cl(²P) decay was affected by addition of HNO₃ to the reaction mixture. On the basis of uncertainties in the individual decay rates, we conservatively estimate that k₂ must be slower than 1 × 10⁻¹⁵ cm³ molecule⁻¹ s⁻¹ at 400 K.

In Table II our rate data for reaction 2 are compared with results reported by other investigators. The earliest measurement of k₂ was reported by Leu and DeMore.¹³ These authors employed the discharge flow-mass spectrometry (DF-MS) technique at total pressures of 1.2 Torr to monitor the decay of HNO₃ in excess Cl atoms. Cl atom concentrations were always less than 10¹⁵/cm³, so the decay of HNO₃ could only be followed down to [HNO₃] ~ 0.8[HNO₃]₀; hence, the results are subject to rather large uncertainties. Poulet et al. also studied reaction 2 using the DF-MS technique with Cl in excess over HNO₃; their experiments employed total pressures of 0.24–1.75 Torr and were done at the elevated temperatures of 439–633 K. Poulet et al. obtained the Arrhenius expression k₂ = 1.5 × 10⁻¹¹ exp(-4400/T). Extrapolation of Poulet et al.'s Arrhenius expression to 298 K gives the extremely low rate coefficient 7 × 10⁻¹⁸ cm³ molecule⁻¹ s⁻¹. However, Poulet et al., upon consideration of potential errors in

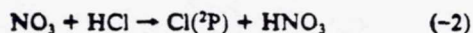
the long extrapolation, suggested 2 × 10⁻¹⁷ cm³ molecule⁻¹ s⁻¹ as an upper limit for k₂(298K). Recently, Poulet and co-workers employed a discharge flow system with EPR detection of Cl(²P) to study reaction 2 at 293 K and obtained an upper limit value of 5 × 10⁻¹⁶ cm³ molecule⁻¹ s⁻¹ for k₂(293K).¹⁷

Clark et al.¹⁵ and Kurylo et al.¹⁶ employed flash photolysis methods to study the kinetics of reaction 2. These authors monitored the decay of Cl(²P) by resonance absorption¹⁵ or resonance fluorescence¹⁶ in the presence of excess HNO₃. The flash photolysis experiments were carried out at total pressures 1–2 orders of magnitude larger than the discharge flow experiments. Both Clark et al. and Kurylo et al. obtained very large values for k₂(298K)—3.6 × 10⁻¹⁴ and 1.7 × 10⁻¹⁴ cm³ molecule⁻¹ s⁻¹, respectively. Neither of these investigators employed HNO₃ concentrations above 3 × 10¹⁵ molecules/cm³ due to attenuation of the chlorine resonance lines by HNO₃. [While we also observed reduction in resonance radiation intensity with added HNO₃, we were able to obtain good quality data even at HNO₃ concentrations above 1 × 10¹⁶ molecules/cm³ (Figure 6).] Potential experimental problems that are specific to flash photolysis experiments include reaction of Cl(²P) with impurities in the HNO₃ sample (particularly NO₂) and reaction of Cl(²P) with flash generated radicals. Although both Clark et al. and Kurylo et al. recognized these potential problems and took measures to minimize them, it appears possible that NO₃, generated via nitric acid photolysis followed by reaction 4, was responsible for a significant fraction of Cl(²P) removal in both earlier flash photolysis studies.^{15,16}

The most recent study of the kinetics of reaction 2 has been reported by Cantrell et al.¹⁸ These authors measured the rate of reaction 2 relative to that for the reaction



They obtained the result k₂/k₁₆ ≤ 0.033. Since k₁₆ ~ 1 × 10⁻¹³ cm³ molecule⁻¹ s⁻¹,³⁵ their result implies that k₂ ≤ 3.3 × 10⁻¹⁵ cm³ molecule⁻¹ s⁻¹. Cantrell et al. also investigated the kinetics of the reverse reaction



They observed that HCl reactions with NO₃ and/or N₂O₃ led to production of ClNO₂, but they attributed ClNO₂ production primarily to heterogeneous pathways. They were able to place an upper limit of 7 × 10⁻¹⁸ cm³ molecule⁻¹ s⁻¹ on the homogeneous gas-phase value for k₂(298K). On the basis of thermodynamic considerations, this result suggests¹⁸ that k₂(298K) is slower than 1.6 × 10⁻¹⁶ cm³ molecule⁻¹ s⁻¹. Our observation of minimal NO₃ production following 351-nm pulsed laser photolysis of Cl₂/HNO₃/He mixtures is in agreement with the low upper limits for k₂(298K) reported by Cantrell et al.¹⁸ and Poulet and co-workers^{14,17} but in conflict with the faster rate coefficients reported by Leu and DeMore,¹³ Kurylo et al.,¹⁵ and Clark et al.¹⁶

Acknowledgment. We thank C. J. Shackelford and E. P. Daykin for assisting with some of the experiments. This work was supported by the National Science Foundation through Grant ATM-86-00892 and by the National Aeronautics and Space Administration through Grant NAGW-1001.

Registry No. F₂, 7782-41-4; Cl₂, 7782-50-5; HNO₃, 7697-37-2; F, 14762-94-8; Cl, 22537-15-1; NO₃, 12033-49-7.

Temperature-Dependent Absorption Cross Sections for Hydrogen Peroxide Vapor

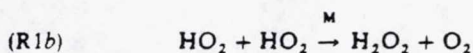
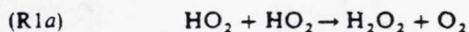
J. M. NICOVICH AND P. H. WINE

Molecular Sciences Branch, Georgia Tech Research Institute, Georgia Institute of Technology, Atlanta

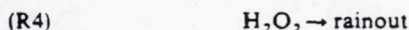
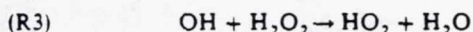
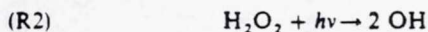
Relative absorption cross sections for hydrogen peroxide vapor were measured over the temperature ranges 285–381 K for $230 \text{ nm} \leq \lambda \leq 295 \text{ nm}$ and 300–381 K for $193 \text{ nm} \leq \lambda \leq 350 \text{ nm}$. The well-established 298 K cross sections at 202.6 and 228.8 nm were used as an absolute calibration. A significant temperature dependence was observed at the important tropospheric photolysis wavelengths, $\lambda > 300 \text{ nm}$. Measured cross sections were extrapolated to lower temperatures, using a simple model which attributes the observed temperature dependence to enhanced absorption by molecules possessing one quantum of O–O stretch vibrational excitation. Upper tropospheric photodissociation rates calculated using the extrapolated cross sections are about 25% lower than those calculated using currently recommended 298 K cross sections.

INTRODUCTION

Hydrogen peroxide (H_2O_2) is an important trace constituent of the atmosphere. H_2O_2 is formed primarily via the HO_2 self reactions,



and is removed from the atmosphere by three processes which occur at similar rates:



Reaction (R2) regenerates the HO_x radicals which were lost in (R1); hence when removed by photolysis, H_2O_2 has acted as an HO_x reservoir. On the other hand, (R1), followed by (R3) and (R4), represents a sink for gas phase HO_x . Both the overall H_2O_2 lifetime and the branching ratios for loss via (R2), (R3), and (R4) must be known quantitatively in order to accurately model atmospheric HO_x chemistry.

Most calculations of the atmospheric H_2O_2 photolysis rate, $j_{\text{H}_2\text{O}_2}$, employ absorption cross sections recommended by the NASA panel for chemical kinetics and photochemical data evaluation [DeMore et al., 1985]. The recommended cross sections are the average of those reported by Lin et al. [1978] and by Molina and Molina [1981]. Both studies were carried out at 298 K, with cross sections reported in 5-nm increments over the range 190–350 nm; they agree very well, except at wavelengths longer than 325 nm, where Molina and Molina report somewhat lower cross sections than Lin et al. In the troposphere and lower stratosphere most H_2O_2 photolysis occurs at wavelengths longer than 310 nm. Hence the differences between the two previous studies do result in small but significant differences in calculated values for $j_{\text{H}_2\text{O}_2}$.

Since photolysis of H_2O_2 in the troposphere occurs exclusively in the long-wavelength tail of the absorption spectrum,

there is a strong possibility that "hot bands," i.e., absorptions originating from excited vibrational levels of the ground electronic state, are responsible for much of the atmospheric photolysis. If atmospheric photodissociation of H_2O_2 does involve hot bands, then $j_{\text{H}_2\text{O}_2}$ will be temperature dependent.

With the above considerations in mind, we have measured absorption cross sections for H_2O_2 over the wavelength range 193–350 nm as a function of temperature. Our results are reported in this paper. Extrapolation of our results to upper tropospheric temperatures leads to significantly lower values for $j_{\text{H}_2\text{O}_2}$ at 5 and 10 km than would be calculated from currently recommended cross sections.

EXPERIMENTAL TECHNIQUE

Cross-section measurements were carried out using the well-established 298 K cross sections at 202.6 and 228.8 nm for absolute calibration [Lin et al., 1978; Molina and Molina, 1981]. A schematic of the experimental apparatus is shown in Figure 1. The measurements were performed in a slow flow system consisting of three absorption cells in tandem. The temperature in the middle cell was varied by circulating thermostated liquid through an outer jacket. A broadband UV light source (deuterium lamp) was used and the wavelength was resolved with a 0.22-m monochromator. The temperature-controlled cell was 244 cm in length. All experiments employed a spectral band pass of 0.6 nm full width at half maximum. The first and last absorption cells were maintained at room temperature, $298 \pm 1 \text{ K}$. A cadmium pen-ray lamp was used as the light source for the first cell, and a narrow band-pass filter was employed to isolate the 228.8-nm Cd resonance line. A zinc hollow cathode lamp was used as a light source for the last absorption cell, and a 0.25-m monochromator was employed to isolate the 202.6-nm Zn^+ line. The first and last absorption cells were 216 and 111 cm in length, respectively. The assumed 298 K cross sections were $4.32 \times 10^{-19} \text{ cm}^2$ at 202.6 nm and $1.86 \times 10^{-19} \text{ cm}^2$ at 228.8 nm.

H_2O_2 was added to the gas flow by diverting some of the N_2 buffer gas through a Pyrex bubbler containing 90% (by weight) H_2O_2 solution. The total pressure was maintained at 100 torr in all experiments. Measurement of the H_2O_2 concentration in the gas flow at both the inlet and outlet from the temperature-controlled cell not only allowed determination of the absolute H_2O_2 concentration, but also allowed potential

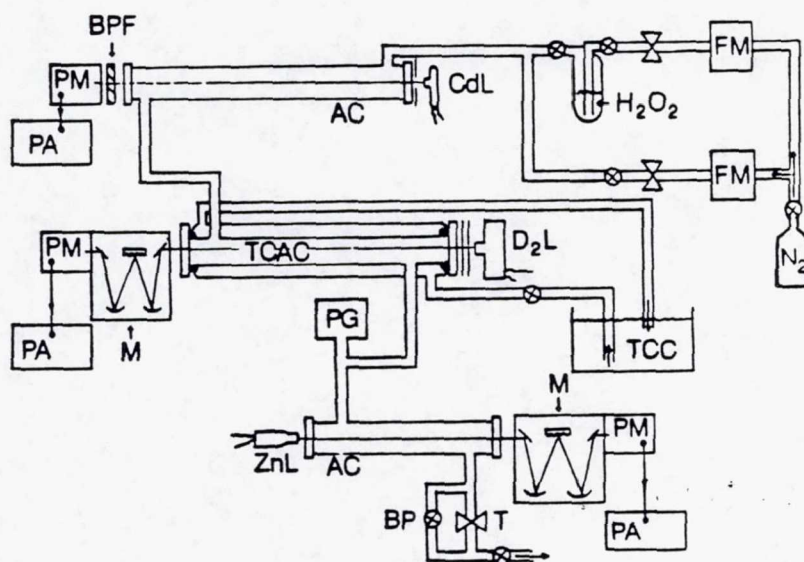


Fig. 1. Schematic of the apparatus. AC, absorption cell; BP, bypass valve; BPF, band-pass filter; CdL, cadmium pen ray lamp; FM, flowmeter; M, monochromator; PA, picoammeter; PG, pressure gauge; PM, photomultiplier; T, throttle valve; TCAC, temperature-controlled absorption cell; TCC, temperature-controlled circulator; ZnL, zinc hollow cathode lamp; D₂L, deuterium lamp.

systematic errors from H_2O_2 loss by decomposition or condensation to be assessed quantitatively. The difference in H_2O_2 concentrations measured at the inlet and outlet of the temperature-controlled cell did not exceed 5% in any of the experiments used to obtain H_2O_2 cross sections. The H_2O_2 concentration in the temperature-controlled cell was always taken to be the temperature-corrected average of the concentrations measured at the inlet and outlet. At temperatures above 381 K, H_2O_2 decomposition became a problem, while the relatively low vapor pressure of H_2O_2 prevented meaningful data from being obtained at temperatures below 285 K.

In preliminary experiments, instead of using a single-pass temperature-controlled absorption cell, a multipass White cell setup was employed. Using a xenon arc lamp light source, a pathlength of 25 m could readily be obtained (70 passes through a 36-cm cell). However, at longer wavelengths, i.e., $\lambda > 300$ nm, a systematic error was uncovered in the multipass absorption measurements. The cross section measured at a given wavelength was found to depend upon the antireflection coating wavelength (of maximum transmission) of the White cell windows. We believe that this effect resulted from a change in refractive index at the gas-window interface due to adsorption of H_2O_2 and/or H_2O to the cell windows. Under certain conditions an improvement in the index match was obtained with H_2O_2 flowing; this resulted in measurement of an apparent negative absorbance! At long wavelengths, where gas phase absorption was very weak, the magnitude of the artifact became intolerable.

Use of a single-pass temperature-controlled absorption cell seemed to overcome this problem. While the pathlength was a factor of 10 shorter than in the White cell arrangement, system stability was somewhat improved. Hence meaningful measurements could be made for $\lambda \leq 350$ nm. To ensure that "window effects" were totally absent, at each temperature and wavelength the absorbance was also measured in a second shorter cell (20.0-cm pathlength) using the same windows as in the

longer cell. Cross sections were then determined using the difference in absorbances and the difference in pathlengths between the long and short cells. Care was taken to collimate the light from the deuterium lamp in such a manner that no reflections from the walls of the absorption cells reached the detector.

RESULTS

Measured H_2O_2 absorption cross sections as a function of temperature and wavelength are tabulated in Table 1. Our 300 K cross sections are in good agreement with current recommendations [Demore *et al.*, 1985] throughout the 193- to 350-nm wavelength range. However, a distinct temperature dependence is observed, which is most pronounced in the atmospherically important 310- to 350-nm wavelength region.

EXTRAPOLATION OF MEASURED CROSS SECTIONS TO LOWER TEMPERATURES

Experimental measurements of H_2O_2 absorption cross sections at temperatures typical of the upper troposphere and lower stratosphere are unavailable and will be extremely difficult to obtain at any time in the future. In the absence of experimental data, we have employed a simple model to extrapolate our results to lower temperatures. The basic assumption in the model is that the observed temperature dependence in the H_2O_2 absorption cross section results from the fact that ground electronic state H_2O_2 with one quantum of O-O stretch excitation absorbs more strongly at longer wavelengths than does unexcited H_2O_2 . Semiempirical and ab initio calculations of ground- and excited-state H_2O_2 potential energy surfaces [Eveith, 1976; Rank and Barriol, 1977; Eveith and Kassab, 1978; Chevaldonnet *et al.*, 1986; Gericke *et al.*, 1986] strongly support this assumption, i.e., the lowest energy spin allowed transition is from the relatively anharmonic X^1A ground state to the steeply repulsive \bar{A}^1A excited state. The O-O stretching frequency is 877 cm^{-1} [Giguère, 1950]. Hence

TABLE 1. Measured Hydrogen Peroxide Absorption Cross Sections as a Function of Wavelength and Temperature

λ , nm	σ , 10^{-21} cm ²				
	285 K	300 K	327 K	355 K	381 K
193		589		582	585
230	182	180	183	182	183
235	152	149	152	151	153
240	124	123	126	125	127
245	102	101	106	103	103
250	83.0	82.1	84.8	84.4	86.7
255	66.8	65.8	68.2	68.1	71.0
260	53.3	52.5	54.8	54.7	57.1
265	42.3	42.0	43.7	44.1	46.3
270	33.3	33.1	34.7	35.0	37.1
275	25.6	25.4	27.0	27.6	29.0
280	20.0	19.8	20.9	21.6	22.3
285	15.0	15.3	16.2	16.8	17.4
290	11.8	11.8	12.4	13.1	13.4
295	8.79	8.85	9.39	9.98	10.2
300		6.58	7.21	7.69	7.81
305		4.97	5.44	5.71	5.90
310		3.66	4.13	4.29	4.46
315		2.65	3.09	3.29	3.36
320		1.99	2.31	2.47	2.59
325		1.43	1.79	1.85	1.93
330		1.10	1.18	1.40	1.57
335		0.82	0.94	1.07	1.18
340		0.54	0.67	0.78	0.92
345		0.51	0.64	0.66	0.74
350		0.43	0.48	0.50	0.60

for $T \leq 400$ K. the fraction of H₂O₂ molecules with one quantum of O-O stretch excitation is ≤ 0.04 and the fraction with more than one quantum of O-O stretch excitation is negligible.

According to our simple model, the absorption cross section at a particular wavelength and temperature is given by the expression

$$\sigma(\lambda, T) = X_0(T)\sigma_0(\lambda) + X_1(T)\sigma_1(\lambda) \quad (1)$$

where the subscripts refer to the number of quanta of O-O stretch excitation. The mole fractions X_0 and X_1 are readily computed from the following equations:

$$Q = 1 + \exp(-\Delta E/RT) \quad (2)$$

$$X_0 = 1/Q \quad (3)$$

$$X_1 = 1 - X_0 = (Q - 1)/Q \quad (4)$$

where ΔE is the energy of one quantum of O-O stretch, i.e., 877 cm⁻¹. It should be noted that (2) is a simplified form for the vibrational partition function which ignores the low-frequency torsional mode. Inclusion of torsional frequencies [Hunt et al., 1965; Helminger et al., 1981; Ticich et al., 1986] has a negligible effect on computed values for X_0 and X_1 .

The data analysis involved least squares fitting the temperature-dependent cross sections at each wavelength to obtain best fit values for $\sigma_0(\lambda)$ and $\sigma_1(\lambda)$. The results are plotted in Figure 2. "Recommended" values for $\sigma_0(\lambda)$ and $\sigma_1(\lambda)$ are obtained from the smoothed results (solid lines in Figure 2); they are tabulated in Table 2. The smooth curve drawn through the $\sigma_1(\lambda)$ data assumes that $\sigma_1(\lambda)$ is wavelength independent for $\lambda < 260$ nm (obviously a rather gross approximation). However, since nearly all absorption at $\lambda < 260$ nm is

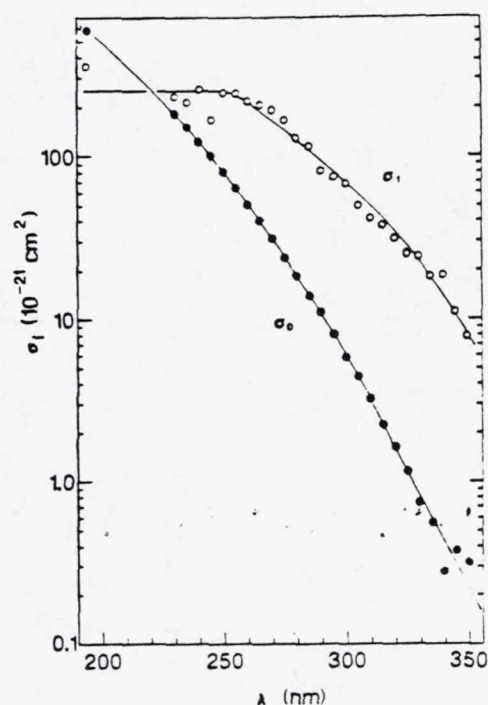


Fig. 2. Best fit values for σ_0 and σ_1 as a function of wavelength.

from vibrationally unexcited H₂O₂, this approximation has little effect on the calculated cross sections (σ).

"Recommended" values for σ as a function of wavelength and temperature can be calculated from the recommended $\sigma_0(\lambda)$ and $\sigma_1(\lambda)$ using (1)-(4). Some representative results are shown in Figure 3, plotted in the form σ versus $1/Q$, which,

TABLE 2. Values for σ_0 and σ_1 Used to Calculate "Recommended" H₂O₂ Absorption Cross Sections as a Function of Wavelength and Temperature

λ , nm	σ_0 , 10^{-21} cm ²	σ_1 , 10^{-21} cm ²
193	591	250
230	181	250
235	150	250
240	122	250
245	99.0	249
250	80.0	244
255	64.0	233
260	50.8	215
265	40.0	189
270	30.9	167
275	23.8	146
280	18.4	127
285	13.9	109
290	11.0	94.5
295	8.00	80.5
300	5.80	68.5
305	4.25	58.5
310	3.08	49.3
315	2.23	41.3
320	1.60	34.3
325	1.15	28.3
330	0.815	23.0
335	0.595	18.4
340	0.428	14.0
345	0.310	10.5
350	0.220	8.0

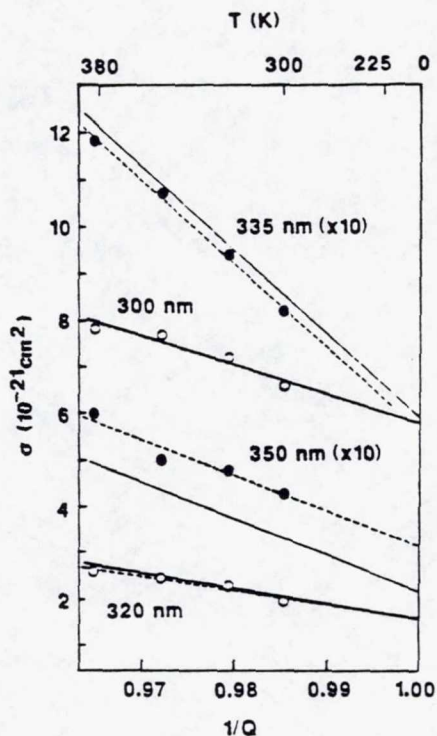


Fig. 3. Plots of σ versus $1/Q$ for $\lambda = 300, 320, 335,$ and 350 nm. Open and closed circles are experimental data. Dashed lines are best fit of the experimental data at each particular wavelength. Solid lines are computed from "recommended" (i.e., smoothed) values of $\sigma_0(\lambda)$ and $\sigma_1(\lambda)$.

according to (1)–(4), should be linear. The open and solid circles in Figure 3 represent experimentally measured cross sections, while the dashed lines are calculated using best fit $\sigma_0(\lambda)$ and $\sigma_1(\lambda)$ values at each individual wavelength (i.e., the data points in Figure 2) and the solid lines are calculated using "recommended" values for $\sigma_0(\lambda)$ and $\sigma_1(\lambda)$ (i.e., solid lines in Figure 2).

PHOTODISSOCIATION AND OTHER ATMOSPHERIC H₂O₂ LOSS PROCESSES

The temperature-dependent absorption cross sections obtained in this study have been employed to calculate atmospheric H₂O₂ photodissociation rates at altitudes of 0, 5, and 10 km, i.e., at temperatures of 288, 257, and 224 K. Solar fluxes were obtained from W. L. Chameides (private communication, 1987) and are appropriate for a zenith angle of 60° (close to the global daytime average zenith angle). The results are summarized in Table 3. One interesting aspect of the results in Table 3 is that about 20% of H₂O₂ photolysis appears to occur at wavelengths longer than 350 nm, where no cross-section data is available. Values for σ at wavelengths longer than 350 nm were obtained by extrapolation (assuming a linear in σ versus λ dependence) and are therefore subject to considerable uncertainty. However, the error in $j_{\text{H}_2\text{O}_2}$ which results from using extrapolated cross sections is much smaller than the error which would result from ignoring all photolysis at wavelengths longer than 350 nm. Since average daytime solar fluxes were used in the calculations, diurnally averaged photolysis rates are a factor of 2 smaller than those given in Table 3. Hence the lifetime of H₂O₂ toward photodissociation is 5.2 days at 0 km, 3.9 days at 5 km, and 3.6 days at 10 km.

TABLE 3. H₂O₂ Photolysis Rates Versus Altitude at a Solar Zenith Angle of 60°

Z, km	T, K	λ , nm	$10^{-13}Q$, cm ⁻² s ⁻¹	$\bar{\sigma}$, 10 ⁻²³ cm ²	$Q\bar{\sigma}$, 10 ⁻⁸ s ⁻¹	j , s ⁻¹
0	288	300–310	3.3	486	16.1	4.43×10^{-6}
		310–320	31.0	267	82.8	
		320–330	73.4	145	106	
		330–340	109.1	80.6	88.0	
		340–350	126.5	44.9	56.8	
		350–360	139.4	26.0	36.3	
		360–370	161.0	15.1	24.3	
		370–380	174.5	8.8	15.4	
		380–390	178.5	5.3	9.5	
		390–400	228.4	3.3	7.4	
5	257	300–310	5.9	462	27.3	5.89×10^{-6}
		310–320	50.7	250	127	
		320–330	112.4	133	149	
		330–340	160.4	72.2	116.	
		340–350	178.7	39.0	69.7	
		350–360	189.9	22.0	41.7	
		360–370	212.9	12.4	26.3	
		370–380	225.2	7.0	15.7	
		380–390	225.1	4.0	9.1	
		390–400	281.3	2.4	6.7	
10	224	300–310	7.9	444	35.2	6.53×10^{-6}
		310–320	64.1	237	152	
		320–330	137.3	123	170	
		330–340	192.6	66.0	127	
		340–350	211.7	34.7	73.4	
		350–360	221.4	19.0	42.1	
		360–370	244.4	10.4	25.3	
		370–380	256.3	5.6	14.4	
		380–390	253.9	3.1	7.8	
		390–400	313.5	1.7	5.5	

Q is equal to the total photon flux in the given wavelength range; $\bar{\sigma}$ is equivalent to the average cross section in the given wavelength range; for $\lambda > 350$ nm, cross sections are estimated by extrapolation; j is equivalent to $\Sigma Q\bar{\sigma}$, the first-order atmospheric photolysis rate.

In Table 4 we compare H₂O₂ photodissociation rates obtained in this work with those calculated using currently recommended absorption cross sections [DeMore *et al.*, 1985] and with estimated rates of H₂O₂ removal by reaction with OH and by rainout. The first-order rate of reaction with OH was calculated using the currently recommended rate coefficient for (R3) [DeMore *et al.*, 1985] and a diurnally averaged OH concentration obtained by interpolating the OH altitude profiles calculated by Logan *et al.* [1981] at 15° and 45°N to a latitude of 41°N; Chameides and Tan [1981] have argued that

TABLE 4. Comparison of Diurnally Averaged H₂O₂ Removal Rates Under Atmospheric Conditions Typical of 41°N Latitude

Z, km	j , 10 ⁻⁷ s ⁻¹			
	NASA ^a	This Work	$k_3[\text{OH}]$, 10 ⁻⁷ s ⁻¹	k_4^b , 10 ⁻⁷ s ⁻¹
0	23	22	9.0	4–40
5	35	29	14	2–20
10	42	33	9.5	0.5–1.5

^aBased on recommendations of DeMore *et al.* [1985].

^bHigh values are predicted when cycling between wet and dry periods is rapid; low values are predicted when storm cycle is long [Giorgi and Chameides, 1985].

41°N is the latitude at which the average daytime solar zenith angle is 60°, as assumed in the *j*-value calculations. A range of values is given in Table 4 for the H₂O₂ rainout rate. It has been argued that for a highly soluble species such as H₂O₂, the time-averaged rainout rate depends not only on the average rainfall, but also on the period of the storm cycle [Thompson and Cicerone, 1982; Giorgi and Chameides, 1985]. The upper limit values for *k*₄ were calculated assuming infinitely rapid cycling between wet and dry periods, while the lower limits are representative of a boundary layer storm cycle of about 1 month [Giorgi and Chameides, 1985].

Values for *j*_{H₂O₂} calculated using currently recommended cross sections are higher than those calculated using our temperature-dependent cross sections by a factor of 1.2 at 5 km and a factor of 1.3 at 10 km. Photodissociation appears to be the single most important H₂O₂ removal mechanism at these altitudes, though both reaction with OH and rainout are important, particularly at 5 km. Incorporation of our results into models of free tropospheric chemistry should result in a small but significant decrease in calculated HO₂ levels.

Acknowledgments. Support for this work was provided by the Fluorocarbon Program Panel of the Chemical Manufacturers Association (contract FC-85-557), The National Aeronautics and Space Administration (grant NAGW 1001), and the National Science Foundation (grant ATM-86-00892). We would like to thank W. L. Chameides for providing the solar photon fluxes and for several helpful discussions. We would also like to thank R. P. Thorn and J. R. Wells for helping with the data analysis and the *j*_{H₂O₂} calculations.

REFERENCES

- Chameides, W. L., and A. Tan, The two-dimensional diagnostic model for tropospheric OH: An uncertainty analysis, *J. Geophys. Res.*, **86**, 5209-5223, 1981.
- Chevaldonnet, C., H. Cardy, and A. Dargelos, Ab Initio CI calculations on the PE and VUV spectra of hydrogen peroxide, *Chem. Phys.*, **102**, 55-61, 1986.
- DeMore, W. B., J. J. Margitan, M. J. Molina, R. T. Watson, D. M. Golden, R. F. Hampson, M. J. Kurylo, C. J. Howard, and A. R. Ravishankara, Chemical kinetics and photochemical data for use in stratospheric modeling, Evaluation 7, *JPL Publ.*, 85-37, 1985.
- Evleth, E. M., Ground and excited state correlations in the rupture of oxygen-oxygen bonds in peroxides, *J. Amer. Chem. Soc.*, **98**, 1637-1639, 1976.
- Evleth, E. M., and E. Kassab, Ground- and excited-state correlations in bond rupture reactions, *J. Amer. Chem. Soc.*, **100**, 7859-7864, 1978.
- Gericke, K.-H., S. Klee, F. J. Comes, and R. N. Dixon, Dynamics of H₂O₂ photodissociation: OH product state and momentum distribution characterized by sub-Doppler and polarization spectroscopy, *J. Chem. Phys.*, **85**, 4463-4479, 1986.
- Giguère, P. A., The infra-red spectrum of hydrogen peroxide, *J. Chem. Phys.*, **18**, 88-92, 1950.
- Giorgi, F., and W. L. Chameides, The rainout parameterization in a photochemical model, *J. Geophys. Res.*, **90**, 7872-7880, 1985.
- Helminger, P., W. C. Bowman, and F. C. DeLucia, A study of the rotational-torsional spectrum of hydrogen peroxide between 80 and 700 GHz, *J. Mol. Spectrosc.*, **85**, 120-130, 1981.
- Hunt, R. H., R. A. Leacock, C. W. Peters, and K. T. Hecht, Internal-rotation in hydrogen peroxide: The far-infrared spectrum and the determination of the hindering potential, *J. Chem. Phys.*, **42**, 1931-1946, 1965.
- Lin, C. L., N. K. Rohatgi, and W. B. DeMore, Ultraviolet absorption cross sections of hydrogen peroxide, *Geophys. Res. Lett.*, **5**, 113-115, 1978.
- Logan, J. A., M. J. Prather, S. C. Wofsy, and M. J. McElroy, Tropospheric chemistry: A global perspective, *J. Geophys. Res.*, **86**, 7210-7354, 1981.
- Molina, L. T., and M. J. Molina, UV absorption cross sections of HO₂NO₂ vapor, *J. Photochem.*, **15**, 97-109, 1981.
- Rank, A., and J. M. Barriol, The computation of oscillator strengths and optical rotary strengths from molecular wavefunctions. The electronic states of H₂O, CO, HCN, H₂O₂, CH₂O, and C₂H₄, *Chem. Phys.*, **25**, 409-424, 1977.
- Thompson, A. M., and R. J. Cicerone, Clouds and wet removal as causes of variability in the trace-gas composition of the marine troposphere, *J. Geophys. Res.*, **87**, 8811-8826, 1982.
- Ticich, T. M., T. R. Rizzo, H. R. Dubal, and F. F. Crim, Unimolecular reactions near threshold: The overtone vibration initiated decomposition of HOOH (*S*_{vOH}), *J. Chem. Phys.*, **84**, 1508-1520, 1986.

J. M. Nicovich and P. H. Wine, Molecular Sciences Branch, Georgia Tech Research Institute, EML, 342 Baker Building, Georgia Institute of Technology, Atlanta, GA 30332.

(Received October 9, 1987;
revised December 8, 1987;
accepted December 10, 1987.)

NDB

520-25
026138

K-102

CLOSE

Reprinted from *The Journal of Physical Chemistry*, 1987, 91, 5118.
 Copyright © 1987 by the American Chemical Society and reprinted by permission of the copyright owner.

Temperature Dependence of the O + HO₂ Rate Coefficient

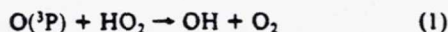
J. M. Nicovich and P. H. Wine*

Molecular Sciences Branch, Georgia Tech Research Institute, Georgia Institute of Technology, Atlanta, Georgia 30332 (Received: February 2, 1987; In Final Form: May 19, 1987)

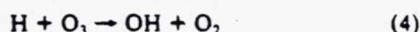
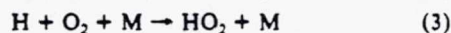
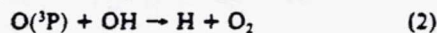
A pulsed laser photolysis technique has been employed to investigate the kinetics of the radical-radical reaction O(³P) + HO₂ → OH + O₂ over the temperature range 266–391 K in 80 Torr of N₂ diluent gas. O(³P) was produced by 248.5-nm KrF laser photolysis of O₃ followed by rapid quenching of O(¹D) to O(³P), while HO₂ was produced by simultaneous photolysis of H₂O₂ to create OH radicals which, in turn, reacted with H₂O₂ to yield HO₂. The O(³P) temporal profile was monitored by using time-resolved resonance fluorescence spectroscopy. The HO₂ concentration was calculated based on experimentally measured parameters. The following Arrhenius expression describes our experimental results: $k_1(T) = (2.91 \pm 0.70) \times 10^{-11} \exp[(228 \pm 75)/T]$ where the errors are 2σ and represent precision only. The absolute uncertainty in k_1 at any temperature within the range 266–391 K is estimated to be ±22%. Our results are in excellent agreement with a discharge flow study of the temperature dependence of k_1 in 1 Torr of He diluent reported by Keyser, and significantly reduce the uncertainty in the rate of this important stratospheric reaction at subambient temperatures.

Introduction

The reaction of ground-state oxygen atoms with hydroperoxyl radicals



is a major odd oxygen destruction pathway in the upper stratosphere and mesosphere. Along with the reactions



reaction 1 plays a major role in controlling the partitioning among H, OH, and HO₂ radicals in the upper atmosphere. Hence, accurate kinetic data for reaction 1 are needed in order to model upper atmospheric chemistry.

Several kinetics studies of reaction 1 are reported in the literature.^{1–7} Four recent direct measurements of k_1 at 298 K are

(1) Burrows, J. P.; Cliff, D. I.; Harris, G. N.; Thrush, B. A.; Wilkinson, J. P. *T. Proc. R. Soc. London, A* 1979, 368, 463.

(2) Hack, W.; Preuss, A. W.; Temps, F.; Wagner, H. *G. Ber. Bunsenges. Phys. Chem.* 1979, 83, 1275.

(3) Liu, R. R.; Sauer, M. C., Jr.; Gordon, S. J. *Phys. Chem.* 1980, 84, 817.

(4) Sridharan, U. C.; Qiu, L. X.; Kaufman, F. J. *Phys. Chem.* 1982, 86, 4469.

* Author to whom correspondence should be addressed.

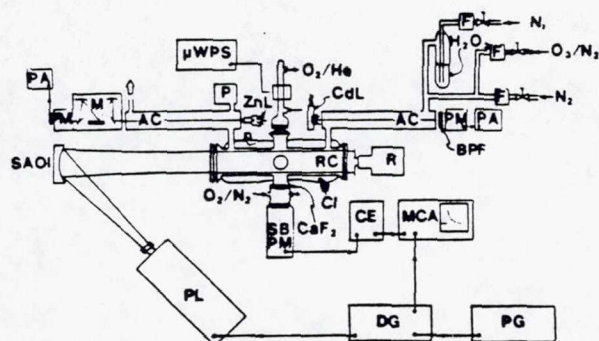


Figure 1. Schematic of the apparatus: AC, absorption cell; BPF, band-pass filter; CdL, cadmium lamp; CE, counting electronics; CI, coolant inlet; DG, delay generator; F, flow meter; M, monochromator; MCA, multichannel analyzer; μ WPS, microwave power supply; PG, pulse generator; PA, picoammeter; P, pressure gauge; PL, photolysis laser; PM, photomultiplier; R, radiometer; RC, reaction cell; SAOI, segmented aperture optical integrator; SBPM, solar blind photomultiplier; ZnL, zinc lamp. For the sake of clarity, the solar blind photomultiplier and resonance lamp are shown at 180°. In reality, the SBPM, resonance lamp, and laser beam were at right angles to each other.

in excellent agreement,⁴⁻⁷ with reported rate coefficients all within the range $(5.2-6.2) \times 10^{-11} \text{ cm}^3 \text{ molecule}^{-1} \text{ s}^{-1}$. However, there has been only one investigation of the temperature dependence of k_1 . Keyser⁵ studied reaction 1 over the temperature range 229–372 K in a discharge flow system at 1-Torr total pressure and observed that $k_1(T)$ increased with decreasing temperature; his reported "negative activation energy" was $\sim 0.4 \text{ kcal mol}^{-1}$. Although Keyser's study of reaction 1 was a high-quality experiment which appears to be free of significant systematic errors, the uncertainty in his reported activation energy will remain undesirably high⁸ until independent confirmation is reported.

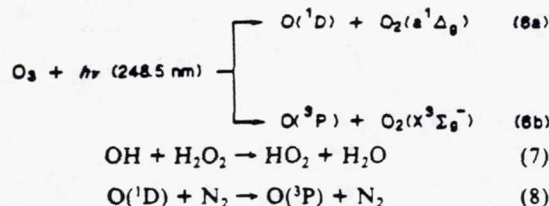
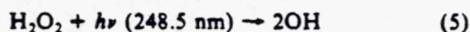
Several years ago, we developed a pulsed laser photolysis technique for studying the kinetics of radical-radical reactions at pressures up to 1 atm. We first applied this technique to investigate reaction 1 at 298 K over the pressure range 10–500 Torr.⁶ In this paper, we report the results of a pulsed laser photolysis-resonance fluorescence study of the temperature dependence of k_1 . Our results, obtained by using a much different experimental approach than that employed by Keyser,⁵ confirm his reported temperature dependence and also demonstrate that k_1 is independent of pressure at subambient temperatures.

Experimental Section

With a few modifications, the experiments were carried out in the same manner as our previous room-temperature study.⁶ A review of the experimental approach, along with details pertinent to this investigation, is given below. A schematic of the apparatus is shown in Figure 1.

All experiments were carried out under slow-flow conditions using a jacketed Pyrex reactor with an internal volume of 320 cm³. The cell was maintained at a constant temperature by circulating ethylene glycol from a thermostated bath through the outer jacket. A copper-constantan thermocouple with a stainless steel jacket was inserted into the reaction zone through a vacuum seal, thus allowing measurement of the gas temperature under the precise pressure and flow conditions of the experiment.

Reactants were produced with HO₂ in excess by 248.5-nm pulsed laser photolysis of H₂O₂/O₃/N₂ mixtures:



A Lambda Physik Model 200E KrF excimer laser was used as the photolysis light source. Kinetic data were obtained by time-resolved resonance fluorescence detection of O(³P). The laser pulse width was 20 ns while, under our experimental conditions, reactions 7 and 8 proceeded at rates of $(3-10) \times 10^5$ and $7 \times 10^7 \text{ s}^{-1}$, respectively. O(³P) decay rates were typically in the range 30–500 s⁻¹.

As in our previous study, the concentration of the excess reactant, HO₂, was not directly measured but was calculated based on experimentally measured and other known parameters. To obtain [HO₂], one must determine [OH]₀, the initial concentration of photolytically produced OH, and the yield of HO₂ from reaction 7 and competing side reactions. The chemistry of conversion of OH to HO₂ is discussed in detail in a later section. Since the concentrations of H₂O₂ and O₃ were such that the system was optically thin at 248.5 nm, [OH]₀ could be calculated from the following relationship

$$[\text{OH}]_0 = \Phi_{\text{OH}} \sigma(\text{H}_2\text{O}_2, 248.5 \text{ nm}, T) [\text{H}_2\text{O}_2] F \quad (I)$$

where Φ_{OH} is the quantum yield for OH production from 248.5-nm photolysis of H₂O₂, $\sigma(\text{H}_2\text{O}_2, 248.5 \text{ nm}, T)$ is the absorption cross section for H₂O₂ at 248.5 nm and temperature T , and F is the laser photon fluence. The determination of each factor in eq I is discussed in detail below.

Φ_{OH} : It is known⁹⁻¹¹ that $\Phi_{\text{OH}} \approx 2$.

$\sigma(\text{H}_2\text{O}_2, 248.5 \text{ nm}, T)$: The absorption cross section for H₂O₂ at 248.5 nm is known to be $8.8 \times 10^{-20} \text{ cm}^2$ at 298 K.⁸ We have recently measured temperature-dependent absorption cross sections for hydrogen peroxide over the wavelength range 193–350 nm.¹² At 248.5 nm, the following expression describes the observed temperature dependence (units are cm² molecule⁻¹):

$$\sigma(\text{H}_2\text{O}_2, 248.5 \text{ nm}, T) = 1.023 \times 10^{-19} \exp\{(-45 \pm 20)/T\} \quad (II)$$

[H₂O₂]: Hydrogen peroxide can be lost in the slow-flow system either by decomposition (particularly at higher temperatures) or by condensation (at lower temperatures). To ensure that the H₂O₂ concentration in the reactor was known, we monitored H₂O₂ by UV photometry before the gas mixture entered the reactor and after the gas mixture exited the reactor. The absorption cells were 216.2 and 90.0 cm in length. The monitoring wavelengths were 228.8 nm in the longer cell (Cd line) and 202.6 nm in the shorter cell (Zn⁺ line). Both cells were kept at ambient temperature, and the absorption cross sections needed to convert absorbance data to H₂O₂ concentration were obtained by interpolation from current NASA recommendations:⁸ $1.86 \times 10^{-19} \text{ cm}^2$ at 228.8 nm and $4.31 \times 10^{-19} \text{ cm}^2$ at 202.6 nm. When the reactor temperature was 350 K or below, the difference in H₂O₂ concentration measured in the two absorption cells was never more than a few percent. At 391 K, the highest temperature at which experiments were performed, 15–20% of the H₂O₂ was lost upon traversal of the reactor. The H₂O₂ concentration in the reaction zone was always taken to be the temperature-corrected average of the concentrations measured in the two absorption cells. Under our experimental conditions, absorption by ozone was negligible compared to absorption by H₂O₂ at 202.6 nm. At 228.8 nm, ozone made a small but significant contribution to the total absorbance. Care was taken to ensure that [O₃] was constant during the I and I_0 measurements required for the [H₂O₂] determination.

(5) Keyser, L. F. *J. Phys. Chem.* 1982, 86, 3439.

(6) Ravishankara, A. R.; Wine, P. H.; Nicovich, J. M. *J. Chem. Phys.* 1983, 78, 6629.

(7) Brune, Wm. H.; Schwab, J. J.; Anderson, J. G. *J. Phys. Chem.* 1983, 87, 4503.

(8) DeMore, W. B.; Margitan, J. J.; Molina, M. J.; Watson, R. T.; Golden, D. M.; Hampson, R. F.; Kurylo, M. J.; Howard, C. J.; Ravishankara, A. R. "Chemical Kinetics and Photochemical Data for Use in Stratospheric Modeling", Evaluation No. 7, JPL Publication 85-37, 1985.

(9) Volman, D. H. *Adv. Photochem.* 1963, 1, 43.

(10) Greiner, N. R. *J. Chem. Phys.* 1966, 45, 99.

(11) Vaghjani, G. L.; Ravishankara, A. R., private communication.

(12) Nicovich, J. M.; Wine, P. H., to be submitted for publication.

F: The photolysis laser beam was made spatially uniform through use of a segmented aperture optical integrator.^{6,13} Virtually the whole cross-sectional area of the cell was irradiated, and the depth of focus of the integrated beam was such that radical concentrations were nearly uniform down the entire length of the cell. The laser beam fluence was measured as the beam exited the reactor by using an EG&G photodiode based radiometer capable of measuring individual pulses. Pulse-to-pulse stability, a requirement for signal averaging in this type of experiment, was found to be very good. Only an occasional pulse energy deviated from the average by more than $\pm 5\%$. In order to avoid having to correct the measured fluence for reflection off the back window, an antireflection coated window with $>99.5\%$ transmission at 248.5 nm was employed. The radiometer was calibrated by using a novel ozone actinometry method which has been described in detail previously.⁶

As mentioned above, all experiments were carried out under slow-flow conditions. The linear flow velocity through the reactor was typically 12 cm s^{-1} , and the laser repetition rate was typically 0.4 Hz. The reactor was 23 cm in length, so the reactor volume was completely replenished with a fresh gas mixture between laser pulses. All experiments employed nitrogen as the buffer gas at a total pressure of 80 Torr. Data were obtained over the temperature range 266–391 K. The temperature range was limited at the low end by the vapor pressure of H_2O_2 and at the high end by the thermal instability of H_2O_2 .

The gases used in this study had the following stated minimum purities: N_2 , 99.999%; O_2 , 99.99%. Hydrogen peroxide was 90 wt % in water. It was concentrated further by bubbling N_2 through the sample for several days before experiments were undertaken and continuously during the course of the experiments. To prevent significant decomposition of H_2O_2 , all components traversed by H_2O_2 between the bubbler and the exit from the last absorption cell were Pyrex or Teflon with the exception of a few stainless steel fittings. The needle valve and flowmeter in the H_2O_2 line were positioned so that N_2 flowed through these components before entering the bubbler. Ozone was prepared by passing O_2 through a commercial ozonator and was stored on silica gel at 197 K. Before use it was degassed at 77 K to remove O_2 . Dilute O_3/N_2 mixtures were prepared in 12-L Pyrex bulbs for use in experiments.

A typical experiment was initiated by flowing $(3\text{--}10) \times 10^{12} \text{ O}_3 \text{ molecules cm}^{-3}$ in 80 Torr of N_2 through the reactor and absorption cells. I_0 and J_0 , the intensities of 228.8- and 202.6-nm light transmitted through the absorption cells, were measured. Next, H_2O_2 was introduced into the gas flow, the N_2 flow was reduced so the total flow rate and total pressure were the same after addition of H_2O_2 as before addition of H_2O_2 , and I and J , the reduced intensities of 228.8- and 202.6-nm light transmitted through the reactor, were measured. Using the measured values of I , I_0 , J , and J_0 , we calculated the concentration of H_2O_2 in the gas stream entering and exiting the reactor; it ranged from $(2\text{--}6) \times 10^{15} \text{ molecules cm}^{-3}$. I and J were continuously monitored during the course of an experiment. The multichannel analyzer was pretriggered before the photolysis laser fired to obtain the background count rate. The concentration of $\text{O}(^3\text{P})$ was monitored as a function of time after the photolysis pulse. A total of 50–200 laser shots were averaged to obtain one pseudo-first-order kinetic decay. The fluence of each laser pulse was measured by using the radiometer and a calibrated aperture. The laser fluence was varied at constant $[\text{O}_3]$ and $[\text{H}_2\text{O}_2]$ to obtain pseudo-first-order decays as a function of $[\text{HO}_2]$. Five to ten fluence values were employed to determine each bimolecular rate constant, k_1 , from the slope of a k' vs. $[\text{HO}_2]$ plot ($k' \equiv$ the $\text{O}(^3\text{P})$ pseudo-first-order decay rate). After the fluence variations were completed, the H_2O_2 flow was turned off, the total pressure and total flow rate were readjusted, and I_0 and J_0 were remeasured. All HO_2 concentrations employed in the k_1 determinations were in the range $(0.15\text{--}8.5) \times 10^{12} \text{ molecules cm}^{-3}$. It should be noted that, in a

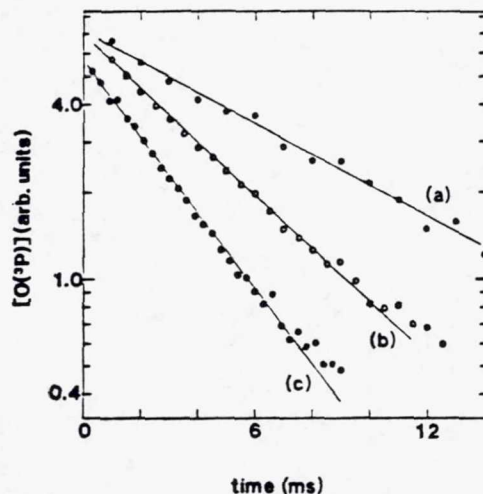


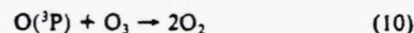
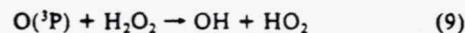
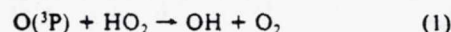
Figure 2. Typical $\text{O}(^3\text{P})$ temporal profiles observed following 248.5-nm pulsed laser photolysis of $\text{O}_3/\text{H}_2\text{O}_2/\text{N}_2$ mixtures. Experimental conditions: $T = 281 \text{ K}$, $P = 80 \text{ Torr}$, $[\text{H}_2\text{O}_2] = 3.9 \times 10^{15} \text{ molecules cm}^{-3}$, $[\text{O}_3] = 6 \times 10^{12} \text{ molecules cm}^{-3}$, laser fluence (in units of mJ cm^{-2}) = (a) 1.95, (b) 4.55, and (c) 6.31. Solid lines are obtained from least-squares analyses of the first two $1/e$ times of $\text{O}(^3\text{P})$ decay and give the following pseudo-first-order decay rates (k'_{exp}): (a) 111 s^{-1} , (b) 210 s^{-1} , (c) 303 s^{-1} .

series of runs involving variation of the laser fluence at constant $[\text{O}_3]$ and $[\text{H}_2\text{O}_2]$, the ratio $[\text{OH}]_0/[\text{O}(^3\text{P})]_0$ is not altered; to change this ratio, the composition of the reaction mixture must be varied.

Results and Discussion

In the absence of competing side reactions which affect the HO_2 concentration, the kinetic system is inherently pseudo-first-order; i.e., all HO_2 lost via reaction 1 is rapidly regenerated via reaction 7. However, as will be discussed in detail below, the importance of certain side reactions is suppressed when $[\text{HO}_2] \gg [\text{O}(^3\text{P})]$. Most of our experiments were carried out under experimental conditions where $[\text{HO}_2] \approx 10[\text{O}(^3\text{P})]_0$, although this ratio was varied as a check on the kinetic model used to extract k_1 . At low temperature, where relatively low H_2O_2 concentrations had to be employed, the HO_2 to $\text{O}(^3\text{P})$ ratio was typically somewhat lower than that employed at higher temperatures.

Photolytically produced $\text{O}(^3\text{P})$ can be lost via the following (pseudo) first-order processes:



$\text{O}(^3\text{P}) \rightarrow$ loss by diffusion from the detector field of view and reaction with background impurities (11)

Under our experimental conditions, reaction 1 dominated $\text{O}(^3\text{P})$ removal except at very low HO_2 levels. Reaction 10 was of negligible importance while reaction 9 was minor but not negligible.¹⁴ k_{11} was directly measured to be $\sim 5 \text{ s}^{-1}$ —1–2 orders of magnitude slower than $k_1[\text{HO}_2]$ under most experimental conditions.

In the absence of competing side reactions which affect the concentrations of $\text{O}(^3\text{P})$ or HO_2 , removal of $\text{O}(^3\text{P})$ should obey first-order kinetics

$$\ln \{ [\text{O}(^3\text{P})]_0 / [\text{O}(^3\text{P})] \} = (k_1[\text{HO}_2] + k_d)t \equiv k'_{\text{exp}}t \quad (\text{III})$$

where

$$k_d \equiv k_9[\text{H}_2\text{O}_2] + k_{10}[\text{O}_3] + k_{11} \quad (\text{IV})$$

(13) Ravishankara, A. R.; Eisele, F. L.; Krutner, N. M.; Wine, P. H. *J. Chem. Phys.* 1981, 74, 2267.

(14) Wine, P. H.; Nicovich, J. M.; Thompson, R. J.; Ravishankara, A. R. *J. Phys. Chem.* 1983, 87, 3948.

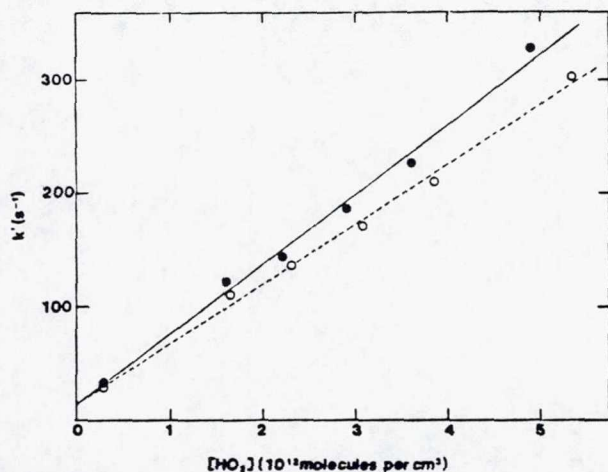


Figure 3. Typical plots of k'_{expt} vs. $[\text{OH}]_0$ (open circles) and k' vs. $[\text{HO}_2]_{\text{max}}$ (closed circles). Experimental conditions: $T = 281 \text{ K}$, $P = 80 \text{ Torr}$, $[\text{H}_2\text{O}_2] = 3.9 \times 10^{15} \text{ molecules cm}^{-3}$, $[\text{O}_3] = 6 \times 10^{12} \text{ molecules cm}^{-3}$. The dashed line is obtained from a linear least-squares analysis of the k'_{expt} vs. $[\text{OH}]_0$ data and gives the "uncorrected" rate coefficient $(5.24 \pm 0.38) \times 10^{-11} \text{ cm}^3 \text{ molecule}^{-1} \text{ s}^{-1}$. The solid line is obtained from a linear least-squares analysis of the k' vs. $[\text{HO}_2]_{\text{max}}$ data and gives the "corrected" rate coefficient $(6.15 \pm 0.54) \times 10^{-11} \text{ cm}^3 \text{ molecule}^{-1} \text{ s}^{-1}$.

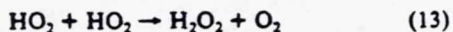
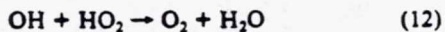
TABLE I: Reaction Set for Computer Simulations

reaction	rate coefficient ^{a,b}
$\text{O} + \text{HO}_2 \rightarrow \text{OH} + \text{O}_2$	$k_1 = 3 \times 10^{-11} \exp(200/T)$
$\text{O} + \text{OH} \rightarrow \text{H} + \text{O}_2$	$k_2 = 2.2 \times 10^{-11} \exp(117/T)$
$\text{H} + \text{O}_3 \rightarrow \text{OH} + \text{O}_2$	$k_4 = 1.4 \times 10^{-10} \exp(-470/T)$
$\text{OH} + \text{H}_2\text{O}_2 \rightarrow \text{HO}_2 + \text{H}_2\text{O}$	$k_7 = 3.1 \times 10^{-12} \exp(-187/T)$
$\text{O} + \text{H}_2\text{O}_2 \rightarrow \text{OH} + \text{HO}_2$	$k_9 = 1.4 \times 10^{-12} \exp(-2000/T)$
$\text{O} + \text{O}_3 \rightarrow 2\text{O}_2$	$k_{10} = 8 \times 10^{-12} \exp(-2060/T)$
$\text{O} \rightarrow \text{loss}$	$k_{11} = 5 \text{ s}^{-1}$
$\text{OH} + \text{HO}_2 \rightarrow \text{O}_2 + \text{H}_2\text{O}$	$k_{12} = 1.7 \times 10^{-11} \exp(416/T) + 3 \times 10^{-31} [\text{M}] \exp(500/T)$
$\text{HO}_2 + \text{HO}_2 \rightarrow \text{H}_2\text{O}_2 + \text{O}_2$	$k_{13} = 2.3 \times 10^{-13} \exp(590/T) + 1.7 \times 10^{-33} [\text{M}] \exp(1000/T)$
$\text{HO}_2 \rightarrow \text{loss}$	$k_{14} = 5 \text{ s}^{-1}$
$\text{HO}_2 + \text{O}_3 \rightarrow \text{OH} + 2\text{O}_2$	$k_{15} = 1.4 \times 10^{-14} \exp(-580/T)$
$\text{H} + \text{HO}_2 \rightarrow 2\text{OH}$	$k_{16} = 6.4 \times 10^{-11} \exp(0/T)$

^aAll rate coefficients are taken from ref 9 except k_{11} which was measured and k_{14} which was set equal to k_{11} . ^bAll rate coefficients except k_{11} and k_{14} are in units of $\text{cm}^3 \text{ molecule}^{-1} \text{ s}^{-1}$.

Figure 2 shows typical plots of $\ln [\text{O}^{(3P)}]$ vs. t . Equation III does indeed appear to be obeyed. If side reactions were unimportant, the bimolecular rate coefficient would be obtained from the slope of a k'_{expt} vs. $[\text{OH}]_0$ plot, such as shown in Figure 3.

Secondary Chemistry. In the paper describing our 298 K study of reaction 1, possible side reactions were considered in detail.⁶ It was concluded that two reactions could significantly affect the HO₂ temporal profile:



To quantify the roles of reactions 12 and 13 in our kinetics experiments, a series of computer simulations were carried out where the temporal profiles of key species were calculated under a variety of experimental conditions by numerical integration of the appropriate rate equations. For completeness, a number of reactions which were expected to play very minor roles in the O^(3P) and HO₂ kinetics were included in the mechanism. The complete sets of reactions and rate coefficients used in the simulations are given in Table I.

Reaction 12 competes with reaction 7 during the period immediately after the laser pulse when OH is being converted to HO₂. Each time reaction 12 occurs, two HO₂ radicals are lost which otherwise would have been present to react with O^(3P). Reaction 12 is most important at high laser fluence (i.e., high

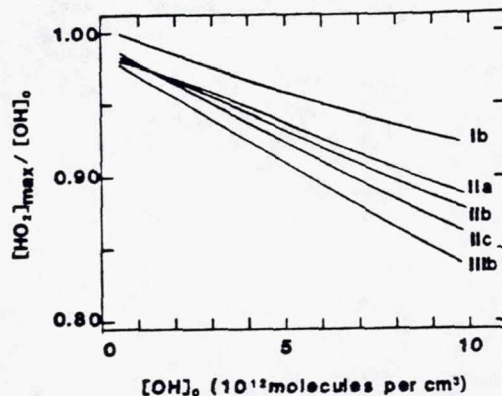


Figure 4. Typical correction curves (obtained from computer simulations) which relate $[\text{HO}_2]_{\text{max}}/[\text{OH}]_0$ to $[\text{OH}]_0$. All curves shown in the figure are from simulations with $[\text{H}_2\text{O}_2] = 4 \times 10^{15} \text{ molecules cm}^{-3}$. Temperature: I, 400 K; II, 300 K; III, 260 K. $[\text{OH}]_0/[\text{O}^{(3P)}]_0$: a, 10⁴; b, 10; c, 4.

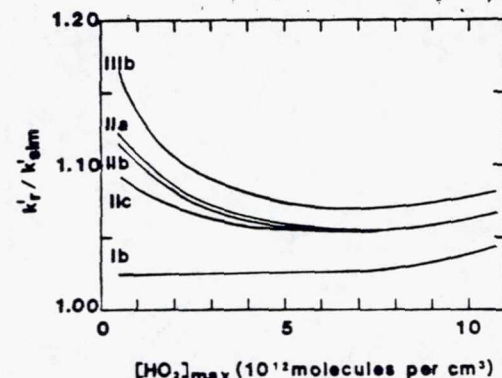


Figure 5. Typical correction curves (obtained from computer simulations) which relate k'_{expt} to k'_{eqm} via eq VI. All curves shown in the figure are from simulations with $[\text{H}_2\text{O}_2] = 4 \times 10^{15} \text{ molecules cm}^{-3}$. Temperature: I, 400 K; II, 300 K; III, 260 K. $[\text{OH}]_0/[\text{O}^{(3P)}]_0$: a, 10⁴; b, 10; c, 4.

$[\text{OH}]_0/[\text{H}_2\text{O}_2]$) and at low temperature. From the computer simulations, a set of curves were constructed which relate $[\text{HO}_2]_{\text{max}}$, the peak amount of HO₂ present after all photolytically produced OH has reacted away but before appreciable HO₂ loss via processes such as reaction 13 has occurred, to $[\text{OH}]_0$. Representative correction curves are plotted in Figure 4. For the 101 experiments used in the $k_1(T)$ determinations, the average value for $[\text{HO}_2]_{\text{max}}/[\text{OH}]_0$ was 0.947 while the minimum value under any set of experimental conditions was 0.845.

As pointed out above, loss of O^(3P) via reactions 1 and 9–11 occurs on a time scale which is long compared to the time scale for HO₂ formation. Hence, if the concentration of HO₂ were constant over the time period of O^(3P) removal, k_1 could be obtained from the slope of a k'_{expt} vs. $[\text{HO}_2]_{\text{max}}$ plot. Unfortunately, small but significant time variation of $[\text{HO}_2]$ can result from the occurrence of reactions 9, 13, and 14. Reactions 9 and

HO₂ → loss by diffusion from the reaction zone and reaction with background impurities (14)

14 are most important at low laser fluences, i.e., low $[\text{HO}_2]$. Reaction 9 is strongly temperature dependent and increases in importance at high temperature. Reaction 9 is also a more important source of HO₂ when $[\text{OH}]_0/[\text{O}^{(3P)}]_0$ is relatively low. Reaction 13 becomes an important HO₂ removal mechanism at relatively high HO₂ concentrations. To avoid large corrections for HO₂ loss via reaction 13, all experiments were carried out with $[\text{HO}_2]_{\text{max}} < 9 \times 10^{12} \text{ molecules cm}^{-3}$ and all data analyses were restricted to two 1/e times of O^(3P) decay; i.e., no data where $[\text{O}^{(3P)}]_0/[\text{O}^{(3P)}]_0 < 0.13$ were used in the data analysis. Computer simulations were carried out under a variety of experimental

TABLE II: Summary of Our O + HO₂ Kinetic Data

T, K	no. of expts ^a	[H ₂ O ₂], 10 ¹⁵ cm ⁻³	[OH] ₀ /[O] ₀	range of k', s ⁻¹	k ₁ , 10 ⁻¹¹ cm ³ molecule ⁻¹ s ⁻¹ , ± 2σ ^b	
					uncorrected ^c	corrected ^d
266	6	2.98	5.0	100-268	5.22 ± 0.51	7.00 ± 0.70
266	6	2.37	6.8	28-209	5.92 ± 0.39	7.14 ± 0.52
275	6	5.61	12	57-608	5.58 ± 0.54	6.60 ± 0.75
281	6	3.90	11	33-327	5.24 ± 0.38	6.15 ± 0.54
298	5	4.22	10	56-558	5.29 ± 0.65	6.30 ± 0.91
300	10	3.57	7.1-17	51-487	5.16 ± 0.30	6.16 ± 0.73
300	6	2.05	6.8	32-293	5.21 ± 0.73	6.34 ± 0.73
300	7	3.81	6.9	66-358	4.81 ± 0.52	5.69 ± 0.56
318	6	5.46	13	73-547	5.48 ± 0.13	6.28 ± 0.09
328	8	3.07	8.0	66-326	5.44 ± 0.24	6.24 ± 0.28
354	6	3.90	16	55-418	5.14 ± 0.45	5.86 ± 0.54
359	5	4.63	15	92-368	4.52 ± 0.69	5.11 ± 0.70
374	8	4.62	15	75-361	4.40 ± 0.40	4.87 ± 0.43
380	7	4.71	19	72-466	5.11 ± 0.39	5.63 ± 0.40
391	9	4.94	11	111-438	4.87 ± 0.32	5.28 ± 0.38

^a Experiment = determination of one pseudo-first-order rate coefficient. ^b Errors represent precision only. ^c Obtained from the slopes of k' vs. [OH]₀ plots. ^d Obtained from the slopes of k' vs. [HO₂]_{max} plots.

TABLE III: Comparison of Our Results with Those of Other Investigators

range of T, K	range of P, Torr	M	exptl method ^a	exptl conditions	A ^b	E/R, K	k ₁ (298 K) ^b	ref
298	1.0	He	DF-LMR	relative to k ₂			2.7 ± 1.0 ^c	1
				relative to k ₇			6.3 ± 2.0 ^c	
298	0.8-2.3	He	DF-LMR/ESR	[O(³ P)] ≫ [HO ₂]			3.7 ± 1.1	2
	2.8-3.4			[HO ₂] ≫ [O(³ P)]			4.2 ± 1.5	
	3.7-5.5			relative to k ₂			3.0 ± 0.9 ^c	
298	1200	Ar/H ₂ /O ₂	PR-UVA	k ₁ extracted by modeling complex chemistry			7 ± 2	3
296 ± 2	2.5	He	DF-RF/LIF	[HO ₂] ≫ [O(³ P)]			5.4 ± 0.9	4
229-372	1.0	He	DF-RF	[HO ₂] ≫ [O(³ P)]	3.1 ± 0.3	200 ± 28	6.1 ± 0.4	5
298	10-500	N ₂	PLP-RF	[HO ₂] ≫ [O(³ P)]			6.1 ± 1.1 ^d	6
300	1.0-4.0	He	DF-LMR/RF/RA	[O(³ P)] ≫ [HO ₂]			5.2 ± 0.8	7
				[HO ₂] ≫ [O(³ P)]				
266-391	80	N ₂	PLP-RF	[HO ₂] ≫ [O(³ P)]	2.9 ± 0.7	228 ± 75	6.2 ± 1.0	this work

^a DF, discharge flow; LMR, laser magnetic resonance; ESR, electron spin resonance; PR, pulsed radiolysis; UVA, ultraviolet absorption; RF, resonance fluorescence; LIF, laser-induced fluorescence; PLP, pulsed laser photolysis; RA, resonance absorption. ^b Units are 10⁻¹¹ cm³ molecule⁻¹ s⁻¹. ^c k₁ recalculated with presently recommended (ref 9) values for the reference reactions. ^d Corrected downward from reported value by 1.5% to account for small change in recommended H₂O₂ absorption cross section.

conditions. The first two 1/e times of the slightly nonexponential computer generated O(³P) temporal profiles were least squares fit to an exponential decay to obtain k'_{sim}, the simulated decay rate. The simulated decay rates were then compared to the "real" decay rates, k'_r, to obtain a set of correction curves, some of which

$$k'_r = k_1[\text{HO}_2]_{\text{max}} + k_9[\text{H}_2\text{O}_2] + k_{10}[\text{O}_3] + k_{11} \quad (\text{V})$$

are shown in Figure 5. The first two 1/e times of each experimental O(³P) temporal profile were least squares fit to eq III to obtain k'_{exptl}. A corrected value of k' was then computed from the expression

$$k' = k'_{\text{exptl}}(k'_r/k'_{\text{sim}}) \quad (\text{VI})$$

One source of uncertainty in the computer simulations concerns the fact that k₁₄ was not measured; it was estimated that k₁₄ = k₁₁ ≈ 5 s⁻¹. Lack of knowledge of the exact value of k₁₄ increases the uncertainty in the k'_r/k'_{sim} factors at low concentrations of HO₂. The low [HO₂] data are relatively unimportant in defining k₁, so the uncertainty in k₁₄ makes only a minor contribution to the overall uncertainty in k₁. For the 101 experiments used in the k₁(T) determinations, the average value of k'_r/k'_{sim} was 1.06 and the maximum value under any set of experimental conditions was 1.18.

As discussed above, k₁ values corrected for secondary chemistry were obtained from the slopes of plots of k' vs. [HO₂]_{max}. Typical data are shown in Figure 3. For all 15 rate coefficients measured, the corrected k₁ values were larger than the values which would have been obtained from plots of k' vs. [OH]₀ (see Figure 3, for example). The magnitude of the secondary chemistry corrections was largest at the lowest temperatures. For the 15 rate coefficients reported, the average difference between the corrected

and uncorrected bimolecular rate coefficients was 16% while the largest difference was 26%.

Summary of Results. The experimental results are summarized in Table II. Errors quoted for individual "corrected" k₁ determinations are 2σ and refer only to the precision of the k' vs. [HO₂]_{max} data. The absolute accuracy of our k₁ determinations is limited not only by precision but also by uncertainties in measurement of the laser photon fluences (F), the H₂O₂ concentration, the correction factor used to obtain [HO₂]_{max} from [OH]₀, the correction factor used to obtain k' from k'_{exptl} (i.e., k'_r/k'_{sim}), and unidentified systematic errors. We estimate the pertinent 2σ uncertainties to be as follows: F, 10%; [H₂O], 5%; [HO₂]_{max}/[OH]₀, 5%; k'_r/k'_{sim}, 10% at 266 K and 5% at 298 K and above; unidentified systematic errors, 5%. Precision did not appear to be temperature dependent and averaged 9%. Hence, the absolute accuracy of an individual k₁ determination is estimated to be ±23% at 266 K and ±21% at 298 K and above.

An Arrhenius plot of our results is shown in Figure 6. An unweighted linear least-squares analysis of the ln k₁ vs. 1/T data gives the following expression (units are cm³ molecule⁻¹ s⁻¹):

$$k_1(T) = (2.91 \pm 0.70) \times 10^{-11} \exp((228 \pm 75)/T) \quad (\text{VII})$$

The uncertainties quoted in the above expression are 2σ and represent precision only.

Comparison with Previous Work. Our results are compared with those reported by other investigators in Table III. The 298 K value reported in this paper is identical with our previously reported value⁶ and at the upper end of the group of recent direct determinations⁴⁻⁷ which span the range (5.2-6.2) × 10⁻¹¹ cm³ molecule⁻¹ s⁻¹. Other than our studies, the other recent direct measurements all employed low-pressure discharge flow systems.

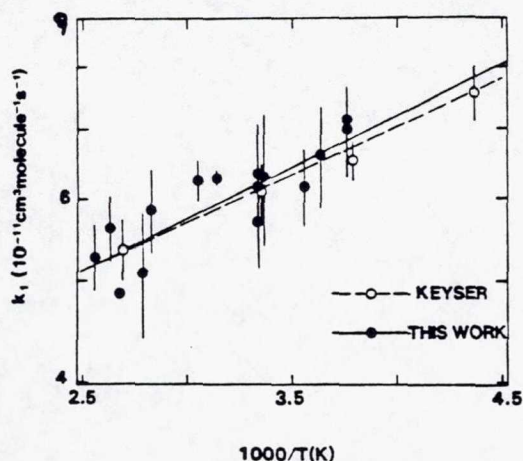


Figure 6. Arrhenius plot for the O + HO₂ reaction.

all measured not only O(³P) but also HO₂ (either directly or indirectly by conversion to OH), and all carefully considered the role of competing side reactions. Hence, there is no obvious reason to prefer one value over another. The early work of Burrows et al.¹ and Hack et al.² give $k_1(298\text{ K})$ values which are considerably lower than those reported in ref 4–7. Possible reasons for the apparently erroneous results reported in ref 1 and 2 are discussed elsewhere.⁵ Lii et al.³ obtained a value for k_1 by comparing computer simulations with HO₂ and O₃ concentration profiles observed following pulsed radiolysis of O₂-H₂-Ar mixtures. Their reported rate coefficient agrees well with our results. However, as pointed out by Keyser,⁵ the experimental data of Lii et al. are very insensitive to the value of k_1 ; hence, their error limits should be ~500% rather than the reported 30%.

Very little temperature-dependent data are available for reaction 1. Values for k_1 of $8 \times 10^{-11}\text{ cm}^3\text{ molecule}^{-1}\text{ s}^{-1}$ at 1600 K¹⁵ and $6 \times 10^{-11}\text{ cm}^3\text{ molecule}^{-1}\text{ s}^{-1}$ at 1050 K¹⁶ have been inferred from flame studies. The only previous temperature dependence study in the atmospheric temperature regime is that of Keyser.⁵ As seen from the comparisons in Table III and Figure 6, our results are in excellent agreement with those of Keyser. Since our experiments were very different in methodology from Keyser's and are subject to different sources of systematic errors, the uncertainty of $k_1(T)$ for atmospheric modeling purposes is now greatly reduced. Keyser's study employed helium buffer gas at a pressure of 1.0 Torr while our study employed nitrogen buffer gas at a pressure of 80 Torr. Thus, agreement between the two studies strongly suggests that k_1 is independent of pressure over the relevant upper atmospheric temperature and pressure ranges.

Reaction 1 could proceed via a hydrogen abstraction mechanism (1a) or via formation of an energized HOOO "pseudo-intermediate" (1b):



Sridharan et al.¹⁷ recently reported an elegant experiment in which ¹⁶OH and ¹⁸OH products from the reaction of ¹⁸O with HO₂ were monitored in a discharge flow system. They found that only ¹⁶OH was produced, implying that O reacts with HO₂ via channel 1b. Thermochemical estimates suggest that HOOO is bound relative to O + HO₂ but is ~12 kcal mol⁻¹ less stable than the OH + O₂ products.^{18,19} Mozurkewich²⁰ points out that since HOOO is bound relative to O + HO₂, we might expect to find a long-range interaction that would produce a transition state for reaction 1 very similar to that expected for formation of HOOO. Mozurkewich's RRKM calculations yield a rate constant for formation of HOOO of $5.5 \times 10^{-11}\text{ cm}^3\text{ molecule}^{-1}\text{ s}^{-1}$, independent of temperature.²⁰ The observed negative activation energy for reaction 1 could probably be reproduced if a small barrier were assumed in the HOOO → OH + O₂ reaction path.²¹

Implications for Atmospheric Chemistry. Model calculations of OH and HO₂ concentration profiles in the upper stratosphere are very sensitive to the choice of $k_1(T)$. Kaye and Jackman,²² considering both sensitivity of their model to various parameters and uncertainties in these parameters, have concluded that the uncertainty of k_1 contributes more to the uncertainty in [OH] and [HO₂] at 35° N, 40-km altitude than any parameter in their model except k_{12} . The currently recommended value⁸ for $k_1(T)$ is

$$k_1(T) = 3.0 \times 10^{-11} \exp[(200 \pm 200)/T] \text{ cm}^3 \text{ molecule}^{-1} \text{ s}^{-1} \quad (\text{VIII})$$

The results reported in this paper will have little effect on the recommended A factor and activation energy but will substantially reduce the uncertainty in the above expression; this will, in turn, significantly reduce the overall uncertainty in model calculations of upper stratospheric OH and HO₂ concentrations and facilitate meaningful comparisons of stratospheric measurements with photochemical models.

Jackman et al.²³ have recently compared O₃ concentrations at 5° N and 43-km altitude measured by LIMS (limb infrared monitor of the stratosphere) with those calculated from a photochemical model using LIMS measurements of H₂O, HNO₃, and NO₂ and temperature and SAMS (stratospheric and mesospheric sounder) measurements of CH₄ as input. The model predicted lower O₃ levels than those actually observed. A sensitivity analysis showed that the overall uncertainty in the model calculation was a factor of 1.7, about the same magnitude as the discrepancy between model and measurement. Of the many parameters used in the model, the uncertainty of k_1 was found to make the sixth largest contribution to the overall uncertainty of the calculation. Our results will therefore result in a small but significant reduction in the model uncertainty.

Acknowledgment. This work was supported by the National Aeronautics and Space Administration through Subcontract 954814 from the Jet Propulsion Laboratory and Grant NAGW 1001.

(17) Sridharan, U. C.; Klein, F. S.; Kaufman, F. *J. Chem. Phys.* **1985**, *82*, 592.

(18) Nangia, P. S.; Benson, S. W. *J. Phys. Chem.* **1979**, *83*, 1138.

(19) Benson, S. W. *Oxid. Commun.* **1982**, *2*, 169.

(20) Mozurkewich, M. *J. Phys. Chem.* **1986**, *90*, 2216.

(21) Mozurkewich, M.; Benson, S. W. *J. Phys. Chem.* **1984**, *88*, 6429.

(22) Kaye, J. A.; Jackman, C. H. *J. Geophys. Res.* **1986**, *91*, 1117.

(23) Jackman, C. H.; Stolarski, R. S.; Kaye, J. A. *J. Geophys. Res.* **1986**, *91*, 1103.

(15) Peeters, J.; Mahnen, G. *Symp. (Int.) Combust., [Proc.]* **1972**, *14*, 133.

(16) Day, M. J.; Thompson, K.; Dixon-Lewis, G. *Symp. (Int.) Combust., [Proc.]* **1972**, *14*, 47.